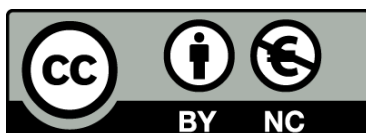




UNIVERSITAT_{DE}
BARCELONA

Stable and efficient photoelectrodes for solar fuels production

Carles Ros Figueras



Aquesta tesi doctoral està subjecta a la llicència **Reconeixement- NoComercial 4.0. Espanya de Creative Commons**.

Esta tesis doctoral está sujeta a la licencia **Reconocimiento - NoComercial 4.0. España de Creative Commons**.

This doctoral thesis is licensed under the **Creative Commons Attribution-NonCommercial 4.0. Spain License**.



UNIVERSITAT DE
BARCELONA

FACULTAT DE FÍSICA



Shaping Energy for a Sustainable Future

GRUP D'EMMAGATZEMATGE
D'ENERGIA I SISTEMES AUTÒNOMS

PROGRAMA DE DOCTORAT EN NANOCIÈNCIES

STABLE AND EFFICIENT PHOTOELECTRODES FOR SOLAR FUELS PRODUCTION

Memòria presentada per optar al títol de doctor per la
Universitat de Barcelona

Autor: CARLES ROS FIGUERAS
Directors: JUAN RAMON MORANTE LLEONART
i TERESA ANDREU ARBELLA
Tutor: JUAN RAMON MORANTE LLEONART

Juny 2019

*"Instruiu-vos, perquè necessitem tota la nostra intel·ligència.
Emocioneu-vos, perquè necessitem tot el nostre entusiasme.
I organitzeu-vos, perquè necessitem tota la nostra força".
Antonio Gramsci*

Molins de Rei, 4 de juliol de 2019

Index

Index

Acknowledgements	1
List of acronyms and abbreviations	5
Preface	9
List of publications included in this thesis	13
Summary of results	15
Authors' contribution to the publications included in this thesis	19
Resum de la tesi (en Català)	23
Chapter 1 General introduction: Broader context and objectives	27
1.1 Photoelectrochemical water splitting: introduction	29
1.2 Fundamental concepts	31
1.3 Metal oxide photoelectrodes and enhancement strategies	37
1.4 Short band gap semiconductors for PEC water splitting	45
1.5 Protective Layers to implement photovoltaic photoabsorbers into water splitting ...	49
1.6 Hetero junctions with the protective layer	69
1.7 Buried homojunctions to maximize efficiency and cell flexibility	76
1.8 Cell implementation strategies and reactors	81
1.9 Resume, perspective and challenges	86
1.10 Scope of this research	91
Chapter 2: Enhancing metal oxide photoelectrodes performance	117
2.1 Hydrogenation and structuration of TiO ₂ nanorod photoanodes: doping level and the effect of illumination in trap-States filling	121
Chapter 3: Titanium dioxide as conductive and protective layer for silicon-based photocathodes	141
3.1 Charge transfer characterization of ALD-grown TiO ₂ protective layers in silicon photocathodes	147

Chapter 4: Adapting protective layers for thin film chalcogenide photoabsorbers ...	161
4.1 Conformal chalcopyrite based photocathode for solar refinery applications	169
4.2 Turning earth abundant kesterite-based solar cells into efficient protected water-splitting photocathodes	177
Chapter 5: Conductivity and endurance of protective layers in alkaline anodic conditions.	187
5.1 Insight into the degradation mechanisms of atomic layer deposited TiO ₂ as photoanode protective layer	195
5.2 About degradation and regeneration mechanisms of NiO protective layers deposited by ALD on photoanodes	227
Conclusions and future work	249
Annex	257
A.1 Enhanced photoelectrochemical water splitting of hematite multilayer nanowire photoanodes by tuning the surface state via bottom-up interfacial engineering.....	265
A.2 Role of Bismuth in the Electrokinetics of Silicon Photocathodes for Solar Rechargeable Vanadium Redox Flow Batteries	315
A.3 Substrate-electrode (SE) interface illuminated photoelectrodes and photoelectrochemical cells	327

Acknowledgements

When I start writing these lines one of the biggest concerns, as always, is to forget mentioning someone important on this journey. A PhD thesis is a long, exhausting and fulfilling path luckily not walked alone: friends and foes, companions and adversaries, all of them have helped me in growing as a scientist but also as a person during this period and I sincerely wanted to thank them all.

The first ones are my supervisors, to give me the opportunity to perform the PhD with them. Dra. Teresa Andreu and Prof. Juan Ramon Morante offered me the possibility to perform the PhD as a full-time job in IREC and put all the necessary resources at hand for my investigations. Also to Dr. Cristian Fábrega, to introduce me to IREC with the master thesis. They have shown me the highly interdisciplinary field of photoelectrochemistry, where intense collaboration between the chemists and physicists communities is not just welcome, but necessary, greatly opening my mind and possibilities. I hope to have contributed with my perspective in this collaborative knowledge gathering in the (not so young any more) Energy Storage and Energy Harvesting group at IREC. I would like to thank all the actual and former members of the group too for all the group meetings, congresses, discussions (scientific, or not), coffee breaks, barbecues, calçotades, room escape's, and beers. The truth is that a PhD without that part would not be the same!

To Dra. Esther Alarcon and Prof. Albert Polman, to accept me for an international internship in the AMOLF FOM institute in Amsterdam. New knowledge, new perspectives and new friends is not enough to resume all what I learned about science and about myself during that period in the 3D Photovoltaics group. Many regards to all those companions I left there and hope to keep meeting.

To my parents and family, always there to support, listen and encourage me to keep on. It is obvious but not less to mention that I would not had gone this far without your efforts and support during these 29 years. Especially to my mom, not everyone is so lucky to have someone who knows what a PhD means at home to guide you.

To all the people I have met during this time the local government, in Molins de Rei's town council and in the E.I. movement. The opportunity this has given me to widen my perspective and to dream and work for a different framework of human, socioeconomic and ecological relationships is invaluable, just comparable to the effort required and I have gladly dedicated.

And to all my friends, the life-long ones, the new ones, those with whom we've shared our intimacy, the ones from the physics faculty, the ones from the student unions, from the party and the movement, and to the ones from none of these or from several. What I value the most is having met you all, learned and shared with you, the debates, the adventures and unbelievable experiences. What I regret the most is not having dedicated enough time to take care of our relationships, or dedicating to you those late hours of the day when I came back completely burn-out. I promise I will try to change it.

List of acronyms and abbreviations

ALD	atomic layer deposition
AFM	atomic force microscopy
AZO	aluminum doped zinc oxide
c-AFC	conductivity-atomic force microscopy
CBD	chemical bath deposition
CIGS	$\text{Cu}(\text{In}_{1-x}\text{Ga}_x)\text{Se}_2$
CIS	CuInSe_2
CV	cyclic voltammogram
CVD	chemical vapor deposition
CZTS	$\text{Cu}_2\text{ZnSnS}_4$
CZTSe	$\text{Cu}_2\text{ZnSnSe}_4$
CZTSSe	$\text{Cu}_2\text{ZnSn}(\text{S}_x\text{Se}_{1-x})_4$
e^-	electron
EC	electrochemical
EDX	energy dispersive X-ray spectroscopy
EELS	electron energy loss spectroscopy
EIS	electrochemical impedance spectroscopy
E_C	conduction band energy
E_F	Fermi level energy
E_g	band gap energy
E_V	valence band energy
FF	fill factor
FTO	fluorine doped tin oxide
FWHM	full width at half maximum
h^+	hole
HC-STH	half-cell solar to hydrogen conversion efficiency

HER	hydrogen evolution reaction
HRTEM	high-resolution transmission electron microscopy
IPCE	incident photon-to-current efficiency
ITO	indium tin oxide ($\text{In}_2\text{O}_3:\text{SnO}_2$)
j_{ph}	photocurrent density
MIS	metal-insulator-semiconductor
OER	oxygen evolution reaction
PEC	photoelectrochemical
PV	photovoltaic
RHE	reversible hydrogen electrode potential
SCLJ	semiconductor-liquid junction
SEM	scanning electron microscopy
SHE	standard hydrogen electrode potential
SIS	semiconductor-insulator-semiconductor
STH	solar to hydrogen conversion efficiency
TCO	transparent conducting oxide
UV	ultraviolet
V_{oc}	open circuit voltage
V_{ph}	photovoltage
XPS	X-ray photoelectron spectroscopy
XRD	X-ray diffraction

Preface

*Publications and summary of the
thesis*

The work included in this PhD thesis covers part of the research developed between 2014 and 2019 by the PhD candidate Carles Ros Figueras at the Catalonia Institute for Energy Research – IREC, in Sant Adrià del Besòs, Barcelona. The research has been performed under the framework of the Nanoscience PhD program from University of Barcelona (UB), and supported by an FPI grant (BES-2015-071618) from the Spanish Ministry of Economy and Competitivity on the project TNT-FUELS (MAT2014-59961-C2-1-R), the WINCOST project (ENE2016-80788-C5-5-R) and the LUXHOR industrial project.

The research has been focused on development of stable and efficient photoelectrodes for solar fuels production, specifically on efficiency enhancement of metal oxide photoelectrodes and stabilization of efficient short band gap photoabsorbers by protective layers. This dissertation covers all the aspects from synthesis optimization and characterization to long-term degradation analysis.

This thesis includes a general introduction as Chapter 1, where the topic is presented and the objectives formulated. The introduction has been written so to be published shortly in a peer-reviewed journal as a review article. The core of the dissertation, Chapters 2 to 5, is based on four published articles and two submitted works in peer-reviewed journals where the PhD candidate is first author, in agreement with the requirements of the Nanoscience doctoral program of the University of Barcelona for a thesis presented as a compilation of publications. A final chapter contains the main conclusions and future work. In the annex, two additional works performed in the topic of the thesis in collaboration with other authors are included, with specific contributions of the PhD candidate. A patent developed during the thesis is also included in the annex.

List of publications included in this thesis

1. Carles Ros, Cristian Fàbrega, Damián Monllor-Satoca, María Dolores Hernández-Alonso, Germán Penelas-Pérez, Juan Ramón Morante, Teresa Andreu. Hydrogenation and Structuration of TiO₂ Nanorod Photoanodes: Doping Level and the Effect of Illumination in Trap-States Filling. *J. Phys. Chem. C* 2018, 122, 3295–3304. <https://doi.org/10.1021/acs.jpcc.7b12468>
2. Carles Ros, Teresa Andreu, María Dolores Hernández-Alonso, Germán Penelas-Pérez, Jordi Arbiol, Juan Ramón Morante. Charge transfer characterization of ALD-grown TiO₂ protective layers in silicon photocathodes. *ACS Appl. Mater. Interfaces* 2017, 9, 17932–17941. <https://doi.org/10.1021/acsami.7b02996>
3. Carles Ros, Teresa Andreu, Sergio Giraldo, Yudania Sánchez, Juan Ramón Morante. Conformal chalcopyrite based photocathode for solar refinery applications. *Solar Energy Materials & Solar Cells*, 158 (2016) 184–188. <https://doi.org/10.1016/j.solmat.2016.01.031>
4. Carles Ros, Teresa Andreu, Sergio Giraldo, Victor Izquierdo-Roca, Edgardo Saucedo, Juan Ramón Morante. Turning Earth Abundant Kesterite-Based Solar Cells Into Efficient Protected Water-Splitting Photocathodes. *ACS Appl. Mater. Interfaces* 2018, 10, 13425–13433. <https://doi.org/10.1021/acsami.8b00062>
5. PengYi Tang, HaiBing Xi, Carles Ros, LiJuan Han, Martí Biset-Peiró, YongMin He, Wesley Kramer, Alejandro Pérez Rodríguez, Edgardo Saucedo, José Ramón Galán-Mascarós, Teresa Andreu, Juan Ramón Morante, Jordi Arbiol. Enhanced Photoelectrochemical Water Splitting of Hematite Multilayer Nanowires Photoanode with Tuning Surface State via Bottom-up Interfacial Engineering. *Energy Environ. Sci.*, 2017, 10, 2124. <https://doi.org/10.1039/C7EE01475A>
6. Cristina Flox, Sebastián Murcia-López, Nina M Carretero, Carles Ros, Juan Ramón Morante, Teresa Andreu. Role of bismuth in the electro-kinetics of silicon photocathodes for solar rechargeable vanadium redox flow batteries. *ChemSusChem* 2018, 11, 125–129. <https://doi.org/10.1002/cssc.201701879>

List of publications submitted in peer-reviewed journals

1. Carles Ros, Nina M. Carretero, Jeremy David, Jordi Arbiol, Teresa Andreu, Juan Ramón Morante. Insight into the degradation mechanisms of Atomic Layer Deposited

TiO₂ as photoanode protective layer. Submitted to *ACS Appl. Mater. Interfaces*. *Under revision*.

2. Carles Ros, Teresa Andreu, Jeremy David, Jordi Arbiol, Juan Ramón Morante. About degradation and regeneration mechanisms of NiO protective layers deposited by ALD on photoanodes. *Under submission*.

List of patents

1. SUBSTRATE-ELECTRODE (SE) INTERFACE ILLUMINATED PHOTOELECTRODES AND PHOTOELECTROCHEMICAL CELLS. Application Number EP15382658.1. Holder: Repsol, S.A. G. Penelas Pérez, M.D. Hernández Alonso, T. Andreu, J. R. Morante, C. Ros, N.M. Carretero, E. Calle, P. Ortega, R. Alcubilla. Date of filling: 23-12-2015. International patent: WO/2017/109108. International publication date: 29-6-2017.

Summary of results

The excessive consumption of non-renewable energy sources such as fossil fuels has led the world to a global climate change, urging for new energy consumption habits together with developing cost-effective alternative renewable technologies. Photoelectrochemical (PEC) water splitting allows for direct conversion of solar light and water into hydrogen and oxygen, storing energy into chemical bonds, solving the storage problem of photovoltaic technology.

PEC water splitting has demonstrated to produce pure hydrogen and oxygen in significant efficiencies, although this technology is not ready for market implementation due to lack of efficient, stable and scalable photoelectrodes. In this work, we undertake a journey from improving the efficiency of stable metal-oxide-based photoanodes to stabilizing efficient photovoltaic materials by the introduction of protective, transparent, conductive and catalytic layers. Efforts have focused on using cost-effective and scalable materials and techniques.

The thesis is structured in five chapters, starting from Chapter 1, Introduction. In this chapter, the topic is first presented to the reader together with an extensive review of the research on photoelectrochemical water splitting up to this thesis, and the main objectives of this thesis research are defined. Firstly, the global energy paradigm is analyzed and the possibilities of PEC technology in facing energy storage challenges, together with some fundamental concepts of semiconductor physics and electrochemistry. The most significant strategies followed during decades to enhance metal oxide photoelectrodes are reviewed, including optimal material selection, band gap tuning, nanoscale structuration, electronic modifications and catalyst and overlayers introduction. The efficiency limitations of metal oxide photoelectrodes are discussed, and the need to study semiconductor materials used by the photovoltaic industry is introduced, together with the corrosion problems of many short band gap materials in acidic or alkaline electrolytes. Thin film protective overlayers are capable to avoid the electrolyte from contacting the semiconductor photoabsorber, but several parameters must be adjusted like transparency, conductivity and stability to enable efficient and durable devices. Highlighted materials and deposition techniques used so far to protect short band gap semiconductors are presented. Finally, tandem-cell and reactor possible configurations are discussed.

The Chapter 2 is focused on metal oxide based photoanodes efficiency enhancement by synthesis and post-treatments optimization. Metal oxide candidate TiO_2 is reported stable in alkaline electrolytes and at anodic potentials, but they present low photon to current conversion efficiencies. This is due to excessively large band gap, absorbing small part of the visible spectra, and small electron and hole mobility. Its efficiency is increased both by microstructuring the substrate and nanostructuring the thin film into nanorods, and by modifying the electronic structure with a reductive H_2 treatment, enhancing potential drop inside the nanorods. This chapter includes the publication “Hydrogenation and Structuration

of TiO₂ Nanorod Photoanodes: Doping Level and the Effect of Illumination in Trap-States Filling”.

In Chapter 3 the strategy is shifted into stabilizing highly efficient short band gap semiconductor materials used by the photovoltaic industry. Silicon based photocathodes are protected by TiO₂ overlayers grown by atomic layer deposition (ALD). The deposition parameters are optimized and temperature is found to play a key role for both efficient film conductivity and stability, being this caused by polycrystalline films formation if sufficient thermal energy is available for crystalline reorganization. ALD enabled high thickness control and pinhole-free layers, together with lower crystallization temperatures (starting at less than 200 °C) than other techniques. The TiO₂-Si interface is studied by high resolution transmission electron microscope (HRTEM) imaging and thin 5 nm Ti interlayer is found to suppress detrimental native SiO₂ formation and enhance TiO₂ nucleation, both beneficial for efficient charge transport from n⁺-Si to TiO₂. This chapter includes the publication “Charge transfer characterization of ALD-grown TiO₂ protective layers in silicon photocathodes”.

Chapter 4 is devoted to implementing thin film chalcogenide solar cells into PEC water splitting. Copper-indium-gallium-selenide (CIGS) solar cells fabricated on flexible stainless steel substrates are protected from corrosion by TiO₂ ALD protective layers. The transparent conductive oxide (TCO) already used in solar cells is found necessary for efficient p-n junction formation and charge transport to the hydrogen evolution reaction. Copper-zinc-tin-sulfide/selenide (CZTS/Se) solar cells, where scarce indium and gallium are substituted by tin and zinc, are implemented for PEC devices with TiO₂ overlayers too. Modifying the S/Se ratio, band gap can be tuned, an especially interesting characteristic for designing tandem PEC devices. The maximum deposition temperature is found at 200 °C, due to affecting the optimized crystallographic imperfection distribution of original cells, particularly affecting the pure sulfide one. Thanks to the possibility to fabricate both solar cells and PEC electrodes based on the same structure, the TiO₂ overlayers and catalyst contributions to electrical and electrochemical charge transfer can be measured, and a series circuit model is presented. This chapter includes the publications “Conformal chalcopyrite based photocathode for solar refinery applications” and “Turning earth abundant kesterite-based solar cells into efficient protected water-splitting photocathodes”.

In Chapter 5, the last one of this thesis, the performance of ALD deposited protective layers is studied in anodic polarizations and alkaline electrolytes. Silicon is used as reference photoabsorber thanks to being unaffected by the used deposition temperatures, 100-300 °C both for TiO₂ and NiO films. In the first work, silicon photoanodes are protected by 100 nm TiO₂ films and 5 nm NiFe is used as catalyst. By varying the deposition temperature of TiO₂, completely amorphous, mixed amorphous and crystalline and fully crystalline films are deposited, and a clear conductivity increase is observed correlated to crystallization. By conductivity atomic force microscopy (c-AFM) preferential conductivity paths are observed

inside crystalline grains, proposed to be related to crystalline defects and grain boundaries. Few hundred hours stability tests revealed significant photocurrent decrease, with no observed dissolution of the Si photoabsorber by scanning electron microscope (SEM). Electrochemical impedance spectroscopy (EIS) revealed an increase of the capacity corresponding to TiO₂ depletion increase. This is attributed to oxidative potentials and electrolyte hydroxides diminishing the n-type semiconductor behavior of TiO₂ and forming a barrier to charge injection into the oxygen evolution reaction. UV superimposed illumination partially recovered conductivity, a persistent photoconductivity effect which could be used to improve photoanodes stability. In the second work included in this chapter, NiO films are ALD-deposited on Si photoanodes. The temperature deposition is studied and conductivity is found to decrease when temperature is increased from 100 to 300 °C, simultaneous to a change in preferential crystal growth direction. Both effects are attributed to a higher stoichiometric film being formed when increasing temperature, decreasing Ni²⁺ vacancies, responsible of the p-type semiconductor behavior. 100 °C deposited films permitted impressive over 1000 hours stability measurements in highly alkaline electrolyte and at anodic potentials. Periodic cyclic voltammetries are found necessary to avoid partial deactivation of the photoanodes, attributed to chemical modifications at the surface in such highly oxidative conditions. This chapter includes two works just submitted in peer-reviewed journals at the moment of finishing this thesis, “Insight into the degradation mechanisms of Atomic Layer Deposited TiO₂ as photoanode protective layer” and “About degradation and regeneration mechanisms of NiO protective layers deposited by ALD on photoanodes”.

The last chapter of this thesis includes the conclusions of the research. In the annex, two other works published in collaboration and a patent are included, which are considered better suited outside the main part of the thesis, since they are the result of collaborative work coming from the knowledge gained through the development of the PhD work.

Authors' contribution to the publications included in this thesis

Chapter 2

1. Carles Ros, Cristian Fàbrega, Damián Monllor-Satoca, María Dolores Hernández-Alonso, Germán Penelas-Pérez, Juan Ramón Morante, Teresa Andreu. *Hydrogenation and Structuration of TiO₂ Nanorod Photoanodes: Doping Level and the Effect of Illumination in Trap-States Filling*. J. Phys. Chem. C 2018, 122, 3295–3304.
 - Impact factor 2018: 4.309
 - 1st quartile by the Journal Citation Report (JCR) in categories: materials science.
 - Carles Ros performed the synthesis and characterization and wrote the manuscript.

Chapter 3

2. Carles Ros, Teresa Andreu, María Dolores Hernández-Alonso, Germán Penelas-Pérez, Jordi Arbiol, Juan Ramón Morante. *Charge transfer characterization of ALD-grown TiO₂ protective layers in silicon photocathodes*. ACS Appl. Mater. Interfaces 2017, 9, 17932–17941.
 - Impact factor 2017: 8.097
 - 1st quartile by the Journal Citation Report (JCR) in categories: materials science and nanoscience and nanotechnology.
 - Carles Ros designed the experiments, performed the ALD synthesis of the protective layers, catalyst incorporation and device encapsulation optimization. Also, performed characterization (Except HRTEM) and wrote the manuscript.

Chapter 4

3. Carles Ros, Teresa Andreu, Sergio Giraldo, Yudania Sánchez, Juan Ramón Morante. *Conformal chalcopyrite based photocathode for solar refinery applications*. Solar Energy Materials & Solar Cells, 2016, 158, 184–188.
 - Impact factor 2016: 4.784
 - 1st quartile by the Journal Citation Report (JCR) in categories: materials science, energy and fuels and applied physics.

- Carles Ros designed the experiments, performed the ALD synthesis of the protective layers, catalyst incorporation and device encapsulation optimization. Also, performed characterization and wrote the manuscript.
4. Carles Ros, Teresa Andreu, Sergio Giraldo, Victor Izquierdo-Roca, Edgardo Saucedo, Juan Ramón Morante. *Turning Earth Abundant Kesterite-Based Solar Cells Into Efficient Protected Water-Splitting Photocathodes*. ACS Appl. Mater. Interfaces 2018, 10, 13425–13433.
 - Impact factor 2018: 8.456
 - 1st quartile by the Journal Citation Report (JCR) in categories: materials science and nanoscience and nanotechnology.
 - Carles Ros designed the experiments, performed the ALD synthesis of the protective layers, catalyst incorporation and device encapsulation. Also, performed characterization (Except the Raman scattering analysis part) and wrote the manuscript.

Chapter 5

5. Carles Ros, Nina M. Carretero, Jeremy David, Jordi Arbiol, Teresa Andreu, Juan Ramón Morante. *Insight into the degradation mechanisms of Atomic Layer Deposited TiO₂ as photoanode protective layer*. Submitted to ACS Appl. Mater. Interfaces. Under revision.
 - Carles Ros designed the experiments, performed the ALD synthesis of the protective layers, catalyst incorporation and device encapsulation. Also, performed characterization (except HRTEM) and wrote the manuscript.
6. Carles Ros, Teresa Andreu, Jeremy David, Jordi Arbiol, Juan Ramón Morante. *About degradation and regeneration mechanisms of NiO protective layers deposited by ALD on photoanodes*. Under submission.
 - Carles Ros designed the experiments, device encapsulation and characterization (except HRTEM) and wrote the manuscript.

Annex

7. PengYi Tang, HaiBing Xi, Carles Ros, LiJuan Han, Martí Biset-Peiró, YongMin He, Wesley Kramer, Alejandro Pérez Rodríguez, Edgardo Saucedo, José Ramón Galán-Mascarós, Teresa Andreu, Juan Ramón Morante, Jordi Arbiol. *Enhanced Photoelectrochemical Water Splitting of Hematite Multilayer Nanowires Photoanode*

with Tuning Surface State via Bottom-up Interfacial Engineering. Energy Environ. Sci., 2017, 10, 2124.

- Impact factor 2017: 30.067
 - 1st quartile by the Journal Citation Report (JCR) in categories: chemistry, energy and fuels, chemical engineering and environmental sciences.
 - Carles Ros participated in the synthesis process by ALD depositing TiO₂ thin-films on the hematite photoelectrodes. Also took part in the results discussion and manuscript revision.
8. Cristina Flox, Sebastián Murcia-López, Nina M Carretero, Carles Ros, Juan Ramón Morante, Teresa Andreu. *Role of bismuth in the electro-kinetics of silicon photocathodes for solar rechargeable vanadium redox flow batteries*. ChemSusChem 2018, 11, 125–129.
- Impact factor 2017: 7.411
 - 1st quartile by the Journal Citation Report (JCR) in categories: chemistry and green & sustainable science & technology.
 - Carles Ros fabricated the photoelectrodes and contributed in results discussion and manuscript revision.

The article in annex chapter by P. Tang et al. is included in his thesis. None of the other articles has been previously used by other co-authors for their doctoral thesis.

Barcelona, 28/06/2019

Dr. Teresa Andreu

Prof. Juan Ramón Morante

Resum de la tesi

L'excés de consum de fonts d'energia no renovables, com ara els combustibles fòssils, ha portat el món cap a un canvi climàtic que ens urgeix a canviar els hàbits de consum energètic i a desenvolupar tecnologies alternatives que siguin renovables. La fotoelectròlisi de l'aigua (PEC) permet una conversió directa de la llum solar i l'aigua en hidrogen i oxigen, emmagatzemant l'energia en l'enllaç químic, resolent el problema d'emmagatzematge de la tecnologia fotovoltaica.

La fotoelectròlisi de l'aigua ha demostrat la producció eficient d'hidrogen i oxigen purs, però no està preparada per ser implementada a escala de mercat per manca de fotoelectrodes eficients, estables i escalables. En aquest treball recorrerem el camí des de millorar l'eficiència de fotoànodes estables basats en òxids metàl·lics cap a l'estabilització de materials fotovoltaics estables mitjançant capes protectores, transparents, conductores i catalítiques. Els esforços s'han centrat en utilitzar materials i tècniques escalables i rentables en cost-eficiència.

La tesi està estructurada en cinc capítols, començant pel Capítol 1, Introducció. En aquest capítol, el tema es presenta al lector juntament amb una revisió extensa de la recerca en fotoelectròlisi de l'aigua fins al punt d'aquesta tesi, i es plantegen l'àmbit i els objectius d'aquesta tesi. Inicialment s'analitza l'estat del model energètic global i les possibilitats de la fotoelectròlisi davant els reptes de l'emmagatzematge de l'energia, juntament amb conceptes fonamentals de la física i l'electroquímica. S'analitzen les estratègies més destacables que s'han utilitzat durant les últimes dècades per millorar els fotoelectrodes basats en òxids metàl·lics, incloent la selecció de materials òptims, l'adaptació de l'ample de banda prohibida, l'estructuració a escala nanomètrica, les modificacions de l'estructura electrònica i la introducció de catalitzadors i capes extres d'altres materials. Les limitacions en quant a eficiència dels òxids metàl·lics es discuteixen, i s'introdueix la necessitat d'estudiar materials semiconductors dels utilitzats per la indústria fotovoltaica, juntament amb els problemes que aquests materials d'ample de banda petit presenten en quant a corrosió en electròlits àcids i alcalins. Les capes fines protectores poden evitar que l'electrolit entri en contacte amb el semiconductor fotoabsorbidor, però hi ha diversos paràmetres que cal complir com transparència, conductivitat i estabilitat per permetre dispositius eficients i duradors. Es presenten els materials i tècniques més destacats per protegir semiconductors d'ample de banda petit. Finalment, es discuteixen les possibles configuracions de cel·la en tàndem i del reactor.

El Capítol 2 es centra en la millora de l'eficiència de fotoànodes basats en òxids metàl·lics via l'optimització dels mètodes de síntesi i els post-tractaments. Els fotoànodes de TiO_2 són coneguts com a estables en electròlits alcalins i a potencials anòdics, però manquen conversions eficients dels fotons en corrent. Això es deu a un ample de banda excessivament gran, que absorbeix només una petita part de l'espectre visible, i una reduïda mobilitat electrònica i dels forats dins del material. S'incrementa l'eficiència tant mitjançant

l'estructuració micromètrica del substrat, la nanomètrica de la capa en nanobarres, i modificant l'estructura electrònica via un tractament reductiu en H_2 que incrementa la caiguda de potencial dins la nanobarra. Aquest capítol inclou la publicació “Hidrogenat i estructurat de fotoànodes de nanobarres de TiO_2 : nivell de dopatge i l'efecte de la il·luminació en saturar estats trampa”.

En el Capítol 3 l'estratègia es reorienta cap a estabilitzar materials semiconductors eficients d'ample de banda petit. Fotocàtodes basats en silici son protegits per capes de TiO_2 crescudes per dipòsit de capa atòmica (ALD). S'optimitzen els paràmetres i es troba que la temperatura es clau tant per bona conductivitat com estabilitat de la capa, causat per la formació de capes policristal·lines si es disposa de suficient energia tèrmica per la reordenació cristal·logràfica. L'ALD permet un elevat control del gruix de la capa i minimitzar-ne els forats, així com temperatures de cristal·lització menors (començant a menys de $200\text{ }^\circ\text{C}$) que altres tècniques. La interfase TiO_2 -Si s'estudia per microscòpia de transmissió electrònica d'altra resolució (HRTEM) i s'observa com les capes intermèdies de 5 nm de Ti eviten la formació de SiO_2 nadiu i incrementen la nucleació del TiO_2 , ambdues coses beneficioses per una transferència de càrrega eficient del n^+ -Si al TiO_2 . Aquest capítol inclou la publicació “Caracterització de la transferència de càrrega de capes protectores de TiO_2 crescudes per ALD en fotocàtodes de silici”.

El Capítol 4 es dedica a implementar cel·les solars de capes fines de calcogenurs en la fotoelectròlisi de l'aigua. Cel·les solars de coure·indi·gal·li·seleni (CIGS) fabricades en substrats flexibles d'acer inoxidable son protegides de la corrosió de l'electròlit mitjançant capes protectores de TiO_2 fabricades via ALD. L'òxid transparent i conductor (TCO) ja present a la cel·la solar és necessari per la formació d'unions p-n eficients i pel transport de càrregues a la reacció d'evolució d'hidrogen. Cel·les solars de coure·zinc·estany·sofre/seleni (CZTS/Se), on els materials escassos indi i gal·li son substituïts per zinc i estany son implementades per la fotoelectròlisi també amb capes de TiO_2 . Variant el rati de S/Se es pot modificar l'ample de banda, una característica especialment interessant per formar cel·les en configuració tàndem. La temperatura màxima de dipòsit va resultar $200\text{ }^\circ\text{C}$, ja que afecta la distribució cristal·logràfica optimitzada d'imperficcions de les cel·les originals, afectant especialment la mostra de pur sofre. Gràcies a la possibilitat de fabricar cel·les solars i elèctrodes fotoelectroquímics basant-nos en la mateixa estructura, es poden mesurar les contribucions de la capa protectora de TiO_2 i del catalitzador a la transferència de càrrega elèctrica i electroquímica, permetent-nos presentar un model de circuit elèctric en sèrie. Aquest capítol inclou les publicacions “Fotocàtode basat en calcopirites conformals per aplicacions en refinaria solar” i “Convertint cel·les solars basades en estructura kesterita i materials abundants en fotocàtodes protegits i eficients per l'electròlisi de l'aigua”.

En el capítol 5, l'últim d'aquesta tesi, s'estudia el comportament de capes protectores dipositades via ALD en condicions de treball de polarització anòdica en electròlits alcalins.

El silici s'utilitza com a fotoabsorbidor de referència gràcies a que no es veu afectat per les temperatures de dipòsit emprades, entre 100 i 300 °C tant pel TiO₂ com pel NiO. En el primer treball d'aquest capítol es protegeixen fotoànodes de silici amb capes de 100 nm de TiO₂ i 5 nm de NiFe s'utilitza com a catalitzador. Modificant la temperatura de dipòsit del TiO₂, es dipositen capes completament amorfes, barreja d'amorfa i cristal·lines i completament cristal·lines, i s'observa un clar augment de la conductivitat correlacionat amb la cristal·lització. Mitjançant microscopi de força atòmica de conductivitat (c-AFM) s'observen camins de conductivitat preferent dins dels grans, on es proposa que estan relacionats amb defectes de cristall i fronteres de gra. Els tests d'estabilitat de pocs centenars d'hores mostren una caiguda significativa de la fotocorrent, sense mostrar dissolució del Si en ser observat via microscopi electrònic d'escombrat (SEM). Les mesures d'espectroscòpia d'impedància electroquímica (EIS) mostren un increment de la capacitat corresponent a la depleció en la capa de TiO₂. S'atribueix a que els potencials d'oxidació i la incorporació d'hidroxils a la capa redueixen la característica de semiconductor tipus-n del TiO₂, formant una barrera per la injecció de les càrregues a la reacció d'evolució d'oxigen. Un extra de llum UV recupera parcialment la conductivitat, un efecte de fotoconductivitat persistent que es podria utilitzar per millorar l'estabilitat dels fotoànodes. En el segon treball d'aquest capítol es dipositen capes de NiO mitjançant ALD en fotoabsorbidors de silici. S'estudia la temperatura de dipòsit i s'observa una reducció de la conductivitat en augmentar de 100 a 300 °C la temperatura de dipòsit, simultani a un canvi de direcció preferent de creixement cristal·logràfic. Tots dos efectes s'atribueixen a la fabricació de capes més estequiomètriques en augmentar la temperatura, reduint el nombre de vacants Ni²⁺, les responsables del comportament com a semiconductor tipus-p. Les capes dipositades a 100 °C van permetre mesures d'estabilitat de més de 1000 h en electròlits altament alcalins i potencials oxidatius. Es va trobar que dur a terme voltametries cícliques de forma periòdica evita una desactivació parcial dels fotoànodes, atribuïda a canvis químics en la superfície en condicions altament oxidants. Aquest capítol inclou dos treballs que, al moment d'acabar aquesta tesi, estan pendents d'acceptació en revistes reconegudes internacionalment, "Percepcions sobre els mecanismes de degradació del TiO₂ dipositat via dipòsit de capa atòmica com a capa protectora per fotoànodes" i "Sobre els mecanismes de degradació i regeneració de les capes protectores de NiO dipositades per ALD en fotoànodes."

L'últim capítol d'aquesta tesi inclou conclusions de la recerca realitzada. A l'annex, s'inclouen dues altres publicacions fetes en col·laboració i una patent.

Chapter 1

Introduction

1. Photoelectrochemical water splitting: introduction

Since the beginning of the industrial revolution, economic growth has been driven by a continuous increase of power consumption¹, which has been possible thanks to the availability, high energy density and low price of fossil fuels. The counter part of its exponential consumption increase has been significant alterations of our planet, some of them irreversible. Global climate change attributed to anthropogenic greenhouse gases emission to the atmosphere, rising sea level and temperatures causing ecological unbalance and exponential growth of species extinction rate are examples. In addition, mineral extraction up to scarcity of some specific elements and the consumption of fossil fuels overcoming the “Peak Oil”, the maximum extraction rate (only sustained nowadays by extremely aggressive techniques such as “fracking”) means fossil fuels and some elements easy and cheap extraction is close to come to an end. Some scientists have considered it a new geological era, the Anthropocene, due to the scale of human-caused modifications on Earth’s crust and its ecosystems².

Renewable energy sources and energy saving strategies should be implemented globally, which must be favored by new legislations and technological improvements. Wind, solar and other clean energy sources have in common their intermittent energy production and thus, the need of energy storage technologies to balance energy production and consumption. Converting the surplus energy into chemical bonds such as hydrogen gas allows for later usage, grid distribution or long-periods storage. Being the sun one of the most abundant energy sources, the photoelectrochemical (PEC) water splitting is postulated as one of the most interesting technologies due to worldwide water availability and pollution-free products, enabling hydrogen as a clean energy vector. Currently, most hydrogen gas feedstock is being produced by methane steam reforming, producing CO₂ as by-product³, so clean methodologies are of great impact in this field.

Photoelectrochemical (PEC) water splitting was discovered in the 70’s by Fujishima and Honda⁴, where TiO₂, an n-type semiconductor material with 3 eV band gap, in contact with an electrolyte, was able to absorb photons and generate enough potential to split the water molecule into hydrogen and oxygen, storing solar energy into chemical bonds, named “solar fuel”⁵. A PEC device can directly convert solar energy into hydrogen and oxygen (Figure 1.1a), although nowadays photovoltaic (PV) cells can be directly coupled to water electrolyzers, such as alkaline electrolysis cells (EC) or proton-exchange-membrane (PEM) electrolyzers⁶, both techniques consisting in mature technologies, as presented in Figure 1.1b. However, one of the main advantages of PEC is being designed to work at lower current densities, in the range of tens of mA·cm⁻², reducing electrochemical overpotentials. This results in lower operation voltages in front of commercial electrolyzers, designed to operate with two orders of magnitude higher currents and thus, significantly higher efficiencies are possible⁷. Lower current densities enable also low cost and earth abundant alternative

catalysts. In addition, PEC approach is a simpler architecture, reducing capital investment costs and transportation losses. However, PEC technology has remaining challenges to overcome: as the device will be in direct contact with the electrolyte, corrosion must be avoided, and device configuration is more limited⁷. For a large-scale implementation of these technologies, costs must be lower than hydrogen produced by fossil fuels, although environmental regulations and taxes could help in this direction. Nowadays, coupled PV-electrolyzer costs are not expected to reduce significantly, but PEC systems have a lot of possibilities ahead^{8,9}.

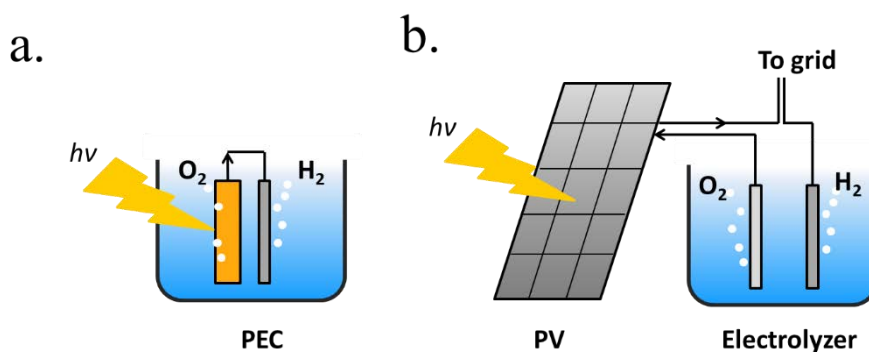


Figure 1.1. a) Scheme of a PEC system immersed in the electrolyte, where one of the electrodes is photoactive. b) scheme of a photovoltaic panel connected to an electrolyzer with the option to give or take current to the electrical grid.

The main requirements to achieve competitive PEC water splitting are: (i) absorption of broad part of the solar spectra. (ii) Efficient photogenerated electron-hole excitation and separation. (iii) Minimized transport losses to the back contact and semiconductor-electrolyte surface. (iv) Minimal overpotential on performing the hydrogen evolution reaction (HER) or the oxygen evolution reaction (OER). (v) Long term stable operation. (vi) Scalable device fabrication techniques. (vii) Utilization of cost-effective and (viii) earth abundant materials.

The aim of this introduction is to show the progress of recent decades investigations in PEC water splitting with a special attention to the main key parameters to drive PEC technology to be upscaled: high productivity, long-term stability and cost-effective materials and techniques. Despite been a significant amount of publications in the field, focus has been put on works with disruptive ideas in the path of obtaining high productivity and stability photoelectrodes capable to fulfill market implementation¹⁰. Metal oxides enhancement are reviewed, together with protective strategies for unstable semiconductors capable to generate higher productivities. Finally, cell implementation strategies and reactor configurations are analysed, as well as future prospective challenges for efficient, stable and scalable PEC cells are discussed.

2. Fundamental concepts

Photoelectrochemical water splitting is a complex process, including several phenomena which must be optimized for an efficient device design. In this section, most fundamental ones are explained and depicted in Figure 1.2: a) light-matter interaction, b) electron-hole pair generation, c) charge separation and transport, d) catalytic charge transfer to the electrolyte and e) the water splitting reaction. As a result of photoelectrochemical water splitting, a current flow (f) is obtained between both electrodes.

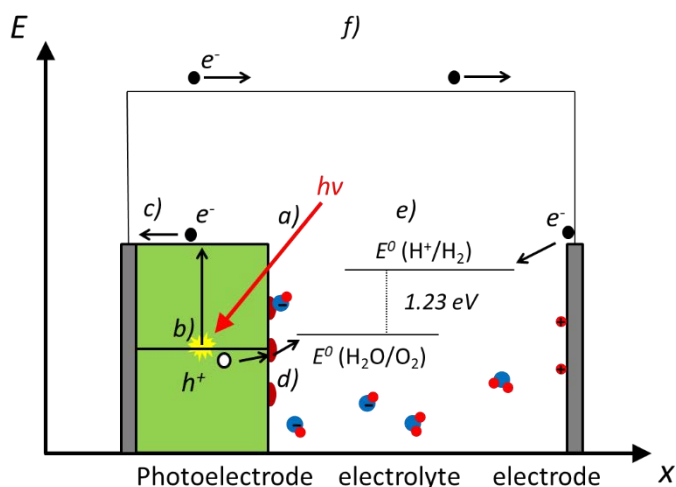


Figure 1.2. Scheme illustrating the principal phenomena of photoelectrochemical water splitting, where a photoanode is immersed in an aqueous electrolyte. a) light-matter interaction, b) electron-hole pair generation, c) charge separation and transport, d) catalysis and e) the water splitting reaction. f) photocurrent associated to the photoelectrochemical (PEC) water splitting.

a) Light-matter interaction

When light strikes on matter it can be absorbed, reflected or transmitted (Figure 1.3a). Across certain media such as liquid electrolytes, light can be slightly absorbed or reflected (scattered), what is considered **attenuation**. Thus, short propagation distances through the electrolyte is necessary to avoid significant losses. At the interface between two different media with different dielectric constant a fraction of the incident light can suffer **reflection**, propagating back in the initial media. Strategies to modulate the divergence between dielectric constants are used in several fields, called “antireflective coatings”, useful to minimize reflection for specific wavelengths range. Once inside the material, photons can be **absorbed** if its energy is higher than the band gap. In this case, photon energy will be transferred to atomic electrons, generating an electron-hole pair. The **penetration depth** is a measure of how deeply an irradiation can penetrate into a medium. It is defined as the depth at which the photons are absorbed by $1/e$ (37%), and is an important parameter in thin film semiconductors, as can

range from 2 μm for Si (at 555 nm wavelengths) to down to few nanometers for iron oxide. The non-reflected or absorbed light is considered **transmitted**.

b) Electron-hole pair excitation

If a material absorbs a photon, the energy is transferred to an electron, which is excited to a higher energy level. In a **semiconductor**'s case, electron states from individual atoms have an overall average energy state distribution forming a **valence band** (E_V) and a **conduction band** (E_C), highest energy states occupied and lowest energy vacant states at absolute zero temperature, respectively. The energy difference between these two bands, where no states are present, is the forbidden energy region, named the **band gap** (E_g).

After photon absorption, some of the valence band **electrons** (e^-) are excited into the conduction band leaving an empty state in the network of covalent bonds, considered a "**hole**" (h^+). If photon's energy is larger than the band gap, the electron will dissipate that extra energy ("thermalize") until stabilizing in the conduction band, giving that extra energy to neighbor atoms in the form of thermal vibration and thus, not storing all original photon's energy in the excited electron-hole pair.

For semiconductors at a certain temperature, some of these atoms are spontaneously ionized, where electrons are excited to the conduction band and holes are created in the valence band. The nature of the majority carriers formed, i.e. free electrons or vacancies in the covalent structure, determines the n- or p-type semiconductor behavior. This is normally governed by alterations in the crystal lattice material covalent network, where modifying the amount of acceptors (accepting a free electron) or donors (giving free electrons) is named "**doping**" the semiconductor, and there are several forms to do it. Among them, the presence of an element with different number of valence electrons (i.e.: a boron atom with 3 electrons in the external shell in a silicon covalent structure consisting on 4-links per atom results in an electron missing in the covalent bonding) or the formation of a sub-stoichiometric material (i.e.: oxygen vacancies in TiO_2 are the responsible of n-type semiconductor behavior). The average states distribution energy is called the **Fermi level** (E_F). If Fermi level is closer to the valence band and majority carriers are holes it is considered a **p-type** semiconductor, and if it is closer to conduction band and electrons are majority carriers, an **n-type** one.

c) Charge separation and transport

Light-induced electron hole pairs need to be separated to avoid eventual **recombination**, the process in which the excited electron releases its energy, "filling" a hole back in the valence band. High recombination rates make impossible to extract any current from photogenerated charges, thus efficient charge separation is needed. Thus, an external potential can be applied, or an internal **built-in potential** can be used to spontaneously **separate photogenerated charges** and consequently, to create a photovoltage and a photocurrent. By putting in contact a p-type and an n-type semiconductors a **p-n junction** is formed, where the average amount

of free electrons or holes (Fermi levels) is equilibrated by charges diffusing from one to the other, forming a **space-charge or depletion region** where there is a strong electric field (Figure 1.3b).

There are several structures forming built-in electric fields, among them:

- **p-n homojunction**, where a semiconductor has two regions with different type character (i.e. p-type and n-type silicon).
- **p-n heterojunction**, where two different materials of different type character are in contact (i.e. n-type TiO₂ and p-type silicon).
- **Schottky junction**, where a semiconductor equilibrates with the free electrons energy level of a metallic film (i.e. Ni metal and n-type silicon).
- A **semiconductor-liquid junction (SCLJ)**, where the semiconductor equilibrates with the ions adsorbed in the surface, forming a Helmholtz double layer (i.e. n-type TiO₂ in an alkaline electrolyte).

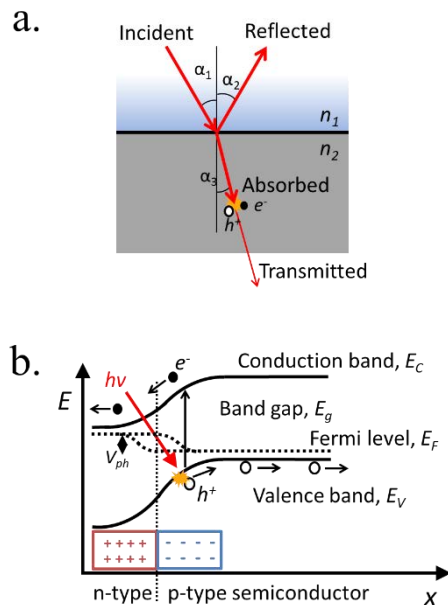


Figure 1.3. a) Scheme of a light beam incident on a two different mediums interface with different refractive index, depicting incident, reflected, absorbed and transmitted light and the formation of an electron-hole pair. b) Energy band diagram of a p-n junction presenting a photon absorbed and the movement of the electron and hole under the built-in electric field, together with the photogenerated voltage between Fermi levels.

Formed electric fields will drift generated charges to opposite directions, i.e. electrons to surface and holes to the back contact (Figure 1.3b). For efficient **charge transport**, high **conductivity** is needed. Conductivity is governed by both carrier mobility and carrier

concentration. Carrier mobility highly depends on impurities and defect concentration: electrons and holes highly scatter on crystallographic defects such as interstitial atoms or vacancies, plane dislocations, stacking faults or grain boundaries, losing some energy and changing direction. Meanwhile, carrier concentration is determined by the doping level, temperature and illumination intensity. All these parameters will be reflected in a higher **resistance** to charge transport.

d) Catalysis and catalyst introduction

Once the electrons/holes reach the surface of the photoabsorber, a chemical reaction takes place. In water splitting, the hydrogen or oxygen evolution reaction, respectively. So, not only the charge separation and transport of electrons/holes to the surface is crucial but also, the efficiency of the water splitting reaction and how the electrons are transferred to the reactants to obtain the products. In this sense, catalysts play an important role, accelerating a chemical reaction.

An electrocatalyst is defined as a material repeatedly enhancing a certain reaction without being consumed. Catalysts introduce alternative reaction paths with lower activation energy through forming alternative intermediate species on its surface. As the reaction will happen on the surface, normally very small amounts of catalysts are needed.

e) The water splitting reaction

The water splitting reaction ($2H_2O \rightarrow 2H_2(g) + O_2(g)$ (eq.1)) is a non spontaneous reaction. At room temperature, water can be split by applying an electrical potential between two electrical contacts, a cathode and an anode, immersed in an aqueous electrolyte, to drive two half-reactions, the hydrogen evolution reaction (HER) and oxygen evolution reaction (OER) (Figure 1.1a and Figure 1.4a). The complete reaction has a Gibbs free energy of 237.18 kJ per mol of produced H_2 , corresponding to a thermodynamic reversible potential of 1.23 V. However, this value is theoretical, assuming ionic concentration of 1 molar, gases pressure of 1 atm. and 298 K, for different conditions, the potential value will vary following the Nernst equation. For instance, at different pHs, the HER and OER standard potential values are:

HER:



OER:



Also, to drive kinetically efficient these reactions, additional potentials are necessary for the catalysis, η_{HER} and η_{OER} , named as overpotentials ($\sim 0.4 \text{ V}$ at $\sim 10 \text{ mA} \cdot \text{cm}^{-2}$ currents for state

of the art catalysts^{11–17}). The overpotential need to drive the reaction efficiently depends not only on the electrocatalyst nature, but also on the basic or acidic character of the electrolyte, the abundance of hydroxides (OH^-) or protons (H^+), which plays a role on the water dissociation kinetics¹⁸. In addition, ionic conductivity is necessary between the two electrodes, which can introduce another extra potential ($\eta_{ionic\ cond.}$) for large distances or reduced ion concentration/conductivity, resulting in an ohmic loss. Gases should be separated to avoid back-reactions if they diffuse to the opposite polarized electrode.

Adding all contributions, a minimum required voltage (V_{min}) is obtained:

$$V_{min}(j) = 1.23\ eV + \eta_{HER}(j) + \eta_{OER}(j) + \eta_{ionic\ cond.}(j)$$

Record values down to $\sim 1.4\ V$ for a current of around $10\ mA \cdot cm^{-2}$ have been obtained^{19,20}.

f) Photoelectrochemical (PEC) water splitting

In PEC water splitting, photons absorbed by the semiconductor create electron-hole pairs, which are separated by the built-in electric field inside the photoelectrode, generated in the semiconductor-liquid junction (SCLJ) by semiconductor and electrolyte Fermi level equilibration. A double layer is formed, first described by Helmholtz²¹ nowadays extended by other authors²² formed by ions physically adsorbed to semiconductor's surface and a diffuse outer layer with exponentially decreasing potential. Electric neutrality is obtained by band bending generated inside the semiconductor²³. The built-in electric field can separate electron-hole pairs, generating photovoltage (V_{ph}) and photocurrent, as depicted in Figure 1.4a and b. In a photoanode, holes are driven to photoelectrode's surface and perform the oxygen evolution, meanwhile electrons are collected by the back contact and close the circuit performing the proton reduction reaction in the counter electrode. Similarly, if the semiconductor built-in electric field drives electrons to the surface to perform the hydrogen evolution, it is considered a photocathode. For a significant photocurrent injected into the electrolyte to perform the water splitting reaction, photogenerated electron-hole pairs will suffer overpotentials for charge-separation (η_{sep}) and for charge transport (η_{trans}) across the semiconductor, from the back contact and other elements in the circuit. Some authors have calculated a minimum band gap ($E_{g\ min}$) of $>2.04\ eV$ ^{23,24} based on:

$$E_{g\ min} = \eta_{trans} + \eta_{sep} + V_{min}$$

If the photopotential is generated by a single photoelectrode is not enough, an external bias can be applied to complete the reaction. This way, external power would be used, but it can help in extracting more power from the photoelectrode too.

Independent analysis of each electrode is possible by measuring in a “three electrode” cell configuration (or half cell) (Figure 1.4c), where a reference electrode is used (at a fixed potential in respect to the electrolyte). In this disposition, the required current is applied in the

counter electrode by an external power supply or potentiostat so that between the working electrode and a reference electrode the desired potential is applied²⁵. With this half-cell configuration, the incoming light conversion efficiency into gas given by this single electrode can be measured, named half-cell solar-to-hydrogen (HC-STH) conversion efficiency²⁶.

$$HC - STH (\%) = \frac{j_{ph} \times (E_{H_2O/O_2} - E)}{P_{sun}} \times 100$$

Where j_{ph} is the photocurrent density obtained under an applied bias (E), E_{H_2O/O_2} is the equilibrium redox potential of oxygen evolution reaction (1.23 V vs. NHE) and P_{sun} is the standard solar irradiation, $100 \text{ mW} \cdot \text{cm}^{-2}$.

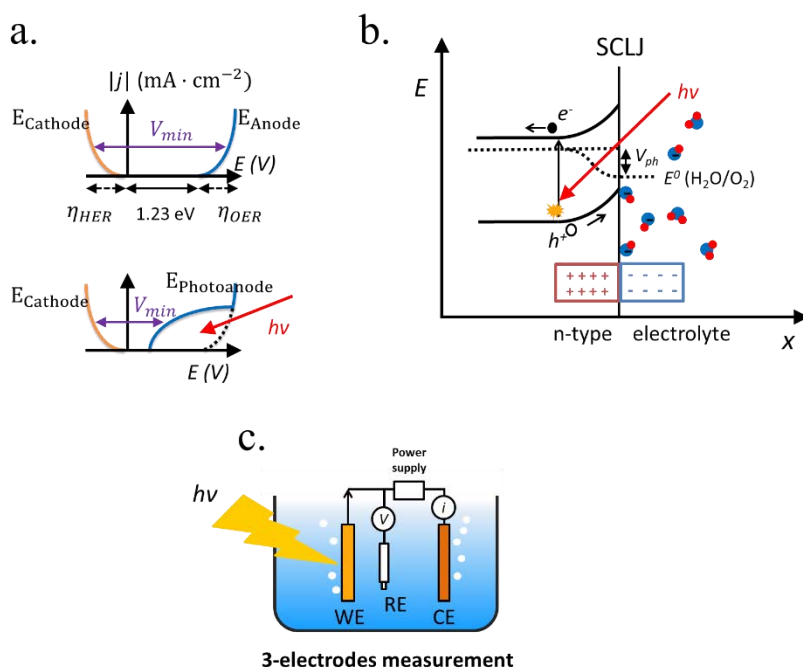


Figure 1.4. a) Absolute current versus voltage of the water splitting reaction with the overpotentials for HER and OER depicted (left) and the shape of the water splitting reaction if one of the electrodes is photoactive (right). b) Energy bands diagram of a photoanode in contact with an alkaline electrolyte, consisting on (left to right) an n-type semiconductor, light-induced electron-hole pair being separated by the space-charge region in the semiconductor-liquid junction (SCLJ), the adsorbed molecules from the electrolyte forming the Helmholtz double layer and the OER redox potential. c) A 3-electrodes measurement system consisting on a working electrode (WE), a reference electrode (RE), a counter electrode (CE) and a potentiostat measurement system, schematically consisting on a voltmeter, a current meter and a power supply.

3. Metal oxide photoelectrodes and enhancement strategies

Metal oxides present several interesting characteristics for PEC compared to other semiconductors, such as earth abundance and a relatively large bandgap that results in high photovoltage, required for water splitting. TiO_2 was the first studied PEC semiconductor, back in the 70's⁴. It is an earth abundant and inexpensive material which has a high stability in alkaline environments and favorable band edge alignment for the OER reaction²⁸, but for decades obtained photocurrents were far below $1 \text{ mA} \cdot \text{cm}^{-2}$. This was mainly caused by a 3.2 eV bandgap, absorbing under a 5% of the solar spectrum corresponding to UV light significant recombination rates and low conductivity due to crystallographic and electronic defects²⁹.

To overcome the intrinsic limitations found for TiO_2 , several strategies were applied following decades³⁰: alternative metal oxide candidates, band gap modification, nanoscale material structuration, controlling electronic defects by new synthesis techniques and post-treatments, surface-decorating with catalysts, creating heterojunctions, etc. With these modifications, significant advancements have been obtained.

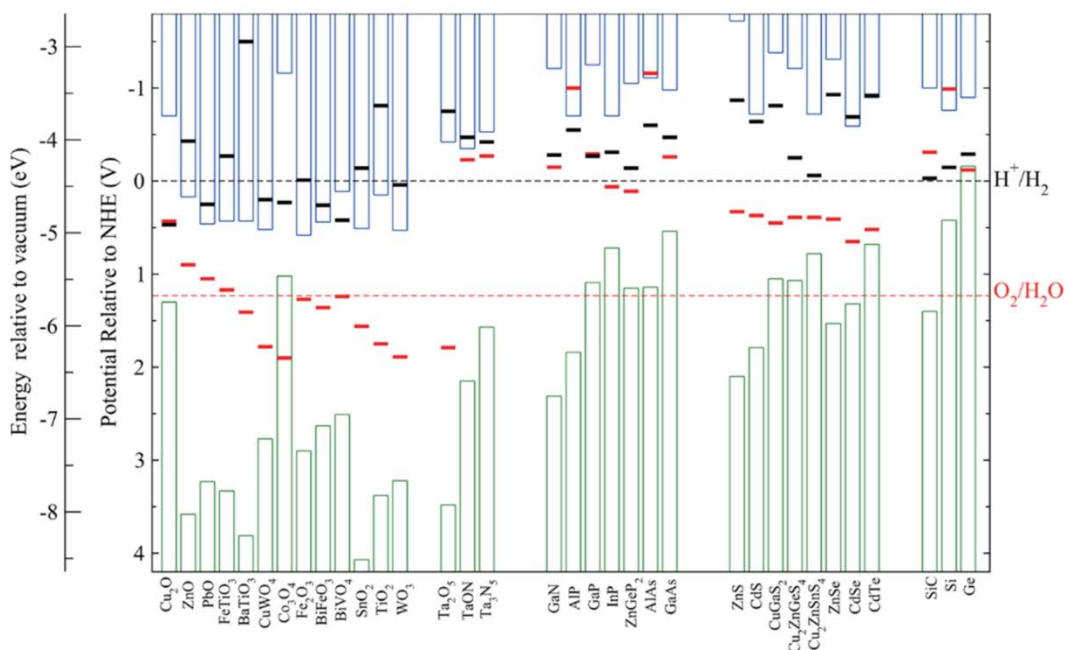


Figure 1.5. Self-oxidation (red bars) and self-reduction potentials (black bars), and conduction (blue bars) and valence bands (green bars) relative to NHE and vacuum potentials for various semiconductors at $\text{pH} = 0$, 298.15 K and 1 bar. Reproduced from Chen et al.³¹

3.1. Metal oxide photoelectrode candidate materials

Among all possible metal oxides, TiO_2 (n-type, 3.2 eV)^{4,32-36} has been always present as one of the most investigated materials, and other candidates have been widely studied too such as Fe_2O_3 (n-type, 2.2 eV)³⁷⁻³⁹, ZnO (n-type, 3.3-3.4 eV)^{40,41}, WO_3 (n-type, 2.6-2.8 eV)⁴²⁻⁴⁴, BiVO_4 (n-type, 2.3-2.5 eV)⁴⁵⁻⁴⁸, NiO (p-type, 3.4 eV)⁴⁹ and Cu_2O (p-type, 2.0 eV)⁵⁰. More materials have been tested but without remarkable success, as there are several criteria to be met: corrosion potentials less favorable than HER/OER reactions, proper band alignment for large photovoltage generation, and favorable band position for the desired redox reaction.

As it can be observed in Figure 1.5, some materials are not useful for water splitting due to unfavorable band alignment, with band edges far from water redox potentials³¹. To perform the HER reaction, conduction band must be at more negative potentials relative to NHE than the H^+/H_2 potential (black dashed line), and for the OER, at more positive potentials than $\text{O}_2/\text{H}_2\text{O}$ (red dashed line). For a bias-free reaction, both conditions must be met.

Bard et al.⁵¹, Gerischer et al.⁵² and other works have discussed in which conditions corrosion reactions are less energetic and thus, thermodynamically more favourable than the HER/OER reaction. S. Chen and L. Wang calculated thermodynamic oxidation and reduction potentials of several semiconductors and compared them to the OER/HER reaction, finding a significant portion of them require protection from corrosion (Figure 1.5)³¹. Generally, a photoelectrode is stable to electron reduction if the self-reduction potentials are more negative relative to NHE than either the H^+/H_2 or conduction band minimum, and to holes oxidation if self-oxidation potentials are more positive than $\text{O}_2/\text{H}_2\text{O}$ or valence band maximum.

Some of these oxides, having 3 eV or higher band gaps limit their theoretical maximum current to values lower than $1.8 \text{ mA}\cdot\text{cm}^{-2}$, such as NiO , TiO_2 or ZnO . Alternative interesting candidates in relation to the mentioned parameters are BiVO_4 , WO_3 , Fe_2O_3 and Cu_2O , with 2.0-2.5 eV band gaps and theoretical photocurrents over $10 \text{ mA}\cdot\text{cm}^{-2}$ ^{253,54}, but they are prone to crystallographic disorder, presenting significant electronic drawbacks: abundant superficial and internal recombination states, low carrier mobility and lifetime. Hence, optimized fabrication of these materials where electronic drawbacks can be overcome has turned into one of the main investigation fields. As an example of photoanode optimization, reducing Fe_2O_3 thickness or their nanostructuring can overcome the extremely short charge diffusion length and lifetime, reaching up to $4.3 \text{ mA}\cdot\text{cm}^{-2}$ at 1.23 V vs RHE, a 34% of its theoretical maximum photocurrent³⁷. Also, WO_3 nanocrystals all grown with a (002) facet orientation have demonstrated to avoid multiple surface energies, and thus, OER overpotentials and kinetics⁴².

Even expecting high stability, thoughtful investigations have observed chemical and performance degradation by high pH electrolytes in photoanodes such as BiVO_4 when protective overlayers or cocatalysts are not used⁵⁵. Further increasing materials complexity

by multiple metal oxides have shown unprecedented photocurrents up to $2.4 \text{ mA} \cdot \text{cm}^{-2}$ at 0.4 V vs RHE for CuFeO_2 combined with NiFe/reduced graphene oxide layers⁵⁶, although much more work is needed in this path.

3.2. Band gap modifications

Large band gap metal oxides have energy band positions prone for water splitting, but lack significant visible light harvesting. Thus, many attempts have been made to modify their bandgap and increase their visible light absorption⁵⁷. Creating new states at energies inside the band gap by forming oxygen vacancies or doping with non-metals or transition metals enable shorter energy differences, thus narrowing the optical band gap. As examples, nitrogen and hydrogen doping on TiO_2 was performed by Wang et al, giving a yellowish material and enhancing quantum efficiency in the previously inactive energy wavelengths of 450-600 nm^{58,59}, or S doping occupied oxygen vacancies and narrowed the band gap achieving visible light absorption⁶⁰, among others⁶¹. However, these improvements have not reached more than a few % efficiency increase, as creating states inside the band gap also creates detrimental recombination paths for photogenerated electron-hole pairs. Similar studies on bandgap modification by doping have been performed to other materials such as WO_3 ^{62,63} and ZnO ⁶⁴⁻⁶⁶.

3.3. Nanoscale material structuration

Controlling material optical and electronic properties gave metal oxide photoelectrodes a significant push, but optimizing material's morphology by controlling growth process at the nanoscale enabled a completely new field. Nanoscale structuration increases the surface area in contact with the electrolyte, reducing electrochemical kinetic overpotentials by lower current densities. Light absorption and charge transport are also enhanced thanks to decoupling light penetration depth and photogenerated charges diffusion length with nanostructures, facilitating charge transport to the electrolyte by enhanced active surface. Planar devices require thicknesses sufficient to absorb of a significant portion of the incident light, and photogenerated charges require diffusion lengths (L_D) enough to reach the surface. In nanostructured devices, the absorption distance for photons is decoupled from the diffusion length of photogenerated charges and thus, allow for higher absorptions meanwhile reducing current loss (Figure 1.6a)⁶⁷. 3D structures such as micrometer-size TiO_2 anodization^{32,59,68-70}, rutile TiO_2 nanorods hydrothermal growth⁷¹⁻⁷³, WO_3 nanowires and nanoflakes^{43,74}, ZnO nanorods^{40,41,65,66}, BiVO_4 ⁴⁵, Cu_2O ⁵³ and Fe_2O_3 ^{39,75} have been fabricated with enhanced PEC performance.

For instance, Cu-Ti-O nanotube arrays formed by anodization demonstrated increased active surface (tube length, pore and wall thickness) and light absorption by changing the Cu-Ti percentage, giving photocurrents from 0.035 to $0.065 \text{ mA} \cdot \text{cm}^{-2}$ at -1 V vs Ag/AgCl⁷⁶. Cu_2O nanowires protected with $\text{ZnO}/\text{TiO}_2/\text{RuO}$ present increased light absorption and charge

separation thanks to nanostructure, $5 \text{ mA}\cdot\text{cm}^{-2}$ for planar and $8 \text{ mA}\cdot\text{cm}^{-2}$ when nanostructured at 0 V vs RHE^{53,77}. By macro-mesoporous optimal structuration, BiVO₄ photoanodes obtained photocurrents of $2 \text{ mA}\cdot\text{cm}^{-2}$ compared with $0.5 \text{ mA}\cdot\text{cm}^{-2}$ at 1 V vs Ag/AgCl of the disordered porous films⁷⁸. Reducing and controlling material thickness can shorten the electrical path for photogenerated charges. I.e., Fe₂O₃ hematite photoanodes, due to few nanometers carrier diffusion lengths, require nanometer-scale thicknesses to minimize recombination losses^{79,80}.

Combining substrate structuration and nanoscale material deposition light absorption and photogenerated charge collection can be improved. High Mo-doped BiVO₄ deposition control in nanocone-shaped substrates, together with Fe/NiOOH catalyst and appropriate phosphate buffered electrolyte achieved up to $6 \text{ mA}\cdot\text{cm}^{-2}$ at 1.23 V vs RHE⁸¹.

3.4. Controlling electronic structure and surface states

To overcome problems such as inefficient charge separation and transport, generating higher and localized potential gradients through electronic doping is key. Metal doping, oxygen vacancy control or hydrogen and nitrogen doping have been studied. $\alpha\text{-Fe}_2\text{O}_3$ has been doped with several cations such as Si, Ti, Pt, Cr, and Mo, finding a decrease of the recombination rate by increasing charge transfer and grain-boundary passivation^{82–85}. Also, partially electrochemical reduction to Fe₂O₄ (a more conductive phase) can form beneficial conduction paths and reduce recombination⁸⁶. BiVO₄ has been modified both with W and Mo dopants and by hydrogen treatment to form oxygen vacancies. For example, porous BiVO₄ can double photoactivity with a 2% Mo incorporation⁸⁷ and potential gradient can be enhanced by gradual incorporation of W during deposition (Figure 1.6b)⁸⁸, or from 0.5 up to $4 \text{ mA}\cdot\text{cm}^{-2}$ at 1.2 V vs Ag/AgCl by hydrogenation at 300 °C thanks to increased donor density, enhancing electron-hole separation and transport⁸⁹. TiO₂ electronic band structure has also been intensively studied, where the depletion region was optimized in nanorod structures by vacancy formation under ammonia atmosphere⁷³.

Also, minimizing superficial electronic states, which act as trap states, is interesting to reduce photogenerated electron-hole recombination and thus, enhancing PEC efficiency. This can be achieved controlling the synthesis and post-treatments, and incorporating other metals on the surface to fill the traps and to act as OER catalysts. Fe₂O₃ photoanodes surface recombination can be reduced by CoO_x⁹⁰, Ga₂O₃^{90,91} or TiO₂⁹² surface states passivation. TiO₂ surface recombination rate was improved by removing detrimental chlorine atoms (blocking oxygen evolution active sites) by a 250 °C annealing treatment⁷¹, or by increasing hydroxyl groups acting as hole trap sites after ammonia treatments⁷³. Depositing atomically-thin films covering the surface is also a very effective strategy to suppress detrimental superficial states, avoiding recombination paths and contributing to shifts in the band positions of the metal oxide photoelectrode respect to the electrolyte, enhancing obtained potentials⁹³.

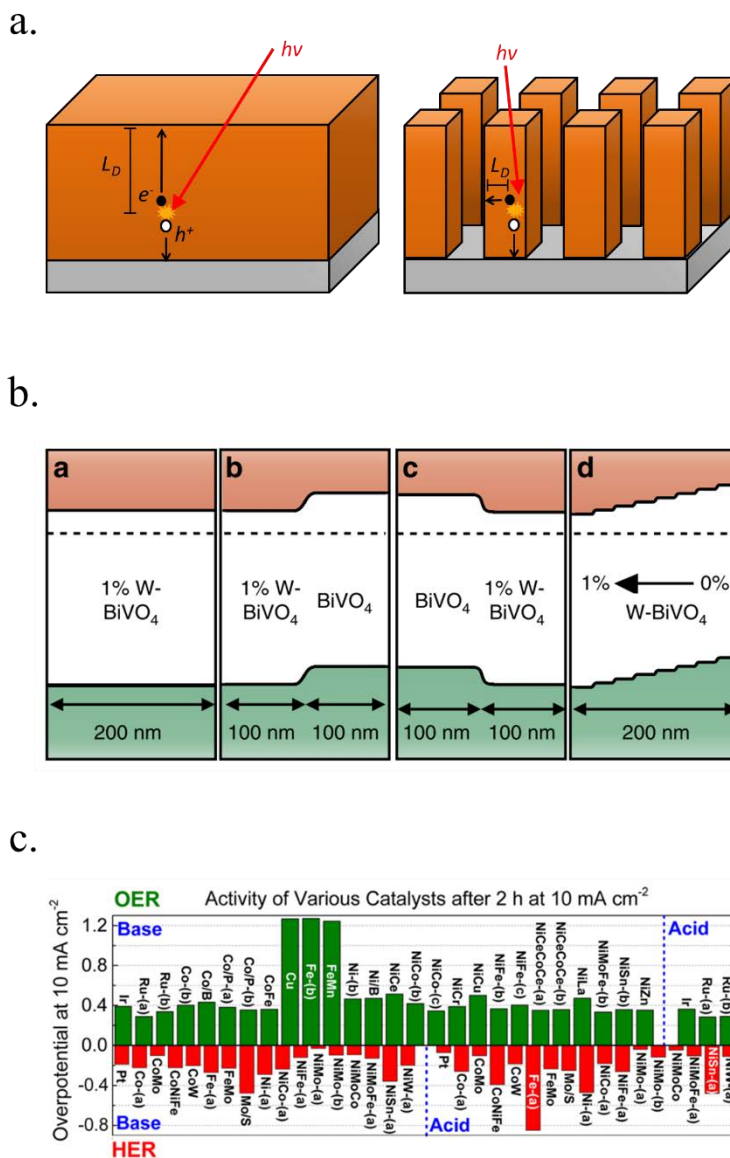


Figure 1.6. a) Planar devices requirements for light absorption and charge diffusion lengths (L_D) (left). In nanostructured devices, the absorption distance for photons is decoupled from the diffusion length of photogenerated charges (right). b) Energy band diagrams of different W doping configurations of BiVO_4 photoanodes, enhancing charge separation and transport. Reproduced from Abdi et al.⁸⁸ c) Overpotentials for 10 mA·cm⁻² currents of several OER and HER catalysts in acidic and basic electrolytes. Reproduced from McCrory et al.⁹⁴

3.5. Surface decoration with cocatalysts

Photoelectrodes such as Fe_2O_3 , CuO_2 or TiO_2 have suitable surface states to directly perform the desired reaction, but the use cocatalysts can enhance their performance thanks to favourable superficial energetics, improving reaction kinetics. Examples of these catalysts are Pt, MoS_2 or RuO_x for the HER reaction and Ni/ FeOOH , CoPi or IrO_x for the OER (Figure 1.6c)^{12,29,95–97}. Some of these cocatalysts are noble metals (Pt, Ru, Ir...), scarce and expensive for large-scale deployment, what has pushed investigation in earth-abundant alternative efficient electrocatalysts^{14,9894}. In the HER case, photocathodes such as Cu_2O have been decorated with Pt (best performing HER catalyst) and RuO_x ⁵³, and also earth abundant MoS_2 cocatalysts^{13,94}. Tilley et al used RuO_x or Pt as catalysts and an AZO/ TiO_2 protective layer (also forming an heterojunction) to obtain over 0.55 V vs RHE onset potential and $5 \text{ mA} \cdot \text{cm}^{-2}$ photocurrents for Cu_2O photocathodes⁹⁹. Amorphous MoS_2 allowed earth-abundant Cu_2O for up to $5.7 \text{ mA} \cdot \text{cm}^{-2}$ at 0 V vs RHE at pH 1¹⁰⁰.

OER reaction is a complex four electron process, with slow kinetics in most of the surfaces⁸⁰. Enhancing reaction kinetics or reducing potential barriers thanks to cocatalysts have improved the performance of TiO_2 and Fe_2O_3 photoanodes¹⁰¹. For example, hierarchically nanostructured TiO_2 photoanodes decorated with Au particles doubled photocurrent up to $2 \text{ mA} \cdot \text{cm}^{-2}$ at 1.23 V vs RHE¹⁰²; or $\alpha\text{-Fe}_2\text{O}_3$ ones obtained up to 15 % current increase and over 200 mV cathodic shift with Cobalt phosphate (Co-Pi) electrocatalyst¹⁰³. Co-Pi also improved BiVO_4 photoanodes performance up to $1.7 \text{ mA} \cdot \text{cm}^{-2}$ ^{47,87}, and FeOOH catalyst incorporation in a 0.1 M KH_2PO_4 + 0.1 M Na_2SO_3 electrolyte, increased BiVO_4 anodic photocurrent to $2.0 \text{ mA} \cdot \text{cm}^{-2}$ at 1.23 vs RHE⁴⁶.

3.6. Metal oxide heterojunctions

Up to now, potential improvements of single metal oxides have been analysed, but their combination opens a whole field of opportunities. By the introduction of other materials layers or substrates, charge separation can be improved by forming an heterojunction.

For photoanodes, several authors have studied the $\text{WO}_3/\text{BiVO}_4$ heterojunction, obtaining up to $4 \text{ mA} \cdot \text{cm}^{-2}$ at 1.23 V vs RHE, almost doubling productivity obtained by each oxide separately^{74,104}. The band energy difference of the two materials enhances charge separation, and different band gaps allow for increased light absorption. Also, a BiVO_4 photoanode with ZnFeO overlayer increased its photocurrent and decreased the onset potential, making it resistant to alkaline electrolytes, sustaining $3 \text{ mA} \cdot \text{cm}^{-2}$ at 1.23 V vs RHE⁴⁵.

For photocathodes, a Cu_2O photoelectrode was covered with an AZO/ TiO_2 /Pt multilayer grown by atomic layer deposition (ALD), obtaining stable and up to $2 \text{ mA} \cdot \text{cm}^{-2}$ photocurrents at 0 V vs RHE⁷⁷. Similar structures but on Cu_2O nanowires and with RuO_x as catalyst increased the photocurrent up to $8 \text{ mA} \cdot \text{cm}^{-2}$ at 0 V vs RHE, almost the double than the same $\text{Cu}_2\text{O}/\text{AZO}/\text{TiO}_2/\text{RuO}_x$ structure on planar photoelectrodes⁵³. Cu_2O is a good example on how combining nanostructuring, synthesis optimization, multilayer heterojunction and

cocatalyst decoration it is possible to approach to theoretical maximum photocurrent of $14 \text{ mA}\cdot\text{cm}^{-2}$.⁵³ Extra layers also protected the photoabsorber from corrosion (which would reduce to metallic Cu, as the redox potentials of monovalent copper oxide lie within the bandgap)⁷⁷.

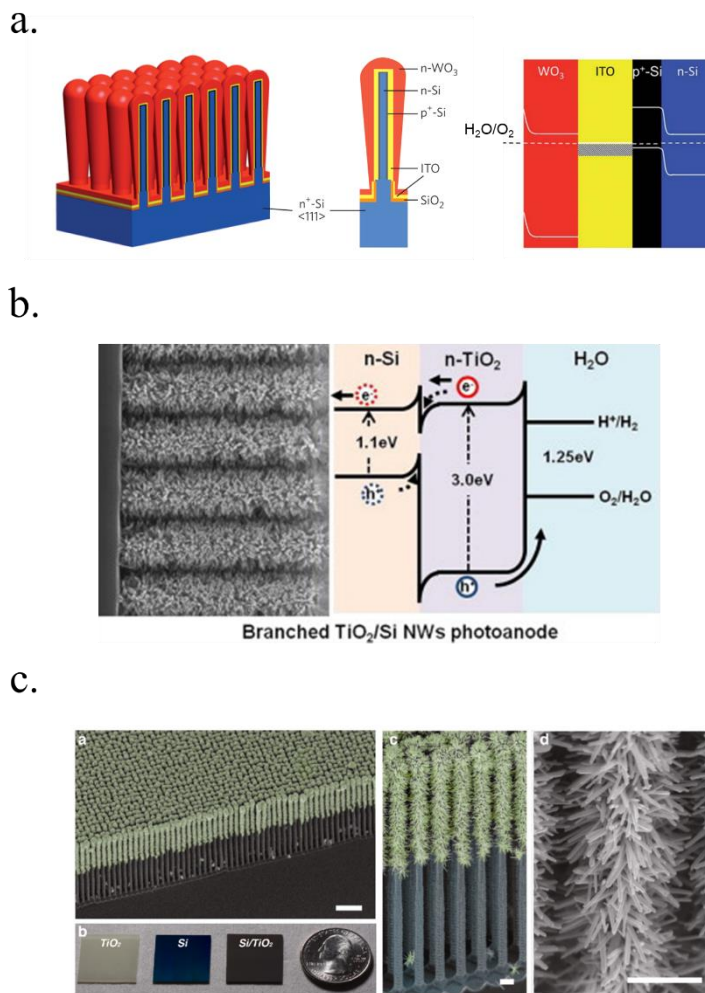


Figure 1.7. a) Scheme of an $np^+\text{-Si}/\text{WO}_3$ tandem structure including an ITO film in-between forming an ohmic contact (left) and its corresponding band diagram (right). Reproduced from Shaner et al.¹⁰⁵ b) SEM image of TiO_2 nanorods grown on $n\text{-Si}$ microwires to form a heterojunction and its corresponding band diagram. Reproduced from Noh et al.¹⁰⁶ c) Fully integrated tandem structure with the top part of Si microwires covered by TiO_2 nanorods and bottom part not, forming a “tree” tandem structure. Reproduced from Liu et al.¹⁰⁷

Other works have used 3D nanostructuring combined with heterojunction formation with different bandgap material use to create core-shell structures to obtain the best of each part. For example, porous WO_3 layers grown on top of Si microwires have been deposited, enhancing light absorption and photogenerated charge collection and transport (Figure 1.7a)^{105,108}. C.Liu et al. demonstrated a Z-scheme photoelectrode depositing TiO_2 nanorods on the top of Si microwires, making each of the tree-like structures a bias-free photoelectrode¹⁰⁷. TiO_2 nanorods on top of Si microwires combine large and small bandgap materials too (Figure 1.7b and c)^{106,107}, although much work is still needed to overcome interfacial detrimental charge recombination paths. The strategy to use small band gap semiconductors such as Si opens a completely new field of scheme possibilities, increased productivities and new challenges, which will be discussed in following sections.

4. Short band gap semiconductors for PEC water splitting

In the previous section, strategies to overcome the main drawbacks presented by metal oxide photoelectrodes for water splitting were discussed. The successful materials obtaining photocurrents higher than $8 \text{ mA} \cdot \text{cm}^{-2}$ with significant photovoltages are very few. In parallel to PEC water splitting development, science and industry of the photovoltaic field (PV) have optimized photoabsorbers and fabrication techniques up to commercial devices with minimal recombination and transport losses. PV productivities have been based on short band gap materials (1-1.5 eV) capable of absorbing the majority of visible spectrum, with materials achieving large carrier mobility thanks to minimized defects and disorder^{109–112}. Monocrystalline silicon-based solar cells, giving photocurrents over $40 \text{ mA} \cdot \text{cm}^{-2}$ and 700 mV open circuit photovoltages are nowadays largely dominating the market thanks to relatively cheap price and material abundance, several years operation stability and efficiencies over 22%. Monocrystalline silicon has not been the only photoabsorber commercialized: polycrystalline and amorphous silicon, together with CdTe, GaAs and CIS/CIGS have been already commercialized, and other semiconductors such as perovskites or CZTSSe are emerging rapidly (Figure 1.8)¹⁰⁹.

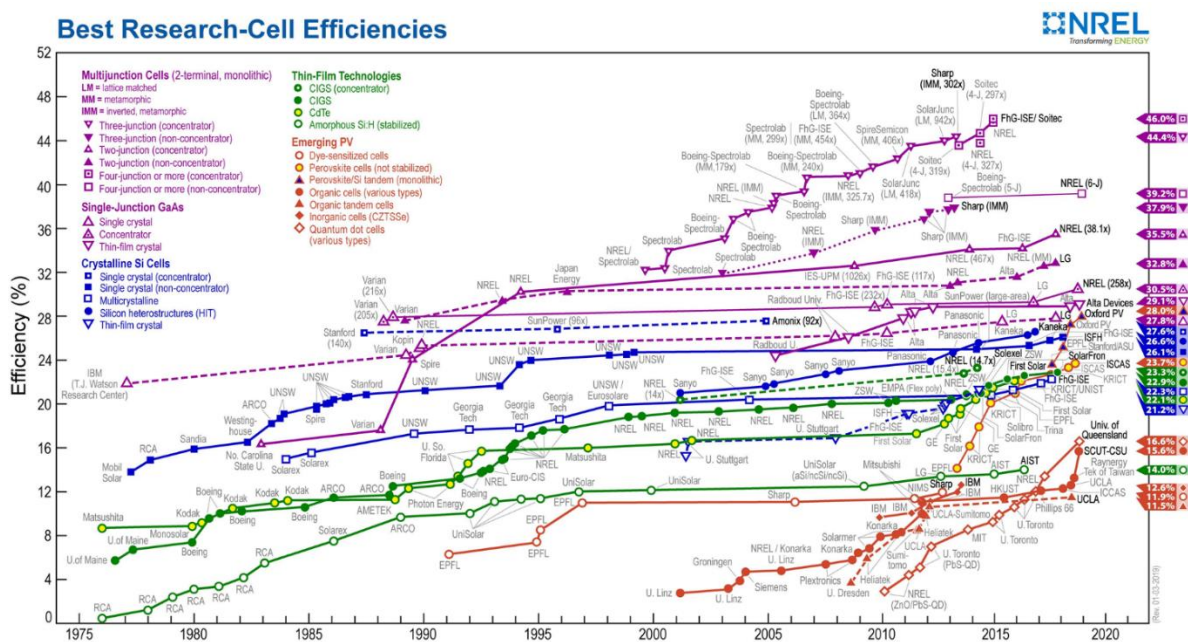


Figure 1.8. 2019 plot of highest-recorded photovoltaic efficiency by year of various photovoltaic devices classified by technology (colours). Prepared by the National Renewable Energy Laboratory (NREL, www.nrel.gov).

During the last decade, implementing short band gap materials in PEC water splitting has attracted much interest, thanks to all the knowledge and development from PV industry and

thus, the possibility to obtain significantly higher outputs than with metal oxides. Although, the use of these photoabsorbers presents extra challenges added to the photovoltaic ones. Not having a large band gap, and thus photovoltage, will require a tandem structure combining ~ 1.1 and $1.6\text{--}1.8$ eV semiconductors photovoltages or an external bias to use all of their capacity, as it will be reviewed in section 8.2, tandem PEC devices. Moreover, monolithic photoelectrodes must be immersed in the electrolyte, preferably in acidic or alkaline electrolytes where the electrochemical activity is highly enhanced. But these electrolytes are normally corrosive for most of the presented photovoltaic materials. Strategies to overcome these instabilities must be found to enable these materials for PEC water splitting.

4.1. Fundamentals of materials corrosion

In PEC devices, years-long photoabsorber sustained activity will be necessary for cost-effective devices, thus materials facing the electrolyte have to be thermodynamically stable in the selected electrolyte or extremely low corrosion kinetics must be involved, as discussed in section 3.1.

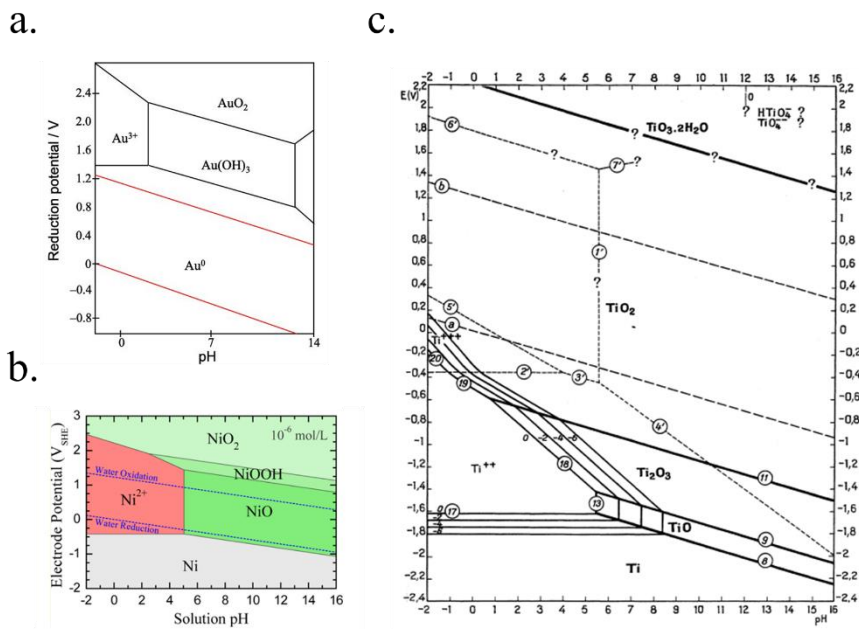


Figure 1.9. Examples of Pourbaix diagrams of a) gold (Reproduced from Huayhuas-Chipana *et al.*¹¹³) b) nickel (Reproduced from Huang *et al.*¹¹⁴) and c) titanium (Reproduced from Parsons.¹¹⁵) in aqueous electrolytes.

Some possible corrosion mechanisms can be material dissolution into the electrolyte, superficial insulator layer formation, or chemical detrimental modifications of the photoabsorber, all of them capable of disabling PEC activity. Pourbaix diagrams, where the

electrochemical stability for different redox states of an element as a function of pH is plotted, present a first approximation to predict the theoretical thermodynamic stability of a certain material in an aqueous environment¹¹⁶. They provide data if there will be a state of oxidation change (i.e. passivation) and/or a phase change (i.e. dissolution) of a certain material when varying the applied potential or electrolyte's pH. Some examples are presented in Figure 1.9.

4.2. Small band gap semiconductors corrosion examples in aqueous electrolytes

Each material is affected by corrosion in different ways, depending on most favourable reaction governed by pH or applied potentials, so it must be analysed in its specific conditions. For example, silicon, by far the most used PV photoabsorber, has been reported to corrode through different processes depending on the used electrolyte^{117–121}. Both in HER or OER potentials, silicon stability will depend on pH, being oxidation in acidic or dissolution in alkaline. The self-limiting passivation reaction of Si forming a thin SiO₂ layer in acidic electrolytes (pH ~ 0)¹²², a transparent but highly insulator layer, will eventually stop charge injection into the water splitting reaction. Whereas, formed SiO₂ dissolves in alkaline electrolytes (pH ~ 14) and will continuously etch the photoelectrode forming recombination paths for photogenerated charges or even dissolving the p-n junction, rapidly losing photocurrent^{117,118,122}. Thus, self-limited SiO₂ formation in specific sites will not significantly affect if the rest of the surface is still protected¹²³, but pinholes in protective layers in alkaline electrolytes will not stop etching the silicon, and thus, will be fatal for the photoelectrode.

Regarding other PV cells based on photoabsorbers such as cadmium-telluride (CdTe), copper-indium/gallium-selenide (CIS/CIGS/CGS) or its earth-abundant alternative, copper-zinc-tin-sulphide/selenide (CZTS/Se), their own structure is based on a multiple materials stack, also containing transparent conductive oxides (TCO, like In:SnO₂ (ITO) or Al:ZnO (AZO)) and n-type CdS, forming the p-n junction. ZnO^{124,125} and SnO₂^{124,126,127} are not stable in highly acidic or alkaline electrolytes or reductive potentials, as they form soluble species^{124,127}. Regarding CdS^{128–130} and also CdTe¹³¹, Cd dissolves in highly acidic and alkaline electrolytes¹³², and is thermodynamically stable only at significant cathodic overpotentials, not attained without applied bias. Cu-based photoabsorber (CIS, CIGS, CZTS...) are complex multielement films, highly electronically sensible to vacancies, and would be significantly degraded in contact with electrolytes, although losing the p-n junction is the main degradation factor.

Among other emerging photovoltaic materials¹⁰⁹, there is none expected to be highly stable for PEC applications under direct contact with the electrolyte. Cells fabricated with silicon, no matter if it is monocrystalline, polycrystalline, HIT, amorphous or micro/nanocrystalline¹³³ will suffer from dissolution or passivation when exposed to alkaline or acidic electrolytes, respectively, as discussed previously. Perovskites, a highly promising PV material, have a main drawback: significant degradation under humidity, what would require encapsulation efforts¹³⁴, especially if put to work in contact with aqueous electrolytes. Organic solar cells

have been implemented in PEC¹³⁵ but require careful selection of redox couples, limiting their efficiency and pointing in stability problems. Dye sensitized solar cells (DSSC) or Grätzel cells, molecular dye decoration of a MO_x framework as an intermediate to OER/HER catalyst presents significant instability of the molecular dye in the used potentials and electrolytes ranges. Thus, low productivities are expected¹³⁶, or full cell encapsulation would be required, then further connected to the electrolyte with an external circuit, forming a PV-EC device configuration¹³⁷.

5. Protective Layers to implement photovoltaic photoabsorbers into water splitting

Several strategies are possible to implement highly active photoabsorber materials into PEC water splitting avoiding their corrosion. Some authors have functionalized the surface of semiconductors with organic reagents like two-step chlorination/alkylation¹³⁸ or by an alkylation through the halogenation/Grignard route¹³⁹ to suppress corrosion, with relative success, but the majority of efforts have been put on depositing inorganic layers onto the photoabsorber to separate it from direct contact with the electrolyte^{93,140}. Protective ultrathin layers of any material must consider even very slow dissolution rates (chemical or mechanical) for long-term operating devices, especially when considering flow systems and direct contact with gas bubbling.

These protective layers must allow electrical conduction, be thermodynamically stable, and optically transparent. M. F. Lichterman et al. stated all the properties under the acronym “SABOR”, meaning “Stable in the thermodynamic, kinetic, and mechanical senses when incorporated onto the semiconductor, immersed in the electrolyte, and operated at the potentials of interest; Active catalytically for the OER/HER, either possessing intrinsic catalytic activity or integrating the activity of a co-catalyst; capable of providing Built-in electronic asymmetry to allow for the separation of electrons and holes, or to allow for a separate buried junction to perform efficiently; Optically transparent to provide optical properties that are optimized for the transmission of light; and, capable of providing low Resistance, to allow for charge-carrier conduction with minimal performance loss due to iR drops”¹⁴¹.

With protective layers incorporation, device’s complexity increases but photovoltage will now be governed by a solid-state junction rather than by the photoabsorber-electrolyte junction, increasing the possible materials candidates to be used. The extra layer can be used either to form an heterojunction, or to protect a buried junction. In addition, if the protective layer is not catalytic, an extra catalyst (layer or particles) must be added to reduce overpotentials. Although several interesting heterojunction strategies have been demonstrated for PEC water splitting electrodes with more or less success, focus will be put on extracting maximum efficiency from the photoabsorbers, using these extra layers to protect the photovoltaic-like junctions and the different techniques to deposit them.

5.1. Thin film deposition techniques

Thin film technology has become one of the main fields of study last decades, from basic sciences to industrial processes. Controlling material deposition at the nanoscale opens a whole new world of possibilities by combining physical and chemical properties from single or multiple element materials with overcoming intrinsic limitations due to phenomena only happening at the nanoscale¹⁴². For example, titanium dioxide, a wide band gap metal oxide,

considered insulator at the macroscale, is conductive at the nanoscale; or metals, highly visible-light reflective and absorptive, can be turned into transparent if deposited few nanometers thick. There are a large amount of deposition techniques and variations among them for diverse applications, but some of the most used ones for inorganic thin film protective layers have been selected.

There are many non-vacuum liquid and chemical-based thin film deposition techniques, but not all of them are used to synthesize protective layers for different reasons. Among the liquid-based thin film deposition techniques, **dip coating**, **spin coating** or **chemical bath deposition (CBD)**¹⁴³ are the more used ones, but require direct contact of the (maybe) sensible photoabsorber with a liquid, which can alter its superficial chemical state and thus, performance. In addition, liquid-based techniques normally produce either porous, not homogeneous at the nanoscale or abundant-pinhole films compared to vacuum technologies, and to eliminate precursor residues or crystallize them they require thermal post-treatments, which can create cracks in the protective layer or affect the photoabsorber. For example, solution-deposited TiO₂ by spin-casting or spray pyrolysis presented significant pinholes, allowing electrolyte to penetrate and dissolve the photoabsorber, being fatal for the device even with 80 nm thick layers¹⁴⁴.

Electroplating is one of the oldest techniques to form metallic thin films since the 19th century. Generally known as **electrochemical deposition**¹⁴⁵, a conductive substrate (in our case, the photoabsorber) is introduced in an electrolyte containing the desired thin film precursor ions and, under controlled polarization, a redox reaction occurs, forming a film of electrodeposited material in the surface of the electrode (Figure 1.10a). It can be extended to any material capable to be deposited in a certain potential window that will depend on the electrolyte media, and is very interesting thanks to its easiness and the wide range of materials possible to be deposited, from metals to metal oxides and sulphides, even with nanoscale morphology control. It requires no vacuum, usually it is carried out at room or moderate temperatures, and with affordable infrastructure, like a power supply, lab equipment and the precursor materials. As drawbacks, it is highly depending on the substrate, that needs to be conductive, and has a moderate throwing power (the capacity to deposit an uniform film over an irregular substrate), not suitable for nanostructured substrates where a high aspect ratio is required. In some cases, nucleation promote the formation of particles rather than a layer, such as electrodeposited Ni oxide/hydroxide, a transparent, chemically resistant and catalytic material, that forms porous layers^{16,146}, not isolating the substrate from electrolyte, whereas NiO deposited by sputtering creates a solid impermeable layer¹⁴⁷. Also, the substrate will be in direct contact with the electrolyte and its properties can be affected. Many works have used electrochemical techniques to deposit catalytic particles or films to enhance OER or HER kinetics on already previously protected semiconductors¹⁴⁸.

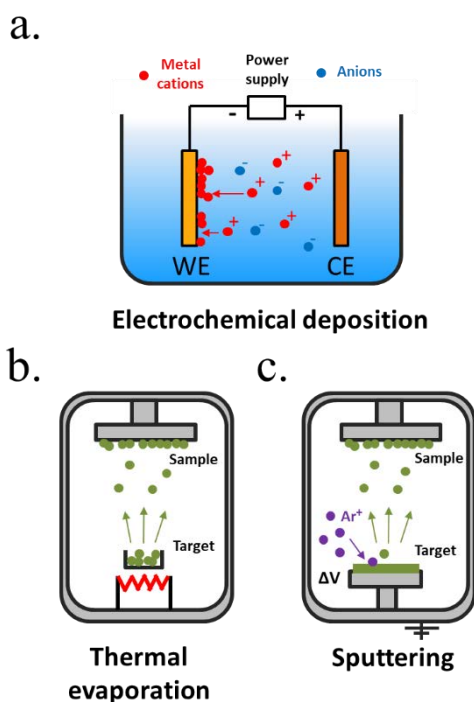


Figure 1.10. Representative schemes of thin film deposition techniques by a) electrochemical deposition, b) thermal evaporation and d) sputtering.

Vacuum technologies allow for an inert and controlled atmosphere deposition, favourable for more homogeneous deposited films and process-control¹⁴³. Among the **physical vapour deposition** (PVD) techniques, **thermal evaporation** is one of the simplest, where a crucible is heated to high temperatures, vaporizing the materials contained^{143,149}. Evaporated particles will travel and solidify forming a film on top of a substrate (Figure 1.10b). However, as different elements vaporize at different temperatures, the technique is useful for single element metals but has reduced stoichiometry reproducibility for mixes elements. Evaporated metallic films have been used as intermediate, protective or catalytic layers in water splitting. **Sputtering deposition**^{150,151} is based on an inert gas (i.e. argon) being ionized and accelerated towards a blank, impacting with high energies and removing particles which will travel until being deposited in our substrate (Figure 1.10c). Direct current (DC) sputtering is useful for conductive blanks (materials to be deposited), and radio-frequency (RF) sputtering allows insulator materials deposition. In reactive sputtering, other gases can be introduced at low pressures in the chamber, reacting with the traveling particles before being deposited (i.e. the oxygen presence can be controlled to tune metal oxides stoichiometry and with this, electrical, optical or other characteristics). Sputtering has been widely used to deposit catalysts¹⁵² and protective layers, thanks to the material possibilities, among them stoichiometry-controlled oxides such as TiO_2 ^{153,154} or NiO ¹⁴⁷ and no dependence on used substrate. Some authors have

required layers such as 8 nm Ti to prevent damaging sensible photoabsorbers such as amorphous Si during the sputtering process, as the process is energetic and the deposition-atmosphere could also affect the absorber¹⁵², and some have reported arcs during plasma attack the deposited film, forming pinholes and more electronically-defective material¹⁴¹. Other less used PVD techniques are **pulsed laser deposition (PLD)**^{155,156}, where very high energy laser pulses vaporize blank's surface with very high stoichiometry control, and **molecular beam epitaxy (MBE)**^{157,158}, a slow and expensive technique where material is formed atomically depositing layer by layer. As PVD techniques are based on high vacuum directional depositions, obtained layers are not conformal, what would not protect highly rugose photoabsorbers or 3D structures.

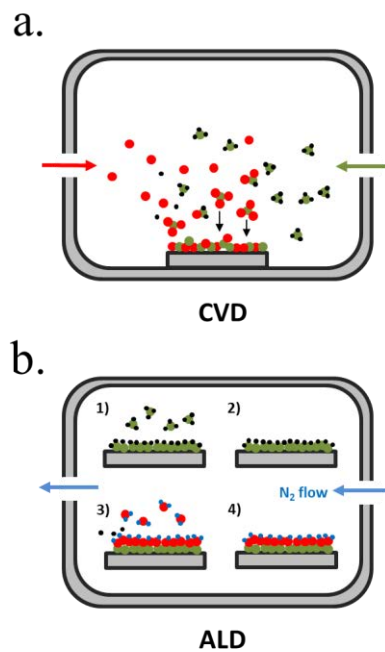


Figure 1.11. Representative schemes of thin film deposition techniques by a) chemical vapour deposition (CVD) and b) atomic layer deposition (ALD).

Chemical vapour-based deposition (CVD) techniques are usually based in temperature-controlled vacuum chambers where introduced precursor gases react, creating the desired products in solid form deposited on a substrate¹⁵⁹ (Figure 1.11a). Single or multiple element layers can be deposited, nitrides, oxides, metals or any other meanwhile the selected precursors react forming a solid product. **Plasma enhanced-CVD (PECVD)** is a variation where precursor gases react or decompose due to an ionizing plasma, arc discharge or microwave excitation, allowing different reactions, precursors or products independent of temperature¹⁶⁰. There is wide experience on metal oxides deposited by CVD, also as protective layers.

Atomic layer deposition (ALD) is a variation of CVD in which precursors are introduced in the chamber sequentially, first reported in the 60' by researchers in the Soviet Union under the name "molecular layering"¹⁶¹. One of the precursors is introduced to the chamber in an inert gas flow, saturating substrate's surface with the precursor, and then all the non-chemisorbed precursor is removed by the gas flow (Figure 1.11b). A second gas is then introduced (normally H₂O, O₃ or NH₃), reacting and forming a conformal submonolayer of the final desired product. This way, control of the layer growth in the sub-nanometer scale is attained, where final thickness depends on the number of cycles of this process¹⁶². ALD is maybe the best candidate to ensure complete surface coverage thanks to saturated deposition steps and thus, to obtain a pinhole-free protective layer¹⁶³. ALD also presents lower temperature crystallization due to absorbed molecule mobility but is much more time consuming than CVD^{67,164}. It has been used for many photoabsorbers and protective materials, even in industrial scale as essential part of high-k gate dielectrics manufacturing, although much more work is needed¹⁶⁴. For covering 3D nanostructures, ALD is the best candidate, due to the self-limited conformal deposition, and has been used in high ratio structures⁶⁷.

5.2. Strategies and materials for protective films

There are many paths to protect semiconductors from corrosion. In Figure 1.12 it was summarized the protective strategies, classified according to an increase in device complexity. From stable semiconductors forming SCLJ with the electrolyte (a), the introduction of metallic layers (thin enough to be transparent) as catalysts and/or to form Schottky junctions (b). Few nanometers thick oxide layers, thin enough to be tunneled, were introduced to increase stability in harsh environments (c). For further stability, thicker transparent films (usually oxides) several tens of nanometers thick can be used, also capable to form an heterojunction with the photoabsorber (d). To maximize charge separation and thus, photoelectrode efficiency, buried junctions can be used, where the protective layer will mainly act as a conductor (e). Finally, the next logical step is use a cable as conductor, forming a non-monolithic device where the photovoltaic part can be located outside of the electrolyte and connected to the electrocatalyzer in a PV-EC configuration(f).

5.2.1. Metallic thin films

Some of the first protective layers used for short bandgap photoelectrodes were metallic (Figure 1.12b), which in contact with the photoabsorber created a Schottky junction, being mandatory proper band alignment to extract maximum photovoltage¹⁶⁵. Noble metals such as platinum, palladium, silver, rhodium, ruthenium and gold were sputtered or thermally/electron-beam evaporated on silicon¹⁶⁶⁻¹⁷⁰ and on other photoabsorbers such as n-GaP¹⁷¹, p-WSe¹⁷¹ or p-InP¹⁷², not achieving significant stabilities. Maier et al.¹⁷³ demonstrated 60 day stability of a electrochemically deposited Pt-protected p-Si photocathode in acidic conditions, although significant series resistance was observed due to SiO₂ interface caused

by acid oxidation, presenting 0.3 V vs RHE onset potential and photocurrents of $10 \text{ mA} \cdot \text{cm}^{-2}$ at 0 V vs RHE, far from Si possibilities.

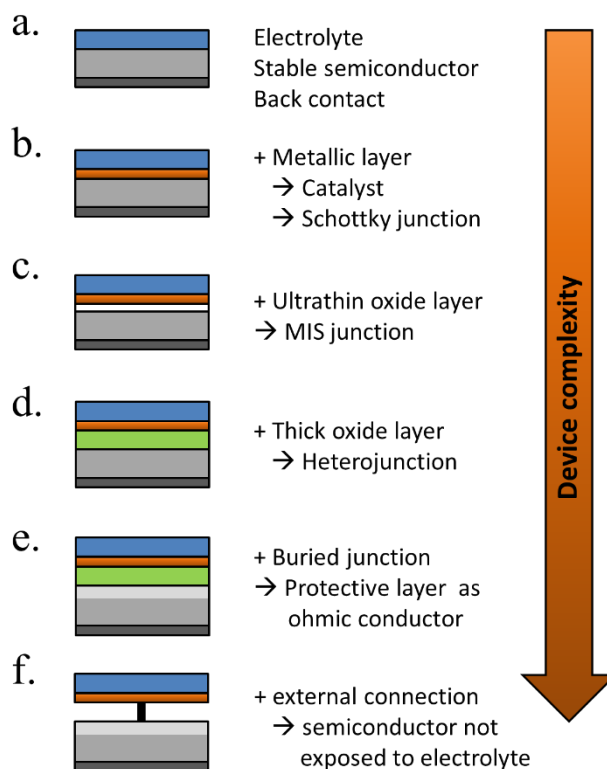


Figure 1.12. Schemes summarizing significant steps in photoelectrode device complexity regarding protective strategies.

Kenney et al.¹⁷⁴ fabricated a Ni-protected silicon photoanode and found that non electrolyte-permeable thick enough metallic layers were also too thick to allow light to reach the photoabsorber. Electrolyte intermixing in the metallic layer (partially oxidized, Ni/NiO) also helped to increase the built-in potential for 2 nm Ni layers, compared with the ≥ 5 nm Ni/n-Si Schottky junction (Figure 1.13a and b). To achieve a good (> 80 h) stability, a K-borate + Li-borate solution (pH 9.5) was used. Metallic film permeability in the few nanometers scale was used by Laskowsk et al.¹⁷⁵ to form an n-Si/5nm-Ni/10nm-Au dual working electrode to simultaneously track Ni redox potentials. In another work, Sartori et al. enhanced a p-Si photocathode's built in potential, and thus onset potential, with a simple 5 nm-Ti protective layer together with Pt catalyst particles¹⁷⁶. Obtained photocurrent reached over $25 \text{ mA} \cdot \text{cm}^{-2}$, but stability was poor. Feng et al. used similar structure but with Ni as catalyst, obtaining more overpotential for the HER reaction¹⁷⁷.

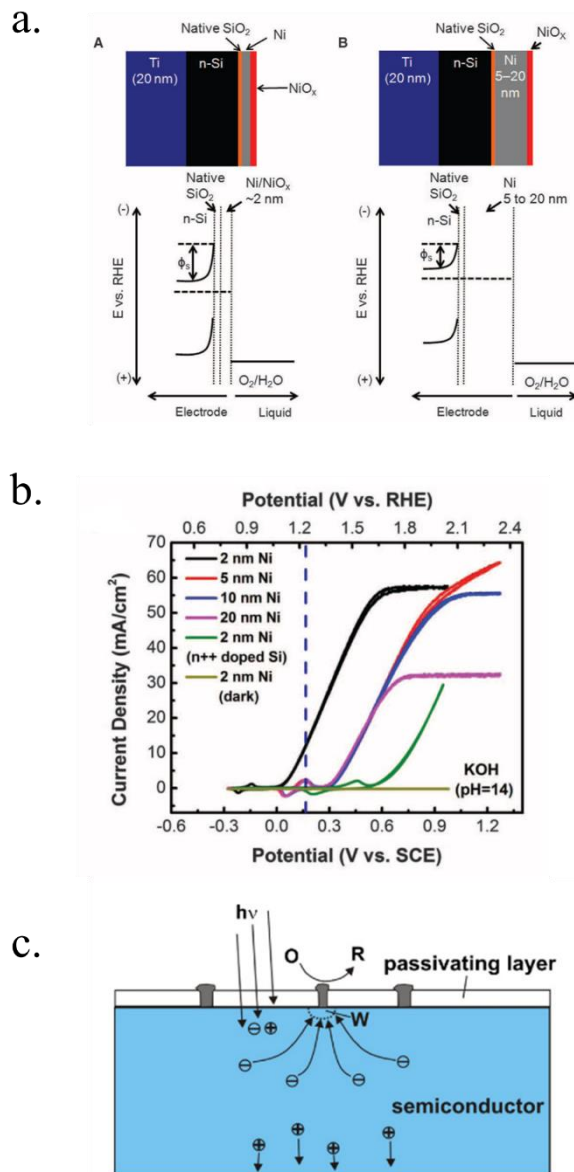


Figure 1.13. a) Scheme of *n*-Si photoanodes protected and catalysed by few nanometer-thick Ni films, demonstrating the effect of extremely thin layers compared to thicker ones. Reproduced from Kenney et al.¹⁷⁴ b) Cyclic voltammogram response of the same Ni-protected silicon photoanodes with different Ni thicknesses, presenting higher photopotential for ~2 nm films and light absorption if thicker than 10 nm. c) Scheme showing photogenerated charges being collected by the depletion formed between a semiconductor and metallic isles embedded in an insulator transparent protective layer. Reproduced from Lewerenz et al.¹²³

Although interesting results have been obtained with a metallic protective layer, the full potential of the photoabsorbers in long-term stabilities cannot be exploited due to insufficient

stability, significant light absorption in the metallic layer and significant recombination in the Schottky junction due to extra states in the interface and Fermi level pinning, lowering photovoltage¹⁷⁸.

To overcome metallic film transparency limitations, some works have proposed microstructured surfaces, with Pt islands (~30 nm thick) in contact with p-Si, and SiO₂ covering the rest of the surface, in a balance between surface coverage of catalytic metal and oxide-protected light absorption regions¹²³ (Figure 1.13c).

Regarding the limitations of metal-photoabsorber Schottky junctions, Seger et. al.¹⁷⁹ proposed a buried silicon p-n homojunction in 2012 to maximize electron-hole separation, with a thin Ti metallic film which partially oxidized to TiO₂ in the acidic electrolyte and using MoS₂ as catalyst. This way, up to 16 mA·cm⁻² were obtained at 0.2 V vs RHE (with 0.6 V photovoltage) and 1 h stability. Similar buried junction structure was used by Mei et. al.¹⁸⁰ using 2-6 nm Ir/IrO_x as protective layer in acidic electrolyte, avoiding detrimental SiO_x formation.

5.2.2. Tunnel-thick protective films

Insulator thin films (Figure 1.12c), mainly oxides, have been studied to protect water splitting photoelectrodes thanks to their chemical stability. However, the system must still be capable to inject the photogenerated charges across the insulator layer and into the electrolyte to perform the water splitting reaction efficiently. For that, tunnelling-distance-thick films in the few nanometers scale have been combined with catalytic films or particles, forming a metal-insulator-semiconductor (MIS) or semiconductor-insulator-semiconductor (SIS) scheme. Advantages of these structures are the passivation of photoabsorber surface states and the suppression of Fermi level pinning^{181,182}, but insulator oxides must be maintained under 3 nm thick to avoid significant tunnelling resistances¹⁶¹. ALD allows the fabrication of ultrathin conformal oxides, expected to be pinhole-free¹⁸³.

Silicon dioxide (SiO₂) was first studied due to its natural occurrence when Si is exposed to acidic electrolytes on a n-Si/SiO₂/Pt photoanode, with poor results¹⁸⁴. Esposito et al.¹⁸⁵ fabricated a 2 nm thick SiO₂ protected MIS photocathode by controlling the oxidation with rapid thermal oxidation (RTO) and depositing 30/20 nm Ti/Pt islands. Pt was used as HER catalyst, but Ti, with lower work function, enhanced photovoltage and also served as adhesion layer. Although 20/30 nm metallic islands are not transparent, controlling the pitch distance and diameter they could maximize light absorption and catalysis up to photocurrents of 20 mA·cm⁻² at 0 V vs RHE and 0.55 V vs RHE onset potential in 0.5 M H₂SO₄, with reported 2 h stability.

n-type silicon photoanodes were fabricated with SiO₂ and Ir as catalyst with photovoltages exceeding 500 mV and saturation photocurrents about 30 mA·cm⁻², although an ultrathin TiO₂ protective layer was needed to stop rapid further Si oxidation at oxidative potentials and

stabilize for over 8 h the photoanodes in acidic, neutral or basic media^{183,186} (Figure 1.14a and b). Planar and nanopillar p-InP was 3 nm n-TiO₂-protected and 2 nm Ru film was added as catalyst, achieving significant photocurrents of 35 mA·cm⁻² stable for some hours and 0.75 V vs NHE onset potentials¹⁸⁷. Photoanodes without the TiO₂ degraded rapidly during the first hour. In this scheme, increasing TiO₂ layer thickness turned into lower trap-mediated thickness-dependent conductivity indicating the importance of using a thin TiO₂ layer for efficient tunnelling-mediated electron transport^{183,188–190}. 490 mV photovoltage was also obtained substituting ultrathin TiO₂ by Al₂O₃, finding that tunnelling layers of a thickness > 2 nm introduce an intermediate resistance, lower than insulator SiO₂ but higher than defect-conductive TiO₂^{191,192}. Crystalline TiO₂ was found to reduce insulator-thickness-dependent photovoltage loss in metal-insulator-semiconductor (MIS) type photoanodes, in comparison with amorphous TiO₂ (ALD-fabricated at 170 °C), due to dielectric constant increase, with a record photovoltage of 623 mV¹⁹³. TiO₂ was proven as one of the best candidates, highly protective, and has been identified to be conductive for thicker than 10 nm layers, where tunnelling is highly non-probable. Indeed, hopping via trap states situated ~1 eV below the conduction band was considered the conduction mechanism in photoanode's case¹⁹⁴, following Campet et al “defect band” first proposed conductivity¹⁹⁵, and will be further discussed in the next section together with other thicker conductive oxides protective layers.

Ultrathin oxides, like metallic thin films, are difficult to fabricate being impermeable and pinhole-free for devices lasting hundreds of hours, and majority of the presented works lack long-term stabilities and device fail mechanisms over large device's area.

5.2.3. Conductive transparent oxides and other protective films

Increasing the protective layers thickness (Figure 1.12d and e) can overcome the stability limitations present in ultrathin metallic or insulating coatings, by avoiding possible electrolyte permeability or reducing pinholes and cracks probability. For films thicker than 5 nm, tunnelling conductivity is not possible, thus material electronic properties (interfacial potential barriers, band alignment, charge mobility, band bending, etc) must be taken into account, in addition to chemical stability (as explained in section 4). Also, protective layers must be intrinsically transparent and conductive, reducing candidates to mid band gap (2-5 eV) semiconductors, transparent to significant part of the visible spectra while not being insulator materials, such as Al₂O₃ and SiO₂ ($E_g > 9$ eV). Luckily the majority of metal oxides studied for protective layers are earth abundant and non-toxic as needed for device scalability¹⁹⁶.

For an efficient conductivity through protection layers, minimal losses in bulk resistance and semiconductor-electrolyte interface must be attained. The protective layers do not need to be as conductive as conventional transparent conductive oxides as only vertical (some tens of nanometers) conductivity is needed, not in-plane several hundred microns as in solar cells. In general, n-type metal oxide semiconductors have been used to protect photocathodes, based

on electrons migrating from the photoabsorber, through the protective layer, and injected in the HER. Fermi level close to the conduction band should help both to form a p-n heterojunction and for favourable alignment with the n-type part of the p-n buried junction. Likewise, p-type semiconductors have been proposed for photoanodes and have efficient OER catalytic surfaces^{97,148,196,197}. The role of cocatalysts on top of the protective layer and the electrolyte is majorly governed by the pinch-off effect, where with few nanometers thick layers, cocatalysts do not really form a Schottky barrier, and rather what is called “adaptive junctions”¹⁹⁸. Although, material specificities and the formation of recombining contacts have made materials such as TiO₂ highly versatile, multiple strategies are possible controlling deposition conditions, oxygen stoichiometry and other metals incorporation for better conductivity or catalysis¹⁹⁰. Transparent and conductive oxides used in the microelectronics industry, such as ITO and AZO, were expected to have good band offsets and conductivity, but their stability and performance resulted very poor^{195,199}. With thick oxides protective layers such as TiO₂, NiO, CoO_x and MnO, among others, better results have been achieved in terms of productivity and stability, with tens of mA·cm⁻², minimal resistances introduced and several hundred hours, even thousands, of operation tests.

a) TiO₂

Titanium dioxide has been one of the most studied materials as protective layer for small band gap photoelectrodes thanks to its transmittance, relatively good electrical properties and chemical stability. It is an earth abundant metal oxide found in nature and with several fabrication routes, such as anodization, hydrothermal, sol-gel and, for protective layers, mostly known to be fabricated by sputtering and ALD, giving compact layers in comparison with other solution-deposited ones¹⁴⁴. TiO₂ is a n-type semiconductor with ~3.2 eV band gap^{153,200}, permitting almost complete optical transmittance for visible light spectra, although thanks to its good chemical stability some works have used it also for back-illuminated photoelectrodes²⁰¹. Its n-type semiconductor behaviour is known to be caused by oxygen vacancies and thus, Ti³⁺ states with energy levels close to the conduction band, giving free electrons. TiO₂ is known to have significant oxygen mobility under polarization or under different atmospheres annealing, locally forming conductive filaments acting as degenerate n-type material across the whole layer, explaining various mechanisms reported depending on fabrication and working conditions¹⁶¹.

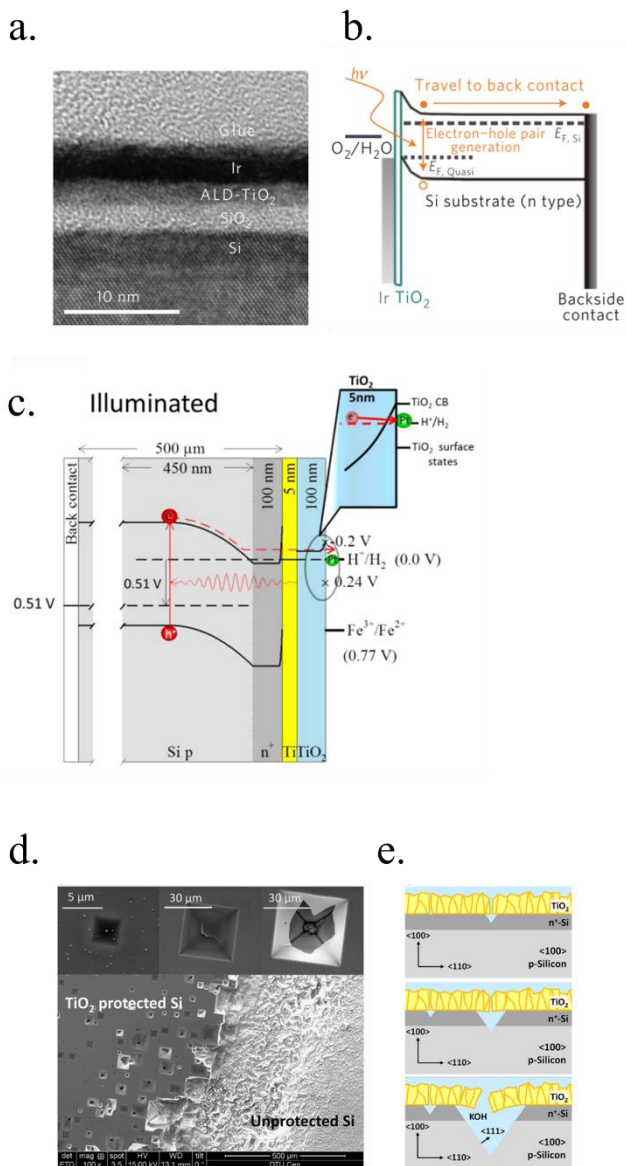


Figure 1.14. a) TEM image of an ultrathin ALD-TiO₂ + SiO₂ protective layer for a silicon photoanode. b) Equivalent energy band diagram under illumination. Reproduced from Chen et al.¹⁸³ c) Energy band diagram of a 5 nm Ti/100 nm-TiO₂ protected silicon photocathode having a buried p-n junction under illumination. Reproduced from Seger et al.²⁰² d) SEM images of a $\langle 100 \rangle$ Si TiO₂-protected and unprotected after immersion in 1 M KOH for 3 days. e) Schematics of the anisotropic etching process forming characteristic inverted pyramids. Reproduced from Bae et al.¹²².

Photocathodic protection with thick (~100 nm) sputtered TiO₂ was first reported in 2013 by Seger et al.²⁰² in a pn⁺-Si/(5 nm)Ti/(100 nm)TiO₂/Pt structure, where favourable band alignment between n⁺-Si, Ti/TiO₂ and TiO₂/Pt interface (behaving like an ohmic contact due to high dopant density of TiO₂ and high energy sputtered Pt, rather than like a Schottky junction^{203,204}) introduced negligible resistance or overpotential (Figure 1.14c). These findings show the system acting equivalently to a solar cell in series with the catalyst metal. They demonstrated conductivity through the conduction band, also explained to be electron polaron hopping through the Ti³⁺ states close to the conduction band (~0.3 eV)²⁰⁵, although the transition temperature between both mechanisms is reported to be about 300 K (room temperature)²⁰⁶ and probably both mechanisms are simultaneously active. Seger et al. introduced a 5 nm Ti layer previous to TiO₂ reactive-sputtering deposition to prevent Si substrate from oxidation, a strategy followed by other works^{122,153,201,207} based on oxygen migration to lowest Gibbs oxide formation energy and thus, oxygen scavenging from Si to Ti^{208,209}. Up to 20 mA·cm⁻² at 0.3 V vs RHE and 70 h of stability were obtained under illumination, corroborating the photoabsorber-protective layer strategy. In following works, durability was studied, reporting the need of 400 °C post-annealing to ALD-TiO₂ protective layers synthesized at 200 °C to reach from 8 to 480 h of stability at 0.3 V vs RHE in 1 M HClO₄²¹⁰. An increase of doping level under the 400 °C annealing was considered to be the reason of significantly higher conductivity, reducing depletion barrier between the TiO₂ and electrolyte, allowing electrons to tunnel through²¹¹, in similar results to Liang et al.²¹² increasing donor level by hydrogen doping upon deposition. Deposition techniques such as high power impulse magnetron sputtering (HPIMS)¹²² have been used to increase layer's density and thus, minimizing pinholes to avoid electrolyte penetration and anisotropic etch corrosion by KOH (Figure 1.14d and e). TiO₂ conduction band is close to the HER potential, and with sufficient dopant levels (i.e. oxygen vacancies), electrons can overcome by tunnelling the small potential barrier formed and reach the catalyst²⁰². Platinum, an expensive noble metal, has been widely used due to its superior cost-efficiency trade-off, and some works have demonstrated the scalability of very small amounts of platinum nanoparticles to drive the PEC water splitting industry to the terawatt level²¹³.

Regarding photoanodes, although TiO₂ should not be expected to be a good hole-conduction layer, in 2014, Hu et al.¹⁹⁴ discovered that depositing amorphous TiO₂ on Si, GaAs, and GaP conduction was possible for films up to 143 nm thick (grown by ALD at 150 °C and Ni coated). Energy states about 1 eV inside the forbidden band were observed by high resolution XPS (Figure 1.15a). Conductivity through intra-band gap levels was also explained by K. Sivula as “Leaky titania” (Figure 1.15b)²¹⁴, based on the concept theorized by Campet et al. time ago¹⁹⁵, and following works performed thoughtful energy band calculations to explain it^{154,215}. Deeper studies are necessary, as weak traces of anatase have been reported down to 140 °C²¹⁶. McDowell et al.¹⁵⁴ found TiO₂ films conduction behaviour not unique to amorphous phase (Figure 1.15c) and with no relation to carbon or nitrogen impurities, although high

temperature treatments turn the system insulator by forming a more-stoichiometric material, reducing available electronic states. Several works have studied thermal treatments under different partial pressures of oxygen and forming gas to understand how conductivity is affected by it^{154,161}. Nb doping could be a strategy to increment TiO₂ conductivity^{217,218}, but very good conductivity has already been demonstrated if properly fabricated. Other photoabsorbers such as CdTe have been protected with “leaky” amorphous TiO₂, with 21 mA·cm⁻² and 435 mV photovoltage²¹⁹. Nickel overlayer was found to be mandatory for proper contact with the conductive TiO₂¹⁹⁴, pinning TiO₂ energies to Ni states and removing the rectifying space-charge region from the TiO₂/solution interface^{141,220}; this is known for Ni as “adaptive” catalyst¹⁹⁸. Up to 100 h stability and 40 mA·cm⁻² at 2 V vs RHE were obtained in 1 M KOH, with 100 nm Ni islands as catalyst¹⁹⁴.

Although, in 2015, B. Mei et al.¹⁵³ designed TiO₂-protected by sputtering at 400 °C photoanodes (and photocathodes) where conduction band electron transport was proposed instead of intra-bandgap hole conduction. In the highly doped p⁺/TiO₂ interface holes from the photoabsorber would recombine with electrons from the conduction band of crystalline TiO₂ and metallic catalyst avoiding TiO₂/electrolyte rectifying junction²¹¹ and would allow efficient OER (Figure 1.15d). In a solid-state measurement for PV applications, Man et al.²²¹ studied n-Si and p-Si devices with amorphous TiO₂ deposited by CVD at 100 °C, and found a clear hole blocking behaviour, what would support conduction-band conductivity. Since then, ALD-TiO₂-protected silicon nanowire photoanodes stability has been pushed up to > 2000 h with 40 nm NiCrO_x catalyst film in 1 M KOH²²².

b) NiO

Several works have also studied nickel oxide (NiO) protective layers for water splitting photoelectrodes due to its abundance and chemical resistance, stability, transparency and catalytic properties. With a 3.8-4 eV bandgap^{223,224} it is not expected to absorb any visible light, although significant defects on NiO structure (Ni reduced atoms) can reduce transparency^{215,225–227}, even presenting electrochromism in specific cases caused by Ni³⁺ species such as NiOOH^{141,226}. It has been mainly used for photoanodes protection due to its p-type semiconductor behaviour²²⁸ prone to hole conductivity (and electron-blocking properties²²⁹) with relatively low resistivity^{227,230}. NiO has high valence band position as it is based on a d-orbital rather than typical O2p²³¹, being slightly reductive to O₂ evolution potential, where an accumulation layer will be formed introducing no band bending overpotential¹³².

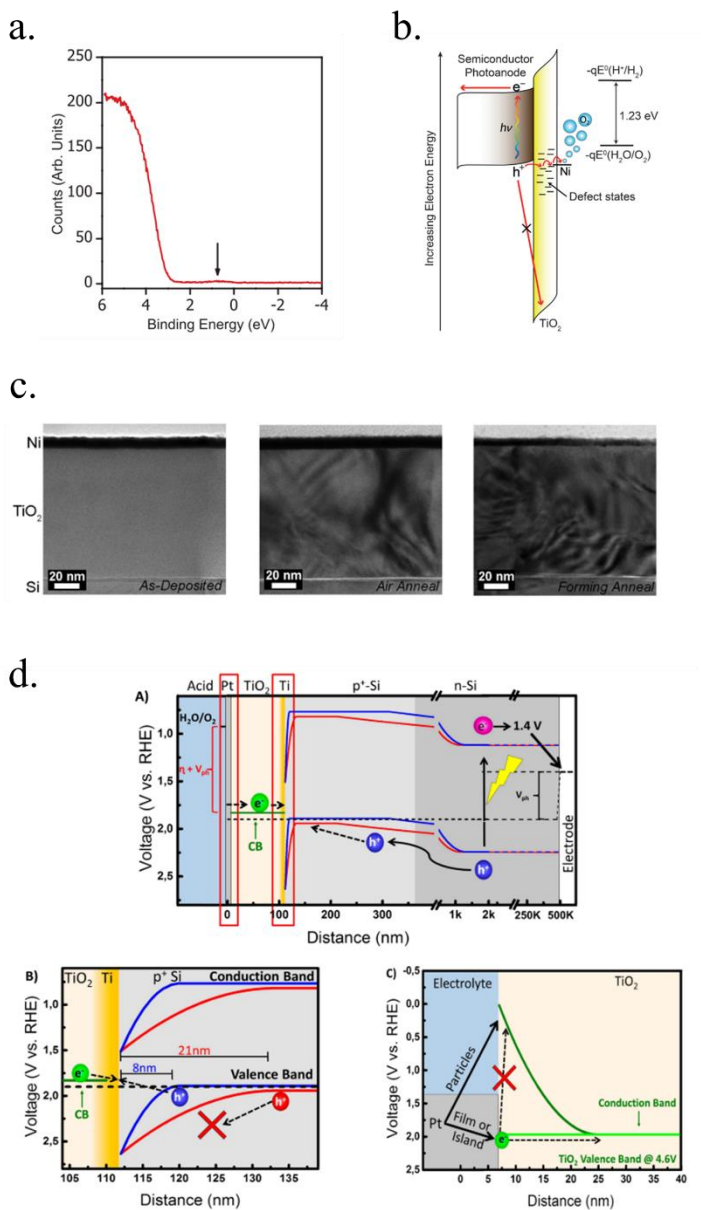


Figure 1.15. a) XPS spectrum of 44 nm-TiO₂ presenting states inside the band gap. Reproduced from Hu et al.¹⁹⁴ b) Schematic energy band diagram to explain the “Leaky” conductivity through intra-band gap states for TiO₂-protected photoanodes. Reproduced from Sivula.²¹⁴ c) Alternative energy band diagram proposed by Mei et al. where electrons are injected into the conduction band and recombine with p⁺-Si in an ohmic contact. Reproduced from Mei et al.²³² d) HRTEM images of as-deposited TiO₂ 100 nm layers, and Air annealed and forming annealed samples presenting crystallinity. Reproduced from McDowell et al.¹⁵⁴

Although, few works have used it for photocathodes, i.e. a Cu_2O electrode 10 nm-NiO protected²³³ with 70% retained current after 20 min in neutral pH, NiO is reduced in acidic electrolytes and cathodic HER potentials²³⁴. Its p-type semiconductivity is given by point defects and Ni^{2+} vacancies, and is explained by the Mott-Hubbard insulator theory¹³². The Ni^{2+} vacancies contribute with extra oxygen in the structure, which is compensated by oxidation of nickel sites to Ni^{3+} states, electron acceptors^{235–238}. Changes in these favorable imperfections due to atomic reorganization caused by temperature treatments, oxygen partial pressure or different layer growth process are crucial in achieving a conductive layer (Figure 1.16a)^{132,224,227,235,239,240}, with significant defects portion affecting on transparency. NiO films are known to present oxygen anions migration under polarization²⁴¹, up to filament formation²⁴², which must be taken in account as stoichiometry modifications can reduce or enhance conductivity.

Also, nickel is known to be one of the best earth-abundant OER catalysts in alkaline media²⁴³, where it is highly stable (but not in acid¹³²). First trials on nickel-based protective layers were performed directly depositing metallic Ni on top of the photoelectrode and letting it oxidize in contact with the electrolyte, but the hydroxide formed is highly porous and permeable^{244–246} after oxy-hydroxide species restructuration (migration) during initial operation²⁴³, hydrating up to 10 nm deep. Thicker Ni films, to protect the semiconductor beneath, would still contain a metallic layer, partially absorbing light and reducing photocurrent¹⁷⁴.

First NiO protected silicon p-n junction was performed in 1987 presenting several high overpotential²⁴⁷. In 2014, Mei et al.²⁴⁸ used reactive sputtering to deposit 50 nm thick NiO layers on a buried np^+ -Si homojunction previously protected with 5 nm Ni, inactive to OER if no pre-treatment in Fe-containing electrolyte was performed (Figure 1.16b). This achieved over 300 h stability of silicon photoanodes in 1 M KOH with $14 \text{ mA}\cdot\text{cm}^{-2}$ at 1.3 V vs RHE. Soon after, Sun et al.¹⁴⁷ reported 75 nm thick RF-sputtered NiO-protected photoanodes giving $30 \text{ mA}\cdot\text{cm}^{-2}$ at 1.73 V vs RHE over 1200 h (Figure 1.16c and d), where some defects attributed to arc-discharges during RF-sputtering were observed and partial oxygen pressure during synthesis is highly important in resulting conductivity²²⁴. III-V semiconductors such as InP could also be protected with the same kind of layers for over 48 h²²⁶ or CdTe, HTJ-Si or a-Si:H over 100 h²²⁴. Significant advance was obtained compared with previous attempts from 2012 with sol-gel NiO reaching $\sim 1 \text{ mA}\cdot\text{cm}^{-2}$ and losing 50% of performance in 1 h²⁴⁹ or 2013 NiRuOx sputtered to form an heterojunction with n-Si giving over 1 h stability with not much photovoltage¹¹⁸. ALD has only been used for NiO electroactive films few times²⁵⁰, with $\text{Ni}(\text{Cp})_2$ and O_3 as precursors at 275 °C deposition temperature. 3-18 nm thick films were found more resistive when ALD deposited than by other techniques together with the need of Fe atoms incorporation for sustained OER current (Figure 1.16e and f).

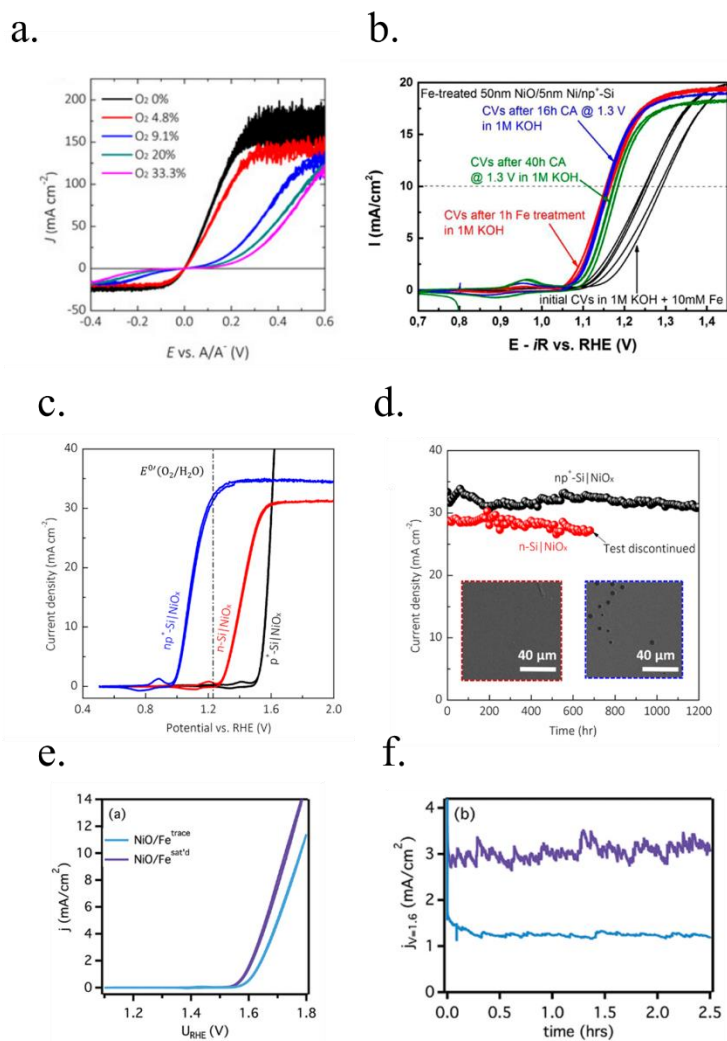


Figure 1.16. a) Cyclic voltammograms of NiO layers in $0.35 M Fe(CN)_6^{3-}/0.050 M Fe(CN)_6^{4-}$ in $1.0 M KCl$ as supporting electrolyte, demonstrating higher oxygen partial pressure during deposition reduces conductivity. Reproduced from Sun et al.²²⁴ b) Cyclic voltammograms of Fe-treated NiO thin films on p^+ -Si photoanodes presenting initial activation. Reproduced from Mei et al.²⁴⁸ c) Cyclic voltammograms and d) stability at 1.73 V vs RHE measurement of NiO layers protecting n -Si and np^+ -Si photoanodes, where higher photopotential can be observed with a buried junction and up to 1200 h stability. Measurements in 1 M KOH and 1 Sun illumination. Reproduced from Sun et al.¹⁴⁷ e) Cyclic voltammograms and f) stability measurements of anodes ALD NiO coated with traces (blue) and saturated (purple) Fe present in the 0.1 M KOH electrolyte, where higher activity and stability is obtained with more Fe present. Reproduced from Nardi et al.²⁵⁰

Nickel-based electrocatalysts are known to be enhanced after cycling at positive potentials¹⁴⁷, related to NiO hydration to NiOOH²²⁴ and incorporation of other metal traces, like Fe^{243,251,252} (with higher activated-state stability with higher amount of Fe incorporated²⁵⁰), Co²⁴³ and Ru¹¹⁸. The surface of nickel oxide is affected in its surface by alkaline electrolytes, forming oxy-hydroxides and porous nanoflakes with high surface area^{243,246} although it is stabilized by the presence of Co, partially inhibiting oxyhydroxide formation and restructuration²⁴³. These hydroxides (Ni(OH)₂) and oxy-hydroxides (NiOOH), important in various fields of chemistry and physics²⁴⁴, are not expected to create significant potential barriers with NiO beneath due to the porous and adaptive junction thanks to abundant electronic states and electrolyte penetration on first nanometers^{198,253}. Also, it is known to be the responsible of the efficient OER catalysis.

c) CoO_x

Cobalt oxide (CoO_x) is a metal oxide similar to NiO in many aspects. With p-type semiconductor behaviour and high conduction band edge, it is favourable to hole conductivity and as electron blocking layer¹³². It is expected to be transparent to large part of visible spectra due to its ~2.3 eV band gap^{254,255}. It is hydroxylated in contact with alkaline media into CoOOH, a known stable and active catalyst for O₂ evolution (OER)²⁵⁶, forming nanosheet/nanoflake structures^{257,258} (Figure 1.17a). Its OER catalysis is highly enhanced by fabricating it already containing Fe²⁵⁸ or incorporating Fe from the electrolyte²⁵⁸ with low overpotentials (~250 mV @ 10 mA·cm⁻²), close to NiFe²⁵⁷. Depositing few nanometers ALD CoO_x on np⁺-Si photoanodes up to 30 mA·cm⁻² were obtained by Yang et al at 1.4 V vs RHE in 1 M NaOH and 1 sun illumination stable for 24 h²⁵⁹.

Bae et al.²⁵⁴ sputter-deposited 50 nm thick NiCoO_x protective layers on back-illuminated photoanodes, reaching stabilities over 72 h and 22 mA·cm⁻² at 1.23 V vs RHE at pH 14 and further enhanced by Fe traces incorporation from the electrolyte. Xing et al.²⁶⁰ co-sputtered CoO_x with 3-8% vanadium 70 nm thick layers on 2 nm Cr protected p⁺n-Si textured photoanodes, with almost 30 mA·cm⁻² at 1.23 V vs RHE. Zhou et al.²⁶¹ CoO_x protected by ALD an n-silicon photoanode containing a thin SiO₂ layer to form a SIS heterojunction, reaching 570 mV photovoltage and 30 mA·cm⁻² at 1.23 V vs RHE and stable for up to 2500 h at 1.63 V vs RHE in 1 M KOH (Figure 1.17b, c and d). Burke et al.²⁵⁸ cathodically electrodeposited Co_{1-x}Fe_x(OH)₂ ~50 nm thick finding that the incorporation of Fe reduced up to 100 times OER overpotential compared to pure CoOOH thanks to strong Co-Fe coupling up to 60% Fe, but at higher amounts, conductivity was reduced and the layer dissolved as FeOOH is soluble in basic mediums unless incorporated in NiOOH or CoOOH. This would suggest CoOOH acts as “conductive, chemically stable, and intrinsically porous/electrolyte-permeable host for Fe, which substitutes Co atoms and serves as the (most) active site for OER catalysis”. Other metals such as Ru or Rh have been combined with CoO_x to further reduce its OER²⁶². Tung et al.²⁵⁶ found one of the causes of long-term instability is volume

expansion on phase change due to hydroxylation to CoOOH , and thus, nanoscale structuration can prevent detachment and efficiency loss.

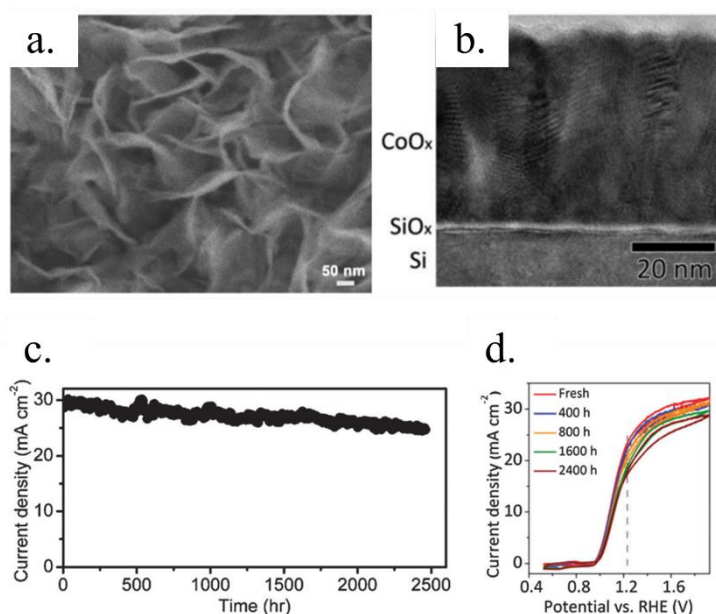


Figure 1.17. a) SEM image of Co(OH)_2 electrodeposited for 2 min. Reproduced from Jiang *et al.*²⁵⁷ b) High resolution cross section TEM images of polycrystalline CoO_x -protected n-Si photoelectrode. c) Stability measurement at 1.63 V vs RHE and d) cyclic voltammogram of the CoO_x -Protected n-Si photoelectrode under 1.1 sun illumination in 1 M KOH. Reproduced from Zhou *et al.*²⁶¹

d) Other conductive protective layers

Back in 1987, Kainthla *et al.*²⁶³ protected n-Si with **MnO** achieving stable photoanode for 650 h giving $1 \text{ mA} \cdot \text{cm}^{-2}$ at 1.3 V vs NHE in 0.5 M K_2SO_4 solution. In 2012, up to 20 nm ALD MnO films were used by Strandwitz *et al.*¹¹⁷ to protect n-Si and obtained almost $30 \text{ mA} \cdot \text{cm}^{-2}$ at 1.5 V vs RHE in 1 M KOH and 550 mV photovoltage, but not stable for more than 10 min. They also found film thickness increase introduced significant resistance, affecting fill factor.

Transparent and conductive thallium oxide (Tl_2O_3) was deposited 3-4 μm thick by Switzer *et al.*²⁶⁴ protecting an n-Si photoanode. A SIS junction was formed, with over 500 mV photovoltage and $33 \text{ mA} \cdot \text{cm}^{-2}$ photocurrent with a $\text{Fe(CN)}_6^{3+/4+}$ redox couple, although thallium is an expensive material with quite low abundance²⁶⁵.

$\sim 100 \text{ nm}$ sputtered n-type Nb_2O_5 formed an heterojunction with p-type GaP in a work by Malizia *et al.*²⁶⁶, achieving 710 mV photovoltage, although its stability was found less than TiO_2 protective layers in 1 M HClO_4 attributed to Nb_2O_5 detachment and thus, Pt cocatalyst loss (Figure 1.18a). Avoiding pinholes corroding photoabsorber beneath is important, as some

materials such as Nb_2O_5 , with expected good stability in acidic environments²⁶⁷, will not stop corrosion from beneath.

For GaP nanowires, Standing et al.²⁶⁸ directly grew a 20 nm electrochemically produced oxide Ga_2O_3 slightly increasing photovoltage and enhancing stability before depositing either Pt or MoS_2 HER catalysts. The list of possible protective layers will probably increase following years, as other authors have proposed other combinatorial metal oxides such as CuWO_4 , Co_3O_4 , SnO_2 , WO_3 , Ta_2O_5 for photoanodes or BaTiO_3 and Ta_2O_5 for photocathodes⁹³.

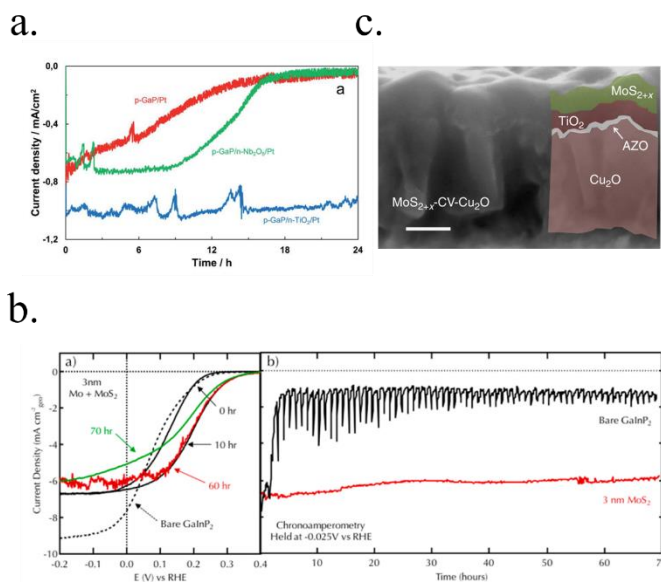


Figure 1.18. a) Stability measurements of GaP photocathodes unprotected (red) Nb_2O_5 (green) and TiO_2 protected (blue) in 1 M HClO_4 . Reproduced from Malizia et al.²⁶⁶ b) Stability measurement of a GaInP photocathode with and without 3 nm MoS_2 catalyst and protective layer. Reproduced from Britto et al.²⁶⁹ c) SEM cross section image of a Cu_2O photocathode AZO/ TiO_2 / MoS_{2+x} protected. Reproduced from Morales-Guio et al.¹⁰⁰

Non-oxide materials have also been studied. Among them, $\text{MoS}_2/\text{MoS}_x$, one of the best performing earth-abundant catalyst for the HER reaction²⁷⁰, has been used few times not just as catalyst, but also as protective layer. 1-5 nm of MoS_2 increases GaInP and Si photoelectrodes stability (Figure 1.18b)²⁶⁹ in acidic electrolytes. However, in 2012 Seger et al.¹⁷⁹ protected an n^+p -Si homojunction with 9 nm Ti and 35 nm MoS_x , and they attributed protection to Ti, on a self-limited oxidation to TiO_2 . Other authors have combined up to 100 nm MoS_x with TiO_2 to protect Cu_2O photocathodes (Figure 1.18c)^{100,271}. Laursen et al.²⁷² protected with MoS_2 a silicon photocathode by sputtering 10 nm Mo and reactive-annealing it with H_2S at 450 °C, obtaining stable photocathode for 120 h in 1 M HClO_4 . Recently, King et al.²⁷³ protected a n^+p -Si with 3.7 nm SiO_2 and ~11 nm $\text{MoO}_x/\text{MoS}_2$ (metallic Mo is

sputtered and further H₂S atmosphere annealed) achieving up to 62 days (1638 h) stability with $> 10 \text{ mA}\cdot\text{cm}^{-2}$ photocurrent at 0 V vs RHE in 0.5 M H₂SO₄.

6. Heterojunctions with the protective layer

Creating effective short band gap photoelectrodes requires highly conductive, transparent, stable and kinetically efficient protective layers and catalysts, but also to maximize the photovoltage of the system. For sensible-to-corrosion photoabsorbers, the electrolyte will not be in contact with the photoabsorber due to the introduction of the protective layer in between and thus, a semiconductor-liquid junction (SCLJ) will not be present to create an electric field to separate and extract photogenerated charges.

Forming an electronic junction between two different materials (at least one of them a semiconductor) forms an heterojunction. In this case, the maximum photovoltage of the photoelectrode is governed by the electronic properties of protective layers, photoabsorbers and interfacial energetics. Introducing heterojunctions results in a more complex device (Figure 1.12b-d), meanwhile it opens the possibility for higher photovoltages thanks to a larger amount of candidates available. Among them, three types of heterojunctions are considered: Schottky junctions (formed between a metal and a semiconductor), metal-insulator-semiconductor (MIS) junctions and semiconductor-semiconductor heterojunctions (composed of different materials).

6.1. Schottky and MIS junctions

In section 5 has been analysed how thin (few nanometers) metallic films can protect a semiconductor from corrosion, forming a Schottky junction (Figure 1.12b). However with limited stability and with significant recombination rates and Fermi level pinning caused by states in the metal-semiconductor interface, limiting electron-hole pseudo-Fermi level separation and thus, the photovoltage¹⁷⁸. Even so, selecting appropriate metals with work functions low for photoanodes and high for photocathodes is mandatory to obtain significant photocurrents and photovoltages¹⁶⁵. Very small photovoltages are obtained from just directly depositing Pt or Ni on p-Si, meanwhile 200 mV more can be generated with a p-Si/5nmTi contact previous to Pt catalyst (Figure 1.19a)^{173,176} or Ni catalyst¹⁷⁷ thanks to higher Schottky barrier created by the favourable work function of Ti.

Introducing few nanometers of insulator materials between the semiconductor and the metal film (Figure 1.12c), such as SiO₂ or Al₂O₃^{178,274}, can passivate interfacial electronic states and enhance energy level separation in the heterojunction (forming a metal-insulator-semiconductor junction, MIS). Specifically, Al₂O₃ is favourable to unpin the Si Fermi level, giving extra built-in potential. Regarding selected metal, Pt has higher work function than Ni and increases photovoltage in n-Si photoanodes (Figure 1.19b)²⁷⁴. Laskowski et al.¹⁷⁵ suggest high barrier regions are formed when Si is oxidized to SiO₂ due to electrolyte (pH 9.8 K-borate buffer) permeability in very thin (~3-5 nm) Ni films, avoiding Ni/n-Si Fermi level pinning and thus, increasing photovoltage (Figure 1.19c and d).

Following this, several works have focused on the passivation of Si surface states with ultrathin semiconductor layers (0-12 nm) such as TiO_2 , although the junction is formed between the metallic film on top and the silicon, and thicker intermediate layers will increase metal to semiconductor separation, reducing formed photovoltage¹⁸⁹. SrTiO_3 epitaxial films, MBE-deposited by Ji et al.^{275,276} on p-Si with patterned 50 nm Ti/Pt catalyst formed a stable (>35 h in 0.5 M H_2SO_4) and effective photocathode ($35 \text{ mA} \cdot \text{cm}^{-2}$ at -0.4 V vs NHE, 450 mV photovoltage) when only few unit cells (4-6, ~ 1.6 nm) of the strontium titanate were deposited. The space-charge region is formed between the p-Si and metallic Ti, with lower work function than Pt, as it has a work function similar to p-Si, and would generate small photovoltage. Although, these insulator layers introduce significant tunnelling resistance if thicker than 3 nm ¹⁶¹ and do not significantly increase stability to corrosion.

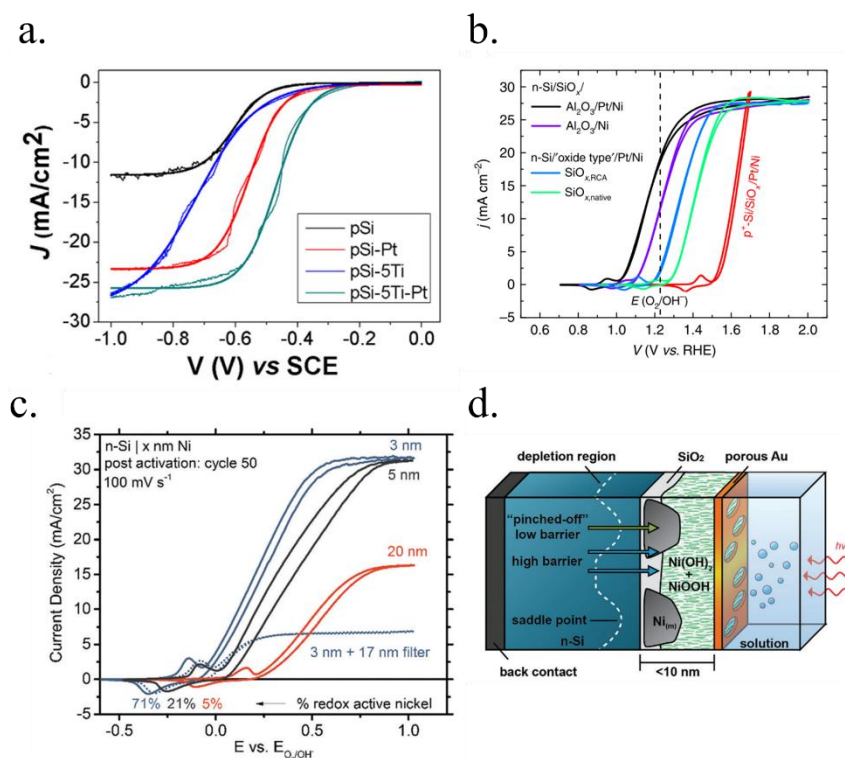


Figure 1.19. a) Cyclic voltammogram of p-Si photoanodes where higher photovoltages can be observed if 5 nm Ti is used to form the Schottky junction and Pt on top as HER catalyst. Reproduced from Sartori et al.¹⁷⁶ b) Cyclic voltammograms of n-Si photoanodes presenting higher MIS photovoltage if Al_2O_3 is used as ultrathin insulator layer and Pt as the metal intervening thanks to its work function, together with Ni as OER electrocatalyst. Reproduced from Digdaya et al.²⁷⁴ c) Cyclic voltammogram and d) scheme depicting the formation of adventitious interfacial ultrathin SiO_2 preventing Fermi level pinning due to electrolyte (pH 9.8 K-borate buffer) penetration, and thus, forming higher photovoltage. Reproduced from Laskowski et al.¹⁷⁵

6.2. Semiconductor–semiconductor heterojunctions with thick oxides

Similar schemes can be formed with thicker conductive oxides semiconductors instead of metals (Figure 1.12d), overcoming metal films limitations on thickness and transparency. In this case, heterojunctions between two semiconductor materials will be formed, where a thin insulator film can be introduced in the interface avoiding Fermi level pinning if necessary (forming a semiconductor-insulator-semiconductor (SIS) junction). Similar electronic structure to section 3.6 will be formed, but doing so with a short band gap material and a wide band gap metal oxide has a great benefit: the major part of photon absorption will occur in the short band gap one, collecting large portion of the visible spectra. Also, short band gap materials such as Si, GaAs or CIGS are very good photoabsorbers, with minimal recombination and transport losses.

Thicker-than-tunnelling metal oxides have been widely used both to protect short band gap semiconductors and to generate a built-in electric field. N-type wide band-gap semiconductors such as ZnO, WO₃ or TiO₂ have favourable energetics to form a heterojunction with p-type photoabsorbers such as Si, InP or CIGS in a similar strategy to SIS solar cells²⁷⁷. In 1996, Yoon et al. tested a different thickness n-type WO₃ on p-Si, achieving a better photovoltage by controlling resistivity, carrier concentration and surface band bending (Figure 1.20a)²⁷⁸. In 1998²⁷⁹ they electron-beam evaporated 50 nm WO₃ on top of p-Si with 1-2 nm Pt as catalyst, and the role of a more efficient built-in field is clearly observed when introducing WO₃, with a better HER catalysis when Pt is incorporated (Figure 1.20b). Although, WO₃ was found not to be stable if Pt was not blocking direct contact of WO₃ with the acidic electrolyte (0.1 M H₂SO₄). By the introduction of an indium-doped tin oxide (ITO) layer, Coridan et al.²⁸⁰ demonstrated not such a good interface is formed between WO₃ and Si, and the ITO layer could also act as an ohmic contact, allowing them to create a tandem cell. Wang et al.²⁸¹ also demonstrated Fe₂O₃ heterojunction with n-Si and p-Si photoelectrodes.

Transparent conductive oxides (TCO) such as ITO and AZO were tested, as theoretically should be good conductive and transparent n-type semiconductors for photocathodes and thus, form good p-n heterojunctions. ZnO (~3.1 eV) was deposited by Sun et al. as a film and as nanorods on planar p-Si and nanowire-grown p-Si²⁸², achieving better light absorption and active surface area thanks to the nanostructures and HER catalysis enhanced by Ni, Pt and Pd cocatalysts (Figure 1.20c). p-type Cu₂O electrodes can also form an heterojunction with n-ZnO reaching more than 7 mA·cm⁻², although TiO₂ was required for higher stability even in 1 M Na₂SO₄ at reductive potentials^{77,100}. Although, stability was limited to few minutes as ZnO is an amphoteric metal oxide unstable in alkaline and even more in acidic electrolytes²⁸³.

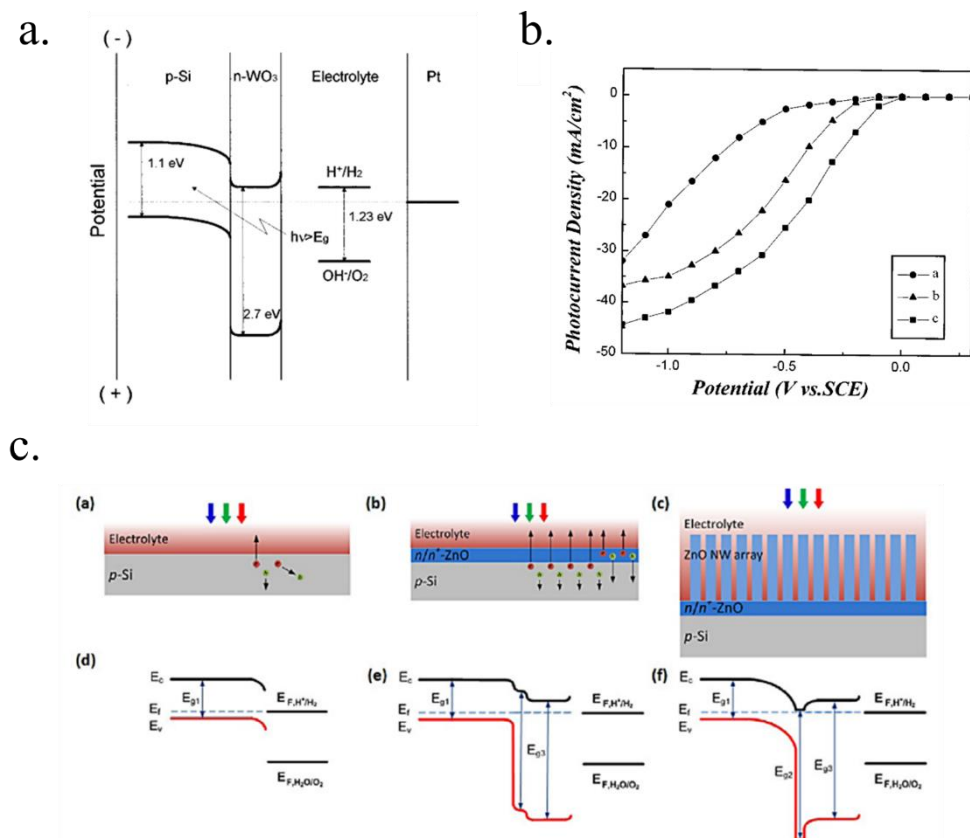


Figure 1.20. a) Scheme of a p-Si/n-WO₃ heterojunction. Reproduced from Yoon et al.²⁷⁸ b) Cyclic voltammograms of a p-Si, a p-Si/n-WO₃ and a p-Si/n-WO₃/Pt catalysed photoelectrodes. Reproduced from Yoon et al.²⁷⁹ c) Schemes (top) and energy band diagrams (bottom) of p-Si (left) p-Si/n⁺-ZnO (center) and p-Si/n⁺-ZnO/ZnO-NW (right). Reproduced from Sun et al.²⁸²

Designing a **photocathode** with TiO₂ as n-type semiconductor and transparent protective oxide forms a p-n junction when put in contact with a p-type photoabsorber such as Si, InP or CIGS. Seger et al.²¹¹ deeply studied the built-in fields generated between p-Si and TiO₂, and in the TiO₂-electrolyte interface (Figure 1.21a-c), with depletions only possible to be tunneled through if doping levels are high enough. Lin et al.²⁸⁴ demonstrated the junction formed between p-InP and 10 nm n-TiO₂ (Figure 1.21d). Azarpira et al.²⁸⁵ deposited ~100 nm n-type Pt-doped anatase TiO₂ on p-type Cu(In,Ga)Se to form the heterojunction of a photocathode, with Pt also enhancing HER catalysis (Figure 1.21e and f). 300 mV photovoltage was achieved, with onset potential at ~ 0.23 V vs RHE but photocurrent saturation (37 mA·cm⁻²) at -0.3 V vs RHE, significantly worse than a commercial CIGSe PV cell. This is because directly depositing one on top of the other does not take into account interfacial recombination, states passivation, etc, which have been circumvented in CIGSe PV devices by highly optimized superficial pre-treatment, n-type CdS chemical bath deposition and

multilayer TCO top contact²⁸⁶. Thus, directly depositing TiO₂ in top of a short band gap photoabsorber is a simpler strategy but maybe not so effective as protecting a buried solar cell cell²⁸⁷.

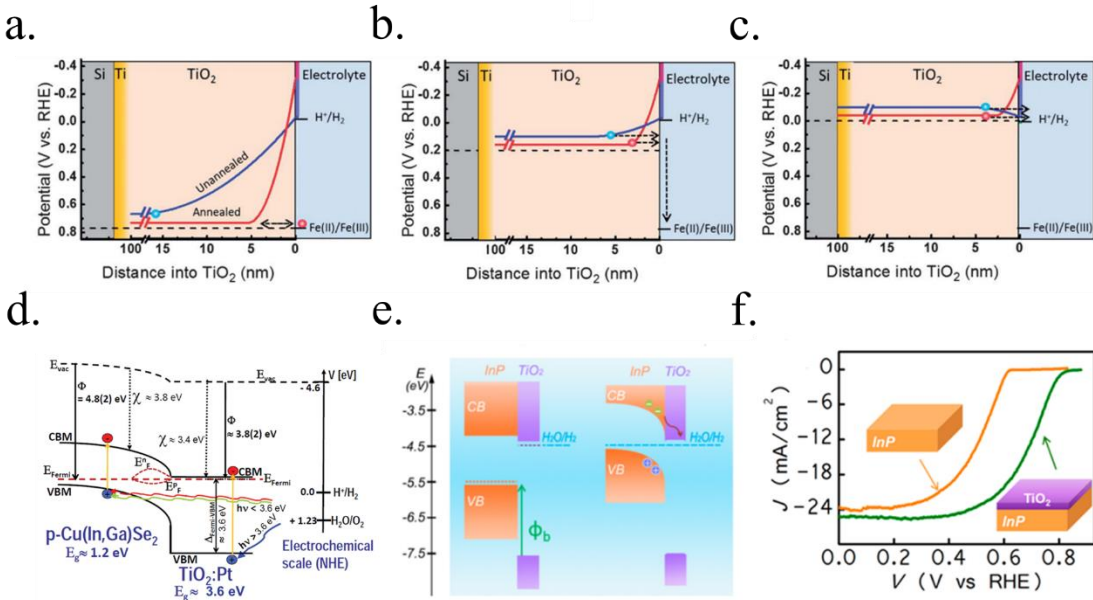


Figure 1.21. The effect of annealed and unannealed TiO₂ protective layers on detrimental superficial band bending at different potentials a) +0.77 V vs RHE, b) +0.2 V vs RHE and c) 0 V vs RHE. Reproduced from Seger et al.²¹¹ d) Heterojunction formed between a p-CIGSe and n-TiO₂:Pt film. Reproduced from Azarpira et al.²⁸⁵ e) energy band diagrams and f) cyclic voltammograms response of an InP/TiO₂ heterojunction. Reproduced from Lin et al.²⁸⁴

Metal oxide protective layers acting as part of the heterojunctions for **photoanodes** also introduce some benefits. Transition metal oxides such as CoO_x^{132,259} or NiO²⁴⁹ have high work function due to oxygen vacancies and cation oxidation states²⁸⁸, what can be used when designing photoelectrodes heterojunction to increase built in electric field and also as hole transporter and electron blocking layers. 37 nm sol-gel nickel oxide can form a 300 mV photovoltage²⁴⁹ and 75 nm sputtered NiO ~350 mV¹⁴⁷ on n-Si. Although, these photoanodes are far from the photovoltages obtained with buried p-n junctions (550-600 mV)¹⁴⁷ due to Fermi level pinning in the Si-MO_x interface. Almost no photovoltage is obtained with a p-NiO/n-InP heterojunction due to strong pinning, whereas with a buried p⁺n-InP ~700 mV were obtained²²⁶. Zhou et al.²⁸⁹ coated n-Si photoanodes having ~2 nm SiO_x or ~2 nm SiO_x/2-3 nm ALD-CoO_x with ~100 nm sputtered NiO, and found the thin CoO_x interlayer introduces up to 165 mV extra photovoltage reaching 560 mV helped by the de pinning caused by the thin SiO₂ (Figure 1.22a and b). CoO_x increases band bending at the interface due to 120 mV larger work function of CoO_x in respect to NiO. This way, photovoltages close to

n^+p -Si junctions and $30 \text{ mA} \cdot \text{cm}^{-2}$ stable for 1700 h (70 days) were obtained. Other p-type semiconductors such as Fe_2O_3 ^{290,291} have been used to form heterojunctions with n-Si.

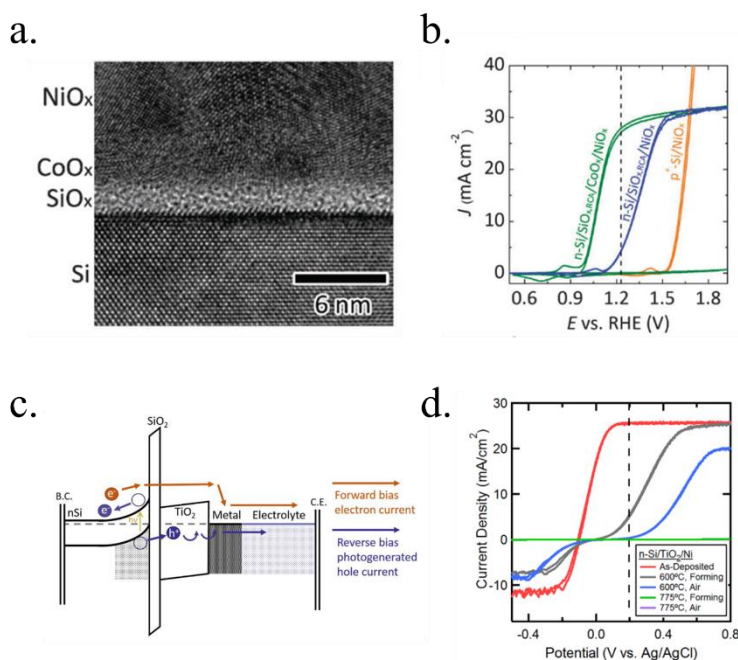


Figure 1.22. a) HRTEM cross section and b) cyclic voltammograms of an $n\text{-Si/SiO}_x/\text{CoO}_x/\text{NiO}_x$ SIS junction (green), where higher photovoltage is obtained thanks to 120 mV greater CoO_x work function. Reproduced from Zhou et al.²⁸⁹ c) Band diagram of an $n\text{-Si/SiO}_2/\text{TiO}_2/\text{Metal}/\text{Electrolyte}$ photoanode presenting hole hopping through TiO_2 intra-band gap states. Reproduced from Scheuermann et al.²⁹² d) Cyclic voltammograms of $n\text{-Si/TiO}_2/\text{Ni}$ photoanodes treated at various temperatures, showing SIS junction detrimental effects with high temperature treatments by reducing states availability in TiO_2 . Reproduced from McDowell et al.¹⁵⁴

As explained in section 5.2.3.a), TiO_2 , although being an n-type semiconductor, has been reported to be efficiently conductive for water oxidation when grown amorphous, with mid-bandgap states ($\sim 1 \text{ eV}$ below the conduction band) allowing hole conductivity by hopping through them^{194,214,292,293} after tunnelling through the thin SiO_2 interface. These energy states are considered to equilibrate with n-Si Fermi level, generating photovoltage (Figure 1.22c). Ni catalyst was reported to be mandatory for properly contacting these states through a less defective TiO_2 surface and thus, allowing connexion with the OER catalysis^{161,194}. The fabrication process (ALD, sputtering) and specific doping conditions of TiO_2 (caused by post-annealing process modifying the Ti states density, carbon contaminants, etc) has been reported to be highly related to final SIS junction photovoltage in a $n\text{-Si/TiO}_2/\text{Ni}$ photoanode (Figure 1.22d)¹⁵⁴. Heterojunctions with the amorphous TiO_2 have also been fabricated with other photoabsorbers, such as $n\text{-CdTe/TiO}_2/\text{Ni}$, with 435 mV photovoltage and $21 \text{ mA} \cdot \text{cm}^{-2}$ ²²¹⁹. If protective layers do not have the optimal energy band levels and interface energetic

states, degenerately doped layers will screen metallic catalyst work function and limit performance¹⁶¹. Meanwhile, slightly doped protective layers, if thicker, will introduce overpotentials from electrical resistivity, proportional to metal oxide thickness. To prevent this, buried junctions can maximize the obtained photovoltage by themselves, not depending on the protective layer.

7. Buried homojunctions to maximize efficiency and cell flexibility

As it has been analysed in previous section many efforts have been put in forming heterojunctions to directly create a built-in field between the metal oxide protective layer and a short band gap semiconductor. So far, even the achieved photovoltages have been significant, they are not as high as the ones for short band gap semiconductors reported for photovoltaic solar cells (with open circuit potentials of up to 750 mV)^{111,294}. Buried p-n junctions (Figure 1.12e) have been proven to generate higher built-in electric fields than SCLJ or Schottky junctions, decoupling photoabsorbers Fermi level from that of the metallic or oxide protective layer or electrolyte, also removing a constrain on the catalyst required work function value^{161,295}. This way, a more flexible device design is possible as each component (photoabsorber, protective layer and catalyst) can be selected more independently as it can be observed in Figure 1.23a and b. Thus, several groups have shifted the strategy and worked on adapting solar cell p-n junctions for water splitting, obtaining the highest reported performances of PEC cells¹³².

Several photovoltaic-used schemes have been studied, being silicon the most implemented one by far. Not only because is the most used one for solar cells, dominating the solar panels market, but also because of the simple and robust cell obtained: a monocrystalline silicon solar cell can be fabricated several tens of centimetres wide, few hundred microns thick and is robust, not requiring any substrate. Also, as p-n junctions are fabricated in silicon wafers by dopant diffusion and incorporation in its crystal lattice at fabrication temperatures of up to 1025 °C¹⁵³, further thermal steps applied at medium temperatures (up to 500 °C) will not damage the p-n junction and will retain original output. In a buried junction electrode, photogenerated charges will migrate to the catalyst/electrolyte interface through protective layers, acting as conductive contacts: n-type semiconductor protective layers should be expected to be prone for electron conductivity in photocathodes (Figure 1.23c), and p-type semiconductors for holes in photoanodes (Figure 1.23d). Although, other strategies such as mid-band gap states in n-type semiconductors have been proposed for hole conduction (Figure 1.23e) or recombining contacts (Figure 1.23f), as will be reviewed later. As example, photovoltages as high as 630 mV have been obtained for silicon with buried p-n junctions²⁹⁴. Other semiconductors have been tested apart from silicon with same protective and catalyst strategies, proving these to be highly reproducible in other photoabsorber materials, increasing device flexibility²⁹⁶.

As it was reported by Scheuermann et al.¹⁸⁹ and Wang et. al.²⁹⁶, once a buried junction is introduced in our device, the requirements of the protective layer or the co-catalyst metallic film are reduced. Optimal work function metallic films or cocatalysts to create high electric field with the photoabsorber are no longer needed, widening material selection possibilities. The protective layer just needs to be chemically stable, highly conductive, transparent and the surface must not create electronic barriers with the electrolyte, together with being kinetically

efficient for the HER or OER reactions, normally achieved by the addition of co-catalyst particles or films. What is equally necessary, though, is that no electrical barriers formed between the top contact of the p-n junction and the protective layer.

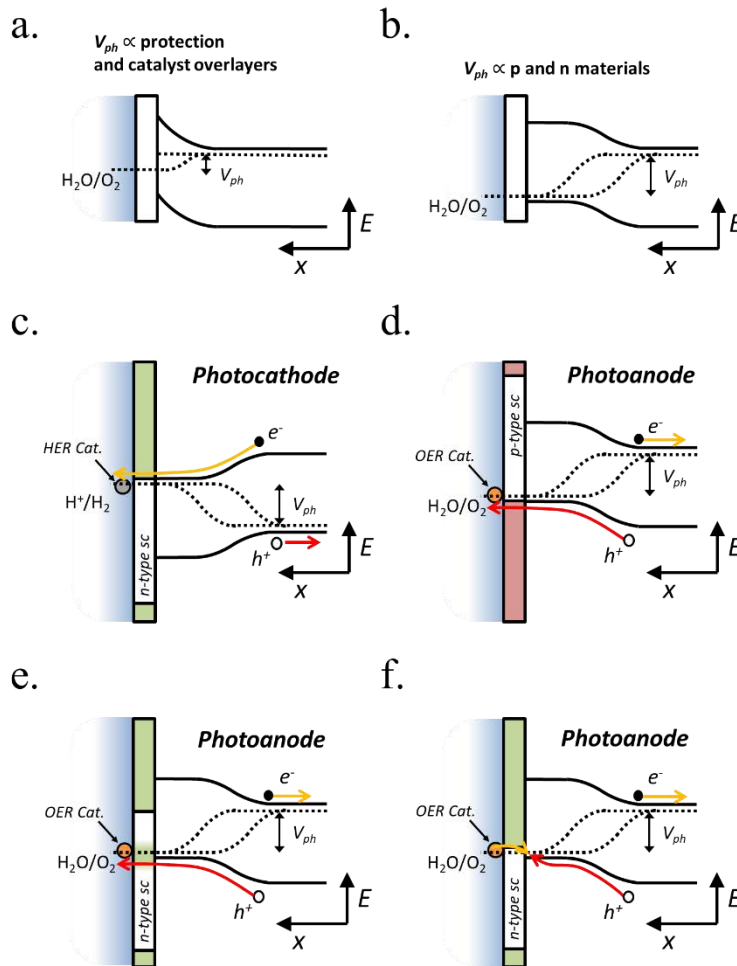


Figure 1.23. Energy band schemes of a) a junction depending on the photoabsorber/electrolyte interface or intermediate layers (i.e.: SCLJ, Schottky, MIS, SIS...) and b) a buried junction, only dependent on the semiconductor materials forming the junction quality (i.e.: n-Si/p-Si, CIGS/CdS...). c) Photocathode protected with an n-type semiconductor layer. d) Photoanode protected by a p-type semiconductor hole transporting layer. Photoanodes protected with n-type semiconductors layers thanks to e) mid-band gap states conducting holes and f) contact for electrons recombining with holes from the photoanode.

Several works have obtained this by creating degenerately doped ohmic contacts, the most used case for silicon being p^+/n^+ (acting like metals) top contacts in the photoanode/photocathode buried junction, shielding the built-in electric field from protective layer's interaction. Even if an upward band bending is present on the n^+/p^+ surface, its depth

would be limited to few nanometers due to the high doping level, easily permitting charge tunneling through these depletions, facilitating the ohmic contact^{180,202,296}. Seger et al. introduced a metallic 5 nm Ti film between n^+p -Si and MoS_x ¹⁷⁹ or TiO_2 ^{122,202}, to form an ohmic contact and to prevent Si oxidation into detrimental insulator SiO_2 (Figure 1.24a), meanwhile in a photoanode, for Mei et al.¹⁵³ a similar structure acted as an ohmic recombining contact between holes from p^+ -Si and electrons from TiO_2 conduction band (Figure 1.24b).

An example of the benefits of a buried junction is the work by Scheuermann et al.¹⁸⁹, where they tried to maximize n -Si photoanodes with few nm SiO_2 and $\text{SiO}_2/\text{TiO}_2$ layers and Ir catalyst, reaching maximum 500 mV highly sensible to SiO_2 thickness, whereas with a buried n^+p -Si junction independent 630 mV were obtained. Similar maximum photovoltages for n -Si/ p -Si and n^+p -Si/ p^+n -Si PEC electrodes were obtained by other authors^{117,140,174,179,180,183,189,194,202,210,297}.

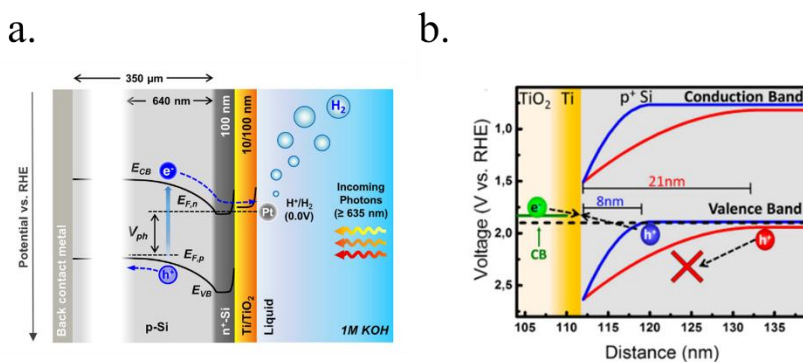


Figure 1.24. Metallic thin Ti films on degenerately-doped silicon assuring ohmic contacts in a) a photocathode (Reproduced from Bae et al.¹²²) and b) a photoanode, where holes recombine with electrons from the conduction band of the protective layer (Reproduced from Mei et al.²³²).

Likewise solar cells prospects¹⁰⁹, decreasing fabrication costs by depositing thin film photoabsorbers on flexible substrates can help on reducing device costs and facilitating technology implementation²⁹⁸. CIGS-CdS buried junctions have been adapted for water splitting^{287,299–302}, together with their earth-abundant³⁰³ equivalent CZTS^{300,304–306} and In_2S_3 ^{304,307} or ZnS ^{308,309} to substitute toxic CdS. The capacity of these cells band gap and thus, photovoltage, to be tuned by compositional variations (1.0–1.5 eV)²⁹⁸ reaching record 741 mV photovoltages and $37.8 \text{ mA}\cdot\text{cm}^{-2}$ can help to form tandem cells^{310–313}. Metallic Mo/Ti films have been used on CIGS/CdS and increased both photocurrent and onset potential, together with laterally transporting charges and avoiding detrimental interfaces with CdS or Pt particles, and also helped to protect the p - n junction (Figure 1.25a and b)²⁸⁷. Efficiently extracting photogenerated charges in polycrystalline defective materials such as CIGS is important to enhance photovoltage and current, as charge diffusion lengths are significantly lower than in silicon³¹⁴. In addition, it is known for solar cells that degenerately doped

transparent conductive oxide (TCO) such as i-ZnO/Al:ZnO have significantly increased photovoltage²⁹⁸. For PEC, directly protecting the p-n junction proved for earth abundant CZTS significantly less effective³¹⁵ than including a degenerate TCO in between n-CdS and TiO₂ protective layer^{285,305} (Figure 1.25c).

In recent years, several other examples of buried junctions can be found, resembling solar cell structures with other materials. In 2014, Kast et al.²⁰⁷ protected a commercial textured n⁺p silicon solar cell with 10 nm Ti/50 nm F:SnO₂/50 nm TiO₂ and 2 nm Ir as HER catalyst to form a photocathode, obtaining onset potentials ~0.6 V vs RHE and >30 mA·cm⁻². 610 mV photovoltages were produced by a CoO_x protected p⁺n-Si photoanode²⁵⁹ or >550 mV with a radial n⁺p junction on Si nanowires²⁹⁵.

Also, Bae et al. fabricated a silicon photoanode²⁵⁴ and a thinned photocathode (Figure 1.25d and e)²⁰¹ to be back-illuminated, a configuration which would easy creating a tandem between two electrodes for a bias-free reaction. For it, they used similar strategies as previously reported: degenerately doped p⁺/n⁺ Si surfaces with 50 nm NiCoO_x / 5 nm Ti-100 nm TiO₂-Pt respectively for efficient OER/HER reactions. In back-illumination there is no need for transparent protective layers, although several tens of nanometers metal oxide layers are some of the best candidates to chemically protect from corrosion and to catalyze the OER reaction.

In the path of burying the photoactive part of the solar cell, 300 nm thick amorphous silicon p-i-n junctions could be adapted and protected with 80 nm TiO₂, producing 930 mV photovoltage¹⁵². Both a HTJ-Si (p⁺-a-Si|i-a-Si|n-c-Si|i-a-Si|n⁺-a-Si) and an n-i hydrogenated amorphous Si (a-Si:H) buried junctions were protected with transparent and catalytic reactive-sputtered 75 nm p-NiO²²⁴, with several hundred hours stability in 1 M KOH and photocurrents of 35 and 5 mA·cm⁻², respectively, similar to equivalent solar cell ones. In another work, an amorphous/crystalline silicon heterojunction (a-Si/c-SiHJ) was fabricated both as photoanode or photocathode, just inverting where the cell is contacted (Figure 1.25f and g), with > 600 mV photovoltages³¹⁶. This structure reported up to 13.26% solar-to-hydrogen conversion efficiency, one of the highest achieved so far.

Moreover, by molecular beam epitaxy (MBE) depositing a 100 nm thick p⁺-InP layer on top of n-InP (1.3 eV band gap), Sun et al.²²⁶ fabricated a photoanode, further protected with sputtered 70 nm NiO, which was capable to generate 700 mV, whereas thinner InP p⁺ layers produced ~350 mV. An amorphous p-i-n silicon carbide (a-SiC) buried junction was also protected with 25 nm TiO₂ and converted into a photocathode using NiMo as catalyst by Digdaya et al.³¹⁷, obtaining the 0.8 V photovoltage expected for the buried junction although limited stability of less than one hour in 1 M KOH was obtained.

Thus, complex buried junction schemes are proven to be readily adapted to PEC with metallic or degenerately doped intermediate layers, confirming the flexibility and advantages of protecting buried junctions²⁹⁶.

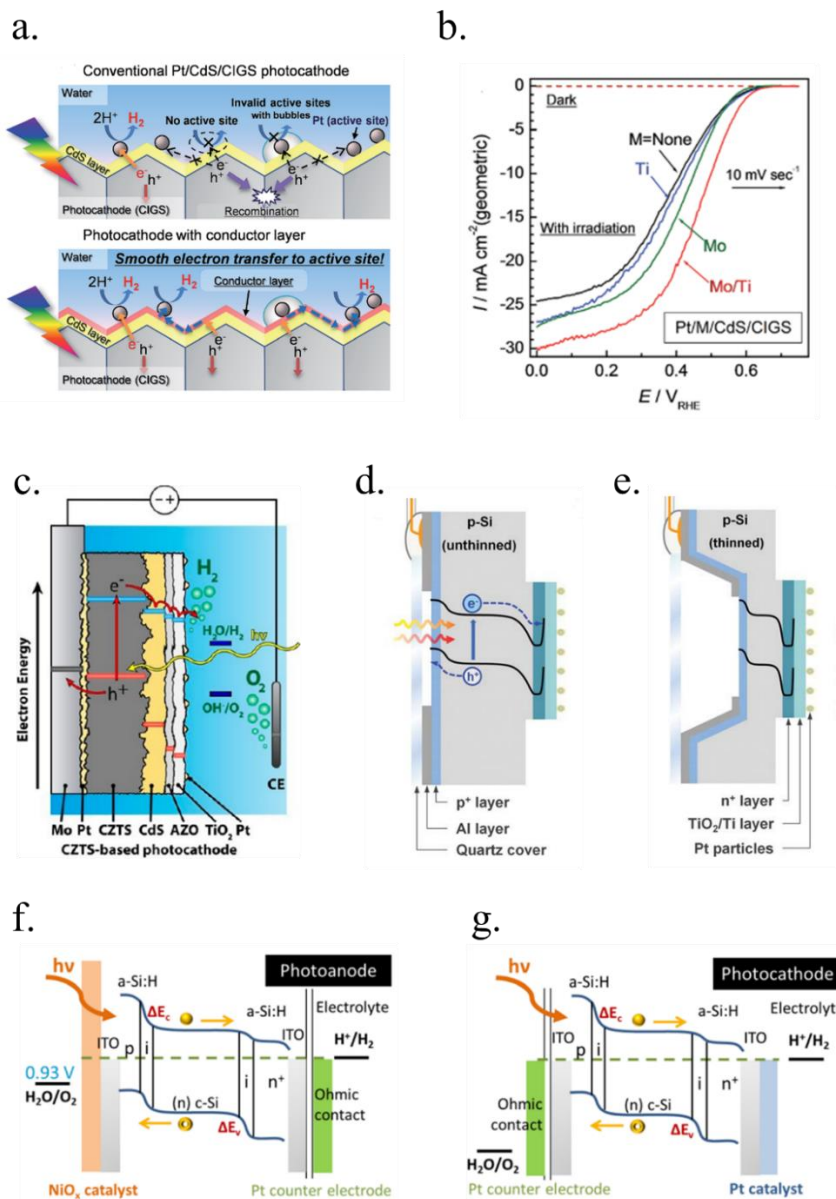


Figure 1.25. a) Charge transfer diagram from the n-type CdS layer to HER catalyst particles (top) and with an intermediate metallic conductive film enabling lateral conduction (bottom) and b) corresponding cyclic voltammograms in $0.5 \text{ M Na}_2\text{SO}_4$, $0.25 \text{ M Na}_2\text{HPO}_4$ and $0.25 \text{ M NaH}_2\text{PO}_4$ (aq.) (pH values adjusted to 6.8 by NaOH addition under AM 1.5G irradiation. Reproduced from Kumagai et al.²⁸⁷ c) Energy band diagram of a CZTS/CdS buried heterojunction protected with AZO/TiO₂ layers and Pt catalysed. Reproduced from Rovelli et al.³⁰⁵ d) Back illuminated photoelectrode before thinning and e) after thinning to properly illuminate the p-n junction energy band diagrams. Reproduced from Bae et al.²⁰¹ Energy band diagrams of p-i-n amorphous silicon f) a photoanode and g) a photocathode showing the role of ohmic contacts, enabling the possibility to easily invert the photoelectrode's structure by simply inverting the buried junction and selecting different catalysts. Reproduced from Wang et al.³¹⁶

8. Cell implementation strategies and reactors

In this work, focus has been put on front-illuminated metal oxide or protected photoelectrodes, the strategy followed majorly by authors in the field. Although, solar energy can be used to drive an electrochemical reaction in different implementation strategies, with different grade of external control and device complexity.

8.1. Photoelectrode configuration

Jacobsson et al.²³ have methodically described all the possible transitions from an independent monolithic PEC device to an electrolyzer powered by Grid-photovoltaic energy, what is depicted in Figure 1.26.

From a monolithic PEC device (a), the first step is separating with an external circuit the second electrode (b). It is depicted as a metal, but the second one could be photoactive too, combining photovoltage in a tandem design (its characteristics will be discussed later). The second step is introducing a protective layer between the photoabsorber and catalyst, where the junction can be formed between the photoabsorber and the electrolyte/catalyst or the layer can intervene in forming a p-n junction (c). A third step is considered if a vertical catalyst structure is perpendicularly set on the photoabsorber (electrically connected), meanwhile the rest of the surface has the protective layer (d). This way, light can still reach the photoactive semiconductor, meanwhile it is no longer possible to form the depletion with the electrolyte, thus a p-n junction is necessary. Once the vertical catalyst is introduced, next step is directly encapsulating the photoactive part (i.e. into polymer) instead of using a protective layer (e). Once completely isolated, there is no more the need of having the photoactive part inside the electrolyte, and connecting the independent catalyst with a wire to the semiconductor allows freely locating the absorber inside the electrolyte or outside (f). Last step consists of substituting the external photoactive semiconductor with connecting the two remaining catalyst structures with grid photovoltaic (or not) electricity, resulting in a PV-electrolyser setup (g). Jacobsson et al. have implemented several of the mentioned designs in CIGS photoelectrodes³⁰¹. As the reader may have realized, the technology readiness is not the same for all configurations⁷: both photovoltaics and electrolyzers are already commercialised technologies, compared to PEC ones which are still under significant investigation. But as discussed in section 1, PEC is designed to work at lower current densities, reducing electrochemical overpotentials and enabling higher conversion efficiencies.

Throughout the whole introduction the vast majority of research has been focused in configurations (b) and (c). In-plane electrodes have been reviewed in increasing complexity, a path to increment its built-in electric field, its photon absorption, stability and catalytic efficiency.

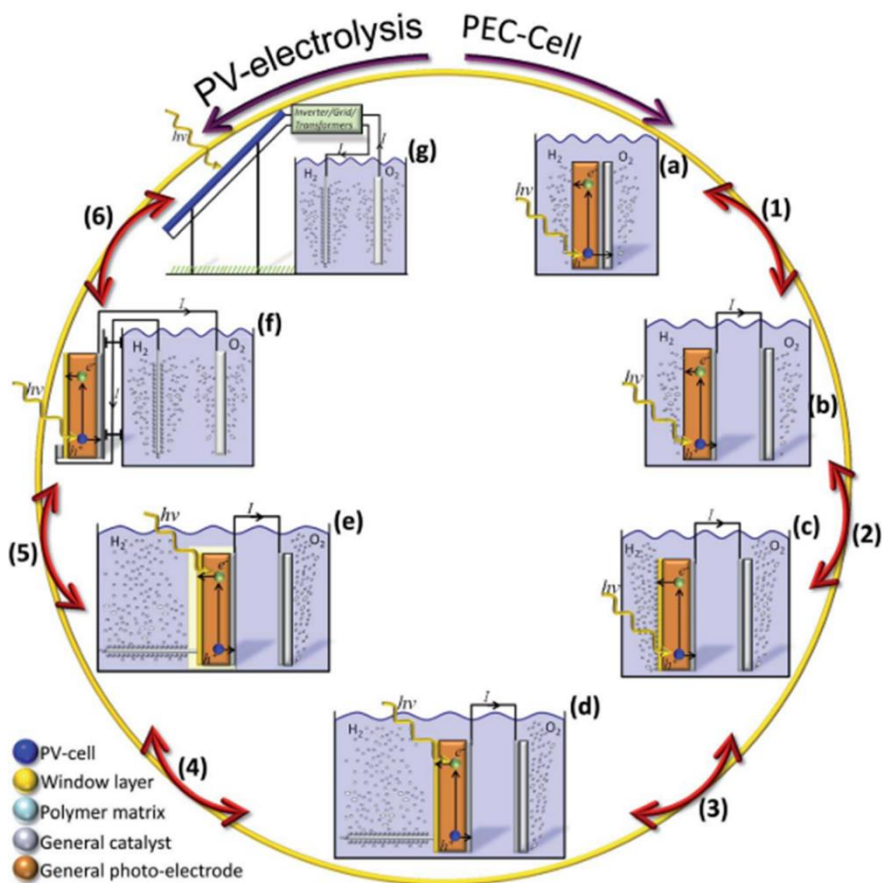


Figure 1.26. Scheme of the possible transitions from a monolithic PEC device to a Photovoltaic-grid powered electrolyser. Reproduced from Jacobsson et al.²³

8.2. Tandem PEC devices

For non-externally biased (unassisted) single light absorber electrodes, only large band gap semiconductors will create enough photovoltage to break the water molecule, meanwhile a dual absorber tandem structure permits absorbing a larger portion of the solar spectra (Figure 1.27a and b)^{96,318}. As Hu et al.³¹⁹ calculated, efficiencies higher than 25% should be obtainable (taking into account earth abundant catalysts overpotential and resistance losses) if band gap semiconductors of ~ 1.1 and 1.6 - 1.8 eV with high performance are found. The short band gap ones are easy to propose, as candidates are already commercial or under development: Si, GaAs, CIGS or perovskites, but the ones with larger band gap still requires more research. Chalcogenides such as CIGS and CZTS have proven the possibility to tune its band gap from 1.0 to 1.6 eV^{109,298,309,320,321}, and also some perovskites³²², what can help in perfect absorption match for both electrodes to be working in the maximum power point.

The possible configuration parameters to form a tandem device are vast, and other authors have already performed thoughtful discussions^{96,318,319,323,324}. For example, both electrodes can be photoactive, combining their performance through the external circuit (Figure 1.27c), or one can be a multijunction photoelectrode, coupled to a metallic counterelectrode (Figure 1.27d). Also, the two photoelectrodes can be connected back-to-back (as in Figure 1.27b) and both may require frontal illumination (Figure 1.27c). Also, either the HER or OER water splitting reaction can be performed in front of the short band gap semiconductor or the large one, what must be decided based on the protection strategy and stability and catalyst selected. Back-illuminated photoelectrodes are good candidates if the large band gap absorber must be deposited on top of them^{201,254} and, in principle, do not require transparent protective layers or catalysts, facilitating the search of appropriate low cost and earth abundant materials.

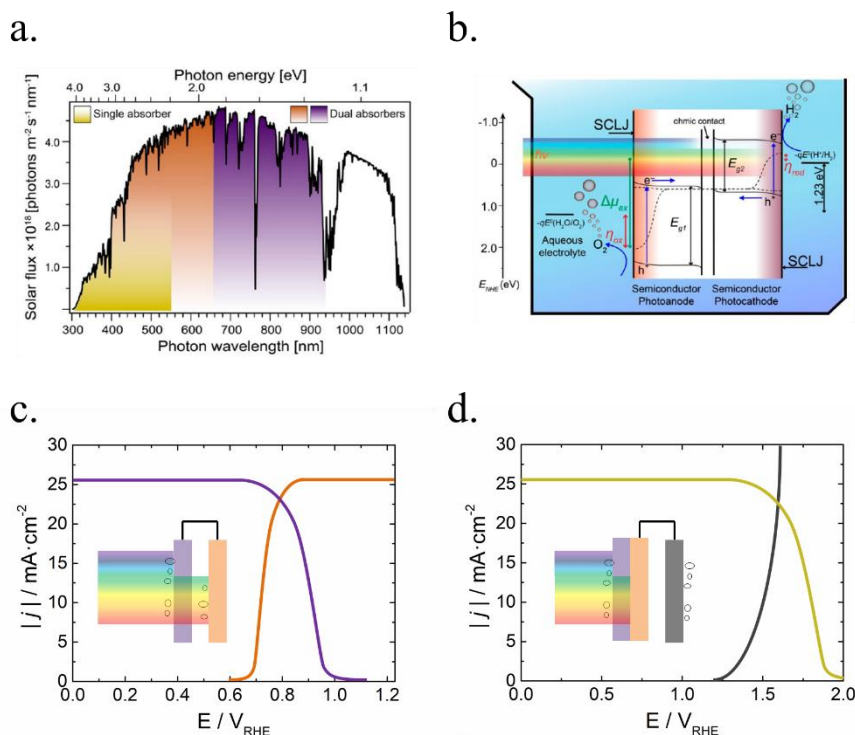


Figure 1.27. a) AM 1.5G solar flux as function of photon wavelength and photon energy. The colored areas represent the portion that can be harvested using a single band gap absorber (yellow) or a tandem one (orange + purple) to perform the bias-free water splitting reaction. b) Tandem monolithic structure with two SCLJ, one front and the other one back illuminated. Reproduced from Sivula et al.³¹⁸ Cyclic voltammograms simulation of c) a two front-illuminated photoelectrodes tandem PEC device and its schematics (inset) and d) a multijunction photoelectrode and a metallic counter electrode with its schematics (inset).

8.3. Electrolyte pH and membranes

Another significant design parameter is the electrolyte pH. As it is commonly known, an alkaline electrolyte enhances the OER, whereas an acidic the HER one. In half-cell lab measurements, this is not a problem, but in a full device electrolytes must be either separated with a membrane or the same electrolyte must be chosen for both electrodes. Also, if no gas-separator-membrane is present, detrimental back reactions can happen of dissolved gases and explosive O_2/H_2 mixtures formed, where a highly pure H_2 and O_2 stream is desired¹⁰. Regarding catalysts availability, Pt, Ir and Pd, or phosphides such as NiP have 100 times higher H-binding energy in acid (beneficial for HER reaction), and only few earth abundant metallic catalysts such as Ni-Mo have been found effective for HER in alkaline media³⁰ (Figure 1.6c). Meanwhile, few expensive catalysts (Ir or Ru) are known to be stable in acid for the OER and all others including earth abundant Ni(Fe) O_xH_y require basic conditions³²⁵. Also, if same electrolyte is used for both reactions, one of the catalysts will have to drive the water dissociation into H^+ and OH^- before OER and HER can happen, introducing significant overpotentials, as described in section 2 e).

Regarding this aspect, bipolar membranes allow different electrolytes to be used for each semi-reaction³²⁵, to have ideal local pHs. These membranes are composed of anion and cation selective layers transporting OH^- and H^+ , respectively, which reacting in the interface. This way no gas or electrolyte crossover is present, and respective pH are maintained allowing the HER and OER to be performed most efficiently. Although, very few studies have been performed in full-cell membrane-divided schemes.

8.4. Reactor schemes

Lab-scale measurements, with devices ranging at most few cm^2 , do not have the problem of current distribution inside the reactor, but large scale devices (several tens of cm^2) must take in account the ionic conductivity of the liquid, and minimize the distance from one electrode's surface to the other. Lewis³⁰ identified four possible reactor schemes to implement monolithic "intrinsically safe" (where H_2 and O_2 are generated in separated compartments) PEC electrodes (Figure 1.28a-d). Nano/microwire electrodes grown integrated with the membrane would introduce almost null ionic resistance, as ions must only travel micrometer distances. Some of these include solar concentration of up to 500 times¹⁰, a strategy to minimize device costs, expected to be significantly higher than bare photovoltaics³²⁶. The main drawback of concentration is increasing the current density on the catalytic surface, which will turn into significant extra overpotential, together with the trade-off on an increase of temperature, enhancing electrocatalysis but reducing photovoltaic efficiency. Several other reactor structures have been analyzed by Minggu et al.³²⁷, for monolithic PEC electrodes or tandem separated ones, set one behind the other or one next to the other (Figure 1.25e-g).

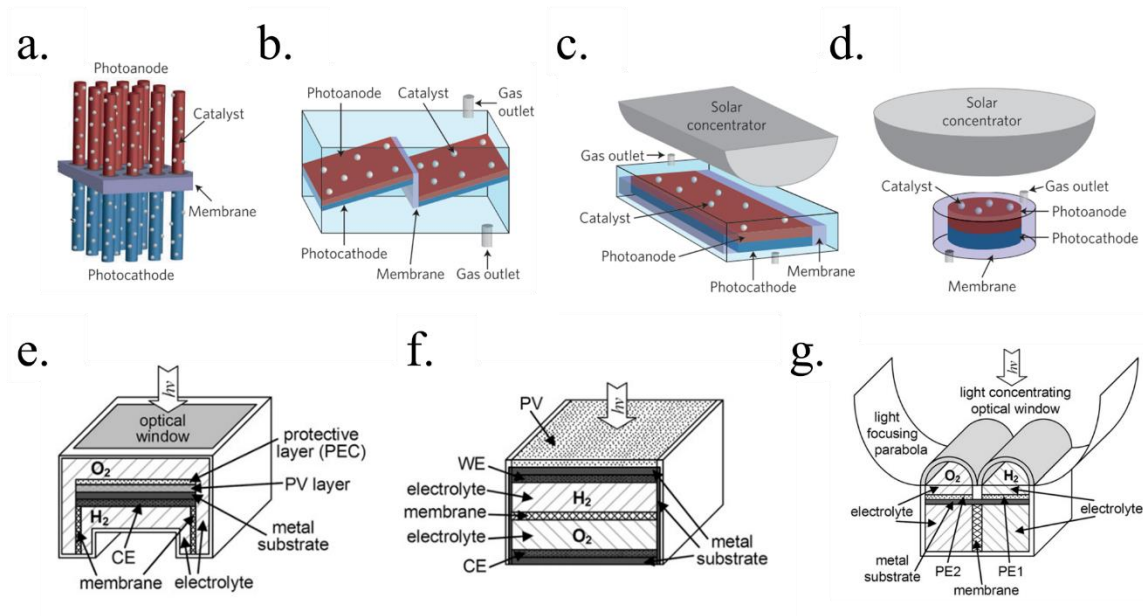


Figure 1.28. a-d) Four possible reactor schemes of monolithic PEC reactors with H_2 and O_2 generated in separated compartments. Reproduced from Lewis et al.³⁰ e) Non-biased PEC electrode, f) PV-biased electrodes and g) laterally-connected tandem electrodes with solar simulator. Reproduced from Minggu et al.³²⁸

9. Resume, perspective and challenges

Renewable energy sources will eventually be implemented globally, together with energy carriers capable to be distributed and used when necessary. PEC water splitting has demonstrated to produce hydrogen from solar energy and water with significant efficiencies, although this technology is not ready for market implementation due to lack of efficient, stable and scalable photoelectrodes.

In this introduction, the pathway of last decades investigations on PEC water splitting cells has been analysed. After first discovery of the semiconductor-liquid junction producing few $\mu\text{A}\cdot\text{cm}^{-2}$ photocurrents on TiO_2 , several other semiconductor materials have been tested and modified in the search of an efficient, stable and scalable device, with significant advances obtained. Other metal oxides such as Fe_2O_3 , WO_3 , BiVO_4 , or Cu_2O have been nanostructured and treated to maximize the built-in electric field to enhance electron-hole separation and transport, together with co-catalyst decoration for a more efficient HER/OER reaction. Metal oxide photoelectrodes present good stability in oxidizing environments and are scalable due to earth abundant materials and low cost deposition techniques, but up to now have lacked of significant photocurrent efficiency.

An alternative approach to overcome this has been adapting short band gap materials such as the ones used for the photovoltaic industry into PEC, mostly III-V semiconductors like GaAs, CdTe or InP, or earth abundant Si, CIGS and CZTS. 1.0 to 1.8 eV band gap semiconductors are capable to absorb broad part of the solar spectra, and some of these materials are band gap tunable by composition variations like In/Ga for CIGS and S/Se in CZTS, easing implementation in tandem devices. Although, their main drawback is the instability in aqueous acidic or alkaline electrolytes.

During las decade, metallic films have been deposited on top both as catalysts and to prevent corrosion, but few nanometer thick layers, thin enough to be transparent, were not passivating enough. Tunnel-distances-thick oxides present similar problems, as resistance increases dramatically if more than ~ 5 nm are deposited. But protecting short band gap photoabsorbers, containing a buried junction, with semiconductor metal oxide transparent conducting and protective layers several tens of nanometers thick has enabled more than 1000 h stable electrodes, with photocurrents and photovoltages resembling photovoltaic cells. TiO_2 and NiO have been the most studied and best performing protective layers, the former with Pt or Ni as HER/OER catalysts and the latter being OER catalytic too.

Yet, electron or hole conduction mechanisms across protective layers are still not fully understood, in photoabsorber-film interface, across the layer or in the layer-catalyst-electrolyte electrolytic surface. Especially for TiO_2 but also for NiO protective layers, the nanoscale disorder and thus, deposition process and temperature have presented significant variations among different studies. Moreover, intrinsic stability for these materials for very

long experiments, intermittent day/night polarization variations, and for all possible crystallographic structures should not be directly assumed. Especially in highly oxidizing or reducing electrolytes, as metal oxide protective layers conductivity relies on cationic or oxygen-deficient electronic structure.

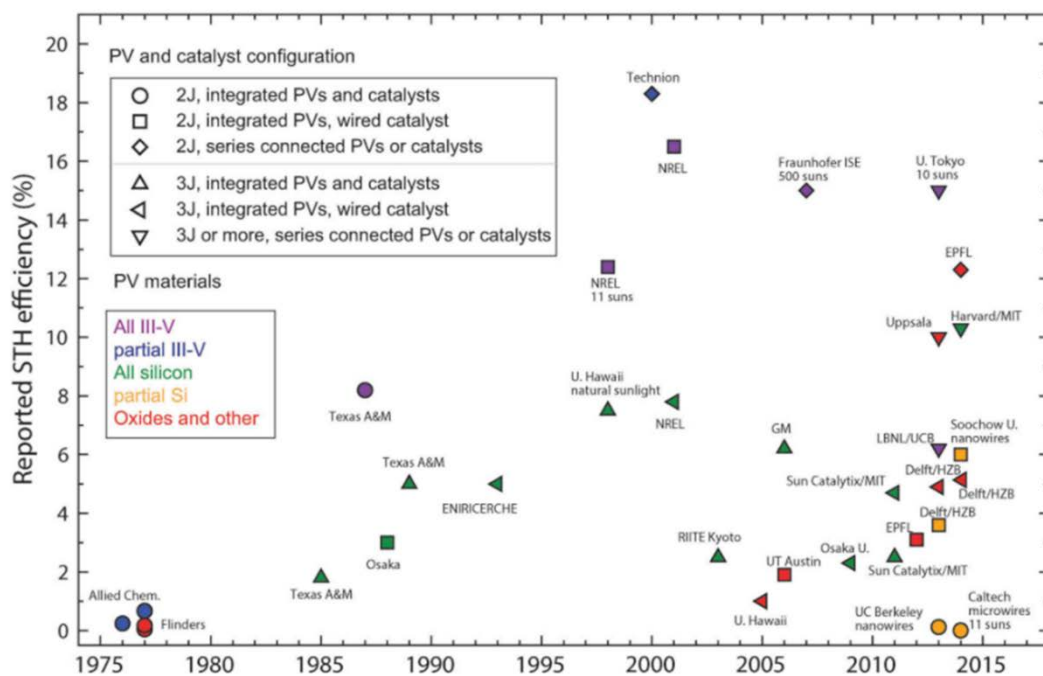


Figure 1.29. Table presenting best-performing PEC devices reported solar-to-hydrogen conversion efficiencies by year, and classified by materials used and number of junctions. Reproduced from Ager et al.¹⁰

In addition, few works have presented complete PEC cells capable to perform bias free solar water splitting efficiently. As can be seen in Figure 1.29¹⁰, systems based on III-V semiconductors have achieved 15-18% solar-to-hydrogen (STH) efficiencies, meanwhile earth abundant materials (silicon or oxides, among others) have reached around 10% STH quite recently. As examples, Licht et al.³²⁹ obtained 18% conversion efficiency with AlGaAs/Si tandem cells with RuO₂/Pt vertical catalysts, and Peharz et al.³³⁰ close values with GaInP cells connected to an electrolyser with a polymer electrolyte membrane as separator and under up to 500 suns illumination. Although, III-V semiconductors are grown by very expensive techniques and thus, scalability is difficult due to price and scarcity. Some authors have studied reactor schemes and costs, where among several strategies, solar concentration is expected to facilitate the amortization of costly cells, reactors, gas separator membranes and pumping systems⁸. In recent years, more works have published high efficiencies with earth abundant materials like silicon, oxides or emerging photovoltaic materials¹⁰. The

Department of Energy (D.O.E.) of the United States fixed a road map for PEC water splitting pointing at 15% STH and \$17.30 per kg H₂ by 2015, 20% STH and \$5.70 per kg H₂ by 2020, and ultimately 25% STH and \$2.10 per kg H₂¹⁰. Efficiencies close to the 2015 and 2020 goals have been obtained nowadays, but on lab-scale devices and with high cost materials.

In order to implement PEC water splitting at industrial scale, efforts must be put into the fabrication of efficient, stable and scalable photoelectrodes. Stable semiconductor materials fulfilling these requirements must be researched and, although some examples like WSe have shown promising results³³¹, the best strategy nowadays is protecting photoabsorbers as such used in PV for long term operation. TiO₂, NiO or CoO_x have been the best performing protective layers so far, fabricated by reactive sputtering, CVD or ALD to minimize pinhole formation. The substitution of high vacuum deposition and time consuming techniques would reduce fabrication costs if non-pinhole layers can be assured, meanwhile self-limited corrosion candidates such as native SiO₂ in silicon protected electrodes in acidic environments must be found (where it is passivated only where pinholes are present in the protective layer)¹³². Using the protective layer as antireflective layer will for sure help in increasing photoelectrodes productivity¹⁴⁷.

More full cell reactor field tests should be performed for sure next decade to fully understand complete device stability and degradation mechanisms³³², especially in less-controlled environments, under day/night intermittent operation, temperature changes and mechanical impact caused by bubbling or electrolyte pumping^{6,333,334}. Regenerative strategies like electrocatalyst re-deposition in dark conditions at night could reduce a constrain, increasing available material candidates^{272,335,336}.

Although some authors have claimed demonstration or early-stage commercial devices would be possible with noble metals if cost-efficiency is matched, earth abundant alternatives must be researched for large scale deployment⁶. Bias-free tandem cells will require medium band-gap semiconductors to be coupled with short ones, and chalcogenides or perovskites (band gap tunable by composition control) have shown promising results for solar cells¹⁰⁹. In addition, finding earth abundant transparent and conductive catalysts, especially inexistent for OER in acid and HER in alkaline, would reduce the constrains on selecting electrolytes and reactions performed on each side. Protective layers with superficial energetics prone to enhance HER or OER catalysis would simplify even more the structures. NiO protective layers surface incorporates Fe and forms Ni(Fe)OOH in alkaline media, one of the most efficient earth abundant OER catalysts¹⁴⁷, or MoS₂ protective and transparent layers have been recently grown and reported stable in acid with good HER catalysis²⁷³.

Furthermore, during last decade some authors have used photoelectrochemistry for other reactions besides water splitting. Carbon dioxide reduction reaction (CO₂RR) is far more complex than water splitting, but enables the possibility to extract the greenhouse gas CO₂ from the atmosphere and turn it into a reusable fuel or chemical. Commercial products like

methane or ethanol production from CO₂ reduction have been studied, which could directly be incorporated into the actual carbon-based fossil fuels market, and several other molecules are possible with appropriate catalysts. The possibility of obtaining liquid products is especially interesting, as highly simplifies distribution and storage (some of the main drawbacks for H₂ as energy vector implementation). Main challenges for CO₂ reduction are finding appropriate catalysts and stable semiconductors to be placed in direct contact with the reaction, as the higher required reductive potentials (~1 extra volt) enhance materials corrosion^{337,338}.

10. Scope of this research

The main objective of this thesis is to study efficient and stable photoelectrodes for PEC water splitting as renewable energy conversion and storage technology for Solar Fuels, using cost-effective materials and scalable techniques. The thesis is mainly focused on improving the efficiency of metal oxide photoelectrodes and on stabilizing efficient photoabsorber semiconductors with protective layers. This includes studying earth abundant efficient materials already known from photovoltaics and optimizing its adaptation into PEC water splitting, mainly charge separation and transport to the electrochemical reaction while avoiding degradation. Some of the specific objectives of this thesis have been:

- Finding appropriate band gap materials to work as photoanodes or photocathodes, with special interest in earth abundant materials, capable of high productivities and long lasting stabilities in harsh acidic and basic electrolytes.
- Maximizing the productivity of metal oxide-based photoelectrodes by nanostructuring and modifying the electronic structure.
- Adapting semiconductors already known from photovoltaic technology as both photocathodes and photoanodes. This includes monocrystalline or other configuration silicon cells and alternative semiconductors.
- Inhibiting corrosion of unstable photoabsorber candidates in highly acidic or basic electrolytes by deposition of protective layers, with special concern on avoiding detrimental affectations on the photoabsorber efficiency.
- Studying atomic layer deposition as protection technique. Controlling the effect of deposition parameters to obtain transparent, conductive and stable protective films.
- Identifying key parameters for efficient conductivity through protective layers both macroscopically and at the nanoscale. Characterizing protective layers before and after long-term operation, with special concern on intrinsic instabilities in harsh electrolytes. This includes identifying the role of introduced overlayers and interfaces.
- Characterizing protected semiconductors as PEC water splitting photo electrodes, identifying the elements limiting productivity related to electrical transport and electrochemical activity.
- Studying the main degradation mechanisms to efficient and long stable photoelectrodes and identifying possible ways to revert them.

Bibliography

- (1) Heinberg, R.; Fridley, D. *Our Renewable Future*; Island Press, 2016.
- (2) Godoy, J. M. 210 Pb Sediment Dating: Redeeming the History of Environmental Pollution in the Anthropocene. *Rev. Virtual Quim.* **2018**, *10* (6), 1733–1757.
- (3) Berry, G. D.; Pasternak, A. D.; Rambach, G. D.; Smith, J. R.; Schock, R. N. Hydrogen as a Future Transportation Fuel. *Energy* **1996**, *21* (4), 289–303.
- (4) Fujishima, A.; Honda, K. Electrochemical Photolysis of Water at a Semiconductor Electrode. *Nature* **1972**, *238* (5358), 37–38.
- (5) Li, Z.; Feng, J.; Yan, S.; Zou, Z. Solar Fuel Production: Strategies and New Opportunities with Nanostructures. *Nano Today* **2015**, 1–19.
- (6) McKone, J. R.; Lewis, N. S.; Gray, H. B. Will Solar-Driven Water-Splitting Devices See the Light of Day? *Chem. Mater.* **2014**, *26* (1), 407–414.
- (7) Ardo, S.; Fernandez Rivas, D.; Modestino, M. A.; Schulze Greiving, V.; Abdi, F. F.; Alarcon-Llado, E.; Artero, V.; Ayers, K. E.; Battaglia, C.; Becker, J.-P.; et al. Pathways to Electrochemical Solar-Hydrogen Technologies. *Energy Environ. Sci.* **2018**, 0–45.
- (8) Shaner, M. R.; Atwater, H. A.; Lewis, N. S.; McFarland, E. W. A Comparative Technoeconomic Analysis of Renewable Hydrogen Production Using Solar Energy. *Energy Environ. Sci.* **2016**, *9* (7), 2354–2371.
- (9) Rothschild, A.; Dotan, H. Beating the Efficiency of Photovoltaics-Powered Electrolysis with Tandem Cell Photoelectrolysis. *ACS Energy Lett.* **2017**, *2* (1), 45–51.
- (10) Ager, J. W.; Shaner, M. R.; Walczak, K. A.; Sharp, I. D.; Ardo, S. Experimental Demonstrations of Spontaneous, Solar-Driven Photoelectrochemical Water Splitting. *Energy Environ. Sci.* **2015**, *8*, 2811–2824.
- (11) Görlin, M.; Chernev, P.; De Araújo, J. F.; Reier, T.; Dresp, S.; Paul, B.; Krähnert, R.; Dau, H.; Strasser, P. Oxygen Evolution Reaction Dynamics, Faradaic Charge Efficiency, and the Active Metal Redox States of Ni-Fe Oxide Water Splitting Electrocatalysts. *J. Am. Chem. Soc.* **2016**, *138* (17), 5603–5614.
- (12) Dutta, A.; Pradhan, N. Developments of Metal Phosphides as Efficient OER Precatalysts. *J. Phys. Chem. Lett.* **2016**, 144–152.
- (13) Benck, J. D.; Hellstern, T. R.; Kibsgaard, J.; Chakhranont, P.; Jaramillo, T. F. Catalyzing the Hydrogen Evolution Reaction (HER) with Molybdenum Sulfide Nanomaterials. *ACS Catal.* **2014**, *4* (11), 3957–3971.
- (14) Yan, Y.; Xia, B.; Xu, Z.; Wang, X. Recent Development of Molybdenum Sulfides as Advanced Electrocatalysts for Hydrogen Evolution Reaction. *ACS Catal.* **2014**, *4* (6), 1693–1705.
- (15) Gong, M.; Dai, H. A Mini Review of NiFe-Based Materials as Highly Active Oxygen Evolution Reaction Electrocatalysts. *Nano Res.* **2014**, *8* (1), 23–39.
- (16) Trotochaud, L.; Ranney, J. K.; Williams, K. N.; Boettcher, S. W. Solution-Cast Metal Oxide Thin Film Electrocatalysts for Oxygen Evolution. *J. Am. Chem. Soc.* **2012**, *134* (41), 17253–17261.

- (17) Sheng, W.; Gasteiger, H. A.; Shao-Horn, Y. Hydrogen Oxidation and Evolution Reaction Kinetics on Platinum: Acid vs Alkaline Electrolytes. *J. Electrochem. Soc.* **2010**, *157* (11), B1529.
- (18) Trasatti, S. The Absolute Electrode Potential : An Explanatory Note. *Pure Appl Chem.*, **1986**, *58* (7), 955–966.
- (19) Li, H.; Chen, S.; Zhang, Y.; Zhang, Q.; Zhang, Q.; Jia, X.; Gu, L.; Sun, X.; Song, L.; Wang, X. Systematic Design of Superaerophobic Nanotube-Array Electrode Comprised of Transition-Metal Sulfides for Overall Water Splitting. *Nat. Commun.* **2018**, *9* (1), 1–12.
- (20) Yu, Z. Y.; Lang, C. C.; Gao, M. R.; Chen, Y.; Fu, Q. Q.; Duan, Y.; Yu, S. H. Ni-Mo-O Nanorod-Derived Composite Catalysts for Efficient Alkaline Water-to-Hydrogen Conversion: Via Urea Electrolysis. *Energy Environ. Sci.* **2018**, *11* (7), 1890–1897.
- (21) Helmholtz, H. Studien Über Electriche Grenzschichten. *Ann. der Phys. und Chemie* **1879**, *243* (7), 337–382.
- (22) Newman, O.; Thomas-Alyea, K. E. *Electrochemical Systems*; John Wiley & Sons, H., Ed.; 2004.
- (23) Jacobsson, T. J.; Fjällström, V.; Edoff, M.; Edvinsson, T. Sustainable Solar Hydrogen Production: From Photoelectrochemical Cells to PV-Electrolyzers and Back Again. *Energy Environ. Sci.* **2014**, *7* (7), 2056.
- (24) Murphy, A. B.; Barnes, P. R. F.; Randeniya, L. K.; Plumb, I. C.; Grey, I. E.; Horne, M. D.; Glasscock, J. A. Efficiency of Solar Water Splitting Using Semiconductor Electrodes. *Int. J. Hydrogen Energy* **2006**, *31* (14), 1999–2017.
- (25) Chen, Z.; Dinh, H. N.; Miller, E. *Photoelectrochemical Water Splitting - Standards, Experimental Methods, and Protocols*; Springer, 2013.
- (26) Jiang, C.; Moniz, S. J. A.; Wang, A.; Zhang, T.; Tang, J. Photoelectrochemical Devices for Solar Water Splitting - Materials and Challenges. *Chem. Soc. Rev.* **2017**, *46* (15), 4645–4660.
- (27) Li, J.; Wu, N. Semiconductor-Based Photocatalysts and Photoelectrochemical Cells for Solar Fuel Generation: A Review. *Catal. Sci. Technol.* **2015**, No. 3, 1360.
- (28) Smith, W. A.; Sharp, I. D.; Strandwitz, N. C.; Bisquert, J. Interfacial Band-Edge Energetics for Solar Fuels Production. *Energy Environ. Sci.* **2015**, *8* (10), 2851–2862.
- (29) Yang, Y.; Niu, S.; Han, D.; Liu, T.; Wang, G.; Li, Y. Progress in Developing Metal Oxide Nanomaterials for Photoelectrochemical Water Splitting. *Adv. Energy Mater.* **2017**, *7* (19), 1–26.
- (30) Lewis, N. S. Developing a Scalable Artificial Photosynthesis Technology through Nanomaterials by Design. *Nat. Nanotechnol.* **2016**, *11* (12), 1010–1019.
- (31) Chen, S.; Wang, L. W. Thermodynamic Oxidation and Reduction Potentials of Photocatalytic Semiconductors in Aqueous Solution. *Chem. Mater.* **2012**, *24* (18), 3659–3666.
- (32) Berger, T.; Monllor-Satoca, D.; Jankulovska, M.; Lana-Villarreal, T.; Gómez, R. The Electrochemistry of Nanostructured Titanium Dioxide Electrodes. *ChemPhysChem* **2012**, *13* (12), 2824–2875.

- (33) Wang, J.; Liu, X.; Li, R.; Qiao, P.; Xiao, L.; Fan, J. TiO₂ Nanoparticles with Increased Surface Hydroxyl Groups and Their Improved Photocatalytic Activity. *Catal. Commun.* **2012**, *19*, 96–99.
- (34) Jankulovska, M.; Berger, T.; Wong, S. S.; Gómez, R.; Lana-Villarreal, T. Trap States in TiO₂ Films Made of Nanowires, Nanotubes or Nanoparticles: An Electrochemical Study. *ChemPhysChem* **2012**, *13* (12), 3008–3017.
- (35) Fan, J.; Fàbrega, C.; Zamani, R. R.; Hao, Y.; Parra, A.; Andreu, T.; Arbiol, J.; Boschloo, G.; Hagfeldt, A.; Morante, J. R.; et al. Enhanced Photovoltaic Performance of Nanowire Dye-Sensitized Solar Cells Based on Coaxial TiO₂@TiO Heterostructures with a Cobalt(II/III) Redox Electrolyte. *ACS Appl. Mater. Interfaces* **2013**, *5* (20), 9872–9877.
- (36) Sá, J.; Friedli, P.; Geiger, R.; Lerch, P.; Rittmann-Frank, M. H.; Milne, C. J.; Szlachetko, J.; Santomauro, F. G.; van Bokhoven, J. a; Chergui, M.; et al. Transient Mid-IR Study of Electron Dynamics in TiO₂ Conduction Band. *Analyst* **2013**, *138* (7), 1966.
- (37) Kim, J. Y.; Magesh, G.; Youn, D. H.; Jang, J. W.; Kubota, J.; Domen, K.; Lee, J. S. Single-Crystalline, Wormlike Hematite Photoanodes for Efficient Solar Water Splitting. *Sci. Rep.* **2013**, *3*, 1–8.
- (38) Dias, P.; Vilanova, A.; Lopes, T.; Andrade, L.; Mendes, A. Extremely Stable Bare Hematite Photoanode for Solar Water Splitting. *Nano Energy* **2016**, *23*, 70–79.
- (39) Sivula, K.; Le Formal, F.; Grätzel, M. Solar Water Splitting: Progress Using Hematite (α -Fe₂O₃) Photoelectrodes. *ChemSusChem* **2011**, *4* (4), 432–449.
- (40) Wei, Y.; Ke, L.; Kong, J.; Liu, H.; Jiao, Z.; Lu, X.; Du, H.; Sun, X. W. Enhanced Photoelectrochemical Water-Splitting Effect with a Bent ZnO Nanorod Photoanode Decorated with Ag Nanoparticles. *Nanotechnology* **2012**, *23* (23).
- (41) Wang, B. S.; Li, R. Y.; Zhang, Z. Y.; Xing-Wang; Wu, X. L.; Cheng, G. A.; Zheng, R. T. An Overlapping ZnO Nanowire Photoanode for Photoelectrochemical Water Splitting. *Catal. Today* **2019**, *321–322* (July 2017), 100–106.
- (42) Zheng, J. Y.; Song, G.; Hong, J.; Van, T. K.; Pawar, A. U.; Kim, D. Y.; Kim, C. W.; Haider, Z.; Kang, Y. S. Facile Fabrication of WO₃nanoplates Thin Films with Dominant Crystal Facet of (002) for Water Splitting. *Cryst. Growth Des.* **2014**, *14* (11), 6057–6066.
- (43) Su, J.; Feng, X.; Sloppy, J. D.; Guo, L.; Grimes, C. A. Vertically Aligned WO₃ Nanowire Arrays Grown Directly on Transparent Conducting Oxide Coated Glass: Synthesis and Photoelectrochemical Properties. *Nano Lett.* **2011**, *11* (1), 203–208.
- (44) Fàbrega, C.; Murcia-López, S.; Monllor-Satoca, D.; Prades, J. D.; Hernández-Alonso, M. D.; Penelas, G.; Morante, J. R.; Andreu, T. Efficient WO₃ Photoanodes Fabricated by Pulsed Laser Deposition for Photoelectrochemical Water Splitting with High Faradaic Efficiency. *Appl. Catal. B Environ.* **2016**, *189*, 133–140.
- (45) Kim, T. W.; Choi, K.-S. Improving Stability and Photoelectrochemical Performance of BiVO₄ Photoanodes in Basic Media by Adding a ZnFe₂O₄ Layer. *J. Phys. Chem. Lett.* **2016**, *7* (3), 447–451.
- (46) Seabold, J. A.; Choi, K. S. Efficient and Stable Photo-Oxidation of Water by a Bismuth Vanadate Photoanode Coupled with an Iron Oxyhydroxide Oxygen Evolution Catalyst. *J. Am.*

- Chem. Soc.* **2012**, *134* (4), 2186–2192.
- (47) Abdi, F. F.; Van De Krol, R. Nature and Light Dependence of Bulk Recombination in Co-Pi-Catalyzed BiVO₄ Photoanodes. *J. Phys. Chem. C* **2012**, *116* (17), 9398–9404.
- (48) Berglund, S. P.; Flaherty, D. W.; Hahn, N. T.; Bard, A. J.; Mullins, C. B. Photoelectrochemical Oxidation of Water Using Nanostructured BiVO₄ Films. *J. Phys. Chem. C* **2011**, *115* (9), 3794–3802.
- (49) Hu, C.; Chu, K.; Zhao, Y.; Teoh, W. Y. Efficient Photoelectrochemical Water Splitting over Anodized P-Type NiO Porous Films. *ACS Appl. Mater. Interfaces* **2014**, *6* (21), 18558–18568.
- (50) Wick, R.; Tilley, S. D. Photovoltaic and Photoelectrochemical Solar Energy Conversion with Cu₂O. *J. Phys. Chem. C* **2015**, *119* (47), 26243–26257.
- (51) Bard, A. J. Thermodynamic Potential for the Anodic Dissolution of N-Type Semiconductors. *J. Electrochem. Soc. Electrochem. Sci. Technol.* **1977**, 1706–1710.
- (52) Gerischer, H. On the Stability of Semiconductor Electrodes against Photodecomposition. *J. Electroanal. Chem.* **1977**, *82*, 133–143.
- (53) Luo, J.; Steier, L.; Son, M. K.; Schreier, M.; Mayer, M. T.; Grätzel, M. Cu₂O Nanowire Photocathodes for Efficient and Durable Solar Water Splitting. *Nano Lett.* **2016**, *16* (3), 1848–1857.
- (54) Li, J.; Wu, N. Semiconductor-Based Photocatalysts and Photoelectrochemical Cells for Solar Fuel Generation: **2015**, *5* (3).
- (55) Toma, F. M.; Cooper, J. K.; Kunzelmann, V.; McDowell, M. T.; Yu, J.; Larson, D. M.; Borys, N. J.; Abelyan, C.; Beeman, J. W.; Yu, K. M.; et al. Mechanistic Insights into Chemical and Photochemical Transformations of Bismuth Vanadate Photoanodes. *Nat. Commun.* **2016**, *7* (May), 1–11.
- (56) Jang, Y. J.; Park, Y. Bin; Kim, H. E.; Choi, Y. H.; Choi, S. H.; Lee, J. S. Oxygen-Intercalated CuFeO₂ Photocathode Fabricated by Hybrid Microwave Annealing for Efficient Solar Hydrogen Production. *Chem. Mater.* **2016**, *28* (17), 6054–6061.
- (57) Yin, W. J.; Tang, H.; Wei, S. H.; Al-Jassim, M. M.; Turner, J.; Yan, Y. Band Structure Engineering of Semiconductors for Enhanced Photoelectrochemical Water Splitting: The Case of TiO₂. *Phys. Rev. B - Condens. Matter Mater. Phys.* **2010**, *82* (4), 1–6.
- (58) Wang, G.; Xiao, X.; Li, W.; Lin, Z.; Zhao, Z.; Chen, C.; Wang, C.; Li, Y.; Huang, X.; Miao, L.; et al. Significantly Enhanced Visible Light Photoelectrochemical Activity in TiO₂ Nanowire Arrays by Nitrogen Implantation. *Nano Lett.* **2015**, *15* (7), 4692–4698.
- (59) Wang, G.; Wang, H.; Ling, Y.; Tang, Y.; Yang, X.; Fitzmorris, R. C.; Wang, C.; Zhang, J. Z.; Li, Y. Hydrogen-Treated TiO₂ Nanowire Arrays for Photoelectrochemical Water Splitting. *Nano Lett.* **2011**, *11* (7), 3026–3033.
- (60) Yang, C.; Wang, Z.; Lin, T.; Yin, H.; Lü, X.; Wan, D.; Xu, T.; Zheng, C.; Lin, J.; Huang, F.; et al. Core-Shell Nanostructured “Black” Rutile Titania as Excellent Catalyst for Hydrogen Production Enhanced by Sulfur Doping. *J. Am. Chem. Soc.* **2013**, *135* (47), 17831–17838.
- (61) Fàbrega, C.; Andreu, T.; Güell, F.; Prades, J. D.; Estradé, S.; Rebled, J. M.; Peiró, F.; Morante, J. R. Effectiveness of Nitrogen Incorporation to Enhance the Photoelectrochemical Activity of

- Nanostructured TiO₂:NH₃ versus H₂-N₂ Annealing. *Nanotechnology* **2011**, *22* (23), 235403.
- (62) Wang, F.; Di Valentin, C.; Pacchioni, G. Doping of WO₃ for Photocatalytic Water Splitting: Hints from Density Functional Theory. *J. Phys. Chem. C* **2012**, *116* (16), 8901–8909.
- (63) Wang, F.; DiValentin, C.; Pacchioni, G. Rational Band Gap Engineering of WO₃ Photocatalyst for Visible Light Water Splitting. *ChemCatChem* **2012**, *4* (4), 476–478.
- (64) Hart, J. N.; Cutini, M.; Allan, N. L. Band Gap Modification of ZnO and ZnS through Solid Solution Formation for Applications in Photocatalysis. *Energy Procedia* **2014**, *60* (C), 32–36.
- (65) Hamid, S. B. A.; Teh, S. J.; Lai, C. W. Photocatalytic Water Oxidation on ZnO: A Review. *Catalysts* **2017**, *7* (3), 93.
- (66) Wang, M.; Ren, F.; Zhou, J.; Cai, G.; Cai, L.; Hu, Y.; Wang, D.; Liu, Y.; Guo, L.; Shen, S. N Doping to ZnO Nanorods for Photoelectrochemical Water Splitting under Visible Light: Engineered Impurity Distribution and Terraced Band Structure. *Sci. Rep.* **2015**, *5* (1), 12925.
- (67) Wang, T.; Luo, Z.; Li, C.; Gong, J. Controllable Fabrication of Nanostructured Materials for Photoelectrochemical Water Splitting via Atomic Layer Deposition. *Chem. Soc. Rev.* **2014**, *43* (22), 7469–7484.
- (68) Kang, Q.; Cao, J.; Zhang, Y.; Liu, L.; Xu, H.; Ye, J. Reduced TiO₂ Nanotube Arrays for Photoelectrochemical Water Splitting. *J. Mater. Chem. A* **2013**, *1* (18), 5766.
- (69) Fàbrega, C.; Hernández-Ramírez, F.; Daniel Prades, J.; Jiménez-Díaz, R.; Andreu, T.; Ramon Morante, J. On the Photoconduction Properties of Low Resistivity TiO₂ Nanotubes. *Nanotechnology* **2010**, *21* (44).
- (70) Yang, Y.; Kao, L. C.; Liu, Y.; Sun, K.; Yu, H.; Guo, J.; Liou, S. Y. H.; Hoffmann, M. R. Cobalt-Doped Black TiO₂ Nanotube Array as a Stable Anode for Oxygen Evolution and Electrochemical Wastewater Treatment. *ACS Catal.* **2018**, *8* (5), 4278–4287.
- (71) Fàbrega, C.; Andreu, T.; Tarancón, A.; Flox, C.; Morata, A.; Calvo-Barrio, L.; Morante, J. R. Optimization of Surface Charge Transfer Processes on Rutile TiO₂ Nanorods Photoanodes for Water Splitting. *Int. J. Hydrogen Energy* **2013**, *38* (7), 2979–2985.
- (72) Wu, J. M.; Zhang, T. W.; Zeng, Y. W.; Hayakawa, S.; Tsuru, K.; Osaka, A. Large-Scale Preparation of Ordered Titania Nanorods with Enhanced Photocatalytic Activity. *Langmuir* **2005**, *21* (15), 6995–7002.
- (73) Fàbrega, C.; Monllor-Satoca, D.; Ampudia, S.; Parra, A.; Andreu, T.; Morante, J. R. Tuning the Fermi Level and the Kinetics of Surface States of TiO₂ Nanorods by Means of Ammonia Treatments. *J. Phys. Chem. C* **2013**, *117* (40), 20517–20524.
- (74) Rao, P. M.; Cai, L.; Liu, C.; Cho, I. S.; Lee, C. H.; Weisse, J. M.; Yang, P.; Zheng, X. Simultaneously Efficient Light Absorption and Charge Separation in WO₃/BiVO₄ Core/Shell Nanowire Photoanode for Photoelectrochemical Water Oxidation. *Nano Lett.* **2014**, *14* (2), 1099–1105.
- (75) Yang, X.; Liu, R.; Lei, Y.; Li, P.; Wang, K.; Zheng, Z.; Wang, D. Dual Influence of Reduction Annealing on Diffused Hematite/FTO Junction for Enhanced Photoelectrochemical Water Oxidation. *ACS Appl. Mater. Interfaces* **2016**, *8* (25), 16476–16485.
- (76) Mor, G. K.; Varghese, O. K.; Wilke, R. H. T.; Sharma, S.; Shankar, K.; Latempa, T. J.; Choi,

- K.; Grimes, C. A. P-Type Cu Ti O Nanotube Arrays and Their Use in Self-Biased Heterojunction Photoelectrochemical Diodes for Hydrogen Generation. **2008**, 0–5.
- (77) Paracchino, A.; Laporte, V.; Sivula, K.; Grätzel, M.; Thimsen, E. Highly Active Oxide Photocathode for Photoelectrochemical Water Reduction. *Nat. Mater.* **2011**, *10* (6), 456–461.
- (78) Zhou, M.; Bao, J.; Xu, Y.; Zhang, J.; Xie, J.; Guan, M.; Wang, C.; Wen, L.; Lei, Y.; Xie, Y. Photoelectrodes Based upon Mo:BiVO₄ Inverse Opals for Photoelectrochemical Water Splitting. *ACS Nano* **2014**, *8* (7), 7088–7098.
- (79) Lopes, T.; Andrade, L.; Le Formal, F.; Gratzel, M.; Sivula, K.; Mendes, A. Hematite Photoelectrodes for Water Splitting: Evaluation of the Role of Film Thickness by Impedance Spectroscopy. *Phys. Chem. Chem. Phys.* **2014**, *16* (31), 16515–16523.
- (80) Klahr, B.; Gimenez, S.; Fabregat-Santiago, F.; Bisquert, J.; Hamann, T. W. Electrochemical and Photoelectrochemical Investigation of Water Oxidation with Hematite Electrodes. *Energy Environ. Sci.* **2012**, *5* (6), 7626.
- (81) Qiu, Y.; Liu, W.; Chen, W.; Zhou, G.; Hsu, P. C.; Zhang, R.; Liang, Z.; Fan, S.; Zhang, Y.; Cui, Y. Efficient Solar-Driven Water Splitting by Nanocone BiVO₄-Perovskite Tandem Cells. *Sci. Adv.* **2016**, *2* (6).
- (82) Cho, S.; Jang, J. W.; Lee, K. H.; Lee, J. S. Research Update: Strategies for Efficient Photoelectrochemical Water Splitting Using Metal Oxide Photoanodes. *APL Mater.* **2014**, *2* (1).
- (83) Glasscock, J. A.; Barnes, P. R. F.; Plumb, I. C.; Savvides, N. Enhancement of Photoelectrochemical Hydrogen Production from Hematite Thin Films by the Introduction of Ti and Si. *J. Phys. Chem. C* **2007**, *111* (44), 16477–16488.
- (84) Hu, Y.; Kleiman-Shwarscstein, A.; Forman, A. J.; Hazen, D.; Park, J.; McFarland, E. W. Pt-Doped α -Fe₂O₃ Thin Films Active for Photoelectrochemical Water Splitting. *Chem. Mater.* **2008**, *20* (12), 3803–3805.
- (85) Kleiman-Shwarscstein, A.; Hu, Y. S.; Forman, A. J.; Stucky, G. D.; McFarland, E. W. Electrodeposition of α -Fe₂O₃ Doped with Mo or Cr as Photoanodes for Photocatalytic Water Splitting. *J. Phys. Chem. C* **2008**, *112* (40), 15900–15907.
- (86) Wang, J.; Waters, J. L.; Kung, P.; Kim, S. M.; Kelly, J. T.; McNamara, L. E.; Hammer, N. I.; Pemberton, B. C.; Schmehl, R. H.; Gupta, A.; et al. A Facile Electrochemical Reduction Method for Improving Photocatalytic Performance of α -Fe₂O₃ Photoanode for Solar Water Splitting. *ACS Appl. Mater. Interfaces* **2017**, *9* (1), 381–390.
- (87) Pilli, S. K.; Furtak, T. E.; Brown, L. D.; Deutsch, T. G.; Turner, J. a.; Herring, A. M. Cobalt-Phosphate (Co-Pi) Catalyst Modified Mo-Doped BiVO₄ Photoelectrodes for Solar Water Oxidation. *Energy Environ. Sci.* **2011**, *4* (12), 5028–5034.
- (88) Abdi, F. F.; Han, L.; Smets, A. H. M.; Zeman, M.; Dam, B.; Van De Krol, R. Efficient Solar Water Splitting by Enhanced Charge Separation in a Bismuth Vanadate-Silicon Tandem Photoelectrode. *Nat. Commun.* **2013**, *4*, 1–7.
- (89) Wang, G.; Ling, Y.; Lu, X.; Qian, F.; Tong, Y.; Zhang, J. Z.; Lordi, V.; Rocha Leao, C.; Li, Y. Computational and Photoelectrochemical Study of Hydrogenated Bismuth Vanadate. *J. Phys. Chem. C* **2013**, *117* (21), 10957–10964.

- (90) Barroso, M.; Mesa, C. A.; Pendlebury, S. R.; Cowana, A. J.; Hisatomi, T.; Sivula, K.; Grätzel, M.; Kluga, D. R.; Durrant, J. R.; Pendlebury, S. R.; et al. Dynamics of Photogenerated Holes in Surface Modified α -Fe₂O₃ Photoanodes for Solar Water Splitting. *PNAS* **2012**, *109* (39), 1–89.
- (91) Hisatomi, T.; Le Formal, F.; Cornuz, M.; Brillet, J.; Tétreault, N.; Sivula, K.; Grätzel, M. Cathodic Shift in Onset Potential of Solar Oxygen Evolution on Hematite by 13-Group Oxide Overlayers. *Energy Environ. Sci.* **2011**, *4* (7), 2512–2515.
- (92) Yang, X.; Liu, R.; Du, C.; Dai, P.; Zheng, Z.; Wang, D. Improving Hematite-Based Photoelectrochemical Water Splitting with Ultrathin TiO₂ by Atomic Layer Deposition. *ACS Appl. Mater. Interfaces* **2014**, *6* (15), 12005–12011.
- (93) Liu, R.; Zheng, Z.; Spurgeon, J.; Yang, X. Enhanced Photoelectrochemical Water-Splitting Performance of Semiconductors by Surface Passivation Layers. *Energy Environ. Sci.* **2014**, *7* (8), 2504–2517.
- (94) McCrory, C. C. L.; Jung, S.; Ferrer, I. M.; Chatman, S. M.; Peters, J. C.; Jaramillo, T. F. Benchmarking Hydrogen Evolving Reaction and Oxygen Evolving Reaction Electrocatalysts for Solar Water Splitting Devices. *J. Am. Chem. Soc.* **2015**, *137* (13), 4347–4357.
- (95) Osgood, H.; Devaguptapu, S. V.; Xu, H.; Cho, J.; Wu, G. Transition Metal (Fe, Co, Ni, and Mn) Oxides for Oxygen Reduction and Evolution Bifunctional Catalysts in Alkaline Media. *Nano Today* **2016**, *11* (5), 601–625.
- (96) Peerakiatkhajohn, P.; Yun, J.-H.; Wang, S.; Wang, L. Review of Recent Progress in Unassisted Photoelectrochemical Water Splitting: From Material Modification to Configuration Design. *J. Photonics Energy* **2016**, *7* (1), 012006.
- (97) Burke, M. S.; Enman, L. J.; Batchellor, A. S.; Zou, S.; Boettcher, S. W. Oxygen Evolution Reaction Electrocatalysis on Transition Metal Oxides and (Oxy)Hydroxides: Activity Trends and Design Principles. *Chem. Mater.* **2015**, *27* (22), 7549–7558.
- (98) Faber, M. S.; Jin, S. Earth-Abundant Inorganic Electrocatalysts and Their Nanostructures for Energy Conversion Applications. *Energy Environ. Sci.* **2014**, *7*, 3519–3542.
- (99) Tilley, S. D.; Schreier, M.; Azevedo, J. J. J.; Stefik, M.; Graetzel, M. Ruthenium Oxide Hydrogen Evolution Catalysis on Composite Cuprous Oxide Water-Splitting Photocathodes. *Adv. Funct. Mater.* **2014**, *24* (3), 303–311.
- (100) Morales-Guio, C. G.; Tilley, S. D.; Vrubel, H.; Grätzel, M.; Hu, X. Hydrogen Evolution from a Copper(I) Oxide Photocathode Coated with an Amorphous Molybdenum Sulphide Catalyst. *Nat. Commun.* **2014**, *5* (1), 1–7.
- (101) Rahimi, N.; Pax, R. A.; Gray, E. M. A. Review of Functional Titanium Oxides. I: TiO₂ and Its Modifications. *Prog. Solid State Chem.* **2016**, *44* (3), 86–105.
- (102) Duan, Y.; Zhou, S.; Chen, Z.; Luo, J.; Zhang, M.; Wang, F.; Xu, T.; Wang, C. Hierarchical TiO₂nanowire/Microflower Photoanode Modified with Au Nanoparticles for Efficient Photoelectrochemical Water Splitting. *Catal. Sci. Technol.* **2018**, *8* (5), 1395–1403.
- (103) Zhong, D. K.; Cornuz, M.; Sivula, K.; Grätzel, M.; Gamelin, D. R. Photo-Assisted Electrodeposition of Cobalt-Phosphate (Co-Pi) Catalyst on Hematite Photoanodes for Solar Water Oxidation. *Energy Environ. Sci.* **2011**, *4* (5), 1759–1764.

- (104) Su, J.; Guo, L.; Bao, N.; Grimes, C. A. Nanostructured WO₃/BiVO₄ Heterojunction Films for Efficient Photoelectrochemical Water Splitting. *Nano Lett.* **2011**, *11* (5), 1928–1933.
- (105) Shaner, M. R.; Fountaine, K. T.; Ardo, S.; Coridan, R. H.; Atwater, H. A.; Lewis, N. S. Photoelectrochemistry of Core-Shell Tandem Junction n-P+/Si/n- WO₃ Microwire Array Photoelectrodes. *Energy Environ. Sci.* **2014**, *7* (2), 779–790.
- (106) Noh, S. Y.; Sun, K.; Choi, C.; Niu, M.; Yang, M.; Xu, K.; Jin, S.; Wang, D. Branched TiO₂/Si Nanostructures for Enhanced Photoelectrochemical Water Splitting. *Nano Energy* **2013**, *2* (3), 351–360.
- (107) Liu, C.; Tang, J.; Chen, H. M.; Liu, B.; Yang, P. A Fully Integrated Nanosystem of Semiconductor Nanowires for Direct Solar Water Splitting. *Nano Lett.* **2013**, *13* (6), 2989–2992.
- (108) Coridan, R. H.; Arpin, K. A.; Brunshwig, B. S.; Braun, P. V.; Lewis, N. S. Photoelectrochemical Behavior of Hierarchically Structured Si/WO₃ Core-Shell Tandem Photoanodes. *Nano Lett.* **2014**, *14* (5), 2310–2317.
- (109) Polman, A.; Knight, M.; Garnett, E. C.; Ehrler, B.; Sinke, W. C.; Summary, R.; Polman, A.; Knight, M.; Garnett, E. C.; Ehrler, B.; et al. Photovoltaic Materials – Present Efficiencies and Future Challenges. *Science (80-)*. **2016**, *352* (6283), 307.
- (110) Aberle, A. G. Surface Passivation of Crystalline Silicon Solar Cells: A Review. *Prog. Photovoltaics Res. Appl.* **2000**, *8* (5), 473–487.
- (111) Lee, Y.; Park, C.; Balaji, N.; Lee, Y.-J.; Dao, V. A. High-Efficiency Silicon Solar Cells: A Review. *Isr. J. Chem.* **2015**, *55* (10), 1050–1063.
- (112) Saga, T. Advances in Crystalline Silicon Solar Cell Technology for Industrial Mass Production. *NPG Asia Mater.* **2010**, *2* (3), 96–102.
- (113) Huayhuas-Chipana, B. C.; Gomero, J. C. M.; Sotomayor, M. D. P. T. Nanostructured Screen-Printed Electrodes Modified with Self-Assembled Monolayers for Determination of Metronidazole in Different Matrices. *J. Braz. Chem. Soc.* **2014**, *25* (9), 1737–1745.
- (114) Huang, L. F.; Hutchison, M. J.; Santucci, R. J.; Scully, J. R.; Rondinelli, J. M. Improved Electrochemical Phase Diagrams from Theory and Experiment: The Ni-Water System and Its Complex Compounds. *J. Phys. Chem. C* **2017**, *121* (18), 9782–9789.
- (115) Parsons, R. Atlas of Electrochemical Equilibria in Aqueous Solutions. *J. Electroanal. Chem. Interfacial Electrochem.* **1967**, *13* (4), 471.
- (116) Acevedo-Pena, P.; Vazquez-Arenas, J.; Cabrera-Sierra, R.; Lartundo-Rojas, L.; Gonzalez, I. Ti Anodization in Alkaline Electrolyte: The Relationship between Transport of Defects, Film Hydration and Composition. *J. Electrochem. Soc.* **2013**, *160* (6), C277–C284.
- (117) Strandwitz, N. C.; Comstock, D. J.; Grimm, R. L.; Nichols-Nielander, A. C.; Elam, J.; Lewis, N. S. Photoelectrochemical Behavior of N-Type Si(100) Electrodes Coated with Thin Films of Manganese Oxide Grown by Atomic Layer Deposition. *J. Phys. Chem. C* **2013**, *117* (10), 4931–4936.
- (118) Sun, K.; Pang, X.; Shen, S.; Qian, X.; Cheung, J. S.; Wang, D. Metal Oxide Composite Enabled Nanotextured Si Photoanode for Efficient Solar Driven Water Oxidation. *Nano Lett.* **2013**, *13* (5), 2064–2072.

- (119) Nikolaychuk, P. A. The Revised Pourbaix Diagram for Silicon. *Silicon* **2014**, 6 (2), 109–116.
- (120) Kim, E.; Osseo-Asare, K. Dissolution Windows for Hydrometallurgical Purification of Metallurgical-Grade Silicon to Solar-Grade Silicon: Eh-PH Diagrams for Fe Silicides. *Hydrometallurgy* **2012**, 127–128, 178–186.
- (121) Milenkovic, S.; Dalbert, V.; Marinkovic, R.; Hassel, A. W. Selective Matrix Dissolution in an Al-Si Eutectic. *Corros. Sci.* **2009**, 51 (7), 1490–1495.
- (122) Bae, D.; Shayestehaminzadeh, S.; Thorsteinsson, E. B.; Pedersen, T.; Hansen, O.; Seger, B.; Vesborg, P. C. K.; Ólafsson, S.; Chorkendorff, I. Protection of Si Photocathode Using TiO₂ Deposited by High Power Impulse Magnetron Sputtering for H₂ Evolution in Alkaline Media. *Sol. Energy Mater. Sol. Cells* **2016**, 144 (JANUARY), 758–765.
- (123) Lewerenz, H. J.; Skorupska, K.; Muñoz, A. G.; Stempel, T.; Nüsse, N.; Lublow, M.; Vo-Dinh, T.; Kulesza, P. Micro- and Nanotopographies for Photoelectrochemical Energy Conversion. II: Photoelectrocatalysis - Classical and Advanced Systems. *Electrochim. Acta* **2011**, 56 (28), 10726–10736.
- (124) Awan, I. Z.; Khan, A. Q.; Awan, I. Z.; Khan, A. Q.; Nationale, E.; Chimie, S. De. Corrosion – Occurrence & Prevention. **2018**, 40 (04), 602–655.
- (125) Beverskog, B.; Puigdomenech, I. Revised Pourbaix Diagrams for Zinc at 25–300 °C. *Corros. Sci.* **1997**, 39 (1), 107–114.
- (126) Buckle, R.; Roy, S. The Recovery of Copper and Tin from Waste Tin Stripping Solution. *Sep. Purif. Technol.* **2008**, 62 (1), 86–96.
- (127) Geiger, S.; Kasian, O.; Mingers, A. M.; Mayrhofer, K. J. J.; Cherevko, S. Stability Limits of Tin-Based Electrocatalyst Supports. *Sci. Rep.* **2017**, 7 (1), 3–9.
- (128) Van Hövell Tot Westerflier, S. W. F. M.; Binsma, J. J. M.; Stein, H. N.; Vandecasteele, C. Solubility of Particulate Cadmium Sulfide at PH=1-14: A Radiotracer Study. *J. Radioanal. Nucl. Chem. Artic.* **1987**, 111 (2), 305–317.
- (129) Tromans, D. Pitting Behavior of Passivated Cadmium Monocrystals. *J. Electrochem. Soc.* **2009**, 156 (11), C367.
- (130) Voloshchuk, A. G.; Tsipishchuk, N. I. Equilibrium Potential-PH Diagram of the CdTe-H₂O System. *Inorg. Mater.* **2002**, 38 (11), 1114–1116.
- (131) A, E. S. S.; Fotouhi, B.; Triboulet, R.; Etman, M. Oxygen Reduction Process on P-Type CdTe in Alkaline Solution. *J. Electroanal. Chem. Interfacial Electrochem.* **1985**, 195, 425–430.
- (132) Bae, D.; Seger, B.; Vesborg, P. C. K.; Hansen, O.; Chorkendorff, I. Strategies for Stable Water Splitting via Protected Photoelectrodes. *Chem. Soc. Rev.* **2017**, 46 (7), 1933–1954.
- (133) Yan, B.; Yue, G.; Yang, J.; Guha, S. High Efficiency Amorphous and Nanocrystalline Silicon Thin Film Solar Cells on Flexible Substrates. *19th Int. Work. Act. Flatpanel Displays Devices - TFT Technol. FPD Mater.* **2012**, 108 (2012), 67–70.
- (134) Guerrero, A.; Bisquert, J. Perovskite Semiconductors for Photoelectrochemical Water Splitting

- Applications. *Curr. Opin. Electrochem.* **2017**, *2* (1), 144–147.
- (135) Guerrero, A.; Haro, M.; Bellani, S.; Antognazza, M. R.; Meda, L.; Gimenez, S.; Bisquert, J. Organic Photoelectrochemical Cells with Quantitative Photocarrier Conversion. *Energy Environ. Sci.* **2014**, *7* (11), 3666–3673.
- (136) Xu, P.; McCool, N. S.; Mallouk, T. E. Water Splitting Dye-Sensitized Solar Cells. *Nano Today* **2017**, *14*, 42–58.
- (137) Brillet, J.; Yum, J.-H.; Cornuz, M.; Hisatomi, T.; Solarska, R.; Augustynski, J.; Graetzel, M.; Sivula, K. Highly Efficient Water Splitting by a Dual-Absorber Tandem Cell. *Nat. Photonics* **2012**, *6* (12), 824–828.
- (138) Bansal, A.; Lewis, N. S. Stabilization of Si Photoanodes in Aqueous Electrolytes through Surface Alkylation. *J. Phys. Chem. B* **1998**, *102* (21), 4058–4060.
- (139) Bansal, A.; Li, X.; Lauermann, I.; Lewis, N. S.; Yi, S. I.; Weinberg, W. H. Alkylation of Si Surfaces Using a Two-Step Halogenation/Grignard Route. *J. Am. Chem. Soc.* **1996**, *118* (30), 7225–7226.
- (140) Hu, S.; Lewis, N. S.; Ager, J. W.; Yang, J.; McKone, J. R.; Strandwitz, N. C. Thin-Film Materials for the Protection of Semiconducting Photoelectrodes in Solar-Fuel Generators. *J. Phys. Chem. C* **2015**, *119* (43), 24201–24228.
- (141) Lichterman, M. F.; Sun, K.; Hu, S.; Zhou, X.; McDowell, M. T.; Shaner, M. R.; Richter, M. H.; Crumlin, E. J.; Carim, A. I.; Saadi, F. H.; et al. Protection of Inorganic Semiconductors for Sustained, Efficient Photoelectrochemical Water Oxidation. *Catal. Today* **2016**, *262*, 11–23.
- (142) Feynman, R. P. There's Plenty of Room at the Bottom. *Miniaturization*. 1960, pp 282–296.
- (143) Lévy, F. Film Growth and Epitaxy: Methods. *Ref. Modul. Mater. Sci. Mater. Eng.* **2016**, No. April 2015, 1–16.
- (144) Kast, M. G.; Enman, L. J.; Gurnon, N. J.; Nadarajah, A.; Boettcher, S. W. Solution-Deposited F:SnO₂/TiO₂ as a Base-Stable Protective Layer and Antireflective Coating for Microtextured Buried-Junction H₂-Evolving Si Photocathodes. *ACS Appl. Mater. Interfaces* **2014**, *6* (24), 22830–22837.
- (145) Oskam, G.; Long, J. G.; Natarajan, A.; Searson, P. C. Electrochemical Deposition of Metals onto Silicon. *J. Phys. D Appl. Phys* **1998**, No. 31, 1927–1949.
- (146) Sun, K.; Shen, S.; Cheung, J. S.; Pang, X.; Park, N.; Zhou, J.; Hu, Y.; Sun, Z.; Noh, S. Y.; Riley, C. T.; et al. Si Photoanode Protected by a Metal Modified ITO Layer with Ultrathin NiOx for Solar Water Oxidation. *Phys. Chem. Chem. Phys.* **2014**, *16* (10), 4612–4625.
- (147) Sun, K.; McDowell, M. T.; Nielander, A. C.; Hu, S.; Shaner, M. R.; Yang, F.; Brunshwig, B. S.; Lewis, N. S. Stable Solar-Driven Water Oxidation to O₂(G) by Ni-Oxide-Coated Silicon Photoanodes. *J. Phys. Chem. Lett.* **2015**, *6* (4), 592–598.
- (148) Roger, I.; Shipman, M. A.; Symes, M. D. Earth-Abundant Catalysts for Electrochemical and Photoelectrochemical Water Splitting Isolda. *Nat. Rev. Chem.* **2017**, *1*, 1–13.
- (149) Park, S. H.; Son, Y. C.; Willis, W. S.; Suib, S. L.; Creasy, K. E. Tin Oxide Films Made by

- Physical Vapor Deposition-Thermal Oxidation and Spray Pyrolysis. *Chem. Mater.* **1998**, *10* (9), 2389–2398.
- (150) Kelly, P. J.; Arnell, R. D. Magnetron Sputtering: A Review of Recent Developments and Applications. **2000**, *56*, 159–172.
- (151) Greene, J. E. Review Article: Tracing the Recorded History of Thin-Film Sputter Deposition: From the 1800s to 2017. *J. Vac. Sci. Technol. A Vacuum, Surfaces, Film.* **2017**, *35* (5), 05C204.
- (152) Lin, Y.; Battaglia, C.; Boccard, M.; Hettick, M.; Yu, Z.; Ballif, C.; Ager, J. W.; Javey, A. Amorphous Si Thin Film Based Photocathodes with High Photovoltage for Efficient Hydrogen Production. *Nano Lett.* **2013**, *13* (11), 5615–5618.
- (153) Mei, B.; Pedersen, T.; Malacrida, P.; Bae, D.; Frydendal, R.; Hansen, O.; Vesborg, P. C. K.; Seger, B.; Chorkendorff, I. Crystalline TiO₂: A Generic and Effective Electron-Conducting Protection Layer for Photoanodes and -Cathodes. *J. Phys. Chem. C* **2015**, *119* (27), 15019–15027.
- (154) McDowell, M. T.; Lichterman, M. F.; Carim, A. I.; Liu, R.; Hu, S.; Brunshwig, B. S.; Lewis, N. S. The Influence of Structure and Processing on the Behavior of TiO₂ Protective Layers for Stabilization of N-Si/TiO₂/Ni Photoanodes for Water Oxidation. *ACS Appl. Mater. Interfaces* **2015**, *7* (28), 15189–15199.
- (155) Lowndes, D. H.; Geohegan, D. B.; Puzos, A. A.; Norton, D. P.; Rouleau, C. M. Synthesis of Novel Thin-Film Materials by Pulsed Laser Deposition. *Science* (80-.). **2012**, *273* (5277), 898–903.
- (156) Orlandi, M.; Caramori, S.; Ronconi, F.; Bignozzi, C. A.; Koura, Z. El; Bazzanella, N.; Meda, L.; Miotello, A. Pulsed-Laser Deposition of Nanostructured Iron Oxide Catalysts for Efficient Water Oxidation. *ACS Appl. Mater. Interfaces* **2014**, *6* (9), 6186–6190.
- (157) Fujii, T.; Groot, F. M. F. De; Sawatzky, G. A. In Situ XPS Analysis of Various Iron Oxide Films Grown by NO₂-Assisted Molecular-Beam Epitaxy. **1999**, *59* (4), 3195–3202.
- (158) Doolittle, W. A.; Carver, A. G.; Henderson, W. Molecular Beam Epitaxy of Complex Metal-Oxides: Where Have We Come, Where Are We Going, and How Are We Going to Get There? *J. Vac. Sci. Technol. B Microelectron. Nanom. Struct.* **2005**, *23* (3), 1272.
- (159) Crowell, J. E. Chemical Methods of Thin Film Deposition: Chemical Vapor Deposition, Atomic Layer Deposition, and Related Technologies. *J. Vac. Sci. Technol. A Vacuum, Surfaces, Film.* **2003**, *21* (5), S88–S95.
- (160) Vasudev, M. C.; Anderson, K. D.; Bunning, T. J.; Tsukruk, V. V.; Naik, R. R. Exploration of Plasma-Enhanced Chemical Vapor Deposition as a Method for Thin-Film Fabrication with Biological Applications. *ACS Appl. Mater. Interfaces* **2013**, *5* (10), 3983–3994.
- (161) Scheuermann, A. G.; McIntyre, P. C. Atomic Layer Deposited Corrosion Protection: A Path to Stable and Efficient Photoelectrochemical Cells. *J. Phys. Chem. Lett.* **2016**, *7* (14), 2867–2878.
- (162) Van Bui, H.; Kovalgin, A. Y.; Wolters, R. A. M. Growth of Sub-Nanometer Thin Continuous TiN Films by Atomic Layer Deposition. *ECS J. Solid State Sci. Technol.* **2012**, *1* (6), P285–P290.

- (163) Mikko Ritala; Markku Leskela. Atomic Layer Epitaxy--a Valuable Tool for Nanotechnology? *Nanotechnology* **1999**, *10*, 19–24.
- (164) M. George, S. Atomic Layer Deposition: An Overview. *Chem. Rev.* **2010**, *110* (1), 111–131.
- (165) Wang, H.; Zhang, L.; Chen, Z.; Hu, J.; Li, S.; Wang, Z.; Liu, J.; Wang, X. Semiconductor Heterojunction Photocatalysts: Design, Construction, and Photocatalytic Performances. *Chem. Soc. Rev.* **2014**, *43* (15), 5234–5244.
- (166) Nakato, Y.; Yano, H.; Nishiura, S.; Ueda, T.; Tsubomura, H. Hydrogen Photoevolution at P-Type Silicon Electrodes Coated with Discontinuous Metal Layers. *J. Electroanal. Chem.* **1987**, *228* (1–2), 97–108.
- (167) Nakato, Y.; Tsubomura, H. Structures and Functions of Thin Metal Layers on Semiconductor Electrodes. *J. Photochem.* **1985**, *29* (1–2), 257–266.
- (168) Nakato, Y.; Tsubomura, H. Silicon Photoelectrodes Modified with Ultrafine Metal Islands. *Electrochim. Acta* **1992**, *37* (5), 897–907.
- (169) Nagasubramanian, G.; Bard, A. J. Semiconductor Electrodes. **1980**, *128* (5), 1055–1060.
- (170) Nakato, K.; Takabayashi, S.; Imanishi, A.; Murakoshi, K.; Nakato, Y. Stabilization of N-Si Electrodes by Surface Alkylation and Metal Nano-Dot Coating for Use in Efficient Photoelectrochemical Solar Cells. *Sol. Energy Mater. Sol. Cells* **2004**, *83* (4), 323–330.
- (171) Harris, L. A. The Role of Metal Overlayers on Gallium Phosphide Photoelectrodes. *J. Electrochem. Soc.* **1977**, *124* (10), 1511.
- (172) Heller, A.; Aharon-Shalom, E.; Bonner, W. A.; Miller, B. Hydrogen-Evolving Semiconductor Photocathodes. Nature of the Junction and Function of the Platinum Group Metal Catalyst. *J. Am. Chem. Soc.* **1982**, *104* (25), 6942–6948.
- (173) Maier, C. U.; Specht, M.; Bilger, G. Hydrogen Evolution on Platinum-Coated p-Silicon Photocathodes. *Int. J. Hydrogen Energy* **1996**, *21* (10), 859–864.
- (174) Kenney, M. J.; Gong, M.; Li, Y.; Wu, J. Z.; Feng, J.; Lanza, M.; Dai, H. High-Performance Silicon Photoanodes Passivated with Ultrathin Nickel Films for Water Oxidation. *Science* (80-). **2013**, *342* (6160), 836–840.
- (175) Laskowski, F. A. L.; Nellist, M. R.; Venkatkarthick, R.; Boettcher, S. W. Junction Behavior of N-Si Photoanodes Protected by Thin Ni Elucidated from Dual Working Electrode Photoelectrochemistry. *Energy Environ. Sci.* **2017**, *10* (2), 570–579.
- (176) Sartori, A.; Orlandi, M.; Berardi, S.; Mazzi, A.; Bazzanella, N.; Caramori, S.; Boaretto, R.; Natali, M.; Fernandes, R.; Patel, N.; et al. Functionalized P-Silicon Photocathodes for Solar Fuels Applications: Insights from Electrochemical Impedance Spectroscopy. *Electrochim. Acta* **2018**, *271*, 472–480.
- (177) Feng, J.; Gong, M.; Kenney, M. J.; Wu, J. Z.; Zhang, B.; Li, Y.; Dai, H. Nickel-Coated Silicon Photocathode for Water Splitting in Alkaline Electrolytes. *Nano Res.* **2015**, *8* (5), 1577–1583.
- (178) Sun, K.; Shen, S.; Liang, Y.; Burrows, P. E.; Mao, S. S.; Wang, D. Enabling Silicon for Solar-Fuel Production. *Chem. Rev.* **2014**, *114* (17), 8662–8719.

- (179) Seger, B.; Laursen, A. B.; Vesborg, P. C. K.; Pedersen, T.; Hansen, O.; Dahl, S.; Chorkendorff, I. Hydrogen Production Using a Molybdenum Sulfide Catalyst on a Titanium-Protected n(+)-p-Silicon Photocathode. *Angew. Chem. Int. Ed. Engl.* **2012**, *51* (36), 9128–9131.
- (180) Mei, B.; Seger, B.; Pedersen, T.; Malizia, M.; Hansen, O.; Chorkendorff, I.; Vesborg, P. C. K. Protection of p + -n-Si Photoanodes by Sputter-Deposited Ir/IrO_x Thin Films. *J. Phys. Chem. Lett.* **2014**, *5* (11), 1948–1952.
- (181) Singh, R.; Green, M. A.; Rajkanan, K. Review of Conductor-Insulator-Semiconductor (CIS) Solar Cells. *Sol. Cells* **1981**, *3* (2), 95–148.
- (182) Green, M. A.; Blakers, A. W. Advantages of Metal-Insulator-Semiconductor Structure for Silicon Solar Cells. *Sol. Cells* **1983**, *8*, 3–16.
- (183) Chen, Y. W.; Prange, J. D.; Dühnen, S.; Park, Y.; Gunji, M.; Chidsey, C. E. D.; McIntyre, P. C. Atomic Layer-Deposited Tunnel Oxide Stabilizes Silicon Photoanodes for Water Oxidation. *Nat. Mater.* **2011**, *10* (7), 539–544.
- (184) Contractor, A. Q.; Bockris, J. O. M. Investigation of a Protective Conducting Silica Film on N-Silicon. *Electrochim. Acta* **1984**, *29* (10), 1427–1434.
- (185) Esposito, D. V.; Levin, I.; Moffat, T. P.; Talin, A. A. H₂ Evolution at Si-Based Metal-Insulator-Semiconductor Photoelectrodes Enhanced by Inversion Channel Charge Collection and H Spillover. *Nat. Mater.* **2013**, *12* (6), 562–568.
- (186) Scheuermann, A. G.; Lu, D. Q.; Ito, T.; Chidsey, C. E. D.; McIntyre, P. C. The Effect of SPA-SiO₂ Tunnel Oxide Thickness for Metal-Insulator-Silicon Photoelectrochemical Cells. *ECS Trans.* **2014**, *64* (9), 265–276.
- (187) Lee, M. H.; Takei, K.; Zhang, J.; Kapadia, R.; Zheng, M.; Chen, Y.-Z.; Nah, J.; Matthews, T. S.; Chueh, Y.-L.; Ager, J. W.; et al. P-Type InP Nanopillar Photocathodes for Efficient Solar-Driven Hydrogen Production. *Angew. Chemie Int. Ed.* **2012**, *51* (43), 10760–10764.
- (188) Scheuermann, A. G.; Prange, J. D.; Gunji, M.; Chidsey, C. E. D.; McIntyre, P. C. Effects of Catalyst Material and Atomic Layer Deposited TiO₂oxide Thickness on the Water Oxidation Performance of Metal-Insulator-Silicon Anodes. *Energy Environ. Sci.* **2013**, *6* (8), 2487–2496.
- (189) Scheuermann, A. G.; Lawrence, J. P.; Kemp, K. W.; Ito, T.; Walsh, A.; Chidsey, C. E. D.; Hurley, P. K.; McIntyre, P. C. Design Principles for Maximizing Photovoltage in Metal-Oxide-Protected Water-Splitting Photoanodes. *Nat. Mater.* **2015**, *15* (October), 1–8.
- (190) Xia, Z.; Zhou, X.; Li, J.; Qu, Y. Protection Strategy for Improved Catalytic Stability of Silicon Photoanodes for Water Oxidation. *Sci. Bull.* **2015**, *60* (16), 1395–1402.
- (191) Scheuermann, A. G.; Kemp, K. W.; Tang, K.; Lu, D. Q.; Satterthwaite, P. F.; Ito, T.; Chidsey, C. E. D.; McIntyre, P. C. Conductance and Capacitance of Bilayer Protective Oxides for Silicon Water Splitting Anodes. *Energy Environ. Sci.* **2016**, *9* (2), 504–516.
- (192) Choi, M. J.; Jung, J. Y.; Park, M. J.; Song, J. W.; Lee, J. H.; Bang, J. H. Long-Term Durable Silicon Photocathode Protected by a Thin Al₂O₃/SiO_x Layer for Photoelectrochemical Hydrogen Evolution. *J. Mater. Chem. A* **2014**, *2* (9), 2928–2933.
- (193) Scheuermann, A. G.; Lawrence, J. P.; Meng, A. C.; Tang, K.; Hendricks, O. L.; Chidsey, C. E. D.; McIntyre, P. C. Titanium Oxide Crystallization and Interface Defect Passivation for High Performance Insulator-Protected Schottky Junction MIS Photoanodes. *ACS Appl. Mater.*

- Interfaces* **2016**, *8* (23), 14596–14603.
- (194) Hu, S.; Shaner, M. R.; Beardslee, J. a; Lichterman, M.; Brunshwig, B. S.; Lewis, N. S. Amorphous TiO₂ Coatings Stabilize Si, GaAs, and GaP Photoanodes for Efficient Water Oxidation. *Science* **2014**, *344* (6187), 1005–1009.
- (195) Campet, G.; Manaud, J. P.; Puprichitkun, C.; Sun, Z. W.; Salvador, P. Protection of Photoanodes against Photo-Corrosion by Surface Deposition of Oxide Films: Criteria for Choosing the Protective Coating. *Act. Passiv. Electron. Components* **1989**, *13* (3), 175–189.
- (196) Ran, J.; Zhang, J.; Yu, J.; Jaroniec, M.; Qiao, S. Z. Earth-Abundant Cocatalysts for Semiconductor-Based Photocatalytic Water Splitting. *Chem. Soc. Rev.* **2014**, *43* (22), 7787–7812.
- (197) Singh, A.; Spiccia, L. Water Oxidation Catalysts Based on Abundant 1st Row Transition Metals. *Coord. Chem. Rev.* **2013**, *257* (17–18), 2607–2622.
- (198) Lin, F.; Boettcher, S. W. Adaptive Semiconductor/Electrocatalyst Junctions in Water-Splitting Photoanodes. *Nat. Mater.* **2014**, *13* (1), 81–86.
- (199) Kraft, A.; Görig, B.; Heckner, K. H. ITO Coated N-GaAs Electrodes for Photoelectrochemical Solar Cells. *Sol. Energy Mater. Sol. Cells* **1994**, *32* (2), 151–158.
- (200) Bard, A. J. Photoelectrochemistry and Heterogeneous Photo-Catalysis at Semiconductors. *J. Photochem.* **1979**, *10* (1), 59–75.
- (201) Bae, D.; Pedersen, T.; Seger, B.; Malizia, M.; Kuznetsov, A.; Hansen, O.; Chorkendorff, I.; Vesborg, P. C. K. Back-Illuminated Si Photocathode: A Combined Experimental and Theoretical Study for Photocatalytic Hydrogen Evolution. *Energy Environ. Sci.* **2015**, *8* (2), 650–660.
- (202) Seger, B.; Pedersen, T.; Laursen, A. B.; Vesborg, P. C. K.; Hansen, O.; Chorkendorff, I. Using TiO₂ as a Conductive Protective Layer for Photocathodic H₂ Evolution. *J. Am. Chem. Soc.* **2013**, *135* (3), 1057–1064.
- (203) Kirner, U. K.; Schierbaum, K. D.; Göpel, W. Interface-Reactions of Pt/TiO₂: Comparative Electrical, XPS-, and AES-Depth Profile Investigations. *Fresenius. J. Anal. Chem.* **1991**, *341* (5–6), 416–420.
- (204) Cerchez, M.; Langer, H.; El Achhab, M.; Heinzl, T.; Ostermann, D.; Lüder, H.; Degenhardt, J. Dynamics of Hydrogen Sensing with Pt/TiO₂ Schottky Diodes. *Appl. Phys. Lett.* **2013**, *103* (3).
- (205) Deskins, N. A.; Dupuis, M. Electron Transport via Polaron Hopping in Bulk TiO₂: A Density Functional Theory Characterization. *Phys. Rev. B - Condens. Matter Mater. Phys.* **2007**, *75* (19), 1–10.
- (206) Bally, A. Electronic Properties of Nano-Crystalline Titanium Dioxide Thin Films. **1999**, *2094*, 140.
- (207) Kast, M. G.; Enman, L. J.; Gurnon, N. J.; Nadarajah, A.; Boettcher, S. W. Solution-Deposited F:SnO₂/TiO₂ as a Base-Stable Protective Layer and Antireflective Coating for Microtextured Buried-Junction H₂-Evolving Si Photocathodes. *ACS Appl. Mater. Interfaces* **2014**, *6* (24), 22830–22837.

- (208) Sabat, K. C.; Rajput, P.; Paramguru, R. K.; Bhoi, B.; Mishra, B. K. Reduction of Oxide Minerals by Hydrogen Plasma: An Overview. *Plasma Chem. Plasma Process.* **2014**, *34* (1), 1–23.
- (209) Satterthwaite, P. F.; Scheuermann, A. G.; Hurley, P. K.; Chidsey, C. E. D.; McIntyre, P. C. Engineering Interfacial Silicon Dioxide for Improved Metal-Insulator-Semiconductor Silicon Photoanode Water Splitting Performance. *ACS Appl. Mater. Interfaces* **2016**, *8* (20), 13140–13149.
- (210) Seger, B.; Tilley, D. S.; Pedersen, T.; Vesborg, P. C. K.; Hansen, O.; Grätzel, M.; Chorkendorff, I. Silicon Protected with Atomic Layer Deposited TiO₂: Durability Studies of Photocathodic H₂ Evolution. *RSC Adv.* **2013**, *3* (48), 25902–25907.
- (211) Seger, B.; Tilley, S. D.; Pedersen, T.; Vesborg, P. C. K.; Hansen, O.; Graetzel, M.; Chorkendorff, I. Silicon Protected with Atomic Layer Deposited TiO₂: Conducting versus Tunnelling through TiO₂. *J. Mater. Chem. a* **2013**, *1* (47), 15089–15094.
- (212) Liang, J.; Tan, H.; Liu, M.; Liu, B.; Wang, N.; Zhang, Q.; Zhao, Y.; Smets, A. H. M.; Zeman, M.; Zhang, X. A Thin-Film Silicon Based Photocathode with a Hydrogen Doped TiO₂ protection Layer for Solar Hydrogen Evolution. *J. Mater. Chem. A* **2016**, *4* (43), 16841–16848.
- (213) Kempainen, E.; Bodin, A.; Sebok, B.; Pedersen, T.; Seger, B.; Mei, B.; Bae, D.; Vesborg, P. C. K.; Halme, J.; Hansen, O.; et al. Scalability and Feasibility of Photoelectrochemical H₂ Evolution: The Ultimate Limit of Pt Nanoparticle as an HER Catalyst. *Energy Environ. Sci.* **2015**, *8* (10), 2991–2999.
- (214) Sivula, K. Defects Give New Life to an Old Material: Electronically Leaky Titania as a Photoanode Protection Layer. *ChemCatChem* **2014**, 2796–2797.
- (215) Hu, S.; Richter, M. H.; Lichterman, M. F.; Beardslee, J.; Mayer, T.; Brunschwig, B. S.; Lewis, N. S. Electrical, Photoelectrochemical, and Photoelectron Spectroscopic Investigation of the Interfacial Transport and Energetics of Amorphous TiO₂/Si Heterojunctions. *J. Phys. Chem. C* **2016**, *120* (6), 3117–3129.
- (216) Aarik, J.; Aidla, A.; Uustare, T.; Sammelselg, V. Morphology and Structure of TiO₂ Thin Films Grown by Atomic Layer Deposition. *J. Cryst. Growth* **1995**, *148* (3), 268–275.
- (217) Lee, H. Y.; Robertson, J. Doping and Compensation in Nb-Doped Anatase and Rutile TiO₂. *J. Appl. Phys.* **2013**, *113* (21).
- (218) Huy, H. A.; Aradi, B.; Frauenheim, T.; Deák, P. Calculation of Carrier-Concentration-Dependent Effective Mass in Nb-Doped Anatase Crystals of TiO₂. *Phys. Rev. B - Condens. Matter Mater. Phys.* **2011**, *83* (15), 1–7.
- (219) Lichterman, M. F.; Carim, A. I.; McDowell, M. T.; Hu, S.; Gray, H. B.; Brunschwig, B. S.; Lewis, N. S. Stabilization of N-Cadmium Telluride Photoanodes for Water Oxidation to O₂(g) in Aqueous Alkaline Electrolytes Using Amorphous TiO₂ Films Formed by Atomic-Layer Deposition. *Energy Environ. Sci.* **2014**, *7* (10), 3334–3337.

- (220) Lichterman, M. F.; Hu, S.; Richter, M. H.; Crumlin, E.; Axnanda, S.; Favaro, M.; Drisdell, W. S.; Hussain, Z.; Mayer, T.; Brunshwig, B. S.; et al. Direct Observation of the Energetics at a Semiconductor/Liquid Junction by Operando X-Ray Photoelectron Spectroscopy. *Energy Environ. Sci.* **2015**, *8*, 2409–2416.
- (221) Man, G.; Schwartz, J.; Sturm, J. C.; Kahn, A. Electronically Passivated Hole-Blocking Titanium Dioxide/Silicon Heterojunction for Hybrid Silicon Photovoltaics. *Adv. Mater. Interfaces* **2016**, *3* (15), 1–8.
- (222) Shaner, M. R.; Hu, S.; Sun, K.; Lewis, N. S. Stabilization of Si Microwire Arrays for Solar-Driven H₂O Oxidation to O₂(g) in 1.0 M KOH(Aq) Using Conformal Coatings of Amorphous TiO₂. *Energy Environ. Sci.* **2015**, *8* (1), 203–207.
- (223) Peng, T. C.; Xiao, X. H.; Han, X. Y.; Zhou, X. D.; Wu, W.; Ren, F.; Jiang, C. Z. Characterization of DC Reactive Magnetron Sputtered NiO Films Using Spectroscopic Ellipsometry. *Appl. Surf. Sci.* **2011**, *257* (13), 5908–5912.
- (224) Sun, K.; Saadi, F. H.; Lichterman, M. F.; Hale, W. G.; Wang, H.-P.; Zhou, X.; Plymale, N. T.; Omelchenko, S. T.; He, J.-H.; Papadantonakis, K. M.; et al. *Stable Solar-Driven Oxidation of Water by Semiconducting Photoanodes Protected by Transparent Catalytic Nickel Oxide Films*; 2015; Vol. 112.
- (225) Patil, P. S.; Kadam, L. D. Preparation and Characterization of Spray Pyrolyzed Nickel Oxide (NiO) Thin Films. *Appl. Surf. Sci.* **2002**, *199* (1–4), 211–221.
- (226) Sun, K.; Kuang, Y.; Verlage, E.; Brunshwig, B. S.; Tu, C. W.; Lewis, N. S. Sputtered NiOx Films for Stabilization of P+n-InP Photoanodes for Solar-Driven Water Oxidation. *Adv. Energy Mater.* **2015**, *5* (1402276), 1–8.
- (227) Sato, H.; Minami, T.; Takata, S.; Yamada, T. Transparent Conducting P-Type NiO Thin Films Prepared by Magnetron Sputtering. *Thin Solid Films* **1993**, *236* (1–2), 27–31.
- (228) Jang, W. L.; Lu, Y. M.; Hwang, W. S.; Hsiung, T. L.; Wang, H. P. Point Defects in Sputtered NiO Films. *Appl. Phys. Lett.* **2009**, *94* (6), 92–95.
- (229) Irwin, M. D.; Buchholz, D. B.; Hains, A. W.; Chang, R. P. H.; Marks, T. J. P-Type Semiconducting Nickel Oxide as an Efficiency-Enhancing Anode Interfacial Layer in Polymer Bulk-Heterojunction Solar Cells. *Proc. Natl. Acad. Sci.* **2007**, *105* (8), 2783–2787.
- (230) D’Amario, L.; Boschloo, G.; Hagfeldt, A.; Hammarström, L. Tuning of Conductivity and Density of States of NiO Mesoporous Films Used in P-Type DSSCs. *J. Phys. Chem. C* **2014**, *118* (34), 19556–19564.
- (231) Bai, S.; Cao, M.; Jin, Y.; Dai, X.; Liang, X.; Ye, Z.; Li, M.; Cheng, J.; Xiao, X.; Wu, Z.; et al. Low-Temperature Combustion-Synthesized Nickel Oxide Thin Films as Hole-Transport Interlayers for Solution-Processed Optoelectronic Devices. *Adv. Energy Mater.* **2014**, *4* (6), 1–6.
- (232) Mei, B.; Pedersen, T.; Malacrida, P.; Bae, D.; Frydendal, R.; Hansen, O.; Vesborg, P. C. K.; Seger, B.; Chorkendorff, I. Crystalline TiO₂: A Generic and Effective Electron-Conducting Protection Layer for Photoanodes and -Cathodes. *J. Phys. Chem. C* **2015**, *119* (27), 15019–15027.

- (233) Lin, C. Y.; Lai, Y. H.; Mersch, D.; Reisner, E. Cu₂O|NiOx Nanocomposite as an Inexpensive Photocathode in Photoelectrochemical Water Splitting. *Chem. Sci.* **2012**, *3* (12), 3482–3487.
- (234) Ciesielczyk, F.; Bartczak, P.; Wieszczycka, K.; Siwińska-Stefańska, K.; Nowacka, M.; Jesionowski, T. Adsorption of Ni(II) from Model Solutions Using Co-Precipitated Inorganic Oxides. *Adsorption* **2013**, *19* (2–4), 423–434.
- (235) Bachmann, J.; Zolotaryov, A.; Albrecht, O.; Goetze, S.; Berger, A.; Hesse, D.; Novikov, D.; Nielsch, K. Stoichiometry of Nickel Oxide Films Prepared by ALD. *Chem. Vap. Depos.* **2011**, *17* (7–9), 177–180.
- (236) Nachman, M.; Cojocaru, L. N.; Rîbco, L. V. Electrical Properties of Non-Stoichiometric Nickel Oxide. *Phys. Status Solidi* **1965**, *8* (3), 773–783.
- (237) Jiang, F.; Choy, W. C. H.; Li, X.; Zhang, D.; Cheng, J. Post-Treatment-Free Solution-Processed Non-Stoichiometric NiOx Nanoparticles for Efficient Hole-Transport Layers of Organic Optoelectronic Devices. *Adv. Mater.* **2015**, *27* (18), 2930–2937.
- (238) Kuanr, S. K.; Vinothkumar, G.; Babu, K. S. Substrate Temperature Dependent Structural Orientation of EBPVD Deposited NiO Films and Its Influence on Optical, Electrical Property. *Mater. Sci. Semicond. Process.* **2018**, *75* (November 2017), 26–30.
- (239) Chen, H. L.; Yang, Y. S. Effect of Crystallographic Orientations on Electrical Properties of Sputter-Deposited Nickel Oxide Thin Films. *Thin Solid Films* **2008**, *516* (16), 5590–5596.
- (240) Jang, W.; Lu, Y.; Hwang, W.; Hsiung, T.; Wang, H. P. Surface & Coatings Technology Effect of Substrate Temperature on the Electrically Conductive Stability of Sputtered NiO Films. *Surf. Coat. Technol.* **2008**, *202* (22–23), 5444–5447.
- (241) Fujii, T.; Arita, M.; Hamada, K.; Takahashi, Y.; Sakaguchi, N. In-Situ Transmission Electron Microscopy of Conductive Filaments in NiO Resistance Random Access Memory and Its Analysis. *J. Appl. Phys.* **2013**, *113* (8).
- (242) Nardi, F.; Deleruyelle, D.; Spiga, S.; Muller, C.; Bouteille, B.; Ielmini, D. Switching of Nanosized Filaments in NiO by Conductive Atomic Force Microscopy. *J. Appl. Phys.* **2012**, *112* (6).
- (243) Dette, C.; Hurst, M. R.; Deng, J.; Nellist, M. R.; Boettcher, S. W. Structural Evolution of Metal (Oxy)Hydroxide Nanosheets during the Oxygen Evolution Reaction. **2018**.
- (244) Hall, D. S.; Lockwood, D. J.; Bock, C.; MacDougall, B. R. Nickel Hydroxides and Related Materials: A Review of Their Structures, Synthesis and Properties. *Proc. R. Soc. A Math. Phys. Eng. Sci.* **2015**, *471* (2174).
- (245) Lin, F.; Bachman, B. F.; Boettcher, S. W. Impact of Electrocatalyst Activity and Ion Permeability on Water-Splitting Photoanodes. *J. Phys. Chem. Lett.* **2015**, *6* (13), 2427–2433.
- (246) Wang, X.; Wang, Y.; Zhao, C.; Zhao, Y.; Yan, B.; Zheng, W. Electrodeposited Ni(OH)₂ Nanoflakes on Graphite Nanosheets Prepared by Plasma-Enhanced Chemical Vapor Deposition for Supercapacitor Electrode. *New J. Chem.* **2012**, *36* (9), 1902–1906.
- (247) Li, G.; Wang, S. Photoelectrochemical Characteristics of Metal-Modified Epitaxial n-Si Anodes. *Electroanal. Chem.* **1987**, *227*, 213–221.
- (248) Mei, B.; Permyakova, A. A.; Frydendal, R.; Bae, D.; Pedersen, T.; Malacrida, P.; Hansen, O.;

- Stephens, I. E. L. L.; Vesborg, P. C. K. K.; Seger, B.; et al. Iron-Treated NiO as a Highly Transparent P-Type Protection Layer for Efficient Si-Based Photoanodes. *J. Phys. Chem. Lett.* **2014**, *5* (20), 3456–3461.
- (249) Sun, K.; Park, N.; Sun, Z.; Zhou, J.; Wang, J.; Pang, X.; Shen, S.; Noh, S. Y.; Jing, Y.; Jin, S.; et al. Nickel Oxide Functionalized Silicon for Efficient Photo-Oxidation of Water. *Energy Environ. Sci.* **2012**, *5* (7), 7872–7877.
- (250) Nardi, K. L.; Yang, N.; Dickens, C. F.; Strickler, A. L.; Bent, S. F. Creating Highly Active Atomic Layer Deposited NiO Electrocatalysts for the Oxygen Evolution Reaction. *Adv. Energy Mater.* **2015**, *5* (17), 1–10.
- (251) Biset-Peiró, M.; Fàbrega, C.; Morante, J. R.; Andreu, T. Multilayer Ni / Fe Thin Films as Oxygen Evolution Catalysts for Solar Fuel Production.
- (252) Trotochaud, L.; Young, S. L.; Ranney, J. K.; Boettcher, S. W. Nickel-Iron Oxyhydroxide Oxygen-Evolution Electrocatalysts: The Role of Intentional and Incidental Iron Incorporation. *J. Am. Chem. Soc.* **2014**, *136* (18), 6744–6753.
- (253) Hamann, T. W. Water Splitting: An Adaptive Junction. *Nat. Mater.* **2014**, *13* (1), 3–4.
- (254) Bae, D.; Mei, B. T.; Frydendal, R.; Pedersen, T.; Seger, B.; Hansen, O.; Vesborg, P. C. K.; Chorkendorff, I. Back-Illuminated Si Based Photoanode with Nickel Cobalt Oxide Catalytic Protection Layer. *ChemElectroChem* **2016**, *3* (10), 1517.
- (255) Deori, K.; Deka, S. Morphology Oriented Surfactant Dependent CoO and Reaction Time Dependent Co₃O₄ Nanocrystals from Single Synthesis Method and Their Optical and Magnetic Properties. *CrystEngComm* **2013**, *15* (42), 8465–8474.
- (256) Tung, C. W.; Hsu, Y. Y.; Shen, Y. P.; Zheng, Y.; Chan, T. S.; Sheu, H. S.; Cheng, Y. C.; Chen, H. M. Reversible Adapting Layer Produces Robust Single-Crystal Electrocatalyst for Oxygen Evolution. *Nat. Commun.* **2015**, *6*, 1–9.
- (257) Jiang, Y.; Li, X.; Wang, T.; Wang, C. Enhanced Electrocatalytic Oxygen Evolution of α -Co(OH)₂ nanosheets on Carbon Nanotube/Polyimide Films. *Nanoscale* **2016**, *8* (18), 9667–9675.
- (258) Burke, M. S.; Kast, M. G.; Trotochaud, L.; Smith, A. M.; Boettcher, S. W. Cobalt-Iron (Oxy)Hydroxide Oxygen Evolution Electrocatalysts: The Role of Structure and Composition on Activity, Stability, and Mechanism. *J. Am. Chem. Soc.* **2015**, *137* (10), 3638–3648.
- (259) Yang, J.; Walczak, K.; Anzenberg, E.; Toma, F. M.; Yuan, G.; Beeman, J.; Schwartzberg, A.; Lin, Y.; Hettick, M.; Javey, A.; et al. Efficient and Sustained Photoelectrochemical Water Oxidation by Cobalt Oxide/Silicon Photoanodes with Nanotextured Interfaces. *J. Am. Chem. Soc.* **2014**, *136* (17), 6191–6194.
- (260) Xing, Z.; Wu, H.; Wu, L.; Wang, X.; Zhong, H.; Li, F.; Shi, J.; Song, D.; Xiao, W.; Jiang, C.; et al. A Multifunctional Vanadium-Doped Cobalt Oxide Layer on Silicon Photoanodes for Efficient and Stable Photoelectrochemical Water Oxidation. *J. Mater. Chem. A* **2018**, *6* (42), 21167–21177.

- (261) Zhou, X.; Liu, R.; Sun, K.; Papadantonakis, K. M.; Brunshwig, B. S.; Lewis, N. S. 570 MV Photovoltage, Stabilized n-Si/CoO_x Heterojunction Photoanodes Fabricated Using Atomic Layer Deposition. *Energy Environ. Sci.* **2016**, No. 9, 892–897.
- (262) Nurlaela, E.; Wang, H.; Shinagawa, T.; Flanagan, S.; Ould-Chikh, S.; Qureshi, M.; Mics, Z.; Sautet, P.; Le Bahers, T.; Cánovas, E.; et al. Enhanced Kinetics of Hole Transfer and Electrocatalysis during Photocatalytic Oxygen Evolution by Cocatalyst Tuning. *ACS Catal.* **2016**, 6 (7), 4117–4126.
- (263) Kainthla, R. C. Protection of N-Si Photoanode against Photocorrosion in Photoelectrochemical Cell for Water Electrolysis. *J. Electrochem. Soc.* **1986**, 133 (2), 248.
- (264) Switzer, J. A. The N-Silicon/Thallium(III) Oxide Heterojunction Photoelectrochemical Solar Cell. *J. Electrochem. Soc.* **1986**, 133 (4), 722.
- (265) Dutch, S. I. Periodic Tables of Elemental Abundance. *J. Chem. Educ.* **1999**, 76 (3), 356.
- (266) Malizia, M.; Seger, B.; Chorkendorff, I.; Vesborg, P. C. K. Formation of a P-n Heterojunction on GaP Photocathodes for H₂ Production Providing an Open-Circuit Voltage of 710 MV. *J. Mater. Chem. A* **2014**, 2 (19), 6847–6853.
- (267) Takeno, N. Atlas of Eh-PH Diagrams. *Natl. Inst. Adv. Ind. Sci. Technol. Tokyo* **2005**, No. 419, 285.
- (268) Standing, A.; Assali, S.; Gao, L.; Verheijen, M. A.; Van Dam, D.; Cui, Y.; Notten, P. H. L.; Haverkort, J. E. M.; Bakkers, E. P. A. M. Efficient Water Reduction with Gallium Phosphide Nanowires. *Nat. Commun.* **2015**, 6 (May), 1–7.
- (269) Britto, R. J.; Benck, J. D.; Young, J. L.; Hahn, C.; Deutsch, T. G.; Jaramillo, T. F. Molybdenum Disulfide as a Protection Layer and Catalyst for Gallium Indium Phosphide Solar Water Splitting Photocathodes. *J. Phys. Chem. Lett.* **2016**, 7 (11), 2044–2049.
- (270) Ding, Q.; Song, B.; Xu, P.; Jin, S. Efficient Electrocatalytic and Photoelectrochemical Hydrogen Generation Using MoS₂ and Related Compounds. *Chem* **2016**, 1 (5), 699–726.
- (271) Gu, J.; Aguiar, J. A.; Ferrere, S.; Steirer, K. X.; Yan, Y.; Xiao, C.; Young, J. L.; Al-Jassim, M.; Neale, N. R.; Turner, J. A. A Graded Catalytic-Protective Layer for an Efficient and Stable Water-Splitting Photocathode. *Nat. Energy* **2017**, 2 (2), 1–8.
- (272) Laursen, A. B.; Pedersen, T.; Malacrida, P.; Seger, B.; Hansen, O.; Vesborg, P. C. K.; Chorkendorff, I. MoS₂- An Integrated Protective and Active Layer on N+p-Si for Solar H₂ evolution. *Phys. Chem. Chem. Phys.* **2013**, 15 (46), 20000–20004.
- (273) King, L. A.; Hellstern, T. R.; Park, J.; Sinclair, R.; Jaramillo, T. F. Highly Stable Molybdenum Disulfide Protected Silicon Photocathodes for Photoelectrochemical Water Splitting. *ACS Appl. Mater. Interfaces* **2017**, 9 (42), 36792–36798.
- (274) Digdaya, I. A.; Adhyaksa, G. W. P.; Trzesniewski, B. J.; Garnett, E. C.; Smith, W. A. Interfacial Engineering of Metal-Insulator-Semiconductor Junctions for Efficient and Stable Photoelectrochemical Water Oxidation. *Nat. Commun.* **2017**, 8 (May), 15968.
- (275) Ji, L.; Mcdaniel, M. D.; Wang, S.; Posadas, A. B.; Li, X.; Huang, H.; Lee, J. C.; Demkov, A. A.; Bard, A. J.; Ekerdt, J. G.; et al. A Silicon-Based Photocathode for Water Reduction with an Epitaxial SrTiO₃ protection Layer and a Nanostructured Catalyst. *Nat. Nanotechnol.* **2015**, 10 (1), 84–90.

- (276) Bao, J. Photoelectrochemical Water Splitting: A New Use for Bandgap Engineering. *Nat. Nanotechnol.* **2015**, *10* (1), 19–20.
- (277) Campet, G.; Sun, Z. W.; Keou, P. Realization of Solar Cells Based on Silicon/Oxide Junctions. *Act. Passiv. Electron. Components* **1990**, *14* (2), 47–52.
- (278) Yoon, K. H.; Shin, C. W.; Kang, D. H. Photoelectrochemical Conversion in a WO₃ Coated P-Si Photoelectrode: Effect of Annealing Temperature. *J. Appl. Phys.* **1997**, *81* (10), 7024–7029.
- (279) Yoon, K. H.; Seo, D. K.; Cho, Y. S.; Kang, D. H. Effect of Pt Layers on the Photoelectrochemical Properties of a WO₃/p-Si Electrode. *J. Appl. Phys.* **1998**, *84* (7), 3954–3959.
- (280) Coridan, R. H.; Shaner, M.; Wiggernhorn, C.; Brunschwig, B. S.; Lewis, N. S. Electrical and Photoelectrochemical Properties of WO₃ / Si Tandem Photoelectrodes. *J. Phys. Chem. C* **2013**, *117*, 6949–6957.
- (281) Wang, X.; Peng, K. Q.; Hu, Y.; Zhang, F. Q.; Hu, B.; Li, L.; Wang, M.; Meng, X. M.; Lee, S. T. Silicon/Hematite Core/Shell Nanowire Array Decorated with Gold Nanoparticles for Unbiased Solar Water Oxidation. *Nano Lett.* **2014**, *14* (1), 18–23.
- (282) Sun, K.; Madsen, K.; Andersen, P.; Bao, W.; Sun, Z.; Wang, D. Metal on Metal Oxide Nanowire Co-Catalyzed Si Photocathode for Solar Water Splitting. *Nanotechnology* **2012**, *23* (19).
- (283) Allen J. Bard. *Standard Potentials in Aqueous Solution*; Routledge: New York, 1985.
- (284) Lin, Y.; Kapadia, R.; Yang, J.; Zheng, M.; Chen, K.; Hettick, M.; Yin, X.; Battaglia, C.; Sharp, I. D.; Ager, J. W.; et al. Role of TiO₂ surface Passivation on Improving the Performance of P-InP Photocathodes. *J. Phys. Chem. C* **2015**, *119* (5), 2308–2313.
- (285) Azarpira, A.; Lublow, M.; Steigert, A.; Bogdanoff, P.; Greiner, D.; Kaufmann, C. A.; Krüger, M.; Gernert, U.; Van De Krol, R.; Fischer, A.; et al. Efficient and Stable TiO₂:Pt-Cu(In,Ga)Se₂ Composite Photoelectrodes for Visible Light Driven Hydrogen Evolution. *Adv. Energy Mater.* **2015**, *5* (12), 1–9.
- (286) Repins, I.; Contreras, M. A.; Egaas, B.; DeHart, C.; Scharf, J.; Perkins, C. L.; To, B.; Noufi, R. 19.9%-Efficient ZnO/CdS/CuInGaSe₂ Solar Cell with 81.2% Fill Factor. *Prog. Photovoltaics Res. Appl.* **2008**, *16* (3), 235–239.
- (287) Kumagai, H.; Minegishi, T.; Sato, N.; Yamada, T.; Kubota, J.; Domen, K. Efficient Solar Hydrogen Production from Neutral Electrolytes Using Surface-Modified Cu(In,Ga)Se₂ Photocathodes. *J. Mater. Chem. A* **2015**, *3* (16), 8300–8307.
- (288) Greiner, M. T.; Chai, L.; Helander, M. G.; Tang, W. M.; Lu, Z. H. Transition Metal Oxide Work Functions: The Influence of Cation Oxidation State and Oxygen Vacancies. *Adv. Funct. Mater.* **2012**, *22* (21), 4557–4568.
- (289) Zhou, X.; Liu, R.; Sun, K.; Friedrich, D.; McDowell, M. T.; Yang, F.; Omelchenko, S. T.; Saadi, F. H.; Nielander, A. C.; Yalamanchili, S.; et al. Interface Engineering of the Photoelectrochemical Performance of Ni-Oxide-Coated n-Si Photoanodes by Atomic-Layer Deposition of Ultrathin Films of Cobalt Oxide. *Energy Environ. Sci.* **2015**, *8*, 2644–2649.

- (290) Osaka, T. Photoelectrochemical Behavior of Iron Oxide/n-Si Heterojunction Electrodes with an Outer Pd Layer. *J. Electrochem. Soc.* **1984**, *131* (7), 1571.
- (291) Morisaki, H.; Ono, H.; Dohkoshi, H.; Yazawa, K. Iron-Oxide Coated n-Si as a Heterostructure Photoanode for the Photoelectrolysis of Water. *Jpn. J. Appl. Phys.* **1980**, *19* (3), L148–L150.
- (292) Scheuermann, A. G.; Chidsey, C. E. D.; McIntyre, P. C. Understanding Photovoltage in Insulator-Protected Water Oxidation Half-Cells. *J. Electrochem. Soc.* **2016**, *163* (3), H192–H200.
- (293) Lichterman, M. F.; Hu, S.; Richter, M. H.; Crumlin, E. J.; Axnanda, S.; Favaro, M.; Drisdell, W.; Hussain, Z.; Mayer, T.; Brunshwig, B. S.; et al. Direct Observation of the Energetics at a Semiconductor/Liquid Junction by *Operando* X-Ray Photoelectron Spectroscopy. *Energy Environ. Sci.* **2015**, *8* (8), 2409–2416.
- (294) Scheuermann, A. G.; Lawrence, J. P.; Kemp, K. W.; Ito, T.; Walsh, A.; Chidsey, C. E. D.; Hurley, P. K.; McIntyre, P. C. Design Principles for Maximizing Photovoltage in Metal-Oxide-Protected Water-Splitting Photoanodes. *Nat. Mater.* **2015**, *15* (October), 99–105.
- (295) Boettcher, S. W.; Warren, E. L.; Putnam, M. C.; Santori, E. A.; Turner-Evans, D.; Kelzenberg, M. D.; Walter, M. G.; McKone, J. R.; Brunshwig, B. S.; Atwater, H. A.; et al. Photoelectrochemical Hydrogen Evolution Using Si Microwire Arrays. *J. Am. Chem. Soc.* **2011**, *133* (5), 1216–1219.
- (296) Wang, T.; Gong, J. Single-Crystal Semiconductors with Narrow Band Gaps for Solar Water Splitting. *Angew. Chemie - Int. Ed.* **2015**, *54* (37), 10718–10732.
- (297) Mei, B.; Permyakova, A. a; Frydendal, R.; Bae, D.; Pedersen, T.; Malacrida, P.; Hansen, O.; Stephens, I. E. L.; Vesborg, P. C. K.; Seger, B.; et al. Iron-Treated NiO as a Highly Transparent p - Type Protection Layer for Efficient Si-Based Photoanodes. *J. Phys. Chem. Lett.* **2014**, *5* (20), 3456–3461.
- (298) Ramanujam, J.; Singh, U. P. Copper Indium Gallium Selenide Based Solar Cells - A Review. *Energy Environ. Sci.* **2017**, *10* (6), 1306–1319.
- (299) Jacobsson, T. J.; Platzer-Björkman, C.; Edoff, M.; Edvinsson, T. CuIn_xGa_{1-x}Se₂ as an Efficient Photocathode for Solar Hydrogen Generation. *Int. J. Hydrogen Energy* **2013**, *38* (35), 15027–15035.
- (300) Chen, Y.; Feng, X.; Liu, M.; Su, J.; Shen, S. Towards Efficient Solar-to-Hydrogen Conversion: Fundamentals and Recent Progress in Copper-Based Chalcogenide Photocathodes. *Nanophotonics* **2016**, *5* (4), 468–491.
- (301) Jacobsson, T. J.; Fjallstrom, V.; Edoff, M.; Edvinsson, T. CIGS Based Devices for Solar Hydrogen Production Spanning from PEC-Cells to PV-Electrolyzers: A Comparison of Efficiency, Stability and Device Topology. *Sol. Energy Mater. Sol. Cells* **2015**, *134*, 185–193.
- (302) Koo, B.; Nam, S. W.; Haight, R.; Kim, S.; Oh, S.; Cho, M.; Oh, J.; Lee, J. Y.; Ahn, B. T.; Shin, B. Tailoring Photoelectrochemical Performance and Stability of Cu(In,Ga)Se₂ Photocathode via TiO₂-Coupled Buffer Layers. *ACS Appl. Mater. Interfaces* **2017**, *9* (6), 5279–5287.
- (303) Septina, W.; Tilley, S. D. Emerging Earth-Abundant Materials for Scalable Solar Water Splitting. *Curr. Opin. Electrochem.* **2017**, *2*, 120–127.

- (304) Jiang, F.; Gunawan; Harada, T.; Kuang, Y.; Minegishi, T.; Domen, K.; Ikeda, S. Pt/In₂S₃/CdS/Cu₂ZnSnS₄ Thin Film as an Efficient and Stable Photocathode for Water Reduction under Sunlight Radiation. *J. Am. Chem. Soc.* **2015**, *137* (42), 13691–13697.
- (305) Rovelli, L.; Tilley, S. D.; Sivula, K. Optimization and Stabilization of Electrodeposited Cu₂ZnSnS₄ Photocathodes for Solar Water Reduction. *ACS Appl. Mater. Interfaces* **2013**, *5* (16), 8018–8024.
- (306) Yokoyama, D.; Minegishi, T.; Jimbo, K.; Hisatomi, T.; Ma, G.; Katayama, M.; Kubota, J.; Katagiri, H.; Domen, K. H₂ Evolution from Water on Modified Cu₂ZnSnS₄ Photoelectrode under Solar Light. *Appl. Phys. Express* **2010**, *3* (10), 101202.
- (307) Septina, W.; Ikeda, S.; Harada, T.; Minegishi, T.; Domen, K.; Matsumura, M. Platinum and Indium Sulfide-Modified CuInS₂ as Efficient Photocathodes for Photoelectrochemical Water Splitting. *Chem. Commun.* **2014**, *50* (64), 8941.
- (308) Guan, Z.; Luo, W.; Zou, Z. Formation Mechanism of ZnS Impurities and Their Effect on Photoelectrochemical Properties on a Cu₂ZnSnS₄ Photocathode. *Crystengcomm* **2014**, 2929–2936.
- (309) Chae, S. Y.; Park, S. J.; Han, S. G.; Jung, H.; Kim, C.-W.; Jeong, C.; Joo, O.-S.; Min, B. K.; Hwang, Y. J. Enhanced Photocurrents with ZnS Passivated Cu(In,Ga)(Se,S)₂ Photocathodes Synthesized Using a Nonvacuum Process for Solar Water Splitting. *J. Am. Chem. Soc.* **2016**, *138*, 15673–15681.
- (310) Ikeda, S.; Nonogaki, M.; Septina, W.; Gunawan, G.; Harada, T.; Matsumura, M. Fabrication of CuInS₂ and Cu(In,Ga)S₂ Thin Films by a Facile Spray Pyrolysis and Their Photovoltaic and Photoelectrochemical Properties. *Catal. Sci. Technol.* **2013**, *3*, 1849.
- (311) Dimitrievska, M.; Fairbrother, A.; Saucedo, E.; Perez-Rodriguez, A.; Izquierdo-Roca, V. Influence of Compositionally Induced Defects on the Vibrational Properties of Device Grade Cu₂ZnSnSe₄ Absorbers for Kesterite Based Solar Cells. *Appl. Phys. Lett.* **2015**, *106*, 073903.
- (312) Chen, S.; Walsh, A.; Gong, X. G.; Wei, S. H. Classification of Lattice Defects in the Kesterite Cu₂ZnSnS₄ and Cu₂ZnSnSe₄ Earth-Abundant Solar Cell Absorbers. *Adv. Mater.* **2013**, *25* (11), 1522–1539.
- (313) Insignares-Cuello, C.; Oliva, F.; Neuschitzer, M.; Fontané, X.; Broussillou, C.; Goislard De Monsabert, T.; Saucedo, E.; Ruiz, C. M.; Pérez-Rodríguez, A.; Izquierdo-Roca, V. Advanced Characterization of Electrodeposition-Based High Efficiency Solar Cells: Non-Destructive Raman Scattering Quantitative Assessment of the Anion Chemical Composition in Cu(In,Ga)(S,Se)₂ Absorbers. *Sol. Energy Mater. Sol. Cells* **2015**, *143*, 212–217.
- (314) Li, G.; Blake, G. R.; Palstra, T. T. M. Vacancies in Functional Materials for Clean Energy Storage and Harvesting: The Perfect Imperfection. *Chem. Soc. Rev.* **2017**, *46* (6), 1693–1706.
- (315) Wang, J.; Zhang, P.; Song, X.; Gao, L. Cu₂ZnSnS₄ Thin Films: Spin Coating Synthesis and Photoelectrochemistry. *RSC Adv.* **2014**, *4*, 21318.
- (316) Wang, H.-P.; Sun, K.; Noh, S. Y.; Kargar, A.; Tsai, M.-L.; Huang, M.-Y.; Wang, D.; He, J.-H. High-Performance A-Si/c-Si Heterojunction Photoelectrodes for Photoelectrochemical Oxygen and Hydrogen Evolution. *Zootaxa* **2011**, No. 2895, 1–34.

- (317) Digdaya, I. A.; Rodriguez, P. P.; Ma, M.; Adhyaksa, G. W. P.; Garnett, E. C.; Smets, A. H. M.; Smith, W. A. Engineering the Kinetics and Interfacial Energetics of Ni/Ni-Mo Catalyzed Amorphous Silicon Carbide Photocathodes in Alkaline Media. *J. Mater. Chem. A* **2016**, *4* (18), 6842–6852.
- (318) Sivula, K.; Prevot, M. S. Photoelectrochemical Tandem Cells for Solar Water Splitting. *J. Phys. Chem. C* **2013**, *117*, 17879–17893.
- (319) Hu, S.; Xiang, C.; Haussener, S.; Berger, A. D.; Lewis, N. S. An Analysis of the Optimal Band Gaps of Light Absorbers in Integrated Tandem Photoelectrochemical Water-Splitting Systems. *Energy Environ. Sci.* **2013**, *6* (10), 2984–2993.
- (320) Fairbrother, A.; Fontané, X.; Izquierdo-Roca, V.; Espindola-Rodriguez, M.; L6pez-Marino, S.; Placidi, M.; L6pez-García, J.; Pérez-Rodríguez, A.; Saucedo, E. Single-Step Sulfo-Selenization Method to Synthesize Cu₂ZnSn(SySe_{1-y})₄ Absorbers from Metallic Stack Precursors. *ChemPhysChem* **2013**, *14* (9), 1836–1843.
- (321) Luo, J.; Tilley, S. D.; Steier, L.; Schreier, M.; Mayer, M. T.; Fan, H. J.; Gratzel, M. Solution Transformation of Cu₂O into CuInS₂ for Solar Water Splitting. *Nano Lett.* **2015**, *15* (2), 1395–1402.
- (322) Yun, S.; Qin, Y.; Uhl, A. R.; Vlachopoulos, N.; Yin, M.; Li, D.; Han, X.; Hagfeldt, A. New-Generation Integrated Devices Based on Dye-Sensitized and Perovskite Solar Cells. *Energy Environ. Sci.* **2018**, *11* (3), 476–526.
- (323) Seger, B.; Hansen, O.; Vesborg, P. C. K. A Flexible Web-Based Approach to Modeling Tandem Photocatalytic Devices. *Sol. RRL* **2016**, 1600013.
- (324) Mayer, M. T. Photovoltage at Semiconductor–Electrolyte Junctions. *Curr. Opin. Electrochem.* **2017**, *2* (1), 104–110.
- (325) Oener, S.; Ardo, S.; Boettcher, S. W. Ionic Processes in Water Electrolysis: The Role of Ion-Selective Membranes. *ACS Energy Lett.* **2017**, No. 2, 2625–2634.
- (326) Pinaud, B. A.; Benck, J. D.; Seitz, L. C.; Forman, A. J.; Chen, Z.; Deutsch, T. G.; James, B. D.; Baum, K. N.; Baum, G. N.; Ardo, S.; et al. Technical and Economic Feasibility of Centralized Facilities for Solar Hydrogen Production via Photocatalysis and Photoelectrochemistry. *Energy Environ. Sci.* **2013**, *6* (7), 1983–2002.
- (327) Minggu, L. J.; Wan Daud, W. R.; Kassim, M. B. An Overview of Photocells and Photoreactors for Photoelectrochemical Water Splitting. *Int. J. Hydrogen Energy* **2010**, *35* (11), 5233–5244.
- (328) Minggu, L. J.; Wan Daud, W. R.; Kassim, M. B. An Overview of Photocells and Photoreactors for Photoelectrochemical Water Splitting. *Int. J. Hydrogen Energy* **2010**, *35* (11), 5233–5244.
- (329) Licht, S.; Wang, B.; Mukerji, S.; Soga, T.; Umeno, M.; Tributsch, H. Over 18% Solar Energy Conversion to Generation of Hydrogen Fuel; Theory and Experiment for Efficient Solar Water Splitting. *Int. J. Hydrogen Energy* **2001**, *26* (7), 653–659.
- (330) Peharz, G.; Dimroth, F.; Wittstadt, U. Solar Hydrogen Production by Water Splitting with a Conversion Efficiency of 18%. *Int. J. Hydrogen Energy* **2007**, *32*, 3248–3252.
- (331) McKone, J. R.; Pieterick, A. P.; Gray, H. B.; Lewis, N. S. Hydrogen Evolution from Pt/Ru-Coated p-Type WSe₂ Photocathodes. *J. Am. Chem. Soc.* **2013**, *135* (1), 223–231.

- (332) Nandjou, F.; Haussener, S. Degradation in Photoelectrochemical Devices: Review with an Illustrative Case Study. *J. Phys. D. Appl. Phys.* **2017**, *50* (12).
- (333) Bae, D.; Seger, B.; Vesborg, P. C. K.; Hansen, O.; Chorkendorff, I. Durability Testing of Photoelectrochemical Hydrogen Production under Day/Night Light Cycled Conditions. *ChemElectroChem* **2018**.
- (334) Rocheleau, R. E.; Miller, E. L.; Misra, A. High-Efficiency Photoelectrochemical Hydrogen Production Using Multijunction Amorphous Silicon Photoelectrodes. *Energy and Fuels* **1998**, *12* (1), 3–10.
- (335) Heremans, G.; Trompoukis, C.; Daems, N.; Bosserez, T.; Vankelecom, I.; Martens, J. A.; Rongé, J. Vapor-Fed Solar Hydrogen Production Exceeding 15% Efficiency Using Earth Abundant Catalysts and Anion Exchange Membrane. *Submitted* **2016**.
- (336) Wang, J.; Ji, L.; Chen, Z. In Situ Rapid Formation of a Nickel-Iron-Based Electrocatalyst for Water Oxidation. *ACS Catal.* **2016**, *6* (10), 6987–6992.
- (337) Montoya, J. H.; Seitz, L. C.; Chakhranont, P.; Vojvodic, A.; Jaramillo, T. F.; Nørskov, J. K. Materials for Solar Fuels and Chemicals. *Nat. Mater.* **2016**, *16* (1), 70–81.
- (338) Kalamaras, E.; Maroto-Valer, M. M.; Shao, M.; Xuan, J.; Wang, H. Solar Carbon Fuel via Photoelectrochemistry. *Catal. Today* **2018**, *317* (February), 56–75.

Chapter 2

*Enhancing metal oxide
photoelectrodes performance*

This chapter is devoted to metal oxide based photoanodes efficiency enhancement by deposition and fabrication optimization and post-synthesis treatments, capable to modify the semiconductor light absorption, charge separation and injection into the electrochemical reaction. Titanium dioxide (TiO_2) has been de selected to fabricate the photoanode as it is an n-type semiconductor material known for significant PEC response. As it was discussed in Chapter 1 section 3, TiO_2 is reported stable in alkaline electrolytes and at oxidative potentials, capable to form a SCLJ with the electrolyte, but the significant band gap and high recombination rates limit their performance. The article included in this chapter focuses on facing the specific detrimental aspects to maximize their performance.

2.1. Hydrogenation and Structuration of TiO_2 Nanorod Photoanodes: Doping Level and the Effect of Illumination in Trap-States Filling

TiO_2 is a 3.2 eV band gap metal oxide, capable to absorb a reduced part of the solar spectra corresponding to the UV part. It was the first discovered photoelectrochemically active semiconductor¹ and has been one of the most studied PEC candidates², but the small portion of visible light converted into photocurrent and relatively high recombination rates are main challenges we will face.

Rutile TiO_2 nanorods hydrothermally grown have achieved significant crystallographic order and thus, enhanced charge mobility. Nanostructured photoanodes allow for significantly higher TiO_2 area in contact with the electrolyte to perform the water oxidation, together with increased light capture. Hydrothermal growth has demonstrated among best performing synthesis routes for TiO_2 , being a relatively facile and inexpensive route requiring a heated autoclave containing the precursor materials and the FTO seeding substrate where the nanorods will hierarchically grow³.

In the first part of this article, we optimized the synthesis by selecting the optimal precursor concentration in the solution, what increased the nanorods packaging and also film thickness. Too high concentration resulted in film detachment. As can be observed in Figure 2.1, the hydrothermal deposition route permits microstructured substrates to be properly covered by TiO_2 nanorods, further enhancing the active area and light absorption. Hydrothermal deposition also includes HCl to create the optimal environment and with Cl^- ions, known as responsible of the hierarchical growth, and requires thermal post-treatments (previously optimized in our group) to eliminate the major part of these ions, incorporated in the crystalline structure⁴.

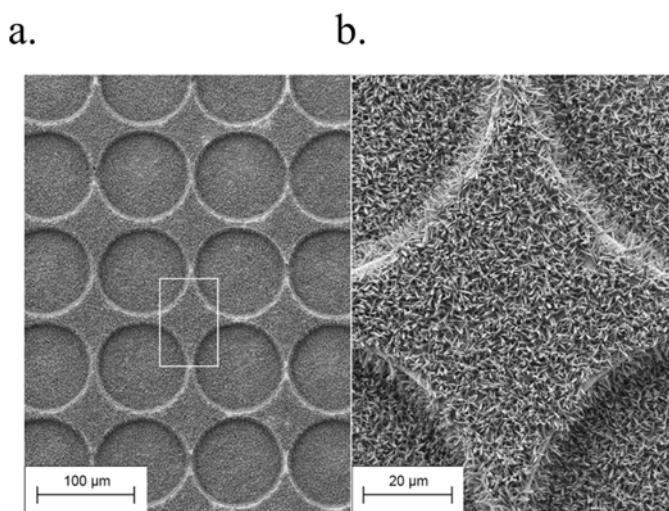


Figure 2.1. a) SEM image of a microstructured TiO_2 photoanode. b) SEM zoomed image, revealing TiO_2 nanorods covering the FTO substrate.

During experiments, incident photon-to-current efficiency (IPCE) measurements revealed significant differences in monochromatic low illumination conditions due to non-filled trap states, and the presence of a light bias was found to increase the effective available charge carriers and to fill trap states. This allowed IPCE measurements better resembling real working conditions (Figure 2.2a).

In a second part of this article, hydrogen post-treatment is used to optimize material's doping level through a reductive process, generating oxygen vacancies. Temperature is optimized so that the hydrogenation caused the optimal states quantity. Depletion layer width adapting to rod's thickness (and thus, the electric field inside the rod) is proposed as the responsible of enhancing charge extraction (reducing recombination and back-reactions), and thus, overall performance, together with increased conductivity by higher doping level (Figure 2.2b). IPCE also revealed the increment in the photogenerated current has been shown to come from a better conversion in the UV part rather than creating states capable to reduce band gap and permit visible light absorption and conversion into photocurrent. Optimized photoanodes reached photocurrent values up to $1.2 \text{ mA} \cdot \text{cm}^{-2}$.

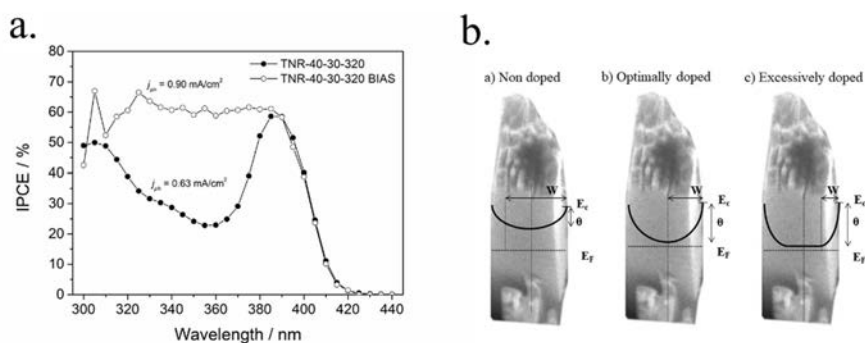


Figure 2.2. a) IPCE conversion efficiencies of a TiO_2 photoanode taken with (empty circles) and without light bias (solid circles). IPCE was measured at 0 V vs Ag/AgCl in a 1 M NaOH electrolyte. Photocurrent densities from integrating the IPCE values to the solar AM 1.5G solar spectra are calculated and indicated. b) Scheme presenting band-bending model for TiO_2 nanorods with an average radius of 100 nm: (a) without any treatment, (b) with the optimal treatment, and (c) with an excessive treatment.

Bibliography

- (1) Fujishima, A.; Honda, K. Electrochemical Photolysis of Water at a Semiconductor Electrode. *Nature* **1972**, 238 (5358), 37–38.
- (2) Berger, T.; Monllor-Satoca, D.; Jankulovska, M.; Lana-Villarreal, T.; Gómez, R. The Electrochemistry of Nanostructured Titanium Dioxide Electrodes. *ChemPhysChem* **2012**, 13 (12), 2824–2875.
- (3) Fàbrega, C.; Monllor-Satoca, D.; Ampudia, S.; Parra, A.; Andreu, T.; Morante, J. R. Tuning the Fermi Level and the Kinetics of Surface States of TiO_2 Nanorods by Means of Ammonia Treatments. *J. Phys. Chem. C* **2013**, 117 (40), 20517–20524.
- (4) Fàbrega, C.; Andreu, T.; Tarancón, A.; Flox, C.; Morata, A.; Calvo-Barrio, L.; Morante, J. R. Optimization of Surface Charge Transfer Processes on Rutile TiO_2 Nanorods Photoanodes for Water Splitting. *Int. J. Hydrogen Energy* **2013**, 38 (7), 2979–2985.

Hydrogenation and Structuration of TiO₂ Nanorod Photoanodes: Doping Level and the Effect of Illumination in Trap-States Filling

C. Ros,^{*,†,‡,§} C. Fàbrega,^{†,‡,§} D. Monllor-Satoca,^{†,||} M. D. Hernández-Alonso,[⊥] G. Penelas-Pérez,[⊥] J. R. Morante,^{†,‡} and T. Andreu^{*,†,‡}

[†]Catalonia Institute for Energy Research (IREC), Jardins de les Dones de Negre 1, 08930 Sant Adrià del Besòs, Barcelona, Spain

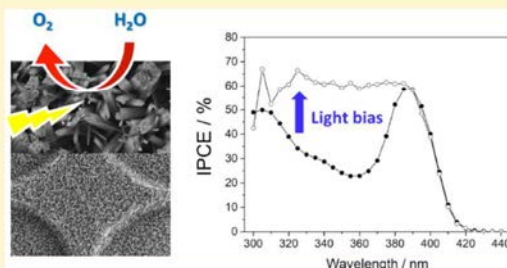
[‡]MIND-Department of Electronics and Biomedical Engineering and [§]Institute of Nanoscience and Nanotechnology (IN²UB), Universitat de Barcelona (UB), c/Martí i Franquès 1, E-08028 Barcelona, Spain

^{||}Department of Analytical and Applied Chemistry, IQS School of Engineering, Universitat Ramon Llull, Via Augusta 390, Barcelona, Spain

[⊥]Repsol Technology Center, Agustín de Betancourt, s/n, 28935 Móstoles, Madrid, Spain

Supporting Information

ABSTRACT: Both electronic properties and light absorption are key features in materials engineering to achieve efficient photoelectrodes for water splitting. Adjusting the potential drop inside the nanostructured semiconductor material through modification of the electronic properties is mandatory to drive efficiently the photogenerated charges. In this work, a hydrogen reduction treatment on titanium dioxide rutile nanorod based photoanodes has been performed in order to adjust the donor density to maximize electron–hole separation. Also, incident photon-to-current efficiency (IPCE) measurements and the effect of a light bias have been elucidated, finding relevant differences in low illumination conditions due to nonfilled trap states. A physical model is proposed to show the role of the donor density on the overall performance of the photoanodes under study. The obtained productivity was enhanced by structuring the conductive glass substrates where TiO₂ nanorods were grown, resulting in a 20% increase of the photocurrent density.



1. INTRODUCTION

In the 1970s, Fujishima and Honda demonstrated the capability of TiO₂ to perform photoelectrochemical (PEC) water splitting, absorbing UV light and dissociating water into hydrogen and oxygen in a single step.¹ Since then, much research has been done toward photoinduced water splitting,^{2–4} but PEC requirements are still so stringent that there is not yet any single cost-effective material capable of overcoming the 10% solar to hydrogen (STH) efficiency needed to make the technology marketable.^{4,5} Among these requirements, at least a 1.8 eV band gap material, no corrosion in aqueous environments, and appropriate conduction band and valence band positions that straddle water oxidation and reduction potentials are conditions that have reduced the possible materials to a few.^{4,6}

Among them, metal oxides such as TiO₂,^{7–11} Fe₂O₃,^{12–14} BiVO₄,^{15–18} and WO₃^{19–21} have demonstrated to be some of the most reliable materials to be implemented in PEC systems, where the former one presents the highest stability and reduced cost.²² However, rutile titanium dioxide has a 3.0 eV band gap, limiting the maximum STH efficiency to a mere 2.2%^{4,3} (corresponding to 1.8 mA cm⁻²), as only 5% of the solar

spectrum is harvested.²⁴ Nonetheless, TiO₂ is still attractive because, thanks to its excellent performance as protective layer and good photoelectrochemical properties toward oxygen evolution reaction (OER), it is being used in the most advanced photoelectrodes recently developed.^{11,25–28}

Among the plethora of nanostructured TiO₂ synthetic routes developed during the past years,²⁹ dense and vertically aligned rutile nanorods grown by hydrothermal methods on fluorinated tin oxide (FTO)-coated glass substrates have proven to be one of the most successful processes in terms of STH efficiency.³⁰ This configuration maximizes the active surface area and reduces the number of TiO₂/substrate interface recombination centers,³¹ as the substrate (i.e., fluorinated tin oxide, FTO) acts as a seed layer for an epitaxial growth. Furthermore, relying on the high temperature and pressure involved in the hydrothermal process, the crystallinity of the obtained TiO₂ is of extreme quality, which hinders the amount of defects along the nanorods.

Received: December 19, 2017

Revised: January 23, 2018

Published: January 23, 2018

In an attempt to enhance the electronic and absorptive properties of TiO_2 , scientists have tried to tune its band gap using additives or dopants such as Nb, W, or Fe^{32-34} or by ammonia treatments^{11,35} but the results obtained so far have not been conclusive and their performance underwhelming. Other authors have also tried to modify electronic properties of titania by electroreducing the material.³⁶

Some studies have proven that hydrogenated TiO_2 nanopowders show an enhanced visible light absorption by adding disorder into the crystal lattice,^{2,37-40} thus creating intraband gap energy levels;⁴¹⁻⁴³ however, the role of these levels has not been completely elucidated. In fact, the increased efficiency of hydrogenated TiO_2 photoanodes has been attributed to the increment of charge carrier density by oxygen vacancies^{44,45} and the introduction of surface states auspicious for the OER.^{38,46}

In this work, we present an optimization of TiO_2 nanorods photoanodes growth process and heating treatment under a hydrogen reductive atmosphere of different duration and at different temperatures, together with substrate patterning for higher active area. A full photoelectrochemical characterization was carried out, paying special attention to the incident photon-to-current efficiency (IPCE) measurements and the effect of a light bias, which is analyzed to be significantly influenced by the extra donors created by the hydrogenation treatment. Working under 1 sunlight bias presented noteworthy differences, pointing out to the need of a light bias for IPCE measurements due to nonfilled states in low light conditions. These findings should encourage other authors to study the need of a light bias in their experiments, or results not representative of the device's working conditions may be obtained. Proper IPCE measurements are especially important for large band gap materials, as these measurements are independent of the used spectra and commercial light sources can have significant deviations from AM1.5G spectra in the UV range.^{47,48} Substrate structuration is known from photovoltaics⁴⁹ but has been analyzed for the first time in water splitting photoanodes up to our knowledge, and we report it is enhancement of device's productivity.

According to the obtained results, we also proposed a model to explain the relation between the increase of charge carrier density and the efficiency improvement of the treated photoanodes.

Combining the strategies of optimization of the growth process, application of a reductive hydrogen treatment, and substrate structuration, we were capable to fabricate a TiO_2 photoanode with photocurrents up to 1.2 mA cm^{-2} and IPCE conversion efficiencies over 65%.

2. MATERIALS AND METHODS

2.1. Photoelectrodes Fabrication. TiO_2 nanorods were grown by hydrothermal synthesis on fluorine-doped tin oxide (FTO) conductive substrates of 20 cm^2 ($4 \times 5 \text{ cm}^2$). Substrates were previously cleaned by sonication for 15 min with a deionized (DI) water, acetone, and isopropanol (1:1:1) solution followed by abundant rinsing in DI water and finally dried under a nitrogen stream. Electrical contacts were made by partially covering the substrates with a Teflon film ($1 \times 5 \text{ cm}^2$) prior to TiO_2 deposition. Teflon was chosen due to its resistance under acidic and moderate temperature conditions.⁵⁰

Teflon-covered FTO substrates were set at an inclination of 45° with the conductive side facing down in a 250 mL Teflon cylindrical reaction chamber. A 100 mL solution was introduced, 18.5 vol % HCl with either 1.36 or 1.53 mL of

titanium butoxide to achieve 40 and 45 mM precursor concentrations, respectively. The Teflon container was sealed into a stainless steel reactor (Parr Instruments Co.), heated up to 200°C at $2^\circ\text{C}/\text{min}$, maintained at 200°C for 120 min, and cooled down to room temperature. Samples were then sonicated in DI water for 10 min and annealed at 500°C for 120 min under air conditions to remove any residuals from the synthetic process.¹¹

We grew two sets of samples using a 40 mM titanium butoxide precursor solution and two more with a 45 mM one. Higher concentrations created thicker TiO_2 layers that detached from the FTO substrate.

These samples were then cut into 40 smaller samples ($\sim 1 \times 2 \text{ cm}^2$) with part of the FTO exposed for electrical contact. All samples were fully characterized and measured in a quartz PEC cell before being subjected to further treatments in order to compare each sample before and after the modifications.

Ten of the samples were annealed under a pure H_2 atmosphere in a sealed Alumina furnace, which was purged with Ar for 15 min, filled with H_2 for 15 min, and heated at different temperatures ranging from 210 to 430°C with $5^\circ\text{C}/\text{min}$ ramp rate and two different dwell times of 30 or 60 min.

Samples were labeled as TNR–precursor concentration (mM)–dwell time (min)–temperature treatment ($^\circ\text{C}$) (i.e., TNR-40-30-320).

To obtain the structured substrate, 500 nm of polycrystalline silicon was deposited by chemical vapor deposition (CVD) on a quartz wafer, followed by deposition of a photoresist exposed with a mask having a pattern of $10 \mu\text{m}$ in diameter circles separated $90 \mu\text{m}$ in a square configuration. A wet etching procedure with a HNO_3 and HF solution was used to transfer the pattern to the polysilicon. A second wet etching process with HF (40 vol %) for 24 min was conducted to pattern the quartz prior to FTO and TiO_2 deposition. The structured substrate was covered with a 550 nm thick layer of FTO ($10 \Omega/\text{square}$) by CVD.

2.2. Characterization. TiO_2 nanorods morphology was observed with a Zeiss Series Auriga field effect scanning electron microscope (FESEM). Structural characterization was carried out by X-ray diffraction (XRD) in a D8 Advance Bruker equipment with a $\text{Cu K}\alpha$ radiation source working at 40 kV and 40 mA. The XRD spectrum has been normalized to the TiO_2 peak. X-ray photoelectron spectroscopy (XPS) measurements were recorded on a PerkinElmer S6000i spectrometer at a pressure lower than 10^{-9} mbar, using a nonmonochromatized Al $\text{K}\alpha$ excitation source (1486.6 eV). Transmission spectrum was obtained with a Pekin-Elmer UV–vis–NIR Lambda 950 spectrometer.

The photoelectrical measurements were obtained with a Princeton Applied Research PARSTAT 2273 potentiostat using saturated Ag/AgCl/KCl as reference electrode and a platinum mesh as counter electrode. The quartz PEC cell was filled with 100 mL of 1 M NaOH electrolyte. Mott–Schottky measurements were collected with a Biologic VMP-300 potentiostat at a frequency of 500 Hz in dark conditions.

Cyclic voltammograms and (at a scan rate of 20 mV/s), saturation, and Faradaic efficiency measurements were obtained using a 300 W xenon lamp with an AM 1.5 solar spectrum filter under the appropriate distance to receive 100 mW cm^{-2} (1 sun). Faradaic efficiency is measured collecting the generated H_2 bubbles with and inverted buret and calculated as presented in Supporting Information. IPCE measurements were performed with an Abet 150 W xenon lamp coupled with an Oriel

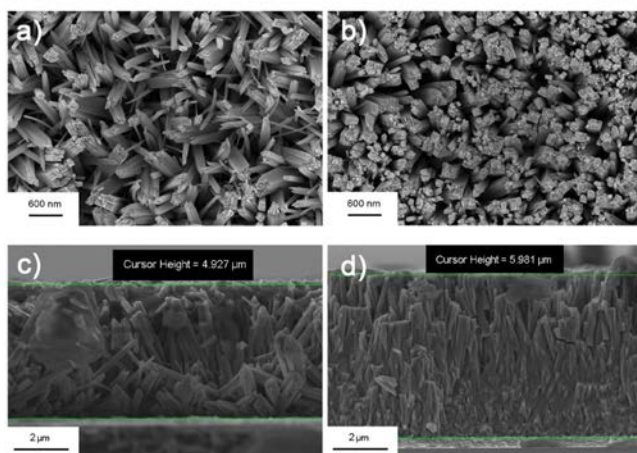


Figure 1. (a) Top view and (c) cross section SEM images of TNR-40 samples. (b) Top view image of a TNR-45 sample and (d) cross section. We can see an increase in density and length of the nanorods with higher precursor concentration.

Cornerstone 260 monochromator, using light pulses of 100 s with 20 s dark, and a light spot smaller than the sample. Light biased IPCE measurements were performed with monochromatic light reaching the sample from the TiO_2 side and 1 sun illumination from the substrate side, as detailed in Figure 1. IPCE is calculated as

$$\text{IPCE (\%)} = \frac{1.24 \times 10^{-3} (\text{nm} \times \mu\text{W} \times \text{A}^{-1}) \times j_{\text{ph}} (\text{A})}{\lambda (\text{nm}) \times P_{\text{lamp}} (\mu\text{W})} \times 100 \quad (1)$$

where j_{ph} is the photocurrent generated by the monochromatic light, λ is the wavelength, and P_{lamp} is the light intensity absorbed by the sample coming from the monochromator.

The half-cell solar-to-hydrogen (HC-STH)⁵¹ conversion efficiency is given by

$$\text{HC-STH (\%)} = \frac{j_{\text{ph}} \times (E_{\text{H}_2\text{O}/\text{O}_2} - E)}{P_{\text{sun}}} \times 100 \quad (2)$$

where j_{ph} is the photocurrent density obtained under an applied bias (E), $E_{\text{H}_2\text{O}/\text{O}_2}$ is the equilibrium redox potential of oxygen evolution reaction (1.23 V vs NHE), and P_{sun} is the standard solar irradiation, 100 mW cm^{-2} .

3. RESULTS AND DISCUSSION

3.1. Characterization Prior to Hydrogen Treatment.

SEM images of the samples grown from 40 and 45 mM precursor solution concentrations presented TiO_2 tetragonal nanorods over FTO substrates (Figure 1). The increasing precursor concentration resulted in a longer (5 and 6 μm for TNR-40 and TNR-45, respectively) and denser concentration of nanorods. In both cases we observed a dispersion in the nanorods diameter, from tens of nanometers up to few hundred nanometers. Looking closer, the nanorods seem to be formed by a mesh of thinner square-section fibers. The nonverticality and disperse thickness can be attributed to the rough FTO substrate.³⁰ The rutile phase is more favorable to grow on the FTO substrate due to lower lattice parameter mismatch (<2%) than anatase (~19%).³⁰ By X-ray diffraction spectroscopy

(XRD) the rutile phase is confirmed together with FTO, with no traces of other TiO_2 phases. Upon annealing treatments, no structural modifications could be seen (Figure 2).

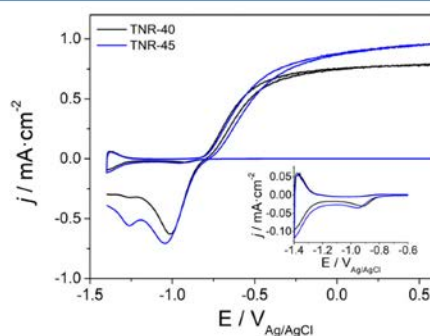


Figure 2. Cyclic voltammograms under 1 sun illumination of TiO_2 nanorods with 40 mM precursor concentrations (black) and 45 mM (blue) with a scan rate of 20 mV/s in 1 M NaOH as electrolyte. Inset: voltammograms in dark conditions.

In Figure 3, UV-vis transmittance spectra of TNR-40 and TNR-45 samples are presented, where a 3.0 eV bandgap can be measured, as expected for TiO_2 nanorods having rutile crystal structure. All UV wavelengths shorter than the band gap are totally absorbed by the sample (0% transmittance). From the visible region, we observe a 70% transmitted light. This absorption can be attributed to light scattering coming from the TiO_2 , the FTO layer, and the glass substrate. TNR-45 has a slightly lower transmittance, attributable to higher scattering from a thicker and denser layer.

All samples were photoelectrochemically characterized before hydrogen treatment. In Figure 2, two cycles of cyclic voltammograms under illumination and in the dark (inset) for rutile nanorods samples are presented. In dark conditions, the reduction peak corresponding to traces of dissolved oxygen appeared in the -1 V vs Ag/AgCl region. This peak is assigned

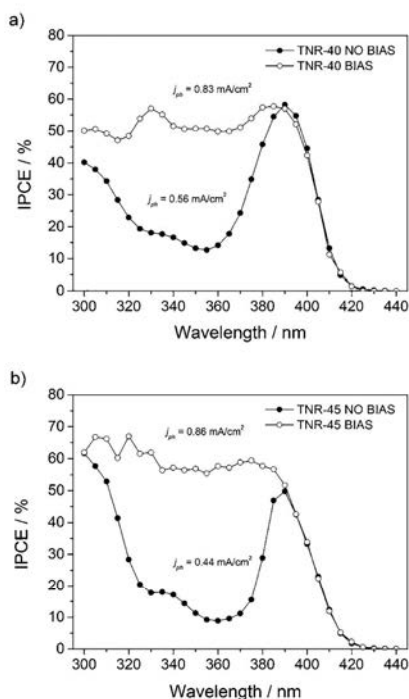


Figure 3. IPCE profiles of TNR-40 (a) and TNR-45 (b) samples with (empty circles) and without light bias (solid circles). IPCE was taken at 0 V vs Ag/AgCl in a 1 M NaOH electrolyte. Photocurrent densities from IPCE integration are indicated.

to surface-related electron trapping occurring at interparticle grain boundaries, corresponding to trap sites with energies inside the band gap;^{10,52} this confirms the active area effect, as with thicker and longer nanorods for TNR-45 more grain boundaries are present.

Under 1 sun illumination, an anodic current is obtained in both samples confirming the n-type semiconductor behavior. A higher photocurrent density is achieved in the case of the 45 mM concentration sample. As it was previously mentioned, a higher surface area is pointed out by the cathodic peak presented in Figure 2 inset, related to surface states. Together with the thicker and denser layer shown in Figure 1, meaning a higher TiO₂ mass load, photocurrent increment with precursor concentration is attributable to a better light absorption and conversion, as less photons will reach the FTO layer and more active area is available for the electrochemical reaction.

TNR-40 samples presented an average photocurrent density of 0.76 mA cm⁻², whereas TNR-45 reached 0.90 mA cm⁻². These values are in the same range of photocurrent for nontreated TiO₂ photoanodes among the literature.^{11,34,35,38,46} In Figure 4, the photocurrent density values of all samples with both precursor concentrations are presented, measured at 0.6 V vs Ag/AgCl, which consistently confirms the increment of photocurrent density at higher precursor concentration.

IPCE of two representative samples from both TNR-40 and TNR-45 are plotted in Figure 3. We can clearly see that both samples show similar IPCE profile as they are both bare TiO₂

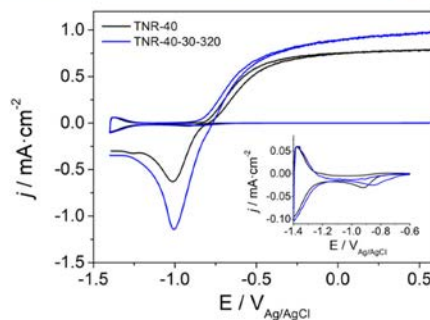


Figure 4. Cyclic voltammograms under 1 sun illumination of TNR-40 before and after treatment at 320 °C for 30 min with a scan rate of 20 mV/s in a 1 M NaOH electrolyte. Inset: voltammograms in dark conditions.

nanorods, but TNR-45 performs slightly better in the UV region (Figure 3b). We also measured the IPCE under 1 sun illumination. In these conditions, we report significantly different IPCE profiles for both samples, obtaining a quite flat efficiency profile at wavelengths lower than the band gap (higher energy), with slightly higher values for TNR-45 (as expected as these samples give higher total photocurrent density).

From IPCE spectra integration (see Supporting Information, eq 1) the photocurrent density we should get under 1 sun illumination was calculated. Both samples presented significantly reduced photocurrent densities without light bias (0.56 mA cm⁻² for TNR-40 and 0.44 mA cm⁻² for TNR-45), which are far from the experimental results obtained from voltammetric measurements, corresponding to 0.75 mA cm⁻² for TNR-40 and 0.87 mA cm⁻² for TNR-45. When a light bias is applied to the system, the calculated photocurrent densities from IPCE measurements are closer to those obtained from the cyclic voltammograms, being 0.83 mA cm⁻² for TNR-40 and 0.86 mA cm⁻² for TNR-45 (Table 1).

Table 1. Photogenerated Currents at 0 V vs Ag/AgCl Measured by Cyclic Voltammograms, Integrated IPCE, and Integrated IPCE under a Light Bias

sample	j_{CV} (mA cm ⁻²)	j_{IPCE} (mA cm ⁻²)	j_{BIAS} IPCE (mA cm ⁻²)
TNR-40	0.75	0.56	0.83
TNR-45	0.87	0.44	0.86

Light bias affects in the same way to samples from both precursor concentrations. This can be attributable to variations only in the layer morphology giving higher surface, with no significant modifications in the electronic structure.

Applying a light bias to TiO₂ generates extra photoexcited electron–hole pairs. In a defective material such as titania, the presence of trap states is expected from oxygen vacancies and hydroxyl groups.^{53,54} Trap states are detrimental for charge extraction, as they will act as recombination centers, reducing the measured photocurrent under very small illuminations (such as the few microwatts illumination generated by the monochromator for a single wavelength). A 1 sunlight bias creates electron–hole pairs which fill trap states, allowing free electrons and holes to be measured as photocurrent. This phenomenon has been previously observed in other semi-

conductor materials.^{53,55} Having these trap states occupied significantly reduces the recombination rate, leading to more realistic IPCE measurements. The described phenomenon is more remarkable for the shortest wavelengths which are absorbed within the first nanometers of the TiO₂ surface, where the density of defects is higher due to crystallographic terminations, reducing IPCE conversions for wavelengths shorter than 380 nm. Thus, it is essential to perform IPCE measurements under a light bias, closer to real operation conditions, or we will be underestimating the photogenerated current, especially in the near-UV region (330–380 nm).

We also tested the capacity of these TiO₂ nanorods to be used under higher illumination intensities, obtaining no saturation up to 500 mW cm⁻² (5 suns) for TNR-45; meanwhile, TNR-40 seems to start saturating after 4 suns (Figure 5). This also corroborates the higher area of the TNR-

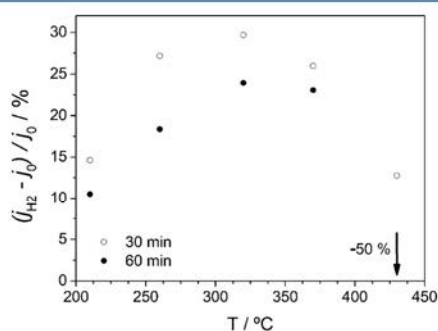


Figure 5. Relative increase of the photocurrent density after hydrogen treatments at different temperatures for 30 min (empty circles) and 60 min (solid circles). Treatment at 430 °C for 60 min (arrow) degraded the FTO substrate, significantly decreasing the sample's performance. Measurements at 0.6 V vs Ag/AgCl.

45 sample. High saturation intensities would allow these photoanodes to work under solar concentration and would be meaningful to reduce full-device fabrication and integration costs.⁵⁶

3.2. Characterization after Hydrogen Treatment. All samples were subjected to hydrogen treatment, at different temperatures ranging from 210 to 430 °C and at two different dwell times of 30 or 60 min. At temperatures above 370 °C, FTO substrates started getting darker and decreasing its conductance. This effect is commonly accepted to be due to a reduction of the tin (Sn) present in the FTO substrate from Sn⁴⁺ (SnO₂) to Sn (metallic) or other nonconductive suboxides such as SnO. As a result, the substrate resistance is increased (at 430 °C) as well as its roughness, leading even to a detachment of the FTO from the glass (at 470 °C), what destroys the sample.⁵⁷

We could also note that TiO₂ nanorods did also change its color, looking yellowish white at 320 °C and grayish at higher temperatures, although this is difficult to distinguish over the FTO change to dark gray.

UV-vis transmission spectra (Figure 6) confirmed that treatments did not modify the band gap of the samples. On the other hand, a reduction of transmitted light for energies lower than the band gap (in the visible region) can be observed for samples treated at higher temperatures (320 and 370 °C). This is considered to be caused by the creation of deep levels inside

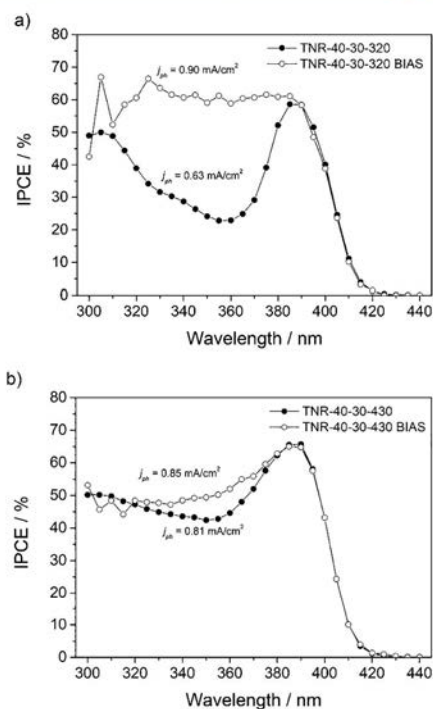


Figure 6. IPCE profiles at 0 V vs Ag/AgCl with (empty circles) and without (solid circles) light bias for samples (a) TNR-40-30-320 and (b) TNR-40-30-430. Photocurrent densities from IPCE integration are indicated in the graph.

the band gap that can be inferred from the 10% increased absorption at 425 nm compared with a 3% at 650 nm.

In Figure 4, cyclic voltammograms of an untreated (TNR-40) and treated sample at 320 °C (TNR-40-30-320) are presented. In dark conditions (inset), the treated sample shows a wider peak at -0.9 V vs Ag/AgCl. As previously mentioned, this peak is attributed to the filling of trap sites related to grain boundaries, and its widening is related to surface traps having deeper energy levels inside the band gap.^{10,52} Under 1 sun illumination, an improvement of the open circuit potential (V_{oc}) of the treated sample is observed. This shift of the V_{oc} to negative potentials can be attributed to a rising in the Fermi level, as the donor density increases with the reduction process caused by the annealing under a H₂ atmosphere. By its reductive action, extra oxygen vacancies are created in the surface and nearby positions, promoting shallow donors near the conduction band and thus shifting the Fermi level closer to the conduction band.^{11,46} Indeed, in Figure 7 is represented all V_{oc} before and after hydrogen treatments for each sample showing an average shift of 45 mV toward more negative potentials. Moreover, the shift of the V_{oc} was translated into an increase in the photocurrent density respect to the nontreated sample. In order to evaluate the hydrogen treatment effect at different temperatures and times on the photocurrent density of the photoanodes, in Figure 5 the ratio between photocurrent densities before and after the treatment for each temperature and both sets of dwell time is depicted.

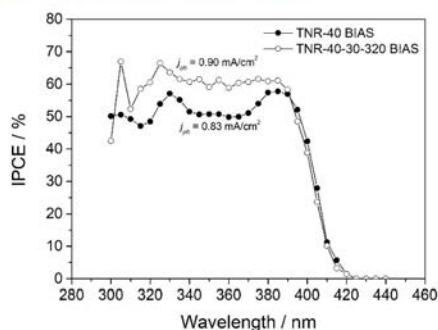


Figure 7. IPCE profiles of the same sample before (solid circles) and after (empty circles) the treatment at optimal parameters (30 min and 320 °C), in both cases under 1 sun bias and at 0 V vs Ag/AgCl in 1 M NaOH.

A maximum relative increment was found at temperatures around 320 °C for both 30 and 60 min treatments. However, lower relative increments were observed in all samples treated for 60 min. This effect is due to a time-dependent reductive effect, where more superficial TiO₂ is reduced and a higher number of surface vacancies were created for longer periods under a H₂ atmosphere.^{11,57,58,45} This raises the Fermi level but also creates extra recombination centers, where photogenerated carriers can recombine, reducing the capacity of the material to effectively separate and transport the photogenerated electron–hole pairs. We must consider that the substrate degradation under reductive atmospheres starts at 370 °C, which makes it impossible to determine if the H₂ temperature treatment has a maximum of performance at 320 °C or other substrates capable of resisting such conditions could allow even higher photocurrents increase without being reduced its conductive performance.

We measured IPCE of all hydrogenated samples (Figure 8) at different temperatures and treatment times, with two representative photoanodes presented in Figure 6. It can be initially seen that zero IPCE conversion is measured at wavelengths below the band gap for all treatment temperatures; thus, the intra-band-gap levels detected in Figure 6 (which absorb light and give its darker color to the treated samples) are inactive, and so no photocurrent comes from the visible region. These intra-band-gap levels are significantly below the H₂O/H₂ reduction potential.⁵⁹

In Figure 6, the IPCE measurements of two representative photoanodes, light biased and nonbiased, are compared. At the top part, the results of a photoanode which had undergone a moderate treatment (TNR-40-30-320 (Figure 6a) are presented, in which we can appreciate a notable increment on the near-UV region (320–380 nm). This sample presented a photocurrent density of 0.89 mA cm⁻² in cyclic voltammogram measurements under real conditions while by integrating the IPCE curve without bias, only 0.63 mA cm⁻² is obtained; meanwhile, under light bias, 0.90 mA cm⁻² is obtained.

On the other hand, a photoanode treated at higher temperatures (TNR-40-30-430 (Figure 6b) led to photocurrent densities of 0.81, 0.81, and 0.85 mA cm⁻² from the voltammetry at real conditions, integration of IPCE with no bias, and integration of IPCE with bias, respectively. The reason for such a small difference in the IPCE between the heavily treated sample with and without light bias can be explained as follows: heavily treated samples (Figure 6b) introduce significant oxygen vacancies, meaning a very high donor density, shifting the Fermi level closer to the conduction band, and filling some of the trap sites without the need of light bias.

To confirm this increment of the donor density in the treated samples, Mott–Schottky measurements were performed, presented in Figure 7. The hydrogenation process is found to increase donor density from 3 × 10¹⁸ cm⁻³ for a pristine sample to 1 × 10¹⁹ cm⁻³ with an optimal treatment (320 °C). Treating the sample with higher temperatures gives less photocurrent increment (as seen in Figure 5) and presents a different Mott–Schottky plot, with higher donors density active in the -0.3 to 0 V vs the Ag/AgCl region.

To summarize all the obtained results, a model is presented in Scheme 1 to illustrate the proposed mechanism as a function of the donor density level (low, optimum, and too high), similar to the one presented by Pesci et al.⁶⁰ The depletion width (W) in a semiconductor is calculated following eq 3:¹¹

$$W = \sqrt{\frac{2\epsilon_0\epsilon_r|\theta_{sc}|}{eN_D}} \quad (3)$$

where ϵ_r is the relative dielectric constant of the semiconductor (170 for rutile TiO₂⁶¹), ϵ_0 is the vacuum permittivity (8.85 × 10⁻¹² C² N⁻¹ m⁻²), e is the fundamental electric charge (1.602 × 10⁻¹⁹ C) and θ_{sc} is the maximum potential drop in the depletion layer, and at 0 V vs Ag/AgCl, $\theta_{sc} = 0.8$ V vs flat band potential. For nontreated samples, a donor density for bare

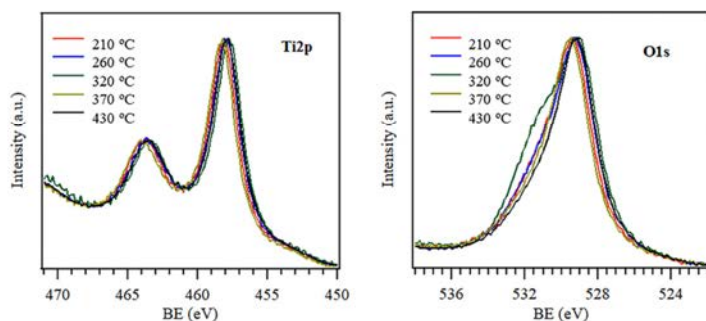
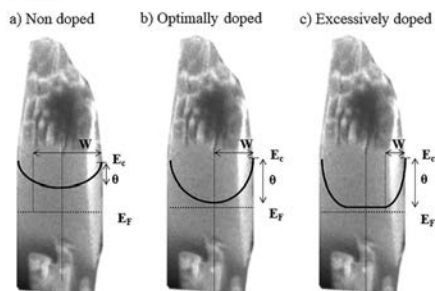


Figure 8. XPS measurements of TNR-40-60 samples in the Ti 2p and O 1s regions.

Scheme 1. Band Bending Model for TiO₂ Nanorods with an Average Radius 100 nm: (a) without Any Treatment, (b) with the Optimal Treatment, and (c) with an Excessive Treatment^a



^a*W* is the depletion region width, *E_c* is the conduction band edge, *E_f* is the de Fermi level energy, and θ is the potential drop within the depletion region.

TiO₂ of $3 \times 10^{18} \text{ cm}^{-3}$ was considered. A depletion width of 71 nm is obtained, being larger than half of the nanorod diameter (75–100 nm diameter). This gives fully depleted nanorods (Scheme 1a). The potential drop inside the nanorods will be lower for fully depleted semiconductors, as dimensions are smaller than the depletion width. With weaker electric fields, the electron–hole separation is hampered, and consequently, higher recombination rate and back-reaction surface rates are derived.

After the reductive treatment, extra oxygen vacancies are created, increasing the free electron density in the semiconductor. With a higher donor density, corresponding to the samples treated at 320 °C, the Fermi level is raised and the depletion width is decreased. Calculating the depletion width with eq 3, with a donors density of $1.05 \times 10^{19} \text{ cm}^{-3}$, dimensions of around 40 nm are achieved, giving fully depleted nanorods but with a potential drop similar to the bulk case (Scheme 1b). This means the presence of higher electric fields, which increase the electron–hole separation and thus less recombination, enhancing the photogenerated current.

When samples are treated under higher temperatures (370 °C and beyond), the donors density increases even more. Taking a donor density of $1.45 \times 10^{19} \text{ cm}^{-3}$, a depletion width of 32 nm is estimated. As Figure 9 shows, the Mott–Schottky plot for an overtreated sample presents two slopes, pointing at deeper change under excessive treatment. Under this condition, the depletion region width is thinner than the diameter of the nanorods, resulting in higher recombination rate, especially in the inner region where no electric field is developed. Combined with the FTO substrate degradation, the photogenerated current is lower in this case.

In Figure 7, a comparison of the IPCE measurements under a light bias is presented for the same sample before and after the treatment at the optimal values, 320 °C for 30 min. The integrated IPCE increment achieves 0.9 mA cm^{-2} , really similar to the 0.88 mA cm^{-2} measured in cyclic voltammetries at 1 sun illumination and 0 V vs Ag/AgCl (Figure 4), proving very good accordance of both measurements. Comparing our results with Wang et al.,³⁸ without the light bias when performing the IPCE, conversion efficiency calculated from the IPCE data and from measured photocurrent have a 30% mismatch. This is a similar difference to the one found in Figures 3a,b and 6a of our work

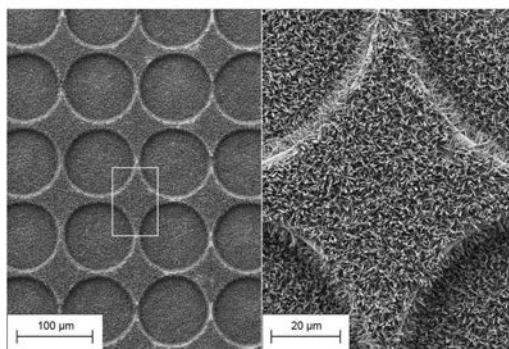


Figure 9. SEM image of a structured substrate with grown TiO₂ nanorods.

when no light bias was used during the measurement, confirming the need of a light bias for proper IPCE measurements.

In addition to the optimization of the doping level and band bending within the semiconductor, other effects on the surface caused by the hydrogen treatment must be taken into account. From the XPS measurements (Figure 8), we clearly see how this treatment creates hydroxyl groups (OH⁻). This is shown as a broadening in the O 1s region, more specifically at 532 eV.^{44,62} This corresponds to the Ti–O–H bond, significantly increased in TNR-40-60-320 sample (the one with higher performance of its set). The presence of hydroxyl groups in the surface of TiO₂ photoanodes has been reported by many authors as related to faster kinetics for OER reaction, through the creation of favorable surface states.^{63,64}

Finally, we evaluated the hydrogen production rate and Faradaic efficiency of the best performing sample (TNR-40-30-320) under 1 sun illumination (Figure 10). We obtained a

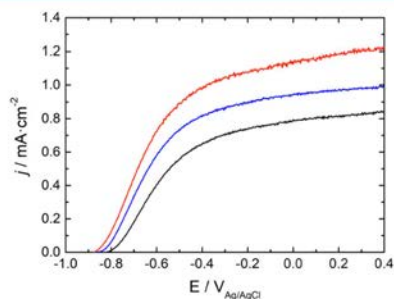


Figure 10. Cyclic voltammograms of TiO₂ nanorods grown on a flat substrate (black), on a structured one (blue), and on a structured substrate and further treated under a hydrogen reductive atmosphere at 320 °C for 30 min (red), under 1 sun illumination with a scan rate of 20 mV/s in a 1 M NaOH electrolyte.

94.3% current to H₂ conversion, very close to 100% and stable for over 2 h, with a hydrogen production rate of $15 \mu\text{mol cm}^{-2} \text{ h}$ under 1 sun exposure. Having a H₂ saturated and pure NaOH electrolyte, together with the widely known stability of TiO₂ in alkaline conditions, this Faradaic efficiency discrepancy must be attributed to a nonperfect H₂ collection.

We applied the optimal treatment (320 °C for 30 min) to one of the best samples grown with 45 mM precursor concentration. Combining the precursor concentration optimization and the hydrogen reductive treatment, we were capable to overcome 1 mA cm^{-2} , reaching 1.02 mA cm^{-2} under 1 sun illumination at 0.6 V vs Ag/AgCl and a HC-STH conversion efficiency of 0.48%.

In an attempt to increase light absorption and the active surface, the substrate was patterned prior to deposition of the FTO contact and TiO₂ hydrothermal growth, applying the TiO₂ growth conditions previously optimized.

From SEM images (Figure 9) it can be observed how the substrate was patterned with 45 μm radius holes in a square packaging, with circles of 8 μm in depth. Using this configuration, a 15.6% increased active area is expected (illustrative figures (Figure S11) and calculations can be found in the Supporting Information). Cyclic voltammograms from a flat sample, a structured one, and a structured one after hydrogen treatment can be seen in Figure 10, and photocurrents of 0.86, 1.0, and 1.20 mA cm⁻² at 0.6 V vs Ag/AgCl are obtained, respectively. The photocurrent increase with substrate structuration was 20%, in the order of the surface area increment. The small disagreement can be attributed to other effects caused by the microscale structuration, such as better electron–hole generation and transport due to lateral incidence to the tilted TiO₂ nanorods. As can be seen in Figure S12, no differences in light absorbance are observed between structured or flat surfaces, being close to 100% in both cases.

Following both strategies, hydrogenation treatment and substrate structuration, the maximum obtained photocurrents reached 1.2 mA cm^{-2} at 0.6 V vs Ag/AgCl corresponding to HC-STH conversion efficiency of up to 0.64%.

4. CONCLUSIONS

In this work, optimization of growth process and structuration of the substrate are conducted with the aim of achieving the highest photocurrents for TiO₂ nanorods grown by the hydrothermal process. Also, the effect of a light bias when measuring the IPCE under low monochromatic illumination intensity has been found to increase the effective available charge carriers and filling trap states, thus giving integrated IPCE currents much more similar to real-operation photocurrents. This gives IPCE a better usability as a comparison parameter independent of the used solar simulator, as they vary significantly in the UV range.

With the temperature treatment under a hydrogen atmosphere, we have demonstrated that the surface oxygen vacancies created by the reduction of TiO₂ increase the doping level. This allowed us to tune the depletion width and to achieve a fully depleted regime. With this, the potential drop inside the nanorods is maximized, optimizing the electron–hole separation and reducing the recombination and back-reaction rates. The increment in the photogenerated current has been shown to come from a better conversion in the UV part of the spectra rather than an enhanced conversion of photons with energies smaller than the band gap. The detected intraband gap levels have shown to absorb visible light, but they are not involved in the photocurrent generation, as they are expected to be located under the H₂/H₂O reduction potential. Substrate structuration increased the available surface area, giving extra total photocurrent and showing there is still way for larger photocurrents increasing active area. Further work can be directed on achieving longer nanorods, finding substrates

capable to resist the highly reductive atmosphere and optimizing the substrate patterning.

■ ASSOCIATED CONTENT

Supporting Information

The Supporting Information is available free of charge on the ACS Publications website at DOI: 10.1021/acs.jpcc.7b12468.

Transmittance measurements, extended calculations, Faradaic efficiency measurements, Mott–Schottky plots, and extra incident photon-to-current efficiency (IPCE) measurements (PDF)

■ AUTHOR INFORMATION

Corresponding Authors

*E-mail cros@irec.cat (C.R.).

*E-mail tandreu@irec.cat (T.A.).

ORCID

C. Ros: 0000-0002-9148-2767

C. Fàbrega: 0000-0001-8337-4056

T. Andreu: 0000-0002-2804-4545

Notes

The authors declare no competing financial interest.

■ ACKNOWLEDGMENTS

This work was supported by Repsol, S.A. Authors from IREC thank Generalitat de Catalunya for financial support through the CERCA Program, M2E (2014SGR1638), and XarMAE network. IREC also acknowledges additional support by the European Regional Development Funds (ERDF, FEDER), by MINECO coordinated projects MAT2014-59961-C2 and ENE2016-80788-C5-5-R and by the FP7 project SOLAR-OGENIX (FP7-NMP-2012-310333). C.R. thanks MINECO for his FPI grant (BES-2015-071618). D. M.-S. acknowledges MINECO for the award of a “Juan de la Cierva-Incorporación” researcher fellowship (IJCI-2014-21969) and “La Caixa” Foundation through project “Ajuts a la Recerca IQS 2017” (2017-LC-11).

■ REFERENCES

- (1) Fujishima, A.; Honda, K. Electrochemical Photolysis of Water at a Semiconductor Electrode. *Nature* **1972**, *238*, 37–38.
- (2) Maeda, K.; Domen, K. Photocatalytic Water Splitting: Recent Progress and Future Challenges. *J. Phys. Chem. Lett.* **2010**, *1*, 2655–2661.
- (3) Ni, M.; Leung, M. K. H.; Leung, D. Y. C.; Sumathy, K. A Review and Recent Developments in Photocatalytic Water-Splitting Using TiO₂ for Hydrogen Production. *Renewable Sustainable Energy Rev.* **2007**, *11*, 401–425.
- (4) Walter, M. G.; Warren, E. L.; McKone, J. R.; Boettcher, S. W.; Mi, Q.; Santori, E. A.; Lewis, N. S. Solar Water Splitting Cells. *Chem. Rev.* **2010**, *110*, 6446–6473.
- (5) Bard, A. J.; Fox, M. A. Artificial Photosynthesis: Solar Splitting of Water to Hydrogen and Oxygen Water Splitting. *Acc. Chem. Res.* **1995**, *28*, 141–145.
- (6) Hu, S.; Xiang, C.; Haussener, S.; Berger, A. D.; Lewis, N. S. An Analysis of the Optimal Band Gaps of Light Absorbers in Integrated Tandem Photoelectrochemical Water-Splitting Systems. *Energy Environ. Sci.* **2013**, *6*, 2984–2993.
- (7) Fàbrega, C.; Andreu, T.; Cabot, A.; Morante, J. R. Location and Catalytic Role of Iron Species in TiO₂:Fe Photocatalysts: An EPR Study. *J. Photochem. Photobiol., A* **2010**, *211*, 170–175.
- (8) Murcia-López, S.; Hidalgo, M. C.; Navío, J. A. Synthesis, Characterization and Photocatalytic Activity of Bi-Doped TiO₂

Photocatalysts under Simulated Solar Irradiation. *Appl. Catal., A* **2011**, *404*, 59–67.

(9) Fàbrega, C.; Andreu, T.; Güell, F.; Prades, J. D.; Estradé, S.; Rebled, J. M.; Peiró, F.; Morante, J. R. Effectiveness of Nitrogen Incorporation to Enhance the Photoelectrochemical Activity of Nanostructured TiO₂:NH₃ versus H₂-N₂ Annealing. *Nanotechnology* **2011**, *22*, 235403.

(10) Berger, T.; Monllor-Satoca, D.; Jankulovska, M.; Lana-Villarreal, T.; Gómez, R. The Electrochemistry of Nanostructured Titanium Dioxide Electrodes. *ChemPhysChem* **2012**, *13*, 2824–2875.

(11) Fàbrega, C.; Monllor-Satoca, D.; Ampudia, S.; Parra, A.; Andreu, T.; Morante, J. R. Tuning the Fermi Level and the Kinetics of Surface States of TiO₂ Nanorods by Means of Ammonia Treatments. *J. Phys. Chem. C* **2013**, *117*, 20517–20524.

(12) Klahr, B.; Gimenez, S.; Fabregat-Santiago, F.; Bisquert, J.; Hamann, T. W. Electrochemical and Photoelectrochemical Investigation of Water Oxidation with Hematite Electrodes. *Energy Environ. Sci.* **2012**, *5*, 7626.

(13) Yang, X.; Liu, R.; Du, C.; Dai, P.; Zheng, Z.; Wang, D. Improving Hematite-Based Photoelectrochemical Water Splitting with Ultrathin TiO₂ by Atomic Layer Deposition. *ACS Appl. Mater. Interfaces* **2014**, *6*, 12005–12011.

(14) Sivula, K.; Formal, F. Le; Grätzel, M. WO₃ – Fe₂O₃ Photoanodes for Water Splitting: A Host Scaffold, Guest Absorber Approach. *Chem. Mater.* **2009**, *21*, 2862–2867.

(15) Murcia-López, S.; Villa, K.; Andreu, T.; Morante, J. R. Improved Selectivity for Partial Oxidation of Methane to Methanol in Presence of Nitrite Ions and BiVO₄ Photocatalyst. *Chem. Commun.* **2015**, *51*, 7249–7252.

(16) Pilli, S. K.; Furtak, T. E.; Brown, L. D.; Deutsch, T. G.; Turner, J. A.; Herring, A. M. Cobalt-Phosphate (Co-Pi) Catalyst Modified Mo-Doped BiVO₄ Photoelectrodes for Solar Water Oxidation. *Energy Environ. Sci.* **2011**, *4*, 5028–5034.

(17) Su, J.; Guo, L.; Bao, N.; Grimes, C. A. Nanostructured WO₃/BiVO₄ Heterojunction Films for Efficient Photoelectrochemical Water Splitting. *Nano Lett.* **2011**, *11*, 1928–1933.

(18) Murcia-López, S.; Fabrega, C.; Monllor-Satoca, D.; Hernández-Alonso, M. D.; Penelas-Pérez, G.; Morata, A.; Morante, J. R.; Andreu, T.; Fàbrega, C.; Monllor-Satoca, D.; et al. Tailoring Multilayered BiVO₄ Photoanodes by Pulsed Laser Deposition for Water Splitting. *ACS Appl. Mater. Interfaces* **2016**, *8*, 4076–4085.

(19) Su, J.; Feng, X.; Sloppy, J. D.; Guo, L.; Grimes, C. A. Vertically Aligned WO₃ Nanowire Arrays Grown Directly on Transparent Conducting Oxide Coated Glass: Synthesis and Photoelectrochemical Properties. *Nano Lett.* **2011**, *11*, 203–208.

(20) Fàbrega, C.; Murcia-López, S.; Monllor-Satoca, D.; Prades, J. D.; Hernández-Alonso, M. D.; Penelas, G.; Morante, J. R.; Andreu, T. Efficient WO₃ Photoanodes Fabricated by Pulsed Laser Deposition for Photoelectrochemical Water Splitting with High Faradaic Efficiency. *Appl. Catal., B* **2016**, *189*, 133–140.

(21) Villa, K.; Murcia-López, S.; Andreu, T.; Morante, J. R. On the Role of WO₃ Surface Hydroxyl Groups for the Photocatalytic Partial Oxidation of Methane to Methanol. *Catal. Commun.* **2015**, *58*, 200–203.

(22) Cowan, A. J.; Leng, W.; Barnes, P. R. F.; Klug, D. R.; Durrant, J. R. Charge Carrier Separation in Nanostructured TiO₂ Photoelectrodes for Water Splitting. *Phys. Chem. Chem. Phys.* **2013**, *15*, 8772.

(23) Murphy, A. B.; Barnes, P. R. F.; Randeniya, L. K.; Plumb, I. C.; Grey, I. E.; Horne, M. D.; Glasscock, J. A. Efficiency of Solar Water Splitting Using Semiconductor Electrodes. *Int. J. Hydrogen Energy* **2006**, *31*, 1999–2017.

(24) Kang, Q.; Cao, J.; Zhang, Y.; Liu, L.; Xu, H.; Ye, J. Reduced TiO₂ Nanotube Arrays for Photoelectrochemical Water Splitting. *J. Mater. Chem. A* **2013**, *1*, 5766.

(25) Irtem, E.; Hernández-Alonso, M. D.; Parra, A.; Fàbrega, C.; Penelas-Pérez, G.; Morante, J. R.; Andreu, T. A Photoelectrochemical Flow Cell Design for the Efficient CO₂ Conversion to Fuels. *Electrochim. Acta* **2017**, *240*, 225–230.

(26) Yin, Y.; Jin, Z.; Hou, F. Enhanced Solar Water-Splitting Efficiency Using Core/sheath Heterostructure CdS/TiO₂ Nanotube Arrays. *Nanotechnology* **2007**, *18*, 495608.

(27) Ros, C.; Andreu, T.; Giraldo, S.; Sánchez, Y.; Morante, J. R. Conformal Chalcopyrite Based Photocathode for Solar Refinery Applications. *Sol. Energy Mater. Sol. Cells* **2016**, *158*, 184–188.

(28) Ros, C.; Andreu, T.; Hernández-Alonso, M. D.; Penelas-Pérez, G.; Arbiol, J.; Morante, J. R. Charge Transfer Characterization of ALD-Grown TiO₂ Protective Layers in Silicon Photocathodes. *ACS Appl. Mater. Interfaces* **2017**, *9*, 17932–17941.

(29) Shakeel Ahmad, M.; Pandey, A. K.; Abd Rahim, N. Advancements in the Development of TiO₂ Photoanodes and Its Fabrication Methods for Dye Sensitized Solar Cell (DSSC) Applications. A Review. *Renewable Sustainable Energy Rev.* **2017**, *77*, 89–108.

(30) Wu, W.-Q.; Lei, B.-X.; Rao, H.-S.; Xu, Y.-F.; Wang, Y.-F.; Su, C.-Y.; Kuang, D.-B. Hydrothermal Fabrication of Hierarchically Anatase TiO₂ Nanowire Arrays on FTO Glass for Dye-Sensitized Solar Cells. *Sci. Rep.* **2013**, *3*, 1352.

(31) Liu, B.; Aydil, E. S. Growth of Oriented Single-Crystalline Rutile TiO₂ Nanorods on Transparent Conducting Substrates for Dye-Sensitized Solar Cells. *J. Am. Chem. Soc.* **2009**, *131*, 3985–3990.

(32) Yang, M.; Ding, B.; Lee, J. K. Surface Electrochemical Properties of Niobium-Doped Titanium Dioxide Nanorods and Their Effect on Carrier Collection Efficiency of Dye Sensitized Solar Cells. *J. Power Sources* **2014**, *245*, 301–307.

(33) Waterhouse, G. I. N.; Wahab, A. K.; Al-Oufi, M.; Jovic, V.; Anjum, D. H.; Sun-Waterhouse, D.; Llorca, J.; Idriss, H. Hydrogen Production by Tuning the Photonic Band Gap with the Electronic Band Gap of TiO₂. *Sci. Rep.* **2013**, *3*, 2849.

(34) Wang, Y.; Zhang, Y. Y.; Tang, J.; Wu, H.; Xu, M.; Peng, Z.; Gong, X. G.; Al, W. E. T.; Zheng, G.; Al, W. E. T.; et al. Simultaneous Etching and Doping of TiO₂ Nanowire Arrays for Enhanced Photoelectrochemical Performance. *ACS Nano* **2013**, *7*, 9375–9383.

(35) Hoang, S.; Berglund, S. P.; Hahn, N. T.; Bard, A. J.; Mullins, C. B. Enhancing Visible Light Photo-Oxidation of Water with TiO₂ Nanowire Arrays via Cotreatment with H₂ and NH₃: Synergistic Effects between Ti³⁺ and N. *J. Am. Chem. Soc.* **2012**, *134*, 3659–3662.

(36) Xie, S.; Zhai, T.; Li, W.; Yu, M.; Liang, C.; Gan, J.; Lu, X.; Tong, Y. Hydrogen Production from Solar Driven Glucose Oxidation over Ni(OH)₂ Functionalized Electroreduced-TiO₂ Nanowire Arrays. *Green Chem.* **2013**, *15*, 2434.

(37) Chen, X.; Liu, L.; Yu, P. Y.; Mao, S. S. Increasing Solar Absorption for Photocatalysis with Black Hydrogenated Titanium Dioxide Nanocrystals. *Science* **2011**, *331* (6018), 746–750.

(38) Wang, G.; Wang, H.; Ling, Y.; Tang, Y.; Fitzer, R. C.; Wang, C.; Zhang, J. Z.; Li, Y. Hydrogen-Treated TiO₂ Nanowire Arrays for Photoelectrochemical Water Splitting. *Nano Lett.* **2011**, *11*, 3026–3033.

(39) Zheng, Z.; Huang, B.; Lu, J.; Wang, Z.; Qin, X.; Zhang, X.; Dai, Y.; Whangbo, M.-H. Hydrogenated Titania: Synergy of Surface Modification and Morphology Improvement for Enhanced Photocatalytic Activity. *Chem. Commun.* **2012**, *48*, 5733.

(40) Janotti, A.; Varley, J. B.; Rinke, P.; Umezawa, N.; Kresse, G.; Van de Walle, C. G. Hybrid Functional Studies of the Oxygen Vacancy in TiO₂. *Phys. Rev. B: Condens. Matter Mater. Phys.* **2010**, *81*, 85212.

(41) Wang, Z.; Yang, C.; Lin, T.; Yin, H.; Chen, P.; Wan, D.; Xu, F.; Huang, F.; Lin, J.; Xie, X.; et al. H-Doped Black Titania with Very High Solar Absorption and Excellent Photocatalysis Enhanced by Localized Surface Plasmon Resonance. *Adv. Funct. Mater.* **2013**, *23*, 5444–5450.

(42) Wang, Z.; Yang, C.; Lin, T.; Yin, H.; Chen, P.; Wan, D.; Xu, F.; Huang, F.; Lin, J.; Xie, X.; et al. Visible-Light Photocatalytic, Solar Thermal and Photoelectrochemical Properties of Aluminium-Reduced Black Titania. *Energy Environ. Sci.* **2013**, *6*, 3007.

(43) Yang, C.; Wang, Z.; Lin, T.; Yin, H.; Lü, X.; Wan, D.; Xu, T.; Zheng, C.; Lin, J.; Huang, F.; et al. Core-Shell nanostructured “black” Rutile Titania as Excellent Catalyst for Hydrogen Production

Enhanced by Sulfur Doping. *J. Am. Chem. Soc.* **2013**, *135*, 17831–17838.

(44) Vázquez Galván, J.; Flox, C.; Fabrega, C.; Ventosa, E.; Parra, A.; Andreu, T.; Morante, J. R. Hydrogen Treated Rutile TiO₂ Shell in Graphite Core Structure as a Negative Electrode for High-Performance Vanadium Flow Batteries. *ChemSusChem* **2017**, *10*, 2089.

(45) Lu, X.; Wang, G.; Zhai, T.; Yu, M.; Gan, J.; Tong, Y.; Li, Y. Hydrogenated TiO₂ Nanotube Arrays for Supercapacitors. *Nano Lett.* **2012**, *12*, 1690–1696.

(46) Fàbrega, C.; Andreu, T.; Tarancón, A.; Flox, C.; Morata, A.; Calvo-Barrio, L.; Morante, J. R. Optimization of Surface Charge Transfer Processes on Rutile TiO₂ Nanorods Photoanodes for Water Splitting. *Int. J. Hydrogen Energy* **2013**, *38*, 2979–2985.

(47) Leary, G.; Switzer, G.; Kuntz, G.; Kaiser, T. Comparison of Xenon Lamp-Based and Led-Based Solar Simulators. *Conf. Rec. IEEE Photovolt. Spec. Conf.* **2016**, *2016*, 3062–3067.

(48) Matson, R. J.; Emery, K. A.; Bird, R. E. Terrestrial Solar Spectra, Solar Simulation and Solar Cell Short-Circuit Current Calibration: A Review. *Sol. Sol. Cells* **1984**, *11*, 105–145.

(49) Yun, M. J.; Sim, Y. H.; Cha, S. I.; Seo, S. H.; Lee, D. Y. High Energy Conversion Efficiency with 3-D Micro-Patterned Photoanode for Enhancement Diffusivity and Modification of Photon Distribution in Dye-Sensitized Solar Cells. *Sci. Rep.* **2017**, *7*, 15027.

(50) Blumm, J.; Lindemann, A.; Meyer, M.; Strasser, C. Characterization of PTFE Using Advanced Thermal Analysis Techniques. *Int. J. Thermophys.* **2010**, *31*, 1919–1927.

(51) Jiang, C.; Moniz, S. J. A.; Wang, A.; Zhang, T.; Tang, J. Photoelectrochemical Devices for Solar Water Splitting - Materials and Challenges. *Chem. Soc. Rev.* **2017**, *46*, 4645–4660.

(52) Jankulovska, M.; Berger, T.; Wong, S. S.; Gómez, R.; Lana-Villarreal, T. Trap States in TiO₂ Films Made of Nanowires, Nanotubes or Nanoparticles: An Electrochemical Study. *ChemPhysChem* **2012**, *13*, 3008–3017.

(53) Wang, X.; Feng, Z.; Shi, J.; Jia, G.; Shen, S.; Zhou, J.; Li, C. Trap States and Carrier Dynamics of TiO₂ Studied by Photoluminescence Spectroscopy under Weak Excitation Condition. *Phys. Chem. Chem. Phys.* **2010**, *12*, 7083.

(54) Sachs, M.; Pastor, E.; Kafizas, A.; Durrant, J. R. Evaluation of Surface State Mediated Charge Recombination in Anatase and Rutile TiO₂. *J. Phys. Chem. Lett.* **2016**, *7*, 3742–3746.

(55) Eisgruber, I.; Granata, J.; Sites, J.; Hou, J.; Kessler, J. Blue-Photon Modification of Nonstandard Diode Barrier in CuInSe₂ Solar Cells. *Sol. Energy Mater. Sol. Cells* **1998**, *53*, 367–377.

(56) King, R. R.; Law, D. C.; Edmondson, K. M.; Fetzer, C. M.; Kinsey, G. S.; Yoon, H.; Sherif, R. A.; Karam, N. H. 40% Efficient Metamorphic GaInP/GaInAsGe Multijunction Solar Cells. *Appl. Phys. Lett.* **2007**, *90*, 183516.

(57) Major, S.; Bhatnagar, M. C.; Kumar, S.; Chopra, K. L. The Degradation of Fluorine Doped Tin Oxide Films in a Hydrogen Plasma. *J. Vac. Sci. Technol., A* **1988**, *6*, 2415–2420.

(58) Berger, T.; Lana-Villarreal, T.; Monllor-Satoca, D.; Gómez, R. Charge Transfer Reductive Doping of Nanostructured TiO₂ Thin Films as a Way to Improve Their Photoelectrocatalytic Performance. *Electrochem. Commun.* **2006**, *8*, 1713–1718.

(59) Sá, J.; Friedli, P.; Geiger, R.; Lerch, P.; Rittmann-Frank, M. H.; Milne, C. J.; Szlachetko, J.; Santomauro, F. G.; van Bokhoven, J. A.; Chergui, M.; et al. Transient Mid-IR Study of Electron Dynamics in TiO₂ Conduction Band. *Analyst* **2013**, *138*, 1966.

(60) Pesci, F. M.; Wang, G.; Klug, D. R.; Li, Y.; Cowan, A. J. Efficient Suppression of Electron-Hole Recombination in Oxygen-Deficient Hydrogen-Treated TiO₂ Nanowires for Photoelectrochemical Water Splitting. *J. Phys. Chem. C* **2013**, *117*, 25837–25844.

(61) Parker, R. A. Static Dielectric Constant of Rutile (TiO₂), 1.6–1060 K. *Phys. Rev.* **1961**, *124*, 1719–1722.

(62) Shi, J.; Wang, X. Hierarchical TiO₂-Si Nanowire Architecture with Photoelectrochemical Activity under Visible Light Illumination. *Energy Environ. Sci.* **2012**, *5*, 7918.

(63) Wang, J.; Liu, X.; Li, R.; Qiao, P.; Xiao, L.; Fan, J. TiO₂ Nanoparticles with Increased Surface Hydroxyl Groups and Their Improved Photocatalytic Activity. *Catal. Commun.* **2012**, *19*, 96–99.

(64) Lana Villarreal, T.; Gómez, R.; Neumann-Spallart, M.; Alonso-Vante, N.; Salvador, P. Semiconductor Photooxidation of Pollutants Dissolved in Water: A Kinetic Model for Distinguishing between Direct and Indirect Interfacial Hole Transfer. I. Photoelectrochemical Experiments with Polycrystalline Anatase Electrodes under Current Doubling and. *J. Phys. Chem. B* **2004**, *108*, 15172–15181.

Hydrogenation and Structuration of TiO₂ Nanorods Photoanodes: Doping Level and the Effect of Illumination in Trap-states Filling.

C. Ros,^a C. Fàbrega,^{a,b,c} D. Monllor-Satoca,^{a,d} M.D. Hernández-Alonso,^e G. Penelas-Pérez,^e J. R. Morante^{a,b} and T. Andreu^a

- ^a. Catalonia Institute for Energy Research (IREC), Jardins de les Dones de Negre 1, 08930 Sant Adrià del Besòs, Barcelona, Spain.
- ^b. MIND-Department of Electronics and Biomedical Engineering, Universitat de Barcelona (UB), c/Martí i Franquès 1, E-08028 Barcelona, Spain.
- ^c. Institute of Nanoscience and Nanotechnology (IN²UB), Universitat de Barcelona (UB), c/Martí i Franquès 1, E-08028 Barcelona, Spain.
- ^d. Department of Analytical and Applied Chemistry, IQS School of Engineering, Universitat Ramon Llull, Via Augusta 390, Barcelona, Spain.
- ^e. Repsol Technology Center, Agustín de Betancourt, s/n, 28935 Móstoles, Madrid, Spain.

Supporting Information

Integrating the areas under the IPCE graph

$$j_{ph} = e \int_0^{\infty} IPCE(\lambda) I_{\lambda}(\lambda) d\lambda \quad (1)$$

Where $I_{\lambda}(\lambda)$ is the incident photon flux passed by the monochromator when set to wavelength λ , IPCE the quantum efficiency of the cell and e is the electronic charge.

Supplementary material:

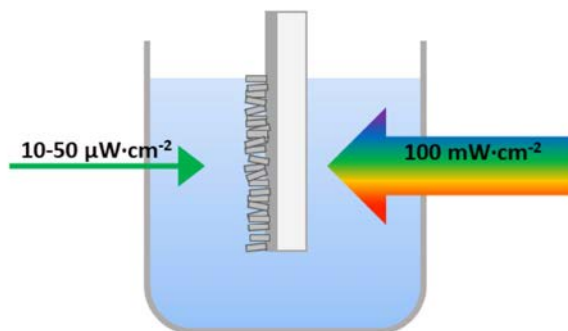


Fig. S. 1: Graphical description of the experimental configuration for the light biased IPCE measurements. Sun AM 1.5G illumination reaches the sample from the back side. Monochromatic illumination, used to generate the IPCE graph, reaches the sample directly in the TiO₂ nanorods.

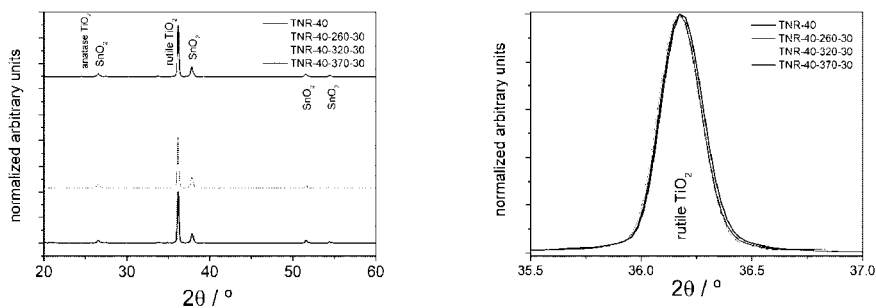


Fig. S. 2: XRD plot of a pristine sample and three treated ones at 260, 320 and 370 $^\circ\text{C}$, representing a small treatment, an optimal one and an over-treated sample. a) Stack graph presenting only the rutile TiO_2 peak and the FTO SnO_2 one. b) Zoom in the rutile TiO_2 peak, showing no visible modification to the TiO_2 peak under hydrogenation treatments.

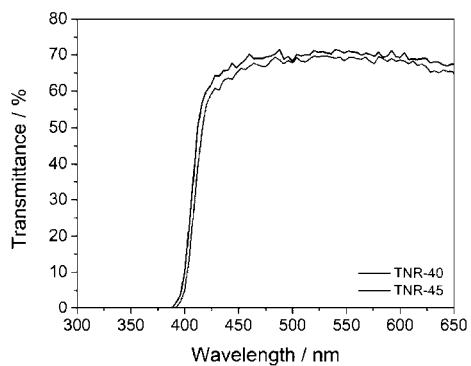


Fig. S. 3: UV-vis transmittance spectra of a TNR-40 sample (black) and a TNR-45 (blue).

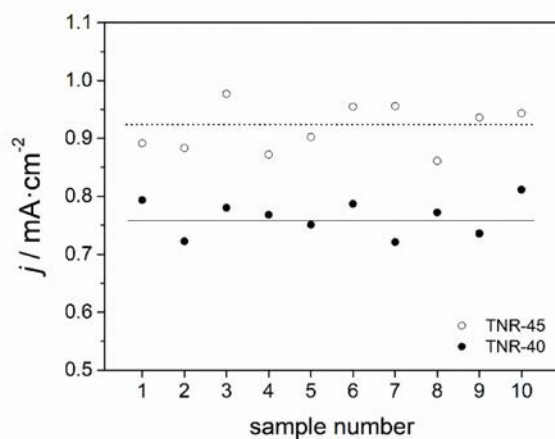


Fig. S. 4: Photogenerated currents of 10 samples grown with 40 (solid circles) and 45 mM (empty circles) precursor concentration. The average photocurrent of each set clearly shows a $0.14 \text{ mA}/\text{cm}^2$ increase for higher precursor concentration.

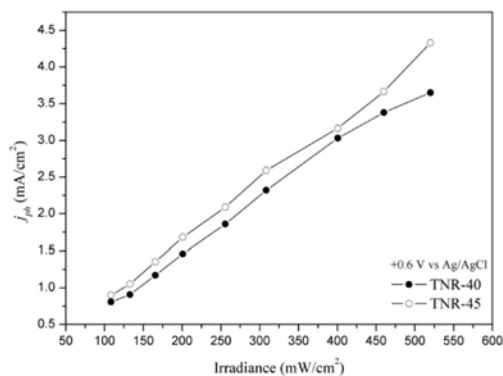


Fig. S. 5: Photocurrent densities generated with increasing solar light intensity. Reaching the 5 suns illumination, we can see a slight saturation tendency for the sample grown with lower precursor concentration, meanwhile there is none for the 45 mM one. These measures should be confirmed by a light source capable of reaching higher intensities. The measures were performed at 0.6 V vs Ag/AgCl .

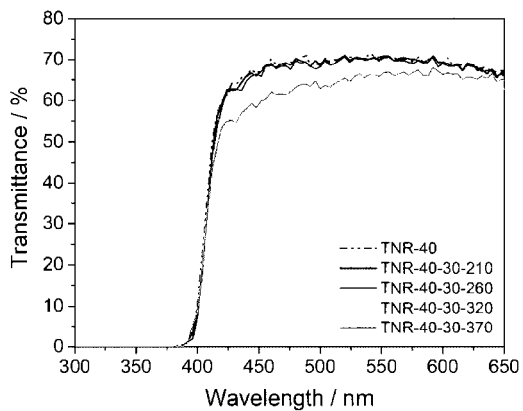


Fig. S. 6: UV-Vis Transmission spectra of all hydrogenated samples for 30 minutes at 210, 260, 320, and 370 °C. Samples under reductive treatments at higher temperatures start absorbing below the TiO₂ band gap.

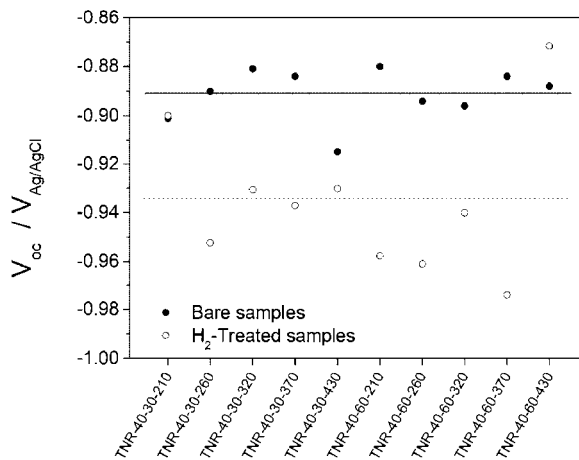


Fig. S. 7: Open circuit potential of all TNR-40 samples under 1 sun exposure, before and after hydrogen treatments.

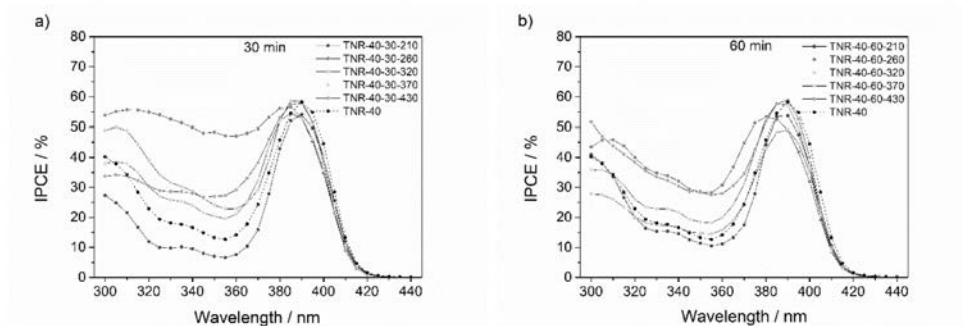


Fig. S. 8: IPCE measurements of all samples after a reductive treatment for a) 30 min and b) 60 min, at different temperatures. Measurements at 0 V vs Ag/AgCl.

Calculating the donors density of hydrogenated Titanium Dioxide Nanorods

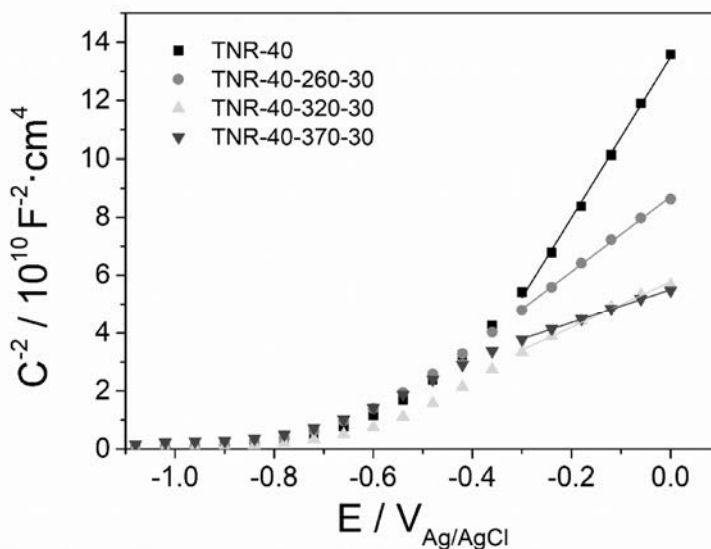


Fig. S. 9: Mott-Schottky plot of a pristine sample and three treated ones at 260, 320 and 370 °C, representing a small treatment, an optimal one and an over-treated sample. Results presented in Table S.1 correspond to the fitted region between -0.3 and 0 V vs Ag/AgCl. Measurements were performed in 1M NaOH in dark conditions.

Sample	Slope $F^{-2} \cdot V^{-1} \cdot cm^4$	N_d / cm^{-3}	W / nm
TNR-40	2.75E+11	3.01E+18	70.66
TNR-40-260-30	1.29E+11	6.41E+18	48.44
TNR-40-320-30	7.86E+10	1.05E+19	37.75
TNR-40-370-30	5.70E+10	1.45E+19	32.14

Table S. 1: Mott-Schottky plot of a pristine sample and three treated ones at 260, 320 and 370 °C, representing a small treatment, an optimal one and an over-treated sample. Results presented in Table S.1 correspond to the fitted region in Fig S.7 between -0.3 and 0 V vs Ag/AgCl.

Calculating the Faradaic efficiency of Titanium Dioxide Nanorods:

The charge, Q measured by the potentiostat is converted into moles, m of H_2 using Faraday's constant, F and n , the numbers of electrons per molecule, 2 in H_2 case:

$$m(\text{mol}) = \frac{Q}{F \times n} (\text{mol})$$

Where $F = 96485.3 \text{ C/mole}$. Now, the volume corresponding to the measured number of moles of H_2 can be calculated following:

$$V(\text{ml}) = \frac{m(\text{mol}) \times T(\text{K}) \times R(\text{L} \cdot \text{Pa} \cdot \text{mol}^{-1} \cdot \text{K}^{-1})}{P_{H_2}(\text{Pa})}$$

Where R is the gas constant, T the temperature and P_{H_2} the hydrogen gas partial pressure.

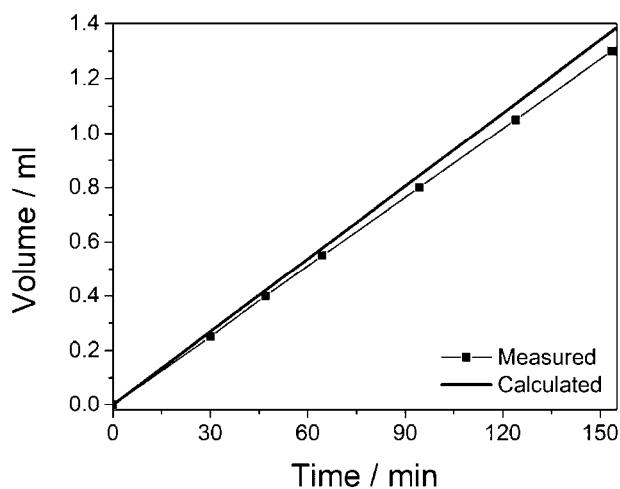


Fig. S. 10: Hydrogen evolution of the TNR-40-30-320 sample and the corresponding theoretical evolution calculated from total charge considering a 100% faradic efficiency. Measured at 0 V vs Ag/AgCl.

Substrate structuration

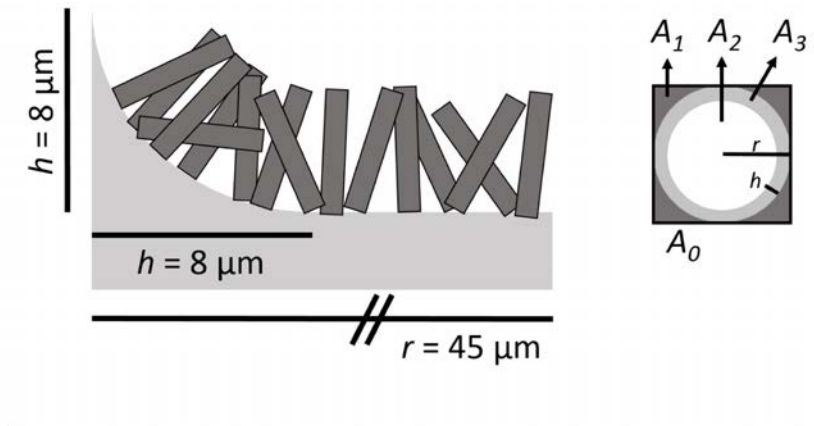


Fig. S. 11: graphical representation of a structured substrate with grown TiO_2 nanorods.

The initial area of a unit cell is:

$$A_0 = 4r^2 = 8100 \mu\text{m}^2$$

And the area of the initial square unit cell minus the etched circle is:

$$A_1 = (4 - \pi)r^2 = 1738.3 \mu\text{m}^2$$

The flat central part of the etched circle is:

$$A_2 = \pi(r - h)^2 = 4300.8 \mu\text{m}^2$$

And half the area of the external part of a torus is:

$$A_3 = \pi^2(r - h)h + 2\pi h^2 = 3323.5 \mu\text{m}^2$$

Which gives a final area increment of:

$$\begin{aligned} \Delta A (\%) &= \frac{(A_1 + A_2 + A_3) - A_0}{A_0} \times 100 = \frac{[(4 - \pi)r^2 + \pi(r - h)^2 + \pi^2(r - h)h + 2\pi h^2] - 4r^2}{4r^2} \times 100 \\ &= \frac{(9362.6 - 8100)\mu\text{m}^2}{8100 \mu\text{m}^2} \times 100 \approx 15.6\% \end{aligned}$$

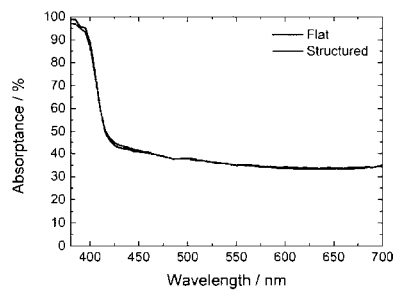


Fig. S. 12: UV-vis absorbance measurements $A(\%) = 100 - R - T$, where R is reflectance and T the transmittance. No appreciable difference can be observed between TiO_2 nanorods samples grown on structured or flat substrates.

Chapter 3

*Titanium dioxide as conductive and
protective layer for silicon-based
photocathodes*

In previous chapter efforts were put into enhancing the productivity of metal-oxide based photoanodes, but even after extensive research last decades and combining substrate microstructuration, nanorods growth and electronic modifications to the semiconductor, obtained photocurrents were below $2 \text{ mA}\cdot\text{cm}^{-2}$. If significant productivities are to be obtained, semiconductors with smaller band gap and more efficient in charge separation and extraction are to be used.

This chapter is focused on implementing silicon p-n junctions to form photocathodes through protecting them from corrosion with ALD-grown TiO_2 protective layers. The strategy has been used for some years, as reported in Chapter 1 section 7, where an homojunction in a short band gap material, highly prone for charge separation and transport (resembling already commercial strategies for photovoltaic technologies) is prevented from contacting the corrosive electrolyte by a conductive, transparent and protective layer. This way, the electron-hole generation and charge separation and extraction can be almost independently optimized in the photoabsorber. The protective layer, thus, must only be highly efficient in transparency and conductivity.

TiO_2 has been selected as protective layer for its large band gap (3.2 eV), transparent to major part of visible light and its known stability and semiconductor n-type behavior, permitting electron conductivity. ALD has been chosen as deposition technique as it permits high deposition thickness control and conformal coverage of any rugosity, minimizing pinholes which would permit the electrolyte to corrode the substrate¹. 100 nm thick layers were selected to assure good protection and to exclude possible tunneling conductivity, thus focusing our analysis on conductivity intrinsic to TiO_2 . The slow deposition process and its relation with TiO_2 layer crystallization will be studied, together with its implications in conductivity and stability.

3.1. Charge transfer characterization of ALD-grown TiO_2 protective layers in silicon photocathodes

In the first article included in this chapter, the aim was to elucidate the fabrication parameters of ALD TiO_2 layers governing especially conductivity and stability in photocathodic hydrogen evolution. Acidic media was selected as it is more prone for the HER reaction together with platinum as highly efficient catalyst. Silicon was chosen as photoabsorber for our photocathodes (Figure 3.1a), as it has long demonstrated efficient light to current conversion of wide part of the solar spectra, and its p-n homojunction is not sensible to the fabrication steps used in this work. This allowed us a study with an invariant photoabsorber part.

Layers were fabricated at deposition temperatures of 100 to 300 °C, and characterized, finding significant morphological, crystallographic and conductivity changes. Layers were homogeneous, amorphous and highly resistive at 100 °C, meanwhile increasing to 200 °C

grains in the anatase-crystalline form of TiO_2 were found to appear, together with significant improvement on photoelectrodes performance. Further increasing temperature to 300 °C improved crystallinity, gran coverage and electrode's performance (Figure 3.1b). A 5 nm Ti layer on top of HF-cleaned silicon was introduced to avoid SiO_2 formation due to atmospheric or H_2O ALD pulses exposure, but was found to enhance anatase- TiO_2 crystallization, thus pushing for more stable and conductive TiO_2 films.

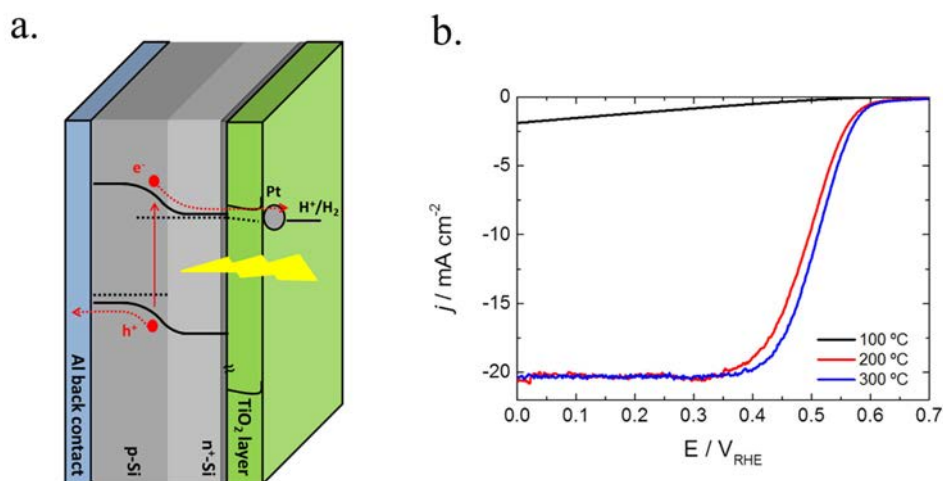


Figure 3.1. a) Energy band diagram model of an $n^+p\text{-Si/Ti/TiO}_2/\text{Pt}$ photocathode. b) Cyclic voltammograms of different photocathodes with protective layers grown at 100, 200 and 300 °C, presenting significant performance increment at higher ALD deposition temperatures.

Deeper analysis by conductivity AFM confirmed the relation between crystallization and conductivity, revealing the crystalline grains present in the deposited film were responsible of electron conductivity (Figure 3.2a). After 300 h stability test in acidic media at reductive potentials, the amorphous regions were found to dissolve, meanwhile fully crystalline layers suffered no alterations (Figure 3.2b). These results are of highly importance for further ALD fabricated TiO_2 protective layers for water splitting photocathodic applications.

Optimizing ALD deposition temperature, highly conductive and stable TiO_2 films were obtained, permitting efficient photocathodes with $20 \text{ mA}\cdot\text{cm}^{-2}$ photocurrents, 640 mV photovoltages and up to 8.1 % HC-STH conversion efficiencies.

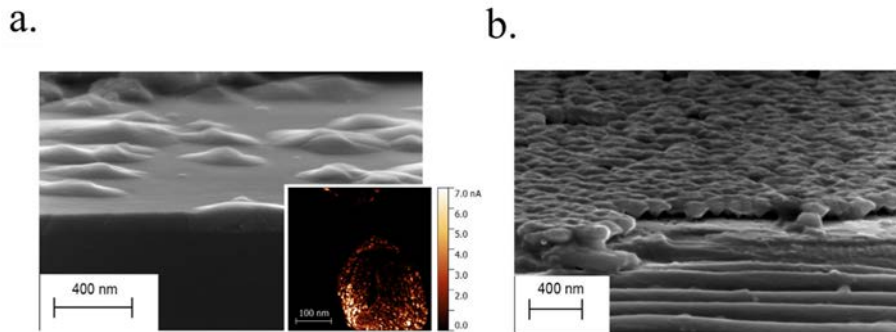


Figure 3.2. a) Cross section SEM image of a TiO_2 layer grown directly on Silicon. Inset: *c*-AFM map showing conductivity is detected where there is a crystal, and no conductivity on amorphous regions. b) Cross section SEM image of a TiO_2 layer after 300 h stability test in acid, presenting dissolution of the amorphous regions.

Bibliography

- (1) Mikko Ritala; Markku Leskela. Atomic Layer Epitaxy--a Valuable Tool for Nanotechnology? *Nanotechnology* **1999**, *10*, 19–24.

Charge Transfer Characterization of ALD-Grown TiO₂ Protective Layers in Silicon Photocathodes

Carles Ros,^{*,†,‡} Teresa Andreu,^{*,†,‡,§} María Dolores Hernández-Alonso,[§] Germán Penelas-Pérez,[§] Jordi Arbiol,^{||,⊥,⊙} and Joan R. Morante^{†,‡}

[†]Catalonia Institute for Energy Research (IREC), Jardins de les Dones de Negre 1, Sant Adrià del Besòs, 08930 Barcelona, Spain

[‡]Universitat de Barcelona (UB), Martí i Franquès, 1, 08028 Barcelona, Spain

[§]Repsol Technology Center, Agustín de Betancourt, s/n, Móstoles, 28935 Madrid, Spain

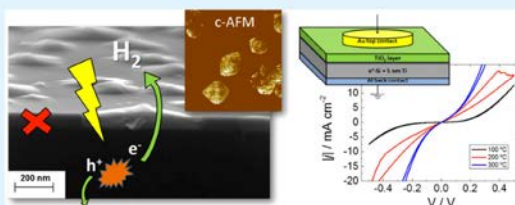
^{||}Catalan Institute of Nanoscience and Nanotechnology (ICN2), CSIC and The Barcelona Institute of Science and Technology (BIST), Campus UAB, Bellaterra, 08193 Barcelona, Spain

[⊥]ICREA, Pg. Lluís Companys 23, 08010 Barcelona, Spain

Supporting Information

ABSTRACT: A critical parameter for the implementation of standard high-efficiency photovoltaic absorber materials for photoelectrochemical water splitting is its proper protection from chemical corrosion while remaining transparent and highly conductive. Atomic layer deposited (ALD) TiO₂ layers fulfill material requirements while conformally protecting the underlying photoabsorber. Nanoscale conductivity of ALD TiO₂ protective layers on silicon-based photocathodes has been analyzed, proving that the conduction path is through the columnar crystalline structure of TiO₂. Deposition temperature has been explored from 100 to 300 °C, and a temperature threshold is found to be mandatory for an efficient charge transfer, as a consequence of layer crystallization between 100 and 200 °C. Completely crystallized TiO₂ is demonstrated to be mandatory for long-term stability, as seen in the 300 h continuous operation test.

KEYWORDS: PEC cells, silicon, protecting overlayers, water splitting, solar hydrogen production, titanium dioxide, atomic layer deposition



1. INTRODUCTION

As society faces the problems derived from global warming, harvesting solar energy and storing it into chemical bonds is one of the most promising paths in the so-called solar fuel economy¹ combined with the introduction of renewable energies. Between them, photoelectrochemical (PEC) water splitting offers the possibility to directly convert water and solar energy into hydrogen and oxygen with competitive efficiencies.² Estimating the actual photovoltaic conversion efficiency and the current commercial electrolyzer yield, the direct conversion of solar energy into chemical energy (solar-to-hydrogen, STH), starts to be competitive above 10%.³

Although this technology has been known for decades,⁴ still many of the published values show conversion efficiencies too low, and only few long-term durability tests have been reported up to now. Combining efficiency and stability, while being cost effective, is the most relevant challenge to overcome.

During the last years, many works have been focused on understanding the capacity of different nonexpensive metal oxide materials, such as TiO₂,⁵ WO₃,⁶ BiVO₄,⁷ or Fe₂O₃,⁸ or oxynitrides, such as TaO_xN_y,⁹ with band gaps large enough to split the water molecule but still capable of harvesting a significant portion of the solar spectra, all of them being

photoanodes due to their n-type semiconductor.^{5,10–13} In parallel, many standard electronic semiconductor materials, such as Si, GaAs, CdTe, or chalcogenides,^{14,15} have also been explored as electrode materials with high photon absorption coefficients for tandem configurations,¹⁶ although with many electrochemical stability limitations, which have required different protection and surface catalyst coating strategies. Many of these semiconductors are well known from the photovoltaic or microelectronic industry, with silicon being the most commercially developed due to its performance and abundance. Nevertheless, silicon, like other standard electronic semiconductors, when exposed to acidic electrolytes has a high surface oxidation rate, limiting its long-term electrochemical performance.^{17,18} To enable silicon to be used as a front-illuminated photocathode for long-term hydrogen evolution, transparent, protective, and conductive coatings are required.¹⁹ The coatings must be stable in aqueous electrolytes, must be transparent to solar spectra to maximize photon absorption,

Received: March 1, 2017

Accepted: May 4, 2017

Published: May 4, 2017

and must have a proper band alignment to facilitate minority carrier injection.^{20–22}

One of the proposed coating candidates is titanium dioxide (TiO₂), as it is known to be stable in a wide range of pH.^{23,24} Moreover, TiO₂ has a 3 eV band gap for rutile and 3.2 eV for the anatase crystalline structure, allowing excellent optical transmittance, making TiO₂ an excellent candidate as a protection layer for photocathodes.^{25,26} In the case of photoanodes, ultrathin (2 nm) TiO₂ has been used to protect them for some hours while conducting by tunneling,²⁷ and recently, thanks to an electronically “leaky” behavior, over 100 nm thick TiO₂ layers were reported to be conductive and stable for over 100 h by the Lewis group despite a large valence band offset between the Si and TiO₂, attributed to Ti³⁺-related midband states closely aligned with the Si valence band,^{28–31} although there is some controversy on the conduction mechanism.³² In the case of photocathodes, it should be taken into account that TiO₂ has n-type semiconductor electrical characteristics due to oxygen vacancies, with its conduction band energetic level almost aligned with the silicon photoabsorber material for an efficient electron transport toward the electrolyte interface for a hydrogen evolution reaction (HER). In this context, other works have deposited TiO₂ by sputtering and some via atomic layer deposition (ALD), all of them requiring a further postannealing process at at least 400 °C for relevant stability.³³ ALD has attracted much attention during the last decade as it allows depositing thin and conformal layers with minimal pinholes, and recently, this technique has been upgraded to industrial production. In spite of these powerful capabilities, there are only few studies about the characteristics of ALD-grown TiO₂ for photocathodic hydrogen evolution.^{34,35} Recently, we have demonstrated the feasibility of using ALD for the fabrication of photocathodes using a CIGSe chalcopyrite absorber,³⁶ where it was proved that, to attain a high STH conversion, optimizing charge transfer processes is required. Although some other works also have used ALD-grown TiO₂, a better understanding of the growth process and evaluation of the final TiO₂ properties as a transparent, protective, and conductive layer is needed. The growth of TiO₂ by ALD is known to produce amorphous or crystalline phases depending on the temperature, precursors, impurities, substrate material, or film thickness³⁷ and hence the charge transfer characteristics from the absorber silicon to the electrolyte through this layer become a function of its deposition parameters.

To the best of our knowledge, there is no detailed microscopic analysis on the influence of electrical characteristics and deposition conditions of ALD coating layers on the final PEC characteristics of TiO₂-protected photocathodes. Among them, temperature is one of the critical factors, with the ALD crystallization temperature being normally lower than that reported for postannealing processes, owing to the surface mobility of intermediate reaction species.^{38,39} Reducing the process temperature while maintaining optimal properties is highly desired to decrease the fabrication costs and to enable novel photoabsorbing materials that are sensitive to temperature.⁴⁰

However, one of the main concerns is relative to the internal interface between silicon and the coated layer. Si native oxidation forms a narrow SiO_x layer. In previous works, controlled SiO_x has been used to maximize the photovoltage owing to the creation of an MIS junction,^{41,42} but in our case the photovoltage is created by the buried n⁺-p silicon junction.

To avoid SiO_x being formed, which in our case would act as a series resistance, a thin metallic titanium layer is deposited on the cleaned silicon surface before TiO₂ deposition to inhibit ambient or ALD-process⁴² oxidation of Si, assuming a small light shielding of the metallic film, and by high-resolution transmission electron microscopy (HRTEM), it is confirmed that no SiO_x is formed. TiCl₄ has been selected as the precursor material owing to its wide deposition range³⁸ compared with other precursors known for ALD TiO₂.⁴³

In the present study, to understand the role of the crystallographic structure on the charge transfer across these coated layers and its stability, TiO₂ layers have been grown by ALD at different deposition temperatures on different silicon-based substrates using TiCl₄ as the precursor. The growth temperature has been modified from 100 to 300 °C, and a model is presented to explain the charge transfer mechanism across the ALD layer.

2. EXPERIMENTAL SECTION

ALD TiO₂ has been grown on n⁺-p silicon buried junctions and simultaneously on n⁺ degenerately doped silicon, to simulate direct injection under dark conditions.

n⁺-Si samples were created by cutting a degenerately doped silicon wafer (0.001 Ω cm) into 1 × 1 cm² pieces, and 50 nm of Al was thermally evaporated as a back contact. To prevent the formation of any native SiO₂ and avoid its potential negative effects, 5 nm of Ti was thermally evaporated on top of some of these samples (Ti/n⁺-Si). The thickness of titanium was controlled by a quartz microbalance.

For the Ti/n⁺-p-Si samples, a 1 cm² active area was lithographically defined by SiO₂ passivation on a silicon p-type wafer (0.1–0.5 Ω cm resistivity). Boron was implanted in the defined front surface and activated by rapid thermal annealing, creating a 200 nm n⁺ region on top of the p-type substrate. The sample's front surface was dipped in HF and immediately coated with 5 nm Ti by sputtering. As back contact, 1 μm Al/0.5% Cu was sputtered on top of 30 nm Ti to form a proper Ohmic contact.

n⁺-Si, Ti/n⁺-Si, and Ti/n⁺-p-Si samples were sonicated for 5 min in a 1:1:1 isopropanol, acetone, and deionized (DI) water cleaning solution, followed by abundant rinsing and further 5 min sonication in DI water. Samples were simultaneously introduced in a R200 Picosun Atomic Layer Deposition system. TiCl₄ was selected as a precursor due to its wide temperature stability range. TiCl₄ and H₂O precursors at 19 °C were used in successive pulses at 8 mbar in a N₂ flow atmosphere, with 0.1 s pulses and 10 s purges. Under these conditions, layers have been grown at deposition temperatures of 100, 200, and 300 °C for 3700 cycles, corresponding to roughly 100 nm layers for 200 °C. The layer thickness was measured by evaluating the reflected spectra with a Sensofar interferometer device with ±0.2 nm error. Finally, platinum was deposited either by thermal evaporation (corresponding to 1 nm measured by a quartz microbalance) or by drop casting 50 μL of 6.5 mM H₂PtCl₆ in isopropanol. The samples were then soldered to a Cu wire using Ag paint and were epoxy-protected, leaving the front area exposed. For I–V measurements, 100 nm of Au was thermally evaporated on TiO₂/Ti/n⁺-Si samples with a circular mask 0.55 cm in diameter.

Surface and cross-section morphology was observed with a Zeiss Series Auriga field effect scanning electron Microscope. Structural characterization was carried out by X-ray diffraction (XRD) in a D8 Advance Bruker equipment with a Cu Kα radiation source working at 40 kV and 40 mA with a 3° offset angle. Crystalline domains are calculated following the Scherrer equation: $D = 0.9\lambda/(\beta \cos \theta)$, where λ is the X-ray wavelength (1.5406 Å), β is the full width of the diffraction line at half-maximum (FWHM), and θ is the Bragg angle. HRTEM, high-angle annular dark field, scanning TEM, and electron energy loss spectroscopy (EELS) spectrum imaging were performed using a TECNAI F20 operated at 200 kV with a point to point resolution of 0.14 nm. AFM and conductivity-AFM measures were taken with a Park Systems XE-100 with platinum conductive

cantilevers. Owing to the n^+ - p -Si built-in voltage, only the samples on n^+ -Si substrates were measured by conductivity-AFM. The PEC measurements were obtained with a Princeton Applied Research PARSTAT 2273 potentiostat using Ag/AgCl/KCl (3 M) ($E^0 = 0.203 V_{\text{RHE}}$) as the reference electrode and a platinum mesh as the counter electrode. A quartz cell with flat faces was used with 100 mL of 0.5 M H_2SO_4 electrolyte and a 300 W xenon lamp with an AM 1.5G filter at an appropriate distance to receive 100 mW/cm^2 , calibrated using a silicon diode (XLPF12-3S-H2-DO; Gentec-EO).

The half-cell STH (HC-STH) efficiency was calculated from the linear sweep voltammograms using the equation $\text{HC-STH} = |j_{\text{ph}}| \times (E_{\text{RHE}} - E_{\text{H}_2/\text{H}^+})/P_{\text{sun}} \times 100\%$, where j_{ph} is the photocurrent density obtained under an applied bias of E_{RHE} , $E_{\text{H}_2/\text{H}^+}$ is the equilibrium redox potential of hydrogen (0 V_{RHE}), and P_{sun} is the power density of the incident solar energy (100 mW/cm^2). I - V curves were obtained with the potentiostat, connecting the working electrode on the back contact and the counter and reference electrodes on the top Au contact. PEC fill factor (FF) was defined equivalently as in photovoltaics assuming the onset potential as the open circuit voltage and the current density at 0 V_{RHE} as the short circuit current.

3. RESULTS AND DISCUSSION

3.1. Electrochemical Characterization. To optimize the charge transfer process of an n^+ - p -Si photocathode, it is needed to consider that the electron injection will be from the doped n^+ -Si to the electrocatalyst through the protective TiO_2 layer. Then, to avoid the resistive effect of the diode under dark conditions, degenerately doped n^+ 0.001 Ω cm Si substrates have been used instead of illuminating n^+ - p -Si junctions, some of them being protected with Ti.

n^+ -Si and Ti/n^+ -Si substrates with nominal TiO_2 growth (100 nm) at different temperatures were tested as electrodes for hydrogen evolution using Pt as an electrocatalyst in sulfuric acid media (0.5 M H_2SO_4) in a 3-electrode configuration. The overall current obtained under polarization is influenced by the intrinsic conductivity of the TiO_2 and a possible extra SiO_2 interlayer and also the surface charge transfer rate, which is assumed to be constant as the HER-deposited catalyst is the same. Thus, any variation in the measured current is attributable to the TiO_2 or the presence of a resistive SiO_2 interlayer. As seen in Figure 1, polarization curves show a clear

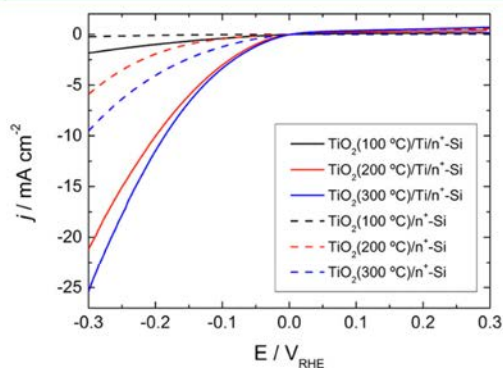


Figure 1. Polarization curves of TiO_2 layers grown at different temperatures on Ti/n^+ -Si substrates (solid lines) and n^+ -Si (dotted lines) ranging from 100 to 300 $^{\circ}\text{C}$. Pt (1 nm) was evaporated on top as the HER catalyst. Measurements were made in 0.5 M H_2SO_4 with Ag/AgCl as the reference electrode and Pt as the counter electrode in a 3-electrode configuration with no illumination.

influence of the ALD deposition temperature. Regardless of the titanium layer presence, the current density reached at the same polarization is higher as the growth temperature increases. Comparing the results obtained with both substrates, n^+ -Si and Ti/n^+ -Si, it can be observed that, under the same experimental conditions, higher current densities were obtained in samples in which the TiO_2 layer was grown on Ti/n^+ -Si. On bare n^+ -Si, the presence of a native SiO_2 layer is expected, introducing significant resistance to the system and lowering the obtained electrochemical current. This native layer can thus be avoided with the metallic 5 nm Ti layer.

3.2. Morphological and Structural Characterization.

No visible pinholes have been detected by direct analysis of the SEM images of the TiO_2 layers grown by ALD (Figure 2a–c) on Ti/n^+ -Si substrates. Increasing the temperature from 100 to 300 $^{\circ}\text{C}$ shows remarkable variation in the film topography, which is proven by XRD to correspond to TiO_2 crystalline growth, starting between 100 and 200 $^{\circ}\text{C}$ and presenting an anatase structure. The deposition temperature range was set up to 300 $^{\circ}\text{C}$ to obtain complete layer crystallization on all substrates.

For ALD layers deposited on Ti/n^+ -Si substrates, XRD shows that at 100 $^{\circ}\text{C}$ amorphous layers are grown, whereas anatase TiO_2 is obtained at 200 and 300 $^{\circ}\text{C}$ (Figure 2d). This is in agreement with electrochemical charge transfer shown in Figure 1, with amorphous layers inhibiting charge transfer; meanwhile, crystallization enables current flow, and more stable TiO_2 phases further reduce electrical resistance. The preferential growth direction with the 25.5 $^{\circ}$ peak is shown at 200 $^{\circ}\text{C}$ but not at 300 $^{\circ}\text{C}$, as the higher nucleation rate inhibits preferential directions to develop.⁴⁴ This phase transition is in accordance with other studies.³⁸

Samples without the intermediate Ti layer (where Si was exposed to air, creating a native SiO_2 layer) show the same behavior but shifted to higher temperatures (Figure S2a–c), with samples grown at 300 $^{\circ}\text{C}$ still showing preferential growth directions (Figure S3).

Crystal nucleation is favored as the temperature increases, starting at a temperature higher than 100 $^{\circ}\text{C}$, as seen in SEM images. At 200 $^{\circ}\text{C}$, grains measuring 180 nm in diameter can be seen on n^+ -Si substrates, whereas those less than 20 nm in diameter can be seen at 300 $^{\circ}\text{C}$ on Ti/n^+ -Si, with a higher grain density and size dispersion due to increased nucleation and competitiveness. Higher thermal energy enhances nucleation kinetics by overcoming its activation energy, favoring nucleation in front of growth and resulting in more and smaller grains. Increasing the temperature is also expected to improve the atomic order in the crystal structure. From XRD data and using the Scherrer equation, the mean size of the crystalline domains has been calculated. Sizes of 33.2 nm at 200 $^{\circ}\text{C}$ and 25.9 nm at 300 $^{\circ}\text{C}$ on n^+ -Si, and 26.3 and 22.2 nm at 200 and 300 $^{\circ}\text{C}$, respectively, on Ti/n^+ -Si substrates have been obtained. The calculated crystallite size suggests that multiple crystallographic domains are present in the same observable grain. The crystal size is reduced when the deposition temperature increases, as is expected for higher nucleation.

The thickness of the layer is also dependent on the crystallographic phase. As can be seen in the cross-section SEM image (Figure 3), grains are thicker than the amorphous layer. We should expect thinner layers where they crystallize into more compact phases, as far as the amount of the precursor is kept constant. However, the anatase phase is more favorable to OH^- adsorption, and higher superficial OH^-

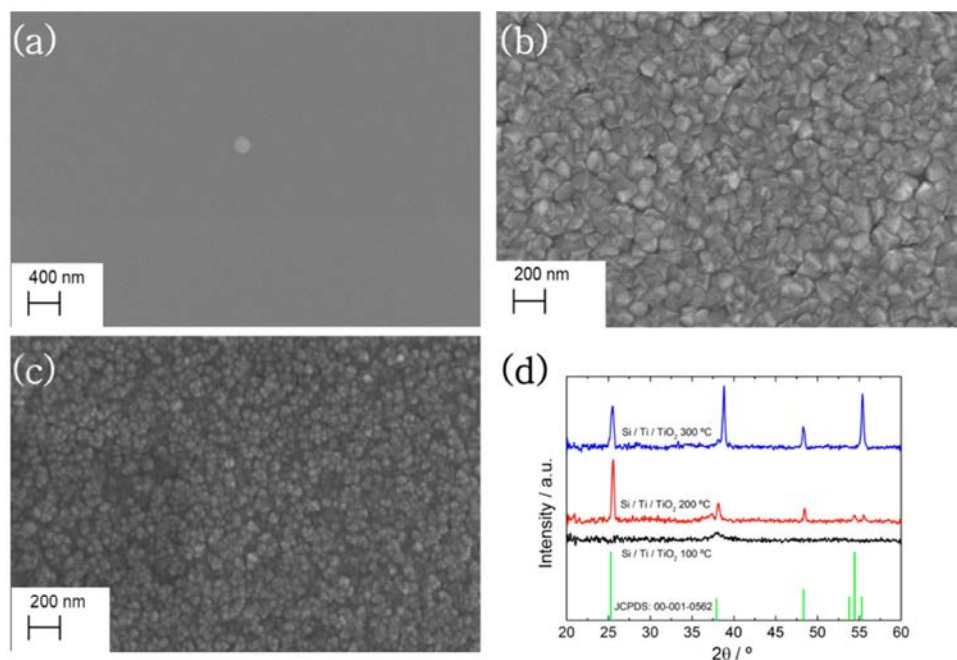


Figure 2. SEM images of TiO₂ layers grown by 3700 ALD cycles of TiCl₄ and H₂O on Ti/n⁺-Si substrates at (a) 100 °C, (b) 200 °C, and (c) 300 °C. (d) XRD patterns of TiO₂ layers grown on Ti/n⁺-Si substrates at 100, 200, and 300 °C.

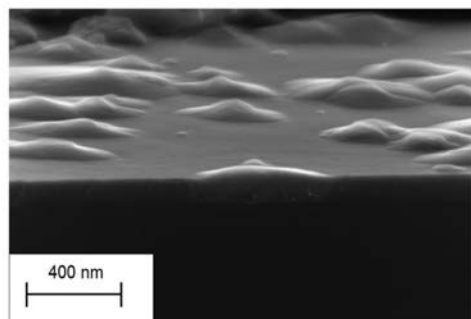


Figure 3. Cross-section SEM image of a 3700-cycle TiO₂ layer on n⁺-Si grown at 200 °C.

density increases the growth per cycle by a higher ALD reactivity, thus generating thicker layers where there is a crystallized zone.³⁵

As seen in the HRTEM cross section (Figure 4) of a processed Ti/n⁺p-Si sample, a native 3.5 nm TiO₂ overlayer is formed on metallic Ti when exposed to air. This layer seems to enhance nucleation and hence, due to growth competition among different grains, reduction of the crystallite size by crystal overlapping takes place. Lower lattice mismatch is the cause of enhanced nucleation on TiO₂/Ti substrates compared with SiO₂/Si, leading to crystallization temperature reduction, as TiO₂ is known to start growing in the amorphous phase for the initial ALD cycles.³⁸ By AFM, it was discarded to be caused by higher substrate rugosity (Figure S4).

From the HRTEM image of TiO₂ on Ti/n⁺p-Si, it is confirmed that the presented ALD crystal has an anatase crystallographic phase (Figure 4). The observed metallic Ti on silicon is 5 nm thick, and its native TiO₂ layer is 3.5 nm. Ti presents a polycrystalline structure with preferential {10 $\bar{1}$ 0} planes parallel to the (001) Si substrate. The native layer is amorphous, as the 200 °C annealing caused by the ALD deposition process is not enough to crystallize it. EELS TEM imaging (Figure S5) confirms progressive reduction of the oxygen content in the native layer, with 5 nm of metallic Ti remaining after ambient exposition during laboratory manipulation and processing, proving that it is thick enough to act as an oxidation barrier, avoiding oxygen diffusion toward the Si photoabsorber. This 5 nm Ti layer is expected to partially block light from reaching the Si, and thus significantly reducing the photon-to-current conversion efficiency.

It is important to note that the bottom part of the ALD layer was crystalline, meaning nucleated crystals not only propagate upward but also laterally.⁴⁵ The substoichiometry of the native oxide layer must prevent its recrystallization. Reciprocal space phase filtered HRTEM presents columnar epitaxial growth from the base to the top of the ALD layer (Figure 4).

3.3. Solid-State Electrical Characterization. A conductivity AFM was used to visualize the conduction path across the TiO₂ layer, similar to the measurements performed by Wang's group on hematite.⁴⁶ From the topography image of a sample grown at 200 °C on bare n⁺-Si substrates (Figure 5a), we can see that successive ALD deposition formed isolated grains, as seen in the SEM image (Figure 3). From conductive measurements (Figure 5b), it is perfectly seen that the whole grain structure is the path for the current flow, with similar current intensities at a fixed voltage. Comparing topography

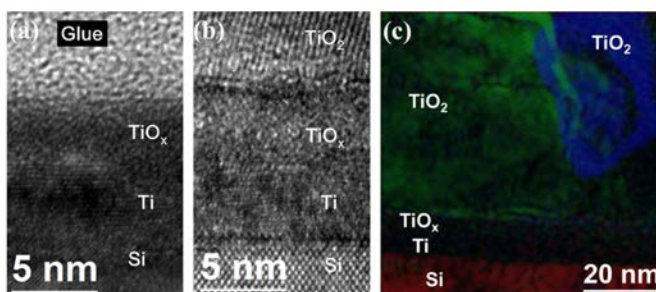


Figure 4. HRTEM images of a Ti/n⁺p-Si substrate (a) before ALD deposition (b) with 3700 ALD cycles of TiO₂ grown at 200 °C. (c) Reciprocal space phase filtered HRTEM image composition. Crystals starting on the native TiO₂ and propagating vertically in a columnar configuration can be seen.

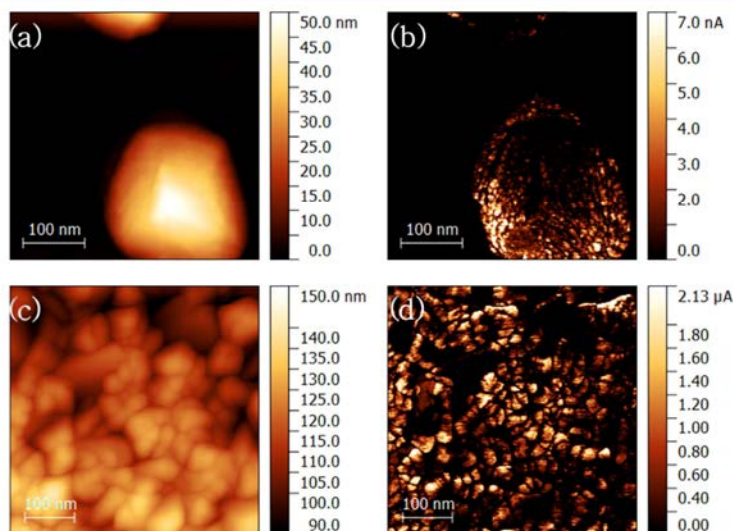


Figure 5. AFM and c-AFM images of TiO₂ ALD layers on an n⁺-Si substrate. (a) Height map of a sample grown at 200 °C, and (b) current intensity image of the same sample. (c) Height map of a sample grown at 300 °C and (d) its current intensity map.

and conductivity AFM measurements, and as suggested by the Scherrer equation, multiple crystallite boundaries can be seen in each grain as more resistive regions. No current is detected from the amorphous regions, as atomic disorder gives significantly reduced electron mobility and larger resistance than crystalline TiO₂. From a sample grown at 300 °C on Ti/n⁺-Si (Figure 5c,d), where no amorphous phase is present, similar current intensity is detected from all grains. Also, grain boundaries are much less conductive.

Columnar grain growth together with conductivity through the crystalline grains is the key for a good electrical transport from the photoabsorbing material to the catalyst to perform the HER. No grain boundaries are seen by HRTEM in the vertical direction, those being one of the main electron mobility barriers for polycrystalline conductive materials. Increasing the deposition temperature increases the number of grain boundaries in the lateral but not in the vertical direction and also enhances the crystallographic order, a parameter for higher electron mobility. This is in accordance with obtaining higher conductivity in the samples grown at higher temperatures.

To deeply analyze and quantify the conduction across ALD-grown TiO₂ layers on Ti/n⁺-Si, 100 nm of Au were deposited by thermal evaporation to form a top, highly conductive and defined contact (Figure 6a). As seen in Figure 6b, a nonlinear behavior and higher currents for negative polarization can be distinguished, meaning that our system presents a rectifying behavior: a Schottky barrier junction, formed between the TiO₂ and the Au top contact. The degenerately doped n⁺-Si/Ti junction and the progressive interface between Ti and TiO₂ (due to the oxygen chemical affinity of Ti) form Ohmic-like contacts, injecting electrons from the n⁺-Si conduction band into the TiO₂ conduction band.⁴⁷ The conductivity increment with higher ALD growth temperatures is clearly shown, presenting the same trend determined by previous electrochemical measurements (Figure 1).

Samples grown at 200 and 300 °C present a reversible switch between a high resistivity (HR) and a low resistivity (LR) state. Anatase-crystallized TiO₂ is known to behave as an n-type semiconductor due to oxygen vacancies, regarded to be fully ionized even at room temperatures, giving free electrons to act

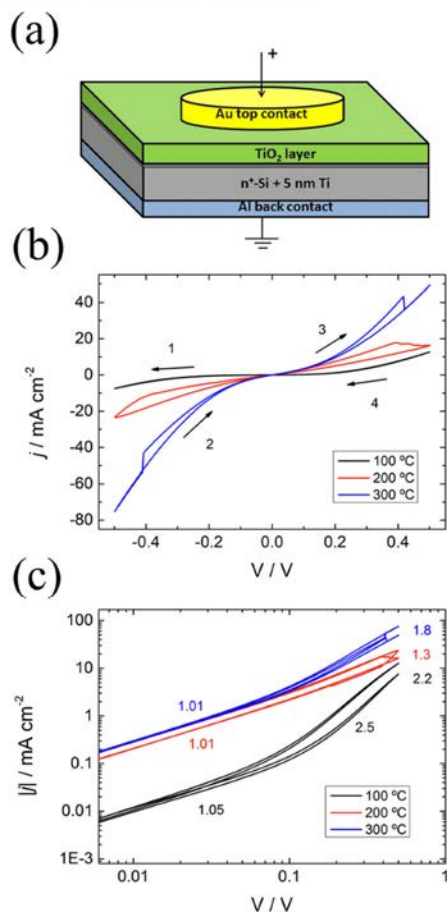


Figure 6. (a) Scheme of the stack. (b) I - V and (c) log-log curves of the Au top-contacted TiO_2 layers grown at 100 °C (black), 200 °C (red), and 300 °C (blue). Numbered arrows show the direction of the polarization curve in (b), and the slope in (c) is indicated for each different segment of the log-log graph. Measurements were recorded at 50 mV/s.

as charge carriers. These changes while cycling have been explained by some papers during the last decade^{47–51} and are attributed to ionic diffusion of the oxygen atoms due to polarization, leaving extra free charges (oxygen vacancies) that enhance the electronic conductivity.⁴⁷ Current flow through defects on the crystallographic structure can create local heating, enhancing ionic diffusion and forming highly conductive paths or filaments, giving the LR state. Reversing the polarization returns the oxygen ions, destroying the filaments and resetting the sample to the HR state. The sample grown at 300 °C has an almost immediate change in the resistivity state, whereas the sample fabricated at 200 °C has a more progressive one. This difference could be justified by the poor crystallographic quality at 200 °C, lowering the ionic mobility together with a general lower conductivity, which gives less local heating.

From the log-log plot (Figure 6c), an Ohmic dependence ($I \propto V$) is observed for all samples on small polarization potentials. Further increasing the potential causes an increase in the slope for all samples. This behavior fits to a space charge limited conduction mechanism ($I \propto V^3$),⁵² together with the Au/ TiO_2 Schottky Barrier junction. For polarization values inside the Ohmic regime, we can measure resistances from 221 $\Omega \text{ cm}^2$ for the sample grown at 100 °C, to 41 and 21 $\Omega \text{ cm}^2$ for 200 and 300 °C-grown samples. If we measure the potential drop in the layer at 5 mA/cm², we obtain 430 mV for 100 °C, 213 and 151 mV for HR and LR states at 200 °C, and 118 and 112 mV for HR and LR at 300 °C.

3.4. PEC Characterization. ALD-grown TiO_2 layers were used to protect n^+ p-Si substrates having a thin ~ 5 nm Ti layer (Ti/ n^+ p-Si) at deposition temperatures of 100, 200, and 300 °C. When exposed to AM 1.5G illumination, the p-n junction properly separates the electron-hole pairs, giving an onset voltage around 0.6 V versus RHE (Figure 7). More than 100 mV/dec potential losses should be expected by the electrochemical kinetics of hydrogen evolution, even when using platinum as a catalyst.⁵³

The layer growth temperature influences significantly the sample's efficiency. Samples grown at 100 °C show a highly resistive response (with a FF of 0.26); meanwhile, FF is significantly improved on increasing the growth temperature. At 200 °C, which corresponds to samples with polycrystalline

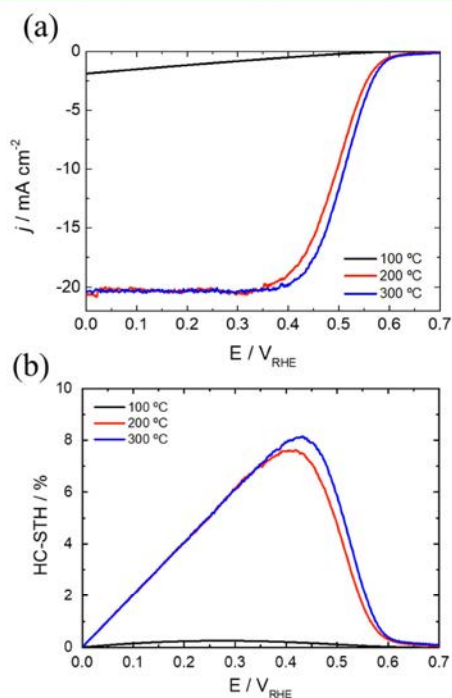


Figure 7. (a) Polarization curves and (b) HC-STH calculations of TiO_2 layers grown at different temperatures on Ti/ n^+ p-Si substrates ranging from 100 to 300 °C. Pt (1 nm) was evaporated on top as the HER catalyst. Measurements under 1 Sun AM 1.5G illumination in 0.5 M H_2SO_4 with Ag/AgCl as the reference electrode and Pt as the counter electrode in a 3-electrode configuration.

anatase layers combined with amorphous regions, an FF of 0.66 is obtained. At 300 °C, the slope of the j - V curve is slightly increased, together with the FF, up to 0.73 (Table 1).

Table 1. Photogenerated Current Densities and Voltages under 1 Sun Illumination of the Samples Grown at Different Temperatures

growth temperature (°C)	j at 0 V_{RHE} (mA/cm ²)	V_{onset} (V_{RHE})	FF	HC-STH (%)
100	1.9	0.59	0.26	0.25
200	20.6	0.63	0.66	7.60
300	20.3	0.64	0.73	8.10

This enhancement in the saturation slope is directly related to the growth temperature via reduction of the resistivity of the deposited layer. With such improvement, a HC-STH conversion efficiency of up to 8.1% can be reached. The effect of TiO₂ layers with different resistivities on the band diagrams of silicon photocathodes is schematically represented in Scheme 1. For highly resistive layers, the voltage drop across the protective layer causes a decrease in the FF. For the more crystalline and less resistive layers, the lower voltage drop allows an optimum electron transfer. Therefore, the main factors contributing to the FF characteristics of the polarization curve are the buried p-n junction and the platinum HER overpotential.

Long-term stability experiments were performed under 1 Sun AM 1.5G illumination at 0.3 V_{RHE} in 0.5 M H₂SO₄ with n⁺p-Si photocathodes protected with either an almost-completely crystalline TiO₂ layer and a fully crystalline one.

After examining the almost-completely crystalline TiO₂ layer by SEM (Figure 8a,b), we can clearly see how the top view is similar to the as-grown layers (Figure 2b), with darker zones between the crystals. The cross-section SEM image evidences that those gaps are missing TiO₂. At reductive potentials and

using an acidic electrolyte (0.5 M H₂SO₄), the amorphous TiO₂ phase dissolves but the anatase crystals do not, leaving inversed conical structures only attached to the Si by the tip. Moreover, silicon is not attacked, and SiO₂ is known to be formed, protecting the silicon from further oxidation but electrically passivating the surface. Fully crystalline TiO₂ layers present no visible dissolution, showing compact columnar crystals by cross-section SEM, proving that the stability of TiO₂ shown in its Pourbaix diagram²³ is only attributable to the crystalline anatase TiO₂ crystal phase. This shows the need to use crystallized ALD layers, together with the conductivity improvement with temperature, as previously shown.

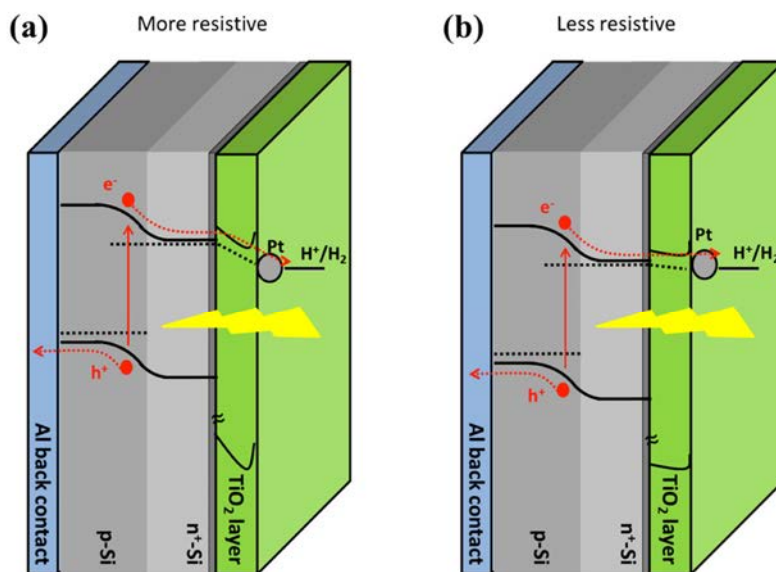
A stability measurement of a photocathode protected with a fully crystalline TiO₂ layer was performed for over 300 h, as shown in Figure 8a. The sample maintained 90% of the initial photocurrent without significant changes in the FF, as seen in Figure S6. This slight current reduction over time has been attributed by other authors to the loss of the poorly attached platinum catalyst.^{25,33} To the best of our knowledge, there are no reports presenting several days' stability of TiO₂-protected photocathodes fabricated at temperatures lower than 400 °C.

4. CONCLUSIONS

In conclusion, we have demonstrated that the ALD growth temperature plays a fundamental role on the charge transfer across protective TiO₂ coatings for front-illuminated silicon photocathodes due to reduced resistivity with increasing deposition temperatures. A minimum growth temperature is required for an efficient charge transfer, as a consequence of layer crystallization between 100 and 200 °C.

From conductive AFM images, we have proven that the conduction path is through the crystalline structure of TiO₂ and that amorphous layers and grain boundaries are highly resistive. Conduction across the protective layer can be increased by using higher deposition temperatures with more stable TiO₂

Scheme 1. Charge Transfer Model in Working Conditions with (a) High-Resistance and (b) Low-Resistance TiO₂ Layers



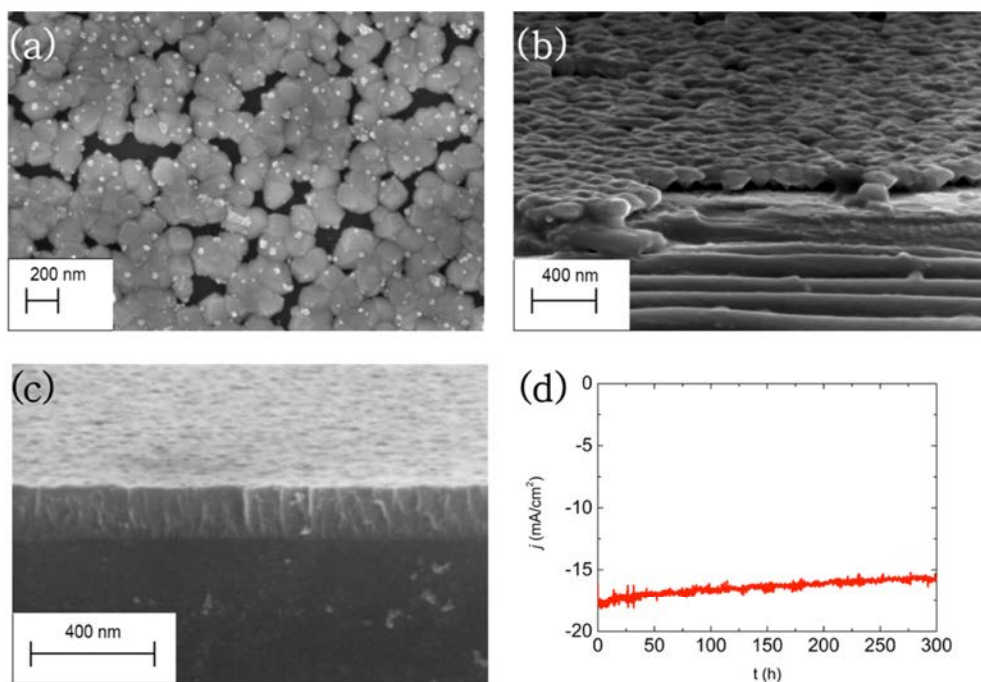


Figure 8. (a) Top and (b) cross-section SEM images of an almost-crystalline TiO_2 layer after a stability test, wherein dissolution of the amorphous region between crystals can be seen. (c) Cross-section of a fully crystallized layer after 300 h stability in 0.5 M H_2SO_4 , with no visible dissolution. (d) Current measurement of the fully crystalline TiO_2 sample for 300 h at 0.3 V_{RHE} under 1 Sun AM 1.5G illumination.

phases and by reducing defects and charge traps and obtaining higher FFs up to 0.73. The thin titanium layer used to protect silicon from oxidation has an important role also in enhancing the TiO_2 nucleation and crystallization, though reducing light transmission. The formation of a TiO_x layer contributes to the nucleation of the TiO_2 ALD layer, thus enhancing crystal density. The negative formation of a resistive SiO_x layer is avoided. In addition, fully crystallized TiO_2 is demonstrated to be mandatory for long-term stability, as seen in the 300 h continuous operation test.

Future studies should be addressed on achieving higher crystallization at lower temperatures, to implement ALD-grown TiO_2 as protective, conductive, and transparent layers for photoabsorbing materials sensitive to temperature processes.

■ ASSOCIATED CONTENT

Supporting Information

The Supporting Information is available free of charge on the ACS Publications website at DOI: 10.1021/acsami.7b02996.

SEM, HRTEM, XRD, and AFM supplementary images, together with a photo of a finished device, are supplied in an additional document (PDF)

■ AUTHOR INFORMATION

Corresponding Authors

*E-mail: cros@irec.cat (C.R.).

*E-mail: tandreu@irec.cat. Tel: (34) 933 562 615 (T.A.).

ORCID

Carles Ros: 0000-0002-9148-2767

Teresa Andreu: 0000-0002-2804-4545

Jordi Arbiol: 0000-0002-0695-1726

Author Contributions

The manuscript was written through contributions of all authors. All authors have given approval to the final version of the manuscript.

Notes

The authors declare no competing financial interest.

■ ACKNOWLEDGMENTS

This work was supported by Repsol, S.A. Authors from IREC thank Generalitat de Catalunya for financial support through the CERCA Program, M2E (2014SGR1638), and XaRMAE network. IREC also acknowledges additional support by the European Regional Development Funds (ERDF, FEDER) and by MINECO coordinated projects MAT2014-59961-C2 and ENE2016-80788-C5-5-R. C.R. thanks MINECO for his FPI grant (BES-2015-071618). ICN2 acknowledges support from the Severo Ochoa Program (MINECO, Grant SEV-2013-0295).

■ REFERENCES

- (1) Lewis, N. S.; Nocera, D. G. Powering the Planet: Chemical Challenges in Solar Energy Utilization. *Proc. Natl. Acad. Sci. U.S.A.* **2006**, *103*, 15729–15735.
- (2) Barber, J.; Tran, P. D. From Natural to Artificial Photosynthesis. *J. R. Soc., Interface* **2013**, *10*, No. 20120984.
- (3) James, B. D.; Baum, G. N.; Perez, J.; Baum, K. N. *Technoeconomic Analysis of Photoelectrochemical (PEC) Hydrogen Production*; Directed Technologies, Inc.: Arlington, VA, 2009; pp 1–128.

- (4) Fujishima, A.; Honda, K. Electrochemical Photolysis of Water at a Semiconductor Electrode. *Nature* **1972**, *238*, 37–38.
- (5) Fàbrega, C.; Monllor-Satoca, D.; Ampudia, S.; Parra, A.; Andreu, T.; Morante, J. R. Tuning the Fermi Level and the Kinetics of Surface States of TiO₂ Nanorods by Means of Ammonia Treatments. *J. Phys. Chem. C* **2013**, *117*, 20517–20524.
- (6) Fàbrega, C.; Murcia-López, S.; Monllor-Satoca, D.; Prades, J. D.; Hernández-Alonso, M. D.; Penelas, G.; Morante, J. R.; Andreu, T. Efficient WO₃ Photoanodes Fabricated by Pulsed Laser Deposition for Photoelectrochemical Water Splitting with High Faradaic Efficiency. *Appl. Catal., B* **2016**, *189*, 133–140.
- (7) Murcia-López, S.; Fàbrega, C.; Monllor-Satoca, D.; Hernández-Alonso, M. D.; Penelas-Pérez, G.; Morata, A.; Morante, J. R.; Andreu, T. Tailoring Multilayered BiVO₄ Photoanodes by Pulsed Laser Deposition for Water Splitting. *ACS Appl. Mater. Interfaces* **2016**, *8*, 4076–4085.
- (8) Yang, X.; Liu, R.; Du, C.; Dai, P.; Zheng, Z.; Wang, D. Improving Hematite-Based Photoelectrochemical Water Splitting with Ultrathin TiO₂ by Atomic Layer Deposition. *ACS Appl. Mater. Interfaces* **2014**, *6*, 12005–12011.
- (9) Abe, R.; Higashi, M.; Domen, K. Facile Fabrication of an Efficient Oxynitride TaON Photoanode for Overall Water Splitting into H₂ and O₂ under Visible Light Irradiation. *J. Am. Chem. Soc.* **2010**, *132*, 11828–11829.
- (10) Maeda, K.; Domen, K. Photocatalytic Water Splitting: Recent Progress and Future Challenges. *J. Phys. Chem. Lett.* **2010**, *1*, 2655–2661.
- (11) Ni, M.; Leung, M. K. H.; Leung, D. Y. C.; Sumathy, K. A Review and Recent Developments in Photocatalytic Water-Splitting Using TiO₂ for Hydrogen Production. *Renewable Sustainable Energy Rev.* **2007**, *11*, 401–425.
- (12) Pilli, S. K.; Furtak, T. E.; Brown, L. D.; Deutsch, T. G.; Turner, J. A.; Herring, A. M. Cobalt-Phosphate (Co-Pi) Catalyst Modified Mo-Doped BiVO₄ Photoelectrodes for Solar Water Oxidation. *Energy Environ. Sci.* **2011**, *4*, 5028–5034.
- (13) Sivula, K.; Formal, F. Le; Grätzel, M. WO₃–Fe₂O₃ Photoanodes for Water Splitting: A Host Scaffold, Guest Absorber Approach. *Chem. Mater.* **2009**, *21*, 2862–2867.
- (14) Wu, X. High-Efficiency Polycrystalline CdTe Thin-Film Solar Cells. *Sol. Energy* **2004**, *77*, 803–814.
- (15) Giraldo, S.; Neuschitzer, M.; Thersleff, T.; López-Marino, S.; Sánchez, Y.; Xie, H.; Colina, M.; Placidi, M.; Pistor, P.; Izquierdo-Roca, V.; Leifer, K.; Pérez-Rodríguez, A.; Saucedo, E. Large Efficiency Improvement in Cu₂ZnSnSe₄ Solar Cells by Introducing a Superficial Ge Nanolayer. *Adv. Energy Mater.* **2015**, *5*, No. 1501070.
- (16) Hu, S.; Xiang, C.; Haussener, S.; Berger, A. D.; Lewis, N. S. An Analysis of the Optimal Band Gaps of Light Absorbers in Integrated Tandem Photoelectrochemical Water-Splitting Systems. *Energy Environ. Sci.* **2013**, *6*, 2984–2993.
- (17) McKone, J. R.; Warren, E. L.; Bierman, M. J.; Boettcher, S. W.; Brunswig, B. S.; Lewis, N. S.; Gray, H. B. Evaluation of Pt, Ni, and Ni–Mo Electrocatalysts for Hydrogen Evolution on Crystalline Si Electrodes. *Energy Environ. Sci.* **2011**, *4*, 3573–3583.
- (18) Boettcher, S. W.; Warren, E. L.; Putnam, M. C.; Santori, E. A.; Turner-Evans, D.; Kelzenberg, M. D.; Walter, M. G.; McKone, J. R.; Brunswig, B. S.; Atwater, H. A.; Lewis, N. S. Photoelectrochemical Hydrogen Evolution Using Si Microwire Arrays. *J. Am. Chem. Soc.* **2011**, *133*, 1216–1219.
- (19) Seger, B.; Pedersen, T.; Laursen, A. B.; Vesborg, P. C. K.; Hansen, O.; Chorkendorff, I. Using TiO₂ as a Conductive Protective Layer for Photocathodic H₂ Evolution. *J. Am. Chem. Soc.* **2013**, *135*, 1057–1064.
- (20) Minggu, L. J.; Wan Daud, W. R.; Kassim, M. B. An Overview of Photocells and Photoreactors for Photoelectrochemical Water Splitting. *Int. J. Hydrogen Energy* **2010**, *35*, S233–S244.
- (21) McKone, J. R.; Lewis, N. S.; Gray, H. B. Will Solar-Driven Water-Splitting Devices See the Light of Day? *Chem. Mater.* **2014**, *26*, 407–414.
- (22) Bae, D.; Shayestehaminzadeh, S.; Thorsteinsson, E. B.; Pedersen, T.; Hansen, O.; Seger, B.; Vesborg, P. C. K.; Ólafsson, S.; Chorkendorff, I. Protection of Si Photocathode Using TiO₂ Deposited by High Power Impulse Magnetron Sputtering for H₂ Evolution in Alkaline Media. *Sol. Energy Mater. Sol. Cells* **2016**, *144*, 758–765.
- (23) Bhola, S. M.; Mishra, B. Effect of Ph on the Electrochemical Properties of Oxides Formed over β -Ti-15Mo and Mixed Ti-6Al-4v Alloys. *Int. J. Electrochem. Sci.* **2013**, *8*, 7075–7087.
- (24) Kast, M. G.; Enman, L. J.; Gurnon, N. J.; Nadarajah, A.; Boettcher, S. W. Solution-Deposited F:SnO₂/TiO₂ as a Base-Stable Protective Layer and Antireflective Coating for Microtextured Buried-Junction H₂-Evolving Si Photocathodes. *ACS Appl. Mater. Interfaces* **2014**, *6*, 22830–22837.
- (25) Seger, B.; Tilley, S. D.; Pedersen, T.; Vesborg, P. C. K.; Hansen, O.; Graetzel, M.; Chorkendorff, I. Silicon Protected with Atomic Layer Deposited TiO₂: Conducting versus Tunneling through TiO₂. *J. Mater. Chem. A* **2013**, *1*, 15089–15094.
- (26) Avasthi, S.; McClain, W. E.; Man, G.; Kahn, A.; Schwartz, J.; Sturm, J. C. Hole-Blocking Titanium-Oxide/silicon Heterojunction and Its Application to Photovoltaics. *Appl. Phys. Lett.* **2013**, *102*, No. 203901.
- (27) Chen, Y. W.; Prange, J. D.; Dühren, S.; Park, Y.; Gunji, M.; Chidsey, C. E. D.; McIntyre, P. C. Atomic Layer-Deposited Tunnel Oxide Stabilizes Silicon Photoanodes for Water Oxidation. *Nat. Mater.* **2011**, *10*, 539–544.
- (28) Hu, S.; Shaner, M. R.; Beardslee, J. A.; Lichterman, M.; Brunswig, B. S.; Lewis, N. S. Amorphous TiO₂ Coatings Stabilize Si, GaAs, and GaP Photoanodes for Efficient Water Oxidation. *Science* **2014**, *344*, 1005–1009.
- (29) Sivula, K. Defects Give New Life to an Old Material: Electronically Leaky Titania as a Photoanode Protection Layer. *ChemCatChem* **2014**, *2796*–2797.
- (30) McDowell, M. T.; Lichterman, M. F.; Carim, A. I.; Liu, R.; Hu, S.; Brunswig, B. S.; Lewis, N. S. The Influence of Structure and Processing on the Behavior of TiO₂ Protective Layers for Stabilization of N-Si/TiO₂/Ni Photoanodes for Water Oxidation. *ACS Appl. Mater. Interfaces* **2015**, *7*, 15189–15199.
- (31) Scheuermann, A. G.; Prange, J. D.; Gunji, M.; Chidsey, C. E. D.; McIntyre, P. C. Effects of Catalyst Material and Atomic Layer Deposited TiO₂ Oxide Thickness on the Water Oxidation Performance of Metal–insulator–silicon Anodes. *Energy Environ. Sci.* **2013**, *6*, 2487.
- (32) Mei, B.; Pedersen, T.; Malacrida, P.; Bae, D.; Frydendal, R.; Hansen, O.; Vesborg, P. C. K.; Seger, B.; Chorkendorff, I. Crystalline TiO₂: A Generic and Effective Electron-Conducting Protection Layer for Photoanodes and -Cathodes. *J. Phys. Chem. C* **2015**, *119*, 15019–15027.
- (33) Seger, B.; Tilley, D. S.; Pedersen, T.; Vesborg, P. C. K.; Hansen, O.; Grätzel, M.; Chorkendorff, I. Silicon Protected with Atomic Layer Deposited TiO₂: Durability Studies of Photocathodic H₂ Evolution. *RSC Adv.* **2013**, *3*, 25902–25907.
- (34) Paracchino, A.; Laporte, V.; Sivula, K.; Grätzel, M.; Thimsen, E. Highly Active Oxide Photocathode for Photoelectrochemical Water Reduction. *Nat. Mater.* **2011**, *10*, 456–461.
- (35) Wang, T.; Luo, Z.; Li, C.; Gong, J. Controllable Fabrication of Nanostructured Materials for Photoelectrochemical Water Splitting via Atomic Layer Deposition. *Chem. Soc. Rev.* **2014**, *43*, 7469–7484.
- (36) Ros, C.; Andreu, T.; Giraldo, S.; Sánchez, Y.; Morante, J. R. Conformal Chalcopyrite Based Photocathode for Solar Refinery Applications. *Sol. Energy Mater. Sol. Cells* **2016**, *158*, 184–188.
- (37) Miikkulainen, V.; Leskelä, M.; Ritala, M.; Puurunen, R. L. Crystallinity of Inorganic Films Grown by Atomic Layer Deposition: Overview and General Trends. *J. Appl. Phys.* **2013**, *113*, No. 021301.
- (38) Aarik, J.; Aidla, A.; Uustare, T.; Sammelselg, V. Morphology and Structure of TiO₂ Thin Films Grown by Atomic Layer Deposition. *J. Cryst. Growth* **1995**, *148*, 268–275.
- (39) Li, W.; Ni, C.; Lin, H.; Huang, C. P.; Shah, S. I. Size Dependence of Thermal Stability of TiO₂ Nanoparticles. *J. Appl. Phys.* **2004**, *96*, 6663.

- (40) Polman, A.; Knight, M.; Garnett, E. C.; Ehler, B.; Sinke, W. C. Photovoltaic Materials – Present Efficiencies and Future Challenges. *Science* **2016**, *352*, No. aad4424.
- (41) Scheuermann, A. G.; Lawrence, J. P.; Kemp, K. W.; Ito, T.; Walsh, A.; Chidsey, C. E. D.; Hurley, P. K.; McIntyre, P. C. Design Principles for Maximizing Photovoltage in Metal-Oxide-Protected Water-Splitting Photoanodes. *Nat. Mater.* **2016**, *15*, 99–105.
- (42) Das, C.; Kot, M.; Henkel, K.; Schmeisser, D. Engineering of Sub-Nanometer SiO_x Thickness in Si Photocathodes for Optimized Open Circuit Potential. *ChemSusChem* **2016**, *9*, 2332–2336.
- (43) Reiners, M.; Xu, K.; Aslam, N.; Devi, A.; Waser, R.; Hoffmann-Eifert, S. Growth and Crystallization of TiO₂ Thin Films by Atomic Layer Deposition Using a Novel Amido Guanidinate Titanium Source and Tetrakis-Dimethylamido-Titanium. *Chem. Mater.* **2013**, *25*, 2934–2943.
- (44) Aarik, J.; Kasikov, A.; Niilisk, A. Spectrophotometric and Raman Spectroscopic Characterization of ALD Grown TiO₂ Thin Films. *Proc. SPIE* **2007**, *6596*, 6596161–6596166.
- (45) Puurunen, R. L.; Sajavaara, T.; Santala, E.; Miikkulainen, V.; Saukkonen, T.; Laitinen, M.; Leskelä, M. Controlling the Crystallinity and Roughness of Atomic Layer Deposited Titanium Dioxide Films. *J. Nanosci. Nanotechnol.* **2011**, *11*, 8101–8107.
- (46) Yang, X.; Liu, R.; Lei, Y.; Li, P.; Wang, K.; Zheng, Z.; Wang, D. Dual Influence of Reduction Annealing on Diffused Hematite/FTO Junction for Enhanced Photoelectrochemical Water Oxidation. *ACS Appl. Mater. Interfaces* **2016**, *8*, 16476–16485.
- (47) Tang, Z.; Fang, L.; Xu, N.; Liu, R. Forming Compliance Dominated Memristive Switching through Interfacial Reaction in Ti/TiO₂/Au Structure. *J. Appl. Phys.* **2015**, *118*, No. 185309.
- (48) Salaoru, I.; Khat, A.; Li, Q.; Berdan, R.; Prodromakis, T. Pulse-Induced Resistive and Capacitive Switching in TiO₂ Thin Film Devices. *Appl. Phys. Lett.* **2013**, *103*, No. 233513.
- (49) Jeong, D. S.; Schroeder, H.; Waser, R. Impedance Spectroscopy of TiO₂ Thin Films Showing Resistive Switching. *Appl. Phys. Lett.* **2006**, *89*, No. 082909.
- (50) Choi, B. J.; Jeong, D. S.; Kim, S. K.; Rohde, C.; Choi, S.; Oh, J. H.; Kim, H. J.; Hwang, C. S.; Szot, K.; Waser, R.; Reichenberg, B.; Tiedke, S. Resistive Switching Mechanism of TiO₂ Thin Films Grown by Atomic-Layer Deposition. *J. Appl. Phys.* **2005**, *98*, No. 033715.
- (51) Bousoulas, P.; Michelakaki, I.; Tsoukalas, D. Influence of Ti Top Electrode Thickness on the Resistive Switching Properties of Forming Free and Self-Rectified TiO₂ - X Thin Films. *Thin Solid Films* **2014**, *571*, 23–31.
- (52) Chiu, F. A Review on Conduction Mechanisms in Dielectric Films. *Adv. Mater. Sci. Eng.* **2014**, *2014*, 1–18.
- (53) Sheng, W.; Gasteiger, H. A.; Shao-Horn, Y. Hydrogen Oxidation and Evolution Reaction Kinetics on Platinum: Acid vs Alkaline Electrolytes. *J. Electrochem. Soc.* **2010**, *157*, B1529.

SUPPORTING INFORMATION

Charge transfer characterization of ALD-grown TiO₂ protective layers in silicon photocathodes

Carles Ros^{a,}, Teresa Andreu^{a,b,*}, María Dolores Hernández-Alonso^c, Germán Penelas-Pérez^c, Jordi Arbiol^{d,e}, Joan R. Morante^{a,b}*

^aCatalonia Institute for Energy Research (IREC). Jardins de les Dones de Negre 1, 08930 Sant Adrià del Besòs, Barcelona, Spain

^bUniversitat de Barcelona (UB), Martí i Franquès, 1, 08028 Barcelona, Spain

^cRepsol Technology Center, Agustín de Betancourt, s/n, 28935 Móstoles, Madrid, Spain.

^dCatalan Institute of Nanoscience and Nanotechnology (ICN2), CSIC and The Barcelona Institute of Science and Technology (BIST), Campus UAB, Bellaterra, 08193 Barcelona, Spain

^eICREA, Pg. Lluís Companys 23, 08010 Barcelona, Spain

AUTHOR INFORMATION

Corresponding Author

*Corresponding authors:

E-mail: cros@irec.cat

E-mail: tandreu@irec.cat

Tel: (34) 933 562 615

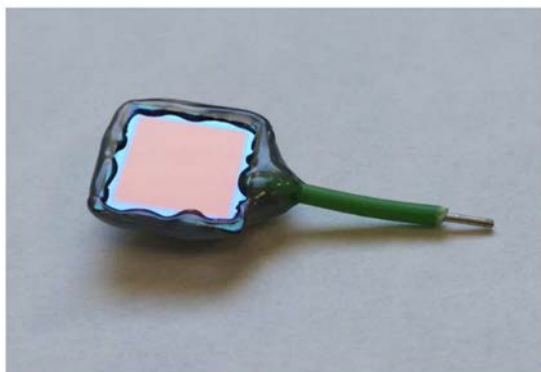


Figure S.1: picture of a $\text{Ti}/n^+\text{p-Si}$ sample with 3700 ALD cycles grown at 300 °C, soldered and epoxy protected.

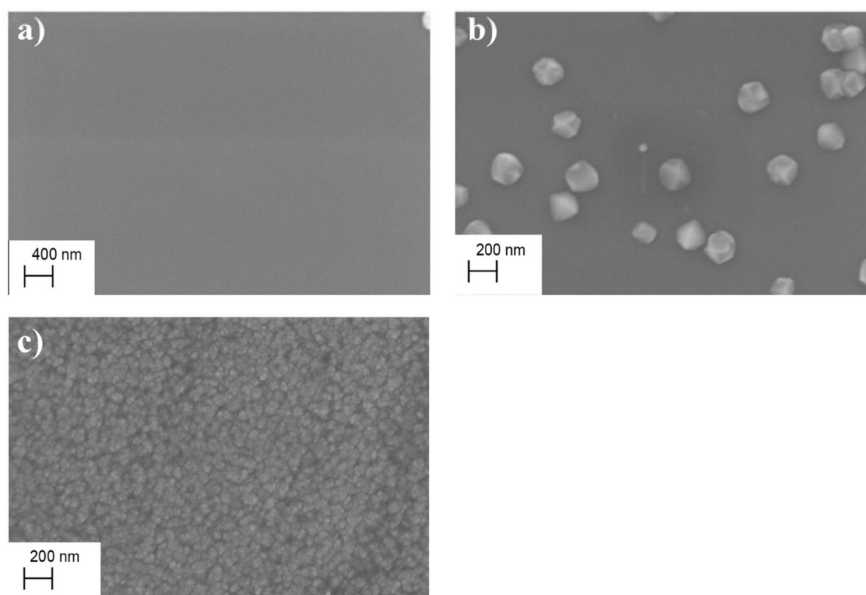


Figure S.2: SEM images of TiO_2 layers grown by 3700 ALD cycles of TiCl_4 and H_2O on $n^+\text{Si}$ substrates at a) 100 °C, b) 200 °C and c) 300 °C. Comparing with the substrates with 5 nm Ti, we can see crystallization is retarded in temperature when the Ti layer is missing.

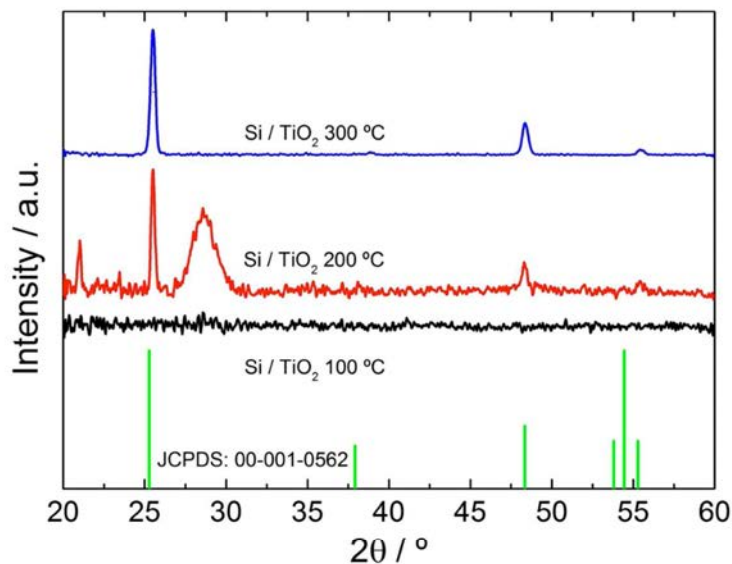


Figure S.3: XRD patterns of TiO₂ layers grown on n⁺Si substrates at 100 °C, 200 °C and 300 °C.

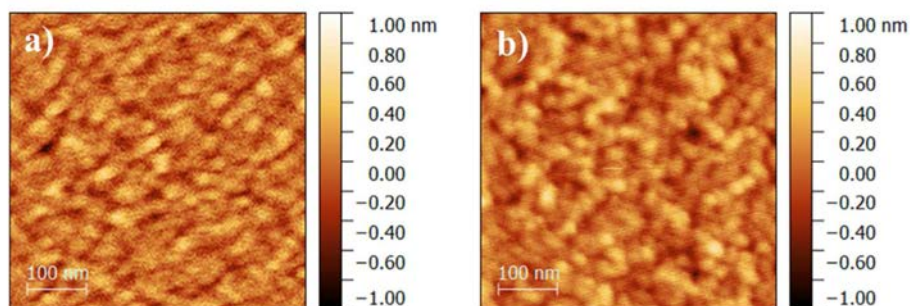


Figure S.4: topography AFM images of the n⁺-Si substrates a) without and b) with 5 nm Ti. We can confirm that the rugosity is the same on both substrates prior to ALD deposition.

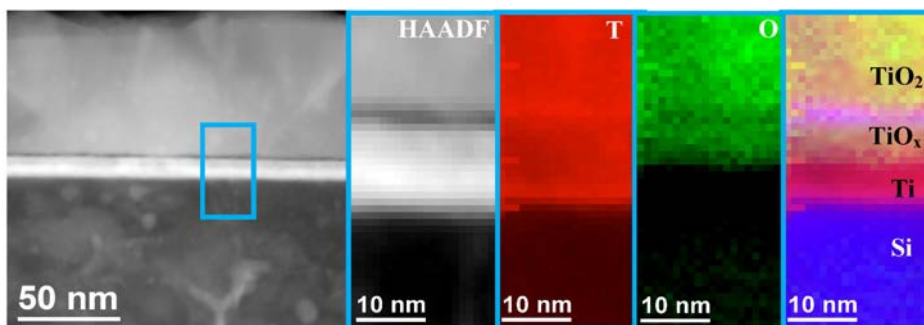


Figure S.5: STEM-EELS image of a Ti/n⁺p-Si substrate with 3700 ALD cycles of TiO₂ grown at 200 °C showing the ALD grown layer, the carbon rich layer on top of the amorphous native TiO₂ layer, the un-oxidized Ti and the Silicon n⁺p photoabsorber.

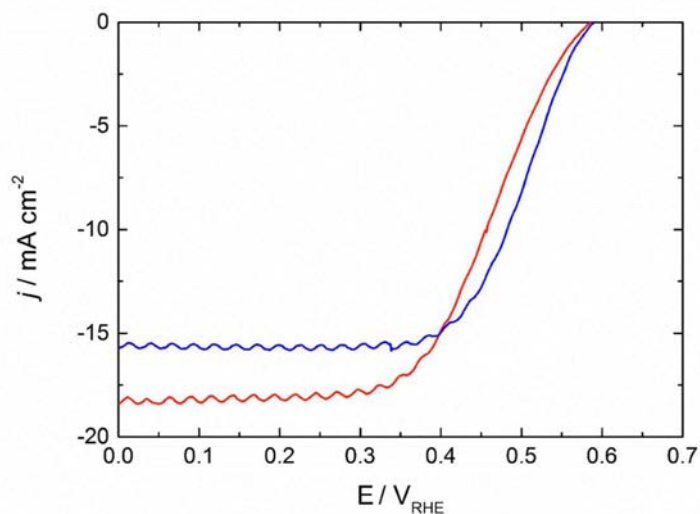


Figure S.6: polarization curves of a fully crystalline sample before (red) and after (blue) 300 h continuous operation at 0.3 V vs RHE. Measurements under 1 sun AM 1.5G illumination in 0.5 M H₂SO₄ with Ag/AgCl as reference and Pt as counter electrode in 3 electrodes configuration. Waves seen in the saturation region of the polarization curves were caused by the lamp used for stability measurements.

Chapter 4

*Adapting protective layers for thin
film chalcogenide photoabsorbers*

In chapter 3, the titanium dioxide protective films were optimized and characterized using silicon as photoabsorber for photocathodic hydrogen evolution. As was mentioned, silicon could be used as a reference semiconductor thanks to its stability, but other emerging photovoltaic semiconductors¹ have shown promising results and present interesting features.

Chalcogenide based photoabsorbers are part of thin film photovoltaic semiconductors, with thicknesses ranging few micrometers thanks to high absorption coefficient and thus, have the possibility to be deposited on glass or on flexible substrates such as steel, aluminum or a polymer, permitting roll-to-roll fabrication². Thin films permit few material consumption and less fabrication costs, pushing for cheaper devices compared to other photovoltaics while achieving high efficiencies³. Moreover, chalcogenide photoabsorbers electronic structure is defined by a complex structure of Cu vacancies acting as electron acceptors and In, Ga, Se substitutions and defects and, by adapting the elemental ratio, its band gap (and thus, photovoltage/saturating photocurrent) can be significantly modified⁴.

Among them, CIGS and CZTS have 1.0 to 1.8 eV variable band gaps varying In/Ga or S/Se ratio respectively. CIGS have already been commercialized and have presented about 20% conversion efficiencies³, while CZTS over 10% with only abundant and non-toxic elements (indium and gallium are replaced by zinc and tin)⁵. The p-n junction is formed normally with n-type CdS or InS ~50 nm layers and ZnO transparent conductive top contact. However, TCO layers are not protective enough against corrosion in acid or alkaline media due to Zn^{2+} and Sn^{2+} forming soluble species⁶ and thus, require further protective layers.

Although, due to the mentioned primordial role of structural imperfections in defining the electronic structure, thermal treatments during late fabrication steps like protective film deposition will significantly influence the photovoltaic efficiency⁷. Thus, optimal coupling of both technologies is of primordial concern. TiO_2 was demonstrated highly stable and conductive for cathodic applications in previous chapter, requiring a crystalline film. For it, ALD is one of the best candidates: thanks to its slow deposition and intermediate species mobility, the necessary TiO_2 crystalline structure can be obtained at lower temperatures than other deposition techniques, often requiring ~400 °C^{8,9}.

4.1. Conformal chalcopyrite based photocathode for solar refinery applications

In the first article of this chapter, chalcopyrite CIGSe/CdS p-n heterojunctions on stainless steel (SS) foil were studied as flexible photocathodes. Due to the known instability of TCO films in acidic conditions, TiO_2 protective layers were applied to analyze the possibility of substituting the TCO. Platinum was used as HER catalyst. Both i-ZnO and AZO layers are found to enhance protected photocathodes efficiency by helping in p-n junction charge separation and film conductivity (Figure 4.1).

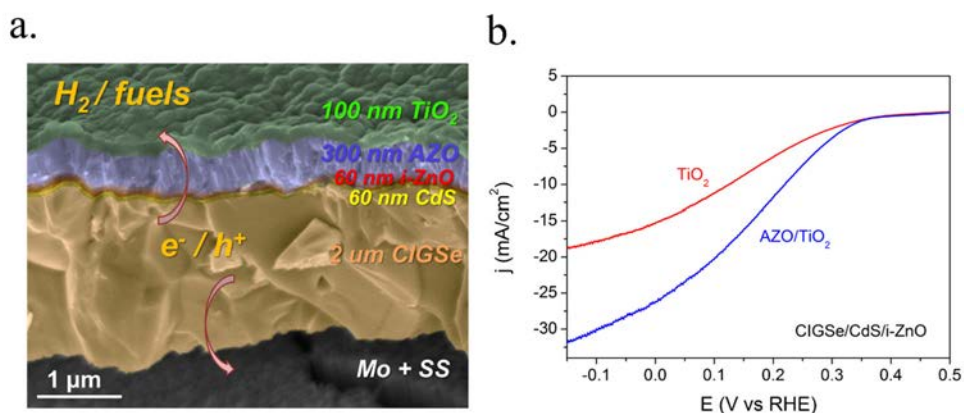


Figure 4.1. a) Cross section SEM image of a CIGS photocathode, with all intermediate layers and thicknesses identified. b) Cyclic voltammogram of CIGSe/CdS/i-ZnO photocathodes with and without an AZO intermediate layer and protected with 100 nm TiO₂ and Pt as catalyst, measured in 0.5 M H₂SO₄ and 1 sun illumination.

10, 50 and 100 nm TiO₂ protective overlayers were deposited. ALD was maintained at 200 °C to prevent damaging the heterojunction. Resistive effect of a 10 nm thin layer is less relevant than 50 nm ones, probably due to tunneling effect and thinner film. Increasing the thickness creates more conductive layer (Figure 4.2a), as more deposition time allows crystals to laterally propagate¹⁰. Cross section SEM shows grainy 100 nm TiO₂ films, with nucleation enhancement expected due to high substrate rugosity.

SS/CIGSe/CdS/i-ZnO/AZO/TiO₂/Pt lab-grown and commercial-based CIGSe cells were protected and adapted into relatively stable photocathodes with up to 40 mA·cm⁻² at 0 V vs RHE photocurrents and over 400 mV photovoltages, meaning up to 6.6% HC-STH conversion efficiencies. Although, post-stability characterization revealed significant cracks in the protective layers, apparently caused by tension on flexing. These cracks do not affect significantly an encapsulated solar cell, but are deadly in a corrosive electrolyte environment, dissolving the cell below the TiO₂ protective layer (Figure 4.2b).

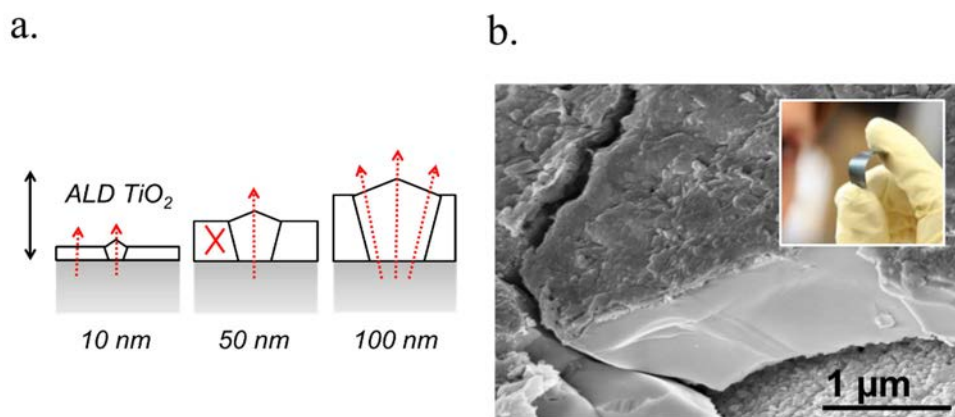


Figure 4.2. a) Scheme describing the possible conduction paths of a 10 nm TiO_2 layer presenting tunneling, a 50 nm one with limited crystal coverage and a 100 nm one, where deposition time gave crystals time to develop and cover significant part of the layer. b) Cross section SEM image of a photocathode after 1h stability, presenting significant cracks and detached film. Inset shows a flexed device.

4.2. Turning earth abundant kesterite-based solar cells into efficient protected water-splitting photocathodes

In this article, the compatibility of ALD- TiO_2 layers to protect earth-abundant copper–zinc–tin–chalcogenide (CZTS/Se) kesterite-based devices is studied, as alternative to CIGS that uses indium, limited in availability. Different stoichiometry CZTSe, CZTSSe and CZTS photoabsorbers, with 1.0, 1.15 and 1.5 eV band gaps are fabricated by modifying the chalcogenide S/Se ratio. Following previous article, CdS/i-ZnO/ITO/100 nm TiO_2 /Pt overlayers were deposited for efficient photovoltaic behavior and charge transfer to the electrolyte (Figure 4.3a).

Chalcogenide kesterites as photoabsorbers show high performance thanks to highly complex structure based on specific phases, lattice parameters, elemental substitution and diffusion and defects distribution, sensible to few hundred Celsius⁷. Temperature-caused alterations on kesterite electronic structure were studied by varying TiO_2 deposition temperature from 200 to 300 °C. As can be observed in Figure 4.3b, 200 °C is the maximum before significantly affecting the CIGSe/CdS junction performance, and over one hour stability was obtained thanks to the TiO_2 protective film. ALD was proven as one of the few techniques capable of protecting kesterite chalcogenides thanks to the low crystallization temperature.

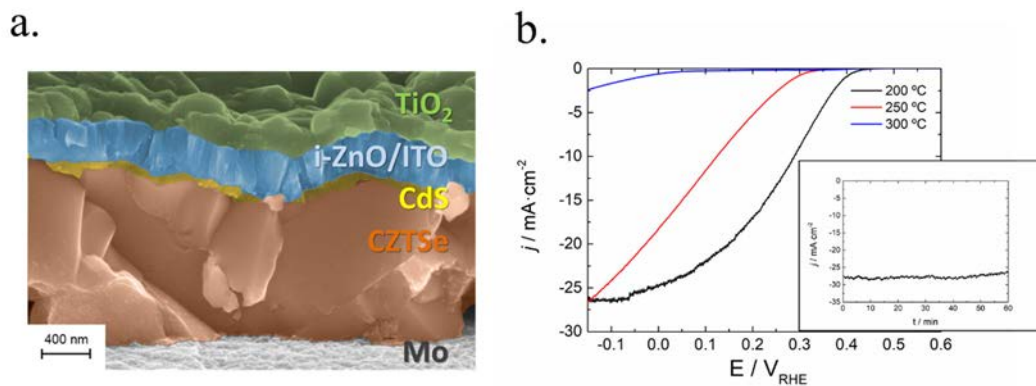


Figure 4.3. a) Colored cross sectional SEM image of a CZTSe-based photocathode. b) Cyclic voltammograms of three CZTSe-based photocathodes protected with TiO_2 deposited at different temperatures, from 200 to 300 °C, presenting p-n junction degradation if higher than 200 °C is used. Inset: Stability measurement presenting over 1 hour performance with minimal degradation. Three electrodes measurements in 0.5 M H_2SO_4 and 1 sun illumination.

The second part of this article was focused on a comparative study thanks to the possibility to measure operational kesterite-based solar cells before and after protecting them to be implemented as photocathodes (Figure 4.4a). Thus, cell and introduced TiO_2 film series resistance, HER Pt catalytic kinetics and solar cell performance alterations (photovoltage or photocurrent variations) could be identified and quantified. The series-circuit model proposed allows for further extrapolations of other photoabsorbers, protective layer materials or HER catalysts combinations in the pursuit of best coupling tandem photoelectrodes (Figure 4.4b).

With this work, we demonstrate the possibility to fabricate band gap tunable photoelectrodes resembling efficient solar cells performance with minimized losses thanks to ALD with over 450 mV photovoltages, $37 \text{ mA} \cdot \text{cm}^{-2}$ and conversion efficiencies up to 7%. Although, pure-sulfide kesterites (CZTS) were more severely affected by the thermal process as was structurally analyzed by Raman, losing its characteristic high photovoltage.

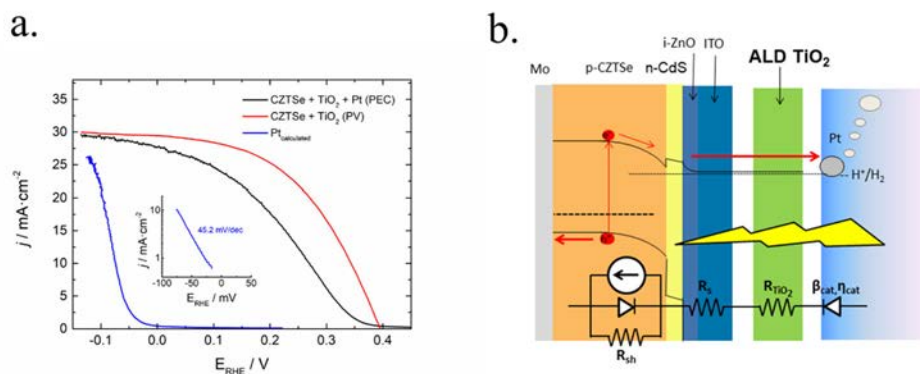


Figure 4.4. a) Cyclic voltammogram PEC measurement of a TiO_2 -protected and Pt catalyzed photocathode (black), photovoltaic I-V curve of a TiO_2 -deposited solar cell (red) and the

calculated HER behavior of the Pt catalyst by subtracting the black curve to the red one (in blue).
b) Scheme of the full photocathode electric series circuit presenting all the calculated electrical elements.

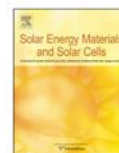
Bibliography

- (1) Polman, A.; Knight, M.; Garnett, E. C.; Ehrler, B.; Sinke, W. C.; Summary, R.; Polman, A.; Knight, M.; Garnett, E. C.; Ehrler, B.; et al. Photovoltaic Materials – Present Efficiencies and Future Challenges. *Science* (80-.). **2016**, 352 (6283), 307.
- (2) Izquierdo-Roca, V.; Caballero, R.; Fontané, X.; Kaufmann, C. A.; Álvarez-García, J.; Calvo-Barrio, L.; Saucedo, E.; Pérez-Rodríguez, A.; Morante, J. R.; Schock, H. W. Raman Scattering Analysis of Cu-Poor Cu(In,Ga)Se₂ Cells Fabricated on Polyimide Substrates: Effect of Na Content on Microstructure and Phase Structure. *Thin Solid Films* **2011**, 519 (21), 7300–7303.
- (3) Repins, I.; Contreras, M. A.; Egaas, B.; DeHart, C.; Scharf, J.; Perkins, C. L.; To, B.; Noufi, R. 19.9%-Efficient ZnO/CdS/CuInGaSe₂ Solar Cell with 81.2% Fill Factor. *Prog. Photovoltaics Res. Appl.* **2008**, 16 (3), 235–239.
- (4) Dimitrievska, M.; Fairbrother, A.; Saucedo, E.; Pérez-Rodríguez, A.; Izquierdo-Roca, V. Secondary Phase and Cu Substitutional Defect Dynamics in Kesterite Solar Cells: Impact on Optoelectronic Properties. *Sol. Energy Mater. Sol. Cells* **2016**, 149, 304–309.
- (5) Wang, W.; Winkler, M. T.; Gunawan, O.; Gokmen, T.; Todorov, T. K.; Zhu, Y.; Mitzi, D. B. Device Characteristics of CZTSSe Thin-Film Solar Cells with 12.6% Efficiency. *Adv. Energy Mater.* **2014**, 4 (7), 1–5.
- (6) Awan, I. Z.; Khan, A. Q.; Awan, I. Z.; Khan, A. Q.; Nationale, E.; Chimie, S. De. Corrosion – Occurrence & Prevention. **2018**, 40 (04), 602–655.
- (7) Neuschitzer, M.; Sanchez, Y.; Olar, T.; Thersleff, T.; Lopez-Marino, S.; Oliva, F.; Espindola-Rodriguez, M.; Xie, H.; Placidi, M.; Izquierdo-Roca, V.; et al. Complex Surface Chemistry of Kesterites: Cu/Zn Reordering after Low Temperature Postdeposition Annealing and Its Role in High Performance Devices. *Chem. Mater.* **2015**, 27 (15), 5279–5287.
- (8) Mei, B.; Pedersen, T.; Malacrida, P.; Bae, D.; Frydendal, R.; Hansen, O.; Vesborg, P. C. K.; Seger, B.; Chorkendorff, I. Crystalline TiO₂: A Generic and Effective Electron-Conducting Protection Layer for Photoanodes and -Cathodes. *J. Phys. Chem. C* **2015**, 119 (27), 15019–15027.
- (9) Malizia, M.; Seger, B.; Chorkendorff, I.; Vesborg, P. C. K. Formation of a P-n Heterojunction on GaP Photocathodes for H₂ Production Providing an Open-Circuit Voltage of 710 mV. *J. Mater. Chem. A* **2014**, 2 (19), 6847–6853.
- (10) Miikkulainen, V.; Leskelä, M.; Ritala, M.; Puurunen, R. L.; Leskelä, M.; Ritala, M.; Puurunen, R. L. Crystallinity of Inorganic Films Grown by Atomic Layer Deposition: Overview and General Trends. *J. Appl. Phys.* **2013**, 113 (2), 021301.



Contents lists available at ScienceDirect

Solar Energy Materials & Solar Cells

journal homepage: www.elsevier.com/locate/solmat

Conformal chalcopyrite based photocathode for solar refinery applications



Carles Ros^a, Teresa Andreu^{a,*}, Sergio Giraldo^a, Yudania Sánchez^a,
Joan Ramon Morante^{a,b,*}

^a Catalonia Institute for Energy Research, IREC, Jardins de les Dones de Negre 1, 08930 Sant Adrià de Besòs, Barcelona, Spain

^b Departament d'Electrònica, Universitat de Barcelona, Martí i Franquès, 1, 08028 Barcelona, Spain

ARTICLE INFO

Article history:

Received 6 September 2015

Received in revised form

17 January 2016

Accepted 27 January 2016

Available online 10 February 2016

Keywords:

PEC cells

CIGSe

Protecting overlayers

Water splitting

Solar hydrogen production

Stainless steel

ABSTRACT

Photoelectrochemical properties of conformal photocathodes based on chalcopyrite built-in on flexible stainless steel foils are shown to give current density level higher than 30 mA cm^{-2} (0 V_{RHE}). These conformal photocathodes can become elements for developing new concepts for PEC cells to obtain solar fuels. The influence on the PEC characteristics of the protective anticorrosion layer based on TiO_2 film deposited by atomic layer deposition technique at very low temperature, 200°C , and using TiCl_4 precursor are analyzed and discussed particularly taking into account the charge transport mechanisms through this layer. Likewise, buffer layer between the used n-type layer and the protective one such as i-ZnO and AZO layers have also been considered to facilitate high efficient photocathode design adaptable for new solar refinery applications for water splitting or CO_2 photoreduction. Improved photocurrent values are obtained with TiO_2 protective values of 100 nm.

© 2016 Elsevier B.V. All rights reserved.

1. Introduction

The identification of stable and inexpensive p-type photocathode materials constitutes a key issue for developing photoelectrochemical (PEC) cells available for implementing new concepts of solar refinery producing hydrogen from water splitting as well as other fuels or chemicals from carbon dioxide reduction. Aside reliable and enduring materials and/or photocathode structures, the development of reliable PEC cells and modules is open to new concepts beyond the usual planar structures commonly reported up to now in the literature. Furthermore, aside these aspects, for commercially viable PEC devices, the overall solar-to-chemical conversion efficiencies are not the only essential parameter. Indeed, other crucial features such as the stability of the device, the use of inexpensive available materials or the manufacturing process employing easily scalable, reproducible, and economical techniques become essential too.

In this panorama, despite silicon band gap, 1.1 eV, does not fit adequately with the theoretical band gap for having maximum absorption from the solar spectra [1], P-type silicon has been extensively investigated as a candidate material [2,3]. Likewise, tunable band gap systems, like III–V semiconductors such as GaInP_2 or, alternatively some metal oxides such as Cu_2O can also be optimized to act as reliable photocathode [4,5]. Nevertheless, any of these proposed materials gather all the requirements for fulfilling conditions –efficiency, low cost, flexible layers,...– for developing adequate conformal enduring electrode structures.

Unlike the previous shown materials, chalcopyrite-type thin film materials, exemplified by CuInS_2 , $\text{CuIn}_x\text{Ga}_{1-x}\text{S}_2$ (CIGS) or $\text{CuIn}_x\text{Ga}_{1-x}\text{Se}_2$ (CIGSe), are Cu-based materials that offer band gap energies around 1.5 eV and thus higher potential solar conversion efficiency. CIGSe has recently shown promising activity as a PEC photocathode [6] as well as the kesterites CZTS [7] which is composed of only inexpensive and readily available elements, since indium and gallium are replaced by zinc and tin which makes it very attractive in view of large scale applications for replacing CIGS or CIGSe. This alternative is structurally similar to CIGS or CIGSe and has also a direct band gap of ca. 1.5 eV although, nowadays, its solar efficiency is still limited below 16% [8,9]. As thin film layers, they can be grown on different substrates such as glass, FTO or flexible metallic foils to define conformal cathode structures. In fact, these photocathodes based on p-type

* Corresponding author. Tel.: +34 933562615; fax: +34 933563802.

** Corresponding author at: Catalonia Institute for Energy Research, IREC, Jardins de les Dones de Negre 1, 08930 Sant Adrià de Besòs, Barcelona, Spain. Tel.: +34 933562615; fax: +34 933563802.

E-mail addresses: tandreu@irec.cat (T. Andreu), jrmorante@irec.cat (J.R. Morante).

<http://dx.doi.org/10.1016/j.solmat.2016.01.031>

0927-0248/© 2016 Elsevier B.V. All rights reserved.

chalcopyrite layers prepared by inexpensive and scalable techniques need also the presence of n-type buffer layers to promote charge separation through the resulting p–n heterojunction. Typically very narrow CdS layers and the less commonly used ZnS or In_2S_3 are used as n-type overlayers. These layers can, in turn, be completed with some protective and conductive layers usually based on zinc oxide with different doping level, aluminum is often used, for facilitating the electron extraction and hence improving the PEC photocurrent for inducing reduction at the cathode surface. However, these layers are not protective enough against corrosion in acid media. Consequently, in all cases, these chalcopyrite based cathode structures require a complementary anticorrosive overlayer that must also be compatible with the flexibility imposed by the metallic foil substrate.

Herein, we report a study on chalcopyrite based photocathodes prepared by inexpensive and scalable techniques on flexible substrate for having conformal cathode structures for future PEC cell design in solar refinery applications. We investigate the role of the different layers used to complete the heterojunction and we further demonstrate the ability to improve and stabilize the photocurrent delivered by chalcopyrite electrodes by protecting their surface using atomic layer TiO_2 deposition overlayers at low temperature for preventing any temperature effect on the previous deposited layers and maintaining the mechanical robustness required for the use of flexible metallic foil.

According to the efforts performed in the photovoltaic field to fabricate chalcopyrite absorbers different technological approaches can be used being electrodeposition and sputtering procedures ones of the best performing considering cost and efficiency. Likewise, different chalcopyrite compositions can be used modifying their semiconductor properties. Among them, CIGS, CIGSe and CZTS kesterites based on abundant elements are the most highlighted. Due to their high absorption coefficients, tunable band gap values (1.0–2.4 eV) by changing In/Ga and/or Se/S ratios, and suitable band alignment for water reduction, these materials are also attractive to be used as photocathodes for H_2 production from water.

In this contribution, focused in optimizing the functionality of TiO_2 layer deposited by atomic layer deposition (ALD) as protective layer for chalcopyrite, we have centered our efforts on CIGSe layer deposited by sputtering as p-type absorbing layer. As ohmic electrical contact we have used molybdenum according the standard route used for the photovoltaic thin film industry. So, for having a flexible structure, these layers were implemented on a molybdenum coated stainless steel foil cover with a chromium buffer layer [10].

To complete the photocathode structure, a PN junction is formed depositing a thin n-type CdS layer following the same criteria than those justifying to design the chalcogenide based photovoltaic device, facilitating the electron hole pair separation induced by the electric field of the space charge zone. This approach involves an appreciable improvement of photocurrent as well as onset potential compared to those of unmodified films.

However, unlike the photovoltaic device, the photoelectrochemical functionality requires to be coated by an anticorrosion protective layer that, at the same time, guarantees the highest values of minority carrier transference from the absorber chalcopyrite layer to the electrolyte.

In this context, TiO_2 is recognized as an adequate material as protective layer due to their characteristics in acid and basic electrolyte and also presents an adequate alignment of its conduction band with the CIGSe/CdS structure [7,11]. Nevertheless, it is well known that at room temperature, considering the wide band gap of the TiO_2 (> 3 eV), the charge transport mechanisms of this material corresponds rather to a nearly insulator dielectric in which the electrical conductivity is very low, that can induce

electrical performance losses modifying the expected photoelectrochemical properties. It should be observed that the conduction current of these layers, at normal applied electric field, could be very small because conductivities could inherently be low depending on the defect densities (i.e. oxygen vacancies). Assuming TiO_2 film thicknesses between 10 and 100 nm, electrical fields around 10^5 – 10^6 V/cm can be estimated through the film, being enough to have noticeable conduction current through the film. So, the conduction mechanisms through these layers could be electrode-limited or bulk-limited. The former mechanism depends on the electrical properties at the electrode-dielectric interface whereas the bulk-limited conduction mechanism depends on the electrical properties of the dielectric itself. Bulk-limited conduction is directly related to the trap level, trap spacing, trap density, carrier drift mobility, dielectric relaxation time, and the density of states in the conduction band. These parameters concern to the film thicknesses as well as to the deposition conditions.

On the other hand, substrate flexibility and mechanical robustness, number of layers and thickness could also be a parameter to take into account.

Therefore, several relevant questions concerning TiO_2 thickness itself, or the need to maintain the ZnO buffer layer and AZO top contact to increase charge transfer efficiency arise in order to define the best flexible Cu-chalcopyrite based photocathode configuration.

2. Experimental

Photoelectrodes were fabricated onto flexible stainless steel (SS). Consequently, samples with/without i-ZnO and AZO (Al:ZnO) layers, and with TiO_2 layer thicknesses of 10 nm, 50 nm and 100 nm were prepared in order to evaluate the effect of these layers on the final PEC performances. Thicknesses and characteristics of the CdS and ZnO layers have been chosen from the background of photovoltaic routes.

- a) Chalcopyrite layer deposition on flexible substrate: CIGSe absorbers were prepared onto 0.3 mm thick stainless steel foil substrates (coated with Cr and Mo) via sequential DC magnetron sputtering deposition (AC450 Alliance Concepts) using Cu, Cu–Ga (50–50%) and In targets (99.99% purity all of them). Reactive annealing under Se atmospheres of the sputtered metallic stacks was used to produce the absorbers. The final compositions were: $\text{Cu}/(\text{In} + \text{Ga}) = 0.90$ and $\text{In}/(\text{In} + \text{Ga}) = 0.28$, and was kept constant in this study. After the thermal annealing, the CIGS absorbers were etched by the classical KCN route (aqueous solution 10% m/v, 25 °C, 120 s), in order to remove possible unwanted Cu_3Se secondary phases at the surface [12].
- b) CdS deposition: CdS was deposited 60 nm thick by Chemical Bath Deposition (CBD) from CdSO_4 and thiourea precursors aqueous solutions, at 75 °C and pH=11, using the methodology reported elsewhere [13].
- c) AZO and ZnO deposition: immediately after CdS growth, the solar cells were completed by DC-pulsed sputtering deposition of i-ZnO (60 nm) and AZO (Al:ZnO, 300 nm) as transparent conductive window layer (Alliance CT100).
- d) Protective TiO_2 overlayer deposition by ALD: samples were simultaneously introduced in a R200 Picosun Atomic Layer Deposition system at 200 °C using TiCl_4 and H_2O precursors at 19 °C in successive pulses in a 8 mbar N_2 flow atmosphere, reaching a growth rate of 0.27 Å/cycle. Some samples were grown simultaneously on silicon substrates to complete characterization of TiO_2 overlayer. Layer thickness was measured by evaluating the reflected spectra with a Sensofar

interferometer device with ± 0.2 nm error and verified by cross section in a Zeiss Series Auriga Field Effect Scanning Electron Microscope (FESEM). Structural characterization was carried out by X-ray diffraction (XRD) in a D8 Advance Bruker equipment with a Cu K α radiation source working at 40 kV and 40 mA with a 3° offset angle.

Photoelectrochemical (PEC) measurements were obtained with a Princeton Applied Research PARSTAT 2273 potentiostat in a three-electrode configuration, using Ag/AgCl/KCl (3 M) ($E^\circ = 0.203$ V_{RHE}) as reference electrode and platinum mesh as a counter electrode. Linear sweep voltammograms were acquired at a scanning rate of 30 mV s⁻¹. A quartz cell with flat faces was used with 100 ml of 0.5 M H₂SO₄ as electrolyte and a 300 W Xenon Lamp to provide simulated AM 1.5G solar light (1 sun, 100 mW cm⁻²), calibrated using a silicon diode (Gentec-EO, XLPF12-3S-H2-DO). The half-cell solar-to-hydrogen efficiency (HC-STH) was calculated from the linear sweep voltammograms using the equation HC-STH = $j_{ph} \times (E_{RHE} - E_{H+/H2}) / P_{sun} \times 100\%$, where j_{ph} is the photocurrent density obtained under an applied bias of E_{RHE} , $E_{H+/H2}$ is the equilibrium redox potential of hydrogen (0 V_{RHE}) and P_{sun} is the power density of the incident solar energy (100 mW cm⁻²). Before measurements, platinum as HER catalyst was generally deposited by H₂PtCl₆ drop casting (which corresponds to a Pt load of 133 μ g/cm²) or by thermal evaporation. Then, samples were scratched to expose the SS substrate, soldered to a Cu wire with Ag paint and protected with an epoxy resin.

3. Results and discussion

TiO₂ layers with different thickness have been deposited simultaneously on the CIGSe photocathodes and on silicon substrates in order to analyze the morphology and structure of the deposited TiO₂ ALD layers under the defined conditions. Fig. 1 shows a scanning electron microscopy image of one of these samples deposited at 200 °C with a thickness of 100 nm using the silicon substrates. Nearly circular crystals can be seen dispersed in a still amorphous layer. The insert in Fig. 1 shows the cross section of one of these anatase crystallized columns embedded in the amorphous layer, where phase composition was depicted from XRD analysis (Fig. S1). Crystallized surface coverage and column diameter size changes with the deposition time and hence with the thickness. Crystallized zones being thicker than the amorphous layer is known from the higher hydroxyl affinity of the anatase crystallographic phase, thus giving a higher ALD growth rate [14].

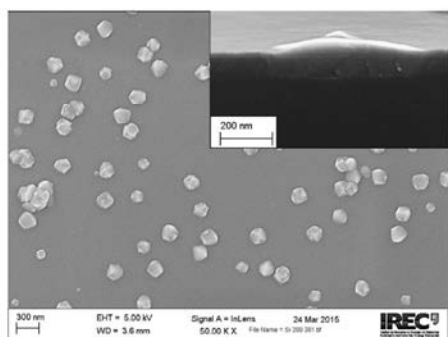


Fig. 1. SEM image of the TiO₂ ALD deposited layer morphology on silicon substrate. Insert: cross section detail of the anatase crystallized vertical column.

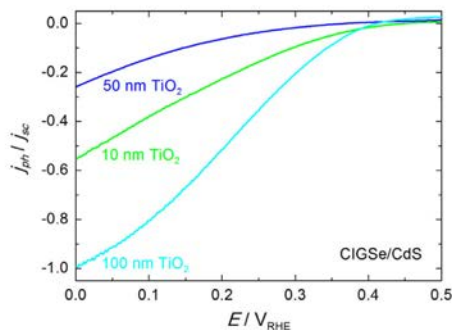


Fig. 2. Linear sweep voltammograms under illumination (1 sun) of CIGSe/CdS heterojunctions with a 10 nm (green), 50 nm (dark blue) or 100 nm (light blue) TiO₂ top layer and 1 nm evaporated Pt as HER. Electrolyte: 0.5 M H₂SO₄. All of the curves have been normalized to the maximum photocurrent at 0 V_{RHE}. (For interpretation of the references to color in this figure legend, the reader is referred to the web version of this article.)

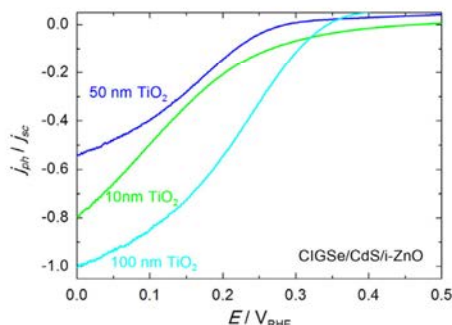


Fig. 3. Linear sweep voltammograms under illumination (1 sun) of CIGSe/CdS/i-ZnO heterojunctions with a 10 nm (green), 50 nm (dark blue) or 100 nm (light blue) TiO₂ top layer and 1 nm evaporated Pt as HER. Electrolyte: 0.5 M H₂SO₄. All of the curves have been normalized to the maximum photocurrent at 0 V_{RHE}. (For interpretation of the references to color in this figure legend, the reader is referred to the web version of this article.)

To preserve the reliability of the chalcopyrite based structure, the growth temperature was not exceeding 200 °C. Then, it is plausible that under the used conditions, the electrical transport properties of the deposited TiO₂ ALD layer can be different at different thickness due to different layer crystallization state.

The influence of the TiO₂ thickness on the photoelectrochemical performance of the chalcopyrite based structure (SS/Cr/Mo/CIGSe/CdS) without or with a i-ZnO buffer layer is shown in Figs. 2 and 3 respectively. For clarity, the obtained photocurrent is plotted normalized versus the value of the 100 nm thickness at 0 V_{RHE}. These data show the effect of different thickness deposited TiO₂ layers. In both cases the maximum photocurrent values are obtained at a thickness of 100 nm with absolute photocurrent value at 0 V_{RHE} in the range of 15–20 mA cm⁻² as it will be shown below.

Likewise, in both cases, the resistive effect of a 10 nm thin layer is less relevant than 50 nm likely due to this thickness still allowing a tunnel conduction through the layer whereas at 50 nm the poor charge transport properties of the layer is preventing to attain a high level of photocurrent due to higher resistance and consequently introducing higher electrical losses. The higher blocking effect in this case is decreasing the charge transfer

capability. Consequently, the photogenerated carriers have a higher residence time in the chalcopyrite based structure before being transferred to the electrolyte and, hence, the recombination rate is increased diminishing the effective photocurrent level.

It can be observed that these resistive effects are much less significant when the i-ZnO buffer layer used in photovoltaic devices for facilitating electron-hole separation is used too, preventing surface recombination. Without the i-ZnO layers, the sample with 50 nm TiO₂ (dark blue line, Fig. 2) approximately transfers 20% of the photocurrent whereas using i-ZnO layer (dark blue line, Fig. 3) there is more than double of the current level. Similar effect exists if we compare the current level for the samples coated with 10 nm of TiO₂.

On the other hand, for these cases of 10 and 50 nm, it is also remarkable the effect of the introduce resistance due to the layer observing the strongly modification in the polarization curve shape especially when i-ZnO layer is not present.

For thickness of 100 nm these limiting effect of the TiO₂ layer with small thicknesses is overcome. High level of photocurrent, charge transport efficiency and better fill factor are recovered pointing out that, at this thickness value, with the low temperature deposition conditions (for preserving chalcopyrite based structure materials stability), the transport properties of the TiO₂ become suitable as protective coating. Furthermore, these results also suggest than it is much better to keep the i-ZnO layer like it is used in the photovoltaic device to facilitate the electron transport and injection through the i-ZnO/TiO₂ interface.

In this direction, we have also analyzed if the introduction of an underlayer of aluminum doped ZnO (AZO) could still improve the final efficiency. In Fig. 4 it is show the positive effect obtained in using the full configuration in extracting electrons according to the fabrication route implemented in photovoltaic devices. Keeping in mind that ALD-TiO₂ has an anatase-amorphous composition with different conductivities (Figure S2), the intermediate layer of the conductive oxide (AZO) between i-ZnO and ALD-TiO₂ is facilitating electrons to find the most conductive pathways of the protective TiO₂ layer, similar to what was proposed by Domen et al. [15]. As it can be seen in Fig. 4, a 26 mA cm⁻² photocurrent level (0 V_{RHE}) has been obtained using the ZnO-AZO configuration, proving the benefits in using the AZO layer too. The fast electron transfer was also validated by measuring the open circuit voltage of the photoelectrodes shown in Fig. 5, where the open circuit voltage decay is higher for the samples without the ZnO-AZO layer, whereas with the layer a virtually constant open circuit voltage was observed, proving that interfacial recombination is suppressed by

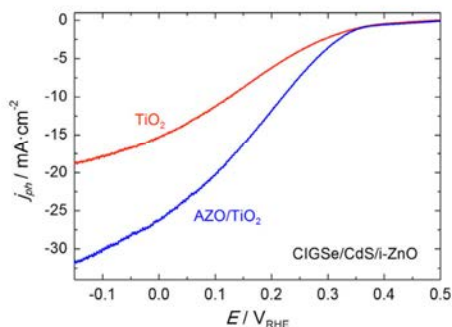


Fig. 4. Linear sweep voltammograms under illumination (1 sun) of CIGSe/CdS/i-ZnO/heterojunctions with 300 nm of AZO (blue) or without the underlayer (red), subsequently protected with 100 nm TiO₂ ALD layer and 133 μg cm⁻² of drop casted Pt as HER. Electrolyte: 0.5 M H₂SO₄. (For interpretation of the references to color in this figure legend, the reader is referred to the web version of this article.)

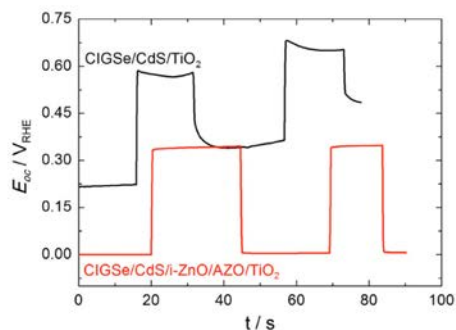


Fig. 5. Open circuit potential measurements of CIGSe CdS heterojunctions with ZnO-AZO layers (red) and without the (black) and with 100 nm TiO₂ top layer and 1 nm Pt evaporated layer as HER. Measurements under chopped illumination (1 sun) in 0.5 M H₂SO₄. (For interpretation of the references to color in this figure legend, the reader is referred to the web version of this article.)

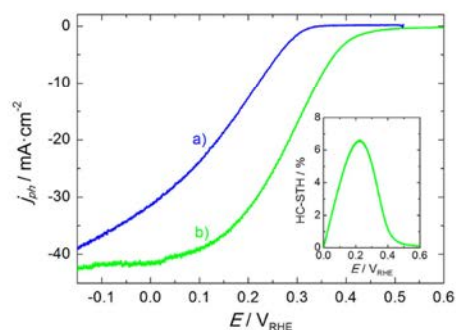


Fig. 6. Linear sweep voltammograms under illumination (1 sun) of CIGSe/CdS/i-ZnO/AZO heterojunctions (blue) or an industrial solar cell (green) with a 100 nm TiO₂ top layer and 1 nm evaporated Pt as HER. Insert, solar to hydrogen (HC-STH) efficiency of the industrial CIGSe/CdS/i-ZnO/AZO/TiO₂/Pt photocathode. Electrolyte: 0.5 M H₂SO₄. (For interpretation of the references to color in this figure legend, the reader is referred to the web version of this article.)

facilitating charge migration through the ZnO-AZO underlayer. According to these analyses it is not suitable to simplify the already optimized electron extraction system and it is mandatory at 200 °C to use a TiO₂ ALD layer of at least 100 nm. We have moved this fabrication recipe to the full standard photovoltaic fabrication route replacing the final metallization step by the ALD deposition. The same has been done for a sample fabricated in an industrial production line. In one case the catalytic platinum was implemented in a different way, which introduces little difference, which origin will be analyzed elsewhere. In Fig. 6 it is shown that photocathodes based on chalcopyrite deposited on flexible stainless steel foils are feasible with a very promising photocurrent level density in the range of 30–40 mA cm⁻², giving a solar to hydrogen (HC-STH) conversion efficiency of 6.6% at 0.23 V_{RHE}, which is in the range of the record HC-STH efficiencies of CIGSe photocathodes using buffered neutral or alkaline electrolytes [15]. Also, stability measurements prove these flexible samples can stand at least for 1 h continuous hydrogen evolution at 0 V_{RHE} giving 20–30 mA cm⁻² (Fig. 7), in acid electrolyte where it was already reported stability issues [6]. Likewise, the combination of In/Ga or alternatively S/Se or even the use of alternative layers to the CdS opens many options for improving the open circuit voltage as well as the overall photoelectrochemical characteristics of this

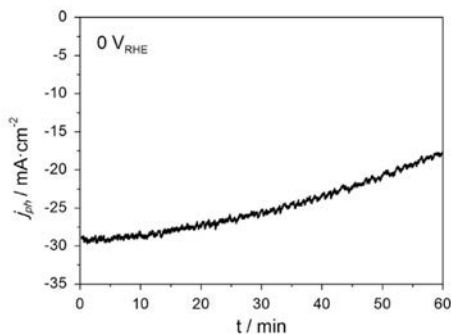


Fig. 7. Stability measurements of a full configuration sample (CIGSe/CdS/i-ZnO/AZO) with 100 nm ALD TiO₂ and 1 nm evaporated Pt HER layer. Measurement at 0 V_{RHE} under 1 sun illumination in 0.5 M H₂SO₄.

Cu-chalcopyrite system. To our knowledge, the observed PEC water splitting activity is clearly competitive among chalcopyrite-based photocathodes reported so far and it is the first time reported on a flexible substrate. Nevertheless, further studies to improve it are now in progress for a second generation of flexible photocathodes.

4. Conclusions

It has been shown the feasibility of the fabrication of highly efficient photocathodes based on Cu-chalcopyrite deposited on flexible stainless steel foil substrates. These cathode structures can take all the advantages of the previously developed thin film technology around the chalcogenides driving new disruptive options for combining different compositions S/Se or Ga/In or just using kesterites systems.

Likewise, it has been proved that atomic layer deposition of TiO₂ deposited at low temperature, 200 °C, using TiCl₄ precursor can accomplish all the requirements for achieving the objective of maximum efficiency from the used p-type absorber layer. For this, electron transport mechanisms through the deposited TiO₂ film has a paramount importance and must be considered to avoid restricting conditions which block charge transfer, accumulating carriers at the interface, increasing the recombination ratio and hence reducing the effective photocurrent. A thickness of at least 100 nm has been demonstrated to be necessary to achieve the maximum charge transfer efficiency. Likewise, it has been proved that, onto the n-type layer of CdS, the use of i-ZnO/AZO (Al:ZnO) layers such as it is used for photovoltaic chalcogenide thin film technology for facilitating the electron extraction is also strongly recommendable for PEC applications in order to achieve photocurrent level, open circuit voltage and fill factor near of those presented for equivalent photovoltaic devices.

The feasibility of Cu-chalcopyrite based photocathodes onto flexible stainless steel foil drives novel PEC cell design towards new conformal developments oriented to develop low cost and high volume applications of multi PEC cell modules under the concept of a solar refinery for obtaining high throughput solar fuels.

Acknowledgments

Authors from IREC and University of Barcelona belong to the M-2E (Electronic Materials for Energy) Consolidated Research Group

and the XaRMAE Network of Excellence on Materials for Energy of the "Generalitat de Catalunya". This work was partially supported by the European Regional Development Funds (ERDF, FEDER) by MINECO projects ENE2012-3651, MAT2014-59961 and the Framework 7 program under the project SOLAROGENIX (FP7-NMP-2012-310333). C.R. and S.G. thank MINECO and FSE for their FPI grants (BES-2015-071618, BES-2014-068533) and Y. S. for the PTA grant (PTA2012-7852-A).

Appendix A. Supplementary material

Supplementary data associated with this article can be found in the online version at <http://dx.doi.org/10.1016/j.solmat.2016.01.031>.

References

- [1] S. Hu, C. Xiang, S. Haussener, A.D. Berger, N.S. Lewis, An analysis of the optimal band gaps of light absorbers in integrated tandem photoelectrochemical water-splitting systems, *Energy Environ. Sci.* 6 (2013) 2984–2993.
- [2] J.R. McKone, E.L. Warren, M.J. Bierman, S.W. Boettcher, B.S. Brunschwig, N. S. Lewis, H.B. Gray, Evaluation of Pt, Ni, and Ni-Mo electrocatalysts for hydrogen evolution on crystalline Si electrodes, *Energy Environ. Sci.* 4 (2011) 3573–3583.
- [3] S.W. Boettcher, E.L. Warren, M.C. Putnam, E.A. Santori, D. Turner-Evans, M. D. Kelzenberg, M.G. Walter, J.R. McKone, B.S. Brunschwig, H.A. Atwater, N. S. Lewis, Photoelectrochemical hydrogen evolution using Si microwave arrays, *J. Am. Chem. Soc.* 133 (2011) 1216–1219.
- [4] D. Yokoyama, T. Minegishi, K. Maeda, M. Katayama, J. Kubota, A. Yamada, M. Konagai, K. Domen, Photoelectrochemical water splitting using a Cu(In,Ga)Se₂ thin film, *Electrochem. Commun.* 12 (2010) 851–853.
- [5] A. Paracchino, V. Laporte, K. Sivula, M. Grätzel, E. Thimsen, Highly active oxide photocathode for photoelectrochemical water reduction, *Nat. Mater.* 10 (2011) 456–461.
- [6] T.J. Jacobsson, V. Fjällström, M. Edoff, T. Edvinsson, CIGS based devices for solar hydrogen production spanning from PEC-cells to PV-electrolyzers: a comparison of efficiency, stability and device topology, *Sol. Energy Mater. Sol. Cells* 134 (2015) 185–193.
- [7] L. Rovelli, S.D. Tilley, K. Sivula, Optimization and stabilization of electrodeposited Cu₂ZnSnS₄ photocathodes for solar water reduction, *ACS Appl. Mater. Interfaces*, 5 (2013) 8018–8024.
- [8] J. Kim, H. Hiroi, T.K. Todorov, O. Gunawan, M. Kuwahara, T. Gokmen, D. Nair, M. Hopstaken, B. Shin, Y.S. Lee, W. Wang, H. Sugimoto, D.B. Mitzi, Solar cells: high efficiency Cu₂ZnSn(S,Se)₄ solar cells by applying a double In₂S₃/CdS emitter, *Adv. Mater.* 26 (2014) 7426–7426.
- [9] T.K. Todorov, O. Gunawan, T. Gokmen, D.B. Mitzi, Solution-processed Cu(In,Ga)(S,Se)₂ absorber yielding a 15.2% efficient solar cell, *Prog. Photovolt. : Res. Appl.* 21 (2013) 82–87.
- [10] S. López-Marino, M. Neuschitzer, Y. Sánchez, A. Fairbrother, M. Espindola-Rodríguez, J. López-García, M. Placidi, L. Calvo-Barrio, A. Pérez-Rodríguez, E. Saucedo, Earth-abundant absorber based solar cells onto low weight stainless steel substrate, *Sol. Energy Mater. Sol. Cells* 130 (2014) 347–353.
- [11] B. Seger, T. Pedersen, A.B. Laursen, P.C.K. Vesborg, O. Hansen, I. Chorkendorff, Using TiO₂ as a conductive protective layer for photocathodic H₂ evolution, *J. Am. Chem. Soc.* 135 (2013) 1057–1064.
- [12] S. Niki, P.J. Fons, A. Yamada, Y. Lacroix, H. Shibata, H. Oyanagi, M. Nishitani, T. Negami, T. Wada, Effects of the surface Cu₂-Se phase on the growth and properties of CuInSe₂ films, *Appl. Phys. Lett.* 74 (1999) 1630–1632.
- [13] M. Neuschitzer, Y. Sanchez, S. López-Marino, H. Xie, A. Fairbrother, M. Placidi, S. Haass, V. Izquierdo-Roca, A. Perez-Rodríguez, E. Saucedo, Optimization of CdS buffer layer for high-performance Cu₂ZnSnS₄ solar cells and the effects of light soaking: elimination of crossover and red kink, *Prog. Photovolt. : Res. Appl.* 23 (2015) 1660–1667.
- [14] M. Reiners, K. Xu, N. Aslam, A. Devi, R. Waser, S. Hoffmann-Eifert, Growth and crystallization of TiO₂ thin films by atomic layer deposition using a novel amido guanidinate titanium source and tetrakis-dimethylamido-titanium, *Chem. Mater.* 25 (2013) 2934–2943.
- [15] H. Kumagai, T. Minegishi, N. Sato, T. Yamada, J. Kubota, K. Domen, Efficient solar hydrogen production from neutral electrolytes using surface-modified Cu(In,Ga)Se₂ photocathodes, *J. Mater. Chem. A* 3 (2015) 8300–8307.

Supplementary Data

Conformal chalcopyrite based photocathode for solar refinery applications

Carles Ros^a, Teresa Andreu^{a,*}, Sergio Giraldo^a, Yudania Sánchez^a, Joan Ramon Morante^{a,b,*}

^a Catalonia Institute for Energy Research, IREC. Jardins de les Dones de Negre 1, 08930 Sant Adrià de Besòs, Barcelona, Spain

^b Departament d'Electrònica, Universitat de Barcelona, Martí i Franquès, 1, 08028 Barcelona, Spain

* Corresponding author: Teresa Andreu, Joan Ramon Morante

Electronic mail: tandreu@irec.cat; jrmorante@irec.cat

Ph.: +34 933562615

Fax: +34 933563802

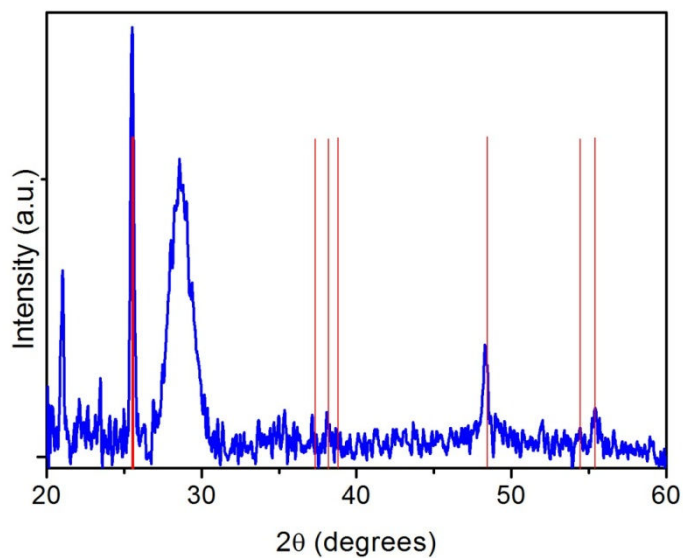


Figure S1. XRD pattern of the TiO₂ ALD deposited layer morphology on silicon substrate.

Red vertical lines corresponds to JCPDS card 1-0562 (anatase).

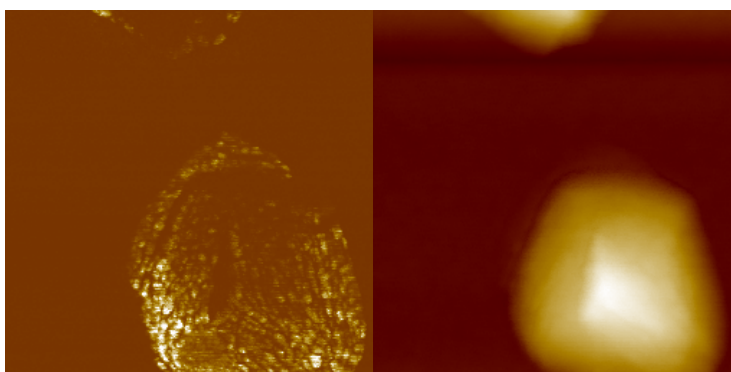


Figure S2: AFM images (conductive tip) of a 200 °C grown TiO₂ ALD layer on an n⁺-Si substrate. Topography image (left) and intensity image (right).

Turning Earth Abundant Kesterite-Based Solar Cells Into Efficient Protected Water-Splitting Photocathodes

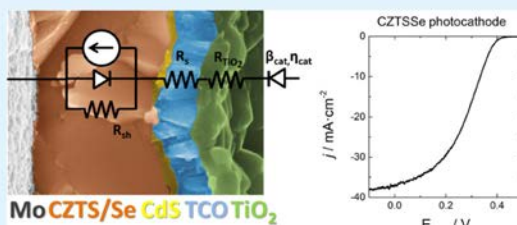
Carles Ros,^{*,†} Teresa Andreu,^{*,†} Sergio Giraldo,[†] Victor Izquierdo-Roca,[†] Edgardo Saucedo,[†] and Joan Ramon Morante^{†,‡}

[†]Catalonia Institute for Energy Research, IREC, Jardins de les Dones de Negre 1, 08930 Sant Adrià de Besòs, Barcelona, Spain

[‡]Universitat de Barcelona, Martí i Franquès, 1, 08028 Barcelona, Spain

ABSTRACT: CZTS/Se kesterite-based solar cells have been protected by conformal atomic layer deposition (ALD)-deposited TiO₂ demonstrating its feasibility as powerful photocathodes for water splitting in highly acidic conditions (pH < 1), achieving stability with no detected degradation and with current density levels similar to photovoltaic productivities. The ALD has allowed low deposition temperatures of 200 °C for TiO₂, preventing significant variations to the kesterite structure and CdS heterojunction, except for the pure-sulfide stoichiometry, which was studied by Raman spectroscopy. The measured photocurrent at 0 V vs reversible hydrogen electrode, 37 mA·cm⁻², is the highest reported to date, and the associated half-cell solar-to-hydrogen efficiency reached 7%, being amongst the largest presented for kesterite-based photocathodes, corroborating the possibility of using them as abundant low-cost alternative photoabsorbers as their efficiencies are improved toward those of chalcopyrites. An electrical circuit has been proposed to model the photocathode, which comprises the photon absorption, charge transfer through the protective layer, and catalytic performance, which paves the way to the design of highly efficient photoelectrodes.

KEYWORDS: kesterite, CZTS, protective layer, TiO₂, hydrogen, water splitting, photocathode



INTRODUCTION

Since the discovery of the photoelectrochemical (PEC) water splitting,¹ much effort has been addressed to develop materials for an industrial scale deployment. The photoelectrode stability and material cost, abundance, and toxicity have become key parameters, together with process efficiency and productivity.

From photovoltaic (PV) point of view, several candidate materials for high solar to current conversion efficiency are known, silicon being one of the most studied. Implementing them in PEC water-splitting devices could overcome the productivity limitations of metal oxides.^{2–7} To overcome material consumption and production costs, second-generation thin-film solar cells are moving to affordable and scalable materials, maintaining high conversion outputs.⁸ Among them, kesterite CZTS/Se (Cu₂ZnSnS₄/Se₄) solar cells are promising low-cost alternatives,^{9,10} similar to CIGS (CuIn_{1–x}Ga_xSe₂) ones^{11–13} but replacing scarce gallium and indium by tin and zinc, which are more abundant, inexpensive, and environment-friendly metals. In this case, cell heterojunctions are formed with a highly n-type CdS layer for an efficient charge separation, normally deposited via chemical bath deposition, a room-temperature process giving excellent results but significantly sensitive to thermal treatments. Additionally, distribution of Cu¹⁺ and Zn²⁺ cations in the crystal structure of kesterite has significant impact on the interface carrier recombination and final performance of the photovoltaic device,^{14,15} and it is also very sensitive to postdevice fabrication thermal processes.

These two facts limit the processing temperature of the PEC device to below 250–300 °C.

On the other hand, another advantage of kesterite-based solar cells is that band gap modification is possible by changing the sulfur–selenium composition, moving from a 1.0 eV band gap pure-selenium CZTSe up to 1.5 eV when substituting selenium by sulfur, allowing 300 mV photovoltage modifications,¹⁶ especially interesting to match the optimum coordination in a tandem device.¹⁷ The CZTS/Se kesterite devices stand for cheap and earth-abundant-materials-based photocathodes, fitting the requirements for the small band gap photoelectrode in tandem cells configuration for large-scale implementation.

One of the main problems faced in implementing kesterites as PEC devices concern the instability of used materials under water-splitting conditions, which require highly acid or basic electrolytes. Moreover, it has recently been demonstrated that for PEC applications, the integration of the absorber based on chalcogenides in the photocathode is improved keeping the top contact transparent layers (normally indium tin oxide (ITO) or aluminum doped zinc oxide (AZO)) typically used in the PV device. This way, these layers contribute to facilitate the charge transfer of photogenerated electrons from the absorber to the

Received: January 2, 2018

Accepted: March 26, 2018

Published: March 26, 2018

hydrogen evolution reaction (HER) catalyst particles.¹⁸ However, these layers lack the chemical stability under working conditions; therefore, the development of layers fulfilling the required properties of pinhole-free, conductivity, transparency, and stability in wide range of pH and electrochemical potentials and compatibility with the kesterite technology are mandatory to implement them into photoelectrochemical systems.¹⁹

In this contribution, we analyze the viability of atomic layer deposition (ALD) of protective layers compatible with the earth-abundant copper–zinc–tin–chalcogenide kesterites ($\text{Cu}_2\text{ZnSnS}_4/\text{Se}_4$)-based devices.^{20–22} These chalcogenides show a complex structure with different phases and lattice parameters under temperature treatment variations, together with diffusion and different distribution of anions (S, Se) and cations (Cu, Zn) already taking place at few hundred degrees Celsius.^{23–27} The main consequences of alterations in these characteristic defects are the modification of the effective band gap values, the change in the open circuit voltage, performance losses in the fill factor, or the variation in the short circuit currents modifying the solar cell characteristics and, hence, its functionality as an active component of a photocathode.¹⁵ In this scenario, once kesterite films are fabricated and the p–n junction formed, low thermal processes are required to overcome these difficulties. However, the protection layer needs some conditions for guaranteeing its functionality.^{28–31} Thus, proper coverage, chemical stability, and high electrical conductivity are simultaneously needed. Furthermore, any electrical resistance introduced by this extra layer must be minimized to avoid efficiency losses.

Here, ALD TiO_2 films have been used as protective coatings, with thicknesses around 100 nm. These layers present excellent results in terms of protection, transparency, and drift conductivity both for anodic and cathodic water-splitting conditions^{31–33} and photoabsorbers such as Si ,^{31,34,35} CuO ,^{36,37} Fe_2O_3 ,⁶ or CuSe .¹⁹ ALD can rule out pinhole generation³⁷ and has lower crystallization deposition temperatures than sputtering or chemical vapor deposition, thanks to intermediate species mobility and a slow layer-by-layer conformal deposition, crystallization being a key characteristic for efficient conductivity.^{31,38,39} These ALD characteristics open the possibility to use it to protect photoabsorbing materials, which would degrade under widely used post-deposition crystallization annealing at moderate temperatures ($\sim 400^\circ\text{C}$).⁴⁰

In this work, to fulfill the above-described requirements, kesterite-based solar cells¹⁰ have been protected with at least 100 nm thick ALD TiO_2 polycrystalline layers. These TiO_2 layers separate the photoabsorber from the corrosive electrolyte, but they can also introduce a certain resistance to the current flow,³¹ reduce the number of photons reaching the photoabsorber (although having a band gap larger than 3 eV),⁴¹ and its deposition process can alter the layers beneath. The kesterite-based photocathodes have been fabricated to resemble the conversion efficiencies of photovoltaic kesterite solar cells while being stable in highly acidic electrolytes.^{42–45}

Significant performance differences have been found between the sulfur-based and selenium-based samples $I(V)$ curves, which have also been corroborated by Raman analysis, pointing out that pure-sulfur samples are especially sensitive to long ALD processes due to the loss of beneficial copper vacancy defects. The photoelectrochemical and photovoltaic behaviors have been compared and individual electrical components have been analyzed assuming an electrical circuit model.^{46,47} Finally, the

performance and stability are tested to obtaining $37\text{ mA}\cdot\text{cm}^{-2}$ at 0 V vs reversible hydrogen electrode (RHE) and the onset potentials up to 450 mV vs RHE, giving a photocathode conversion efficiency of 7% for a CZTSSe kesterite. These values enhance this technology to be a very promising and low-cost approach, as kesterite-based PV efficiencies have increased during the last years up to 12.6%,⁴⁸ which is beyond the efficiencies used in this work. This gives promising expectations to achieve the conversion efficiencies above 10% using kesterite-based photocathodes in the near future.

EXPERIMENTAL SECTION

Preparation of CZTS/Se Thin Films. CZTSe layers were synthesized on Mo-coated soda lime glass by annealing the Cu/Sn/Cu/Zn metallic multistacks in a reactive atmosphere with S, Se, or the combination of S and Se. Precursor absorber films were approximately 800–840 nm thick, with composition ratios of $\text{Cu}/(\text{Zn} + \text{Sn}) = 0.77–0.87$ and $\text{Zn}/\text{Sn} = 1.24–1.49$. When combining S and Se, a mixed atmosphere post-treatment was used, resulting in a sulfur/selenium ratio $\text{S}/(\text{S} + \text{Se}) = 0.166$, fabricated as in previous works.^{16,49} The as-prepared absorbers were then subjected to several etching processes to remove the secondary phases and passivate the surface, as reported elsewhere.^{50,51} Afterward, the solar cells are finished by a chemical bath deposition of a CdS buffer layer (60 nm), followed immediately by pulsed direct current (DC)-magnetron sputtering deposition of 50 nm intrinsic ZnO and 450 nm $\text{In}_2\text{O}_3/\text{SnO}_2$ (90/10 atom %) window layer (CT100 Alliance Concepts).

For simplicity, complete solar cells including the $\text{Cu}_2\text{ZnSnS}_4/\text{Se}_4$ photoabsorbing material, the CdS, the $i\text{-ZnO}$, and the top contact ITO will be named based on the photoabsorber, namely, CZTSe, CZTSSe, and CSTS. CZTS/Se will be used to mention the chalcogenide compounds with mixed S/Se stoichiometry used in this work.

Protection with Transparent Conductive TiO_2 . The samples were introduced in a R200 Picosun Atomic Layer Deposition system at the deposition temperatures $T_d = 200, 250,$ and 300°C using TiCl_4 and H_2O precursors at 19°C in successive pulses in a 12 mbar N_2 flow atmosphere, similar to previous works,³¹ reaching a growth rate of 0.43 Å per cycle, with a fixed number of 3300 cycles. Some samples were grown simultaneously on silicon substrates for complete characterization of the TiO_2 overlayer. The annealing processes simulating ALD conditions were performed in the same ALD chamber in N_2 flow vacuum, but with no precursor being introduced during 18 h (the time corresponding to 3300 ALD cycles).

HER Catalysts. Before measurements, platinum as HER catalyst was deposited by drop-casting using 6.5 mM H_2PtCl_6 in isopropanol (corresponding to a Pt load of $66\text{ }\mu\text{g}\cdot\text{cm}^{-2}$). Then, the samples were scratched to expose the Mo substrate soldered to a Cu wire with an Ag paint and protected with a nontransparent epoxy resin, leaving no scratched border exposed to electrolyte.

Structural Characterization. TiO_2 layer thickness was measured by evaluating the reflected spectra with a Sensofar interferometer device with $\pm 0.2\text{ nm}$ error and verified by cross section in a Zeiss Series Auriga field effect scanning electron microscope. The structural characterization was carried out by X-ray diffraction (XRD) in a D8 Advance Bruker equipment with a $\text{Cu K}\alpha$ radiation source working at 40 kV and 40 mA. The XRD diffractogram has been normalized to the TiO_2 peak. The crystalline domains are calculated following the Scherrer equation: $D = 0.9 \times \lambda / (\text{FWHM} \times \cos \theta)$, where λ is the X-ray wavelength (1.5406 Å), full width at half-maximum (FWHM) is the full width of the diffraction line at half-maximum and θ is the Bragg angle. The Raman scattering measurements were performed in backscattering configuration with 785 and 532 nm excitation wavelength using an IREC developed Raman setup based in an iHR320 Horiba Jobin Yvon spectrometer system. All the measurements were performed with a spot diameter of around 70 μm and keeping the power density below $100\text{ W}\cdot\text{cm}^{-2}$. All the spectra have been calibrated using a reference monocrystalline silicon sample and imposing the Raman shift of the main peak at 520 cm^{-1} .

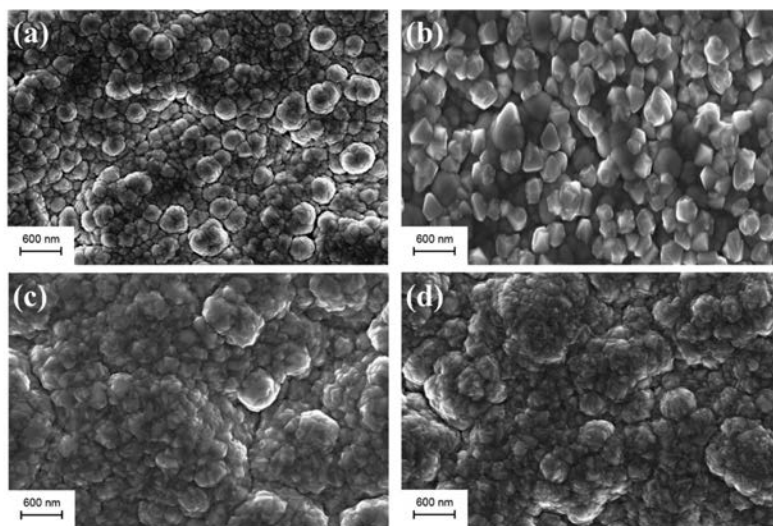


Figure 1. SEM images of CZTSe solar cells (a) as finished and with 3300 cycles of ALD-TiO₂ deposited at (b) 200, (c) 250, and (d) 300 °C.

Photovoltaic and Photoelectrochemical Characterization. Photovoltaic J - V measurements were performed with an AAA class ABET 3000 Solar Simulator under AM 1.5 conditions. The photoelectrochemical (PEC) measurements were obtained with a Princeton Applied Research PARSTAT 2273 potentiostat in a three-electrode configuration, using Ag/AgCl/KCl (3 M) ($E = 0.203 V_{\text{RHE}}$) as the reference electrode and platinum mesh as the counter electrode. 0.5 M H₂SO₄ (pH = 0.3) was used as the electrolyte. Linear sweep voltammograms were acquired at a scanning rate of 30 mV·s⁻¹. A quartz cell with flat faces was used with 100 mL of electrolyte and a 300 W xenon lamp to provide simulated solar light (AM 1.5G filter, 1 sun, 100 mW·cm⁻²) calibrated using a silicon diode (Gentec-EO, XLPF12-3S-H2-DO).

The performance and quality of the prepared photoelectrodes were determined by measuring the half-cell solar-to-hydrogen efficiency (HC-STH) using a three-electrode configuration. It was calculated from the data obtained in the linear sweep voltammograms using the equation HC-STH = $j_{\text{ph}} \times (E_{\text{RHE}} - E_{\text{H}^+/\text{H}_2}) / P_{\text{sun}} \times 100\%$, where j_{ph} is the photocurrent density obtained under an applied bias of E_{RHE} , $E_{\text{H}^+/\text{H}_2}$ is the equilibrium redox potential of hydrogen (0 V_{RHE}), and P_{sun} is the power density of the incident solar energy (100 mW·cm⁻²). Shunt (R_{sh}) and series (R_{s}) resistances have been calculated as the slope in the $I(V)$ curve in short-circuit and open-circuit conditions, respectively.

RESULTS AND DISCUSSION

Influence of the Structural, Morphological, and Electrical Parameters. TiO₂ layers ranging between 130 and 140 nm in thickness (depending on the growth temperature) have been deposited on CZTSe/CdS/i-ZnO/ITO solar cells at 200, 250, and 300 °C. At least 100 nm thick TiO₂ layers are highly recommended for proper crystallization of the ALD-grown TiO₂ in the anatase phase, as reported in our previous work.¹⁹ The deposition temperature was tested up to 300 °C to obtain more crystalline layers, which would increase its conductivity and stability and enhance the solar-to-hydrogen conversion efficiency.^{31,52} From the scanning electron microscopy (SEM) images (Figure 1), we can see grains of around 200 nm diameter when grown at $T_{\text{d}} = 200$ °C (Figure 1b), and the size is reduced and nucleation enhanced when the

deposition temperature is increased to 250 and 300 °C (Figure 1c,d). The surface appearance becomes less rugose. From the cross-sectional SEM (Figure 2) of a sample deposited at $T_{\text{d}} = 200$ °C, we corroborate the proper coverage of the ITO layer by TiO₂.

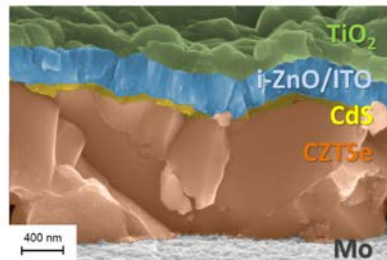


Figure 2. SEM cross-sectional image of a CZTSe device protected with a 3300 cycles TiO₂ layer grown at 200 °C. We can identify CZTSe (brown), CdS (yellow), i-ZnO/ITO (blue), and TiO₂ (green).

The XRD analysis confirms the presence of the anatase TiO₂ phase (25.5° peak) (Figure 3). According to the XRD diffractogram, the crystalline domain (D) is reduced, together with increase in the residual compressive strain, at higher deposition temperatures. The increase in layer strain is caused by higher nucleation and nanocrystal growth competition. Higher nucleation is a direct and known effect of increasing deposition temperature, facilitating atomic ordering, in this case, of intermediate species of the ALD deposition process.³¹ All these results are resumed in Table 1.

From the photoelectrochemical (PEC) measurements of the samples with TiO₂ layers grown at different temperatures (Figure 4a), we can see how the onset potential of our samples was reduced, from 0.43 V vs RHE for $T_{\text{d}} = 200$ °C to 0.33 V vs RHE for $T_{\text{d}} = 250$ °C and almost nothing for $T_{\text{d}} = 300$ °C. Thus, the deposition process, consisting on 18 h in the ALD,

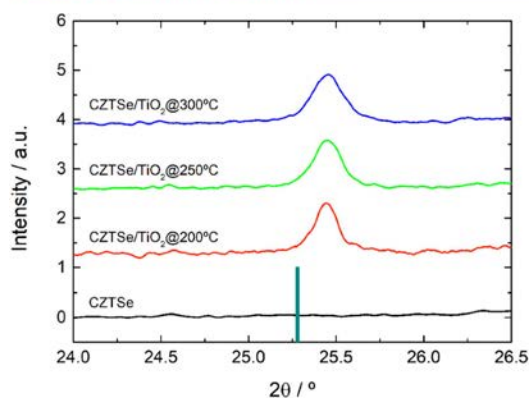


Figure 3. XRD diffractogram of the complete device around one of the TiO_2 peaks for a sample before the TiO_2 deposition (black) and with the protective layer grown at 200 (red), 250 (green), and 300 °C (blue). The anatase reference peak is shown with a dark green bar.

Table 1. Peak Maximum Position, Full Width at Half-Maximum (FWHM), Crystalline Domain (D), Interatomic Planar Spacing (d), and Compressive Strain Measured from the XRD Diffractogram Presented in Figure 3

	2θ (°)	FWHM (°)	D (nm)	d (Å)	strain, $\Delta d/d_{ref}$ (%)
TiO_2 ref 53	25.28			3.5191	
TiO_2 200 °C	25.5091	0.1506	53.4	3.4877	0.89
TiO_2 250 °C	25.5495	0.1829	44.0	3.4824	1.04
TiO_2 300 °C	25.5604	0.2194	36.7	3.4808	1.09

has a negative effect on the buried p–n junction of the thin-film kesterite solar cell for temperatures above 200 °C, as well as on the structure of the buried kesterite layer. At these temperatures, especially the CdS but also the TCO n-type semiconductor layers are modified by defect redistribution and recrystallization,⁵⁴ which changes the electronic parameters and degrades the device performance. This effect has been seen in sulfur- and selenium-based kesterite solar cells when 250–300 °C post-treatments are applied.^{54,55} For this reason, the temperature for further experiments was kept at 200 °C. The sample grown at 200 °C was tested in 0.5 M H_2SO_4 for stability at 0 V vs RHE and showed over 1 h stability, giving almost 27 $\text{mA}\cdot\text{cm}^{-2}$ with no significant losses (Figure 4b). After 1 h, when the sample started to lose current, we stopped the experiment. It was not possible to measure the stability of the same device without the TiO_2 protective layer, as acid-sensitive upper layers (ITO⁵⁶ and CdS⁵⁶) are completely corroded inside the electrolyte in few seconds, inhibiting any measurable photoelectrochemical current.

We present in Figure 5 images of an unprotected device before, during, and after a 0.5 M H_2SO_4 droplet was put on top, where significant corrosion can be seen in 1 min. TiO_2 -protected photocathodes presented small circular regions with different colors after 1 h stability measurements (Figure 5b, top). By SEM (Figure 5b, down), we can corroborate that these visually different regions correspond to defects in the protective layer, where the electrolyte corroded the layers beneath the TiO_2 . The backscattered SEM images allow us to see regions where the layers beneath the TiO_2 have been dissolved. Point

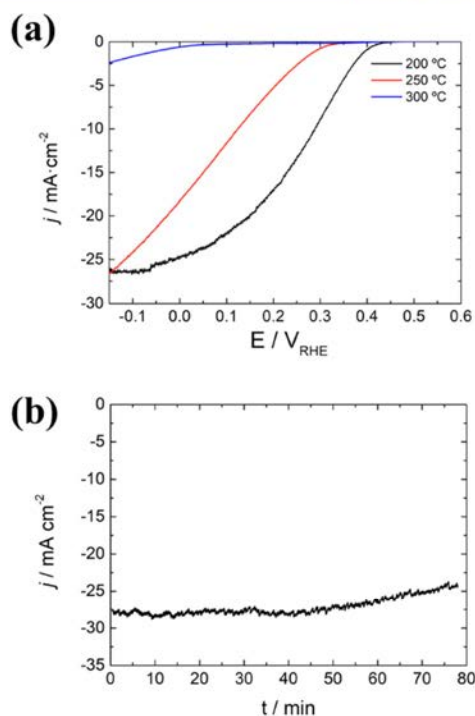


Figure 4. (a) Polarization curves of CZTSe devices with TiO_2 layers grown at different temperatures ranging from 250 to 300 °C. (b) Stability measurement of the sample with TiO_2 grown at 200 °C. Pt was drop-casted on top as HER catalyst. Measurements under 1 sun AM 1.5G illumination in 0.5 M H_2SO_4 with Ag/AgCl as reference and Pt as counter electrode at 0 V vs RHE.

defects or cracks due to thermal stress should be taken into account for an industrial-scale production.

Once the deposition temperature has been determined, to check the variations in the kesterite layer properties due to thermal treatment at 200 °C during 18 h, we compared the photovoltaic $I(V)$ curves of as-fabricated CZTSe solar cell (CZTSe with no TiO_2 layer), an identical solar cell without TiO_2 layer after an 18 h postannealing treatment at 200 °C and after the ALD TiO_2 deposition at 200 °C lasting 18 h (Figure 6). We can see the overall cell performance is enhanced with the thermal treatment, with a 49 mV and 1 $\text{mA}\cdot\text{cm}^{-2}$ increase in the open-circuit potential (V_{OC}) and the short-circuit current density (J_{sc}), respectively. The thermal treatment also reduced the series resistance (R_s) and enhanced the shunt resistance (R_{sh}). This enhancement in the heterojunction performance has been attributed by Neuschitzer et al.⁵⁷ to a slight Cu depletion taking place mainly in the grain boundaries and to a Zn enrichment of the CZTSe absorber surface, together with an increase of the Cu content inside the CdS layer. In our case, the top TiO_2 coating layer introduces extra resistance up to 3.7 Ω and lowers by 2.7 $\text{mA}\cdot\text{cm}^{-2}$ the short-circuit current density (together with significantly lowering the shunt resistance), slightly reducing the fill factor of the cell. All these results are summarized in Table 2.

It is plausible to consider that the thermal effects on the solar cell heterojunction are similar both for ALD TiO_2 deposition

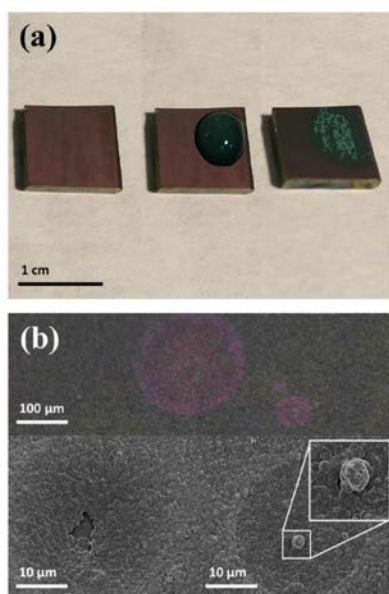


Figure 5. (a) Left to right: a CZTSe device before, during, and after depositing a droplet of 0.5 M H₂SO₄ electrolyte, completely etching the upper layers in a 1 min experiment. (b) Visual (top) and SEM (down) images of a photocathode after 1 h stability at 0 V vs RHE.

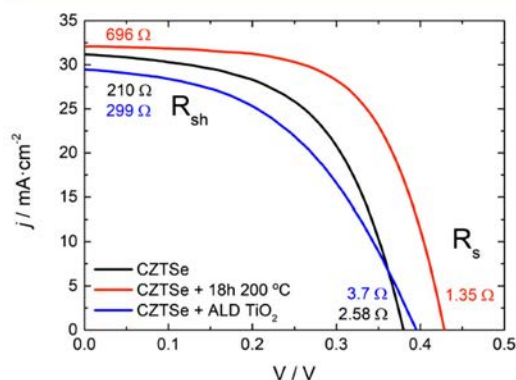


Figure 6. $J(V)$ curve of an as-finished (black) CZTSe solar cell after an 18 h annealing process inside the ALD (red) and with a deposited protective layer of ALD-TiO₂ (blue).

Table 2. Open-Circuit Potential, Short-Circuit Current Density, Total Series Resistance, and Shunt Resistance of as-Finished CZTSe Solar Cells after an 18 h Annealing Process or after the Deposition of 3300 Cycles of TiO₂ by ALD

	V_{OC} (mV)	J_{sc} (mA·cm ⁻²)	$R_{s, total}$ (Ω)	R_{sh} (Ω)
CZTSe	379	31.1	2.58	210
CZTSe + 18 h	428	32.1	1.35	696
CZTSe + ALD	394	29.4	3.7	299

and by the equivalent time and temperature treatment with no deposition. Then, it is possible to estimate the resistance

introduced by the protective layer (TiO₂) as the difference between the series resistance after the two processes, which is 2.35 Ω. The short-circuit current loss can be attributed to nonoptimal antireflective coating by the introduction of the TiO₂ layer. The effect of TiO₂ protective layers on extra series resistance (2.35 Ω) and incident light transmittance (92%) are in agreement with the previous results found on silicon.³¹

Contribution of the photovoltaic and electrochemical components to the overall photoelectrochemical system.

As this TiO₂-introduced layer plays a role as intermediate layer between photon absorption and electrochemical charge transfer, it is highly interesting to identify the contribution of each component on the overall photoelectrochemical performance. Some authors have performed similar analyses;^{16,47} however, for photocathodes requiring protective layers, it is highly interesting to identify its role. By subtracting the photovoltaic $J(V)$ curve of a device coated with TiO₂ to the PEC curve in 0.5 M H₂SO₄, we can isolate the deposited HER catalyst's behavior and deduce its Tafel slope (Figure 7a). To perform this calculation, we assumed the electrical circuit model presented in Figure 7b and considered the voltage drop of each component to depend on the current. We drop-casted

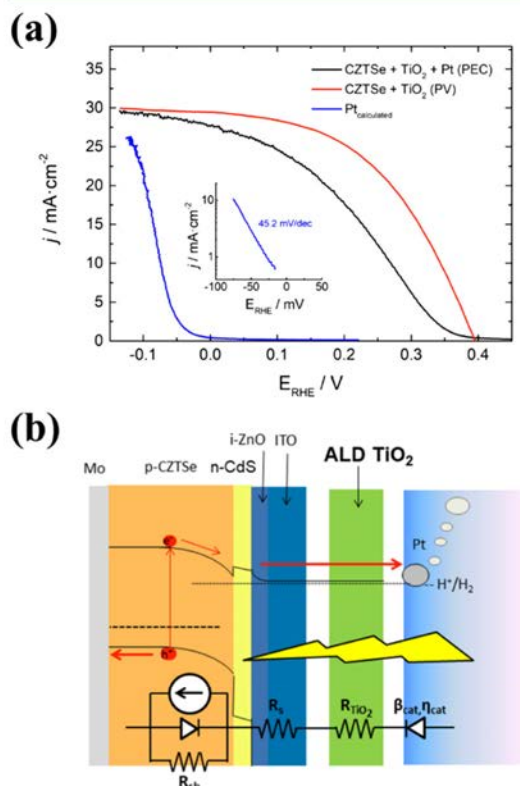


Figure 7. (a) Graph combining a polarization curve of a CZTSe PEC device, TiO₂ protected and Pt decorated in a 3-electrode cell, with 0.5 M H₂SO₄ electrolyte, Ag/AgCl as the reference electrode, and Pt as the counter electrode, corrected to RHE (black), $J(V)$ curve of a CZTSe solar cell TiO₂ protected (red), and the difference between black and red curves (blue). (b) Scheme of the complete PEC device.

platinum on top of the TiO₂ protective layer and compared the photoelectrochemical performance, obtaining a 28 mV overpotential (η_{cat}) at 1 mA·cm⁻² and a Tafel slope (β_{cat}) of 45.2 mV·dec⁻¹, which is in the range of 33–51 mV·dec⁻¹ found in the literature for platinum HER catalysts in 0.5 M H₂SO₄.^{58–60} Following this independent-component approach, it is possible to separate the contribution of each element to the final performance of the PEC device, proving that the electrochemical performance is maintained and photovoltaic characteristics are only partially affected, having a few ohms extra resistance due to the introduced anticorrosion TiO₂ layer.

Band Gap Modification. To maximize the coordination between a photocathode and a photoanode in a tandem configuration, it is important to match the maximum output of each component. Thanks to the possibility to modify the sulfur/selenium composition of the kesterite photoabsorber, we were able to fabricate solar cells with 1, 1.12, and 1.5 eV band gaps (Figure 8a). It is important to note that the state-of-the-art kesterite solar cells outperform the ones used in this work with efficiencies over 11%, thanks to a better fill factor and short-circuit currents up to 35 mA·cm⁻².⁶¹ Similar to the previous

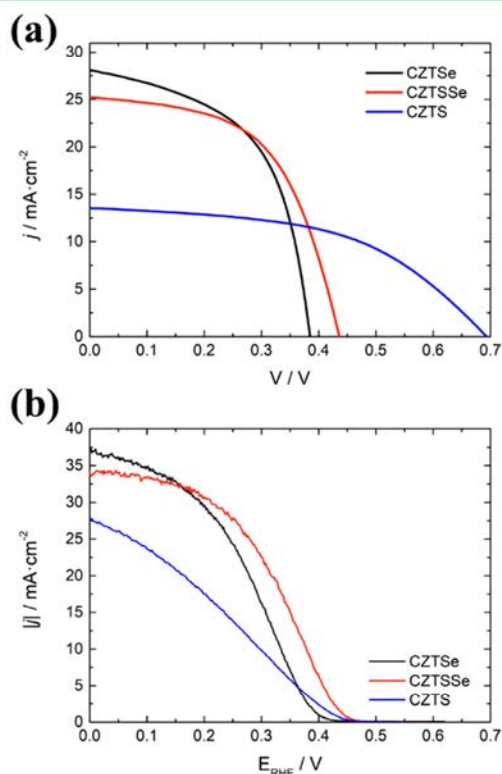


Figure 8. (a) $J(V)$ curves of CZTSe (black), CZTSSe (red), and CZTS (blue) solar cells as synthesized and (b) polarization curves of the same solar cells protected with TiO₂ layers grown at 200 °C and Pt drop-casted on top as HER catalyst. All the measurements were performed under 1 sun AM 1.5G illumination and photoelectrochemical polarization curves in 0.5 M H₂SO₄ with Ag/AgCl as the reference electrode and Pt as the counter electrode.

electrode, our solar cells were further ALD-TiO₂ protected, Pt deposited, and measured in 0.5 M H₂SO₄ (pH = 0.3). The resulting photocathodes showed conversion efficiencies of 6.2, 7, and 3.6% for CZTSe, CZTSSe, and CZTS (Figure 8b), respectively.

Analyzing the polarization curves, we can observe that CZTSe and CZTSSe photoabsorber-based photocathodes have similar fill factors to the photovoltaic $J(V)$ curves. The improvement in the CZTSe and CZTSSe photocathodes compared to the original photovoltaic cell is caused, as it was presented above, by the formation of the widely known copper depletion region in the kesterite surface.⁵⁷ Meanwhile, the sulfur-based cell (CZTS) has a significant loss of photovoltage.

To investigate why the sulfur-based samples are sensitive to the ALD process, the CZTS PV devices have been analyzed by Raman spectroscopy before and after the TiO₂ deposition at 200 °C under nonresonant (532 nm) and preresonant (785 nm) excitation conditions (Figure 9). The analysis of the

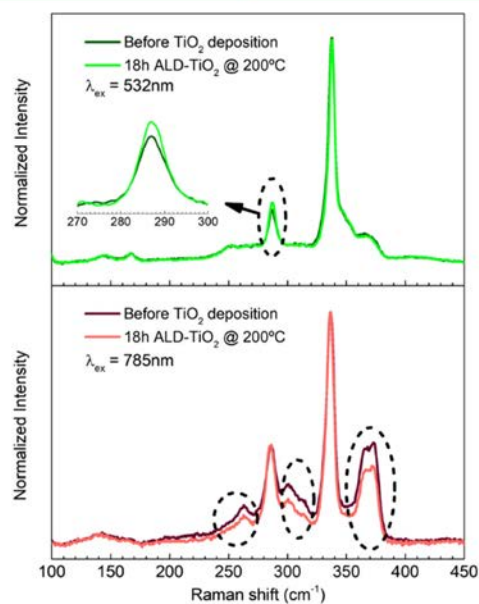


Figure 9. Raman spectra of a CZTS finished solar cell before ALD deposition (dark green and red) and after 3300 cycles of TiO₂ ALD at 200 °C (bright green and red) using a 532 nm (top) and 785 nm (bottom) laser light.

spectra acquired under the 785 nm shows clear differences between before and after the TiO₂ deposition. Similar changes have been attributed by Scragg et al.⁶² to the reordering of the Cu and Zn in the kesterite structure. The comparison of the Raman spectra of the CZTS devices before and after the TiO₂ deposition suggests the improvement of the crystal quality by the reduction of the Cu_{Zn} and Zn_{Cu} antisite defects.⁶² On the other hand, the analysis under 532 nm excitation wavelength also detects small variations in the Raman spectra features: changes in both FWHM of the main A' mode (337 cm⁻¹) and intensity of the 278 cm⁻¹ peak. The reduction of the FWHM is a clear indicator of the improvement of the CZTS crystal quality,⁶³ whereas the increase in the intensity of the 278 cm⁻¹

peak requires a more detailed discussion. Similar peak modifications under postannealing treatments have been analyzed for the selenium-based kesterite (CZTSe) in other works,^{64,65} and the increase in the intensity in the second main peak observed at 175 cm^{-1} has been reported as the reduction of the V_{Cu} defects concentration. This change can be observed after a soft annealing process (<250 °C), as it has been reported by Dimitrievska et al.⁵⁴ Additionally, the intensity changes in the peak linked with the V_{Cu} concentration are correlated with the modification of the V_{OC} of the PV devices.^{54,66} In the CZTS case, the peak observed at 278 cm^{-1} is assigned to the same origin as the CZTSe peaks at 175 cm^{-1} ; therefore, the interpretation of the changes in the 175 cm^{-1} peak in the CZTSe to the 278 cm^{-1} peak of the CZTS spectra can be extended, attributing the changes in this peak to a variation in the V_{Cu} defect concentration. All these changes observed in the V_{Cu} defect concentration are variations from the optimized solar cell and have been correlated to significant V_{OC} variations,⁶⁶ like we can see reflected in the protected CZTS photocathodes onset potential loss (Figure 7a).

To sum up the Raman characterization, the TiO_2 deposition by ALD process on the CZTS device at 200 °C induces a reduction in the V_{Cu} defects concentration and a reduction in the disorder induced by the Cu_{Zn} and Zn_{Cu} antisites, which promotes an improvement of the crystal quality (reduction of the FWHM of the dominant Raman peak). These effects have a strong impact on the electrical properties of the material modifying the doping (defects) and the electronic energy levels among other effects, and can contribute significantly to lowering the V_{OC} and, thus, the degradation of the PV device performance after the TiO_2 deposition. Pure-sulfur samples being more affected by the 200 °C temperature process have not been studied, but point in the direction that the efficiency vs temperature plateau between 175 and 250 °C presented for selenium-based CZTSe in Figure 2 of Dimitrievska et al.⁵⁴ is expected at similar temperatures. This effect needs to be corroborated and is currently under investigation, but is out of the scope of this work.

To date, very few works have deployed a heterojunction approach using these chalcogenide-based materials capable of achieving high photocurrents densities,⁴⁵ and most of them have used buffered neutral or alkaline pH electrolytes to avoid corrosion.^{42,67} To our knowledge, this is the first time when a protected kesterite-based heterojunction has been used as a photocathode and measured in acidic conditions to achieve over 1 h stability with no detected degradation, with currents comparable to photovoltaic productivities. The measured photocurrent at 0 V vs RHE is the highest reported to date, and the HC-STH efficiency reached 7%, being among the largest presented for kesterite-based photocathodes.^{43–45,68,69} Likewise, according to the analysis performed on individual elements, it is plausible to think that as the kesterite solar cell efficiency increases in the near future, so will the PEC efficiency, even being feasible to overcome the 10% efficiency barrier.

CONCLUSIONS

We have demonstrated the possibility to implement earth-abundant CZTS/Se-based kesterite thin-film photovoltaic cells into photoelectrochemistry through protection with chemically stable, transparent, and conductive TiO_2 layers. ALD has been used to deposit crystalline protective layers at lower temperatures (200 °C) than other methods, such as DC sputtering

(normally 400 °C). Low-temperature synthesis has been proven to be mandatory to avoid defect redistribution and recrystallization in the CdS but also the TCO layers, which degrades the p–n heterojunction and final device performance. By tuning the band gap through modification of the S/Se stoichiometry and with TiO_2 protective layers and Pt as HER catalyst, we were able to obtain up to 7% HC-STH conversion efficiencies. Specifically, the CZTS/Se photovoltaic cells are limited to thermal treatments up to 200 °C, which still enhances its efficiency through defects reorganization. For devices with sulfur-based kesterite photoabsorbers (CZTS), it was not possible to avoid a significant efficiency loss due to nonoptimal thermal treatment even with treatments at 200 °C and, thus, less efficient defect distribution, meanwhile maintaining crystalline TiO_2 deposition temperatures, as PV device is optimized for shorter thermal treatments. However, it has been pointed out that the introduction of a partial percentage of sulfur slightly improves the photovoltaic and the photoelectrochemical characteristics.

A series circuit model has been applied to separately analyze the role of each component: the photovoltaic part, the protective layer, and the HER catalyst. The series resistance and transmittance losses from the TiO_2 protective layer have been identified to represent roughly 2.35 Ω and 8% loss of photocurrent, which can be attributed not only to TiO_2 absorbance but also to changes in thin film reflectivity. Individually measuring the inner elements allowed us to isolate the catalyst behavior, overpotential, and Tafel slope, allowing easy calculations of a final Pt-free device with other HER catalysts.

Future studies should be directed toward achieving appropriate conversion of sulfur-based CZTS solar cells into photoelectrodes and to analyze other S/Se stoichiometries and their synergistic influence to facilitate the band gap adaptation for tandem configuration of PEC cells, designed both as photoanodes and photocathodes.

AUTHOR INFORMATION

Corresponding Authors

*E-mail: cros@irec.cat (C.R.).

*E-mail: tandreu@irec.cat (T.A.).

ORCID

Carles Ros: 0000-0002-9148-2767

Teresa Andreu: 0000-0002-2804-4545

Sergio Giraldo: 0000-0003-4881-5041

Notes

The authors declare no competing financial interest.

ACKNOWLEDGMENTS

Authors thank Generalitat de Catalunya for financial support through the CERCA Programme, M2E (2014SGR1638), and XARMAE network. IREC also acknowledges the support by the European Regional Development Funds (ERDF, FEDER) and by MINECO coordinated projects TNT-FUELS, MAT2014-59961-C2, ENE2014-56237-C4-1-R, and ENE2016-80788-C5-5-R. C.R. also thanks MINECO for his FPI grant (BES-2015-071618) and S.G. for his FPI grant (BES-2014-068533).

REFERENCES

- (1) Fujishima, A.; Honda, K. Electrochemical Photolysis of Water at a Semiconductor Electrode. *Nature* 1972, 238, 37–38.

- (2) Wang, G.; Wang, H.; Ling, Y.; Tang, Y.; Yang, X.; Fitzmorris, R. C.; Wang, C.; Zhang, J. Z.; Li, Y. Hydrogen-Treated TiO₂ Nanowire Arrays for Photoelectrochemical Water Splitting. *Nano Lett.* **2011**, *11*, 3026–3033.
- (3) Fàbrega, C.; Monllor-Satoca, D.; Ampudia, S.; Parra, A.; Andreu, T.; Morante, J. R. Tuning the Fermi Level and the Kinetics of Surface States of TiO₂ Nanorods by Means of Ammonia Treatments. *J. Phys. Chem. C* **2013**, *117*, 20517–20524.
- (4) Su, J.; Guo, L.; Bao, N.; Grimes, C. A. Nanostructured WO₃/BiVO₄ Heterojunction Films for Efficient Photoelectrochemical Water Splitting. *Nano Lett.* **2011**, *11*, 1928–1933.
- (5) Sivula, K.; Le Formal, F.; Grätzel, M. WO₃–Fe₂O₃ Photoanodes for Water Splitting: A Host Scaffold, Guest Absorber Approach. *Chem. Mater.* **2009**, *21*, 2862–2867.
- (6) Yang, X.; Liu, R.; Du, C.; Dai, P.; Zheng, Z.; Wang, D. Improving Hematite-Based Photoelectrochemical Water Splitting with Ultrathin TiO₂ by Atomic Layer Deposition. *ACS Appl. Mater. Interfaces* **2014**, *6*, 12005–12011.
- (7) Murcia-López, S.; Fàbrega, C.; Monllor-Satoca, D.; Hernández-Alonso, M. D.; Penelas-Pérez, G.; Morata, A.; Morante, J. R.; Andreu, T. Tailoring Multilayered BiVO₄ Photoanodes by Pulsed Laser Deposition for Water Splitting. *ACS Appl. Mater. Interfaces* **2016**, *8*, 4076–4085.
- (8) Polman, A.; Knight, M.; Garnett, E. C.; Ehrler, B.; Sinke, W. C. Photovoltaic Materials – Present Efficiencies and Future Challenges. *Science* **2016**, *352*, No. aad4424.
- (9) Katagiri, H. Cu₂ZnSnS₄ Thin Film Solar Cells. *Thin Solid Films* **2005**, *480–481*, 426–432.
- (10) Giraldo, S.; Neuschitzer, M.; Thersleff, T.; López-Marino, S.; Sánchez, Y.; Xie, H.; Colina, M.; Placidi, M.; Pistor, P.; Izquierdo-Roca, V.; Leifer, K.; Pérez-Rodríguez, A.; Saucedo, E. Large Efficiency Improvement in Cu₂ZnSnSe₄ Solar Cells by Introducing a Superficial Ge Nanolayer. *Adv. Energy Mater.* **2015**, *5*, No. 1501070.
- (11) Repins, I.; Contreras, M. A.; Egaas, B.; DeHart, C.; Scharf, J.; Perkins, C. L.; To, B.; Noufi, R. 19.9%-Efficient ZnO/CdS/CuInGaSe₂ Solar Cell with 81.2% Fill Factor. *Prog. Photovoltaics* **2008**, *16*, 235–239.
- (12) Yin, G.; Knight, M. W.; van Lare, M.-C.; Solà Garcia, M. M.; Polman, A.; Schmid, M. Optoelectronic Enhancement of Ultrathin CuIn 1-X Ga X Se 2 Solar Cells by Nanophotonic Contacts. *Adv. Opt. Mater.* **2017**, No. 1600637.
- (13) Insignares-Cuello, C.; Oliva, F.; Neuschitzer, M.; Fontané, X.; Broussillou, C.; Gouillard De Monsabert, T.; Saucedo, E.; Ruiz, C. M.; Pérez-Rodríguez, A.; Izquierdo-Roca, V. Advanced Characterization of Electrodeposition-Based High Efficiency Solar Cells: Non-Destructive Raman Scattering Quantitative Assessment of the Anion Chemical Composition in Cu(In,Ga)(S,Se)₂ Absorbers. *Sol. Energy Mater. Sol. Cells* **2015**, *143*, 212–217.
- (14) Neuschitzer, M.; Sanchez, Y.; López-Marino, S.; Xie, H.; Fairbrother, A.; Placidi, M.; Haass, S.; Izquierdo-Roca, V.; Perez-Rodríguez, A.; Saucedo, E. Optimization of CdS Buffer Layer for High-Performance Cu₂ZnSnSe₄ Solar Cells and the Effects of Light Soaking: Elimination of Crossover and Red Kink. *Prog. Photovoltaics* **2015**, *23*, 1660–1667.
- (15) Kaur, K.; Kumar, N.; Kumar, M. Strategic Review of Interface Carrier Recombination in Earth Abundant Cu–Zn–Sn–S–Se Solar Cells: Current Challenges and Future Prospects. *J. Mater. Chem. A* **2017**, *5*, 3069–3090.
- (16) Fairbrother, A.; Fontané, X.; Izquierdo-Roca, V.; Espindola-Rodríguez, M.; López-Marino, S.; Placidi, M.; López-García, J.; Pérez-Rodríguez, A.; Saucedo, E. Single-Step Sulfo-Selenization Method to Synthesize Cu₂ZnSn(SySe_{1-y})₄ Absorbers from Metallic Stack Precursors. *ChemPhysChem* **2013**, *14*, 1836–1843.
- (17) Hu, S.; Xiang, C.; Haussener, S.; Berger, A. D.; Lewis, N. S. An Analysis of the Optimal Band Gaps of Light Absorbers in Integrated Tandem Photoelectrochemical Water-Splitting Systems. *Energy Environ. Sci.* **2013**, *6*, 2984–2993.
- (18) Kumagai, H.; Minegishi, T.; Sato, N.; Yamada, T.; Kubota, J.; Domen, K. Efficient Solar Hydrogen Production from Neutral Electrolytes Using Surface-Modified Cu(In,Ga)Se₂ Photocathodes. *J. Mater. Chem. A* **2015**, *3*, 8300–8307.
- (19) Ros, C.; Andreu, T.; Giraldo, S.; Sánchez, Y.; Morante, J. R. Conformal Chalcopyrite Based Photocathode for Solar Refinery Applications. *Sol. Energy Mater. Sol. Cells* **2016**, *158*, 184–188.
- (20) Ahmed, S.; Reuter, K. B.; Gunawan, O.; Guo, L.; Romankiw, L. T.; Deligianni, H. A High Efficiency Electrodeposited Cu₂ZnSnS₄ Solar Cell. *Adv. Energy Mater.* **2012**, *2*, 253–259.
- (21) Rand, B. P.; Genoe, J.; Heremans, P.; Poortmans, J. Solar Cells Utilizing Small Molecular Weight Organic Semiconductors. *Prog. Photovoltaics* **2007**, *15*, 659–676.
- (22) Todorov, T. K.; Reuter, K. B.; Mitzi, D. B. High-Efficiency Solar Cell with Earth-Abundant Liquid-Processed Absorber. *Adv. Mater.* **2010**, *22*, E156–E159.
- (23) Schorr, S. The Crystal Structure of Kesterite Type Compounds: A Neutron and X-Ray Diffraction Study. *Sol. Energy Mater. Sol. Cells* **2011**, *95*, 1482–1488.
- (24) Chen, S.; Walsh, A.; Gong, X. G.; Wei, S. H. Classification of Lattice Defects in the Kesterite Cu₂ZnSnS₄ and Cu₂ZnSnSe₄ Earth-Abundant Solar Cell Absorbers. *Adv. Mater.* **2013**, *25*, 1522–1539.
- (25) Li, G.; Blake, G. R.; Palstra, T. T. M. Vacancies in Functional Materials for Clean Energy Storage and Harvesting: The Perfect Imperfection. *Chem. Soc. Rev.* **2017**, *46*, 1693–1706.
- (26) Bishop, D. M.; McCandless, B.; Gershon, T.; Lloyd, M. A.; Haight, R.; Birkmire, R. Modification of Defects and Potential Fluctuations in Slow-Cooled and Quenched Cu₂ZnSnSe₄ Single Crystals. *J. Appl. Phys.* **2017**, *121*, No. 065704.
- (27) Bosson, C. J.; Birch, M. T.; Halliday, D. P.; Knight, K. S.; Gibbs, A. S.; Hatton, P. D. Cation Disorder and Phase Transitions in the Structurally Complex Solar Cell Material Cu₂ZnSnS₄. *J. Mater. Chem. A* **2017**, *5*, 16672–16680.
- (28) Bae, D.; Seger, B.; Vesborg, P. C. K.; Hansen, O.; Chorkendorff, I. Strategies for Stable Water Splitting via Protected Photoelectrodes. *Chem. Soc. Rev.* **2017**, *46*, 1933–1954.
- (29) Lichterman, M. F.; Sun, K.; Hu, S.; Zhou, X.; McDowell, M. T.; Shaner, M. R.; Richter, M. H.; Crumlin, E. J.; Carim, A. I.; Saadi, F. H.; Brunschwig, B. S.; Lewis, N. S. Protection of Inorganic Semiconductors for Sustained, Efficient Photoelectrochemical Water Oxidation. *Catal. Today* **2016**, *262*, 11–23.
- (30) Scheuermann, A. G.; McIntyre, P. C. Atomic Layer Deposited Corrosion Protection: A Path to Stable and Efficient Photoelectrochemical Cells. *J. Phys. Chem. Lett.* **2016**, *7*, 2867–2878.
- (31) Ros, C.; Andreu, T.; Hernández-Alonso, M. D.; Penelas-Pérez, G.; Arbiol, J.; Morante, J. R. Charge Transfer Characterization of ALD-Grown TiO₂ Protective Layers in Silicon Photocathodes. *ACS Appl. Mater. Interfaces* **2017**, *9*, 17932–17941.
- (32) Bhola, S. M.; Mishra, B. Effect of Ph on the Electrochemical Properties of Oxides Formed over β-Ti-15Mo and Mixed Ti-6Al-4v Alloys. *Int. J. Electrochem. Sci.* **2013**, *8*, 7075–7087.
- (33) Chen, S.; Wang, L. W. Thermodynamic Oxidation and Reduction Potentials of Photocatalytic Semiconductors in Aqueous Solution. *Chem. Mater.* **2012**, *24*, 3659–3666.
- (34) Hu, S.; Shaner, M. R.; Beardslee, J. A.; Lichterman, M.; Brunschwig, B. S.; Lewis, N. S. Amorphous TiO₂ Coatings Stabilize Si, GaAs, and GaP Photoanodes for Efficient Water Oxidation. *Science* **2014**, *344*, 1005–1009.
- (35) Seger, B.; Pedersen, T.; Laursen, A. B.; Vesborg, P. C. K.; Hansen, O.; Chorkendorff, I. Using TiO₂ as a Conductive Protective Layer for Photocathodic H₂ Evolution. *J. Am. Chem. Soc.* **2013**, *135*, 1057–1064.
- (36) Paracchino, A.; Laporte, V.; Sivula, K.; Grätzel, M.; Thimsen, E. Highly Active Oxide Photocathode for Photoelectrochemical Water Reduction. *Nat. Mater.* **2011**, *10*, 456–461.
- (37) Wu, Y.; Yang, X.; Chen, H.; Zhang, K.; Qin, C.; Liu, J.; Peng, W.; Islam, A.; Bi, E.; Ye, F.; Yin, M.; Zhang, P.; Han, L. Highly Compact TiO₂ Layer for Efficient Hole-Blocking in Perovskite Solar Cells. *Appl. Phys. Express* **2014**, *7*, No. 052301.

- (38) Aarik, J.; Aidla, A.; Uustare, T.; Sammelselg, V. Morphology and Structure of TiO₂ Thin Films Grown by Atomic Layer Deposition. *J. Cryst. Growth* **1995**, *148*, 268–275.
- (39) Li, W.; Ni, C.; Lin, H.; Huang, C. P.; Shah, S. I. Size Dependence of Thermal Stability of TiO₂ Nanoparticles. *J. Appl. Phys.* **2004**, *96*, 6663.
- (40) Seger, B.; Tilley, D. S.; Pedersen, T.; Vesborg, P. C. K.; Hansen, O.; Grätzel, M.; Chorkendorff, I. Silicon Protected with Atomic Layer Deposited TiO₂: Durability Studies of Photocathodic H₂ Evolution. *RSC Adv.* **2013**, *3*, 25902–25907.
- (41) Busani, T.; Devine, R. A. B. Dielectric and Infrared Properties of TiO₂ Films Containing Anatase and Rutile. *Semicond. Sci. Technol.* **2005**, *20*, 870–875.
- (42) Chen, Y.; Feng, X.; Liu, M.; Su, J.; Shen, S. Towards Efficient Solar-to-Hydrogen Conversion: Fundamentals and Recent Progress in Copper-Based Chalcogenide Photocathodes. *Nanophotonics* **2016**, *5*, 524–547.
- (43) Jiang, F.; Gunawan, Harada, T.; Kuang, Y.; Minegishi, T.; Domen, K.; Ikeda, S. Pt/In₂S₃/CdS/Cu₂ZnSnS₄ Thin Film as an Efficient and Stable Photocathode for Water Reduction under Sunlight Radiation. *J. Am. Chem. Soc.* **2015**, *137*, 13691–13697.
- (44) Rovelli, L.; Tilley, S. D.; Sivula, K. Optimization and Stabilization of Electrodeposited Cu₂ZnSnS₄ Photocathodes for Solar Water Reduction. *ACS Appl. Mater. Interfaces* **2013**, *5*, 8018–8024.
- (45) Yokoyama, D.; Minegishi, T.; Jimbo, K.; Hisatomi, T.; Ma, G.; Katayama, M.; Kubota, J.; Katagiri, H.; Domen, K. H₂ Evolution from Water on Modified Cu₂ZnSnS₄ Photoelectrode under Solar Light. *Appl. Phys. Express* **2010**, *3*, No. 101202.
- (46) Rocheleau, R.; Miller, E. L. Photoelectrochemical Production of Hydrogen: Engineering Loss Analysis. *Int. J. Hydrogen Energy* **1997**, *22*, 771–782.
- (47) Becker, J. P.; Urbain, F.; Smirnov, V.; Rau, U.; Ziegler, J.; Kaiser, B.; Jaegermann, W.; Finger, F. Modeling and Practical Realization of Thin Film Silicon-Based Integrated Solar Water Splitting Devices. *Phys. Status Solidi A* **2016**, *213*, 1738–1746.
- (48) Wang, W.; Winkler, M. T.; Gunawan, O.; Gokmen, T.; Todorov, T. K.; Zhu, Y.; Mitzi, D. B. Device Characteristics of CZTSSe Thin-Film Solar Cells with 12.6% Efficiency. *Adv. Energy Mater.* **2014**, *4*, No. 1301465.
- (49) Xie, H.; López-Marino, S.; Olar, T.; Sánchez, Y.; Neuschitzer, M.; Oliva, F.; Giraldo, S.; Izquierdo-Roca, V.; Lauermann, I.; Pérez-Rodríguez, A.; Saucedo, E. Impact of Na Dynamics at the Cu₂ZnSn(S,Se)₄/CdS Interface during Post Low Temperature Treatment of Absorbers. *ACS Appl. Mater. Interfaces* **2016**, *8*, 5017–5024.
- (50) Xie, H.; Sánchez, Y.; López-Marino, S.; Espindola-Rodríguez, M.; Neuschitzer, M.; Sylla, D.; Fairbrother, A.; Izquierdo-Roca, V.; Pérez-Rodríguez, A.; Saucedo, E. Impact of Sn (S, Se) Secondary Phases in Cu₂ZnSn(S, Se)₄ Solar Cells: A Chemical Route for Their Selective Removal and Absorber Surface Passivation. *ACS Appl. Mater. Interfaces* **2014**, *6*, 12744–12751.
- (51) López-Marino, S.; Sánchez, Y.; Placidi, M.; Fairbrother, A.; Espindola-Rodríguez, M.; Fontané, X.; Izquierdo-Roca, V.; López-García, J.; Calvo-Barrio, L.; Pérez-Rodríguez, A.; Saucedo, E. ZnSe Etching of Zn-Rich Cu₂ZnSnSe₄: An Oxidation Route for Improved Solar-Cell Efficiency. *Chem. - Eur. J.* **2013**, *19*, 14814–14822.
- (52) Mäkeläinen, V.; Leskelä, M.; Ritala, M.; Puurunen, R. L. Crystallinity of Inorganic Films Grown by Atomic Layer Deposition: Overview and General Trends. *J. Appl. Phys.* **2013**, *113*, No. 021301.
- (53) Theivasanthi, T.; Alagar, M. Titanium Dioxide (TiO₂) Nanoparticles XRD Analyses: An Insight, 2013, arXiv:1307.1091. arXiv.org e-Print archive. <https://arxiv.org/abs/1307.1091> (accessed Jul 2, 2013).
- (54) Dimitrievska, M.; Giraldo, S.; Pistor, P.; Saucedo, E.; Pérez-Rodríguez, A.; Izquierdo-Roca, V. Raman Scattering Analysis of the Surface Chemistry of Kesterites: Impact of Post-Deposition Annealing and Cu/Zn Reordering on Solar Cell Performance. *Sol. Energy Mater. Sol. Cells* **2016**, *157*, 462–467.
- (55) Scragg, J. J. S.; Choubrac, L.; Lafond, A.; Ericson, T.; Platzer-Björkman, C. A Low-Temperature Order-Disorder Transition in Cu₂ZnSnS₄ Thin Films. *Appl. Phys. Lett.* **2014**, *41911*, 1–5.
- (56) Walker, P.; Tarn, W. H. *CRC Handbook of Metal Etchants*; CRC Press, 1990.
- (57) Neuschitzer, M.; Sanchez, Y.; Olar, T.; Thersleff, T.; Lopez-Marino, S.; Oliva, F.; Espindola-Rodríguez, M.; Xie, H.; Placidi, M.; Izquierdo-Roca, V.; Lauermann, I.; Leifer, K.; Perez-Rodríguez, A.; Saucedo, E. Complex Surface Chemistry of Kesterites: Cu/Zn Reordering after Low Temperature Postdeposition Annealing and Its Role in High Performance Devices. *Chem. Mater.* **2015**, *27*, 5279–5287.
- (58) Dešić, M. N.; Popović, M. M.; Obradović, M. D.; Vračar, L. M.; Grgur, B. N. Study of Gold-Platinum and Platinum-Gold Surface Modification and Its Influence on Hydrogen Evolution and Oxygen Reduction. *J. Serb. Chem. Soc.* **2005**, *70*, 231–242.
- (59) Liu, C.; Zhou, D.; Zhou, J.; Xie, Z.; Xia, Y. Synthesis and Characterization of Tungsten Carbide and Application to Electro-catalytic Hydrogen Evolution. *RSC Adv.* **2016**, *6*, 76307–76311.
- (60) Tominaka, S.; Wu, C.-W.; Momma, T.; Kuroda, K.; Osaka, T. Perpendicular Mesoporous Pt Thin Films: Electrodeposition from Titania Nanopillars and Their Electrochemical Properties. *Chem. Commun.* **2008**, 2888–2890.
- (61) Todorov, T. K.; Tang, J.; Bag, S.; Gunawan, O.; Gokmen, T.; Zhu, Y.; Mitzi, D. B. Beyond 11% Efficiency: Characteristics of State-of-the-Art Cu₂ZnSn(S,Se)₄ Solar Cells. *Adv. Energy Mater.* **2013**, *3*, 34–38.
- (62) Scragg, J. J. S.; Choubrac, L.; Lafond, A.; Ericson, T.; Platzer-Björkman, C. A Low-Temperature Order-Disorder Transition in Cu₂ZnSnS₄ Thin Films. *Appl. Phys. Lett.* **2014**, *104*, No. 041911.
- (63) Dimitrievska, M.; Fairbrother, A.; Pérez-Rodríguez, A.; Saucedo, E.; Izquierdo-Roca, V. Raman Scattering Crystalline Assessment of Polycrystalline Cu₂ZnSnS₄ Thin Films for Sustainable Photovoltaic Technologies: Phonon Confinement Model. *Acta Mater.* **2014**, *70*, 272–280.
- (64) Dimitrievska, M.; Fairbrother, A.; Saucedo, E.; Pérez-Rodríguez, A.; Izquierdo-Roca, V. Influence of Compositionally Induced Defects on the Vibrational Properties of Device Grade Cu₂ZnSnSe₄ Absorbers for Kesterite Based Solar Cells. *Appl. Phys. Lett.* **2015**, *106*, No. 073903.
- (65) Oliva, F.; Arqués Farré, L.; Giraldo, S.; Dimitrievska, M.; Pistor, P.; Martínez-Pérez, A.; Calvo-Barrio, L.; Saucedo, E.; Pérez-Rodríguez, A.; Izquierdo-Roca, V. In *Raman Scattering Assessment of the Point Defects in Kesterite Semiconductors: UV Resonant Raman Characterization for Advanced Photovoltaics*, IEEE Proceedings; IEEE, 2017.
- (66) Dimitrievska, M.; Fairbrother, A.; Saucedo, E.; Pérez-Rodríguez, A.; Izquierdo-Roca, V. Secondary Phase and Cu Substitutional Defect Dynamics in Kesterite Solar Cells: Impact on Optoelectronic Properties. *Sol. Energy Mater. Sol. Cells* **2016**, *149*, 304–309.
- (67) Wang, J.; Yu, N.; Zhang, Y.; Zhu, Y.; Fu, L.; Zhang, P.; Gao, L.; Wu, Y. Synthesis and Performance of Cu₂ZnSnS₄ Semiconductor as Photocathode for Solar Water Splitting. *J. Alloys Compd.* **2016**, *688*, 923–932.
- (68) Wang, J.; Zhang, P.; Song, X.; Gao, L. Cu₂ZnSnS₄ Thin Films: Spin Coating Synthesis and Photoelectrochemistry. *RSC Adv.* **2014**, *4*, 21318.
- (69) Ma, G.; Minegishi, T.; Yokoyama, D.; Kubota, J.; Domen, K. Photoelectrochemical Hydrogen Production on Cu₂ZnSnS₄/4-Mesh Thin-Film Electrodes Prepared by Electroplating. *Chem. Phys. Lett.* **2011**, *501*, 619–622.

Chapter 5

*Conductivity and endurance of
protective layers in alkaline anodic
conditions*

In this chapter, focus is put into protective layers for photoanodes in alkaline electrolytes, more prone for the OER reaction. Silicon as photoabsorber has been previously studied and used as reference material in chapter 3 thanks to the high performance and not being affected by post-treatments at few hundred Celsius as they are fabricated at ~ 1000 °C¹. In addition, as was discussed in chapter 1 section 4, alkaline electrolytes corrode silicon with significant anisotropic etching dissolution, thus corrosion can be observed and used to characterize the protective capacity of the overlayers.

Silicon is a highly versatile semiconductor. A p-n junction designed so that the HER or OER are performed on its frontal side only requires inverting the n or p-type extrinsic doping order. By using n-type wafers with a p⁺ top region, holes are conducted to the electrolyte. Protective layers thus should be favorable to hole conduction and energetically aligned to avoid forming any detrimental barrier with p⁺-Si or the OER electrocatalyst. Although, this is not the only way¹.

Two strategies were followed in this article, both using ALD thanks to its minimal-pinholes, layer thickness control and low deposition temperatures, among others. The first one is using TiO₂, an n-type semiconductor proven with some works to be highly conductive for anodic current, and with scientific debate on which is the specific conductivity mechanism. NiFe-based catalysts will be used. The second one is based on NiO protective layers, a p-type semiconductor that forms, in contact with alkaline electrolytes, favorable oxyhydroxides highly catalytic to the OER.

5.1. Insight into the degradation mechanisms of atomic layer deposited TiO₂ as photoanode protective layer

In the first article of this chapter, n-type TiO₂ as protective layer for silicon photoanodes in alkaline electrolytes is characterized. Two aspects are studied: first, the conductivity mechanism, considered mid-band gap states mediated hole conductivity through amorphous TiO₂ in some works² or conduction band electron transport in crystals in others¹, and the second is the stability of these oxygen-defective layers in highly oxidative electrolytes and potentials.

ALD wide temperature window is used to fabricate completely amorphous layers (deposited at 100 °C), and partially crystalline (150 °C) and fully crystalline ones (300 °C) on p⁺n-Si photoelectrodes and further 5 nm NiFe decorated. PEC measurements revealed strong correlation of performance and deposition temperature, with no photocurrent at 100 °C and significant photodiode saturation of >20 mA·cm⁻² at 300 °C (Figure 5.1a). HRTEM and Raman characterization revealed multicrystalline TiO₂ grains at already 150 °C deposition temperatures (Figure 5.2b), and c-AFM maps showed preferential conductivity regions only in the crystalline parts.

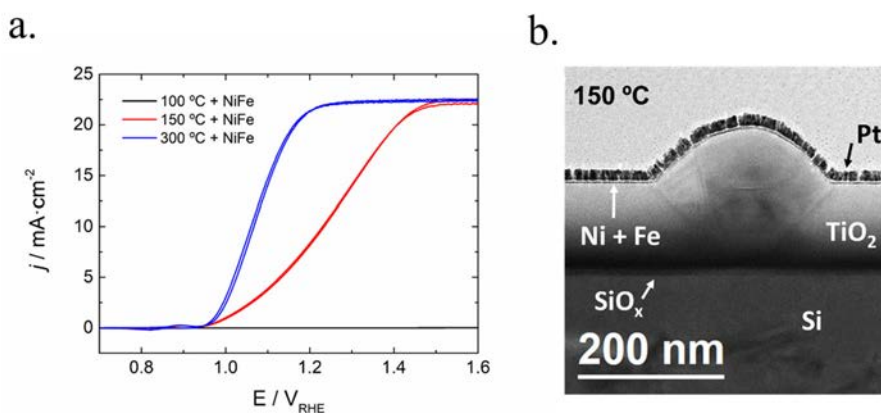


Figure 5.1. a) Cyclic voltammograms of p^+n -Si photoanodes protected with 100 nm TiO_2 layers grown at 100 °C, 150 °C and 300 °C, with 5 nm of nickel-iron thermally evaporated as OER catalyst. b) Cross section HRTEM image of a 150 °C grown TiO_2 layer, presenting a crystalline grain where several grain boundaries inside can be observed, embedded in an amorphous homogeneous TiO_2 film.

In the article a conductivity scheme is proposed, based on electron injection from the OER adaptive oxidized NiFeOOH catalyst into the conduction band of defective TiO_2 regions acting as preferential conductivity paths. ~ 2 nm SiO_2 detected by HRTEM, inherent of the fabrication process, would help unpinning TiO_2/p^+ -Si bands and achieving an ohmic recombining contact (Figure 5.2a).

Stability measurements presented significant logarithmic decay over 480 h, a possible sign of metal oxide self-limited oxidative passivation. Electrochemical impedance spectroscopy (EIS) measurements allowed for in-situ tracking of the electrical components affecting charge transfer (Figure 5.2b), and over-time increase of a solid-state depletion region attributed within the TiO_2 protective layer was observed. As TiO_2 conductivity highly depend on its n -type semiconductor behavior, given by structural defects and oxygen vacancies, it can be highly affected by the direct contact with oxidative electrolyte OH^- ions and OER potentials. Extra UV superimposed illumination was used to partially recover TiO_2 film conductivity, attributed to altering the density of states within the TiO_2 electronic structure. Persistent photoconductivity was observed, as the de-occupation of localized states will eventually be compensated and oxidized again.

These findings highlight the need to take in account the degradation mechanisms of TiO_2 in alkaline OER conditions.

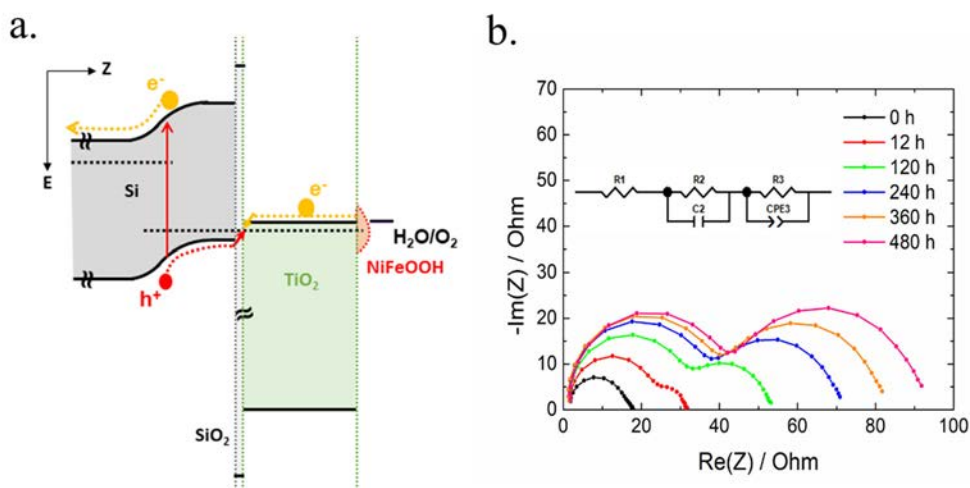


Figure 5.2. a) Band diagram of a p⁺n-Si photoanode, TiO₂ protected and with cycled Ni(Fe)OOH OER catalyst. b) Nyquist plot of the electrochemical impedance spectroscopy (EIS) data from a 300 °C TiO₂-protected photoanode obtained every 12 h under potentiostatic conditions at 1.8 V vs RHE. The inset shows the equivalent electric circuit used to fit the EIS data.

5.2. About degradation and regeneration mechanisms of NiO protective layers deposited by ALD on photoanodes.

In the second work included in this chapter ALD-grown NiO layers on silicon photoanodes have been studied. NiO was selected as a candidate, expected to be intrinsically stable to oxidation conditions as it is a p-type semiconductor material, caused by point defects such as cationic Ni²⁺ vacancies³. In addition, a nickel-based protective layer in contact with alkaline electrolytes is expected to form OER-favorable oxyhydroxides in the surface⁴, enhancing the catalysis kinetics and thus, not requiring any extra added catalyst.

ALD was selected as deposition technique due to low temperature crystallographic transitions and their consequent changes in electric behavior for other materials (as reported in previous chapters) and as it had not previously been studied to deposit NiO protective layers on photoanodes. ~50 nm thick layers at 100, 200 and 300 °C were deposited.

Morphological, electrical and photoelectrochemical characterization revealed a transition in crystallographic orientation caused by temperature, together with relative resistance to charge conduction significantly increased with higher deposition temperatures (Figure 5.3). This is caused by a more stoichiometric ALD-NiO fabrication when increasing deposition temperature, forming a less Ni-deficient material (the cause of Ni³⁺ acceptor-doping states). ALD, basing its deposition on surface precursor saturation, produced more stoichiometric films than other techniques.

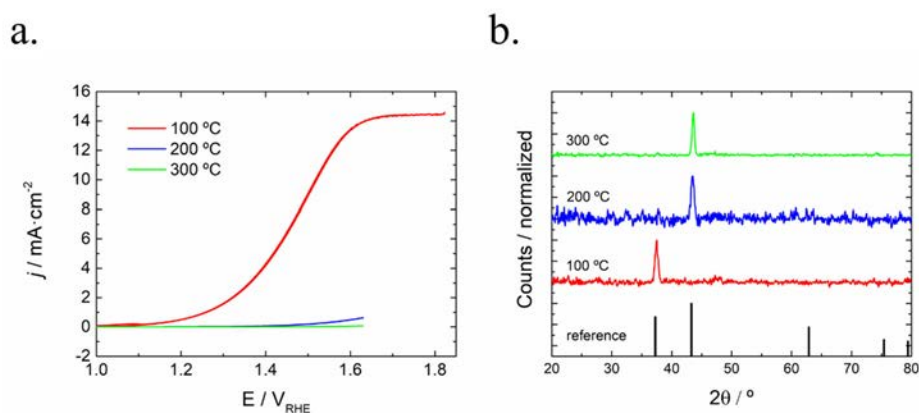


Figure 5.3. a) Cyclic voltammograms of silicon photoanodes ALD-protected with NiO deposited at 100, 200 and 300 °C showing significantly higher performance at low deposition temperatures. b) Corresponding XRD patterns of NiO films where the same crystalline structure is observed with a change in the orientation between 100 and 200 °C.

Thanks to the very high conformal deposition of ALD, minimal etched sites caused by pinholes were detected after over 1000 h of $>10 \text{ mA}\cdot\text{cm}^{-2}$ continuous oxygen evolution in 1 M KOH. Deactivation was detected over several tens of hours, although with periodical cycling a regeneration was possible, proving exceptional protection capabilities of NiO layers (Figure 5.4).

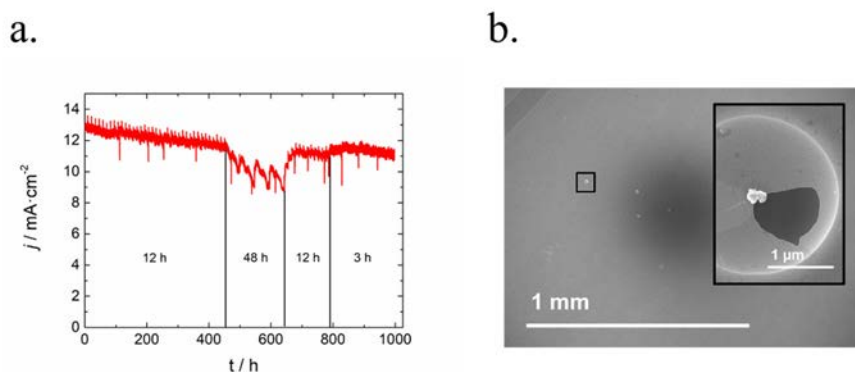


Figure 5.4. a) Stability measurement of a silicon photoanode protected at 100 °C performed under 1 sun illumination and 1 M KOH as electrolyte. Cyclic voltammograms were performed during the stability at different intervals, temporally recovering the performance of the photoelectrode. b) SEM images of the same photoelectrode after 1000 h stability in 1 M KOH, presenting very few etched sites, related to pinholes caused by defects present during fabrication.

Bibliography

- (1) Mei, B.; Pedersen, T.; Malacrida, P.; Bae, D.; Frydendal, R.; Hansen, O.; Vesborg, P. C. K.; Seger, B.; Chorkendorff, I. Crystalline TiO₂: A Generic and Effective Electron-Conducting Protection Layer for Photoanodes and -Cathodes. *J. Phys. Chem. C* **2015**, *119* (27), 15019–15027.
- (2) Sivula, K. Defects Give New Life to an Old Material: Electronically Leaky Titania as a Photoanode Protection Layer. *ChemCatChem* **2014**, 2796–2797.
- (3) Nachman, M.; Cojocaru, L. N.; Ribco, L. V. Electrical Properties of Non-Stoichiometric Nickel Oxide. *Phys. Status Solidi* **1965**, *8* (3), 773–783.
- (4) Dette, C.; Hurst, M. R.; Deng, J.; Nellist, M. R.; Boettcher, S. W. Structural Evolution of Metal (Oxy)Hydroxide Nanosheets during the Oxygen Evolution Reaction. **2018**.

Insight into the degradation mechanisms of Atomic Layer Deposited TiO₂ as photoanode protective layer.

Carles Ros^{a,*}, Nina M. Carretero^a, Jeremy David^c, Jordi Arbiol^{c,d}, Teresa Andreu^{a,*}, Joan R. Morante^{a,b}

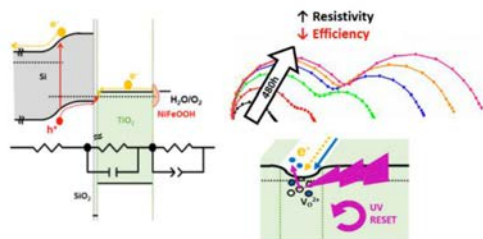
^a Catalonia Institute for Energy Research (IREC), Jardins de les Dones de Negre 1, 08930 Sant Adrià del Besòs, Barcelona, Spain

^b Universitat de Barcelona (UB), Martí i Franquès, 1, 08028 Barcelona, Spain

^c Catalan Institute of Nanoscience and Nanotechnology (ICN2), CSIC and BIST, Campus UAB, Bellaterra, 08193 Barcelona, Spain

^d ICREA, Pg. Lluís Companys 23, 08010 Barcelona, Spain

KEYWORDS: TiO₂, water splitting, photoanode, protective layer, ALD, degradation.



ABSTRACT

Around 100 nm thick TiO₂ layers deposited by atomic layer deposition (ALD) have been investigated as anticorrosion protective films for silicon based photoanodes decorated with 5 nm NiFe catalyst in highly alkaline electrolyte. Completely amorphous layers presented high resistivity, meanwhile the ones synthesized at 300°C, having a fully anatase crystalline TiO₂ structure, introduced insignificant resistance, showing direct correlation between crystallization degree and electrical conductivity. The conductivity through crystalline TiO₂ layers has been found not to be homogeneous, presenting preferential conduction paths attributed to grain boundaries and defects within the crystalline structure. A correlation between the c-AFM measurements and grain interstitials can be seen, supported by HRTEM cross sectional images presenting defective regions in crystalline TiO₂ grains. It was found that the conduction mechanism goes through the injection of electrons coming from water oxidation from the electrocatalyst into the TiO₂ conduction band. Then,

electrons are transported to the Si/SiO₂/TiO₂ interface where electrons recombine with holes given by the p⁺n-Si junction. No evidences of intra band gap states in TiO₂ responsible of conductivity have been detected. Stability measurements of fully crystalline samples over 480 h in anodic polarization show a continuous current decay. Electrochemical impedance spectroscopy allows to identify that the main cause of deactivation is associated to the loss of TiO₂ electrical conductivity, corresponding to a self-passivation mechanism. This is proposed to reflect the effect of OH⁻ ions diffusing in the TiO₂ structure in anodic conditions by the electric field. This fact proves that a modification takes place in the defective zone of the layer, blocking the ability to transfer electrical charge through the layer. According to this mechanism, a regeneration of the degradation process is demonstrated possible based on ultraviolet illumination, which contributes to change the occupancy of TiO₂ electronic states and to recover the defective zones conductivity. These findings confirm the connection between the structural properties of the ALD-deposited polycrystalline layer and the degradation mechanisms, and thus highlight main concerns towards fabricating long-lasting metal oxide protective layers for frontal illuminated photoelectrodes.

1. INTRODUCTION

Our society faces a significant challenge regarding energy production and climate change, where renewable energy sources are called to be crucial. However, the

high variability on renewables such as wind and solar power is one of the main drawbacks nowadays. Storing solar energy into chemical bonds is an interesting candidate to face this variability, the so called “solar fuels”.¹⁻⁴ Among them, hydrogen produced from water electrolysis is a promising candidate as energy vector, substituting natural gas as heat source⁵ or fossil fuels used for transportation.⁶ Photoelectrochemical (PEC) water splitting was discovered by Fujishima and Honda in the late 70's,⁷ but solar to hydrogen (STH) efficiencies have been far from industrial requirements for decades, although remarkable efforts have been put in understanding and enhancing photoactive metal oxide semiconductors and catalysts to perform the water splitting reaction.⁸⁻¹⁸

With the significant increase in productivity and cost reduction of the photovoltaic industry, which has led to its large scale implementation, many authors have put their attention into implementing these semiconductor materials and fabrication methods in PEC water splitting.¹⁹⁻²¹ Many materials such as monocrystalline²²⁻²⁴ and amorphous silicon,²⁵ chalcogenide-based compounds,^{26,27} III-V semiconductors²⁸⁻³² and even perovskites³³ have been proposed. However, all of these semiconductors face a common problem: the chemical stability of such materials when exposed to the highly acidic or alkaline electrolytes necessary for kinetically-efficient oxygen and hydrogen evolution reactions (OER and HER).²⁰ To overcome this, the use of protective layers was suggested, avoiding the contact between the electrolyte and the sensible photoabsorber materials, but their fabrication routes should assure that the photoabsorber suffers no harm or alteration. In addition, protective layers for frontal illuminated photoelectrodes need to be conductive, transparent, chemically stable. These requirements reduce the candidate materials and methods. Among them, TiO₂ is found to be one of the best performing candidates,^{21,34-38} and among deposition techniques, atomic layer deposition (ALD) allows high layer thickness control, conformal layers almost pinhole free, and low crystallization temperatures thanks to intermediate-species mobility, avoiding alterations of inner layers of the photoelectrode.³⁹⁻⁴² For instance, recent studies have reported interesting characteristics of ALD-TiO₂ such as increased adhesion on Si photoanodes⁴³ or enhanced plasmonic resonance in photovoltaic devices⁴⁴.

Photocathodes protected with polycrystalline TiO₂ have been widely reported as the conduction band alignment between the silicon and the TiO₂ metal oxide facilitates the electron transfer from the photocathode to the electrolyte through the TiO₂ layer that is n-type.^{26,45-50}

Regarding TiO₂ protecting silicon based photoanodes, there is a totally different casuistic. In this case, the photo-generated minority carriers, holes, must be transferred to the electrolyte through a protective n-type TiO₂ layer. Different works have studied TiO₂ as protective layer for photoanodes, mainly using silicon as the photoabsorbing material, either forming a heterojunction between the TiO₂ and the n-Si⁵¹⁻⁵⁶ or with a buried p⁺-n junction in silicon.^{28,57,58} Under these boundaries, as a n-type metal oxide layer was expected to be highly resistive when thicker than the tunnelling distance, first works with TiO₂ grown via ALD as protective layer were using thicknesses ranging of only few nanometers.^{51,52,56,58,59} However, these assumptions were put in evidence by the studies carried out by Hu *et al.*²⁸ These authors used layers with thicknesses over 100 nm which were found to have conductivity enough to validate the use of TiO₂ for photoanodes as feasible. They propose state-mediated hole transport through intra-band gap levels as the conduction path caused by the disorder of amorphous TiO₂ (“electronically leaky layer”), in alignment with the silicon valence band, following the same mechanism postulated decades ago by Campet *et al.*⁶⁰ Hu *et al.* attribute these electronic defects arise from amorphous structural disorder and/or chemical impurities from ALD precursors tetrakis- dimethylamidotitanium (TDMAT) and water.

Other authors that claim not identifying this mid bandgap levels in their samples have proposed a mechanism based on a MIM-like (Metal-Insulator-Metal) structure defined by a TiO₂ layer between the photoabsorber and the electrocatalyst. Thus, Mei *et al.*⁵⁷ proposed that electrons were conducted through the conduction band for a p⁺-Si/Ti/TiO₂/Pt structure. So, under this model, electrons from the oxygen evolution reaction are easily injected to the conduction band of the sputtered titanium dioxide layer through the electrocatalyst. Through it they are transferred to the internal Si/TiO₂ interface at the photoanode where they recombine with the photogenerated holes. However, these works generally do not consider the

polycrystalline nature of the TiO₂ layer and neither their degradation mechanisms, which they are often overlooked.

So, there is still significant controversy in the field whether the conduction mechanism through TiO₂ layers is based on the crystalline or amorphous structure of the film. Moreover, debate is open on if it is related to the role of the precursor contaminants some processes such as ALD can have, although McDowell et al.⁵⁴ found TiO₂ films conduction behaviour not unique to amorphous phase and with no relation to carbon or nitrogen impurities. Surprisingly, insufficient studies have used TiCl₄ as precursor for TiO₂ protective films, although it can be applied in a significantly wider ALD regime of 100 to 500 °C than other precursors TDMAT⁶¹ and TTIP⁶². TiCl₄ is also a less complex molecule, requires no precursor pre-heating and has a lower cost.⁶³ Moreover, some works have considered amorphous films at ALD deposition temperatures of 150 °C²⁸, although weak traces of anatase have been reported down to 140 °C⁶⁵. Thus, deposition temperatures to be considered amorphous films might require to be lower, together with more sensible characterization techniques.

In this context, this work aims at revealing the role of the amorphous / polycrystalline nature of the atomically deposited TiO₂ layer using TiCl₄ as precursor, considering its defective zones, to determine the electrical conductivity pathways and their evolution over time as a consequence of the degradation mechanisms that take place, which determines the endurance to the use of the protective layers based on TiO₂ in silicon photoanodes for water splitting.

2. EXPERIMENTAL SECTION

TiO₂ coatings have been grown by ALD on p⁺-n silicon buried junctions and simultaneously on p⁺ degenerately doped silicon, to simulate direct injection of carriers in dark conditions.

p⁺-Si samples were created by cutting a degenerately doped silicon wafer (0.001 Ω·cm) in 1x1 cm² pieces, and 50 nm of Al were thermally evaporated as back contact.

For the p⁺n-Si samples, a 1 cm² active area was lithographically defined by SiO₂ passivation on a silicon

n-type wafer (0.1-0.5 Ω·cm resistivity). Boron was implanted in the defined front surface and activated by rapid thermal annealing, creating a 200 nm n⁺ region on top of the n-type substrate. As back contact, 1 μm of Al/0.5%Cu was sputtered on top of 30 nm of Ti to form a proper ohmic contact.

p⁺-Si and p⁺n-Si samples were sonicated for 5 min in a 1:1:1 isopropanol, acetone and DI water cleaning solution, followed by abundant rinsing and further 5 min sonication in DI water. Before ALD deposition, front surface was cleaned with 0.1M HF for 5 min, rinsed in DI water and immediately introduced in the ALD chamber.

A R200 Picosun Atomic Layer Deposition system was used to grow TiO₂ layers. TiCl₄ was selected as precursor because of its wide deposition window and lower cost compared with other metalorganic compounds. Thus, TiCl₄ and H₂O precursors at 19 °C were used in successive pulses at 8 mbar in N₂ flow atmosphere, with 0.1 s pulses and 10 s purges. Under these conditions, layers were grown at deposition temperatures of 100, 150 and 300 °C for 3300 cycles, corresponding to roughly 100 nm layers. Layer thickness was measured by evaluating the reflected spectra with a Sensofar interferometer device with ± 0.2 nm error. Finally, nickel-iron (NiFe) was deposited by thermal evaporation using an Oerlikon Univex 250 equipment, with a thickness of 5 nm measured by a quartz microbalance. Samples were then soldered to a Cu wire using Ag paint and epoxy protected leaving the front area exposed (Figure S1).

Surface morphology was observed with a Zeiss Series Auriga Field Emission Scanning Electron Microscope (FESEM). Structural characterization was carried out by X-ray diffraction (XRD) in a D8 Advance Bruker equipment with a Cu K_α radiation source working at 40 kV and 40 mA with a 3 ° offset angle. Raman spectroscopy was performed using a Horiba LabRam HR 800 with 532 nm laser light with a 100x objective and an output power of 5 mW, 10 s acquisition time and 10 accumulations. High resolution transmission electron microscopy (HRTEM), high angle annular dark field (HAADF) scanning TEM (STEM) and electron energy loss spectroscopy (EELS) spectrum imaging (S.I.) were performed using a TECNAI F20 operated at 200 kV with a point to point resolution of 0.19 nm, with

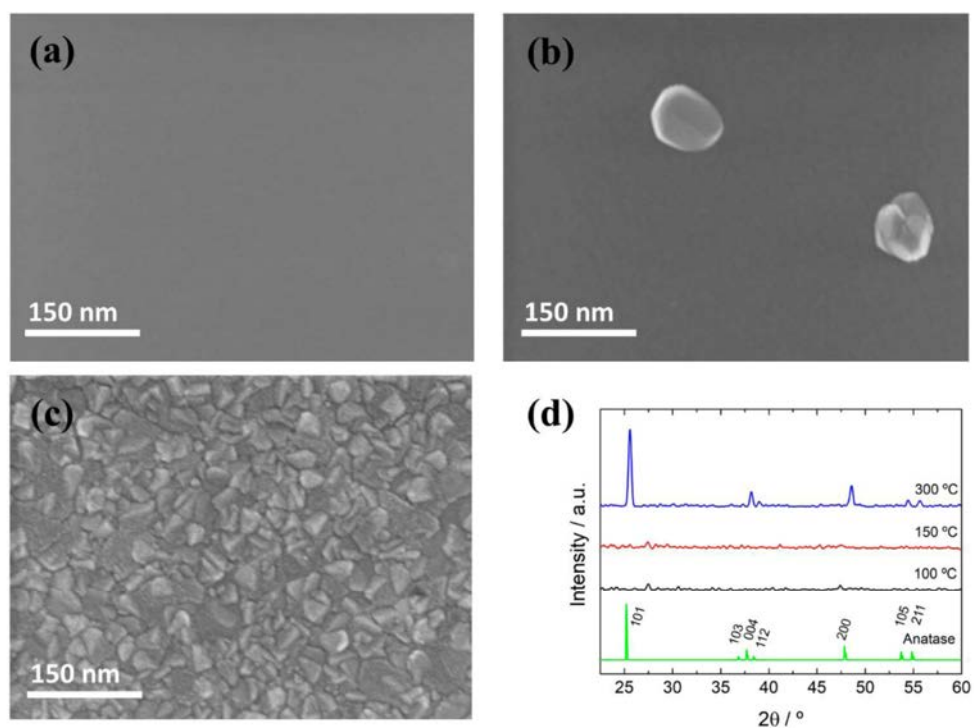


Figure 1. Top view SEM images of n^+p -Si photoanodes protected with 100 nm TiO_2 grown at 100 °C (a), 150 °C (b) and 300 °C (c). (d) XRD spectra of TiO_2 layers grown at 100 °C (black), 150 °C (red) and 300 °C (blue) compared to the reference anatase pattern RRUFF R060277.9 (green).

a coupled GATAN QUANTUM EELS detector. HRTEM samples were prepared using a focused ion beam (FIB) to select the desired region to image, previous protecting the surface with deposited Pt. AFM and conductivity AFM (c-AFM) measures were taken with a Park Systems XE-100 with platinum conductive cantilevers biasing the sample at +1 V. Due to the p^+n -

Si built-in voltage, only the samples on p^+ -Si substrates were measured by c-AFM. The photoelectrochemical measurements (cyclic voltammetries, chronoamperometries and electrochemical impedance

spectroscopy) were obtained with a Biologic VMP-300 potentiostat using $\text{Ag}/\text{AgCl}/\text{KCl}$ (3M) ($E^0 = 0.203 \text{ V}_{\text{RHE}}$) as reference electrode and platinum mesh as counter electrode. A quartz cell with flat faces was used with 100 ml of 1M KOH electrolyte and a 300 W xenon lamp with an AM 1.5G filter adjusted to $100 \text{ mW}/\text{cm}^2$, calibrated using a silicon diode (Gentec-EO, XLPF12-

3S-H2-DO). $20 \text{ mW}\cdot\text{cm}^{-2}$ 365 nm UV light is obtained from a 200 W Hg-Xe Hamamatsu LC8 light source lamp. I-V curves were obtained in two-electrode configuration depositing 50 nm of Au as top contact.

3. RESULTS AND DISCUSSION

3.1. Morphological and structural characterization

In this work, we have fabricated silicon photoanodes protected with TiO_2 layers prepared by Atomic Layer Deposition (ALD) in a temperature range from 100 to 300 °C from TiCl_4 precursor, which permits a wide temperature deposition window.⁶⁴

Figure 1 shows SEM surface images of the ALD TiO_2 coatings synthesized at the different temperatures. For the film obtained at 100°C (Figure 1a), a homogeneous coating is observed with no presence of grains, whereas using deposition temperatures of 150 °C some regions

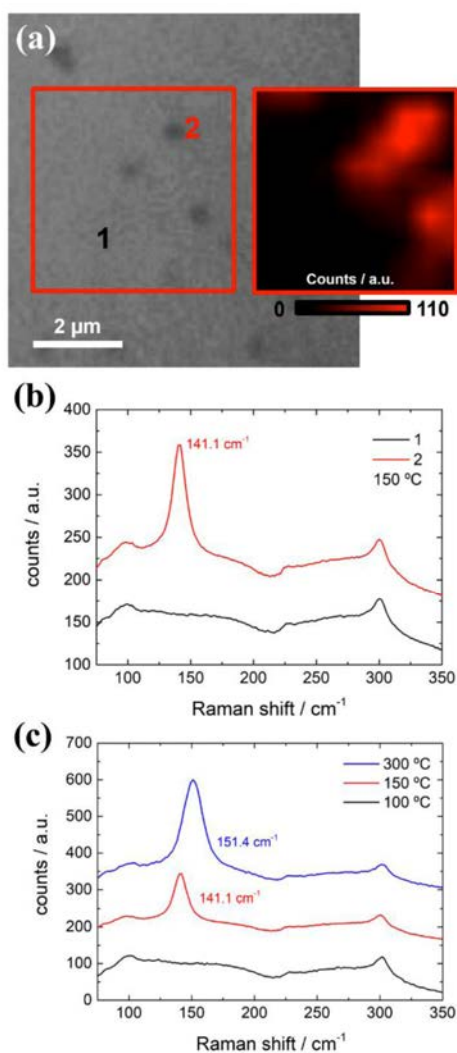


Figure 2. (a) Optical image of a protected silicon with TiO_2 grown by ALD at 150°C . Right inset, counts map of the Eg Raman shift of the indicated region. (b) Raman shift spectra of two different positions of image a) corresponding to an amorphous region (1, black) or a crystalline grain (2, red). c) Raman shift spectra of ALD- TiO_2 layers grown at 100°C (black), 150°C (red) and 300°C (blue). The presented Raman shift spectra for the sample synthesized at 150°C corresponds to a position where a TiO_2 grain can be seen. Peak maximum position is indicated for 150 and 300°C .

with different contrast appear, corresponding to grains embedded in an amorphous matrix (Figure 1b). Further

increasing deposition temperature up to 300°C (Figure 1c), yields to a highly crystalline surface with smaller grain sizes. These grains are related to the TiO_2 anatase phase, as can be seen in the XRD diffraction pattern for the sample synthesized at 300°C (Figure 1d). The TiO_2 anatase phase is more favourable to OH^- adsorption and thus causing higher ALD growth rate.^{22,65} No anatase

XRD peaks or other crystalline phases are detected at 100 or 150°C , as previously observed in literature.^{66,67}

As it can be seen in the SEM image for the sample synthesized at 150°C (Figure 1b) the density of embedded crystals is rather low, and therefore XRD measurement does not allow the identification of the crystalline structure, being below the resolution. We used Raman spectroscopy equipped with an optical microscope, in order to carry out a more localised analysis. Optical view of the Si chip with an ALD- TiO_2 layer grown at 150°C is shown in Figure 2a, where it is seen the presence of dark spots embedded in a homogenous grey film, which may be attributed to the submicron size crystals identified by SEM.⁶⁸ Figure 2b presents the Raman spectra of two different spots, with a clear appearance of an intense peak in the darker spot, corresponding to the Eg mode of anatase located at 141.4 cm^{-1} . The peak is red-shifted with respect to the expected 144 cm^{-1} value,⁶⁹ being a sign of tensile stress, probably caused by partial amorphousness of the interface and reduced crystalline size.⁷⁰ A Raman mapping scan of the Eg main peak is shown in the inset of Figure 2a, which allows us to correlate the dark spots seen in the optical image with anatase crystallographic order presence.

Complete analysis by micro Raman spectroscopy of TiO_2 layers grown at 100 , 150 and 300°C is shown in Figure 2c. None of the spots analyzed of the sample synthesized at 100°C present the anatase peak, whereas is present at any spot at 300°C samples, confirming the existence of a fully polycrystalline layer, in accordance with the XRD results and SEM. A deeper analysis of the Raman spectra shows a more intense peak for 300°C layers compared with 150°C crystalline zones, and a blue shift of the Eg mode (of 10.3 cm^{-1}), that can be attributed to either surface pressure or phonon confinement effect that usually exist in nanometer-sized materials.⁷¹ As seen in SEM images (Fig. 1c), nucleation is enhanced with increased deposition

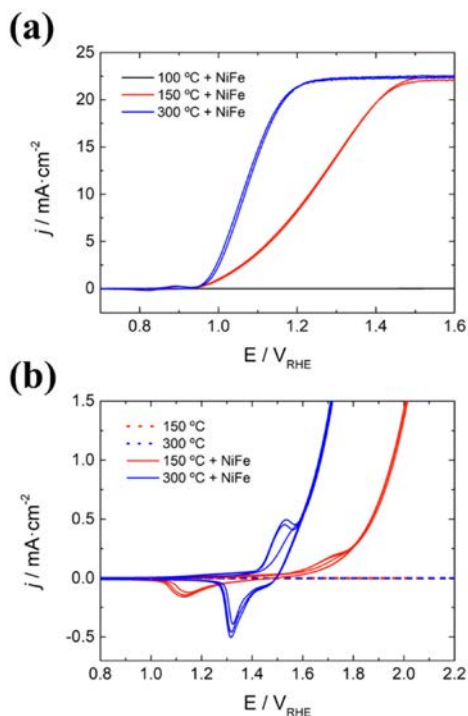


Figure 3. (a) Cyclic voltammeteries (1 sun AM 1.5G) of *p-n*-Si photoanodes protected with 100 nm TiO_2 layers grown at 100 °C, 150 °C and 300 °C, with 5 nm of nickel-iron thermally evaporated as OER catalyst. (b) Cyclic voltammeteries in dark of *p-n*-Si substrates protected either with 150 °C or 300 °C TiO_2 layers and decorated or not with 5 nm of thermally evaporated nickel-iron. 1 M KOH was used as electrolyte.

temperature and smaller grains are obtained by competitive growth.

3.2. Electrochemical characterization

In Figure 3a, cyclic voltammeteries of three illuminated *p-n*-Si homojunctions are shown. The photoanodes, previously cleaned with HF (to eliminate the SiO_x) and immediately ALD-protected with TiO_2 grown at 100, 150 and 300 °C were then coated with a 5 nm film of thermally evaporated NiFe, to act as OER catalyst. For samples grown at 100 °C, no photocurrent can be observed. However, for samples deposited at 150 °C and 300 °C the same onset potential is obtained (around 0.96 V vs RHE) and whereas significant photocurrent is obtained for the former, highly increased currents are

observed for the later. This fact, together with the saturation regime reached at more anodic potentials for the 150 °C sample, indicate a more resistive layer. The saturation current value, 22.5 mA/cm², is given by the photovoltaic quality of the prepared silicon-based

homojunctions that were not optimized, and the lack of adjusted antireflective strategies.⁷²

In dark conditions, the same tendency observed for photoanodes is obtained in TiO_2 -protected *p-n*-Si anodes: increasing deposition temperature from 150 to 300 °C enhances OER current (Figure 3b). The nickel-iron catalyst is necessary for efficient charge injection into the electrolyte^{28,73–76}, and if it is not present, no oxidative current is obtained in the studied range of potentials (dotted line in Figure 3b). In fact, Ni(Fe)OOH is the real catalytic phase obtained after cycling in alkaline electrolytes such as standard KOH solutions, one of the earth-abundant OER catalyst with lower overpotentials^{38,77–86}. The voltage difference between oxidative and reductive redox peaks of Ni hydroxide/oxyhydroxide is decreased when increasing TiO_2 deposition temperature (0.592 and 0.216 V for 150 and 300 °C). This fact is in accordance with the slopes of the OER current both in photoelectrodes (Figure 3a) and electrodes (Figure 3b), and it is related to higher series resistance in the system. Likewise, Ni²⁺/Ni³⁺ redox peaks present smaller area for the 150 °C sample than for the one synthesized at 300 °C, which indicates less active catalyst in the former sample, as the deposited NiFe quantity is the same in both samples. This fact may point out that charge transfer is boosted in the 300 °C sample in comparison with the 150 °C one.

3.3. Conduction pathways in TiO_2 -ALD protected photoanodes

In Figure 4, we present the topography and conductivity atomic force microscopy maps (c-AFM) of ALD- TiO_2 samples grown on degenerately doped *p-n*-Si substrates at 150 °C and 300 °C with 5 nm NiFe thermally evaporated on top. Measurements of TiO_2 /NiFe layers were performed at +1 V, simulating the electron flow from the tip to the substrate across the layer, like in OER

anodic conditions. Without NiFe catalyst, no current could be measured in the used range of potentials. As it can be seen in Figure 4 e-f, there is a correlation between

topography maps and regions where current signal is detected: crystalline boundary regions, more abundant in the 300 °C sample than in the 150 °C, and no current in the amorphous regions. Additional images pointing in the same direction are presented in supporting information Figure S2. Localized conduction of TiO₂-ALD layers observed by c-AFM has been also reported

by other works. To explain the preferential conduction paths, Yu et. al.⁸⁷ suggested the presence of crystallographically metastable regions, and Murakami et. al.⁸⁸ assumed an inhomogeneous distribution of oxygen vacancies (V_{ox}) known to be mobile under applied potentials and capable to agglomerate, defining preferential electron trap-assisted tunneling conductivity paths or conductive filaments, or Magneli phases in the grain boundaries such as it has been identified in the development of TiO₂ memristors.⁸⁹⁻⁹²

Figure 5 shows the HRTEM images of the cross section obtained by FIB for the samples synthesized at 150 and 300°C, where multiple crystal orientations, grain

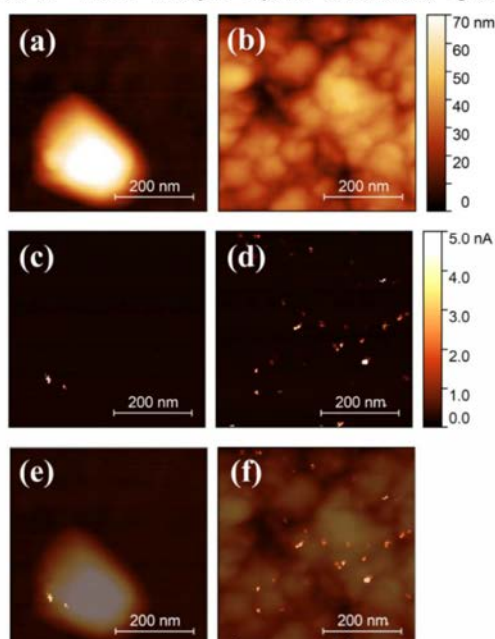


Figure 4. AFM height map of TiO₂ + NiFe layers grown at 150°C (a) and 300 °C (b), and its respective current intensity maps, (c) and (d) obtained at +1 V. (e) and (f) shows the overlays of the topography and current maps for each sample.

boundaries and twin-like defects can be seen, embedded in an amorphous matrix for the 150 °C sample . Thus, unevenly distributed defects and oxygen vacancies should be expected, affecting the electrical states distribution. More HRTEM analysis is further depicted in Figure S3.

Columnar grains are present in both samples synthesized at 150 and 300 °C, but nucleation is significantly different. The HRTEM image of the sample grown at 150 °C shows that TiO₂ is crystalline

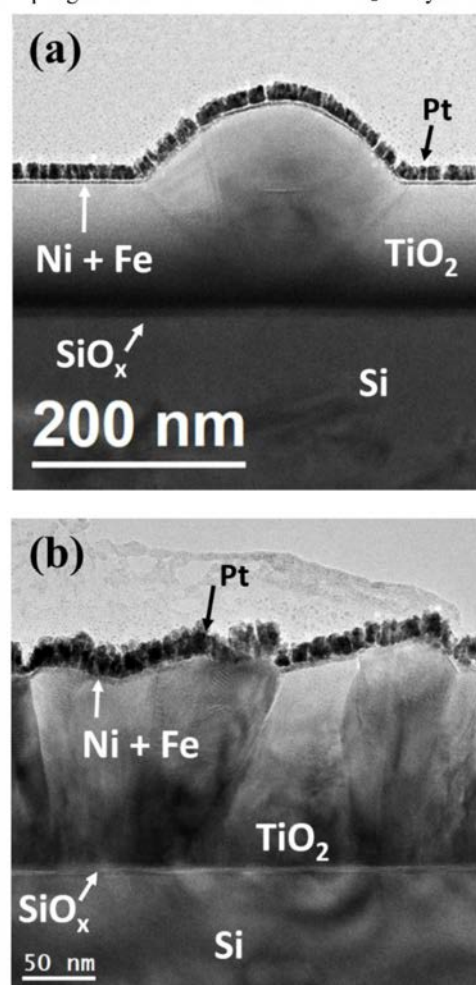


Figure 5. HRTEM cross sectional images of TiO₂ layers grown by ALD at 150 °C (a) and 300 °C (b). A Pt layer was deposited on top to protect the sample during the FIB sample preparation process.

only in a few-nanometer dome-like region close to the substrate, while the rest of the TiO_2 layer remains amorphous. However, the one prepared at 300°C shows that the whole TiO_2 layer is crystalline. This can be attributed to the higher deposition temperature used, which enhances nucleation and lateral crystal propagation, together with crystal competition.⁴¹

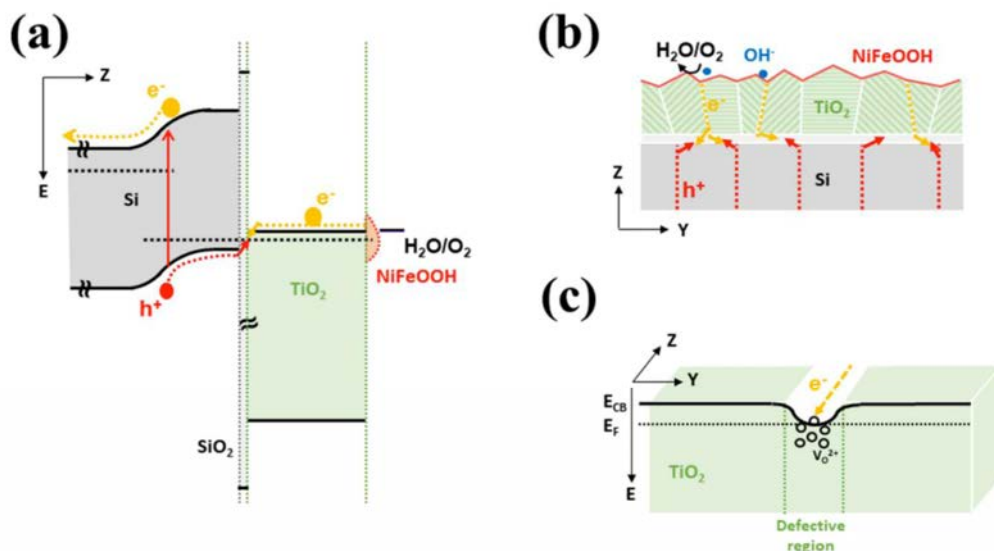
The TiO_2/NiFe interface can be analysed by HRTEM EELS. In those as-prepared samples, the $\sim 5\text{nm}$ apparently homogeneous NiFe catalyst layer can be seen (Figure S4a). After cycling in 1 M KOH (Figure S4b), a thicker layer can be observed, and the oxygen presence throughout the whole NiFe layer is increased, indicating oxidation of the metallic layer and OH^- incorporation, as reported in other works, where a restructuring of the NiFe towards a three dimensional nanoflakes porous layer takes place.⁹³ Moreover, there is no presence of Ni or Fe incorporation in the TiO_2 crystalline structure, or O or Ti concentration gradient can be detected above the EELS system resolution threshold, neither in the amorphous or crystalline structures nor the grain boundaries (Figures S5, S6).

To study the surface chemical composition of the layer, XPS analysis was performed, which is discussed in the

supplementary information and Figure S7 and Table S1. To sum up, for as prepared samples, a 2.8:1 Ni:Fe ratio is observed, natively oxidized before anodic cycling and with higher oxygen content afterwards, caused by OH^- intercalation and oxidation of the coatings. Ni 2p spectra presents Ni(0) metallic peaks before but not after immersion in the electrolyte. For the cycled sample, multiple Ni(II) and Ni(III) peaks can be fitted (Figure S7a), probably by the presence of multiple chemical states such as NiO, $\text{Ni}(\text{OH})_2$ and NiOOH, not easy to differentiate by XPS⁹⁴, and also correlated to Fe(III) forming Ni(Fe)OOH, as reported in other works^{38,74,93,95–97}.

XPS analysis also allows to obtain valence band (VB) positions of the superficial electrons, through the density and occupancy of electronic states of the surface

(Figure S8). On one hand, as prepared TiO_2 layers at 150 and 300°C present valence band potentials of ~ 2.75 eV under Fermi level, pointing at a higher n-type behaviour for the sample grown at 300°C (larger Fermi level to valence band energies). On the other hand, no signal from intra-bandgap states is detected with a fine analysis of the 0-3 eV region in accordance with another works²⁸, although the small signal-to-noise ratio could



Scheme 1. (a) Band diagram of a p-n-Si photoanode, TiO_2 protected with cycled Ni(Fe)OOH catalyst. (b) Cross section diagram with electron and holes flow paths depicted. (c) Energy and cross section diagram corresponding to a preferential path or defective region, showing how extra states in interfacial defects generate a preferential path.

be hindering the detection (Figure S9). Also, the oxidation of the metallic NiFe layer after immersion in the electrolyte at anodic potentials is revealed by the XPS spectra, still presenting slight free electrons behaviour. The most significant result is the excellent band alignment between TiO_2 conduction band and the Ni(Fe)OOH catalyst, that justify the injection of electrons from the oxygen evolution catalyst to the TiO_2 conduction band. The results obtained can be summarized in the mechanism proposed in Scheme 1,

basing the conductivity in preferential charge transport pathways. The increased conductivity pathways density present for 300 °C deposited samples with respect to 150 °C ones (Figure 4 e-f) must be especially highlighted, in

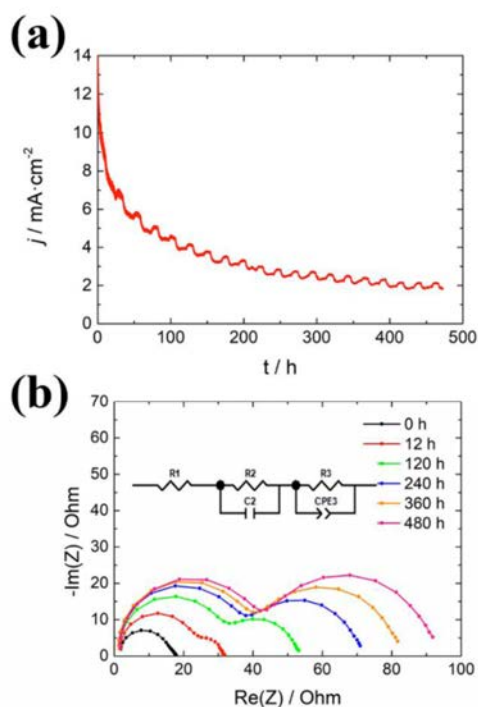


Figure 6. (a) Chronoamperometry of a p^- -Si anode protected with ALD-deposited TiO_2 at 300 °C and NiFe decorated in 1 M KOH at a fixed potential of 1.8 V vs RHE. (fluctuations are due to daily temperature changes). (b) Nyquist plot of the electrochemical impedance spectroscopy (EIS) data from the same sample obtained every 12 h under potentiostatic 1.8 V vs RHE potential from 1 Hz to 50 kHz and an amplitude of 25 mV. The inset shows the equivalent electric circuit used to fit the EIS data.

agreement with reported data in Figure 3. In addition, several features can be underlined:

1) The Si- TiO_2 interface has been found not to introduce significant electrical barrier to charge transport. A recombining contact for holes from the p^- -Si valence band and electrons from the TiO_2 preferential paths conduction band is expected, facilitated by tunnelling through the ALD-caused SiO_x similar to the schemes proposed by other authors.²⁰

2) The transversal section to charge transport has been proven to be not homogeneous. Lower resistivity regions detected by c-AFM are attributed to more defective crystalline TiO_2 regions than bulk crystal grains, forming preferential conductivity paths through the grain boundaries and defects within the crystalline structure.⁸⁹

3) There is a favourable electron transfer from the Ni(Fe)OOH to the TiO_2 conduction band. This is facilitated by the permeable to electrolyte and energetically adaptive characteristics of the catalyst due to ionic diffusion, avoiding the energetic barrier formed between TiO_2 and the electrolyte and facilitating OER reaction.^{74,98}

3.4. Endurance test: degradation mechanisms and stability

Crystalline TiO_2 -protected p^+ -Si anodes and p^+ -n-Si photoanodes were tested for stability in a 1 M KOH electrolyte at anodic potentials. The obtained current density values show significant decay for both electrodes (Figures 6 and 7). To further analyse these samples, Electrochemical Impedance Spectroscopy (EIS) was applied before and during stability test.

For the p^+ -Si anode in dark conditions, the current measured for more than 480 h at 1.8 V vs RHE, shows an exponential decay (Figure 6a), which indicates a degradation of the electrode. The EIS measurement shows two clear semicircles increasing over time (Figure 6b) revealing degradation correlated with two processes in series defined by different RC time constants, which allows us to propose an equivalent electrical circuit shown in Figure 6b. As seen in Figure S10 and Table S2, the first semicircle (R_2/C_2) is independent from the applied potential and the second

Table 1. Values obtained after fitting the data presented in Figure 6b according to the circuit proposed.

Time (h)	R ₁ (Ω)	R ₂ (Ω)	C ₂ (F·cm ⁻²)	R ₃ (Ω)	CPE ₃ (F·cm ⁻² ·s ^{0.3-1})	α ₃
0	1.40	13.56	2.11·10 ⁻⁶	2.83	6.54·10 ⁻⁴	0.787
12	1.33	22.58	1.80·10 ⁻⁶	7.30	1.22·10 ⁻⁴	0.992
120	1.22	31.32	1.83·10 ⁻⁶	19.84	1.22·10 ⁻⁴	0.955
240	1.03	37.04	1.84·10 ⁻⁶	31.53	1.14·10 ⁻⁴	0.955
360	0.92	39.30	1.79·10 ⁻⁶	40.40	1.18·10 ⁻⁴	0.940
480	1.29	40.37	1.67·10 ⁻⁶	50.45	1.41·10 ⁻⁴	0.901

one varies significantly between open circuit potential (OCP) and OER working conditions, proving a non-ohmic dependence of this second one. Our electrode has been modelled to an ohmic resistance, R₁ (corresponding to all resistive system contributions given by cables, back contact and substrate and electrolyte conductivity), a R₂/C₂ parallel circuit in series (corresponding to the depletion region within the TiO₂ protective layer) and a Randles circuit (R₃/CPE₃, corresponding to the electrocatalytic OER charge transfer on Ni(Fe)OOH).

Fitting the proposed EIS circuit to our experiments (Table 1), a clear relation is observed between the current loss during stability tests and the semicircles increase. The current diminution rate is initially high, and it is reduced as current values decrease, pointing towards a relation between current passing and conductivity degradation. The resistance R₂ corresponding to the current flow through the TiO₂ layer increases logarithmically over time at 1.8 V vs RHE, meanwhile R₃, the resistance attributed to charge transfer in the OER reaction, increases lineally (Figure S11).

Owing to the fact that the interfacial SiO_x layer does not increase in thickness after stability test (Figure S12), the increase of R₂ over time can be related with the intrinsic self-passivating process of metal oxide surfaces, following a logarithmic rate law.⁹⁹ This is highlighting an interaction of OH⁻ ions from the electrolyte and the polycrystalline TiO₂ driven by the electric field due to anodic polarization. Some authors have previously reported chemical interaction of OH⁻ migration and defective regions, nulling preferential charge transport paths.¹⁰⁰

The significant decrease of crystalline TiO₂ conductivity has not previously been stated, but a deep review of the bibliography does not deny its plausibility. Other works have shown the possibility of OH⁻ to penetrate through a permeable Ni catalyst layer and diffuse through the TiO₂⁸⁷ or ALD-TiO₂ dissolution on few hours scale¹⁰⁰. Oxygen mobility under polarization in TiO₂ has been known for years, forming preferential paths in the form of conductive filaments.^{101,102} The presence of such oxidant molecules, OH⁻, inside the TiO₂ structure can easily interact with the states responsible of the n-type semiconductor properties and conductivity.¹⁰³ This fact has been depicted in Scheme S1a and b.

On the other hand, according to the Tafel equation describing the charge transfer at the electrode/electrolyte interface (eq. 1)¹⁰⁴, overpotential (η) depends logarithmically on the current density. Assuming both elements are in series (*i*₂ equals *i*₃, *i*), and the resistance of the TiO₂ layer (R₂) increases while applied potential is kept constant, the current reaching the OER reaction (measured in EIS as R₃) will decrease logarithmically, giving an inverse logarithmic dependence of R₃ with R₂ (eq. 2), represented in Figure S13. A 5 times increase in the total resistance (R₂ + R₃) is in accordance with the equivalent current reduction observed after the 480 h stability test under anodic polarization.

$$\log\left(\frac{1}{R_{ct}}\right) = \frac{di}{d\eta} = a * \eta + b; \quad (1)$$

where $R_{ct} = R_3$ and $\eta = V - i * R_2$, giving:

$$\log\left(\frac{1}{R_3}\right) \propto (-R_2) \quad (2)$$

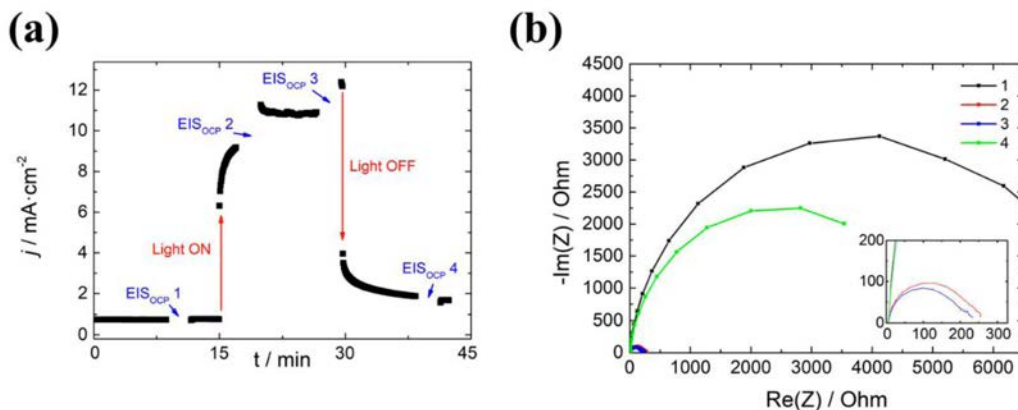


Figure 7. a) Chronoamperometry measurement at 1.3 V vs RHE of a p-n-Si photoanode protected with TiO₂ ALD-deposited at 300 °C and NiFe under solar irradiation and superimposed UV light, after 333 h of stability test b) EIS measurement at OCP of a UV temporarily illuminated degraded photoanode, partially recovering the photocurrent via light-induced states. Measurements performed under 1 sun illumination, using 1 M KOH as electrolyte.

Following these equations, if $R_2 \propto \log(t)$ as it has been demonstrated in Figure S11, and substituting in eq. 2, we obtain $R_3 \propto t$.

In his turn, capacitance of the TiO₂ semicircle is not significantly modified as expected, as it corresponds to the thickness and dielectric constant of the TiO₂ and these are maintained.

Similar stability test was performed with a p⁺-n-Si photoanode with TiO₂ deposited at 300 °C and NiFe decorated. Likewise, after 333 h at 1.3 V vs RHE photocurrent has been reduced significantly (Figure S14).

To validate the previously described degradation mechanism, superimposed UV illumination was used to modify the density of states within the TiO₂ electronic structure, achieving a significant recovery of the photocurrent (Figure 7a). This can be explained by the photoconductivity effect on TiO₂,¹⁰⁵ where the UV photons create electron-hole pairs changing the occupation of localized states, causing a significant reduction of R_2 (Figure 7b, Table S3).¹⁰⁶ Switching off UV light gave a few-seconds decay followed by a several minutes persistent photoconductivity (PPC). These states created by oxygen desorption will eventually be compensated again by OH⁻ diffusing inside the material, as illustrated in Scheme S1. This

UV-light effect should only be expected in the near-surface region of TiO₂ due to small UV photon penetration depth, precisely where higher OH⁻ interaction would be. More studies should be performed regarding TiO₂ degradation and recovery in the near future to fully understand this phenomena.

4. CONCLUSIONS

TiO₂ protective layers grown by ALD have been deposited on silicon photoanodes to avoid corrosion, while allowing charge transfer to the electrolyte to perform the oxygen evolution reaction using a NiFe earth abundant catalyst. Layers consisting of approximately 100 nm have been grown at 100, 150 and 300 °C, corresponding to completely amorphous, partially crystalline and fully crystalline TiO₂.

Completely amorphous layers presented high resistivity, meanwhile the ones synthesized at 300°C, having a fully anatase crystalline TiO₂ structure, introduced insignificant resistance, showing direct correlation between crystallization degree and electrical conductivity. The conductivity through crystalline TiO₂ layers has been found not to be homogeneous, presenting preferential conduction paths attributed to grain boundaries and defects within the crystalline structure. A correlation between the c-AFM measurements and grain interstitials can be seen,

supported by HRTEM cross sectional images presenting defective regions in crystalline TiO₂ grains.

A conduction mechanism has been proposed assuming electrons coming from water oxidation are injected into the TiO₂ conduction band in preferential regions through the electrocatalyst. Then, electrons are transported to the Si/SiO_x/TiO₂ interface where electrons recombine with holes given by the p⁺n-Si junction. No evidences of intra band gap states in TiO₂ responsible of conductivity have been detected.

On the other hand, current decay under continuous polarization was found, where OH⁻ ions are considered to diffuse into TiO₂ under anodic conditions and alter conduction paths conductivity. These changes were analysed under long-time (> 480 h) stability measurements at fixed voltage, which presented current decay over time. Deeper EIS analysis show two different time constant RC elements changing during endurance test, and allowed to track electrical variations in a series circuit structure. Associated TiO₂ resistance increases logarithmically over time, as expected for metal oxide surface passivation, corroborating a self-limited degradation. A 5 times increase on the EIS measured resistances associated to TiO₂ conductivity and OER catalysis is in accordance with the total current reduction observed after 480 h stability test in anodic polarization.

To corroborate this model, UV illumination was used to modify states occupancy, presenting persistent conductivity thanks to the partial recovery of the electronic states lost under working conditions. Further studies focused on higher resolution analysis than this work are needed to identify OH⁻ diffusion into TiO₂ structure and states loss, specifically in preferential regions. UV illumination constitutes a promising method to partially recover degradation. This confirms that the degradation mechanisms of TiO₂ still needs to be taken into consideration to enhance its long term use endurance as a transparent conductive and protective layer for frontal illumination water splitting photoanodes.

ASSOCIATED CONTENT

AFM, HRTEM, XPS, and EIS supplementary data, together with a photo of a finished device and a scheme of UV recovery, are supplied in an additional document

AUTHOR INFORMATION

Corresponding Author

*cros@irec.cat

*tandreu@irec.cat

Author Contributions

The manuscript was written through contributions of all authors. All authors have given approval to the final version of the manuscript.

ACKNOWLEDGMENT

This work was partially supported by Repsol, S.A. and Enagas S.A. Authors from IREC thank Generalitat de Catalunya for financial support through the CERCA Programme, M2E (2017SGR1246) and XaRMAE network. IREC also acknowledges additional support by the European Regional Development Funds (ERDF, FEDER) and by MINECO coordinated projects MAT2014-59961-C2 and ENE2016-80788-C5-5-R. C.R. thanks to MINECO for his FPI grant (BES-2015-071618). ICN2 acknowledge funding from Generalitat de Catalunya 2017 SGR 327 and the Spanish MINECO project ENE2017-85087-C3. ICN2 is supported by the Severo Ochoa program from Spanish MINECO (Grant No. SEV-2017-0706) and is funded by the CERCA Programme / Generalitat de Catalunya. JD has received funding from the European Union's Horizon 2020 research and innovation programme under the Marie Skłodowska-Curie grant agreement No 665919 (P-SPHERE) co-funded by Severo Ochoa Programme.

REFERENCES

- (1) Lewis, N. S.; Nocera, D. G. Powering the Planet: Chemical Challenges in Solar Energy Utilization. *Proc. Natl. Acad. Sci. U. S. A.* **2006**, *103* (43), 15729–15735.
- (2) Wang, M. Fuel Choices for Fuel-Cell Vehicles: Well-to-Wheels Energy and Emission Impacts. *J. Power Sources* **2002**, *112* (1), 307–321.
- (3) James, B. D.; Baum, G. N.; Perez, J.; Baum, K. N. Technoeconomic Analysis of Photoelectrochemical (PEC) Hydrogen Production. **2009**, 1–128.
- (4) Barber, J.; Tran, P. D. From Natural to Artificial Photosynthesis. *J. R. Soc. Interface* **2013**, *10* (81), 20120984.
- (5) Haeseldonckx, D.; D'haeseleer, W. The Use of the Natural-Gas Pipeline Infrastructure for Hydrogen

- Transport in a Changing Market Structure. *Int. J. Hydrogen Energy* **2007**, *32* (10–11), 1381–1386.
- (6) Berry, G. D.; Pasternak, A. D.; Rambach, G. D.; Smith, J. R.; Schock, R. N. Hydrogen as a Future Transportation Fuel. *Energy* **1996**, *21* (4), 289–303.
- (7) Fujishima, A.; Honda, K. Electrochemical Photolysis of Water at a Semiconductor Electrode. *Nature* **1972**, *238* (5358), 37–38.
- (8) Bard, A. J.; Fox, M. A. Artificial Photosynthesis: Solar Splitting of Water to Hydrogen and Oxygen Water Splitting. *Acc. Chem. Res* **1995**, *28*, 141–145.
- (9) Murphy, A. B.; Barnes, P. R. F.; Randeniya, L. K.; Plumb, I. C.; Grey, I. E.; Horne, M. D.; Glasscock, J. A. Efficiency of Solar Water Splitting Using Semiconductor Electrodes. *Int. J. Hydrogen Energy* **2006**, *31* (14), 1999–2017.
- (10) Ros, C.; Fàbrega, C.; Monllor-Satoca, D.; Hernández-Alonso, M. D.; Penelas-Pérez, G.; Morante, J. R.; Andreu, T. Hydrogenation and Structuration of TiO₂ Nanorods Photoanodes: Doping Level and the Effect of Illumination in Trap-States Filling. *J. Phys. Chem. C* **2018**, *122* (6), 3295–3304.
- (11) Ni, M.; Leung, M. K. H.; Leung, D. Y. C.; Sumathy, K. A Review and Recent Developments in Photocatalytic Water-Splitting Using TiO₂ for Hydrogen Production. *Renewable and Sustainable Energy Reviews*, April 2007, pp 401–425.
- (12) Maeda, K.; Domen, K. Photocatalytic Water Splitting: Recent Progress and Future Challenges. *J. Phys. Chem. Lett.* **2010**, *1* (18), 2655–2661.
- (13) Fàbrega, C.; Andreu, T.; Cabot, A.; Morante, J. R. Location and Catalytic Role of Iron Species in TiO₂:Fe Photocatalysts: An EPR Study. *J. Photochem. Photobiol. A Chem.* **2010**, *211* (2–3), 170–175.
- (14) Murcia-López, S.; Hidalgo, M. C.; Navío, J. A. Synthesis, Characterization and Photocatalytic Activity of Bi-Doped TiO₂ Photocatalysts under Simulated Solar Irradiation. *Appl. Catal. A Gen.* **2011**, *404* (1–2), 59–67.
- (15) Sivula, K.; Formal, F. Le; Grätzel, M. WO₃-Fe₂O₃ Photoanodes for Water Splitting: A Host Scaffold, Guest Absorber Approach. *Chem. Mater.* **2009**, *21* (13), 2862–2867.
- (16) Fàbrega, C.; Murcia-López, S.; Monllor-Satoca, D.; Prades, J. D.; Hernández-Alonso, M. D.; Penelas, G.; Morante, J. R.; Andreu, T. Efficient WO₃ Photoanodes Fabricated by Pulsed Laser Deposition for Photoelectrochemical Water Splitting with High Faradaic Efficiency. *Appl. Catal. B Environ.* **2016**, *189*, 133–140.
- (17) Murcia-López, S.; Fàbrega, C.; Monllor-Satoca, D.; Hernández-Alonso, M. D.; Penelas-Pérez, G.; Morata, A.; Morante, J. R.; Andreu, T. Tailoring Multilayered BiVO₄ Photoanodes by Pulsed Laser Deposition for Water Splitting. *ACS Appl. Mater. Interfaces* **2016**, *8* (6), 4076–4085.
- (18) Tang, P.; Xie, H.; Ros, C.; Han, L.; Biset-Peiró, M.; He, Y.; Kramer, W.; Rodríguez, A. P.; Saucedo, E.; Galán-Mascarós, J. R.; Andreu, T.; Morante, J. R.; Arbiol, J. Enhanced Photoelectrochemical Water Splitting of Hematite Multilayer Nanowire Photoanodes by Tuning the Surface State via Bottom-up Interfacial Engineering. *Energy Environ. Sci.* **2017**, *10* (10), 2124–2136.
- (19) Chu, S.; Li, W.; Yan, Y.; Hamann, T.; Shih, I.; Wang, D.; Mi, Z. Roadmap on Solar Water Splitting: Current Status and Future Prospects. **2017**.
- (20) Bae, D.; Seger, B.; Vesborg, P. C. K.; Hansen, O.; Chorkendorff, I. Strategies for Stable Water Splitting via Protected Photoelectrodes. *Chem. Soc. Rev.* **2017**, *46* (7), 1933–1954.
- (21) Wang, T.; Gong, J. Single-Crystal Semiconductors with Narrow Band Gaps for Solar Water Splitting. *Angew. Chemie - Int. Ed.* **2015**, *54* (37), 10718–10732.
- (22) Ros, C.; Andreu, T.; Hernández-Alonso, M. D.; Penelas-Pérez, G.; Arbiol, J.; Morante, J. R. Charge Transfer Characterization of ALD-Grown TiO₂ Protective Layers in Silicon Photocathodes. *ACS Appl. Mater. Interfaces* **2017**, *9* (21), 17932–17941.
- (23) Seger, B.; Laursen, A. B.; Vesborg, P. C. K.; Pedersen, T.; Hansen, O.; Dahl, S.; Chorkendorff, I. Hydrogen Production Using a Molybdenum Sulfide Catalyst on a Titanium-Protected n(+)-Silicon Photocathode. *Angew. Chem. Int. Ed. Engl.* **2012**, *51* (36), 9128–9131.
- (24) McKone, J. R.; Warren, E. L.; Bierman, M. J.; Boettcher, S. W.; Brunschwig, B. S.; Lewis, N. S.; Gray, H. B. Evaluation of Pt, Ni, and Ni–Mo Electro catalysts for Hydrogen Evolution on Crystalline Si Electrodes. *Energy Environ. Sci.* **2011**, *4* (9), 3573–3583.
- (25) Turan, B.; Becker, J.-P.; Urbain, F.; Finger, F.; Rau, U.; Haas, S. Upscaling of Integrated Photoelectrochemical Water-Splitting Devices to Large Areas. *Nat. Commun.* **2016**, *7*, 12681.
- (26) Ros, C.; Andreu, T.; Giraldo, S.; Sánchez, Y.; Morante, J. R. Conformal Chalcopyrite Based Photocathode for Solar Refinery Applications. *Sol. Energy Mater. Sol. Cells* **2016**, *158*, 184–188.
- (27) Ros, C.; Andreu, T.; Giraldo, S.; Izquierdo-Roca, V.; Saucedo, E.; Morante, J. R. Turning Earth Abundant Kesterite-Based Solar Cells into Efficient Protected Water Splitting Photocathodes. *ACS Appl. Mater. Interfaces* **2018**, *10*, 13425–13433.
- (28) Hu, S.; Shaner, M. R.; Beardslee, J. a; Lichterman,

- M.; Brunchwitz, B. S.; Lewis, N. S. Amorphous TiO₂ Coatings Stabilize Si, GaAs, and GaP Photoanodes for Efficient Water Oxidation. *Science* **2014**, *344* (6187), 1005–1009.
- (29) Khaselev, O.; Turner, J. A.; Khaselev, O.; Turner, J. A. A Monolithic Photovoltaic-Photoelectrochemical Device for Hydrogen Production via Water Splitting R EPORTS A Monolithic Photovoltaic-Photoelectrochemical Device for Hydrogen Production via Water Splitting. *Science (80-)*. **1998**, *280*, 425–429.
- (30) Moniz, S. J. A.; Shevlin, S. A.; Martin, D. J.; Guo, Z. X.; Tang, J. Visible-Light Driven Heterojunction Photocatalysts for Water Splitting—a Critical Review. *Energy and Environmental Science*. Royal Society of Chemistry 2015, pp 731–759.
- (31) Lee, M. H.; Takei, K.; Zhang, J.; Kapadia, R.; Zheng, M.; Chen, Y.-Z.; Nah, J.; Matthews, T. S.; Chueh, Y.-L.; Ager, J. W.; Javey, A. P-Type InP Nanopillar Photocathodes for Efficient Solar-Driven Hydrogen Production. *Angew. Chemie Int. Ed* **2012**, *51* (43), 10760–10764.
- (32) Sun, K.; Kuang, Y.; Verlage, E.; Brunchwitz, B. S.; Tu, C. W.; Lewis, N. S. Sputtered NiOx Films for Stabilization of P+n-InP Photoanodes for Solar-Driven Water Oxidation. *Adv. Energy Mater.* **2015**, *5* (1402276), 1–8.
- (33) Guerrero, A.; Bisquert, J. Perovskite Semiconductors for Photoelectrochemical Water Splitting Applications. *Curr. Opin. Electrochem.* **2017**, *2* (1), 144–147.
- (34) Liu, R.; Zheng, Z.; Spurgeon, J.; Yang, X. Enhanced Photoelectrochemical Water-Splitting Performance of Semiconductors by Surface Passivation Layers. *Energy Environ. Sci.* **2014**, *7* (8), 2504–2517.
- (35) Hu, S.; Lewis, N. S.; Ager, J. W.; Yang, J.; McKone, J. R.; Strandwitz, N. C. Thin-Film Materials for the Protection of Semiconducting Photoelectrodes in Solar-Fuel Generators. *J. Phys. Chem. C* **2015**, *119* (43), 24201–24228.
- (36) Lichterman, M. F.; Sun, K.; Hu, S.; Zhou, X.; McDowell, M. T.; Shaner, M. R.; Richter, M. H.; Crumlin, E. J.; Carim, A. I.; Saadi, F. H.; Brunchwitz, B. S.; Lewis, N. S. Protection of Inorganic Semiconductors for Sustained, Efficient Photoelectrochemical Water Oxidation. *Catal. Today* **2016**, *262*, 11–23.
- (37) Lewis, N. S. Developing a Scalable Artificial Photosynthesis Technology through Nanomaterials by Design. *Nat. Nanotechnol.* **2016**, *11* (12), 1010–1019.
- (38) Digdaya, I. A.; Adhyaksa, G. W. P.; Trzesniewski, B. J.; Garnett, E. C.; Smith, W. A. Interfacial Engineering of Metal-Insulator-Semiconductor Junctions for Efficient and Stable Photoelectrochemical Water Oxidation. *Nat. Commun.* **2017**, *8* (May), 15968.
- (39) Wang, T.; Luo, Z.; Li, C.; Gong, J. Controllable Fabrication of Nanostructured Materials for Photoelectrochemical Water Splitting via Atomic Layer Deposition. *Chem. Soc. Rev.* **2014**, *43* (22), 7469–7484.
- (40) Wen, L.; Zhou, M.; Wang, C.; Mi, Y.; Lei, Y. Nanoengineering Energy Conversion and Storage Devices via Atomic Layer Deposition. *Adv. Energy Mater.* **2016**, *6* (23), 1600468.
- (41) Miikkulainen, V.; Leskelä, M.; Ritala, M.; Puurunen, R. L.; Leskelä, M.; Ritala, M.; Puurunen, R. L. Crystallinity of Inorganic Films Grown by Atomic Layer Deposition: Overview and General Trends. *J. Appl. Phys.* **2013**, *113* (2), 021301.
- (42) Seger, B.; Tilley, D. S.; Pedersen, T.; Vesborg, P. C. K.; Hansen, O.; Grätzel, M.; Chorkendorff, I. Silicon Protected with Atomic Layer Deposited TiO₂: Durability Studies of Photocathodic H₂ Evolution. *RSC Adv.* **2013**, *3* (48), 25902–25907.
- (43) Tang-Kong, R.; Winter, R.; Brock, R.; Tracy, J.; Eizenberg, M.; Dauskardt, R. H.; McIntyre, P. C. The Role of Catalyst Adhesion in ALD-TiO₂ Protection of Water Splitting Silicon Anodes. *ACS Appl. Mater. Interfaces* **2018**, *10* (43), 37103–37109.
- (44) Karbalaei Akbari, M.; Hai, Z.; Wei, Z.; Detavernier, C.; Solano, E.; Verpoort, F.; Zhuiykov, S. ALD-Developed Plasmonic Two-Dimensional Au-WO₃-TiO₂ Heterojunction Architectonics for Design of Photovoltaic Devices. *ACS Appl. Mater. Interfaces* **2018**, *10* (12), 10304–10314.
- (45) Seger, B.; Pedersen, T.; Laursen, A. B.; Vesborg, P. C. K.; Hansen, O.; Chorkendorff, I. Using TiO₂ as a Conductive Protective Layer for Photocathodic H₂ Evolution. *J. Am. Chem. Soc.* **2013**, *135* (3), 1057–1064.
- (46) Seger, B.; Tilley, S. D.; Pedersen, T.; Vesborg, P. C. K.; Hansen, O.; Grätzel, M.; Chorkendorff, I. Silicon Protected with Atomic Layer Deposited TiO₂: Conducting versus Tunnelling through TiO₂. *J. Mater. Chem. a* **2013**, *1* (47), 15089–15094.
- (47) Bae, D.; Shayestehaminzadeh, S.; Thorsteinsson, E. B.; Pedersen, T.; Hansen, O.; Seger, B.; Vesborg, P. C. K.; Ólafsson, S.; Chorkendorff, I. Protection of Si Photocathode Using TiO₂ Deposited by High Power Impulse Magnetron Sputtering for H₂ Evolution in Alkaline Media. *Sol. Energy Mater. Sol. Cells* **2016**, *144* (JANUARY), 758–765.
- (48) Gu, J.; Aguiar, J. A.; Ferrere, S.; Steirer, K. X.; Yan, Y.; Xiao, C.; Young, J. L.; Al-Jassim, M.; Neale, N. R.; Turner, J. A. A Graded Catalytic-Protective Layer for an Efficient and Stable Water-Splitting

- Photocathode. *Nat. Energy* **2017**, 2 (2), 1–8.
- (49) Engel, J.; Bishop, S. R.; Vayssieres, L.; Tuller, H. L. In Situ Electrical Characterization of Anatase TiO₂ quantum Dots. *Adv. Funct. Mater.* **2014**, 24 (31), 4952–4958.
- (50) Ros, C.; Andreu, T.; Hernández-Alonso, M. D.; Penelas-Pérez, G.; Arbiol, J.; Morante, J. R. Charge Transfer Characterization of ALD-Grown TiO₂ Protective Layers in Silicon Photocathodes. *ACS Appl. Mater. Interfaces* **2017**, 9, 17932–17941.
- (51) Chen, Y. W.; Prange, J. D.; Dühnen, S.; Park, Y.; Gunji, M.; Chidsey, C. E. D.; McIntyre, P. C. Atomic Layer-Deposited Tunnel Oxide Stabilizes Silicon Photoanodes for Water Oxidation. *Nat. Mater.* **2011**, 10 (7), 539–544.
- (52) Scheuermann, A. G.; Prange, J. D.; Gunji, M.; Chidsey, C. E. D.; McIntyre, P. C. Effects of Catalyst Material and Atomic Layer Deposited TiO₂ Oxide Thickness on the Water Oxidation Performance of Metal–Insulator–Silicon Anodes. *Energy Environ. Sci.* **2013**, 6 (8), 2487.
- (53) Satterthwaite, P. F.; Scheuermann, A. G.; Hurley, P. K.; Chidsey, C. E. D.; McIntyre, P. C. Engineering Interfacial Silicon Dioxide for Improved Metal–Insulator–Semiconductor Silicon Photoanode Water Splitting Performance. *ACS Appl. Mater. Interfaces* **2016**, 8 (20), 13140–13149.
- (54) McDowell, M. T.; Lichterman, M. F.; Carim, A. I.; Liu, R.; Hu, S.; Brunshwig, B. S.; Lewis, N. S. The Influence of Structure and Processing on the Behavior of TiO₂ Protective Layers for Stabilization of n-Si/TiO₂/Ni Photoanodes for Water Oxidation. *ACS Appl. Mater. Interfaces* **2015**, 7 (28), 15189–15199.
- (55) Hu, S.; Richter, M. H.; Lichterman, M. F.; Beardslee, J.; Mayer, T.; Brunshwig, B. S.; Lewis, N. S. Electrical, Photoelectrochemical, and Photoelectron Spectroscopic Investigation of the Interfacial Transport and Energetics of Amorphous TiO₂/Si Heterojunctions. *J. Phys. Chem. C* **2016**, 120 (6), 3117–3129.
- (56) Xia, Z.; Zhou, X.; Li, J.; Qu, Y. Protection Strategy for Improved Catalytic Stability of Silicon Photoanodes for Water Oxidation. *Sci. Bull.* **2015**, 60 (16), 1395–1402.
- (57) Mei, B.; Pedersen, T.; Malacrida, P.; Bae, D.; Frydendal, R.; Hansen, O.; Vesborg, P. C. K.; Seger, B.; Chorkendorff, I. Crystalline TiO₂: A Generic and Effective Electron-Conducting Protection Layer for Photoanodes and -Cathodes. *J. Phys. Chem. C* **2015**, 119 (27), 15019–15027.
- (58) Scheuermann, A. G.; Lawrence, J. P.; Kemp, K. W.; Ito, T.; Walsh, A.; Chidsey, C. E. D.; Hurley, P. K.; McIntyre, P. C. Design Principles for Maximizing Photovoltage in Metal-Oxide-Protected Water-Splitting Photoanodes. *Nat. Mater.* **2015**, 15 (October), 99–105.
- (59) Moehl, T.; Suh, J.; Sévery, L.; Wick-Joliat, R.; Tilley, S. D. Investigation of (Leaky) ALD TiO₂ Protection Layers for Water Splitting Photoelectrodes. *ACS Appl. Mater. Interfaces* **2017**, acsami.7b12564.
- (60) Campet, G.; Manaud, J. P.; Puprichkun, C.; Sun, Z. W.; Salvador, P. Protection of Photoanodes against Photo-Corrosion by Surface Deposition of Oxide Films: Criteria for Choosing the Protective Coating. *Act. Passiv. Electron. Components* **1989**, 13 (3), 175–189.
- (61) Abendroth, B.; Moebus, T.; Rentrop, S.; Strohmeier, R.; Vinnichenko, M.; Weling, T.; Stöcker, H.; Meyer, D. C. Atomic Layer Deposition of TiO₂ from Tetrakis(Dimethylamino) Titanium and H₂O. *Thin Solid Films* **2013**, 545, 176–182.
- (62) Aarik, J.; Aidla, A.; Uustare, T.; Ritala, M.; Leskela, M. TTIP as A Precursor for ALD Characterization. Pdf. **2000**, 385–395.
- (63) Aarik, J.; Aidla, A.; Uustare, T.; Sammelselg, V. Morphology and Structure of TiO₂ Thin Films Grown by Atomic Layer Deposition. *J. Cryst. Growth* **1995**, 148 (3), 268–275.
- (64) Aarik, J.; Aidla, A.; Uustare, T.; Sammelselg, V. Morphology and Structure of TiO₂ Thin Films Grown by Atomic Layer Deposition. *J. Cryst. Growth* **1995**, 148 (3), 268–275.
- (65) Reiners, M.; Xu, K.; Aslam, N.; Devi, A.; Waser, R.; Hoffmann-Eifert, S. Growth and Crystallization of TiO₂ Thin Films by Atomic Layer Deposition Using a Novel Amido Guanidinate Titanium Source and Tetrakis-Dimethylamido-Titanium. *Chem. Mater.* **2013**, 25 (15), 2934–2943.
- (66) McDowell, M. T.; Lichterman, M. F.; Carim, A. I.; Liu, R.; Hu, S.; Brunshwig, B. S.; Lewis, N. S. The Influence of Structure and Processing on the Behavior of TiO₂ Protective Layers for Stabilization of n-Si/TiO₂/Ni Photoanodes for Water Oxidation. *ACS Appl. Mater. Interfaces* **2015**, 7 (28), 15189–15199.
- (67) Scheuermann, A. G.; Lawrence, J. P.; Meng, A. C.; Tang, K.; Hendricks, O. L.; Chidsey, C. E. D.; McIntyre, P. C. Titanium Oxide Crystallization and Interface Defect Passivation for High Performance Insulator-Protected Schottky Junction MIS Photoanodes. *ACS Appl. Mater. Interfaces* **2016**, 8 (23), 14596–14603.
- (68) Heiss, M.; Conesa-Boj, S.; Ren, J.; Tseng, H. H.; Gali, A.; Rudolph, A.; Uccelli, E.; Peiró, F.; Morante, J. R.; Schuh, D.; Reiger, E.; Kaxiras, E.; Arbiol, J.; Fontcuberta I Morral, A. Direct Correlation of

- Crystal Structure and Optical Properties in Wurtzite/Zinc-Blende GaAs Nanowire Heterostructures. *Phys. Rev. B - Condens. Matter Mater. Phys.* **2011**, *83* (4), 1–11.
- (69) Ohsaka, T.; Izumi, F.; Fujiki, Y. Raman Spectrum of Anatase, TiO₂. *J. Raman Spectrosc.* **1978**, *7* (6), 321–324.
- (70) Guerra-Nuñez, C.; Zhang, Y.; Li, M.; Chawla, V.; Erni, R.; Michler, J.; Park, H. G.; Utke, I. Morphology and Crystallinity Control of Ultrathin TiO₂ Layers Deposited on Carbon Nanotubes by Temperature-Step Atomic Layer Deposition. *Nanoscale* **2015**, *7* (24), 10622–10633.
- (71) Gupta, S. K.; Desai, R.; Jha, P. K.; Sahoo, S.; Kirin, D. Titanium Dioxide Synthesized Using Titanium Chloride: Size Effect Study Using Raman Spectroscopy and Photoluminescence. *J. Raman Spectrosc.* **2010**, *41* (3), 350–355.
- (72) Saga, T. Advances in Crystalline Silicon Solar Cell Technology for Industrial Mass Production. *NPG Asia Mater.* **2010**, *2* (3), 96–102.
- (73) Chen, L.; Toma, F. M.; Cooper, J. K.; Lyon, A.; Lin, Y.; Sharp, I. D.; Ager, J. W. Mo-Doped BiVO₄ Photoanodes Synthesized by Reactive Sputtering. *ChemSusChem* **2015**, *8* (6), 1066–1071.
- (74) Smith, W. A.; Sharp, I. D.; Strandwitz, N. C.; Bisquert, J. Interfacial Band-Edge Energetics for Solar Fuels Production. *Energy Environ. Sci.* **2015**, *8* (10), 2851–2862.
- (75) Mills, T. J.; Lin, F.; Boettcher, S. W. Theory and Simulations of Electrolyte-Coated Semiconductor Electrodes for Solar Water Splitting. *Phys. Rev. Lett.* **2014**, *112* (14), 1–5.
- (76) Lichterman, M. F.; Hu, S.; Richter, M. H.; Crumlin, E.; Axnanda, S.; Favaro, M.; Drisdell, W. S.; Hussain, Z.; Mayer, T.; Brunschwig, B. S.; Lewis, N.; Liu, Z.; Lewerenz, H.-J. Direct Observation of the Energetics at a Semiconductor/Liquid Junction by Operando X-Ray Photoelectron Spectroscopy. *Energy Environ. Sci.* **2015**, *8*, 2409–2416.
- (77) Louie, M. W.; Bell, A. T. An Investigation of Thin-Film Ni-Fe Oxide Catalysts for the Electrochemical Evolution of Oxygen. *J. Am. Chem. Soc.* **2013**, *135* (33), 12329–12337.
- (78) Corrigan, D. A. The Catalysis of the Oxygen Evolution Reaction by Iron Impurities in Thin Film Nickel Oxide Electrodes. *J. Electrochem. Soc.* **1987**, *134* (2), 377.
- (79) Biset-Peiró, M.; Fàbrega, C.; Morante, J. R.; Andreu, T.; Murcia-López, S.; Fàbrega, C.; Morante, J. R.; Andreu, T. Multilayer Ni/Fe Thin Films as Oxygen Evolution Catalysts for Solar Fuel Production. *J. Phys. D. Appl. Phys.* **2017**, *50* (10).
- (80) Gong, M.; Dai, H. A Mini Review of NiFe-Based Materials as Highly Active Oxygen Evolution Reaction Electrocatalysts. *Nano Res.* **2014**, *8* (1), 23–39.
- (81) Kenney, M. J.; Gong, M.; Li, Y.; Wu, J. Z.; Feng, J.; Lanza, M.; Dai, H. High-Performance Silicon Photoanodes Passivated with Ultrathin Nickel Films for Water Oxidation. *Science (80-)*. **2013**, *342* (6160), 836–840.
- (82) Kiseok Oh, a Cristelle Meriadec, b Benedikt Lassalle-Kaiser, c Vincent Dorcet, a Bruno Fabre, A.; Soraya Ababou-Girard, b Loic Joanny, d F. G. and G. L.; Oh, K.; Meriadec, C.; Lassalle-Kaiser, B.; Dorcet, V.; Fabre, B.; Ababou-Girard, S.; Joanny, L.; Gouttefangeas, F.; Loget, G. Elucidating the Performance and Unexpected Stability of Partially Coated Water-Splitting Silicon Photoanodes. *Energy Environ. Sci.* **2018**, 0–11.
- (83) Dette, C.; Hurst, M. R.; Deng, J.; Nellist, M. R.; Boettcher, S. W. Structural Evolution of Metal (Oxy)Hydroxide Nanosheets during the Oxygen Evolution Reaction. **2018**.
- (84) Trotochaud, L.; Young, S. L.; Ranney, J. K.; Boettcher, S. W. Nickel-Iron Oxyhydroxide Oxygen-Evolution Electrocatalysts: The Role of Intentional and Incidental Iron Incorporation. *J. Am. Chem. Soc.* **2014**, *136* (18), 6744–6753.
- (85) Nardi, K. L.; Yang, N.; Dickens, C. F.; Strickler, A. L.; Bent, S. F. Creating Highly Active Atomic Layer Deposited NiO Electrocatalysts for the Oxygen Evolution Reaction. *Adv. Energy Mater.* **2015**, *5* (17), 1–10.
- (86) Zhu, K.; Luo, W.; Zhu, G.; Wang, J.; Zhu, Y.; Zou, Z.; Huang, W. Interface-Engineered Ni(OH)₂/β-like FeOOH Electrocatalysts for Highly Efficient and Stable Oxygen Evolution Reaction. *Chem. - An Asian J.* **2017**, *12* (20), 2720–2726.
- (87) Yu, Y.; Sun, C.; Yin, X.; Li, J.; Cao, S.; Zhang, C.; Voyles, P. M.; Wang, X. Metastable Intermediates in Amorphous Titanium Oxide: A Hidden Role Leading to Ultra-Stable Photoanode Protection. *Nano Lett.* **2018**, *18* (8), 5335–5342.
- (88) Murakami, K.; Rommel, M.; Hudec, B.; Rosová, A.; Hušková, K.; Dobročka, E.; Rammula, R.; Kasikov, A.; Han, J. H.; Lee, W.; Song, S. J.; Paskaleva, A.; Bauer, A. J.; Frey, L.; Fröhlich, K.; Aarik, J.; Hwang, C. S. Nanoscale Characterization of TiO₂ Films Grown by Atomic Layer Deposition on RuO₂ Electrodes. *ACS Appl. Mater. Interfaces* **2014**, *6* (4), 2486–2492.
- (89) Tang, K.; Meng, A. C.; Hui, F.; Shi, Y.; Petach, T.; Hitzman, C.; Koh, A. L.; Goldhaber-Gordon, D.; Lanza, M.; McIntyre, P. C. Distinguishing Oxygen Vacancy Electromigration and Conductive Filament Formation in TiO₂ Resistance Switching Using

- Liquid Electrolyte Contacts. *Nano Lett.* **2017**, *17* (7), 4390–4399.
- (90) Kim, S. K.; Kim, K. M.; Jeong, D. S.; Jeon, W.; Yoon, K. J.; Hwang, C. S. Titanium Dioxide Thin Films for Next-Generation Memory Devices. *J. Mater. Res.* **2013**, *28* (3), 313–325.
- (91) Du, Y.; Kumar, A.; Pan, H.; Zeng, K.; Wang, S.; Yang, P.; Wee, A. T. S. The Resistive Switching in TiO₂ Films Studied by Conductive Atomic Force Microscopy and Kelvin Probe Force Microscopy. *AIP Adv.* **2013**, *3* (082107), 1–7.
- (92) Kwon, D.-H.; Kim, K. M.; Jang, J. H.; Jeon, J. M.; Lee, M. H.; Kim, G. H.; Li, X.-S.; Park, G.-S.; Lee, B.; Han, S.; Kim, M.; Hwang, C. S. Atomic Structure of Conducting Nanofilaments in TiO₂ Resistive Switching Memory. *Nat. Nanotechnol.* **2010**, *5* (2), 148–153.
- (93) Han, T.; Shi, Y.; Song, X.; Mio, A.; Valenti, L.; Hui, F.; Privitera, S.; Lombardo, S.; Lanza, M. Ageing Mechanisms of Highly Active and Stable Nickel-Coated Silicon Photoanodes for Water Splitting. *J. Mater. Chem. A* **2016**, *4* (21), 8053–8060.
- (94) Biesinger, M. C.; Lau, L. W. M.; Gerson, A. R.; Smart, R. S. C. The Role of the Auger Parameter in XPS Studies of Nickel Metal, Halides and Oxides. *Phys. Chem. Chem. Phys.* **2012**, *14* (7), 2434–2442.
- (95) Zhou, H.; Yu, F.; Zhu, Q.; Sun, J.; Qin, F.; Yu, L.; Bao, J.; Yu, Y. Water Splitting by Electrolysis at High Current Density under 1.6 Volt. *Energy Environ. Sci.* **2018**, No. 60 mL, 3–5.
- (96) Biesinger, M. C.; Payne, B. P.; Grosvenor, A. P.; Lau, L. W. M.; Gerson, A. R.; Smart, R. S. C. Resolving Surface Chemical States in XPS Analysis of First Row Transition Metals, Oxides and Hydroxides: Cr, Mn, Fe, Co and Ni. *Appl. Surf. Sci.* **2011**, *257* (7), 2717–2730.
- (97) Mei, B.; Permyakova, A. a; Frydendal, R.; Bac, D.; Pedersen, T.; Malacrida, P.; Hansen, O.; Stephens, I. E. L.; Vesborg, P. C. K.; Seger, B.; Chorkendor, I. Iron-Treated NiO as a Highly Transparent p - Type Protection Layer for Efficient Si-Based Photoanodes. *J. Phys. Chem. Lett.* **2014**, *5* (20), 3456–3461.
- (98) Seger, B.; Tilley, S. D.; Pedersen, T.; Vesborg, P. C. K.; Hansen, O.; Grätzel, M.; Chorkendorff, I. Silicon Protected with Atomic Layer Deposited TiO₂: Conducting versus Tunnelling through TiO₂. *J. Mater. Chem. A* **2013**, *1* (47), 15089–15094.
- (99) Samin, A. J.; Taylor, C. D. An Analysis of Limiting Cases for the Metal Oxide Film Growth Kinetics Using an Oxygen Defects Model Accounting for Transport and Interfacial Reactions. **2018**, *43* (4), 317–326.
- (100) Hannula, M.; Ali-Löytty, H.; Lahtonen, K.; Sarlin, E.; Saari, J.; Valden, M. Improved Stability of Atomic Layer Deposited Amorphous TiO₂ Photoelectrode Coatings by Thermally Induced Oxygen Defects. *Chem. Mater.* **2018**, acs.chemmater.7b02938.
- (101) Tang, K.; Meng, A. C.; Hui, F.; Shi, Y.; Petach, T.; Hitzman, C.; Koh, A. L.; Goldhaber-Gordon, D.; Lanza, M.; McIntyre, P. C. Distinguishing Oxygen Vacancy Electromigration and Conductive Filament Formation in TiO₂ Resistance Switching Using Liquid Electrolyte Contacts. *Nano Lett.* **2017**, *17* (7), 4390–4399.
- (102) Kim, K. M.; Jeong, D. S.; Hwang, C. S. Nanofilamentary Resistive Switching in Binary Oxide System; A Review on the Present Status and Outlook. *Nanotechnology* **2011**, *22* (25).
- (103) Agrell, H. G.; Boschloo, G.; Hagfeldt, A. Conductivity Studies of Nanostructured TiO₂ Films Permeated with Electrolyte. *J. Phys. Chem. B* **2004**, *108* (33), 12388–12396.
- (104) Han, I.; Tang, P.; Reyes-Carmona, Á.; Rodríguez-García, B.; Torrén, M.; Morante, J. R.; Arbiol, J.; Galan-Mascaros, J. R. Enhanced Activity and Acid pH Stability of Prussian Blue-Type Oxygen Evolution Electrocatalysts Processed by Chemical Etching. *J. Am. Chem. Soc.* **2016**, *138* (49), 16037–16045.
- (105) Fàbrega, C.; Hernández-Ramírez, F.; Daniel Prades, J.; Jiménez-Díaz, R.; Andreu, T.; Ramon Morante, J. On the Photoconduction Properties of Low Resistivity TiO₂ Nanotubes. *Nanotechnology* **2010**, *21* (44).
- (106) Nakajima, A.; Watanabe, T.; Wang, R.; Hashimoto, K.; Minabe, M.; Koizumi, S.; Fujishima, A. Photocatalytic Activity and Photoinduced Hydrophilicity of Titanium Dioxide Coated Glass. *Thin Solid Films* **2002**, *351* (1–2), 260–263.

Supplementary Information

Insight into the degradation mechanisms of Atomic Layer Deposited TiO₂ as photoanode protective layer.

Carles Ros^{a,}, Nina M. Carretero^a, Jeremy David^c, Jordi Arbiol^{c,d}, Teresa Andreu^{a,*}, Joan R. Morante^{a,b}*

^a Catalonia Institute for Energy Research (IREC). Jardins de les Dones de Negre 1, 08930 Sant Adrià del Besòs, Barcelona, Spain

^b Universitat de Barcelona (UB), Martí i Franquès, 1, 08028 Barcelona, Spain

^c Catalan Institute of Nanoscience and Nanotechnology (ICN2), CSIC and BIST, Campus UAB, Bellaterra, 08193 Barcelona, Spain

^d ICREA, Pg. Lluís Companys 23, 08010 Barcelona, Spain



Figure S1. Picture of a n⁺p-Si photoanode presenting the 1.2 x 1.2 cm² Si chip with an active area of 1 x 1 cm², defined by a perimeter of 100 nm of SiO₂ thick insulator layer. The Si chip was protected by TiO₂-ALD and Ag paint soldered to a Cu wire, and further encapsulated with epoxy resin.

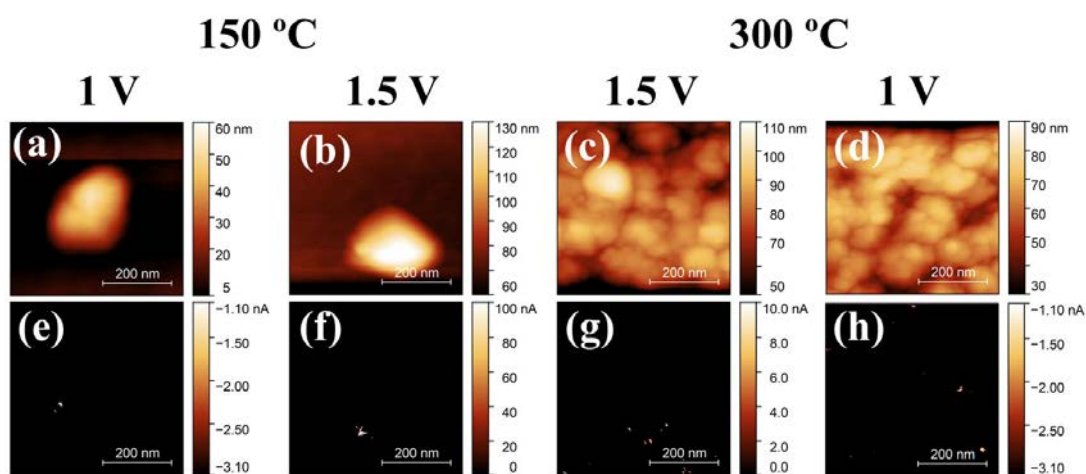


Figure S2. AFM height map of TiO₂ + NiFe layers grown at 150 °C (a, b, e, f) and 300 °C (c, d, g, g)), and its respective current intensity maps, at potentials of 1 (e, h) and 1.5 V (f, g) in different sample regions.

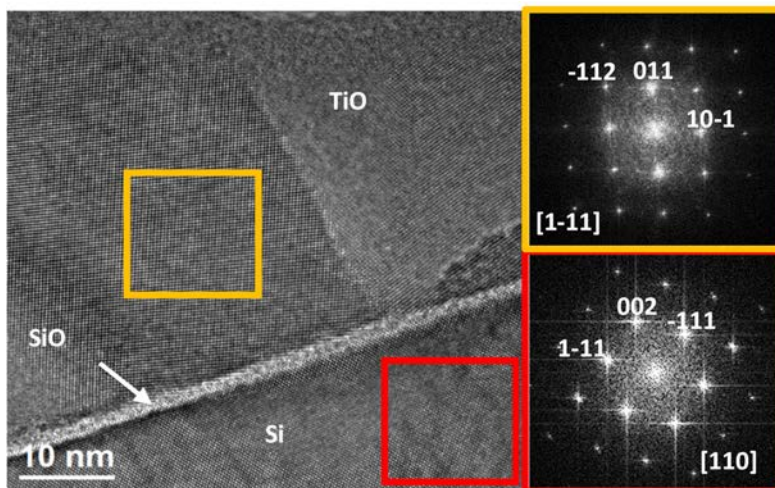


Figure S3. HRTEM image of the TiO_2 -300 °C interface with Si chip. Insets present the FFT of indicated regions: in yellow, anatase TiO_2 crystal planes are observed; in red, the silicon monocrystalline substrate.

An intermediate 1.5-2 nm amorphous SiO_x native oxide layer can be seen between Si/ TiO_2 interface. As Si photoanodes had been HF-etched immediately before ALD- TiO_2 deposition, the formation of this observed SiO_x is attributed to the ALD process, when H_2O pulses first reach Si during synthesis.

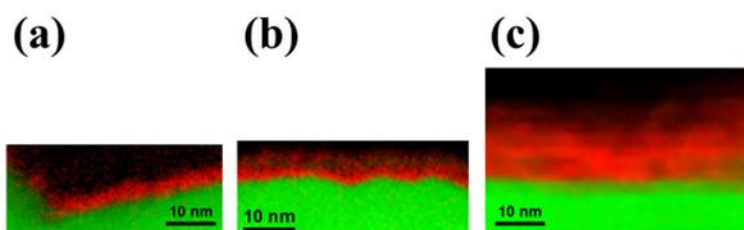
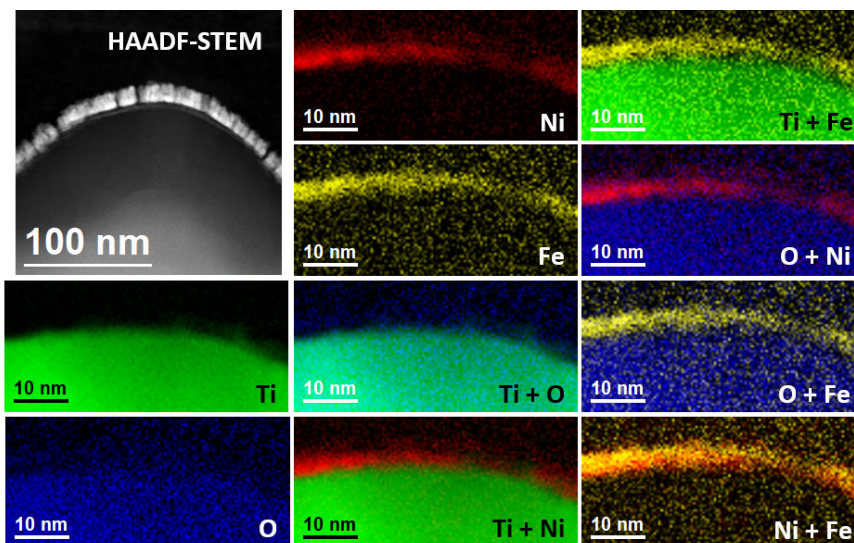


Figure S4. EELS maps (Ti in green and Ni in red) of a p⁺n-Si photoanode protected with TiO_2 ALD-deposited at 300 °C and NiFe decorated a) after fabrication, b) after 100 cycles in 1 M KOH and c) after 400 h stability test in 1 M KOH at 1.3 V vs RHE under 1 sun illumination.

(a)



(b)

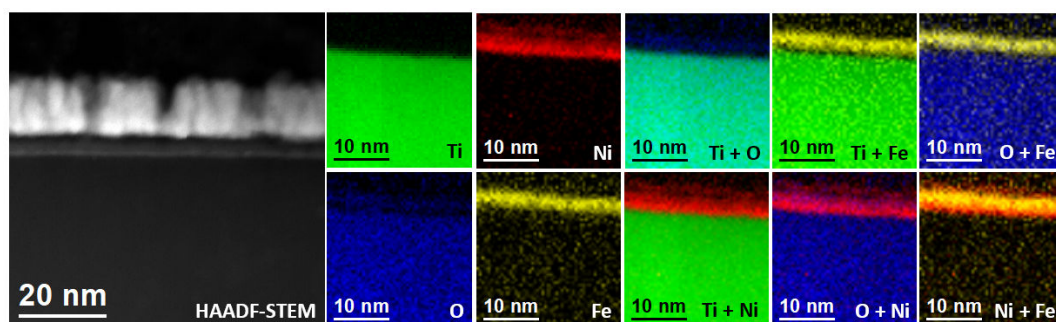


Figure S5: HAADF-STEM image and EELS maps of a p⁺n-Si photoanode protected with TiO₂ ALD-deposited at 150 °C and NiFe decorated before (a) and after electrochemical cycling (b)

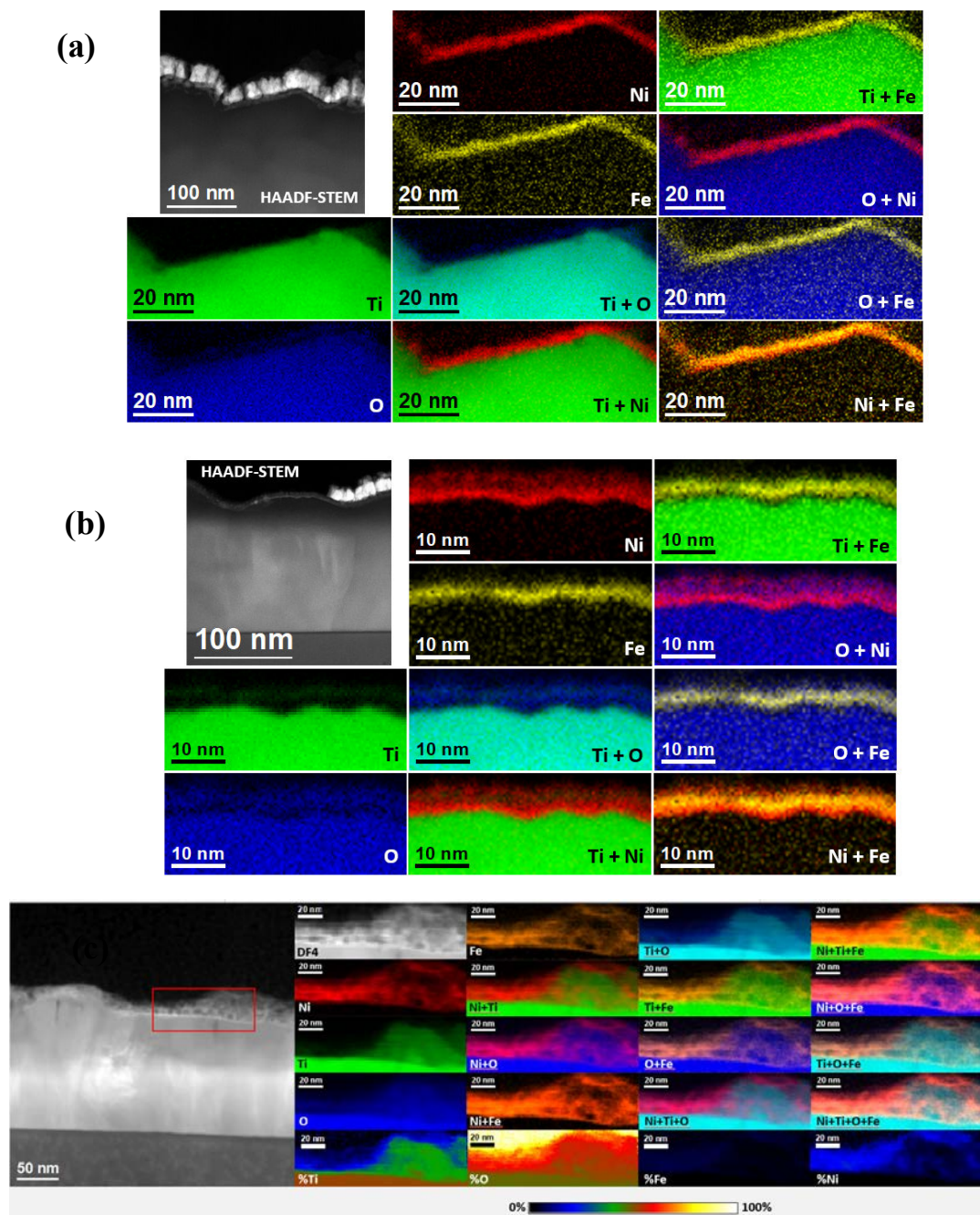


Figure S6: HAADF-STEM image and EELS maps of a p⁺n-Si photoanode protected with TiO₂ ALD-deposited at 300 °C and NiFe decorated, as synthesized (a), after electrochemical cycling (b), and after stability (c)

XPS analysis.

Table S1: XPS detection percentage of selected elements for photoanodes with different ALD growth temperature and NiFe decorated, as prepared and after cycling in 1 M KOH.

	C1s (%)	O1s (%)	Ti2p (%)	Fe2p (%)	Ni2p (%)
150 °C + NiFe	52.47	34.09	0.19	3.13	10.12
150 °C + NiFe cycled	39.93	41.5	0.35	4.93	13.29
300 °C + NiFe	47.75	35.89	0.37	4.67	11.32
300 °C + NiFe cycled	35.56	45.56	0.47	4.95	13.46

The catalyst presents an average Ni:Fe ratio of 2.8:1. An increase of the oxygen content can be detected after cycling, pointing at oxidation of the catalyst layer by the alkaline electrolyte, OH⁻ intercalation and the anodic electrochemical potentials applied during cycling, corroborating the previous results obtained by HRTEM and EELS.

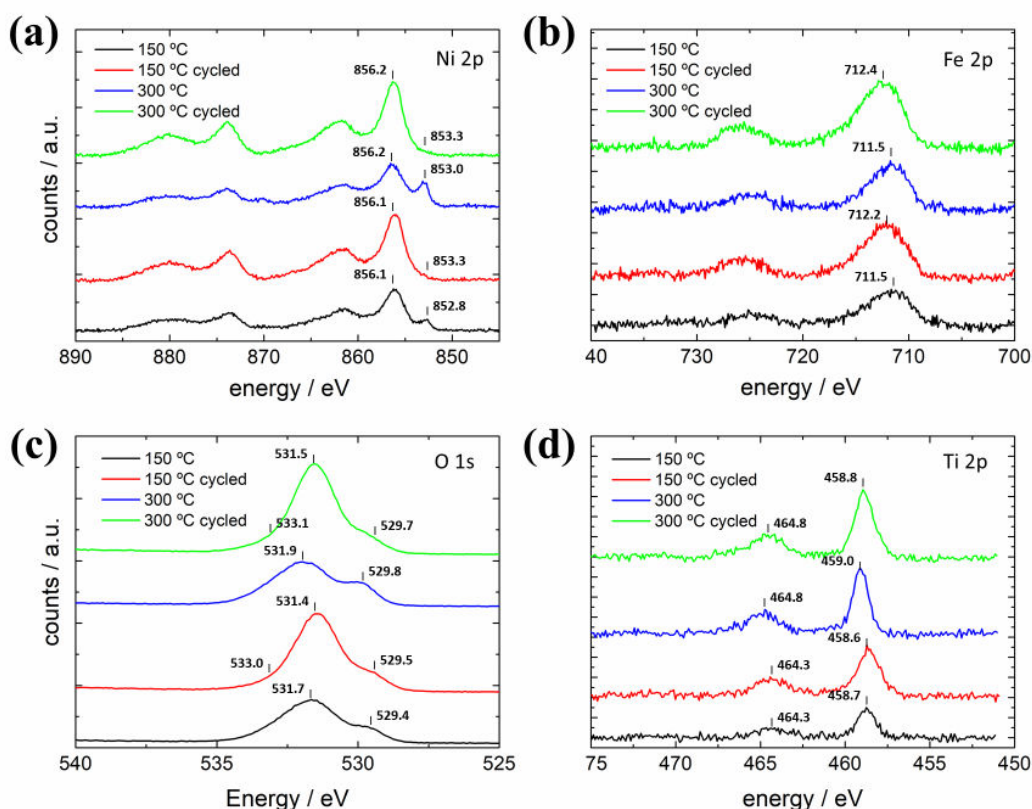


Figure S7. XPS spectra of samples with 150 °C and 300 °C deposited TiO₂ layers and NiFe catalyst as prepared and after cycling in 1 M KOH of a) Ni 2p b) Fe 2p c) O 1s and d) Ti 2p peaks.

Analyzing the electronic core-level photoemission peaks more in detail, significant differences are observed for samples with TiO₂ deposition temperatures of 150 and 300 °C and after cycling them in 1 M KOH (Figure S7).

Analyzing the **Ni2p_{3/2} peak**, we can observe at bonding energy of ~853 eV the presence of the Ni(0) metallic peak in the samples as prepared, which indicates the incomplete native oxidation caused by atmospheric oxygen¹ and completely disappearing after cycling, which indicates complete oxidation, also corroborated by the increase in the Ni(II) and Ni(III) peaks (~856.2 eV). Apart from this, fitting the Ni2p peaks to a specific Ni(II) or Ni(III) chemical state is difficult, as NiO, Ni(OH)₂, and NiOOH share various peak energies², but differ on the ratio between these peaks³. The high percentage detected for the peak at ~856.2 eV (> 40%) correlated with Ni(OH)₂/NiO/NiOOH species, demonstrates that most probably, the catalytic film is composed of all of these chemical states^{4,5}.

Concerning the **Fe2p3/2 peak**, there is no presence of metallic iron, and the signal can be attributed to Fe (III) species as the binding energy is around 711,5 eV, and for Fe(II) species this value is lower. After cycling, peaks suffer a slight shift towards higher energies (~ 0.5 eV). The signal-to-noise ratio, although showing Fe(III) peaks, does not allow us to differentiate between NiFe_2O_4 , FeOOH or Fe_2O_3 ^{6,7}. As Fe is almost 3 times less abundant than Ni in these samples, all of it can be expected to be intercalated forming mostly Ni(Fe)OOH .

O1s signal is mainly attributed either to Ni or Fe coordination. Two clear peaks can be seen for uncycled samples, one corresponding to metal oxides (~ 529.5 eV) and another one which could be ascribed to metal hydroxides (~ 531.5 eV)³. In the cycled samples, a third peak is detected at 533.1 eV, which is attributed to physisorbed water (533.5 eV)³. Also, the hydroxide peak becomes much more predominant over the oxides, as it should be expected^{1,6}, together with absolute higher oxygen content detected, caused by the oxidation of the metallic Ni-Fe and the corresponding OH intercalation.

Regarding the **Ti2p peaks** of all samples, the main peak at ~ 458.7 eV can be attributed to the Ti (IV) 2p3/2 with the corresponding 2p1/2 peak at 464.3 eV⁸.

Valence Band Studies. After 5 nm NiFe coating is thermally evaporated on top of TiO_2 grown at 150 and 300 °C, metallic behaviour is detected. NiFe layer before cycling has mainly a metallic nature with a partial contribution of a native oxide, which predominantly oxidized afterwards but still with free electrons, being former ones the responsible of signal at lower than 0 eV. Two slopes can be assigned for cycled samples (Fig.S8 cyan and pink), one to p-type semiconductor and another one to free electrons at energies slightly lower than 0 eV. The active catalyst, named as nanostructured Ni(Fe)OOH presents electronic structures significantly different from bulk NiO due to significant interaction with the alkaline electrolyte, surface states, three dimensional flakes nanostructure, and porosity⁹. The slightly higher Fermi level for 300 °C sample is translated to lower energies for all cases, as all Fermi levels must equilibrate. Samples with NiFe have around ~ 3 eV lower energy than bare TiO_2 ones. This matches TiO_2 valence band plus TiO_2 band gap, meaning there is a good band alignment between TiO_2 conduction band and the NiFe catalyst.

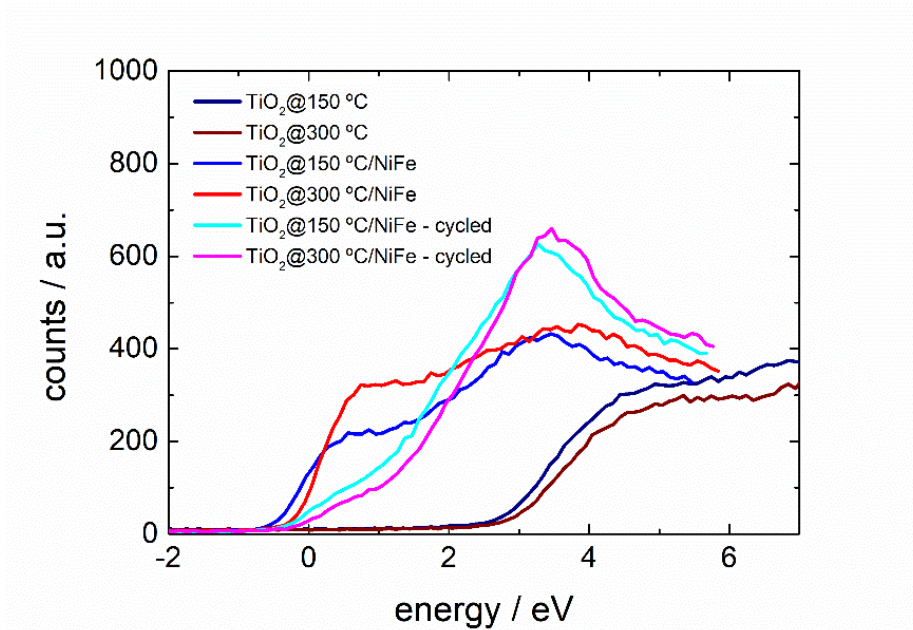


Figure S8. XPS spectra of samples with TiO₂ protective layers ALD grown at 150 and 300 °C, without NiFe catalyst, with it, and with the catalyst after cycling to oxidative potentials in 1 M KOH under 1 sun illumination.

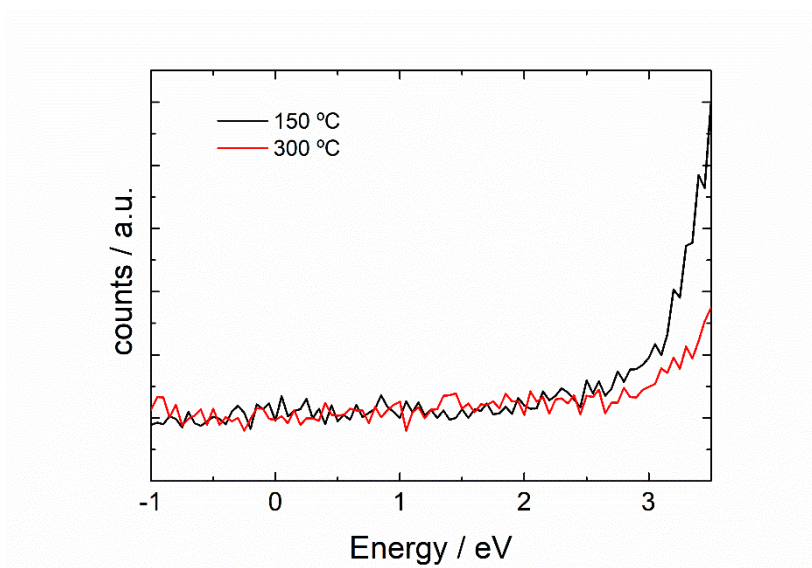


Figure S9. Fine XPS analysis of the 0-3 eV region presenting no visible intra-band gap states such as other works have shown¹⁰ for samples grown at 150 and 300 °C.

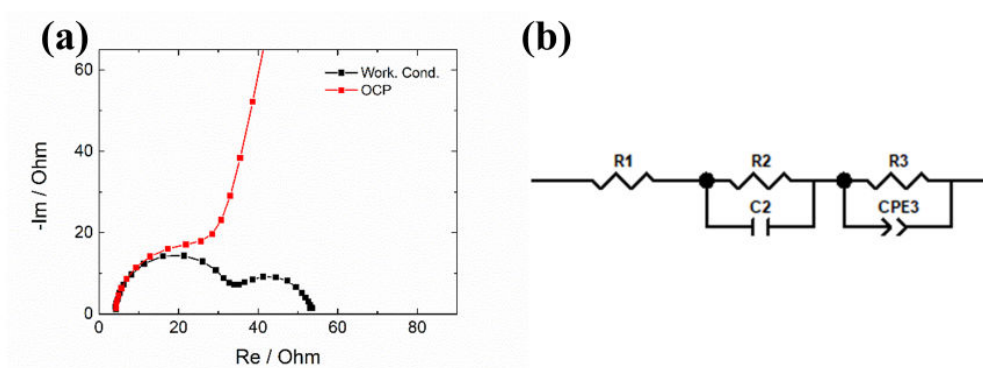


Figure S10. a) EIS measurements of a p^+ -Si anode TiO_2 protected at $300\text{ }^\circ\text{C}$ and NiFe decorated set to 1.8 V vs RHE (Working Conditions) and to open circuit potential (OCP) in dark and in 1 M KOH as electrolyte. The first semicircle is independent of applied potential and the second one varies significantly, proving a non-Ohmic dependence of this second one. b) scheme of the electrical circuit used to fit measured impedance data.

Table S2. Fitted values of Figure S10

	R_1 (Ω)	R_2 (Ω)	C_2 ($\text{F} \cdot \text{cm}^{-2}$)	R_3 (Ω)	CPE_3 ($\text{F} \cdot \text{cm}^{-2} \cdot \text{s}^{\alpha_3-1}$)	α_3
1.8 V VS RHE	4.148	27.8	1.59E-06	21.79	2.67E-04	0.85
OCP	4.108	23.51	1.50E-06	3.15E+05	2.99E-05	0.87316

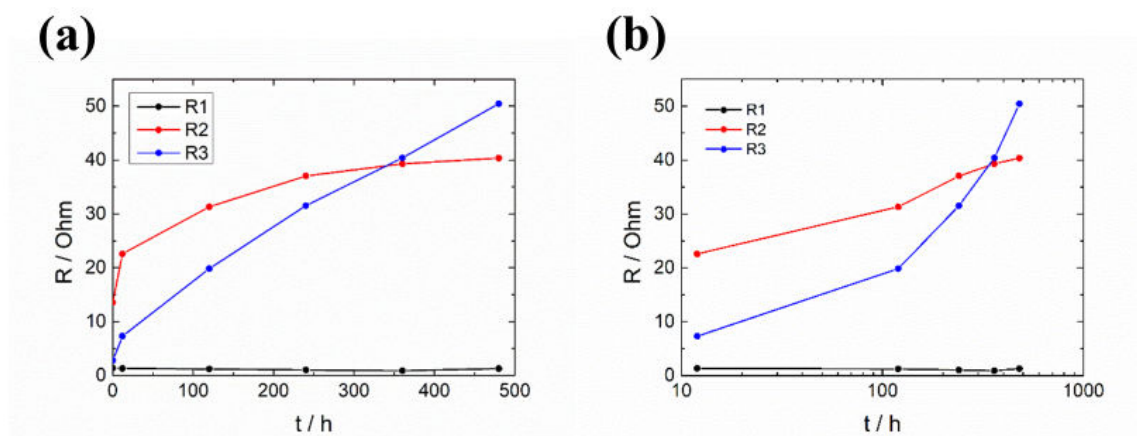


Figure S11. Variation of resistances over time in linear scale (a) and linear-log scale (b) for a p^+ -Si anode protected with TiO_2 ALD-deposited at 300°C and NiFe decorated in 1 M KOH at a fixed potential of 1.8 V vs RHE.

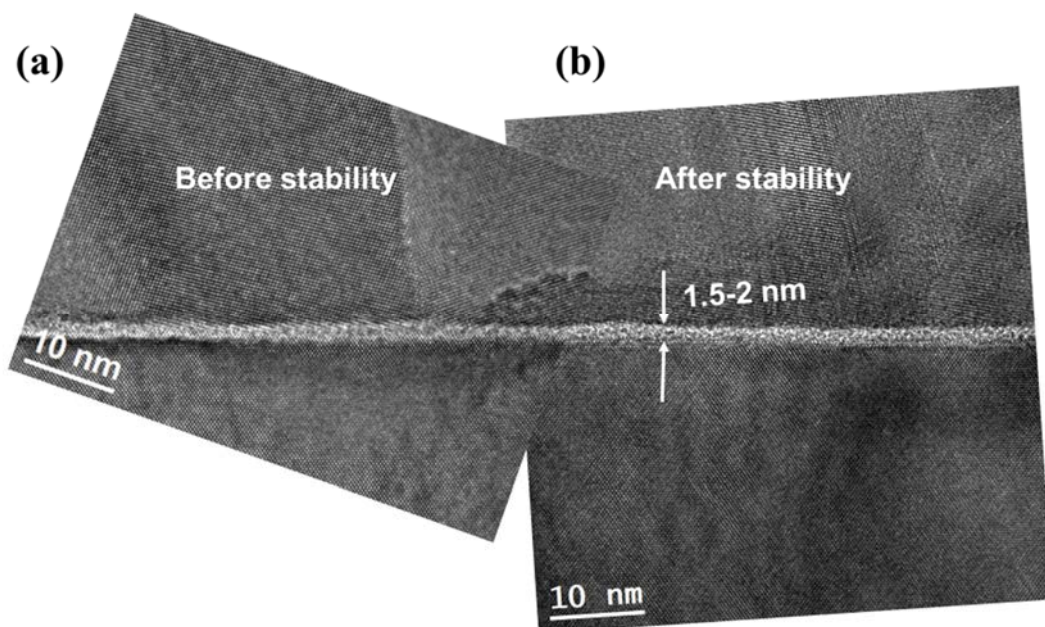


Figure S12. HTREM analysis of the SiO_x layer a) before and b) after the stability measurement of a photoanode after 400 hours of stability at 1.8 V vs RHE. No significant growth can be observed. Increase of the SiO_2 interlayer could be a reason to dramatically increase tunnelling resistivity¹¹, as reported in other works¹².

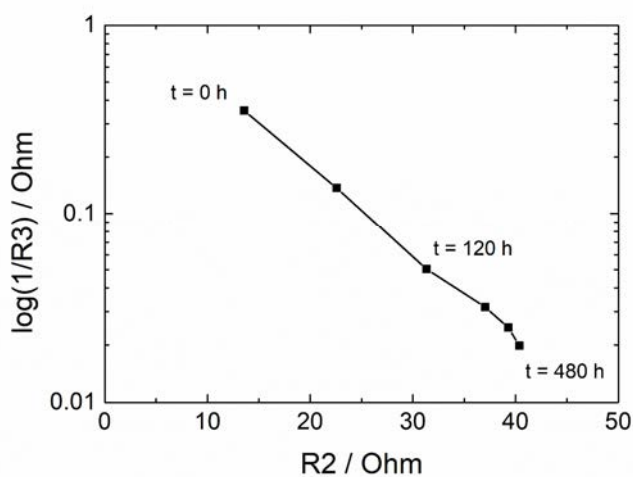
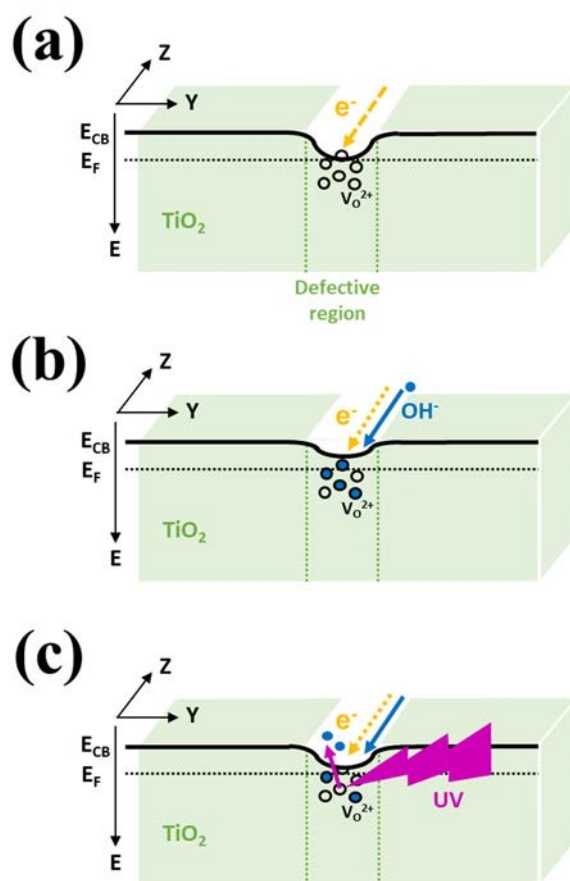


Figure S13. Representation of fitted values in Table S3, $\log(1/R_3)$ as a function of R_2 .

Table S3. EIS fittings in open circuit potential (OCP) conditions corresponding to Figure 7b measured data.

#measure	R_1 ($\text{Ohm}\cdot\text{cm}^2$)	R_2 ($\text{Ohm}\cdot\text{cm}^2$)	C_2 ($\text{F}\cdot\text{cm}^{-2}$)	R_3 ($\text{Ohm}\cdot\text{cm}^2$)	CPE_3 ($\text{F}\cdot\text{cm}^{-2}\cdot\text{S}^{\text{A}_3-1}$)	A_3
1	5.49	4753.0	$1.95\cdot 10^{-6}$	3581.0	$1.85\cdot 10^{-5}$	0.817
2	4.50	167.2	$1.79\cdot 10^{-6}$	118.3	$3.97\cdot 10^{-4}$	0.561
3	4.49	145.2	$1.77\cdot 10^{-6}$	113.4	$5.44\cdot 10^{-4}$	0.530
4	5.27	3686.0	$1.76\cdot 10^{-6}$	1948.0	$4.79\cdot 10^{-5}$	0.742



Scheme S1: energy and cross section diagram corresponding to a preferential path region, showing a) extra states in interfacial defects generate a preferential path, b) OH^- diffusion and oxygen vacancy occupation and c) UV excitation of these states, partially recovering the initial oxygen vacancy abundance.

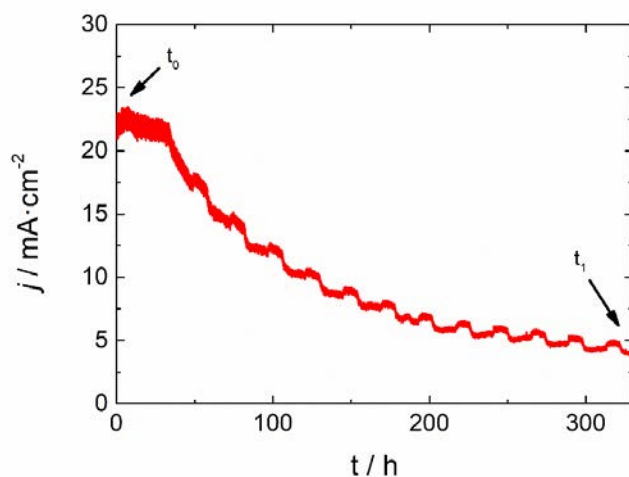


Figure S14. a) Current stability measurement of a p⁺n-Si photoanode protected with TiO₂ ALD-deposited at 300 °C and NiFe decorated at a fixed potential of 1.3 V vs RHE (Observed undulations every 24h are caused by lab temperature variations at night and day). Measurements performed under 1 sun illumination, using 1 M KOH as electrolyte.

References

- (1) Han, T.; Shi, Y.; Song, X.; Mio, A.; Valenti, L.; Hui, F.; Privitera, S.; Lombardo, S.; Lanza, M. Ageing Mechanisms of Highly Active and Stable Nickel-Coated Silicon Photoanodes for Water Splitting. *J. Mater. Chem. A* 2016, 4 (21), 8053–8060.
- (2) Biesinger, M. C.; Lau, L. W. M.; Gerson, A. R.; Smart, R. S. C. The Role of the Auger Parameter in XPS Studies of Nickel Metal, Halides and Oxides. *Phys. Chem. Chem. Phys.* 2012, 14 (7), 2434–2442.
- (3) Biesinger, M. C.; Payne, B. P.; Grosvenor, A. P.; Lau, L. W. M.; Gerson, A. R.; Smart, R. S. C. Resolving Surface Chemical States in XPS Analysis of First Row Transition Metals, Oxides and Hydroxides: Cr, Mn, Fe, Co and Ni. *Appl. Surf. Sci.* 2011, 257 (7), 2717–2730.
- (4) Digdaya, I. A.; Adhyaksa, G. W. P.; Trzesniewski, B. J.; Garnett, E. C.; Smith, W. A. Interfacial Engineering of Metal-Insulator-Semiconductor Junctions for Efficient and Stable Photoelectrochemical Water Oxidation. *Nat. Commun.* 2017, 8 (May), 15968.

- (5) Mei, B.; Permyakova, A. a; Frydendal, R.; Bae, D.; Pedersen, T.; Malacrida, P.; Hansen, O.; Stephens, I. E. L.; Vesborg, P. C. K.; Seger, B.; et al. Iron-Treated NiO as a Highly Transparent p - Type Protection Layer for Efficient Si-Based Photoanodes. *J. Phys. Chem. Lett.* 2014, 5 (20), 3456–3461.
- (6) Zhou, H.; Yu, F.; Zhu, Q.; Sun, J.; Qin, F.; Yu, L.; Bao, J.; Yu, Y. Water Splitting by Electrolysis at High Current Density under 1.6 Volt. *Energy Environ. Sci.* 2018, No. 60 mL, 3–5.
- (7) Lu, Z.; Xu, W.; Zhu, W.; Yang, Q.; Lei, X.; Liu, J.; Li, Y.; Sun, X.; Duan, X. Three-Dimensional NiFe Layered Double Hydroxide Film for High-Efficiency Oxygen Evolution Reaction. *Chem. Commun.* 2014, 50 (49), 6479–6482.
- (8) Biesinger, M. C.; Lau, L. W. M.; Gerson, A. R.; Smart, R. S. C. Resolving Surface Chemical States in XPS Analysis of First Row Transition Metals, Oxides and Hydroxides: Sc, Ti, V, Cu and Zn. *Appl. Surf. Sci.* 2010, 257 (3), 887–898.
- (9) Dette, C.; Hurst, M. R.; Deng, J.; Nellist, M. R.; Boettcher, S. W. Structural Evolution of Metal (Oxy)Hydroxide Nanosheets during the Oxygen Evolution Reaction. 2018.
- (10) Hu, S.; Shaner, M. R.; Beardslee, J. a; Lichterman, M.; Brunshwig, B. S.; Lewis, N. S. Amorphous TiO₂ Coatings Stabilize Si, GaAs, and GaP Photoanodes for Efficient Water Oxidation. *Science* 2014, 344 (6187), 1005–1009.
- (11) Scheuermann, A. G.; Kemp, K. W.; Tang, K.; Lu, D. Q.; Satterthwaite, P. F.; Ito, T.; Chidsey, C. E. D. D.; McIntyre, P. C.; McIntyre, P. C. Conductance and Capacitance of Bilayer Protective Oxides for Silicon Water Splitting Anodes. *Energy Environ. Sci.* 2016, 9 (2), 1–26.
- (12) Kiseok Oh, a Cristelle Meriadec, b Benedikt Lassalle-Kaiser, c Vincent Dorcet, a Bruno Fabre, A.; Soraya Ababou-Girard, b Loic Joanny, d F. G. and G. L.; Oh, K.; Meriadec, C.; Lassalle-Kaiser, B.; Dorcet, V.; Fabre, B.; Ababou-Girard, S.; Joanny, L.; Gouttefangeas, F.; et al. Elucidating the Performance and Unexpected Stability of Partially Coated Water-Splitting Silicon Photoanodes. *Energy Environ. Sci.* 2018, 0–11.

About degradation and regeneration mechanisms of NiO protective layers deposited by ALD on photoanodes

Carles Ros^{a,*}, Teresa Andreu^{a,b,*}, Jordi Arbiol^{c,d}, Joan R. Morante^{a,b}

^aCatalonia Institute for Energy Research (IREC). Jardins de les Dones de Negre 1, 08930 Sant Adrià del Besòs, Barcelona, Spain

^bUniversitat de Barcelona (UB), Martí i Franquès, 1, 08028 Barcelona, Spain

^cCatalan Institute of Nanoscience and Nanotechnology (ICN2), CSIC and The Barcelona Institute of Science and Technology (BIST), Campus UAB, Bellaterra, 08193 Barcelona, Spain

^dICREA, Pg. Lluís Companys 23, 08010 Barcelona, Spain

KEYWORDS: ALD, protective layers, water splitting, nickel oxide, degradation, regeneration.

ABSTRACT

The use of high pH electrolytes requires protective layers to avoid corrosion in photoanodes based on semiconductors like silicon. NiO is one of the materials that complies the requirements of transparency, conductivity, chemical stability and catalysis on its surface in contact with the electrolyte. Here, these layers have been deposited by atomic layer deposition (ALD) at low temperatures, and their stability is analyzed over 1000 hours. Due to the layer structure characteristics, best overall performance has been achieved at 100 °C deposition temperature due to increased native defects and Ni²⁺ vacancies. Progressive time dependent degradation under anodic working conditions is observed, attributed to the formation of higher nickel oxidation states at the electrode/electrolyte interface, resulting in an OER overpotential increase. A regeneration process based on an in situ periodic cyclic voltammetries, bringing the electrodes to cathodic conditions every 3, 12 or 48 hours, has shown to partially recover the main degradation mechanism achieving 85% of stability over 1000 hours with over 11 mA·cm⁻² photocurrents.

INTRODUCTION

As our society turns in the direction of a renewable based energy system, new challenges appear¹. To store one of the most abundant energy sources, the sun, to be used when it is not available, photoelectrochemical (PEC) water splitting offers a clean and direct path²⁻⁴. The produced hydrogen can be either stored for further conversion into electricity with fuel cell technologies^{5,6} or used in

chemical process such as CO₂ revalorization⁷ and other chemical products fabrication.

For many years metal oxides have been investigated and optimized, but efficiencies are limited and far from productivity requirements to industrialize this technique^{4,8-11}. During the last decade significant efforts have been put into using already known efficient photovoltaic materials such as Si¹²⁻¹⁴, InP^{15,16}, GaAs¹⁷⁻¹⁹, CIGS/CZTS²⁰⁻²⁴, but corrosion in highly acidic or alkaline electrolytes must be avoided. Covering the photoabsorbing materials with chemically resistant, electrically conductive, optically transparent and catalytic layers has given significant results, but there is still room to reduce degradation, device fabrication complexity, costs and adaptation to photoabsorber limitations^{4,25-28}.

TiO₂ has been the most used protective layer for photoanodes during last years, always combined with a catalyst layer or particles such as IrO₂, Pt, Ni, or Ni-Fe^{19,26,29,30}. In a recently submitted article, we have shown our findings on the role of the conduction mechanisms of TiO₂ concerning the identified instability over long periods when in contact with alkaline environments at anodic oxidative potentials. The mechanisms related to the OH⁻ diffusion inside TiO₂ and passivation of Ti states, changing the conductivity through the protective layer, are analyzed. Following this finding, there is still room for alternative materials which can assure better performance for very long-term under OER conditions.

In this study, we use NiO layers grown by atomic layer deposition (ALD) on silicon p-n junctions to efficiently fulfil all the required parameters as

protective layers for PEC water splitting in alkaline environments (chemical resistance, photoabsorber protection, conductivity, transparency and catalytic effectivity for the oxygen evolution reaction (OER)) in a single step at low temperature fabrication process. NiO has a 3.8-4 eV band gap³¹, with expected low visible spectra absorption coefficient. Moreover, it is also expected to be highly stable in alkaline media, forming nickel compounds in its surface, some of them more favorable for the OER water splitting reaction³². Likewise, NiO is known to have p-type semiconductor behavior³³, although some works report even three orders of magnitude lower conductivity than titanium dioxide^{34,35}.

A standard silicon based frontal photoanode has been selected as supporting electrode for this study. ALD allows for very conformal and pinhole-free layers, characteristics highly favorable for protective layers³⁶. Low crystallization temperature is also a characteristic of ALD^{14,37}, and is needed to avoid degradation of sensible photoabsorbers such as CIGS and CZTS as we demonstrated in other works^{23,24}.

In this work we report the degradation and regeneration mechanisms over 1000 hours anodic photocurrent of the NiO protected layers deposited at low temperature (100 °C) in a single-step ALD deposition. However, due to higher crystallinity and stoichiometry with increasing deposition temperature (100 to 300°C), reducing acceptors density, the higher electrical conductivity has been found to the lower temperature. Although, at this lowest temperature, the optical transmittance is smaller. Likewise, NiO regeneration capabilities are shown with an in situ periodic cyclic voltammetry process, bringing the electrodes to cathodic conditions after periods of different duration. Under these procedures, a partial recovery has been shown, achieving 85% of stability over 1000 hours. This opens a route for potential self-regeneration strategies of the catalyst/protective layers.

MATERIALS AND METHODS

ALD NiO has been grown on laboratory standard p⁺n silicon buried junctions prepared as frontal photoanodes and simultaneously on p⁺ degenerately doped silicon, to simulate direct injection in dark conditions.

p⁺-Si samples were created by cutting in 1x1 cm² pieces a degenerately doped silicon wafer (0.001

ohm·cm), and 50 nm Al were thermally evaporated as back contact.

p⁺n-Si samples were fabricated as in previous works^{14,38}, where a 0.5 cm² active area was lithographically defined by SiO₂ passivation on a silicon n-type wafer (0.1-0.5 ohm·cm resistivity). Boron was implanted in the defined front surface and activated by rapid thermal annealing, creating a 200 nm p⁺ region on top of the n-type substrate. As back contact, 1 μm Al/0.5%Cu was sputtered on top of 30 nm Ti to form a proper ohmic contact.

p⁺-Si, and p⁺n-Si samples were sonicated for 5 min in a 1:1:1 isopropanol, acetone and DI water cleaning solution, followed by abundant rinsing and further 5 min sonication in DI water. Before ALD deposition, sample's front surface was dipped in 0.1 M HF for 5 min, rinsed in DI water and immediately introduced in the ALD chamber.

A Cambridge Savannah 100 Atomic Layer Deposition system was used to grow NiO layers. NiCp₂ (nickelocene, bis(cyclopentadienyl)nickel) was selected as precursor and ozone (O₃) as reactant^{39,40}. NiCp₂ container was heated at 80 °C during the process. Successive pulses in N₂ flow atmosphere were introduced to the chamber, 4 s pulses, 10 s maintained in the chamber ("expo" mode) and 20 s purges for NiCp₂, and 20 s pulse and 40 s purge for O₃. Under these conditions, layers have been grown at deposition temperatures of 100, 200 and 300 °C for 1000 cycles, corresponding to roughly 50 nm layers, too thick for real protective layers but robust enough for manipulation during the degradation experiments. Samples were then soldered to a Cu wire using Ag paint and epoxy protected leaving the front area exposed (Fig. S. 1).

Surface morphology and cross section were observed with a Zeiss Series Auriga Field Effect Scanning Electron Microscope (FESEM). Structural characterization was carried out by X-ray diffraction (XRD) in a D8 Advance Bruker equipment with a Cu K α radiation source working at 40 kV and 40 mA with a 1 ° offset angle. Crystalline domains are calculated following the Scherrer equation: $D = 0.9 * \lambda / (\beta * \cos \theta)$, where λ is the X-ray wavelength (1.5406 Å), β is the full width of the diffraction line at half maximum (FWHM), and θ is the Bragg angle. High resolution transmission electron microscopy (HRTEM) was performed using a TECNAI F20 operated at 200 kV with a point to point resolution of 0.14 nm. AFM and conductivity AFM (c-AFM) measures were taken with a Park Systems XE-100 with platinum conductive cantilevers and biasing the

sample at +1.5 V respect to the tip. Due to the p⁺n-Si built-in voltage, only the samples on p⁺-Si substrates were measured by c-AFM. The photoelectrochemical measurements were obtained with a Biologic VMP-300 potentiostat using Ag/AgCl/KCl(sat) ($E^0 = 0.197 \text{ V}_{\text{RHE}}$) as reference electrode and platinum mesh as counter electrode. A quartz cell with flat faces was used with 100 ml of 1 M KOH electrolyte and a 300 W xenon lamp with an AM 1.5G filter under the appropriate distance to receive 100 mW/cm^2 , calibrated using a silicon diode (Gentec-EO, XLPF12-3S-H2-DO). Electrochemical impedance spectroscopy was obtained with 25 mV amplitude and scanning from 100 kHz to 1 Hz.

I-V curves were obtained depositing 50 nm of Ni and measuring with the potentiostat, connecting the working electrode on the back contact and the counter and reference electrodes on the top Ni contact.

RESULTS AND DISCUSSION

Photoelectrochemical, electrical and morphological characterization

NiO layers grown by ALD were fabricated at 100, 200 and 300 °C deposition temperatures on top of p⁺n-Si, p⁺-Si, FTO and glass. This range was selected to investigate low deposition temperatures, as some photoabsorbers require avoiding high temperatures in order to prevent any alteration^{23,24}. In Fig. 1 and Fig. S.2 we present representative cyclic voltammograms of the first 100 cycles measured for these samples. In dark conditions, measurements were performed using layers deposited on top of p⁺ silicon anodes, and, under 1 sun simulated illumination, using layers deposited on top of p⁺n-Si junctions. A clear dependence can be seen in both cases, with significantly higher currents when depositing at 100 °C than at 200 °C, further reduced when increasing to 300 °C. Clear Ni²⁺/Ni³⁺ peaks can be seen more cathodic than the OER onset potential, corresponding to Ni active sites^{32,41,42} presenting steady increase with cycling. Transmittance on top of glass substrates was measured to be in the range of 40 to 80% (Fig. S. 3), reduced with lower deposition temperatures³⁵. NiO is known to be less transparent when increasingly defective^{35,43,44}. This is expected to be directly translated into reduced maximum saturation photocurrent for photoanodes under illumination.

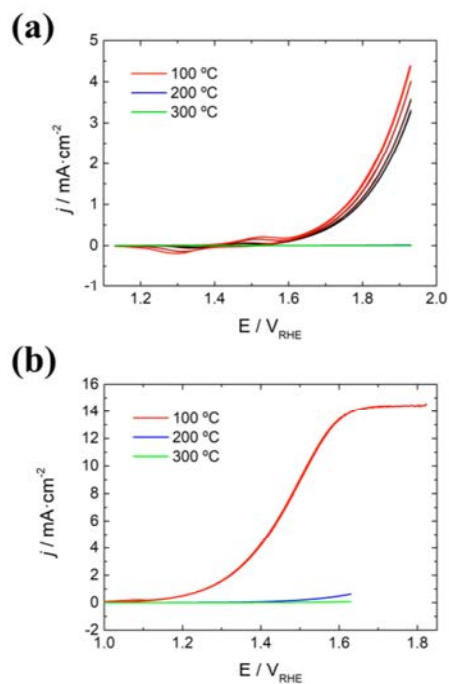


Fig. 1: cyclic voltammograms in 1 M KOH of a) p -Si anodes protected with ALD deposited NiO layers at 100 °C (red) 200 °C (blue) and 300 °C (green), cycles 1, 10, 50 and 100 from darker to clearer color. Zoom in the 200 and 300 °C is presented in Fig. S. 2. b) p -n Si photoanodes under 1 sun illumination.

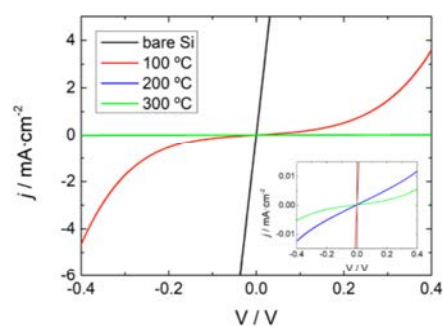


Fig. 2: I-V measurements of NiO layers grown on p -Si at ALD deposition temperatures of 100, 200 and 300 °C and further 50 nm Ni deposited as top contact. A sample with Ni directly deposited on top of p -Si is considered as reference.

To exclude any influence of the electrolyte contact, Ni metallic contacts were deposited on top of p⁺-Si devices and I-V measurements were also carried out. In Fig. 2 it can clearly be seen conductivity to depend on deposition temperature as it has been seen in Fig. 1. Likewise, 100 °C deposited layers are significantly more resistive than the p⁺-Si/Ni contact with a rectifying behavior.

From SEM analysis (Fig. 3, a-c), we do not observe any significant differences upon deposition temperature. Samples present complete surface coverage, with a measurable thickness by cross section of around 50 nm, as predicted (Fig. 4). A granular rugose surface is observed for all deposition temperatures in the range of ~20 nm,

close to the resolution limit of the SEM, slightly more pronounced for 300 °C deposition temperature. Main differences are deduced from the XRD spectra. Bunsenite crystallographic structure is measured for all the deposition temperatures, but major orientation changes happen when increasing it. At 100 °C a single exposed crystallographic facet is measured, with a diffraction angle of 37.37 ° associated to the 111 direction. On the contrary, for the 200 and 300 °C deposition temperatures, a preferential peak of 43.48 ° is measured. Crystalline interplanar spacing (d) was measured to be reduced at higher temperatures, together with the full width at half maximum (β , FWHM). Using the Scherrer equation, crystalline domains (D) are measured to be

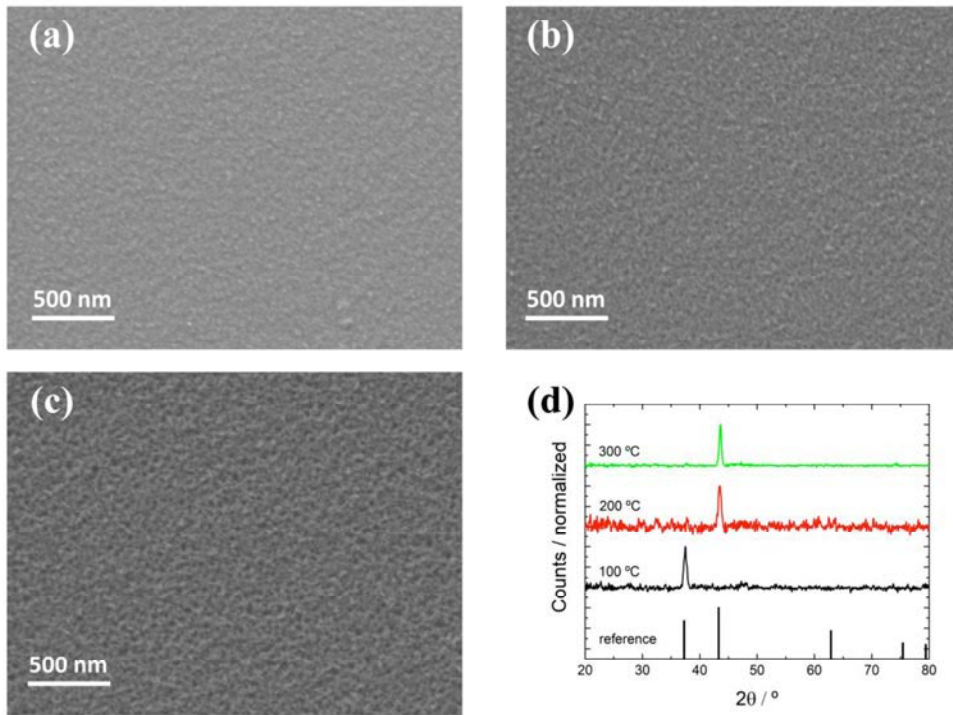


Fig. 3: SEM images of NiO films grown on top of Si at a) 100 b) 200 and c) 300 °C. d) XRD patterns of NiO films grown at different temperatures, compared to reference data JCPDS 00-047-1049.

Sample	Preferential peak	2θ (°)	β , FWHM (°)	d (Å)	D (nm)
Ref	1 1 1	37.249	-	2.412	-
Ref	2 0 0	43.276	-	2.089	-
100 °C	1 1 1	37.37	0.5314	2.40639	18.8
200 °C	2 0 0	43.48	0.7439	2.08135	14.7
300 °C	2 0 0	43.61	0.4536	2.07364	24.1

Table 1: XRD measurements of NiO layers grown at 100, 200 and 300 °C and compared to reference data from bunsenite NiO, corresponding to JCPDS 00-047-1049. Crystal orientation change can be observed between 100 and 200 °C.

18.8, 14.7 and 24.1 nm for 100, 200 and 300 °C. All this information is resumed in Table 1. The variation with temperature are difficult to analyze, as there is a simultaneous change in the dominant orientation from 111 to 200. These trends are coherent with the results found for the sputter-deposited NiO films, which nucleate and grow preferentially in the (111) plane direction at room temperature if sufficient oxygen is available, whereas they show a (200) crystal orientation if deposition temperature is increased⁴⁵⁻⁴⁷. The slight shift to higher diffraction angles from 200 to 300 °C can be attributed to compressive stress or to stoichiometry enhancement, reducing the cell volume (interplanar spacing, d)⁴⁸.

HRTEM of NiO layers grown at 100 °C and 200 °C (Fig. 4) present polycrystalline layers matching the bunsenite structure, with observed crystals being 10-20 nm, in the same range as crystalline domain (D) measured by XRD. FFT filtered images show crystals longer in vertical growth direction than horizontal, some of them propagating from substrate to surface.

Likewise, the HRTEM analysis reveals the existence of an unwanted SiO₂ layer of about 5 nm thick, independent of deposition temperature. This parasitic layer is expected to introduce an extra tunnelling resistance to the system⁴⁹, and is attributed to the use of ozone, oxidizing the Si substrate during the first stages of the ALD deposition⁵⁰, as it is known to be an aggressive

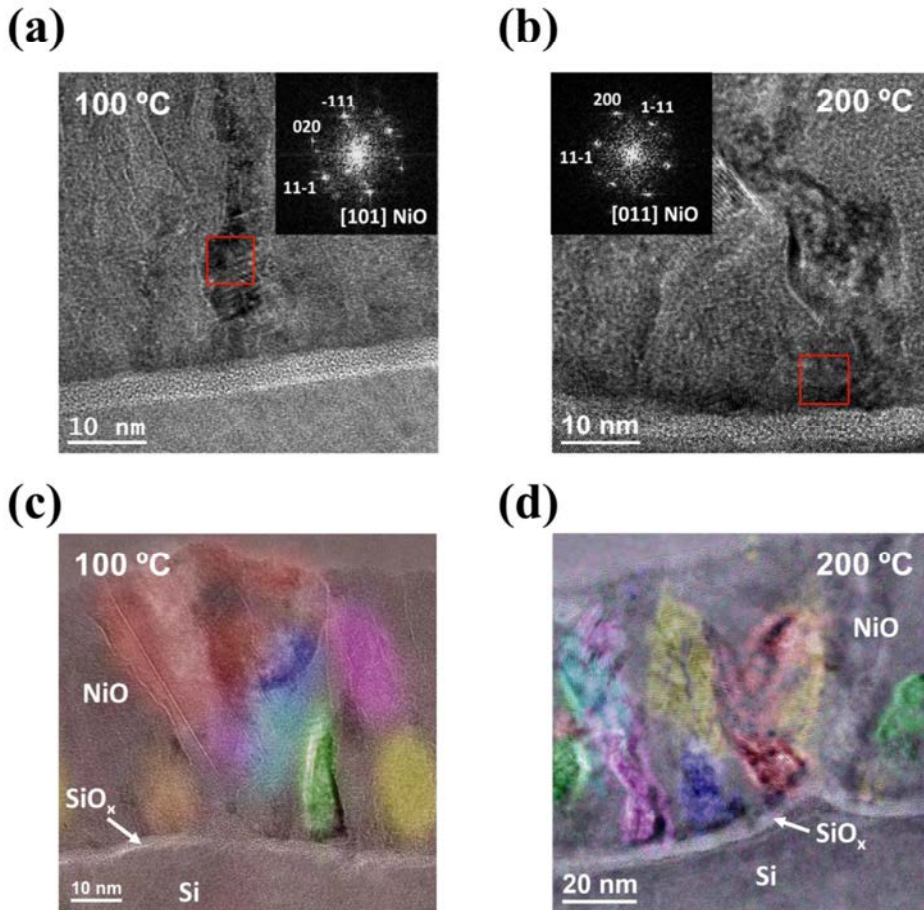


Fig. 4: HRTEM images of NiO films grown on Si at 100 (a and c) and 200 °C (b and d). SiO₂ films of ~ 5 nm can be observed, not modified with temperature. NiO grains can be observed in colored FFT filtered HRTEM, few of them being columnar from base to top. Non-flat surface of Si chips is caused by successive etching steps from masked p-n junction formation and isolation process.

oxidant^{51,52}. Although it should be avoided in order to improve the overall protected photoanode performances, it does not prevent the endurance analysis of these layers.

Current mapping was measured by AFM. Again, lower conductivity is determined as deposition temperature is increased, following the same tendency as for cyclic voltammograms (Fig. 1) and I-V measurements (Fig. 2). No current is detected in grain boundary zones, which are observed much thinner when increasing deposition temperature, probably by a better crystallization (such as it has been determined by XRD). For 100 °C, all grains appear as conductive, with a +/- 30% current dispersion. For 200 and 300 °C, smaller grains are the ones appearing to be more conductive, although overall conductivity is lower compared to 100 °C (observe the different current scale). NiO is known to present oxygen anions migration under applied

potentials⁵³, up to filament formation⁵⁴, although is not observed in our potential range.

Gathering all these results, we find a relation between the deposition temperature, the crystal orientation and the conductivity, determining the overall benefit in using 100 °C deposited layers. As can be seen in Fig. 3d, increasing deposition temperature in ALD changes the preferential growth direction too. Higher deposition temperature gives more thermal energy, allowing the adsorbed atoms to diffuse longer distances and minimize surface energy to form more thermodynamically stable crystal structures, shifting from (111) XRD preferential plane orientation to the (200) one, improving crystallinity (Fig. 3d). This reduces point defects such as cationic Ni²⁺ vacancies, responsible of creating Ni³⁺ states^{51,55-57} acting as acceptors. Changes in these favorable imperfections due to atomic reorganization caused by temperature

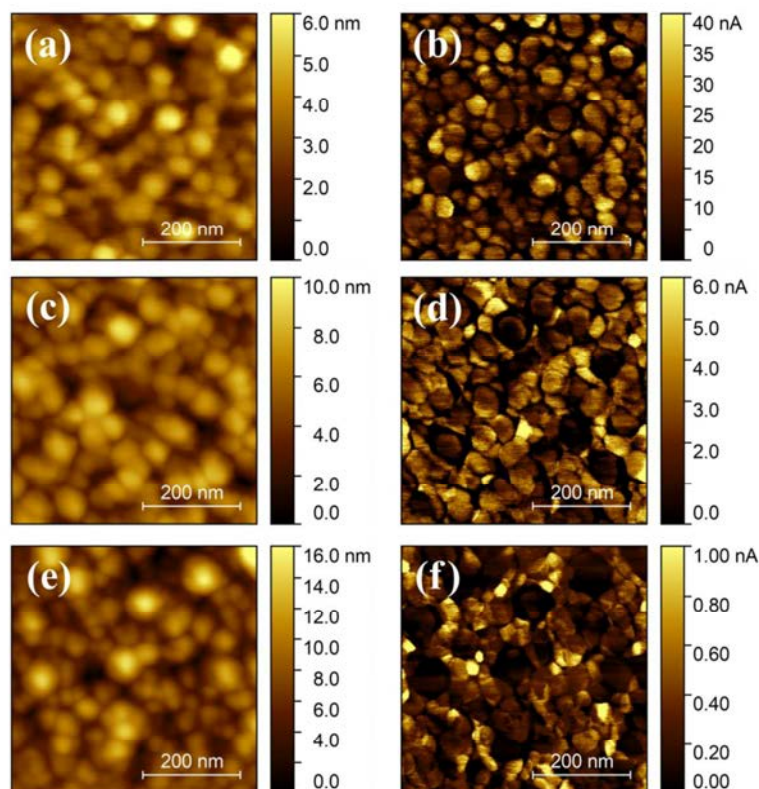


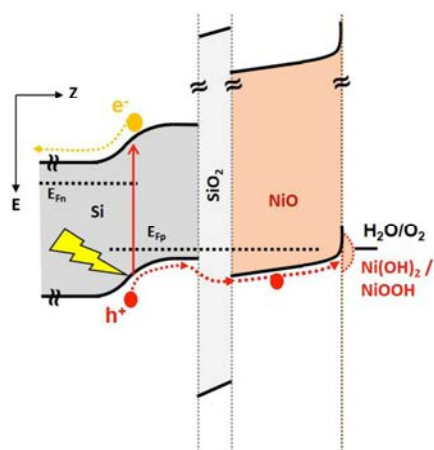
Fig. 5: Topography (a, c, e) and current (b, d, f) AFM images of NiO layers grown at 100 (a, b), 200(c, d) and 300 °C (e, f). Grain size and distribution is not observed to vary, but rugosity increases with deposition temperature. Overall conductivity is reduced when deposition temperature is increased, with some crystals more conductive than others and grain boundaries observed as not conductive. Measurements performed biasing the sample at +1.5 V respect to the tip.

treatments or different layer growth process are crucial in achieving a conductive layer^{35,51}. This diminishment on Ni²⁺ vacancies with increasing deposition temperature reduces NiO available acceptor levels, which are the majority charge carriers in p-type semiconductors, thus reducing film conductivity^{35,45–47,58}.

Scheme 1 describes a band structure where the photogenerated holes are injected into the NiO valence band through the tunnel barrier introduced by the parasitic SiO₂ layer. These injected holes must travel to the NiO/electrolyte interface overcoming the internal voltage losses caused by the low NiO layer conductivity.

When immersed in alkaline electrolytes and at anodic potentials, the NiO surface reacts with OH⁻ to form NiOOH and Ni(OH)₂, known to modify the OER catalyst performance of the NiO surface^{59–63}. Moreover, residual Fe ion traces are known to be incorporated from electrolyte impurities, being beneficial for efficient OER⁴¹. With the valence band maximum located below the water oxidation level, there is no resistance expected as NiO surface has an accumulation zone in contact with the catalytic region⁵⁸.

Electrochemical and photoelectrochemical stability characterization.



Scheme 1: Energy band diagram of a p-n-Si photoanode, with the O₂-caused SiO₂ layer and ALD-NiO protected and with Ni(OH)₂/NiOOH as OER catalyst.

100 °C sample was analyzed by electrochemical impedance spectroscopy (EIS), and two semicircles were observed (Fig. 6a and Table S. 1). The one at high frequencies (left) is attributed to a depletion barrier in NiO film in its internal interface and the one at low frequencies (right) to OER catalysis. This one is drastically reduced at potentials more anodic than OER (~1.6 V vs RHE). Comparing with the EIS of a Ni foil in the same conditions, a single semicircle is observed for the metallic foil, with similar R and C values (at similar current) to the low

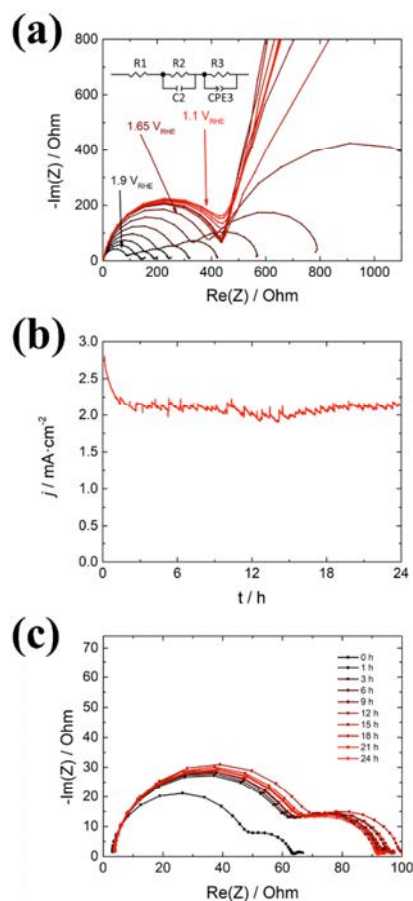


Fig. 6: a) EIS measurements at potentials from 1.1 to 1.9 V vs RHE in 1 M KOH of an ALD protected p⁺-Si with 100 °C NiO. The fitted circuit is represented in the inset. Obtained fitted values are presented in Table S. 1. b) 24 h stability measurement of the same sample at 1.9 V vs RHE in 1 M KOH. c) Periodical EIS measurements at 1.9 V vs RHE corroborating non-significant changes after initial decay. Obtained fitted values are presented in Table S. 3.

frequency arc of NiO, confirming it can be attributed to OER catalysis (Fig. S. 4 and Table S. 2).

100 °C sample was left 24 h in stability at 1.9 V vs RHE (Fig. 6b) and initial anodic current decay was observed from 3 towards 2 mA·cm⁻² during first two hours, then stabilized. This decay points toward a logarithmic dependence of current on time (Fig. S. 5), and could suggest the formation of a self-passivation layer and its corresponding introduced charge transfer resistance, lowering the current. The increase in resistance is also observed in periodical EIS (Fig. 6c and Table S. 3). Due to the temperature fluctuations in the laboratory affecting reaction kinetics, some variations are observed in current.

Thus, SEM images of 100 °C sample revealed the presence of ~200 nm bumps formed on the surface after electrochemical testing (Fig. 7a and b), which were confirmed by EDX to be elementally composed of Ni and O (Fig. S. 6 and Table S. 4). 200 and 300 °C ones presents no observable morphological changes (Fig. S. 7) after cycling (Fig. 1a) together with no significant measured current. These rounded porous structures are known to be characteristic of Ni(OH)₂⁶⁴⁻⁶⁶. Cross section SEM

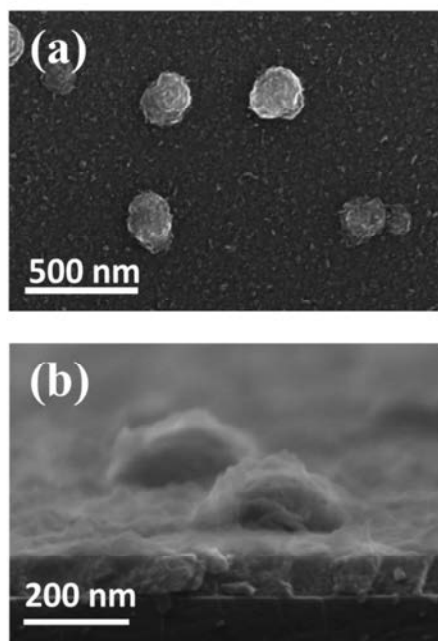


Fig. 7: a) SEM images of a NiO layer grown at 100 °C on top of a p-Si anode in 1 M KOH after finishing the stability measurement and b) cross section.

revealed the NiO film does not show any evidence of significant variation of initially deposited ~50 nm.

Stability measurements were performed using a p⁺n-Si photoanode, protected by a 100 °C grown NiO layer (Fig. 8). Sample was polarized to 1.7 V vs RHE, the lowest potential to be considered in saturation regime. Initially, this photoanode was cycled 6 times (voltage inversion from cathodic to anodic conditions) in 12 h intervals under 1 sun AM 1.5G illumination. After 500 h, the cycling period was increased to 48 h. Under these conditions, a higher current density decay can be observed from 12 to 9 mA·cm⁻². If the cycling is reset to 12 h, the photocurrent recovers up to 11 mA·cm⁻², and further reducing it to 3 h gives a slightly extra photocurrent reaching 12 mA·cm⁻² at 1.7 V vs RHE (Fig. 8a). This test measurement was performed during 1000 h, where we stopped the experiment to be capable to further characterize the sample. Constant decay of 1 mA·cm⁻² every 500 h over the whole experiment was observed. Also some small fluctuations are visible (especially in Fig. 8b) due to lab temperature variations, which affect the catalysis kinetics.

These results reveal the more frequent application of cyclic voltammograms allows increased partial recovery of the passivation layer, and density current values are recovered.

Worthy information about these degradation and regeneration mechanisms can be deduced from a detailed analysis of the cyclic voltammograms measured during the 1000 h stability test (Fig. 8, c and d), presenting several remarkable characteristics.

First, an increase of the Ni²⁺/Ni³⁺ redox peaks, which suggests a progressive increase of the nickel involved in the reaction, related bumps and flakes formed as observed comparing Fig. 3a and Fig. 7.

Second, a decrease of the electrochemical activity giving by a lowering of the slope in the 1.4-1.8 V vs RHE range. This lower slope reveals either an increase of internal voltage losses or points out an increase of the electrochemical overpotential due to the modification of the Ni(OH)₂/NiOOH catalytic surface.

Third, a decrease of the saturation current, which must be attributed to a decrease of the amount of light reaching the photodiode. For NiO, it is reported the existence of electrochromic darkening caused by surface ion adsorption⁴⁶ or electrochemical

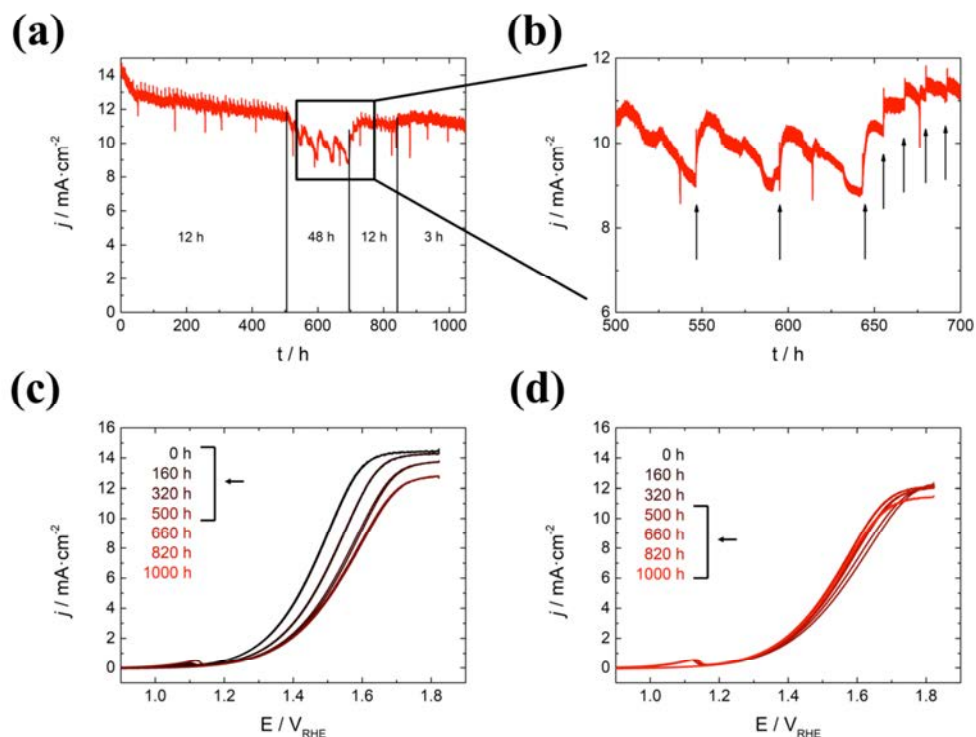


Fig. 8: p - n -Si photoanode protected with NiO deposited at 100 °C and measured under 1 sun illumination in 1 M KOH. a) 1000 h stability measurement at 1.7 V vs RHE cycled 6 times every 12, 48 or 3h as indicated. b) Zoom of the region cycled every 48 h and 12 h, corresponding to the arrows. c) Cyclic voltammograms measured during first 500 h of the stability test, showing saturation current decrease and small hysteresis increase. d) Cyclic voltammograms starting on the last 48 h interval, where the sample was most degraded, and further recovered by smaller cycling intervals.

formation of less transparent NiOOH, with more Ni^{3+} in the surface, having lower optical band gap

and higher absorption coefficient than NiO and $\text{Ni}(\text{OH})_2$ ⁴⁴. This deactivation was discarded to be related with transmittance variations caused by NiO deactivation, as we demonstrated on a NiO-

protected FTO substrate (Fig. S. 8). We attribute the constant decay over 1000 h to slow electrolyte impurities absorbed in the surface reducing transparency.

Other authors have related similar degradations to chemical changes of the electrocatalytic surface, caused by less active Ni-Fe oxides being formed or Fe dissolution in alkaline electrolytes^{67,68}. Observing the electrode potential–pH (Pourbaix) phase map diagram of NiO in aqueous electrolytes⁶⁹, our anodic applied potentials are close to the NiO_2 region,

where nickel oxyhydroxides (most favorable phase to OER catalysis) is no more the principal nickel phase.

Finally, the SEM analysis presents few spots where the silicon beneath had been etched, 5 in a 1 mm² area (Fig. S. 9a-c), after 1000 h stability tests. Analyzing them closely, we can see the protective layer is still present, and the alkaline electrolyte found a path in few specific spots to reach the silicon etching it. On these few spots, in one case a particle was present and in the other one a hole, both of them exactly in the center. So, these pinholes in the protective layer can be attributed to extrinsic or unwanted fabrication defects and not to intrinsic instability of the protection film, and thus, should be eliminated with optimal fabrication.

CONCLUSIONS

NiO transparent, protective, conductive and catalytic films grown by ALD have been used to avoid corrosion on frontal illuminated silicon photoanodes in alkaline electrolytes and anodic potentials while performing the oxygen evolution reaction.

Layers grown at 100, 200 and 300 °C with thicknesses in the range of 50 nm present a polycrystalline structure with a change in preferential orientation when increasing from 100 °C to 200 and 300 °C, correlated with conductivity diminishment and transparency slight increase. The sample grown at 100°C presents the best electrical conductivity and optical transparency compromise.

Stability measurements on best-performing 100 °C NiO-protected photoanodes present degradation mechanisms. Current density decays following a logarithmic time dependency, pointing at the formation of a self-passivation layer. This is attributed to the interaction of the NiO layer and the alkaline electrolyte under anodic working conditions, forming of higher nickel oxidation states at the electrode/electrolyte interface, resulting in an OER overpotential increase.

Nevertheless, the application of periodic cycling ranging from anodic to cathodic voltage conditions corroborates the existence of a recovery procedure based the cathodic scans promoting the reduced forms at the surface of the NiO layer.

Applying this methodology under 3 hours cycling periodicity, over 1000 h stability measurements were possible with over 11 mA·cm⁻² photocurrents, an 85% of the initial photocurrent.

The few corrosion spots observed have been correlated to extrinsic origin and thus, NiO ALD was demonstrated as a successful technique for long-lasting protective layers in anodic and alkaline conditions, avoiding corrosion of Si photoelectrodes. Such low deposition temperature (100 °C) would allow for temperature-sensitive photoabsorbers to be implemented in anodic conditions.

Consequently, this procedure opens a promising strategy for driving stability in photoelectrochemical devices. This regenerative protocol represents less than 1% of the working time under anodic conditions. However, there is still room to fully

understand regenerative pathway's and to enable very long stability, and thus should be studied also in other materials suffering from electrochemical deactivation.

ASSOCIATED CONTENT

Supporting Information. Transmittance, SEM and EDX supplementary images, together with a photo of a finished device, are supplied in an additional document.

AUTHOR INFORMATION

Corresponding Author

*Corresponding authors:

E-mail: cros@irec.cat

E-mail: tandreu@irec.cat

Tel: (34) 933 562 615

Author Contributions

The manuscript was written through contributions of all authors. All authors have given approval to the final version of the manuscript.

Funding Sources

ACKNOWLEDGMENT

Authors from IREC thank Generalitat de Catalunya for financial support through the CERCA Programme, M2E (2014SGR1638) and XaRMAE network. IREC also acknowledges additional support by the European Regional Development Funds (ERDF, FEDER) and by MINECO coordinated projects MAT2014-59961-C2 and ENE2016-80788-C5-5-R. C.R. thanks to MINECO for his FPI grant (BES-2015-071618). ICN2 acknowledges support from the Severo Ochoa Program (MINECO, Grant SEV-2013-0295).

REFERENCES

- (1) Lewis, N. S.; Nocera, D. G. Powering the Planet: Chemical Challenges in Solar Energy Utilization. *Proc. Natl. Acad. Sci. U. S. A.* **2006**, *103* (43), 15729–15735.
- (2) Tuller, H. L. Solar to Fuels Conversion Technologies: A Perspective. *Mater. Renew. Sustain. Energy* **2017**, *6* (1), 1–16.

- (3) James, B. D.; Baum, G. N.; Perez, J.; Baum, K. N. Technoeconomic Analysis of Photoelectrochemical (PEC) Hydrogen Production. *2009*, 1–128.
- (4) Lewis, N. S. Developing a Scalable Artificial Photosynthesis Technology through Nanomaterials by Design. *Nat. Nanotechnol.* **2016**, *11* (12), 1010–1019.
- (5) Berry, G. D.; Pasternak, A. D.; Rambach, G. D.; Smith, J. R.; Schock, R. N. Hydrogen as a Future Transportation Fuel. *Energy* **1996**, *21* (4), 289–303.
- (6) Wang, M. Fuel Choices for Fuel-Cell Vehicles: Well-to-Wheels Energy and Emission Impacts. *J. Power Sources* **2002**, *112* (1), 307–321.
- (7) Yao, Y.; Liu, X.; Hildebrandt, D.; Glasser, D. Fischer–Tropsch Synthesis Using H₂/CO/CO₂ Syngas Mixtures over an Iron Catalyst. *Ind. Eng. Chem. Res.* **2011**, *50* (19), 11002–11012.
- (8) Fujishima, A.; Honda, K. Electrochemical Photolysis of Water at a Semiconductor Electrode. *Nature* **1972**, *238* (5358), 37–38.
- (9) Rahimi, N.; Pax, R. A.; Gray, E. M. A. Review of Functional Titanium Oxides. I: TiO₂ and Its Modifications. *Prog. Solid State Chem.* **2016**, *44* (3), 86–105.
- (10) Tang, P.; Xie, H.; Ros, C.; Han, L.; Biset-Peiró, M.; He, Y.; Kramer, W.; Rodríguez, A. P.; Saucedo, E.; Galán-Mascarós, J. R.; et al. Enhanced Photoelectrochemical Water Splitting of Hematite Multilayer Nanowire Photoanodes by Tuning the Surface State via Bottom-up Interfacial Engineering. *Energy Environ. Sci.* **2017**, *10* (10), 2124–2136.
- (11) Ros, C.; Fabrega, C.; Monllor-Satoca, D.; Hernández-Alonso, M. D.; Penelas-Pérez, G.; Morante, J. R.; Andreu, T. Hydrogenation and Structuration of TiO₂ Nanorods Photoanodes: Doping Level and the Effect of Illumination in Trap-States Filling. *J. Phys. Chem. C* **2018**, *122* (6), 3295–3304.
- (12) Xia, Z.; Zhou, X.; Li, J.; Qu, Y. Protection Strategy for Improved Catalytic Stability of Silicon Photoanodes for Water Oxidation. *Sci. Bull.* **2015**, *60* (16), 1395–1402.
- (13) Sun, K.; Shen, S.; Liang, Y.; Burrows, P. E.; Mao, S. S.; Wang, D. Enabling Silicon for Solar-Fuel Production. *Chem. Rev.* **2014**, *114* (17), 8662–8719.
- (14) Ros, C.; Andreu, T.; Hernández-Alonso, M. D.; Penelas-Pérez, G.; Arbiol, J.; Morante, J. R. Charge Transfer Characterization of ALD-Grown TiO₂ Protective Layers in Silicon Photocathodes. *ACS Appl. Mater. Interfaces* **2017**, *9* (21), 17932–17941.
- (15) Lee, M. H.; Takei, K.; Zhang, J.; Kapadia, R.; Zheng, M.; Chen, Y.-Z.; Nah, J.; Matthews, T. S.; Chueh, Y.-L.; Ager, J. W.; et al. P-Type InP Nanopillar Photocathodes for Efficient Solar-Driven Hydrogen Production. *Angew. Chemie Int. Ed.* **2012**, *51* (43), 10760–10764.
- (16) Wang, T.; Gong, J. Single-Crystal Semiconductors with Narrow Band Gaps for Solar Water Splitting. *Angew. Chemie - Int. Ed.* **2015**, *54* (37), 10718–10732.
- (17) Licht, S.; Wang, B.; Mukerji, S.; Soga, T.; Umeno, M.; Tributsch, H. Over 18% Solar Energy Conversion to Generation of Hydrogen Fuel; Theory and Experiment for Efficient Solar Water Splitting. *Int. J. Hydrogen Energy* **2001**, *26* (7), 653–659.
- (18) Qiu, J.; Zeng, G.; Ha, M.-A.; Hou, B.; Mecklenburg, M.; Shi, H.; Alexandrova, A. N.; Cronin, S. B. Microscopic Study of Atomic Layer Deposition of TiO₂ on GaAs and Its Photocatalytic Application. *Chem. Mater.* **2015**, *27* (23), 7977–7981.
- (19) Hu, S.; Shaner, M. R.; Beardslee, J. a; Lichterman, M.; Brunschwig, B. S.; Lewis, N. S. Amorphous TiO₂ Coatings Stabilize Si, GaAs, and GaP Photoanodes for Efficient Water Oxidation. *Science* **2014**, *344* (6187), 1005–1009.
- (20) Gunawan, Septina, W.; Ikeda, S.; Harada, T.; Minegishi, T.; Domen, K.; Matsumura, M. Platinum and Indium Sulfide-Modified CuInS₂ as Efficient Photocathodes for Photoelectrochemical Water Splitting. *Chem. Commun.* **2014**, *50* (64), 8941.
- (21) Luo, J.; Tilley, S. D.; Steier, L.; Schreier, M.; Mayer, M. T.; Fan, H. J.; Gratzel, M. Solution Transformation of Cu₂O into CuInS₂ for Solar Water Splitting. *Nano Lett.* **2015**, *15* (2), 1395–1402.
- (22) Wang, J.; Zhang, P.; Song, X.; Gao, L. Cu₂ZnSnS₄ Thin Films: Spin Coating Synthesis and Photoelectrochemistry. *RSC Adv.* **2014**, *4*, 21318.
- (23) Ros, C.; Andreu, T.; Giraldo, S.; Izquierdo-

- Roca, V.; Saucedo, E.; Morante, J. R. Turning Earth Abundant Kesterite-Based Solar Cells into Efficient Protected Water Splitting Photocathodes. *ACS Appl. Mater. Interfaces* **2018**, *10*, 13425–13433.
- (24) Ros, C.; Andreu, T.; Giraldo, S.; Sánchez, Y.; Morante, J. R. Conformal Chalcopyrite Based Photocathode for Solar Refinery Applications. *Sol. Energy Mater. Sol. Cells* **2016**, *158*, 184–188.
- (25) Liu, R.; Zheng, Z.; Spurgeon, J.; Yang, X. Enhanced Photoelectrochemical Water-Splitting Performance of Semiconductors by Surface Passivation Layers. *Energy Environ. Sci.* **2014**, *7* (8), 2504–2517.
- (26) Hu, S.; Lewis, N. S.; Ager, J. W.; Yang, J.; McKone, J. R.; Strandwitz, N. C. Thin-Film Materials for the Protection of Semiconducting Photoelectrodes in Solar-Fuel Generators. *J. Phys. Chem. C* **2015**, *119* (43), 24201–24228.
- (27) Lichterman, M. F.; Sun, K.; Hu, S.; Zhou, X.; McDowell, M. T.; Shaner, M. R.; Richter, M. H.; Crumlin, E. J.; Carim, A. I.; Saadi, F. H.; et al. Protection of Inorganic Semiconductors for Sustained, Efficient Photoelectrochemical Water Oxidation. *Catal. Today* **2016**, *262*, 11–23.
- (28) Wang, T.; Luo, Z.; Li, C.; Gong, J. Controllable Fabrication of Nanostructured Materials for Photoelectrochemical Water Splitting via Atomic Layer Deposition. *Chem. Soc. Rev.* **2014**, *43* (22), 7469–7484.
- (29) Mei, B.; Pedersen, T.; Malacrida, P.; Bae, D.; Frydendal, R.; Hansen, O.; Vesborg, P. C. K.; Seger, B.; Chorkendorff, I. Crystalline TiO₂: A Generic and Effective Electron-Conducting Protection Layer for Photoanodes and -Cathodes. *J. Phys. Chem. C* **2015**, *119* (27), 15019–15027.
- (30) Mei, B.; Seger, B.; Pedersen, T.; Malizia, M.; Hansen, O.; Chorkendorff, I.; Vesborg, P. C. K. Protection of p + -n-Si Photoanodes by Sputter-Deposited Ir/IrO_x Thin Films. *J. Phys. Chem. Lett.* **2014**, *5* (11), 1948–1952.
- (31) Peng, T. C.; Xiao, X. H.; Han, X. Y.; Zhou, X. D.; Wu, W.; Ren, F.; Jiang, C. Z. Characterization of DC Reactive Magnetron Sputtered NiO Films Using Spectroscopic Ellipsometry. *Appl. Surf. Sci.* **2011**, *257* (13), 5908–5912.
- (32) Dette, C.; Hurst, M. R.; Deng, J.; Nellist, M. R.; Boettcher, S. W. Structural Evolution of Metal (Oxy)Hydroxide Nanosheets during the Oxygen Evolution Reaction. **2018**.
- (33) Jang, W. L.; Lu, Y. M.; Hwang, W. S.; Hsiung, T. L.; Wang, H. P. Point Defects in Sputtered NiO Films. *Appl. Phys. Lett.* **2009**, *94* (6), 92–95.
- (34) D'Amario, L.; Boschloo, G.; Hagfeldt, A.; Hammarström, L. Tuning of Conductivity and Density of States of NiO Mesoporous Films Used in P-Type DSSCs. *J. Phys. Chem. C* **2014**, *118* (34), 19556–19564.
- (35) Sato, H.; Minami, T.; Takata, S.; Yamada, T. Transparent Conducting P-Type NiO Thin Films Prepared by Magnetron Sputtering. *Thin Solid Films* **1993**, *236* (1–2), 27–31.
- (36) Scheuermann, A. G.; McIntyre, P. C. Atomic Layer Deposited Corrosion Protection: A Path to Stable and Efficient Photoelectrochemical Cells. *J. Phys. Chem. Lett.* **2016**, *7* (14), 2867–2878.
- (37) Miikkulainen, V.; Leskelä, M.; Ritala, M.; Puurunen, R. L.; Leskelä, M.; Ritala, M.; Puurunen, R. L. Crystallinity of Inorganic Films Grown by Atomic Layer Deposition: Overview and General Trends. *J. Appl. Phys.* **2013**, *113* (2), 021301.
- (38) Flox, C.; Murcia-López, S.; Carretero, N. M.; Ros, C.; Morante, J. R.; Andreu, T. Role of Bismuth in the Electrokinetics of Silicon Photocathodes for Solar Rechargeable Vanadium Redox Flow Batteries. *ChemSusChem* **2017**, *08028*, 125–129.
- (39) Lu, H. L.; Scarel, G.; Wiemer, C.; Perego, M.; Spiga, S.; Fanciulli, M.; Pavia, G. Atomic Layer Deposition of NiO Films on Si(100) Using Cyclopentadienyl-Type Compounds and Ozone as Precursors. *J. Electrochem. Soc.* **2008**, *155* (10), H807.
- (40) Lindahl, E.; Ottosson, M.; Carlsson, J. O. Atomic Layer Deposition of NiO by the Ni(Thd)₂/H₂O Precursor Combination. *Chem. Vap. Depos.* **2009**, *15* (7–9), 186–191.
- (41) Trotochaud, L.; Young, S. L.; Ranney, J. K.; Boettcher, S. W. Nickel-Iron Oxyhydroxide Oxygen-Evolution Electrocatalysts: The Role of Intentional and Incidental Iron Incorporation. *J. Am. Chem. Soc.* **2014**, *136* (18), 6744–6753.
- (42) Nardi, K. L.; Yang, N.; Dickens, C. F.;

- Strickler, A. L.; Bent, S. F. Creating Highly Active Atomic Layer Deposited NiO Electrocatalysts for the Oxygen Evolution Reaction. *Adv. Energy Mater.* **2015**, *5* (17), 1–10.
- (43) Hassan, A. J. Study of Optical and Electrical Properties of Nickel Oxide (NiO) Thin Films Deposited by Using a Spray Pyrolysis Technique. **2014**, No. December, 2184–2191.
- (44) Sun, K.; Kuang, Y.; Verlage, E.; Bruntschwig, B. S.; Tu, C. W.; Lewis, N. S. Sputtered NiOx Films for Stabilization of P+n-InP Photoanodes for Solar-Driven Water Oxidation. *Adv. Energy Mater.* **2015**, *5* (1402276), 1–8.
- (45) Chen, H. L.; Yang, Y. S. Effect of Crystallographic Orientations on Electrical Properties of Sputter-Deposited Nickel Oxide Thin Films. *Thin Solid Films* **2008**, *516* (16), 5590–5596.
- (46) Sun, K.; Saadi, F. H.; Lichterman, M. F.; Hale, W. G.; Wang, H.-P.; Zhou, X.; Plymale, N. T.; Omelchenko, S. T.; He, J.-H.; Papadantonakis, K. M.; et al. *Stable Solar-Driven Oxidation of Water by Semiconducting Photoanodes Protected by Transparent Catalytic Nickel Oxide Films*; 2015; Vol. 112.
- (47) Jang, W.; Lu, Y.; Hwang, W.; Hsiung, T.; Wang, H. P. Surface & Coatings Technology Effect of Substrate Temperature on the Electrically Conductive Stability of Sputtered NiO Films. *Surf. Coat. Technol.* **2008**, *202* (22–23), 5444–5447.
- (48) B.D. Cullity. *Elements of X-RAY DIFFRACTION Second Edition*; 1978.
- (49) Scheuermann, A. G.; Kemp, K. W.; Tang, K.; Lu, D. Q.; Satterthwaite, P. F.; Ito, T.; Chidsey, C. E. D. D.; McIntyre, P. C.; McIntyre, P. C. Conductance and Capacitance of Bilayer Protective Oxides for Silicon Water Splitting Anodes. *Energy Environ. Sci.* **2016**, *9* (2), 1–26.
- (50) Dueñas, S.; Castán, H.; García, H.; Andrés, E. S.; Toledano-Luque, M.; Mártel, I.; González-Díaz, G.; Kukli, K.; Uustare, T.; Aarik, J. A Comparative Study of the Electrical Properties of TiO₂ Films Grown by High-Pressure Reactive Sputtering and Atomic Layer Deposition. *Semicond. Sci. Technol.* **2005**, *20* (10), 1044–1051.
- (51) Bachmann, J.; Zolotaryov, A.; Albrecht, O.; Goetze, S.; Berger, A.; Hesse, D.; Novikov, D.; Nielsch, K. Stoichiometry of Nickel Oxide Films Prepared by ALD. *Chem. Vap. Depos.* **2011**, *17* (7–9), 177–180.
- (52) Niinistö, J.; Putkonen, M.; Niinistö, L.; Arstila, K.; Sajavaara, T.; Lu, J.; Kukli, K.; Ritala, M.; Leskelä, M. HfO₂ Films Grown by ALD Using Cyclopentadienyl-Type Precursors and H₂O or O₃ as Oxygen Source. *J. Electrochem. Soc.* **2006**, *153* (3), F39.
- (53) Fujii, T.; Arita, M.; Hamada, K.; Takahashi, Y.; Sakaguchi, N. In-Situ Transmission Electron Microscopy of Conductive Filaments in NiO Resistance Random Access Memory and Its Analysis. *J. Appl. Phys.* **2013**, *113* (8).
- (54) Nardi, F.; Deleruyelle, D.; Spiga, S.; Muller, C.; Bouteille, B.; Ielmini, D. Switching of Nanosized Filaments in NiO by Conductive Atomic Force Microscopy. *J. Appl. Phys.* **2012**, *112* (6).
- (55) Nachman, M.; Cojocaru, L. N.; Ribco, L. V. Electrical Properties of Non-Stoichiometric Nickel Oxide. *Phys. Status Solidi* **1965**, *8* (3), 773–783.
- (56) Jiang, F.; Choy, W. C. H.; Li, X.; Zhang, D.; Cheng, J. Post-Treatment-Free Solution-Processed Non-Stoichiometric NiO Nanoparticles for Efficient Hole-Transport Layers of Organic Optoelectronic Devices. *Adv. Mater.* **2015**, *27* (18), 2930–2937.
- (57) Kuanr, S. K.; Vinothkumar, G.; Babu, K. S. Substrate Temperature Dependent Structural Orientation of EBPVD Deposited NiO Films and Its Influence on Optical, Electrical Property. *Mater. Sci. Semicond. Process.* **2018**, *75* (November 2017), 26–30.
- (58) Bae, D.; Seger, B.; Vesborg, P. C. K.; Hansen, O.; Chorkendorff, I. Strategies for Stable Water Splitting via Protected Photoelectrodes. *Chem. Soc. Rev.* **2017**, *46* (7), 1933–1954.
- (59) Hamann, T. W. Water Splitting: An Adaptive Junction. *Nat. Mater.* **2014**, *13* (1), 3–4.
- (60) Digdaya, I. A.; Adhyaksa, G. W. P.; Trzesniewski, B. J.; Garnett, E. C.; Smith, W. A. Interfacial Engineering of Metal-Insulator-Semiconductor Junctions for

- Efficient and Stable Photoelectrochemical Water Oxidation. *Nat. Commun.* **2017**, *8* (May), 15968.
- (61) Mills, T. J.; Lin, F.; Boettcher, S. W. Theory and Simulations of Electrocatalyst-Coated Semiconductor Electrodes for Solar Water Splitting. *Phys. Rev. Lett.* **2014**, *112* (14), 1–5.
- (62) Lin, F.; Boettcher, S. W. Adaptive Semiconductor/Electrocatalyst Junctions in Water-Splitting Photoanodes. *Nat. Mater.* **2014**, *13* (1), 81–86.
- (63) Lin, F.; Bachman, B. F.; Boettcher, S. W. Impact of Electrocatalyst Activity and Ion Permeability on Water-Splitting Photoanodes. *J. Phys. Chem. Lett.* **2015**, *6* (13), 2427–2433.
- (64) Sharel, P. E.; Liu, D.; Lazenby, R. A.; Sloan, J.; Vidotti, M.; Unwin, P. R.; Macpherson, J. V. Electrodeposition of Nickel Hydroxide Nanoparticles on Carbon Nanotube Electrodes: Correlation of Particle Crystallography with Electrocatalytic Properties. *J. Phys. Chem. C* **2016**, *120* (29), 16059–16068.
- (65) Wang, X.; Wang, Y.; Zhao, C.; Zhao, Y.; Yan, B.; Zheng, W. Electrodeposited Ni(OH)₂ Nanoflakes on Graphite Nanosheets Prepared by Plasma-Enhanced Chemical Vapor Deposition for Supercapacitor Electrode. *New J. Chem.* **2012**, *36* (9), 1902–1906.
- (66) Hall, D. S.; Lockwood, D. J.; Bock, C.; MacDougall, B. R. Nickel Hydroxides and Related Materials: A Review of Their Structures, Synthesis and Properties. *Proc. R. Soc. A Math. Phys. Eng. Sci.* **2015**, *471* (2174).
- (67) Zou, S.; Burke, M. S.; Kast, M. G.; Fan, J.; Danilovic, N.; Boettcher, S. W. Fe (Oxy)Hydroxide Oxygen Evolution Reaction Electrocatalysis: Intrinsic Activity and the Roles of Electrical Conductivity, Substrate, and Dissolution. *Chem. Mater.* **2015**, *27* (23), 8011–8020.
- (68) Zhu, K.; Luo, W.; Zhu, G.; Wang, J.; Zhu, Y.; Zou, Z.; Huang, W. Interface-Engineered Ni(OH)₂ /β-like FeOOH Electrocatalysts for Highly Efficient and Stable Oxygen Evolution Reaction. *Chem. - An Asian J.* **2017**, *12* (20), 2720–2726.
- (69) Huang, L. F.; Hutchison, M. J.; Santucci, R. J.; Scully, J. R.; Rondinelli, J. M. Improved Electrochemical Phase Diagrams from Theory and Experiment: The Ni-Water System and Its Complex Compounds. *J. Phys. Chem. C* **2017**, *121* (18), 9782–9789.

About degradation and regeneration mechanisms of NiO protective layers deposited by ALD on photoanodes

Carles Ros^{a,*}, Teresa Andreu^{a,b,*}, Jordi Arbiol^{c,d}, Joan R. Morante^{a,b}

^a Catalonia Institute for Energy Research (IREC). Jardins de les Dones de Negre 1, 08930 Sant Adrià del Besòs, Barcelona, Spain

^b Universitat de Barcelona (UB), Martí i Franquès, 1, 08028 Barcelona, Spain

^c Catalan Institute of Nanoscience and Nanotechnology (ICN2), CSIC and The Barcelona Institute of Science and Technology (BIST), Campus UAB, Bellaterra, 08193 Barcelona, Spain

^d ICREA, Pg. Lluís Companys 23, 08010 Barcelona, Spain

Supporting Information

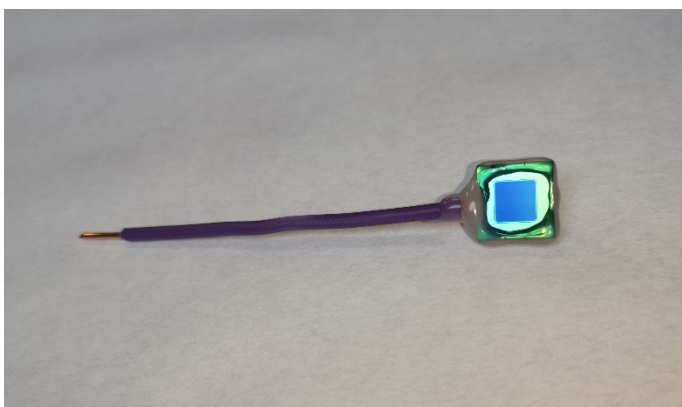


Fig. S. 1: p^+n -Si photoanode, where a 0.5 cm^2 active area (darker region) was lithographically defined by SiO_2 passivation on a silicon n -type wafer (0.1 - 0.5 ohm.cm resistivity), ALD-protected and further Ag paint soldered to a Cu wire and isolated with thermoplastic.

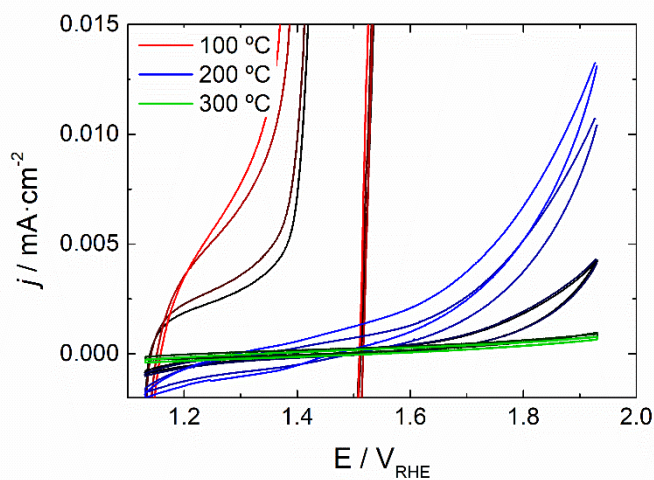


Fig S. 2: Zoom in the 200 and 300 °C region of cyclic voltammograms presented in Fig. 1, in 1 M KOH of a) p^+ -Si anodes protected with ALD deposited NiO layers at 100 °C (red) 200 °C (blue) and 300 °C (green), cycles 1, 10, 50 and 100 from darker to clearer color.

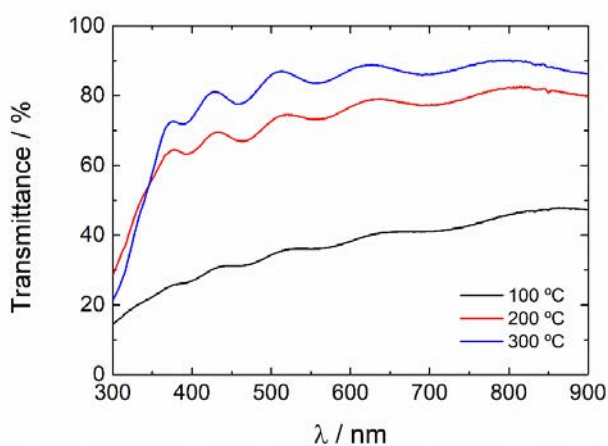


Fig S. 3: transmittance measurements of NiO layers grown at 100 (black), 200 (red) and 300 °C (blue) on top of glass substrates.

<u>V vs RHE</u>	<u>$R1$ / Ohm</u>	<u>$R2$ / Ohm</u>	<u>$C2$ / F</u>	<u>$R3$ / Ohm</u>	<u>$CPE3-T$ / $F \cdot S^{A3-1}$</u>	<u>$A3$</u>
1.1	2.293	426.9	1.40E-06	3.01E+18	1.01E-04	0.83
1.2	2.229	428.9	1.39E-06	5.10E+11	1.38E-04	0.83
1.3	2.093	419.1	1.38E-06	7244	4.89E-04	0.76
1.4	2.407	430.1	1.37E-06	6.46E+11	4.43E-04	0.87
1.5	2.054	430.5	1.36E-06	6104	3.11E-04	0.88
1.6	2.13	371.1	1.35E-06	447.9	2.74E-04	0.83
1.7	2.223	246.1	1.32E-06	179.2	2.39E-04	0.82
1.8	2.366	144.7	1.25E-06	97.5	1.93E-04	0.85
1.9	1.822	82.2	1.19E-06	56.59	2.05E-04	0.85

Table S. 1: EIS fitted values of Fig. 6a using the modelled circuit presented in Fig. 6a (inset).

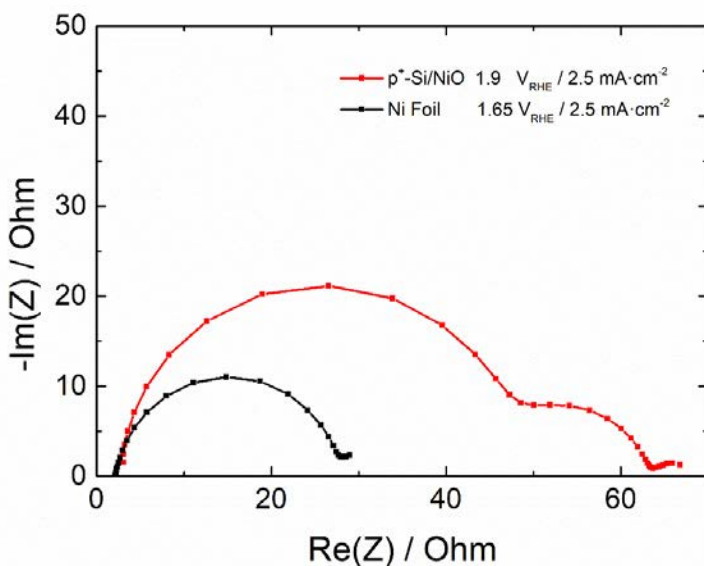


Fig. S. 4: EIS measurements of a Ni Foil and a protected p⁺-Si with 100 °C NiO by ALD at similar current values and thus, at different potential using the modelled circuit presented in Fig. 6a (inset). Results are presented in Table S. 3.

<u>t / h</u>	<u>R1 / Ohm</u>	<u>R2 / Ohm</u>	<u>C2 / F</u>	<u>R3 / Ohm</u>	<u>CPE3-T / F·S^{A3-1}</u>	<u>A3</u>
<i>Ni Foil</i>	2.15	0	0	26.04	8.92E-04	0.89
<i>100 °C NiO p⁺-Si</i>	2.99	41.96	1.16E-06	18.9	3.80E-04	0.78

Table S. 2: EIS fitted values of Fig. S. 3 using the modelled circuit presented in Fig. 6a (inset).

<u>t / h</u>	<u>R1 / Ohm</u>	<u>R2 / Ohm</u>	<u>C2 / F</u>	<u>R3 / Ohm</u>	<u>CPE3-T / F·S^{A3-1}</u>	<u>A3</u>
<i>0</i>	2.9	41.9	1.16E-06	18.9	3.80E-04	0.78
<i>1</i>	3.6	52.8	1.16E-06	36.3	2.63E-04	0.78
<i>3</i>	3.5	54.3	1.14E-06	35.8	2.48E-04	0.79
<i>6</i>	3.6	55.2	1.14E-06	35.7	2.51E-04	0.79
<i>9</i>	3.8	57.1	1.13E-06	35.3	2.36E-04	0.80
<i>12</i>	3.6	55.7	1.16E-06	34.3	2.46E-04	0.80
<i>15</i>	4.0	59.7	1.12E-06	37.1	2.41E-04	0.79
<i>18</i>	3.5	57.7	1.18E-06	35.8	2.56E-04	0.78
<i>21</i>	3.7	56.8	1.14E-06	33.8	2.40E-04	0.79
<i>24</i>	3.8	56.1	1.13E-06	32.8	2.45E-04	0.79

Table S. 3: EIS fitted values of Fig. 6c using the modelled circuit presented in Fig. 6a (inset).

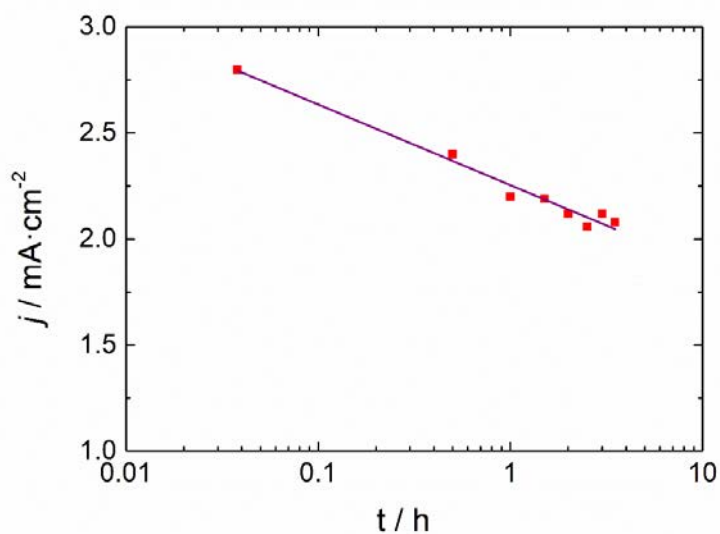


Fig. S. 5: Stability measurement of the same sample represented in Fig. 6b in a logarithmic time scale and the correspondent fitting of the measured values, polarized at 1.9 V vs RHE in 1 M KOH.

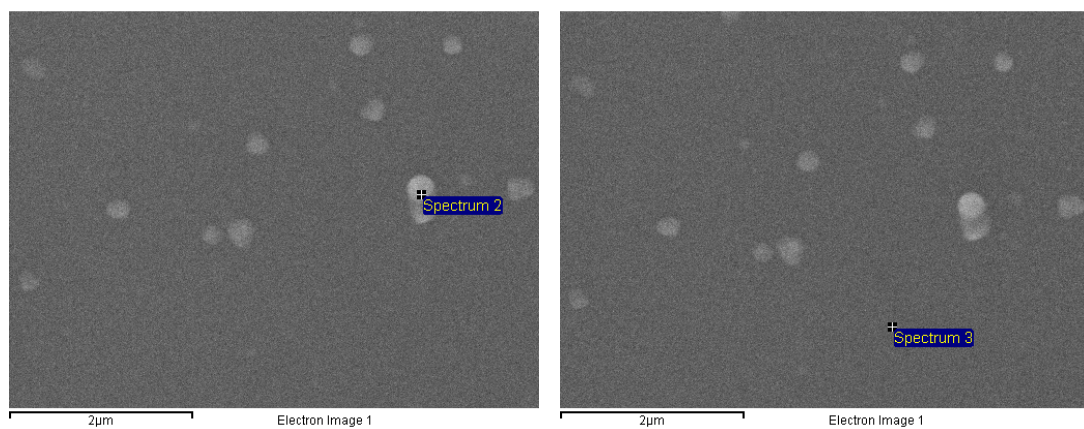
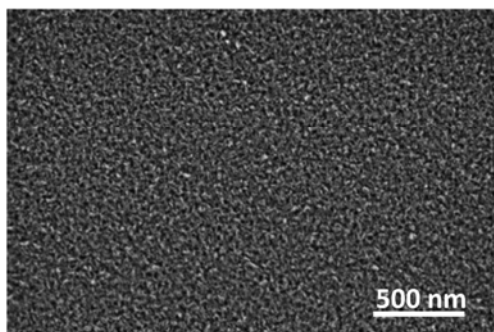


Fig. S. 6: selected spots where the EDX measurements presented in Table S.1 were performed.

Spectrum 2			Spectrum 3		
Element	Weight%	Atomic%	Element	Weight%	Atomic%
C K	15.84	28.17	C K	30.38	48.55
O K	15.34	20.49	O K	8.57	10.28
F K	7.06	7.94	F K	1.73	1.75
Al K	0.29	0.23	Al K	0.00	0.00
Si K	52.31	39.79	Si K	56.13	38.36
S K	0.14	0.10	S K	0.08	0.05
Ni K	9.01	3.28	Ni K	3.12	1.02
Totals	100.00		Totals	100.00	

Table S. 4: EDX quantifications of spots selected in Fig. S. 4, presenting significant extra Ni and O where bumps are visible by SEM.

(a)



(b)

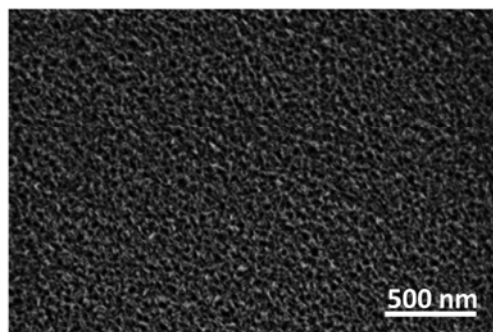


Fig. S. 7: SEM images of NiO layers grown on top of Si at deposition temperatures of 200 °C (left) and 300 °C (right) after 100 cycles between 1.1 and 2 V vs RHE in 1 M KOH electrolyte in dark conditions. No morphology changes can be seen.

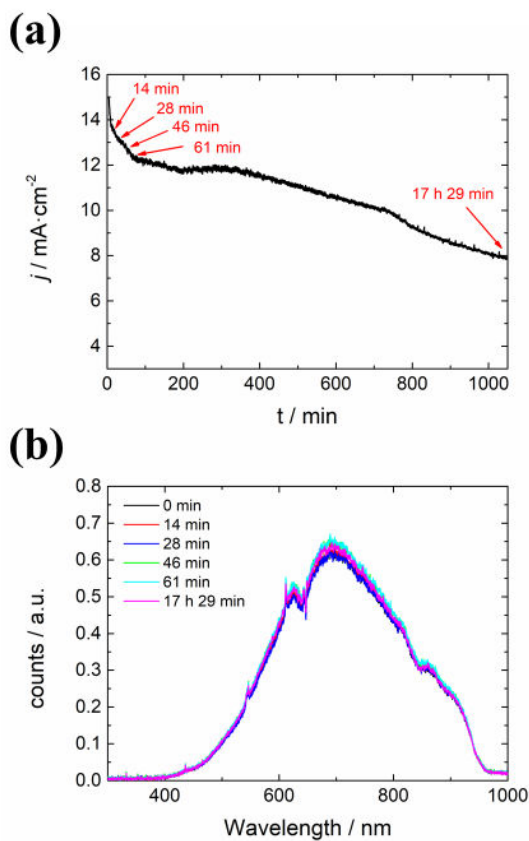


Fig. S. 8: a) Stability measurement of a FTO covered with 50 nm of NiO at 100 °C and under stability for 18h at 1.9 V vs RHE in 1 M KOH. b) In-situ transmittance measurement of the FTO and NiO layers showing no apparent variation after 18 h stability and ~40% current decay.

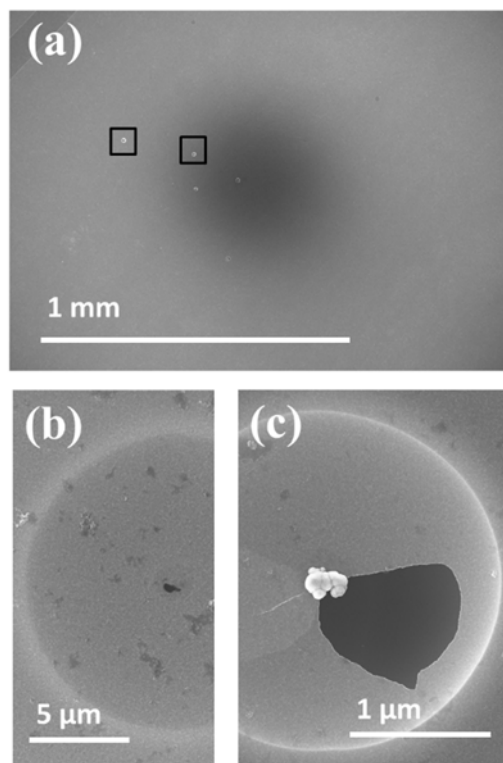


Fig. S. 9: a) SEM top view image of the n^+p -Si photoanode NiO protected at 100 °C presenting very few etched regions. Zoom in two of the etching regions, where b) a few tens of nanometers hole can be seen and c) a particle is present, both probable fabrication defects of the NiO layer allowing KOH to etch the silicon beneath.

Conclusions and future work

The main objective of this thesis has been to study efficient and stable front illuminated photoelectrodes for photoelectrochemical water splitting, with special attention on cost-effective materials. Focus has been put on characterizing materials performance and stability for the two considered configurations, metal oxide based photoelectrodes and protective layers on unstable short band gap photoabsorbers. The protection of silicon and chalcogenide based photoelectrodes resulted in significantly superior productivities than studied metal oxide photoanodes, thus centering most of our efforts. For better understanding of protective layers characteristics, conductivity and degradation analyses were also performed at the nanoscale level.

In the first part of this thesis, titanium dioxide (TiO₂) based photoanodes are studied, giving to the following conclusions:

- Performance increases with thicker and denser nanorods film, caused by higher active area, which is obtained with increasing precursor concentration during hydrothermal growth. There is a maximum precursor concentration of 45 mM, over which TiO₂ film detaches from substrate.
- Substrate microstructuration further enhances productivity by increased direct and scattered light absorption and electrode's area.
- A thermal treatment in a reductive H₂ atmosphere increases the n-type semiconductor level. This way, the semiconductor-liquid junction (SCLJ) was optimized to maximize nanorods potential drop, enhancing charge separation and transport and thus, increasing photoanodes performance.
- By incident photon-to-current efficiency (IPCE) it was corroborated that the performance increase after the H₂ treatment was caused by a better charge extraction in the UV range rather than absorption of visible light by treatment-created states inside the band gap.
- Collaterally, it was observed remarkable different spectral response of TiO₂ photoanodes with and without a light bias, increasing effective available charge carriers and filling trap states active under low monochromatic illumination intensities. This finding helps for more reliable future IPCE measurements.
- Up to 1.2 mA·cm⁻² photocurrent at 1.23 V vs RHE was obtained by these morphological, microscopical and electronic modifications, which corresponds to about a 65% of its theoretical maximum photocurrent.

A 3.0 eV semiconductor is limited to absorb a ~5% of the solar spectra, the UV part. Even with the triple strategy followed to enhance TiO₂ photoanodes performance, results are limited. More complex configurations, involving more efficient and short band gap semiconductors, must be implemented to obtain higher productivities.

In the second part of this thesis, buried short band gap semiconductor junctions, already known from photovoltaic technology, are implemented for photocathodic hydrogen evolution in acidic electrolytes, to favor the hydrogen evolution reaction (HER). Atomic layer deposited (ALD) TiO₂ protective layers are used to inhibit corrosion of unstable photoabsorber candidates, first optimized on silicon. Platinum is used as a model HER catalyst since its overpotential is close to 0, thus studying catalysts was not the scope of this work. The main conclusions of this section are:

- The deposition temperature is found to be a key parameter for stability and conductivity, directly related to crystallization, starting between 100 and 200 °C. Films deposited at 300 °C presented high conductivity, transparency, and polycrystalline morphology, allowing over 20 mA·cm⁻² at 0.4 V vs RHE stable for over 300 h in 0.5 M H₂SO₄.
- Crystalline grains are responsible for electron conduction, revealed by conductive atomic force microscopy (c-AFM), unlike amorphous zones where no current can be measured.
- Amorphous TiO₂ regions present in mixed amorphous-crystalline films are found to dissolve in cathodic conditions and acidic electrolytes, exposing the substrate to the electrolyte.
- 5 nm Ti intermediate layer between Si and TiO₂ is found to help in ALD-TiO₂ crystalline nucleation and to prevent native SiO₂ detrimental formation at the Si/TiO₂ interface.

These protective layers are also deposited on chalcogenide photoabsorbers, from which it were depicted the following conclusions:

- Copper-indium-gallium-selenide (CIGS) photoabsorbers on flexible stainless steel substrates can be converted in efficient PEC devices with over 40 mA·cm⁻² photocurrents and 450 mV photovoltages.
- The use of the complete multilayer stack (n-CdS/i-ZnO/AZO) used for CIGS solar cells is needed for efficient charge separation and electron transport to the hydrogen evolution reaction.
- Devices fabricated on flexible substrates result in detrimental cracks in the protective layer, allowing acid to corrode the photocathode.
- Indium and gallium can be substituted by zinc and tin, earth abundant elements. These kesterite-structured copper-zinc-tin-sulfide/selenide (CZTS/Se) based solar cells can also be transformed into photocathodes by ALD-TiO₂ protection and Pt catalyst decoration.
- By modifying the sulfur/selenium ratio, the optical band gap can be tuned (1.0-1.5 eV), together with the final cathode photovoltage. This characteristic is highly interesting to form tandem PEC devices.

- The kesterite-based cells electronic structure and p-n junction, defined by optimized distribution of copper vacancies and Cu/Zn antisite defects, is highly sensible to thermal post treatments, limiting ALD deposition temperatures to 200 °C. ALD is especially interesting deposition technique due forming crystalline films at such low deposition temperature, given by intermediate species mobility and slow deposition. Pure-sulfide kesterites suffer from partial band gap decrease even at 200 °C.
- ALD has demonstrated to protect kesterite-based solar cells on glass substrates giving over 25 mA·cm⁻² stable photocurrent for more than 1 h in acidic electrolyte.
- Thanks to the possibility to measure solar cells with and without the protective layer, the electrical resistance and changes in its performance can be measured and the catalytic response calculated, allowing us to describe a series circuit model including the role of each component.

In the last part of the thesis, TiO₂ and NiO protective layers are studied in anodic conditions and alkaline electrolytes (favorable for the oxygen evolution reaction, OER). Silicon (with buried homojunctions) is used as reference photoabsorber as it is unaffected by the range of temperatures used for ALD deposition (100-300 °C).

In the first work, TiO₂ layers are deposited, followed by 5 nm NiFe as catalyst (which is hydroxylated to Ni(Fe)OOH in contact with alkaline electrolytes, one of the best catalyst for oxygen evolution). The main findings are:

- Conductivity is enabled when crystallinity is present. This is demonstrated by depositing completely amorphous, mixed amorphous-crystalline and completely crystalline TiO₂ films. Preferential paths in crystalline grains are observed to be the responsible of conductivity in TiO₂ by micro-Raman and c-AFM measurements. This points towards electron injection from the catalyst to the conduction band of TiO₂ and a tunneling recombining contact constituted by the p⁺-Si/2.5 nm SiO₂/TiO₂ interface.
- HRTEM analysis presents polycrystallinity inside the observed grains, and preferential conductivity paths are attributed to grain boundaries and defects within the crystalline structure.
- TiO₂-based protective films present logarithmic current decay under continuous polarization over 480 h stability tests. Electrochemical impedance spectroscopy (EIS) corroborates an increase of the capacity attributed to depletions inside the TiO₂ film. OH⁻ ions are considered to diffuse into TiO₂ under anodic conditions and alter semiconductor's conduction paths conductivity
- UV superimposed illumination partially recovers conductivity of the film, considered a persistent photoconductivity effect on TiO₂ due to modifications on states occupancy.

Alternatively, a one-step ALD deposition of NiO films at 100, 200 and 300 °C creates protected photoanodes with optimal catalytic surface in contact with alkaline electrolytes, where:

- The most conductive layers were formed at low deposition temperature of 100 °C, attributed to less stoichiometric films, with more Ni²⁺ vacancies, responsible of the p-type semiconductor conductivity. Temperature increase was found to result in a crystalline growth direction variation, simultaneous to conductivity reduction.
- Current density decays following a logarithmic time dependency, pointing at the formation of a self-passivation layer. This is attributed to the interaction of the NiO layer and the alkaline electrolyte under anodic working conditions, forming of higher nickel oxidation states at the electrode/electrolyte interface, resulting in an OER overpotential increase.
- Nevertheless, the application of periodic cycling ranging from anodic to cathodic voltage conditions corroborates the existence of a recovery procedure based the cathodic scans promoting the reduced forms at the surface of the NiO layer.
- Applying this methodology under 3 hours cycling periodicity, over 1000 h stability measurements were possible with over 11 mA·cm⁻² photocurrents, an 85% of the initial photocurrent.

In conclusion, the works included in this thesis are significant contributions to the study of fundamental properties of materials and more specifically, stable and efficient photoelectrodes for photoelectrochemical water splitting and their degradation mechanisms. A broad study is performed on ALD deposition of metal oxides and the relationship of these protective thin films with buried semiconductor p-n junctions. The results included have allowed a great improvement of IREC's both maximum productivities and knowledge on short band gap semiconductors and protective layers for harsh chemical environments. In the end, the presented results contribute in the multidisciplinary field of photoelectrochemistry, and should bring stable and efficient photoelectrodes a step closer to commercial application.

Future work:

Nevertheless, despite all the knowledge gained during recent years, efficient and long-stable photoelectrochemical devices have still some challenges to overcome for their large-scale implementation. Silicon presents optimal characteristics for absorbing the red part of visible spectra in tandem structures, but efficient ~1.7 eV band gap earth abundant candidates (absorbing only the blue and green part of the visible spectra) must be found. In this direction, chalcogenide-based photoelectrodes have been demonstrated especially interesting due to the possibility of adapting their band gap by varying the chalcogenide composition. Simplifying the multilayer structure for chalcogenide based PEC devices, i.e. with chemically stable metal oxides acting directly as TCO, might increase their stability in harsh electrolytes and reduce

fabrication costs. The substitution of high vacuum deposition and time-consuming techniques would reduce fabrication costs if pinhole-free layers can be assured. Optimizing the protective layer thickness as antireflective layer will surely help in increasing photoelectrodes productivity. Very long-term stability measurements, in intermittent day/night operation will be necessary to prove protective layers strategy viable in years-lasting devices.

Annex

In the annex chapter of this thesis three works are included, which are considered better suited outside the main part of the thesis, since they are the result of collaborative work coming from the knowledge gained through the development of the PhD work. In the first article, related to hematite photoanodes, the contribution of the thesis author has been minor, related to the TiO₂-ALD deposition prior to anneal treatment, to form the Fe₂TiO₅ superficial layer helping to control surface states and electronic interface coupling. In the second one, the n⁺p-Si/Ti/TiO₂ photocathodes described in Chapter 3 are implemented in another energy storage technology, vanadium redox flow batteries. Due to the evident divergence with water splitting focus of this thesis it has been considered better suited in the annex. The third work included in this chapter is a patent published in collaboration with an industry, where interdigitated back contact (IBC) solar cells are implemented for PEC water splitting with different protective strategies, one of them ALD-deposited TiO₂ films. Due to intellectual property reasons, only the patented content of the work related to this study is reprinted here.

A.1. Enhanced photoelectrochemical water splitting of hematite multilayer nanowire photoanodes by tuning the surface state via bottom-up interfacial engineering

In the first article included in this chapter a sequential study on detrimental interfacial electron-hole recombination of hematite based photoanodes is performed. Multilayered nanowires ITO/Fe₂O₃/Fe₂TiO₅/FeNiOOH are fabricated, with optimized deposition and post-treatments, to facilitate charge transport from the electrochemical reaction into the back contact.

Fe₂O₃ nanowires were grown by a hydrothermal process on and different-thickness indium-doped tin oxide (ITO) covered or no-ITO FTO substrates. Further post-treatments and quenching in air with none or few nanometers ALD-TiO₂ on top allowed forming the Fe₂TiO₅ superficial layer. FeNiOOH nanodots are later photoelectrodeposited on top. The characterization of the photoelectrodes with and without extra interfaces helped elucidating the role of each one.

The systematic electrochemical measurements, and extensive HRTEM and STEM-EELS analysis permitted defining the elemental distribution inside the nanostructures and modeling the electronic interface coupling (Figure A.1a). Epitaxial growth and optimal control of thermal treatments help improve the ITO/Fe₂O₃ interface, with Sn diffusing as doping in Fe₂O₃ structure, reducing back contact recombination. ALD-TiO₂ followed by thermal post-treatments formed Fe₂TiO₅, with favorable energetics for charge separation and Ti atoms passivating detrimental sites in a core-shell nanowire structure. Together with FeNiOOH nanodots increasing electrochemically active sites for OER, electron-hole recombination rates are reduced.

With reported interface coupling optimization, an order of magnitude photocurrent enhancement has been obtained from 0.205 to 2.2 mA·cm⁻² at 1.23 V vs RHE (Figure A.1b), also presenting high stability.

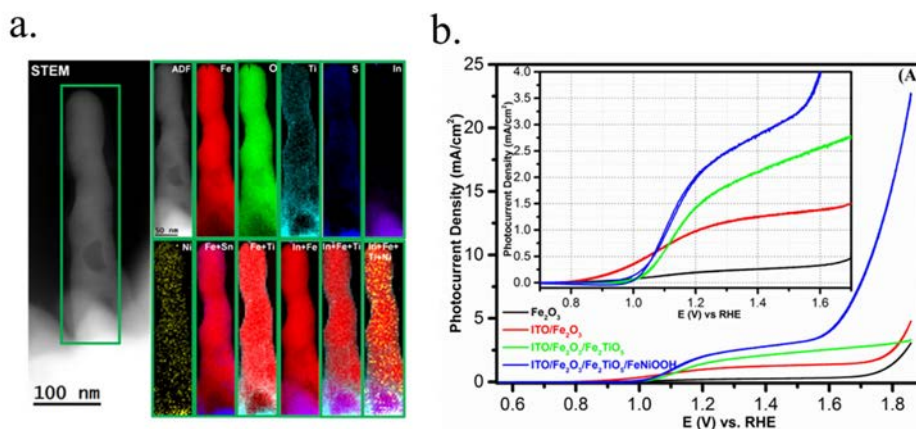


Figure A.1. a) STEM ADF and EELS images of an ITO/Fe₂O₃/Fe₂TiO₅/FeNiOOH photoanodes nanowire. b) Cyclic voltammogram (inset is the magnified plot) for the Fe₂O₃, ITO/Fe₂O₃, ITO/Fe₂O₃/Fe₂TiO₅, and ITO/Fe₂O₃/Fe₂TiO₅/FeNiOOH electrodes.

A.2. Role of Bismuth in the Electrokinetics of Silicon Photocathodes for Solar Rechargeable Vanadium Redox Flow Batteries

In the second article of this chapter, described n⁺p-Si/Ti/TiO₂ photocathodes (Chapter 3), with no Pt as catalyst, were used for a different electrochemical reaction rather than water splitting. The silicon photocathodes were used to perform the vanadium V³⁺/V²⁺ redox reaction, using solar light to recharge the redox battery in the so-called solar-powered electrochemical energy storage (SPEES)¹. As vanadium redox flow batteries operate in acidic environments, silicon must be protected from corrosion.

TiO₂-protected silicon photocathodes supplied photovoltage, reducing the necessary potential for the redox reaction, with significant current conversion. A scheme is depicted in Figure A.2. Moreover, the TiO₂-finished surface is not favorable for the H⁺/H₂ reaction, parasitic for redox flow batteries, restricting H₂ formation by strong proton adsorption². This way the faradaic efficiency to the desired vanadium reaction is enhanced, increasing the efficiency on charging the battery.

In this article, bismuth is used as additive, catalyzing the V³⁺/V²⁺ redox reaction and increasing its reversibility while retarding the HER. Lower charge transfer resistance is detected in Nyquist open circuit plots with the additive. With bismuth, less negative voltages are necessary for the vanadium redox and thus, less reductive potentials will be applied in

working conditions in the TiO_2 protective layer, increasing its stability. Although, Bi^0 deposition on the TiO_2 surface is detected, partially reducing light absorption and maximum photocurrent.

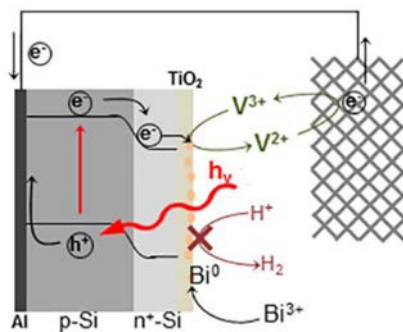


Figure A.2. Scheme illustrating electron-hole pair generated by light in the buried junction and thus, photovoltage; V^{3+}/V^{2+} reaction occurring by injected electrons; the HER reaction inhibited and Bi^0 deposition, together with a counter electrode performing the opposite V^{2+}/V^{3+} reaction.

A.3 Substrate-electrode (SE) interface illuminated photoelectrodes and photoelectrochemical cells

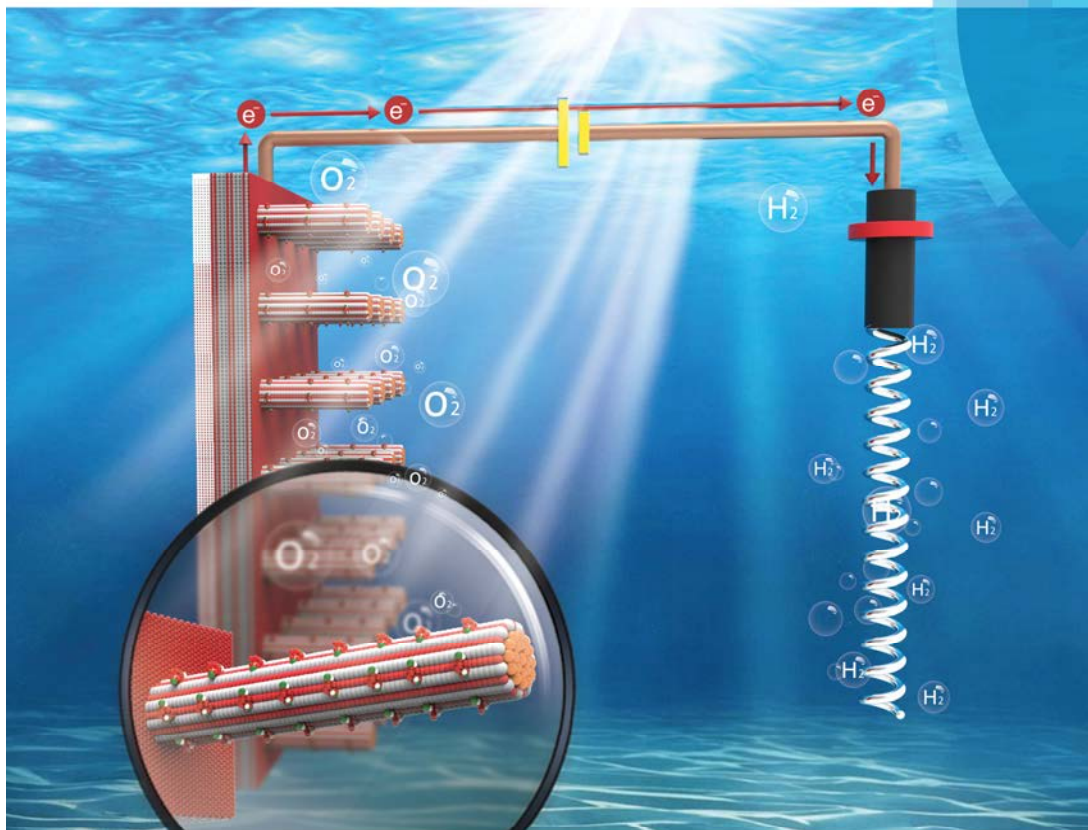
In the third work included in this annex chapter (patent WO/2017/109108, first page reprinted in page 327), interdigitated back contact (IBC) solar cells are implemented for PEC water splitting. Selectively, a resin layer isolates one of the back contacts (collector) from performing any reaction with the electrolyte. The non-isolated one (emitter) charges are conducted through a passivation layer and reaching electrocatalyst, performing the desired reaction. In one of the strategies presented in this patent, ALD-grown TiO₂ layers as reported in Chapter 3 are used as protective, conductive layers together with platinum as HER catalyst. In this strategy, the transparency of these layers is not an issue as IBC solar cells are illuminated from the substrate-electrode (SE) interface side. The possibility of this scheme is demonstrated, together with high current densities equivalent to the photovoltaic ones and over one hour stability.

Bibliography

- (1) Yu, M.; McCulloch, W. D.; Huang, Z.; Trang, B. B.; Lu, J.; Amine, K.; Wu, Y. Solar-Powered Electrochemical Energy Storage: An Alternative to Solar Fuels. *J. Mater. Chem. A* **2016**, *4* (8), 2766–2782.
- (2) Vázquez-Galván, J.; Flox, C.; Fàbrega, C.; Ventosa, E.; Parra, A.; Andreu, T.; Morante, J. R. Hydrogen-Treated Rutile TiO₂ Shell in Graphite-Core Structure as a Negative Electrode for High-Performance Vanadium Redox Flow Batteries. *ChemSusChem* **2017**, *10* (9), 2089–2098.

Energy & Environmental Science

rsc.li/ees



ISSN 1754-5706



PAPER

Jordi Arbiol *et al.*
Enhanced photoelectrochemical water splitting of hematite multilayer nanowire photoanodes by tuning the surface state via bottom-up interfacial engineering

PAPER



Cite this: *Energy Environ. Sci.*,
2017, 10, 2124

Enhanced photoelectrochemical water splitting of hematite multilayer nanowire photoanodes by tuning the surface state *via* bottom-up interfacial engineering†

PengYi Tang,^{b,ab} HaiBing Xie,^{b,a} Carles Ros,^{b,a} LiJuan Han,^c Martí Biset-Peiró,^{b,a} YongMin He,^d Wesley Kramer,^e Alejandro Pérez Rodríguez,^a Edgardo Saucedo,^a José Ramón Galán-Mascarós,^{b,cf} Teresa Andreu,^{b,a} Joan Ramon Morante^a and Jordi Arbiol^{b,*bf}

The optimization of multiple interfaces in hematite (α -Fe₂O₃) based composites for photoelectrochemical water splitting to facilitate charge transport in the bulk is of paramount importance to obtain enhanced solar-to-fuel efficiency. Herein, we report the fabrication of ITO/Fe₂O₃/Fe₂TiO₅/FeNiOOH multi-layer nanowires and a series of systematic experiments designed to elucidate the mechanism underlying the interfacial coupling effect of the quaternary hematite composite. The hierarchical ITO/Fe₂O₃/Fe₂TiO₅/FeNiOOH nanowires display photocurrents that are more than an order of magnitude greater than those of pristine Fe₂O₃ nanowires (from 0.205 mA cm⁻² to 2.2 mA cm⁻² at 1.23 V vs. RHE and 1 Sun), and higher than those of most of the recently reported state-of-the-art hematite composites. Structural, compositional and electrochemical investigations disclose that the surface states (SS) are finely regulated *via* the atomic addition of an Fe₂TiO₅ layer and FeNiOOH nanodots, while the upgrading of back contact conductivity and charge donor densities originate from the epitaxial relationship and enhanced Sn doping contributed from the ITO underlayer. We attribute the superior water oxidation performance to the interfacial coupling effect of the ITO underlayer (Sn doping and back contact conductivity promoter), the atomic level Fe₂TiO₅ coating (Ti doping, surface state density and energy level modulation) and the FeNiOOH nanodot electrocatalyst (regulating surface state energy level). Our work suggests an effective pathway for rational designing of highly active and cost-effective integrated photoanodes for photoelectrochemical water splitting.

Received 26th May 2017,
Accepted 18th July 2017

DOI: 10.1039/c7ee01475a

rs.li/ees

Broader context

Conversion of solar energy to hydrogen energy using photoelectrochemical (PEC) water splitting is one of the key technologies to tackle serious energy and environmental problems. Hematite is a promising candidate for PEC photoanodes as its bandgap is well-suited for absorption of the solar spectrum. However, issues like poor charge transport, surface charge recombination, and slow charge transfer kinetics have limited its practical application. In light of this, an increasing number of investigations have focused on hematite heterostructures that incorporate a second material to tackle some of the inherent material limitations. While individual components of these heterostructured materials have been studied independently, there remains a wealth of untapped knowledge concerning the integration strategy. Herein we report the design and fabrication of ITO/Fe₂O₃/Fe₂TiO₅/FeNiOOH multilayer nanowires which display greatly enhanced PEC performance. By systematically comparing the pristine and representative integrated electrodes, we shed light on the working mechanism of the integrated heterojunction photoanodes. The function of each component in the integrated photoanodes has been identified, as well as the ways in which they couple together to regulate the donor density and surface state density. Additionally, the investigation of the charge transfer kinetics at the semiconductor/electrolyte interface highlights the role of the surface state density/donor density ratio in determining the charge transfer efficiency. This report presents a more complete and clear picture with which to understand the integrated photoanodes for PEC water splitting.

^a Catalonia Institute for Energy Research (IREC), Jardins de les Dones de Negre 1, Sant Adrià del Besòs, Barcelona 08930, Catalonia, Spain

^b Catalan Institute of Nanoscience and Nanotechnology (ICN2), CSIC and The Barcelona Institute of Science and Technology (BIST), Campus UAB, Bellaterra, 08193 Barcelona, Catalonia, Spain. E-mail: arbiol@icrea.cat

^c Institute of Chemical Research of Catalonia (ICIQ), The Barcelona Institute of Science and Technology (BIST), Avinguda Paisos Catalans 16, Tarragona 43007, Catalonia, Spain

^d School of Physical Science and Technology, Lanzhou University, Lanzhou 730000, China

^e Beckman Institute and Division of Chemistry and Chemical Engineering, California Institute of Technology, 1200 East California Boulevard, Pasadena, California 91125, USA

^f ICREA, Pg. Lluís Companys 23, 08010 Barcelona, Catalonia, Spain

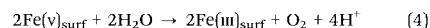
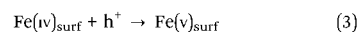
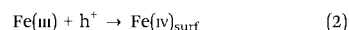
† Electronic supplementary information (ESI) available: XRD, UV-Vis spectrum, SEM, EDS, TEM, STEM-EELS maps, PEC characteristics, PEIS, equivalent circuit, Mott-Schottly plots, XPS spectra and crystal model. See DOI: 10.1039/c7ee01475a

1. Introduction

Hematite based photoanodes have been intensively investigated on account of several promising properties which make them a potential candidate as a water splitting photoanode. Hematite materials are low cost, and environmentally friendly owing to their high natural abundance. More importantly, in terms of its applications in PEC, hematite possesses high photo-chemical stability, a narrow bandgap (1.9–2.2 eV), and a theoretical maximum solar-to-hydrogen (STH) efficiency of 15.4%, corresponding to 12.5 mA cm⁻² at Air-Mass 1.5 Global solar illumination, which exceeds the STH benchmark efficiency of 10% required for practical applications.^{1,2} However, its relatively low absorption coefficient, short excited-state lifetime (10⁻⁶ s),^{3,4} poor oxygen evolution reaction kinetics, short hole diffusion length, and poor electrical conductivity lead to multiple electron-hole recombination pathways occurring in the bulk, interfaces, and surfaces and significantly limit the photoelectrochemical (PEC) activity of hematite.² Since rapid charge transport and transfer between the back substrate, photoactive semiconductor, catalyst and electrolyte is necessary for efficient STH performance, the electronic and structural properties of back substrate/semiconductor/catalyst/electrolyte interfaces play a vital role in PEC performance.^{5–10} The electron-hole recombination at the interface of the back substrate and hematite is critical for electron transport from bulk hematite to the current collector and thus affects the overall PEC photocurrent response.^{2,9,11–14} For instance, Zheng *et al.* reported an integrated hematite, TiO₂ and FeOOH photoanode and obtained a photocurrent of around 1.5 mA cm⁻², which is still much lower than the theoretical value (12.5 mA cm⁻²) of hematite.¹² Even though this design simultaneously reduces charge recombination in the bulk and surface of hematite, the obtained photocurrent response suffers from intensive back electron-hole recombination between hematite nanowires and the FTO substrate. This phenomenon is likely derived from the Sn loss in the FTO substrate during the high temperature (1000 °C) sintering treatment which leads to poor electron conductivity in the back contact.^{13,14} Therefore, it is essential to optimize the back interface of the FTO substrate and hematite. This may be accomplished by introducing a conductive buffer layer, such as an ITO underlayer between hematite and the FTO substrate. Moreover, the energetic and electronic structures of hematite can be tuned by forming an advantageous heterojunction interface, which can reduce the charge recombination at the semiconductor junction interface and thus facilitates hole transport to the electrolyte for the oxygen evolution reaction (OER).^{10,12} Recently, we prepared a mesoporous hematite-Fe₂TiO₅ heterojunction film, with an optimized 10% TiO₂ doping, which possessed a 15-fold photocurrent increment (up to 1.3 mA cm⁻² at 1.23 V vs. RHE).¹⁰ Furthermore, iron-nickel oxide hydroxides (FeNiOOH) have attracted widespread attention as oxygen evolution catalysts (OEC) due to their unique structure and good OER activity in alkaline medium, whose OER activity can be adjusted according to film thickness.^{15–17} Coupling FeNiOOH OECs on hematite photoanodes is supposed to effectively suppress the electron-hole pair recombination and accelerate reaction

kinetics at the photoactive semiconductor/electrolyte interface (SEI).^{18,19} In light of this, it is therefore of high interest to design an integrated quaternary multilayer photoanode with a high electrical conductive underlayer (ITO layer, to protect against Sn loss from the FTO substrate), an advantageous heterojunction (Fe₂O₃/Fe₂TiO₅),¹⁰ and an efficient OEC layer (FeNiOOH) to simultaneously reduce the interfacial, bulk and surface charge recombination as well as to enhance its PEC performance.

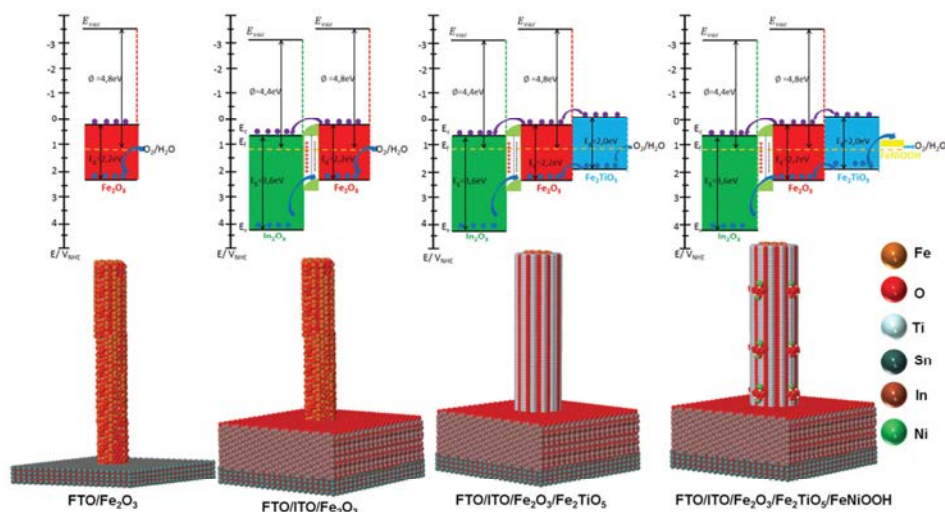
On the other hand, the kinetic process of water oxidation at the SEI^{10,20–22} and the identification of the active sites^{2,3–25} for water splitting have drawn the attention of many researchers. Peter *et al.* employed photoelectrochemical impedance spectroscopy (PEIS) for the kinetic analysis of the multistep water oxidation reaction and proposed that the OER in hematite involves high-valent iron states formed at the surface.²⁰ Water oxidation on the hematite surface is a 4-electron process, which occurs following eqn (1–4), with the holes being 'stored' in the Fe(IV) and Fe(V) intermediate states.²⁰



Hamann *et al.* illustrated a general physical model and systematically discussed the suitable equivalent circuit for illustrating the EIS data for the hematite electrode, including surface states (SS) at the SEI where holes accumulate.²¹ Most recently, Hamann *et al.* investigated the water-oxidation reaction on hematite *via in situ* infrared spectroscopy; and the existence of an Fe^{IV}=O group (an intermediate in the PEC water oxidation reaction) was directly observed, which is the origin of the presence of hematite surface states.²⁶ Moreover, our previous investigation proposed a charge transfer mechanism through hole trapping at the surface state and its isoenergetic transfer to water for a hematite/Fe₂TiO₅ composite system and demonstrated that the surface state density of hematite can be tuned by controlling the amount of TiO₂.¹⁰ In addition, it is well established that SS exist due to the termination of lattice periodicity at the species' surface, and the unpaired electrons in the dangling bonds of surface atoms interact with each other forming an electronic state with a narrow energy band (mid band) at the semiconductor band gap.^{27,28} In this regard, we propose that, by integrating the hematite nanowires with an ITO underlayer, and Fe₂TiO₅ and FeNiOOH coating layers step-wise, the SS would be finely regulated because the chemical environment of Fe^{IV}=O present at the SEI will vary slightly during the water oxidation process.^{29–32}

2. Results

Based on the wealth of reported band gap information for In₂O₃, hematite, Fe₂TiO₅ and FeNiOOH,^{10,33} a type II band alignment composed of multiple ITO/hematite/Fe₂TiO₅/FeNiOOH interfaces can be constructed *via* gradual incorporation of ITO, Fe₂TiO₅ and FeNiOOH layers in hematite nanowires.^{27,34} As illustrated



Scheme 1 Top: Thermodynamic scheme for the charge transfer processes at 1.23 V vs. RHE of SEI under illumination for the Fe_2O_3 , ITO/ Fe_2O_3 , ITO/ $\text{Fe}_2\text{O}_3/\text{Fe}_2\text{TiO}_5$, and ITO/ $\text{Fe}_2\text{O}_3/\text{Fe}_2\text{TiO}_5/\text{FeNiOOH}$ electrodes. The black arrows indicate the bandgap of In_2O_3 (ITO matrix), hematite and Fe_2TiO_5 . The dark blue arrow refers to the hole transfer process at the heterojunction interfaces. The purple arrow refers to the electron transfer process present at the heterojunction interfaces. For simplicity, interfacial charge transfer is considered to occur through the E_V and/or E_C states directly, without the intervention of interfacial SS. In all photoanodes, 4 electron–hole couples per visible active semiconductor are depicted. In_2O_3 (main ingredient of ITO matrix): green; Fe_2O_3 : red; Fe_2TiO_5 : indigo; FeNiOOH : yellow. Bottom: The atomic supercell models illustrate the interfaces existing at In_2O_3 (ITO matrix), hematite, Fe_2TiO_5 and FeNiOOH species in the integrated electrodes.

in Scheme 1, upon light illumination, the pristine Fe_2O_3 electrode suffers from a large recombination rate that yields a low photo-current, as holes are sluggishly transferred to water. For the ITO/ Fe_2O_3 electrode, since both In_2O_3 and hematite are n-type semiconductors with different work functions, a heterojunction with a potential barrier will form at their interface. In_2O_3 (main ingredient of ITO) has a lower work function compared to hematite, thus the electrons in the Fermi level (E_f) of In_2O_3 will migrate to the E_f of Fe_2O_3 until their E_f equalize.³³ At the equilibrium state, an electron depletion layer (marked as double layer charge between hematite and In_2O_3) will be generated at the heterojunction interface and thus a built-in electron field will be formed, which will accelerate the separation of photo-generated charge carriers and reduce the recombination rate and thus result in enhanced photocurrent.^{27,35} Since Fe_2TiO_5 and hematite's relative conduction band (CB) and valence band (VB) edge positions enable a cascade of charge migration, holes are transferred from Fe_2O_3 to Fe_2TiO_5 and conversely electrons are transferred from Fe_2TiO_5 to Fe_2O_3 in a conveyor belt fashion.¹⁰ Upon coating of ultrathin Fe_2TiO_5 onto ITO/ Fe_2O_3 nanowires, the hematite nanowires can accommodate the ultrathin pseudobrookite phase shell at the surface, forming the advantageous $\text{Fe}_2\text{O}_3/\text{Fe}_2\text{TiO}_5$ heterojunction. The heterojunctions in the ITO/ $\text{Fe}_2\text{O}_3/\text{Fe}_2\text{TiO}_5$ electrode reduce the grain boundary recombination by preventing charge accumulation in the nanowires and at the interfaces, and thus are expected to further enhance the photocurrent response. Finally, there is consensus that coupling FeNiOOH on photoanodes effectively suppresses the

charge recombination and accelerates reaction kinetics at the SEI.^{36–42} The deposition of FeNiOOH onto the ITO/ $\text{Fe}_2\text{O}_3/\text{Fe}_2\text{TiO}_5$ nanowires should further increase the surface work function, resulting in a remarkable enhancement of the barrier height and built-in electric field for the migration of photogenerated holes to the electrode surface.^{36–38} With this in mind, an ITO/hematite/ $\text{Fe}_2\text{TiO}_5/\text{FeNiOOH}$ heterojunction nanowire was designed and fabricated *via* a combination of sputtering, hydrothermal, ALD and photo-electrochemical deposition techniques, as displayed in Fig. 2 (top).

2.1 XPS spectrum

The surface electronic states and composition of each electrode were analysed by XPS and all binding energies were corrected for sample charging effects regarding the C 1s line at 284.6 eV. Fig. 1 and Fig. S1 (ESI†) present the Sn 3d, O 1s, Fe 2p, In 3d, Ti 2p and Ni 2p core level XPS scans at higher resolution over smaller energy windows. The Fe 2p_{1/2} and 2p_{3/2} peaks at the binding energies of 710.39 eV and 724.00 eV confirm the presence of the Fe element in these four electrodes. Additionally, two satellite peaks of the Fe 2p main line are present at approximately 8.1–8.5 eV lower energy than the main line, indicating the presence of Fe^{3+} species.^{10,43} A positive shift of the Fe peaks after the sputtering of the ITO underlayer reflects a decrease in the electron density of the Fe_2O_3 due to electron transfer from Fe_2O_3 to the ITO layer. Conversely, a negative shift of the Fe peak is detected after the deposition of Fe_2TiO_5 and FeNiOOH layers. These shifts can be ascribed to the surface binding

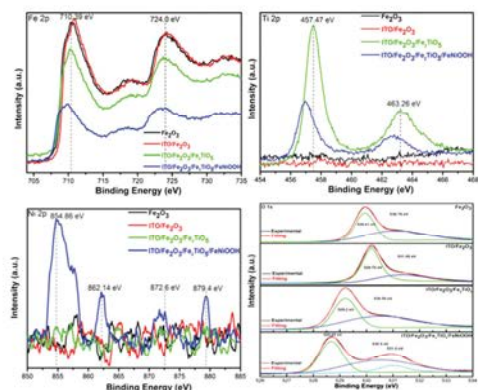


Fig. 1 High resolution XPS spectra of Fe 2p, Ti 2p, Ni 2p and O 1s, from the Fe_2O_3 , ITO/ Fe_2O_3 , ITO/ Fe_2O_3 / Fe_2TiO_5 , and ITO/ Fe_2O_3 / Fe_2TiO_5 / FeNiOOH electrodes.

interaction between ITO, Fe_2O_3 , Fe_2TiO_5 and FeNiOOH , which induces an electron transfer in the integrated photoanode following the order: $\text{FeNiOOH} \rightarrow \text{Fe}_2\text{TiO}_5 \rightarrow \text{Fe}_2\text{O}_3 \rightarrow \text{ITO}$ as depicted in Scheme 1.⁴⁴ The Sn $3d_{3/2}$ and Sn $3d_{5/2}$ peaks (Fig. S1, ESI[†]) at 494.80 and 486.26 eV with a splitting energy of 8.54 eV are consistent with reported values of Sn^{4+} .^{33,45} Furthermore, the In $2p_{1/2}$ and $2p_{3/2}$ core level XPS spectrum (Fig. S1, ESI[†]) has two weak, broad peaks around 451.60 and 444.76 eV, in good agreement with In_2O_3 .³³ Compared with the strong intensity of the Sn 3d peaks, the relatively weak intensity of the In 2p peaks means that the formation of In^{3+} ions is closer to the substrate, indicating that Sn doping dominates the Fe_2O_3 nanowires rather than In doping. The Ti $2p_{1/2}$ and $2p_{3/2}$ peaks at 463.26 and 457.27 eV reveal the successful coating of Fe_2TiO_5 for ITO/ Fe_2O_3 / Fe_2TiO_5 and ITO/ Fe_2O_3 / Fe_2TiO_5 / FeNiOOH electrodes.¹⁰ Coinciding with the observed shift of Fe 2p peaks, after the FeNiOOH deposition, the Ti peaks shift in the negative binding energy direction, again implying electron transfers from the FeNiOOH to the Fe_2TiO_5 layer. Moreover, the presence of Ni in FeNiOOH was also investigated. The weak Ni $2p_{1/2}$ and $2p_{3/2}$ core level XPS peaks located at 872.60 eV and 854.86 eV and the associated satellite peaks at 862.14 eV and 879.40 eV are observed in the ITO/ Fe_2O_3 / Fe_2TiO_5 / FeNiOOH electrode, confirming the presence of FeNiOOH .⁴⁴ The O 1s XPS spectrum of the ITO/ Fe_2O_3 / Fe_2TiO_5 / FeNiOOH electrode is composed of three peaks. The low binding energy at 529.41 eV and the higher binding energy component at 531.05 eV are attributed to the coordination of oxygen bound to iron atoms from the Fe_2O_3 moiety and surface adsorbed OH groups, respectively.⁴⁶ The shift behaviour of these two O 1s peaks of Fe_2O_3 is in accordance with shifts observed for the Fe 2p and Ti 2p peaks. Whereas, the 531.00 eV O1s peak can be assigned to the OOH bonding likely to the FeNiOOH species.⁴¹ The consistent shifts in the binding energy observed in the XPS data for these electrodes indicate charge transfer processes that benefit electron-hole separation, further supporting the

well-constructed multiple ITO/hematite/ Fe_2TiO_5 / FeNiOOH heterojunction with type II band alignment.

2.2 Structural characterization

The morphology and crystal phase evolution of these electrodes were monitored by SEM, EDS, XRD, TEM and STEM-EELS maps. Vertically aligned Fe_2O_3 nanowires were grown on an FTO or 105 nm ITO coated FTO substrate (the corresponding SEM images of these two substrates are displayed in Fig. S18, ESI[†]) via a previously reported hydrothermal method.⁴⁷ The Fe_2O_3 nanowires have a diameter range of 50 to 100 nm (Fig. 2A–D). Subsequently, an ultrathin TiO_2 layer was coated onto the ITO/ Fe_2O_3 nanowires by ALD (30 cycles). The surface TiO_2 was subsequently transformed into Fe_2TiO_5 through a post-quenching process in ambient atmosphere at 750 °C for 30 min. As displayed in Fig. 2E and F, the Fe_2TiO_5 coating onto ITO/ Fe_2O_3 is homogeneous with no change in the nanowire configuration. Interestingly, the ITO/ Fe_2O_3 / Fe_2TiO_5 nanowires appear to be straighter than the ITO/ Fe_2O_3 nanowires; this is likely due to the confinement effect from the ultrathin Fe_2TiO_5 layer (this phenomenon is similar to the function of SiO_2 in the fabrication of mesoporous Fe_2O_3 , reported by K. Sivula *et al.*).⁴⁸ When 10 mC FeNiOOH was further photo-electrodeposited onto the ITO/ Fe_2O_3 / Fe_2TiO_5 nanowires, no visible nanostructure could be observed on the nanowire surface (Fig. 2G and H), indicating its ultrathin configuration. The crystal phase and elemental information were characterized by XRD (Fig. S2A, ESI[†]) and EDS (Fig. S3, ESI[†]), confirming the presence of In_2O_3 , hematite, pseudobrookite and FeNiOOH in the corresponding electrodes.

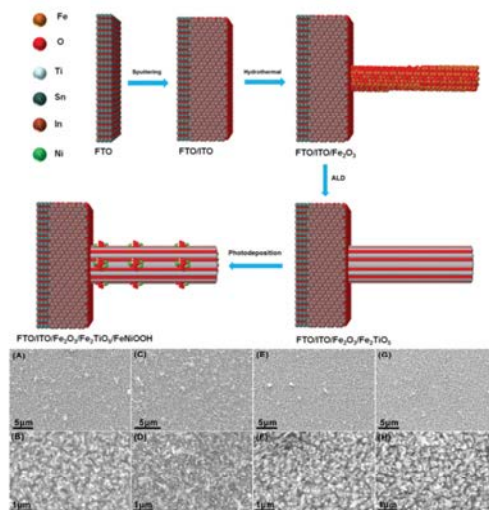


Fig. 2 Top: Atomic supercell model illustration of the synthetic procedure for the ITO/ Fe_2O_3 / Fe_2TiO_5 / FeNiOOH integrated photoanodes. Bottom: SEM images (top view) of the Fe_2O_3 (A and B), ITO/ Fe_2O_3 (C and D), ITO/ Fe_2O_3 / Fe_2TiO_5 (E and F), and ITO/ Fe_2O_3 / Fe_2TiO_5 / FeNiOOH (G and H) electrodes.

To identify each crystal phase *via* HRTEM and probe the spatial distribution of these components in the integrated electrodes, we created crystal models based on the single crystal data in the Inorganic Crystal Structure Database (ICSD), as displayed in Fig. S4 (ESI[†]). With these crystal models, the diffraction patterns visualized from different zone axes of each phase can be simulated. Then, the simulated diffraction pattern is compared with the power spectrum (FFT) obtained on the atomic resolution HRTEM experimental images for the identification of the crystal phases in the composite electrodes. Fig. S5 (ESI[†]) shows low magnification TEM images of the Fe₂O₃ electrode with nanowire-like morphology, while its HRTEM and detailed atomic structure are displayed in Fig. 3A. The corresponding temperature coloured power spectrum (Fig. 3A right) indicates that the structure corresponds to the trigonal Fe₂O₃, [R3-CH]-space group 167, also known as hematite, with lattice parameters of $a = b = 0.50342$ nm, $c = 1.37483$ nm, and $\alpha = \beta = 90^\circ$ and $\gamma = 120^\circ$ as visualized along the [21-2] direction. The HRTEM and atomic structure detail of the ITO/Fe₂O₃ electrode in Fig. 3B demonstrate that the modification of the FTO substrate with a 105 nm ITO underlayer does not alter the crystal phase of the Fe₂O₃ nanowires. The temperature coloured power spectrum (right of Fig. 3B) of the ITO/Fe₂O₃ electrodes indicates that the nanowires retain their single crystal hematite nature as visualized along the [110] direction; this is further supported by Fig. S6 and S7 (ESI[†]). Fig. 3C (left) shows the HRTEM image of the edge region of a single ITO/Fe₂O₃/Fe₂TiO₅ nanowire extracted from the ITO/Fe₂O₃/Fe₂TiO₅ electrode nanowire array. The corresponding power spectrum (Fig. 3C right) shows that the nanowire is composed of a hematite core (Fe₂O₃) and a Fe₂TiO₅ shell ([BBMM]-space group 63, with lattice parameters of $a = 0.9793$ nm, $b = 0.9979$ nm, $c = 0.3732$ nm, and $\alpha = \beta = \gamma = 90^\circ$), as visualized along the [42-1] and [001] directions, respectively. RGB coloured phase filtered images corresponding to the selected area of the ITO/Fe₂O₃/Fe₂TiO₅ electrode in Fig. 3C are exhibited on the right. Fig. S8 and S9 (ESI[†]) clearly confirm the homogenous coating of the Fe₂TiO₅ layer on the surface of the Fe₂O₃ nanowires. Moreover, the atomic density profile in the inset of the left HRTEM image in Fig. 3C, reveals that the thickness of the Fe₂TiO₅ shell is 0.78 ± 0.02 nm, in agreement with the estimated 0.81 nm from the ALD process. Fig. 3D displays a HRTEM image (left) of the electrode after the deposition of FeNiOOH to form the quaternary ITO/Fe₂O₃/Fe₂TiO₅/FeNiOOH structure. The presence of hematite and pseudobrookite phases was identified from their power spectrum (Fig. 3D middle). It is noteworthy that the crystal diffraction spots of FeNiOOH, while visible, are weak showing few crystallites (low magnification TEM images are displayed in Fig. S10, ESI[†]), consistent with the XRD results indicating that it is primarily amorphous.^{44,49-52} Moreover, the corresponding RGB phase filtered image (Fig. 3D right) illustrates the localized presence of hematite (nanowire core), pseudobrookite (shell) and FeNiOOH nanodots (surface crystallites in blue, showing a 0.256 nm plane distance corresponding to its (021) plane).⁵²⁻⁵⁵

The chemical compositions of the interfaces in the ITO/Fe₂O₃/Fe₂TiO₅/FeNiOOH electrodes were investigated by

EELS mapping using the K edge for O, M edges for In and Sn, and L edges for Fe, Ti and Ni. The STEM-EELS composition maps of the Fe₂O₃ (Fig. S11 and S12), ITO/Fe₂O₃ (Fig. S13 and S14) and ITO/Fe₂O₃/Fe₂TiO₅ (Fig. S15 and S16) electrodes are included in the ESI[†]. As displayed in the STEM image of Fig. 4, the Fe₂O₃/Fe₂TiO₅/FeNiOOH composite nanowire (green squared region) is grown directly onto the ITO matrix (brighter bottom region). The individual Fe, Sn and Fe + Sn RGB composite EELS maps in Fig. 4 show that the Sn from the ITO matrix diffuses into the hematite nanowires, revealing an intensive Sn doping throughout the ITO/Fe₂O₃/Fe₂TiO₅/FeNiOOH electrode as compared to the weak Sn signal detected in the nanowires corresponding to the Fe₂O₃ electrode (Fig. S11 and S12, ESI[†]). By contrast, In, in the form of In₂O₃, is only present in the bottom region of the electrode corresponding to the ITO underlayer, as supported by the individual In and O EELS mappings shown in Fig. 4 and HRTEM result in Fig. S6 (ESI[†]). Together with the STEM-EELS maps obtained in the ITO/Fe₂O₃ electrode (Fig. S13 and S14, ESI[†]) and the ITO/Fe₂O₃/Fe₂TiO₅ electrode (Fig. S15 and S16, ESI[†]), these data demonstrate that there is almost no In doping into the Fe₂O₃ nanowires upon the sputtering of the ITO underlayer, which is consistent with the XPS result. The Fe, Ti and Fe + Ti RGB composite EELS elemental maps obtained on the ITO/Fe₂O₃/Fe₂TiO₅/FeNiOOH electrode (Fig. 4) show complete coverage of the ultrathin Fe₂TiO₅ shell over the Fe₂O₃ nanowires. The individual Fe, Ni, and O EELS elemental maps illustrate the presence of discontinuous distributed FeNiOOH species decorated on the nanowires, in good agreement with the nanodot-like FeNiOOH structure observed in Fig. 3D and Fig. S10, S17 (ESI[†]). RGB composite EELS elemental maps of In + Fe, In + Fe + Ti and In + Fe + Ti + Ni together illustrate the successful construction of the quaternary ITO/Fe₂O₃/Fe₂TiO₅/FeNiOOH heterojunction nanowires *via* step-wise incorporation of ITO, Fe₂O₃, Fe₂TiO₅ and FeNiOOH.

2.3 PEC performance characterization

To determine the optimum conditions for the integration of ITO/Fe₂O₃/Fe₂TiO₅/FeNiOOH electrodes, different synthesis parameters, including ITO thickness, TiO₂ cycles, post-quench sintering conditions and FeNiOOH deposition charge, were examined (for details see Fig. S18–S27 and associated discussions in the ESI[†]). The PEC performance measured for the optimized four representative photoanodes is displayed in Fig. 5. The CVs of pristine Fe₂O₃ nanowires (Fig. 5A) show a relatively low photoresponse over the whole potential window with a photocurrent density of 0.205 mA cm^{-2} at 1.23 V vs. RHE, the thermodynamic potential for the OER. Upon introduction of the ITO underlayer, the photocurrent density increases to 1.05 mA cm^{-2} at 1.23 V vs. RHE. The onset potential of ITO/Fe₂O₃ still remains at 0.85 V, which is the same as that of the pristine Fe₂O₃ electrode. Besides, the CV curve of Fe₂O₃ and ITO/Fe₂O₃ electrodes at high potential region (over 1.7 V) exhibits the same trend, indicating the presence of a similar Fe₂O₃/electrolyte interface.¹⁵ In contrast, the ITO/Fe₂O₃/Fe₂TiO₅ electrode exhibits an anodic shift in the onset potential to 1.0 V vs. RHE, along with an increase in the photocurrent density to 1.56 mA cm^{-2} at 1.23 V vs. RHE.

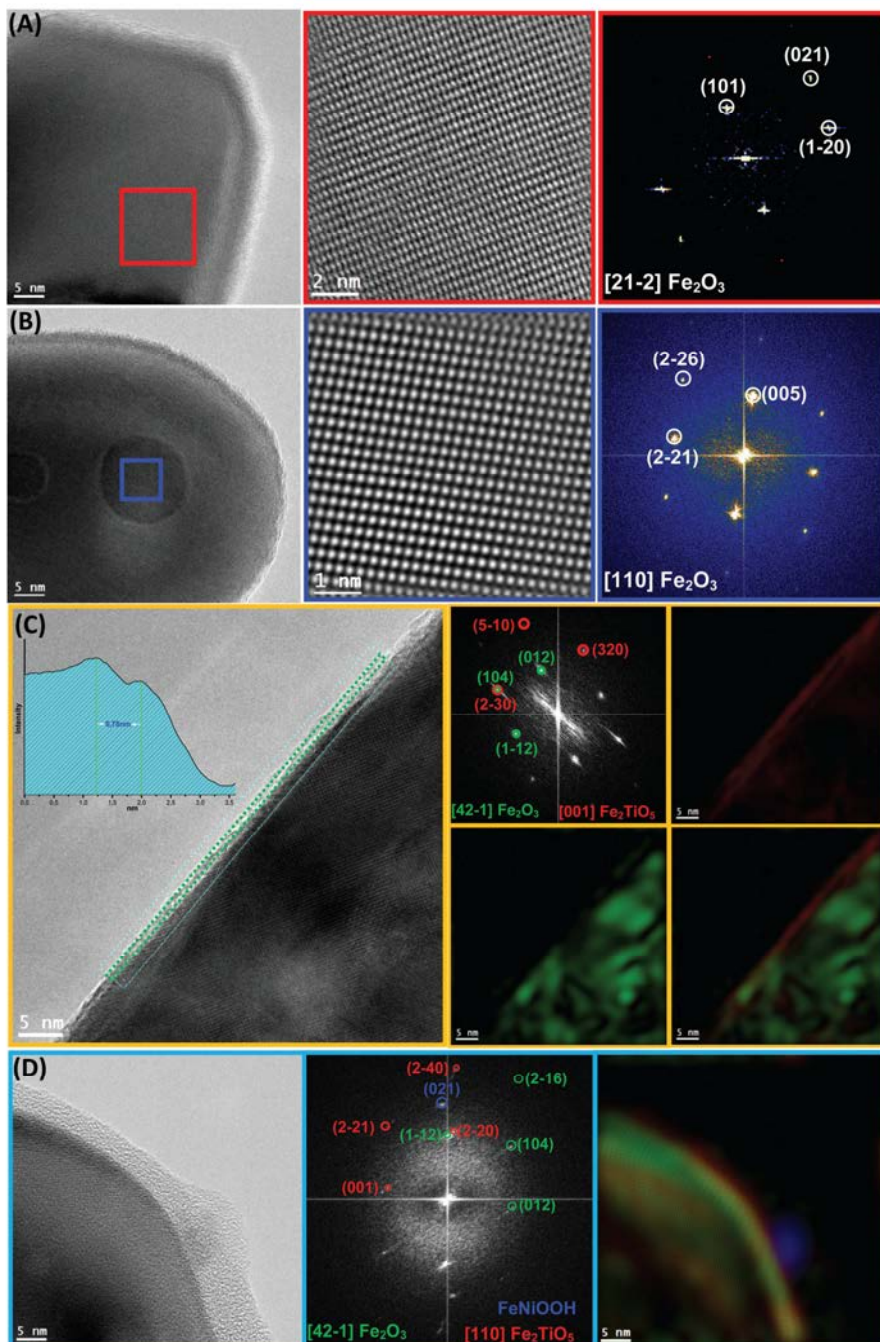


Fig. 3 HRTEM, power spectrum and RGB coloured phase filtered structural images of the Fe_2O_3 (A), ITO/ Fe_2O_3 (B), ITO/ Fe_2O_3 / Fe_2TiO_5 (C) and ITO/ Fe_2O_3 / Fe_2TiO_5 / FeNiOOH (D) electrodes.

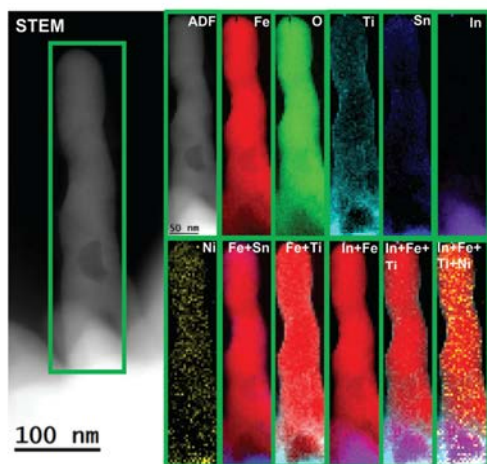


Fig. 4 EELS chemical composition maps obtained from the green rectangled area on the ADF-STEM micrograph selected on one of the nanowires extracted from the ITO/Fe₂O₃/Fe₂TiO₅/FeNiOOH electrode sample. Individual Fe (red), O (green), Sn (blue), In (purple), Ti (indigo) and Ni (yellow) maps and their RGB composite.

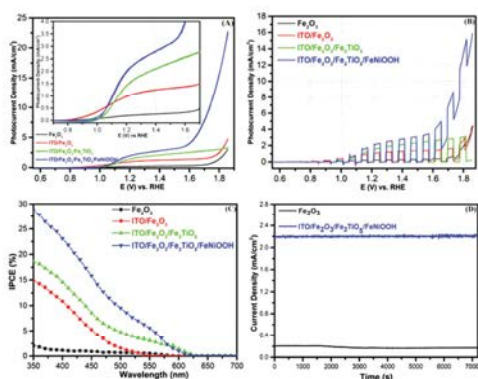


Fig. 5 (A) Cyclic voltammetry (the inset shows its magnified plot), (B) chopped light photocurrent-potential curves, (C) IPCE and (D) photoelectrochemical stability test operated at 1.23 V vs. RHE for the Fe₂O₃, ITO/Fe₂O₃, ITO/Fe₂O₃/Fe₂TiO₅, and ITO/Fe₂O₃/Fe₂TiO₅/FeNiOOH electrodes. All polarization potentials reported here are relative to the reversible hydrogen electrode (RHE), and current densities are per geometric area.

The positive shift in the onset potential upon coating Fe₂TiO₅ onto the hematite nanowires is consistent with the result reported by Zhong *et al.*,⁵³ which is probably due to the suppressing of the surface state density at a potential lower than 1.0 V vs. RHE when compared with that of the ITO/Fe₂O₃ electrode, as displayed in Fig. 7A. While, the CV curve of the ITO/Fe₂O₃/Fe₂TiO₅ electrodes at high potential (over 1.7 V) is somehow suppressed compared with that of the Fe₂O₃ and ITO/Fe₂O₃ electrodes, illustrating its SEI variation. Despite some improvement, the PEC performance for the

ITO/Fe₂O₃/Fe₂TiO₅ nanowires remains unsatisfactory, likely caused by the slow water oxidation kinetics.⁵⁴ Thus, an optimized OEC (Fig. S24 and S25, ESI[†]), 10 mM FeNiOOH, was deposited on the surface of the ITO/Fe₂O₃/Fe₂TiO₅ nanowires. In the case of the ITO/Fe₂O₃/Fe₂TiO₅/FeNiOOH electrode, a cathodic shift in the onset potential for the OER to 0.95 V is observed relative to the ITO/Fe₂O₃/Fe₂TiO₅ electrode. Its photocurrent density of 2.2 mA cm⁻² at 1.23 V vs. RHE represents the highest value among these four photoanodes, and is even higher than the photocurrent response of recently reported state-of-the-art Fe₂O₃ composite photoanodes (Table S2, ESI[†]). The tremendous increment of the photocurrent at high potential (over 1.6 V, dominated by the dark current response from the OEC) implies the successful combination of the merits of the photocatalytic activity of ITO/Fe₂O₃/Fe₂TiO₅ and the electrocatalytic activity of FeNiOOH.¹⁵ Besides, there is a photocurrent plateau for all electrodes, which is derived from the transition of the hole acceptor from OH⁻ to water in the electrolyte according to the report of Zhao *et al.*²² Furthermore, transient photocurrent measurements, based on the CVs under chopped light illumination, were performed for each photoanode. As shown in Fig. 5B, all electrodes exhibit a prompt and reproducible photocurrent response with respect to the irradiation signal ON-OFF cycles. The current density of these electrodes under illumination follows an ascending order of: Fe₂O₃ < ITO/Fe₂O₃ < ITO/Fe₂O₃/Fe₂TiO₅ < ITO/Fe₂O₃/Fe₂TiO₅/FeNiOOH photoanodes. This is in good agreement with the CV results and further demonstrates the enhancement in PEC performance provided by addition of ITO, Fe₂TiO₅ and FeNiOOH to hematite nanowires.

The incident photon-to-current conversion efficiency (IPCE) was measured to understand the relationship between the photocatalytic activity and light absorption. All samples exhibit photocatalytic activity in the visible light region (Fig. 5C). The maximum IPCEs obtained at 350 nm for Fe₂O₃, ITO/Fe₂O₃, ITO/Fe₂O₃/Fe₂TiO₅, and ITO/Fe₂O₃/Fe₂TiO₅/FeNiOOH photoanodes are 2.1%, 14.8%, 18.6%, and 28.7%, respectively. The large enhancement of IPCE for the ITO/Fe₂O₃/Fe₂TiO₅/FeNiOOH nanowires further supports the integrated coupling effect of ITO, Fe₂TiO₅ and FeNiOOH to the PEC performance. Additionally, the IPCE curves for all of these electrodes correlate with the UV-Vis absorption spectrum of Fe₂O₃ presented in Fig. S2B (ESI[†]), indicating that the Fe₂O₃ indeed acts as the sole visible light responsive semiconductor material. Thus, the enhanced PEC performance is preliminarily attributed to a synergistic effect between ITO, Fe₂O₃, Fe₂TiO₅ and FeNiOOH rather than the primitively tandem function of each semiconductor material. The photoelectrochemical stability is operated by chronopotentiometric response at a constant applied working potential of 1.23 V vs. RHE, as shown in Fig. 5D. The photocurrent of Fe₂O₃ slightly decreases from 0.205 mA cm⁻² to 0.17 mA cm⁻² over the course of the 2 h experiment. In contrast, no photocurrent degradation was observed for the ITO/Fe₂O₃/Fe₂TiO₅/FeNiOOH electrode during the stability test and it maintained a photocurrent of 2.2 mA cm⁻² throughout.

2.4 PEIS and OER mechanism investigations

All the above results illustrate that the incorporation of ITO, Fe₂TiO₅ and FeNiOOH largely improves the PEC performance

of the hematite nanowire photoanode. A physical model of the illuminated SEI for SS-mediated, indirect hole transfer has been well established and occurs in two consecutive steps: (i) hole trapping by SS, and (ii) hole transfer from SS to water molecules at the SEI.^{10,23,24} To gain further insight into the mechanism of this interfacial coupling effect, primary PEIS (Fig. S28 and S29, ESI†) has been employed to identify the functions of the ITO, Fe₂O₃, Fe₂TiO₅ and FeNiOOH in the integrated ITO/Fe₂O₃/Fe₂TiO₅/FeNiOOH electrodes. PEIS measurements were performed at potentials ranging from 0.65 V vs. RHE (before the onset of photocurrent) to 1.36 V vs. RHE (before the light-flux limited photocurrent region) because the effect of SS is more prevalent when unaffected by the light-flux limited and dark oxygen evolution factors.¹⁰ The obtained PEIS data was fitted based on the equivalent circuit displayed in Scheme S1A (ESI†).

Typically, the R_s , series resistance, includes the resistance at the interface between the FTO substrate, or ITO underlayer, and Fe₂O₃ nanowires.^{9,20} A substantial reduction in R_s is observed from ca. 70 Ω cm⁻² for the pristine Fe₂O₃ electrode to ca. 35 Ω cm⁻² for the composite Fe₂O₃ electrodes modified with the ITO underlayer, as displayed in Fig. 6A. These results mean that the ITO underlayer is able to efficiently improve the back electrical contact and facilitate the electron transport from Fe₂O₃ to the FTO substrate. This improvement is attributed to the enhanced Sn doping in hematite nanowires^{13,14} and the epitaxial relationship between the Fe₂O₃ and In₂O₃ phases, as demonstrated by the HRTEM and STEM-EELS map results. However, the capacitance associated with charge accumulation in the bulk (C_{bulk} , Fig. S30, ESI†) was measured to be on the same order of magnitude for these electrodes with the exception of an abrupt peak at ca. 0.9 V for the ITO/Fe₂O₃/Fe₂TiO₅, and

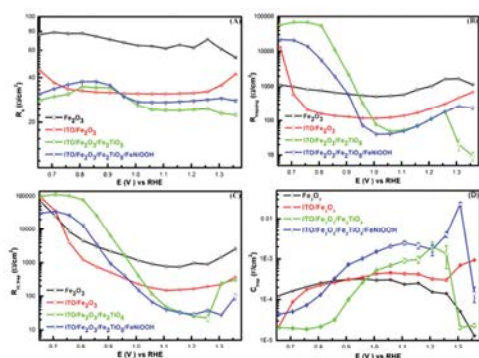


Fig. 6 Equivalent circuit parameters obtained from fitting IS data for the Fe₂O₃, ITO/Fe₂O₃, ITO/Fe₂O₃/Fe₂TiO₅, and ITO/Fe₂O₃/Fe₂TiO₅/FeNiOOH electrodes in contact with 1 M NaOH electrolytes under 1 Sun illumination. R_s (A), $R_{\text{ct,trap}}$ (B), $R_{\text{ct,trap}}$ (C) and C_{trap} (D) as a function of the applied potential. R_s , resistance associated with the electric contacts of the electrode, electrolyte, etc. R_{trapping} , resistance associated with charge trapping at surface states. $R_{\text{ct,trap}}$, resistance associated with the charge transfer process from surface states. C_{trap} , capacitance associated with charge accumulation on the surface states.

ITO/Fe₂O₃/Fe₂TiO₅/FeNiOOH electrodes. It may be due to the addition of the ultrathin Fe₂TiO₅ shell, which slightly changes the electronic state of the electrodes.³⁵ Fig. 6B shows the lowest value of R_{trapping} for the ITO/Fe₂O₃/Fe₂TiO₅/FeNiOOH electrode as compared to the Fe₂O₃, ITO/Fe₂O₃ and ITO/Fe₂O₃/Fe₂TiO₅ electrodes at the potential window (0.9 V to 1.36 V).¹⁰ This is consistent with the correlation of a dip in the $R_{\text{ct,trap}}$ and a peak in the C_{trap} profile resulting in more efficient charge transfer kinetics during PEC.⁵⁵ Work by Hamann and coworkers^{21,56,57} suggests that a large C_{trap} and a low $R_{\text{ct,trap}}$ would eventually render larger photocurrents, provided that the charge is transferred from the SS to the electrolyte. As shown in Fig. 6C, for each of these four electrodes, a gradual decrease in $R_{\text{ct,trap}}$ is observed as the applied potential increases implying a increment of the associated photocurrent response. Notably, the ITO/Fe₂O₃/Fe₂TiO₅/FeNiOOH photoanode possesses a relative minimum $R_{\text{ct,trap}}$ from 0.9 V to 1.25 V, in line with the larger photocurrent variation at this region dominated by SS (Fig. 5A). The $R_{\text{ct,trap}}$ at 1.25 V for the ITO/Fe₂O₃/Fe₂TiO₅/FeNiOOH photoanode is ca. 34 times lower than that of the pristine Fe₂O₃ nanowires, further evidencing its best photocurrent response. Meanwhile, the C_{bulk} (Fig. S30, ESI†) and C_{trap} (Fig. 6D) show opposite tendencies. With the potential increase, the C_{bulk} decreases, whereas the C_{trap} increases, implying a larger percentage of charge located on SS; similarly, a relative optimum value ($C_{\text{trap}}/C_{\text{bulk}}$ at 1.23 V. RHE) is observed in the ITO/Fe₂O₃/Fe₂TiO₅/FeNiOOH electrode. Fig. S31 and Table S1 (ESI†) reveal that the bulk donor density for the ITO/Fe₂O₃ electrode (2.75×10^{19} cm⁻³) is 6 times higher than that for the pristine Fe₂O₃ electrode (4.60×10^{18} cm⁻³). This effect is derived from the enhanced Sn doping in the hematite nanowires that results from the addition of the ITO underlayer (Fig. S13 and S14, ESI†) and is in good agreement with the significantly improved photocurrent response of the ITO/Fe₂O₃ electrode.^{13,14} With the coating of Fe₂TiO₅ onto the ITO/Fe₂O₃ electrode, the bulk donor density is further improved to 5.80×10^{19} cm⁻³, indicating that there may be a small amount of Ti doping in the Fe₂O₃ nanowires and thus additional photocurrent enhancement (1.56 mA cm⁻²) observed for the ITO/Fe₂O₃/Fe₂TiO₅ electrode.¹⁰

The general behaviour of the integrated multi-layer nanowires has been interpreted and phenomenologically correlated with the SS; a deeper investigation of the photo-induced processes (*i.e.* charge generation and the subsequent transport to and transfer from the interfaces) is required to elucidate the interfacial charge transfer mechanism. In order to highlight the role of SS in the interfacial charge transfer process, we calculated the values for their density of surface states (DOSS) from the C_{trap} using eqn (5):^{10,21}

$$N_{\text{SS}}(E) = C_{\text{trap}}(E)/q \quad (5)$$

where $N_{\text{SS}}(E)$ is the DOSS (cm⁻² eV⁻¹) as a function of applied potential and q is the electron charge (1.602×10^{-19} C). As shown in Fig. 7A, it is possible to observe the SS energy distribution located below the photocurrent onset with its Fermi level pinned at the SS.²¹

Our previous report¹⁰ demonstrated that there is a direct correlation between the percentage of available filled surface

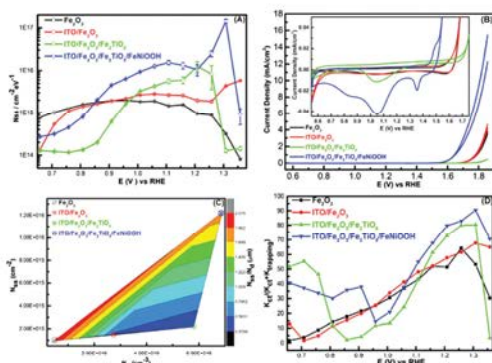


Fig. 7 (A) Density of surface states (DOSS) as a function of the applied potential on the Fe_2O_3 , ITO/ Fe_2O_3 , ITO/ $\text{Fe}_2\text{O}_3/\text{Fe}_2\text{TiO}_5$, and ITO/ $\text{Fe}_2\text{O}_3/\text{Fe}_2\text{TiO}_5/\text{FeNiOOH}$ electrodes. Error bars stem from the goodness of the EIS data fittings. (B) CV curves scanned in the dark at 20 mV s^{-1} immediately after holding the electrode potential at 1.85 V vs. RHE for 1 min under illumination of the Fe_2O_3 , ITO/ Fe_2O_3 , ITO/ $\text{Fe}_2\text{O}_3/\text{Fe}_2\text{TiO}_5$, and ITO/ $\text{Fe}_2\text{O}_3/\text{Fe}_2\text{TiO}_5/\text{FeNiOOH}$ electrodes. (The inset shows its magnified plot.) (C) Total surface state density (N_{SS}), donor density (N_{d}), and their ratio ($N_{\text{SS}}/N_{\text{d}}$) for the Fe_2O_3 , ITO/ Fe_2O_3 , ITO/ $\text{Fe}_2\text{O}_3/\text{Fe}_2\text{TiO}_5$, and ITO/ $\text{Fe}_2\text{O}_3/\text{Fe}_2\text{TiO}_5/\text{FeNiOOH}$ electrodes. N_{d} was estimated from the slopes of the Mott–Schottky plots in the dark (Fig. S31, ESI †), whereas N_{SS} was obtained from integration of the DOSS profiles (A). Colour bar with a unit of μm^2 is plotted on the right Y axis for $N_{\text{SS}}/N_{\text{d}}$. (D) Ratio of the charge transfer rate constant (k_{ct}) and the sum of k_{ct} and trapping rate constant (k_{trapping}) at different potentials, calculated with eqn (6).

states (larger DOSS) near the thermodynamic potential for the OER, and the observed photocurrent response at 1.23 V vs. RHE due to the required isoenergetic hole transfer process at the SEI.^{21,58} As displayed in Fig. 7A, the N_{SS} of the four photoanodes follows the order: $\text{Fe}_2\text{O}_3 < \text{ITO}/\text{Fe}_2\text{O}_3 < \text{ITO}/\text{Fe}_2\text{O}_3/\text{Fe}_2\text{TiO}_5 < \text{ITO}/\text{Fe}_2\text{O}_3/\text{Fe}_2\text{TiO}_5/\text{FeNiOOH}$ across the entire SS dominated region (0.9 V to 1.36 V). The extended SS distribution from 0.65 V to 1.36 V in Fe_2O_3 and ITO/ Fe_2O_3 electrodes probably spans inside the CB and triggers a deleterious Fermi level pinning at SS, which could be responsible for their relatively low photocurrent response. Moreover, the potential of the DOSS peak for the photoanodes shifts to more positive values, e.g., 0.9 V, 0.95 V, and 1.25 V for the Fe_2O_3 , ITO/ Fe_2O_3 , ITO/ $\text{Fe}_2\text{O}_3/\text{Fe}_2\text{TiO}_5$ electrodes, respectively. Interestingly, the DOSS curve for the ITO/ $\text{Fe}_2\text{O}_3/\text{Fe}_2\text{TiO}_5/\text{FeNiOOH}$ electrode displays two peaks located at ca. 1.1 V and 1.3 V. This peak splitting phenomenon displayed by the ITO/ $\text{Fe}_2\text{O}_3/\text{Fe}_2\text{TiO}_5/\text{FeNiOOH}$ photoanode was further investigated by obtaining the CV curves scanned in the cathodic direction in the dark at 20 mV s^{-1} of these electrodes immediately after holding the electrode potential at 1.85 V vs. RHE for 1 min under illumination to photoelectrochemically oxidize the surface states.^{26,29,59} As displayed in Fig. 7B, for the ITO/ $\text{Fe}_2\text{O}_3/\text{Fe}_2\text{TiO}_5/\text{FeNiOOH}$ electrode, two cathodic peaks appear at around 1.05 V and 1.35 V, which is relatively consistent with the DOSS peak positions for the ITO/ $\text{Fe}_2\text{O}_3/\text{Fe}_2\text{TiO}_5/\text{FeNiOOH}$ electrode. Besides, Hamann *et al.* quantitatively correlated the C_{trap} measured by both cyclic voltammetry and

impedance spectroscopy with the absorption peak at 572 nm *via* operando UV-vis experiments, corresponding to the formation of an Fe(IV) intermediate.²⁹ The splitting of one C_{trap} peak into two C_{trap} peaks was also observed upon coating an ultrathin ALD aluminium layer onto the hematite film, which is derived from the insufficient covering of the aluminium overlayer and partial exposure of the hematite film.²⁹ Moreover, Irie *et al.* investigated preliminary *in situ* UV-vis absorption spectra of FeNiOOH; and the incorporation of Fe into NiOOH was found to induce an increase in the absorption peak similar to that observed for the hematite electrode, demonstrating the formation of an Fe(IV) intermediate in the FeNiOOH during the electrochemical test.³⁰ In our case, the DOSS peak splitting performance of the ITO/ $\text{Fe}_2\text{O}_3/\text{Fe}_2\text{TiO}_5/\text{FeNiOOH}$ electrode can be attributed to the incomplete coverage of FeNiOOH nanodots on the nanowire surface in a manner consistent with the aluminium coated hematite reported by Hamann *et al.*²⁹ The peak located at 1.1 V vs. RHE likely arises from $\text{Fe}^{\text{IV}}=\text{O}$ surface intermediates on the partially exposed Fe_2TiO_5 coating,³¹ as the same DOSS peak is observed for the ITO/ $\text{Fe}_2\text{O}_3/\text{Fe}_2\text{TiO}_5$ electrode. The DOSS peak located at 1.3 V can then be assigned to the $\text{Fe}^{\text{IV}}=\text{O}$ intermediates localized on the discontinuously distributed FeNiOOH nanodots.³⁰ In brief, the atomic level of the Fe_2TiO_5 and FeNiOOH nanodot coatings can regulate the surface state density and energy level of the hematite nanowires, which is probably attributed to the chemical environment variation of $\text{Fe}^{\text{IV}}=\text{O}$ intermediates. After all, the identification of OER active sites in the integrated hematite photoanode⁶⁰ and further insights into the evolution of $\text{Fe}^{\text{IV}}=\text{O}$ intermediates in these electrodes will need *in situ* TEM experiments,⁶¹ which is beyond the scope of this work.

A combined comparison of the N_{SS} , N_{d} and $N_{\text{SS}}/N_{\text{d}}$ ratio is presented in Fig. 7C and Table S1 (ESI †). A large $N_{\text{SS}}/N_{\text{d}}$ ratio does not ensure good photoactivity because the number of donors in the hematite nanowires may not be high enough to endow the nanowires with good conductivity. This is demonstrated by the pristine Fe_2O_3 electrode which displays a high $N_{\text{SS}}/N_{\text{d}}$ ratio but poor PEC performance. In stark contrast, the ITO/ Fe_2O_3 and ITO/ $\text{Fe}_2\text{O}_3/\text{Fe}_2\text{TiO}_5$ electrodes display a relatively low $N_{\text{SS}}/N_{\text{d}}$ ratio, and possess enough donors in the nanowires to provide good conductivity, but a lack of surface reactive sites still limits the PEC performance of these electrodes. In the case of the ITO/ $\text{Fe}_2\text{O}_3/\text{Fe}_2\text{TiO}_5/\text{FeNiOOH}$ electrode, a relatively high $N_{\text{SS}}/N_{\text{d}}$ ratio corresponds to a scenario in which N_{SS} and N_{d} are both numerous enough to give a larger photocurrent response. In addition, the charge transfer efficiency at the SEI is estimated through (eqn (6)):^{10,20}

$$\text{Transfer efficiency (\%)} = \frac{k_{\text{ct}}}{k_{\text{ct}} + k_{\text{trapping}}} = \frac{R_{\text{trapping}}}{R_{\text{ct,trap}} + R_{\text{trapping}}} \quad (6)$$

where k_{ct} and k_{trapping} are the charge transfer and trapping rate constants, respectively. The charge transfer efficiency obtained from the PEIS data is shown in Fig. 7D. The abnormally high transfer efficiency (TE) in the low applied potential region (before the onset potential) might be due to deviations of the

charge transfer kinetic models at the region, where the effect of SS is less prevalent.^{10,62} In essence, although the application of the ITO underlayer provides an additional Sn doping amount, it does not affect the rate of surface electron-hole recombination at the Fe_2O_3 /electrolyte interface, evidenced by the same trend of TE values in the Fe_2O_3 and ITO/ Fe_2O_3 electrodes. In both cases, significant surface electron-hole recombination is expected. The surface surface electron-hole recombination in the ITO/ Fe_2O_3 / Fe_2TiO_5 and ITO/ Fe_2O_3 / Fe_2TiO_5 / FeNiOOH electrodes has been suppressed; and in the case of the ITO/ Fe_2O_3 / Fe_2TiO_5 / FeNiOOH electrode, over 80% of the holes are being transferred into the electrolyte at 1.23 V vs. RHE. The calculated TE values of these electrodes also agree well with the steady-state current-voltage relationship (Fig. 5A). Our result here highlights the effectiveness of the atomic level Fe_2TiO_5 and FeNiOOH nanodot coating on regulating the surface state density and energy level of hematite nanowires as well as reducing the surface electron-hole recombination rate to speed up the water oxidation rate.

3. Conclusions

In summary, an ITO/ Fe_2O_3 / Fe_2TiO_5 / FeNiOOH nanowire electrode with a quaternary multilayer heterostructure has been successfully integrated by stepwise deposition of an ITO underlayer, ultrathin Fe_2TiO_5 and FeNiOOH nanodots onto Fe_2O_3 nanowires. The resulting quaternary multilayer nanowires exhibit significantly enhanced PEC performance, including a large photocurrent (2.2 mA cm^{-2}) and a high stability. A deep and careful investigation into the mechanism responsible for the enhanced PEC performance has been conducted. These studies show that: (i) the ITO underlayer is used as a high quality electrical back contact to reduce the back-contact interface charge recombination and as a Sn doping source for tuning the donor density, (ii) the atomic level Fe_2TiO_5 coating serves as the surface state density and energy level modulation layer, and effectively suppresses the charge recombination at the semiconductor junction interface, and (iii) the FeNiOOH nanodots increase the surface active sites, and thus accelerate the OER kinetics at the SEL. The interfacial coupling effect between the ITO underlayer, the ultrathin Fe_2TiO_5 and the FeNiOOH nanodots in the ITO/ Fe_2O_3 / Fe_2TiO_5 / FeNiOOH photoanodes simultaneously enhances the charge separation and water oxidation efficiency, and suggests a path forward to design improved integrated photoanodes.

4. Experimental

4.1 Chemicals and materials

All commercially available reagents and solvents were used as received without further purification unless otherwise indicated. All chemical reagents were purchased from Sigma-Aldrich. If not specified, all solutions were prepared with Milli-Q water (*ca.* $18.2 \text{ M}\Omega \text{ cm}$ resistivity). The fluorine-tin-oxide (FTO) coated glass substrate (735167-1EA, $7 \Omega \text{ sq}^{-1}$) was purchased from Sigma-Aldrich.

4.2 Electrode preparation

FTO substrates were cut into small pieces with $1 \text{ cm} \times 3 \text{ cm}$ area and washed by sonicating in a (1 : 1 : 1) mixture of acetone (Sigma-Aldrich, 99.9%), isopropanol (Sigma-Aldrich, 99.9%) and water. After rinsing the FTO substrates thoroughly with distilled water, the substrates were washed in ethanol (Fluka, 99.8%) and then dried in air at $300 \text{ }^\circ\text{C}$ for 1 h (heating rate: $8.5 \text{ }^\circ\text{C min}^{-1}$). A part of the substrates (*ca.* $1 \text{ cm} \times 2 \text{ cm}$) was covered using a polymer tape (Kaptons[®] Foil, VWR International) prior to the following process. The uncoated part of the FTO was later employed as the electric contact for the electrodes in the photo-electrochemical cell.

Fe_2O_3 electrodes. Hematite nanowires were prepared following a slightly adapted procedure.⁴⁷ A 200 ml Teflon-lined stainless steel autoclave was filled with 60 ml of an aqueous solution containing 0.15 M ferric chloride (FeCl_3 , 97%) and 1 M sodium nitrate (NaNO_3 , 99%) and 316 μl hydrochloric (HCl , wt 37%). Six pieces of washed FTO substrate were put into the autoclave and heated at $95 \text{ }^\circ\text{C}$ for 4 hours. A uniform layer of iron oxyhydroxide (FeOOH) nanowires was formed on the FTO substrate, as displayed in Fig. S32 (ESI[†]). The FeOOH -coated substrate was then washed with deionized water to remove any residual salt, and subsequently sintered in air at $550 \text{ }^\circ\text{C}$ (heating rate: $8.5 \text{ }^\circ\text{C min}^{-1}$) for 2 hours. During this pre-sintering process, the FeOOH nanowires were converted into hematite nanowires without deterioration of the nanowire structure, as shown Fig. S33 (ESI[†]). To further reduce the surface defective sites, the hematite nanowires were treated at $750 \text{ }^\circ\text{C}$ for an additional 30 min and subsequently quenched in air within 1 min (post-quenching process).

ITO/ Fe_2O_3 electrodes. Different thicknesses (49 nm, 105 nm, 149 nm, 196 nm and 245 nm) of indium doped tin dioxide (ITO, $\text{In}_2\text{O}_3 : \text{SnO}_2 = 90/10 \text{ wt}\%$) were deposited onto the FTO substrate by DC-pulsed sputtering according to our previous report.⁶³ After that, the ITO coated FTO substrates were subjected to the same hydrothermal and pre-sintering process for Fe_2O_3 electrode as described above to grow hematite nanowires on the surface of the ITO/FTO substrates. For the post-quenching process of ITO/ Fe_2O_3 , a quenching condition at $750 \text{ }^\circ\text{C}$ for 30 min has been employed.

ITO/ Fe_2O_3 / Fe_2TiO_5 electrodes. The obtained ITO/ Fe_2O_3 samples after the pre-sintering process were further subjected to a TiO_2 atomic layer deposition (ALD) process.⁶⁴ The ALD was performed in an R200 Picosun Atomic Layer Deposition system at $150 \text{ }^\circ\text{C}$ with TiCl_4 (Sigma-Aldrich, 99%) and water as the precursors in an 8 mbar N_2 flow atmosphere, reaching a growth rate of $0.27 \text{ \AA cycle}^{-1}$. The typical pulse time for the TiCl_4 and water was 0.1 s and the purge time was 10 s. The TiO_2 thickness of the ITO/ Fe_2O_3 / Fe_2TiO_5 electrode was controlled by changing the number of deposition cycles, *i.e.*, 15 cycles, 30 cycles, 50 cycles, 100 cycles and 150 cycles. After that, a varying quenching time slot (10 min, 30 min, 40 min and 80 min) at $750 \text{ }^\circ\text{C}$ has been tuned to optimize the sintering conditions and transform the ALD TiO_2 into Fe_2TiO_5 .

ITO/ Fe_2O_3 / Fe_2TiO_5 / FeNiOOH electrodes. The optimized ITO/ Fe_2O_3 / Fe_2TiO_5 electrodes were further coated with FeNiOOH *via* photo-electrodeposition.^{18,39,41,54} Photo-electrodeposition of

FeNiOOH on the ITO/Fe₂O₃/Fe₂TiO₃ electrodes was carried out in a mixture solution containing 0.01 M FeSO₄·7H₂O (≥99%) and 0.1 M NiSO₄·6H₂O (99%). Prior to the photo-electrodeposition of FeNiOOH, the solution was purged with nitrogen gas for 30 min. A three-electrode cell was used, composed of an ITO/Fe₂O₃/Fe₂TiO₃ electrode (work electrode), Pt wire (counter electrode), and Ag/AgCl (3 M KCl, reference electrode). A 150 W AM 1.5G solar simulator (Solar Light Co., 16S-300-002 v4.0) with an incident light intensity set at 1 Sun (100 mW cm⁻²) was used as the light source, and the light density was calibrated using a thermopile (Gentec-EO, XLPF12-3S-H2-DO) coupled with an optical power meter (Gentec-EO UNO). The light was illuminated through the glass side (back-side illumination) and the light intensity was 100 mW cm⁻². For clarification, the FeOOH grown on the back side of the FTO glass during the hydrothermal process has been carefully removed for all samples by lens wiping paper before the sintering treatment. To facilitate the photoelectrodeposition, an external bias of ca. 0.25 V vs. Ag/AgCl (3 M KCl) was applied. During illumination, the holes generated in the valence band of Fe₂O₃ were used to oxidize Fe²⁺/Ni²⁺ ions to Fe³⁺/Ni³⁺ ions, which precipitate as FeNiOOH on the surface of the ITO/Fe₂O₃/Fe₂TiO₃ electrode (Fe²⁺/Ni²⁺(aq) + h⁺ + 3OH⁻ → FeNiOOH(s) + H₂O).^{18,54} Various deposition charges (*i.e.*, 5 mC, 10 mC, 15 mC and 20 mC) were deposited onto the surface of the ITO/Fe₂O₃/Fe₂TiO₃ nanowires by controlling the deposition time. The fabrication process of the ITO/Fe₂O₃/Fe₂TiO₃/FeNiOOH electrode is displayed in Fig. 2 (top).

4.3 Optical, structural and morphological characterization

The grazing incidence X-ray diffraction (XRD) analyses were performed on a Bruker D4 X-ray powder diffractometer using Cu K α radiation (1.54184 Å) and a 1D Lynkey detector, which is equipped with a Gobel mirror in the incident beam and equatorial Soller slits in the diffracted beam (51 incidence angle, 2° step⁻¹). Optical properties of all electrodes were characterized by using a UV-vis spectrophotometer (Lambda 950, Perkin Elmer) equipped with an integrating sphere (150 mm diameter sphere covered with Spectralon as the reflecting material, Perkin Elmer). Absorbance (*A*) measurements were obtained from measured reflectance (*R*, %) and transmission (*T*, %), using a wavelength range of 350 to 800 nm and a step of 5 nm, respectively. The morphology of the films was characterized using a field emission gun scanning electron microscope (FE-SEM, Zeiss Series Auriga microscope) equipped with an electron dispersive X-ray spectroscopy (EDX) detector. X-ray photoelectron spectroscopy (XPS) was performed with a Phoibos 150 analyser (SPECS GmbH, Berlin, Germany) in ultra-high vacuum conditions (base pressure 4 × 10⁻¹⁰ mbar) with a monochromatic aluminium K α X-ray source (1486.74 eV). The energy resolution as measured by the FWHM of the Ag 3d_{5/2} peak for a sputtered silver foil was 0.8 eV. All the samples for HRTEM and STEM were prepared by using a mechanical process, as displayed in Scheme S2 (ESI[†]) and published elsewhere.⁶⁵ HRTEM and STEM images have been obtained by using a FEI Tecnai F20 field emission gun microscope with a 0.19 nm point-to-point resolution at 200 kV equipped with an embedded Quantum Gatan Image Filter for

EELS analyses. Images have been analysed by means of Gatan Digital Micrograph software. Atomic supercell modelling was performed by the Eje-Z, Rhodius and JMOL software packages with the corresponding crystal phase parameters of each species obtained from ICSD, which were verified by HRTEM and STEM-EELS mapping.⁶⁵⁻⁶⁸

4.4 Photo-electrochemical measurements

Photocurrent (*j*, mA cm⁻²) vs. potential (*E*, V) curves were taken using an undivided three-electrode cell. The working, counter and reference electrodes were the aforementioned composite hematite nanowires (1 cm² geometric area), a Pt wire and an Ag/AgCl (3 M KCl) electrode (Metrohm, *E* = 0.203 vs. NHE), respectively. The electrolyte was a 1 M NaOH solution (pH 13.6). The electrolyte was purged with N₂ during the experiments. CV was taken using a computer-controlled potentiostat (VMP3, BioLogic Science Instruments). The potential was scanned from -0.45 V vs. Ag/AgCl to 0.85 V vs. Ag/AgCl, with a scan rate of 20 mV s⁻¹. The photocurrent density is referenced to the geometric area. All potentials were corrected at 80% for the ohmic drop, which was determined using the automatic current interrupt (CI) method implemented by the potentiostat,¹⁵ and are converted and reported with respect to the reversible hydrogen electrode (RHE): *E* (V vs. RHE) = *E* (V vs. Ag/AgCl) + 0.0592 × pH + 0.203. Light illumination was performed using a 150 W AM 1.5G solar simulator (Solar Light Co., 16S-300-002 v 4.0) with an incident light intensity set at 1 Sun (100 mW cm⁻²), as measured using a thermopile (Gentec-EO, XLPF12-3S-H2-DO) coupled with an optical power meter (Gentec-EO UNO). In the PEC characterization, the light came from the front side (electrode-electrolyte interface, front side illumination). PEIS data were acquired with an alternate current (AC) perturbation of 5 mV in amplitude and a 100 mHz to 1 MHz frequency range, both in the dark and under illumination, and under selected direct current (DC) potentiostatic conditions (-0.45 V vs. Ag/AgCl). Nyquist plots (imaginary vs. real components of impedance, *Z*_{Im} vs. *Z*_{Re}) were fitted to the corresponding equivalent circuits using Z-fit (BioLogic Associates). Fitted capacitances and resistances are referred to the electrode geometric area (1 cm × 1 cm). Error bars stem from the goodness of the EIS data fittings.

4.5 Incident photon to current efficiency (IPCE)

IPCE was characterized using a xenon light source (Abet 150 W Xenon Lamp) coupled with a monochromator (Oriol Cornerstone 260 1/4 m monochromator). The wavelength was scanned from 350 to 800 nm (step: 10 nm step⁻¹) keeping the voltage fixed at 1.23 V vs. RHE. To calculate IPCE, the following relation was used:⁵⁵

$$\text{IPCE (\%)} = (1240/\lambda) \times (j/j_{\text{light}}) \times 100 \quad (7)$$

where *I* is the photocurrent density (mA cm⁻²) obtained using a potentiostat (mentioned earlier) recording the *i*-*t* curve at 1.23 V vs. RHE, λ is the incident light wavelength (nm) from monochromatic light, and *j*_{light} (mW cm⁻²) is the power density of monochromatic light at a specific wavelength. A source

Paper

Energy & Environmental Science

meter (Keithley Instruments Inc., model no. 2400) coupled with the standard Silicon Photodiode (Thorlabs, S120VC) was used to measure the power density of monochromatic light.

Author contribution

PengYi Tang, Jordi Arbiol and Joan Ramon Morante designed the experiments. PengYi Tang carried out the XRD, UV-Vis spectra, SEM, EDS, TEM, STEM-EELS maps, atomic supercell models, hydrothermal reaction, sintering process, photo-electrodeposition, and electrochemical experiments. HaiBing Xie, Alejandro Pérez Rodríguez and Edgardo Saucedo carried out the ITO sputtering experiments. Carles Ros, Martí Biset-Peiró and Teresa Andreu carried the ALD TiO₂ deposition experiments. Lijuan Han and José Ramón Galán-Mascarós participated in part of the PEIS experiments and PEIS data analysis. Guillaume Sauthier carried out the XPS spectrum experiments. PengYi Tang, Jordi Arbiol, YongMin He, Wesley Kramer and Joan Ramon Morante co-wrote the manuscript and all authors edited the manuscript.

Acknowledgements

This work was supported by the Spanish Ministerio de Economía y Competitividad (MINECO, grant CTQ2015-71287-R) through coordinated Projects TNT-FUELS, e-TNT (MAT2014-59961-C2), WINCOST ENE2016-80788-C5, the BIST Ignite Project inWOC and the Generalitat de Catalunya (2014-SGR-797 and 2014-SGR-1638). Part of the present work was performed in the framework of Universitat Autònoma de Barcelona Materials Science PhD program. We acknowledge Dr Guillaume Sauthier from the ICN2 for the XPS measurements. ICN2 and ICIQ acknowledge support from the Severo Ochoa Program (MINECO, Grant SEV-2013-0295 and SEV-2013-0319). ICN2 and ICIQ are funded by the CERCA Programme/Generalitat de Catalunya.

References

- 1 K. Sivula and R. V. D. Krol, *Nat. Rev. Mater.*, 2016, **1**, 15010.
- 2 S. H. Shen, S. A. Lindley, X. Y. Chen and J. Z. Zhang, *Energy Environ. Sci.*, 2016, **9**, 2744–2775.
- 3 Z. Q. Huang, Y. J. Lin, X. Xiang, W. Rodríguez-Córdoba, K. J. McDonald, K. S. Hagen, K. S. Choi, B. S. Brunshwig, D. G. Musaev, C. L. Hill, D. W. Wang and T. Q. Lian, *Energy Environ. Sci.*, 2012, **5**, 8923–8926.
- 4 S. R. Pendlebury, A. J. Cowan, M. Barroso, K. Sivula, J. H. Ye, M. Grätzel, D. R. Klug, J. W. Tang and J. R. Durrant, *Energy Environ. Sci.*, 2012, **5**, 6304–6312.
- 5 T. A. Pham, Y. Ping and G. Galli, *Nat. Mater.*, 2017, **16**, 401–408.
- 6 J. T. Li, S. K. Cushing, P. Zheng, F. K. Meng, D. Chu and N. Q. Wu, *Nat. Commun.*, 2013, **4**, 2651.
- 7 M. E. McBriarty, G. F. V. Rudorff, J. E. Stubbs, P. J. Eng, J. Blumberger and K. M. Rosso, *J. Am. Chem. Soc.*, 2017, **139**, 2581–2584.
- 8 B. Iandolo, B. Wickman, E. Svensson, D. Paulsson and A. Hellman, *Nano Lett.*, 2016, **16**, 2381–2386.
- 9 Y. C. Qiu, S. F. Leung, Q. P. Zhang, B. Hua, Q. F. Lin, Z. H. Wei, K. H. Tsui, G. Zhang, S. H. Yang and Z. Y. Fan, *Nano Lett.*, 2014, **14**, 2123–2129.
- 10 D. M. Satoca, M. Bartsch, C. Fabrega, A. Gen, S. Reinhard, T. Andreu, J. Arbiol, M. Niederberger and J. R. Morante, *Energy Environ. Sci.*, 2015, **8**, 3242–3254.
- 11 Y. J. Lin, S. Zhou, S. W. Sheehan and D. W. Wang, *J. Am. Chem. Soc.*, 2011, **133**, 2398–2401.
- 12 I. S. Cho, H. S. Han, M. Logar, J. Park and X. L. Zheng, *Adv. Energy Mater.*, 2015, 1501840.
- 13 A. Annamalai, A. Subramanian, U. Kang, H. Park, S. H. Choi and J. S. Jang, *J. Phys. Chem. C*, 2015, **119**, 3810–3817.
- 14 P. S. Shinde, A. Annamalai, J. H. Kim, S. H. Choi, J. S. Lee and J. S. Jang, *Sol. Energy Mater. Sol. Cells*, 2015, **141**, 71–79.
- 15 L. J. Han, P. Y. Tang, A. Reyes-Carmona, B. Rodríguez-García, M. Torrents, J. R. Morante, J. Arbiol and J. R. Galán-Mascarós, *J. Am. Chem. Soc.*, 2016, **138**, 16037–16045.
- 16 F. Song and X. Hu, *Nat. Commun.*, 2014, **5**, 4477.
- 17 Y. Zhao, X. Jia, G. Chen, L. Shang, G. I. Waterhouse, L. Z. Wu, C. H. Tung, D. O'Hare and T. Zhang, *J. Am. Chem. Soc.*, 2016, **138**, 6517–6524.
- 18 T. W. Kim and K. S. Choi, *Science*, 2014, **343**, 990–994.
- 19 L. Wang, F. Dionigi, N. T. Nguyen, R. Kirchgeorg, M. Gliech, S. Grigorescu, P. Strasser and P. Schmuki, *Chem. Mater.*, 2015, **27**, 2360–2366.
- 20 K. G. U. Wijayantha, S. Saremi-Yarahmadi and L. M. Peter, *Phys. Chem. Chem. Phys.*, 2011, **13**, 5264–5270.
- 21 B. Klahr, S. Gimenez, F. Fabregat-Santiago, T. W. Hamann and J. Bisquert, *J. Am. Chem. Soc.*, 2012, **134**, 4294–4302.
- 22 Y. C. Zhang, H. N. Zhang, H. W. Ji, W. H. Ma, C. C. Chen and J. C. Zhao, *J. Am. Chem. Soc.*, 2016, **138**, 2705–2711.
- 23 Y. D. Su, C. L. Liu, S. Brittan, J. Y. Tang, A. Fu, N. Kornienko, Q. Kong and P. D. Yang, *Nat. Nanostruct.*, 2016, **11**, 609–612.
- 24 J. B. Sambur, T. Y. Chen, E. Choudhary, G. Q. Chen, E. J. Nissen, E. M. Thomas, N. M. Zou and P. Chen, *Nature*, 2016, **530**, 77–80.
- 25 S. C. Warreni, K. Voitchovsky, H. Dotan, C. M. Leroy, M. Cornuz, F. Stellacci, C. Hébert, A. Rothschild and M. Grätzel, *Nat. Mater.*, 2013, **12**, 842–849.
- 26 O. Zandi and T. W. Hamann, *Nat. Chem.*, 2016, **8**, 778–783.
- 27 Z. Zhang and J. T. Yates Jr, *Chem. Rev.*, 2012, **112**, 5520–5551.
- 28 B. Iandolo and A. Hellman, *Angew. Chem.*, 2014, **53**, 13404–13408.
- 29 B. Klahr and T. Hamann, *J. Phys. Chem. C*, 2014, **118**, 10393–10399.
- 30 T. Takashima, K. Ishikawa and H. Irie, *J. Phys. Chem. C*, 2016, **120**, 24827–24834.
- 31 Q. H. Liu, J. F. He, T. Yao, Z. H. Sun, W. R. Cheng, S. He, Y. Xie, Y. H. Peng, H. Cheng, Y. F. Sun, Y. Jiang, F. C. Hu, Z. Xie, W. S. Yan, Z. Y. Pan, Z. Y. Wu and S. Q. Wei, *Nat. Commun.*, 2014, **5**, 5122.
- 32 M. R. Nellist, F. A. L. Laskowski, F. D. Lin, T. J. Mills and S. W. Boettcher, *Acc. Chem. Res.*, 2016, **49**, 733–740.
- 33 Z. M. Zhang, C. T. Gao, Y. X. Li, W. H. Han, W. B. Fu, Y. M. He and E. Q. Xie, *Nano Energy*, 2016, **30**, 892–899.

- 34 J. Resasco, H. Zhang, N. Kornienko, N. Becknell, H. Lee, J. H. Guo, A. L. Briseno and P. D. Yang, *ACS Cent. Sci.*, 2016, **2**, 80–88.
- 35 T. T. Yao, R. T. Chen, J. J. Li, J. F. Han, W. Qin, H. Wang, J. Y. Shi, F. T. Fan and C. Li, *J. Am. Chem. Soc.*, 2016, **138**, 13664–13672.
- 36 I. Roger, M. A. Shipman and M. D. Symes, *Nat. Rev. Chem.*, 2017, **1**, 3.
- 37 J. C. Hill, A. T. Landers and J. A. Switzer, *Nat. Mater.*, 2015, **14**, 1150–1155.
- 38 F. D. Lin and S. W. Boettcher, *Nat. Mater.*, 2014, **13**, 81–86.
- 39 M. W. Louie and A. T. Bell, *J. Am. Chem. Soc.*, 2013, **135**, 12329–12337.
- 40 D. Friebel, M. W. Louie, M. Bajdich, K. E. Sanwald, Y. Cai, A. M. Wise, M. J. Cheng, D. Sokaras, T. C. Weng, R. Alonso-Mori, R. C. Davis, J. R. Bargar, J. K. Nørskov, A. Nilsson and A. T. Bell, *J. Am. Chem. Soc.*, 2015, **137**, 1305–1313.
- 41 L. Trotochaud, S. L. Young, J. K. Ranney and S. W. Boettcher, *J. Am. Chem. Soc.*, 2014, **136**, 6744–6753.
- 42 H. S. Ahn and A. J. Bard, *J. Am. Chem. Soc.*, 2016, **138**, 313–318.
- 43 P. Y. Tang, L. J. Han, A. Gen, Y. M. He, X. Zhang, L. Zhang, J. R. Galán-Mascarós, J. R. Morante and J. Arbiol, *Nano Energy*, 2016, **22**, 189–201.
- 44 F. Y. Ning, M. F. Shao, S. M. Xu, Y. Fu, R. K. Zhang, M. Wei, D. G. Evans and X. Duan, *Energy Environ. Sci.*, 2016, **9**, 2633–2643.
- 45 Z. M. Zhang, C. T. Gao, Z. M. Wu, W. H. Han, Y. L. Wang, W. B. Fu, X. D. Li and E. Q. Xie, *Nano Energy*, 2016, **19**, 318–327.
- 46 A. Brauna, Y. L. Hu, F. Boudoieira, D. K. Boraa, D. D. Sarmad, M. Grätzel and C. M. Eggleston, *Catal. Today*, 2016, **260**, 72–81.
- 47 Y. C. Ling, G. M. Wang, D. A. Wheeler, J. Z. Zhang and Y. Li, *Nano Lett.*, 2011, **11**, 2119–2125.
- 48 J. Brilllet, M. Gratzel and K. Sivula, *Nano Lett.*, 2010, **10**, 4155–4160.
- 49 J. Y. C. Chen, L. N. Dang, H. F. Liang, W. L. Bi, J. B. Gerken, S. Jin, E. E. Alp and S. S. Stahl, *J. Am. Chem. Soc.*, 2015, **137**, 15090–15093.
- 50 M. Görlin, P. Chernev, J. F. d. Araújo, T. Reier, S. Drespe, B. Paul, R. Krähnert, H. Dau and P. Strasser, *J. Am. Chem. Soc.*, 2016, **138**, 5603–5614.
- 51 X. W. Yu, M. Zhang, W. J. Yuan and G. Q. Shi, *J. Mater. Chem. A*, 2015, **3**, 6921–6928.
- 52 J. J. Deng, X. X. Lv, H. Zhang, B. H. Zhao, X. H. Sun and J. Zhong, *Phys. Chem. Chem. Phys.*, 2016, **18**, 10453–10458.
- 53 J. J. Deng, X. X. Lv, K. Q. Nie, X. L. Lv, X. H. Sun and J. Zhong, *ACS Catal.*, 2017, **7**, 4062–4069.
- 54 K. J. McDonald and K. S. Choi, *Energy Environ. Sci.*, 2012, **5**, 8553–8557.
- 55 P. S. Bassi, R. P. Antony, P. P. Boix, Y. N. Fang, J. Barber and L. H. Wong, *Nano Energy*, 2016, **22**, 310–318.
- 56 B. Klahr, S. Gimenez, F. Fabregat-Santiago, J. Bisquert and T. W. Hamann, *J. Am. Chem. Soc.*, 2012, **134**, 16693–16700.
- 57 B. Klahr, S. Gimenez, F. Fabregat-Santiago, J. Bisquert and T. W. Hamann, *Energy Environ. Sci.*, 2012, **5**, 7626–7636.
- 58 T. L. Villarreal, R. Gomez, M. Neumann-Spallart, N. Alonso-Vante and P. Salvador, *J. Phys. Chem. B*, 2004, **108**, 15172–15181.
- 59 O. Zandi and T. W. Hamann, *J. Phys. Chem. Lett.*, 2014, **5**, 1522–1526.
- 60 Z. X. Su, J. S. Baskin, W. Z. Zhou, J. M. Thomas and A. H. Zewail, *J. Am. Chem. Soc.*, 2017, **139**, 4916–4922.
- 61 B. H. Han, K. A. Stoerzinger, V. Tileli, A. D. Gamalski, E. A. Stach and S. H. Yang, *Nat. Mater.*, 2017, **16**, 121–126.
- 62 W. Li, D. He, S. W. Sheehan, Y. M. He, J. E. Thorne, X. H. Yao, G. W. Brudvig and D. W. Wang, *Energy Environ. Sci.*, 2016, **9**, 1794–1802.
- 63 M. Neuschitzer, Y. Sanchez, T. Olar, T. Thersleff, S. Lopez-Marino, F. Oliva, M. Espindola-Rodriguez, H. B. Xie, M. Placidi, V. Izquierdo-Roca, I. Lauerman, K. Leifer, A. Perez-Rodriguez and E. Saucedo, *Chem. Mater.*, 2015, **27**, 5279–5287.
- 64 C. Ros, T. Andreu, M. D. Hernández-Alonso, G. Penelas-Pérez, J. Arbiol and J. R. Morante, *ACS Appl. Mater. Interfaces*, 2017, **9**, 17932–17941.
- 65 M. D. L. Mata, R. Leturcq, S. R. Plissard, C. Rolland, C. Magen, J. Arbiol and P. Caroff, *Nano Lett.*, 2016, **16**, 825–833.
- 66 S. Bernal, F. J. Botana, J. J. Calvino, C. Lopez-Cartes, J. A. Perez-Omil and J. M. Rodriguez-Izquierdo, *Ultramicroscopy*, 1998, **72**, 135–164.
- 67 R. R. Zamani, M. Ibanez, M. Luysberg, N. Garcia-Castello, L. Houben, J. D. Prades, V. Grillo, R. E. Dunin-Borkowski, J. R. Morante, A. Cabot and J. Arbiol, *ACS Nano*, 2014, **8**, 2290–2301.
- 68 J. Arbiol, A. Cirera, F. Peiró, A. Cornet, J. R. Morante, J. J. Delgado and J. J. Calvino, *Appl. Phys. Lett.*, 2002, **80**, 329–331.

Electronic Supplementary Material (ESI) for Energy & Environmental Science.
This journal is © The Royal Society of Chemistry 2017

Electronic Supplementary Information

Enhanced Photoelectrochemical Water Splitting of Hematite Multilayer Nanowires Photoanode with Tuning Surface State via Bottom-up Interfacial Engineering

PengYi Tang,^{a,b} HaiBing Xie,^a Carles Ros,^a LiJuan Han,^c Martí Biset-Peiró,^a YongMin He,^d Wesley Kramer,^e Alejandro Pérez Rodríguez,^a Edgardo Saucedo,^a José Ramón Galán-Mascarós,^{c,f} Teresa Andreu,^a Joan Ramon Morante,^a Jordi Arbiol^{b,f,*}

^a Catalonia Institute for Energy Research (IREC), Jardins de les Dones de Negre 1, Sant Adrià del Besòs, Barcelona 08930, Catalonia, Spain.

^b Catalan Institute of Nanoscience and Nanotechnology (ICN2), CSIC and The Barcelona Institute of Science and Technology (BIST), Campus UAB, Bellaterra, 08193 Barcelona, Catalonia, Spain.

^c Institute of Chemical Research of Catalonia (ICIQ), The Barcelona Institute of Science and Technology (BIST), Avinguda Paisos Catalans 16, Tarragona 43007, Catalonia, Spain.

^d School of Physical Science and Technology, Lanzhou University, Lanzhou 730000, China.

^e Beckman Institute and Division of Chemistry and Chemical Engineering, California Institute of Technology, 1200 East California Boulevard, Pasadena, California 91125, United States.

^f ICREA, Pg. Lluís Companys 23, 08010 Barcelona, Catalonia, Spain.

*Emails: arbiol@icrea.cat

CONTENTS

Figure S1. High resolution XPS spectra of C 1s, Sn 3d and In 3d of Fe ₂ O ₃ , ITO/Fe ₂ O ₃ , ITO/Fe ₂ O ₃ /Fe ₂ TiO ₅ , and ITO/Fe ₂ O ₃ /Fe ₂ TiO ₅ /FeNiOOH electrodes.....	(4)
Figures S2. (A): Grazing incidence XRD patterns of Fe ₂ O ₃ , ITO/Fe ₂ O ₃ , ITO/Fe ₂ O ₃ /Fe ₂ TiO ₅ , and ITO/Fe ₂ O ₃ /Fe ₂ TiO ₅ /FeNiOOH electrodes. (B): Absorbance of Fe ₂ O ₃ , ITO/Fe ₂ O ₃ , ITO/Fe ₂ O ₃ /Fe ₂ TiO ₅ , and ITO/Fe ₂ O ₃ /Fe ₂ TiO ₅ /FeNiOOH electrodes.....	(5)
Figure S3. EDS obtained on Fe ₂ O ₃ , ITO/Fe ₂ O ₃ , ITO/Fe ₂ O ₃ /Fe ₂ TiO ₅ , and ITO/Fe ₂ O ₃ /Fe ₂ TiO ₅ /FeNiOOHelectrodes.....	(6)
Figure S4. 1*1*1 unit crystal model of hematite, In ₂ O ₃ , Fe ₂ TiO ₅ and FeNiOOH create based on the crystal data in ICSD and reported data for the identification of the phase.....	(7)
Figure S5. Low magnification TEM images of Fe ₂ O ₃ electrode.....	(8)
Figure S6-S7. TEM images of ITO/Fe ₂ O ₃ electrode.	(9-10)
Figure S8-S9. TEM images of ITO/Fe ₂ O ₃ /Fe ₂ TiO ₅ electrode.	(11)
Figure S10. TEM images of ITO/Fe ₂ O ₃ /Fe ₂ TiO ₅ /FeNiOOH electrode.....	(12)
Figure S11-S12. STEM-EELS chemical composition maps of Fe ₂ O ₃ electrode.....	(13-14)
Figure S13-S14. STEM-EELS chemical composition maps of the ITO/Fe ₂ O ₃ electrode.....	(15)
Figure S15-S16. STEM-EELS chemical composition maps of the ITO/Fe ₂ O ₃ /Fe ₂ TiO ₅ electrode.(16)	(16)
Figure S17. STEM-EELS chemical composition maps of the ITO/Fe ₂ O ₃ /Fe ₂ TiO ₅ /FeNiOOH electrode.....	(17)
Figure S18. SEM images of the pristine FTO substrate, ITO-105 nm, ITO-245 nm, ITO-105 nm-Fe ₂ O ₃ and ITO-245 nm-Fe ₂ O ₃ electrodes.....	(18)
Figure S19. Top: the atomic model for optimized ITO/Fe ₂ O ₃ electrodes. Bottom: Left: CV curves of the ITO/Fe ₂ O ₃ electrodes with different ITO thickness sintering on 750 °C for 30min under illumination; Right: the photocurrent density at 1.23 V vs. RHE related to the ITO thickness.	(19)
Figure S20. SEM images of the ITO/Fe ₂ O ₃ /Fe ₂ TiO ₅ electrodes with different ALD cycles (TiO ₂ thickness), e.g. 15 cycles, 30 cycles, 50 cycles, 100 cycles and 150 cycles.....	(20)
Figure S21. Top: the atomic model for optimized ITO/Fe ₂ O ₃ /Fe ₂ TiO ₅ electrodes. Bottom: Left: CV curves of the ITO/Fe ₂ O ₃ /Fe ₂ TiO ₅ electrodes with different ALD TiO ₂ cycles (thickness) sintering on 750 °C for 30 min under illumination; Right: the photocurrent density at 1.23 V vs. RHE related to the ALD TiO ₂ cycles.....	(21)
Figure S22. SEM images of the ITO/Fe ₂ O ₃ /Fe ₂ TiO ₅ -30 cycles electrodes with different sintering time at 750°C, e.g. 10 min, 30 min, 40 min and 80 min.....	(22)
Figure S23. Top: the atomic model for optimized ITO/Fe ₂ O ₃ /Fe ₂ TiO ₅ electrodes. Bottom: Left: CV curves of the ITO/Fe ₂ O ₃ /Fe ₂ TiO ₅ -30 cycles electrodes with different sintering time on 750 °C under illumination; Right: the photocurrent density at 1.23 V vs. RHE related to the sintering time.....	(23)
Figure S24. SEM images of the ITO/Fe ₂ O ₃ /Fe ₂ TiO ₅ /FeNiOOH electrodes with different FeNiOOH deposition charge.....	(24)
Figure S25. Top: the atomic model for optimized ITO/Fe ₂ O ₃ /Fe ₂ TiO ₅ /FeNiOOH electrode. Bottom: Left: CV curves of the ITO/Fe ₂ O ₃ /Fe ₂ TiO ₅ /FeNiOOH electrodes with different FeNiOOH deposition charge under illumination; Right: the photocurrent density at 1.23 V vs. RHE related to the FeNiOOH deposition charge.....	(25)
Figure S26. SEM images of the Fe ₂ O ₃ /Fe ₂ TiO ₅ -30 cycles electrodes with different sintering time at 750 °C. e.g. 10 min. 30min. 1 h and 2 h.....	(26)

- Figure S27.** Top: the atomic model for optimized $\text{Fe}_2\text{O}_3/\text{Fe}_2\text{TiO}_5$ -30 cycles electrode. Bottom: Left: CV curves of the $\text{Fe}_2\text{O}_3/\text{Fe}_2\text{TiO}_5$ -30 cycles electrodes with different sintering conditions under illumination; Right: the photocurrent density at 1.23 V vs. RHE related to the sintering conditions.....(27)
- Schematic S1.** A: Equivalent circuit (EC) for the charge transfer process of hematite composite under illumination. B: simple Randles circuit for the charge transfer process of hematite composite under dark.....(28)
- Figure S28.** Nyquist (Imaginary vs. Real component of impedance) plots under light illumination of Fe_2O_3 , $\text{ITO}/\text{Fe}_2\text{O}_3$, $\text{ITO}/\text{Fe}_2\text{O}_3/\text{Fe}_2\text{TiO}_5$, and $\text{ITO}/\text{Fe}_2\text{O}_3/\text{Fe}_2\text{TiO}_5/\text{FeNiOOH}$ electrodes.....(29)
- Figure S29.** Nyquist (Imaginary vs. Real component of impedance) plots in the dark of Fe_2O_3 , $\text{ITO}/\text{Fe}_2\text{O}_3$, $\text{ITO}/\text{Fe}_2\text{O}_3/\text{Fe}_2\text{TiO}_5$, and $\text{ITO}/\text{Fe}_2\text{O}_3/\text{Fe}_2\text{TiO}_5/\text{FeNiOOH}$ electrodes.....(30)
- Figure S30.** C_{bulk} of Fe_2O_3 , $\text{ITO}/\text{Fe}_2\text{O}_3$, $\text{ITO}/\text{Fe}_2\text{O}_3/\text{Fe}_2\text{TiO}_5$, and $\text{ITO}/\text{Fe}_2\text{O}_3/\text{Fe}_2\text{TiO}_5/\text{FeNiOOH}$ electrodes under 1 sun illumination.....(31)
- Figure S31.** Mott-Schottky plots (C^{-2} vs. E) of Fe_2O_3 , $\text{ITO}/\text{Fe}_2\text{O}_3$, $\text{ITO}/\text{Fe}_2\text{O}_3/\text{Fe}_2\text{TiO}_5$, and $\text{ITO}/\text{Fe}_2\text{O}_3/\text{Fe}_2\text{TiO}_5/\text{FeNiOOH}$ electrodes.(32)
- Table S1.** Flat band potential values (E_{fb}), bulk donor densities (N_{d}) and total surface state density (N_{ss}) of the Fe_2O_3 , $\text{ITO}/\text{Fe}_2\text{O}_3$, $\text{ITO}/\text{Fe}_2\text{O}_3/\text{Fe}_2\text{TiO}_5$, and $\text{ITO}/\text{Fe}_2\text{O}_3/\text{Fe}_2\text{TiO}_5/\text{FeNiOOH}$ electrodes.....(32)
- Figure S32.** SEM images of FeOOH nanowires on FTO substrate.....(33)
- Figure S33.** SEM images of FeOOH nanowires on FTO substrate after sintering at 550°C for 2h.....(33)
- Schematic S2** The sample preparation process of $\text{FTO}/\text{ITO}/\text{Fe}_2\text{O}_3/\text{Fe}_2\text{TiO}_5/\text{FeNiOOH}$ electrode for TEM and STEM-EELS characterization.....(34)
- Table S2.** Photo-electrochemical performance comparison of hematite based electrodes.....(35)
- References**

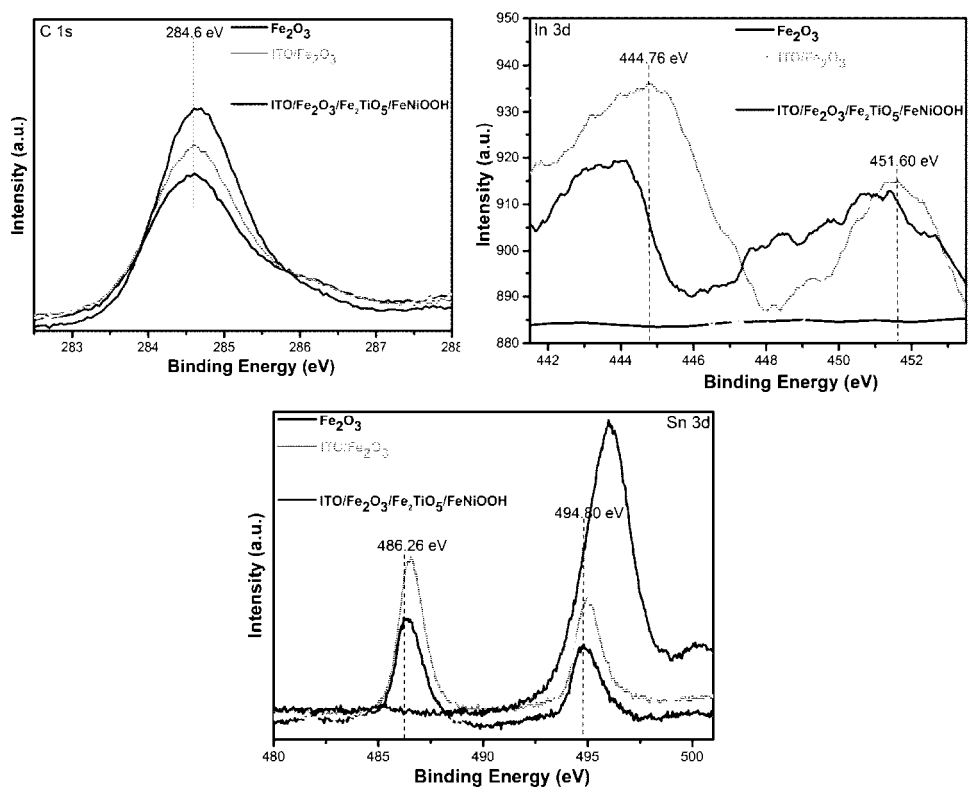


Figure S1. High resolution XPS spectra of C 1s, Sn 3d and In 3d of the Fe₂O₃, ITO/Fe₂O₃, ITO/Fe₂O₃/Fe₂TiO₅, and ITO/Fe₂O₃/Fe₂TiO₅/FeNiOOH electrodes.

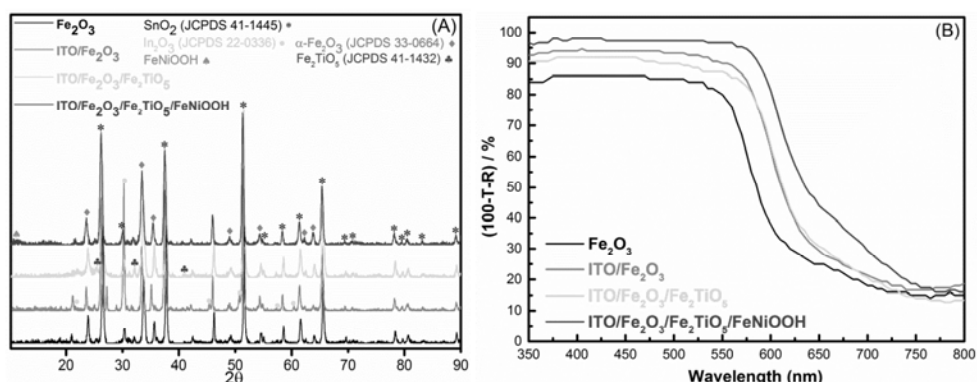


Figure S2. (A): Grazing incidence XRD patterns of the Fe₂O₃, ITO/Fe₂O₃, ITO/Fe₂O₃/Fe₂TiO₅, and ITO/Fe₂O₃/Fe₂TiO₅/FeNiOOH electrodes. (B): Absorbance of the Fe₂O₃, ITO/Fe₂O₃, ITO/Fe₂O₃/Fe₂TiO₅, and ITO/Fe₂O₃/Fe₂TiO₅/FeNiOOH electrodes; this plot was obtained from transmittance (T, %) and total reflectance (R, %) measurements on these electrodes by UV-Vis spectrum.

Characteristic XRD peaks of Fe₂O₃ (JCPDS no. 33-0664) and SnO₂ (JCPDS no. 41-1445, mainly derived from FTO substrate) can be observed in the four electrodes shown in Figure S2A. The XRD pattern of the ITO/Fe₂O₃, ITO/Fe₂O₃/Fe₂TiO₅, and ITO/Fe₂O₃/Fe₂TiO₅/FeNiOOH electrodes exhibit the diffraction peaks assigned to In₂O₃ (JCPDS no. 22-0336) from the initial sputtered ITO underlayer. The diffraction peaks related to the pseudobrookite (Fe₂TiO₅, JCPDS no. 41-1432) phase of ITO/Fe₂O₃/Fe₂TiO₅, and ITO/Fe₂O₃/Fe₂TiO₅/FeNiOOH electrodes are very weak, which is attributed to the ultrathin shell (30 ALD cycles, estimated ca. 0.81 nm) of Fe₂TiO₅ coating.¹ Besides, there is a weak broad peak located at 11°, which can be assigned to the FeNiOOH,²⁻⁴ indicating its poor crystalline structure. UV-vis absorbance spectra are obtained to account for the photo-activity of the Fe₂O₃, ITO/Fe₂O₃, ITO/Fe₂O₃/Fe₂TiO₅, and ITO/Fe₂O₃/Fe₂TiO₅/FeNiOOH electrodes, as shown in Figure S2B. All photoanodes exhibit an overall high absorption in the visible region (wavelength < 580 nm) with a relative steep absorption edge at approximately 580 nm.

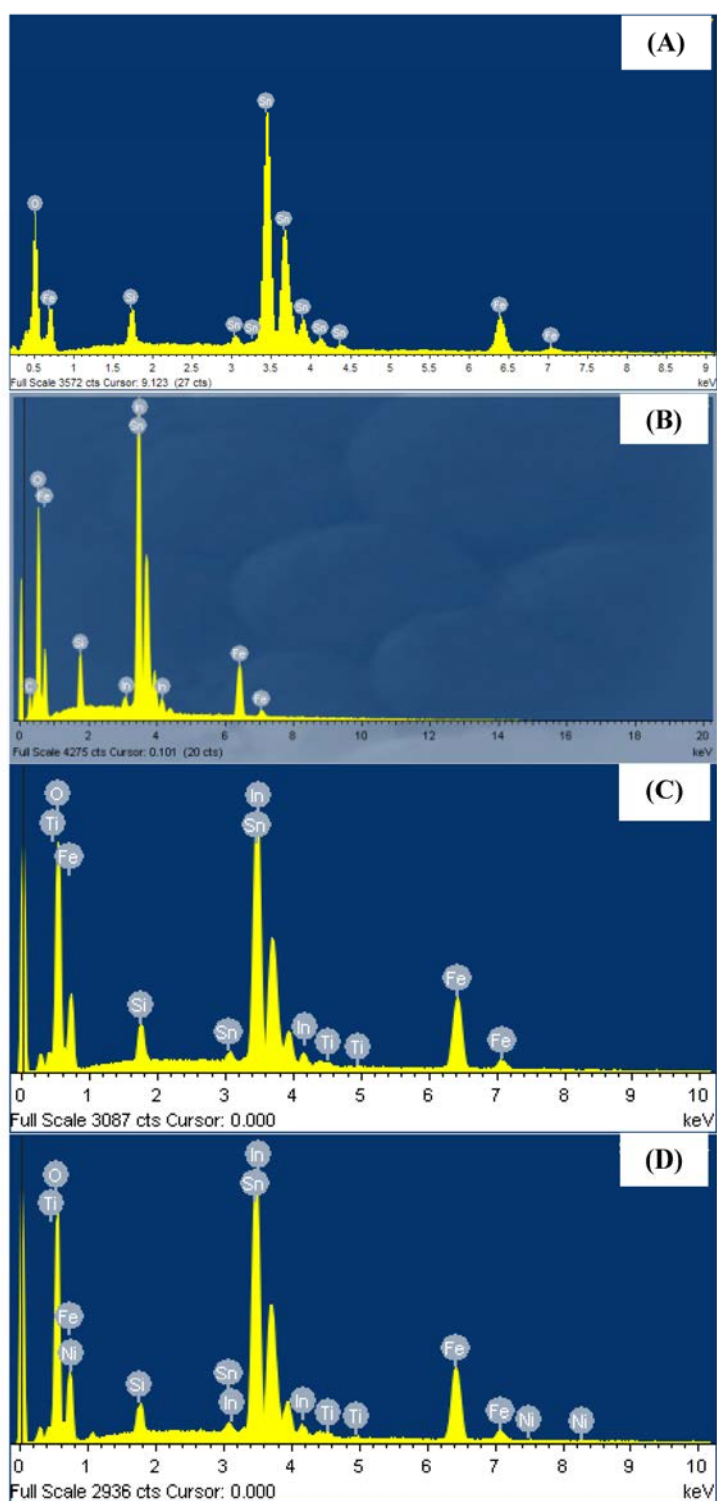


Figure 53. EDS obtained on the Fe_2O_3 (A), ITO/ Fe_2O_3 (B), ITO/ Fe_2O_3 / Fe_2TiO_5 (C), and ITO/ Fe_2O_3 / Fe_2TiO_5 / FeNiOOH (D) electrodes.

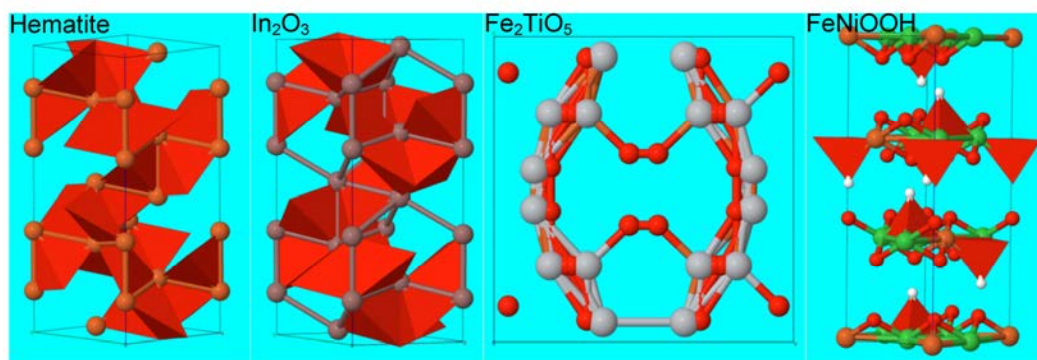


Figure S4. 1*1*1 unit crystal model of hematite, In₂O₃, Fe₂TiO₅ and FeNiOOH based on the crystal data in ICSD and reported data⁵ for the identification of the crystal phase.

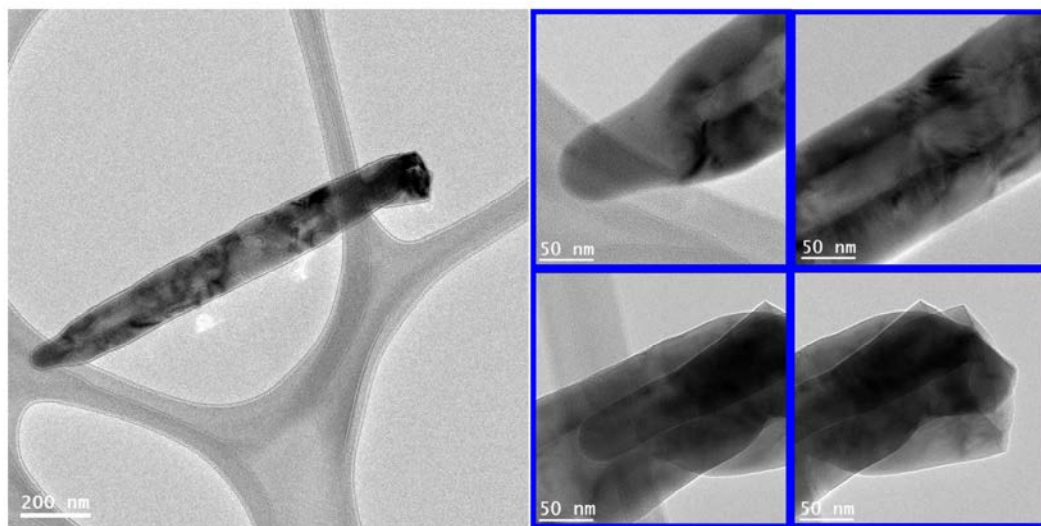


Figure S5. Low magnification TEM images of a nanowire from the Fe_2O_3 electrode. Left: low magnification TEM micrograph shows the nanowire morphology of the Fe_2O_3 electrode; Right: several TEM images showing the detailed structure of the Fe_2O_3 nanowire.

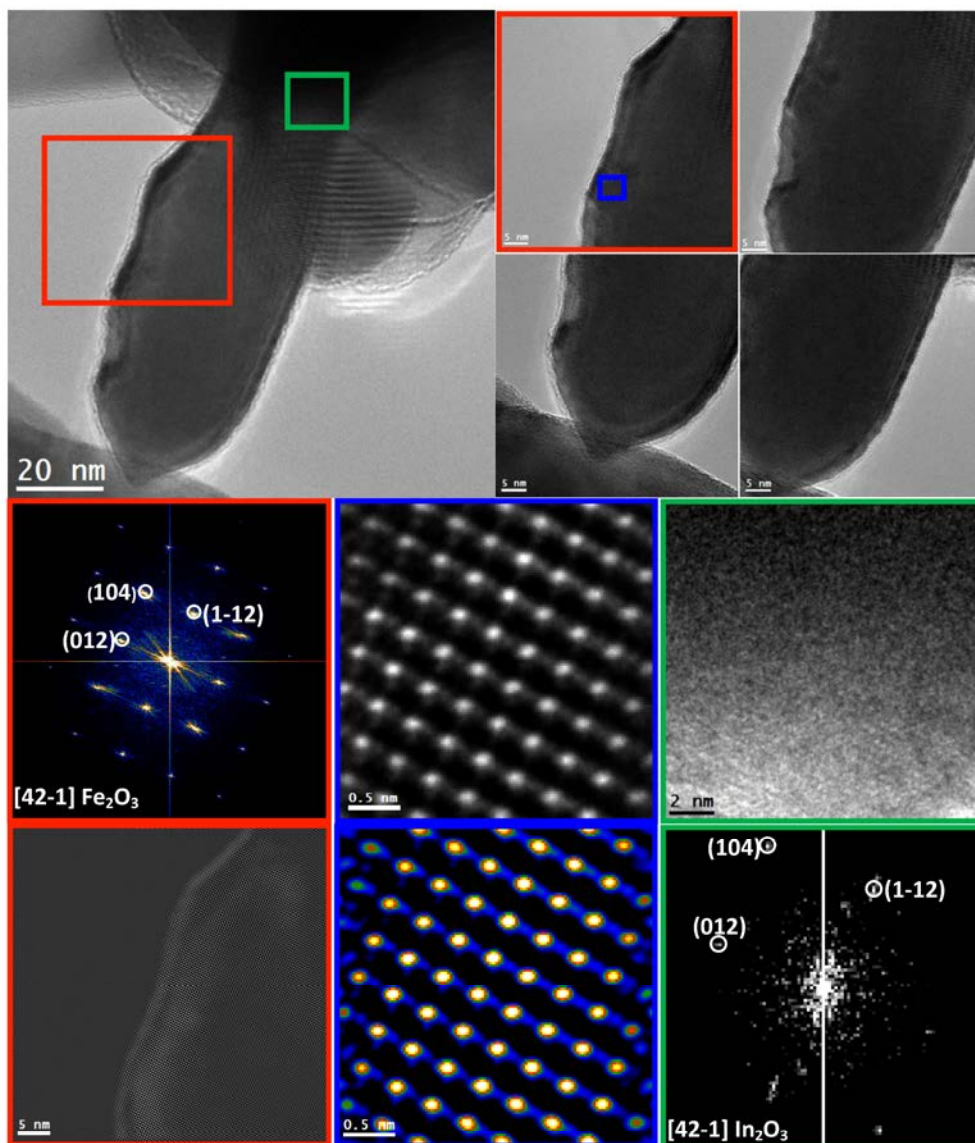


Figure S6. HRTEM, FFT spectrum and IFFT images obtained on a nanowire extracted from the ITO/Fe₂O₃ electrode.

Top rows: left: the low magnification TEM micrograph shows the morphology of a small Fe₂O₃ nanowire directly grown on ITO matrix; Right: the detailed crystal structure of different regions of the small nanowire.

Bottom rows: left column: the power spectrum of the red squared area indicating its single crystal structure corresponding to trigonal Fe₂O₃, [R3-CH]-Space group 167, also known as hematite, with lattice parameters of $a = b = 0.50342$ nm, $c = 1.37483$ nm, and $\alpha = \beta = 90^\circ$ and $\gamma = 120^\circ$ as visualized along the [42-1] direction; and the IFFT image of the red squared area. Middle column: the atomic HRTEM and temperature colored HRTEM of the blue squared area shows the ordered structure of hematite. Right column: the HRTEM of the green squared area and the corresponding reduced FFT spectrum indicates that the species can be assigned to Trigonal In₂O₃, [R3-CH]-space group 167, with lattice parameters of $a = b = 0.5438$ nm, $c = 1.4474$ nm, and $\alpha = \beta = 90^\circ$ and $\gamma = 120^\circ$ as visualized along [42-1] direction.

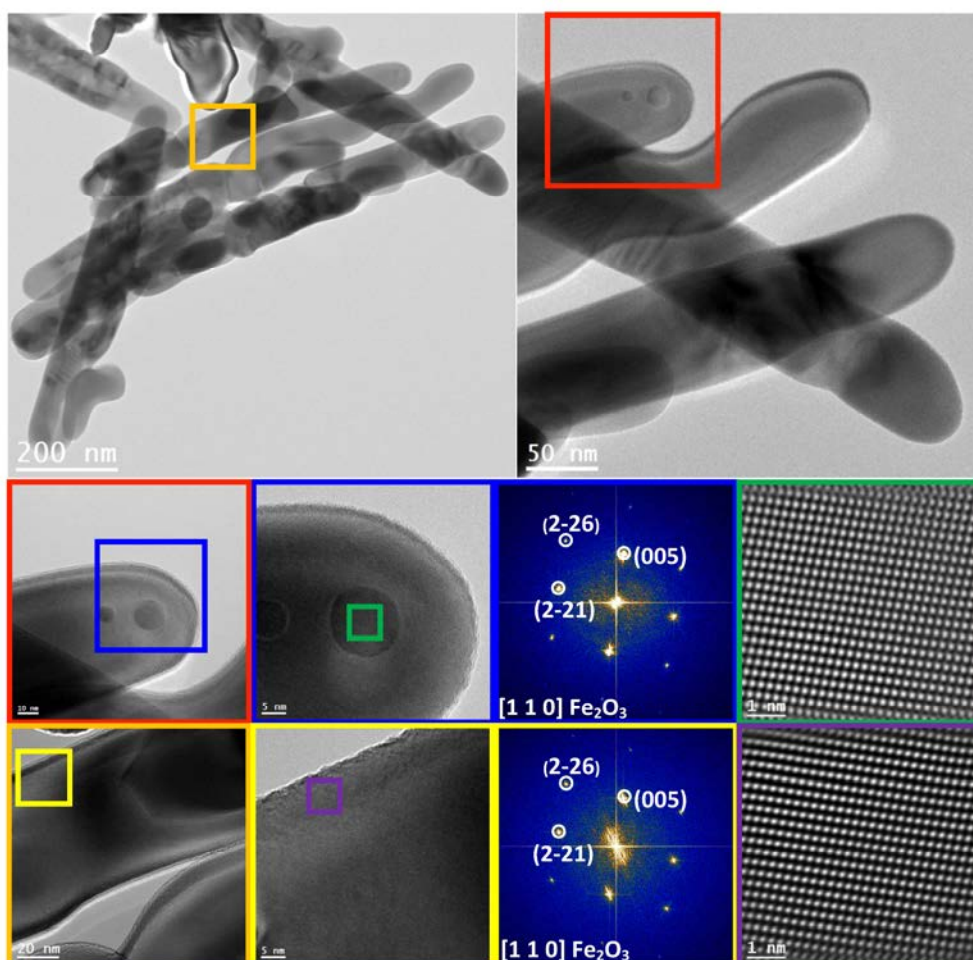


Figure S7. HRTEM, FFT spectrum and IFFT images corresponding to nanowire-like structures extracted from the ITO/Fe₂O₃ electrode. Top rows: left: low magnification TEM micrograph shows the distribution of several nanowires; Right: the magnified TEM images of these nanowires. Middle rows: left: HRTEM obtained on the red squared area; Middle: the detailed structure obtained on the blue squared area and its corresponding power spectrum indicating its hematite single crystal structure as visualized along the [110] direction; Right: atomic IFFT image of the green squared area. Bottom rows: left: HRTEM micrograph corresponding to the orange squared area; Middle: detail structure in the yellow squared area and the corresponding power spectrum indicating its hematite single crystal structure as visualized along the [110] direction; Right: atomic IFFT image of the purple squared area.

As can be seen from Figure S6, Trigonal In₂O₃ phase is identified at the bulk matrix, where the small Fe₂O₃ nanowires are directly grown onto. It is noteworthy that the Fe₂O₃ nanowires grown with a ITO under layer presents single crystal hematite phase, as confirmed by the FFT spectrum and atomic resolution HRTEM displayed in Figures S6 and S7. The improved crystal quality of Fe₂O₃ nanowires may be derived from the epitaxial relationship between Fe₂O₃ and In₂O₃ phase since they belong to the same Space group-167 [R3-CH] and with similar crystal constant. Besides, Figure S7 indicates that even the nanowire structure shows a slightly curved-shape, the nanowires crystal orientation does not vary at different regions.

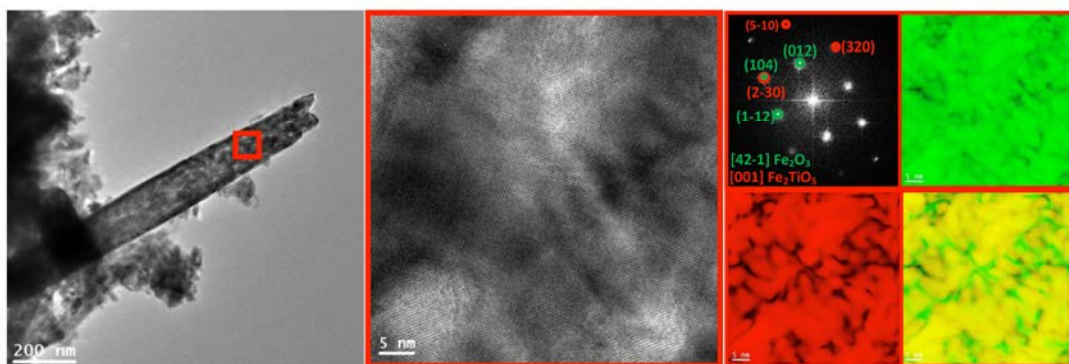


Figure S8. HRTEM and RGB IFFT images of ITO/Fe₂O₃/Fe₂TiO₅ electrode. left: low magnification TEM image showing a Fe₂O₃/Fe₂TiO₅ composite nanowire directly grown on the ITO matrix; Middle: detail of structure at the red squared area; Right: the corresponding power spectrum indicating it is composed of hematite and pseudobrookite visualized along [42-1] and [001] directions, respectively; and the RGB IFFT images of hematite, pseudobrookite and their composite, indicating the homogeneously coating of pseudobrookite on the surface of the hematite nanowires.

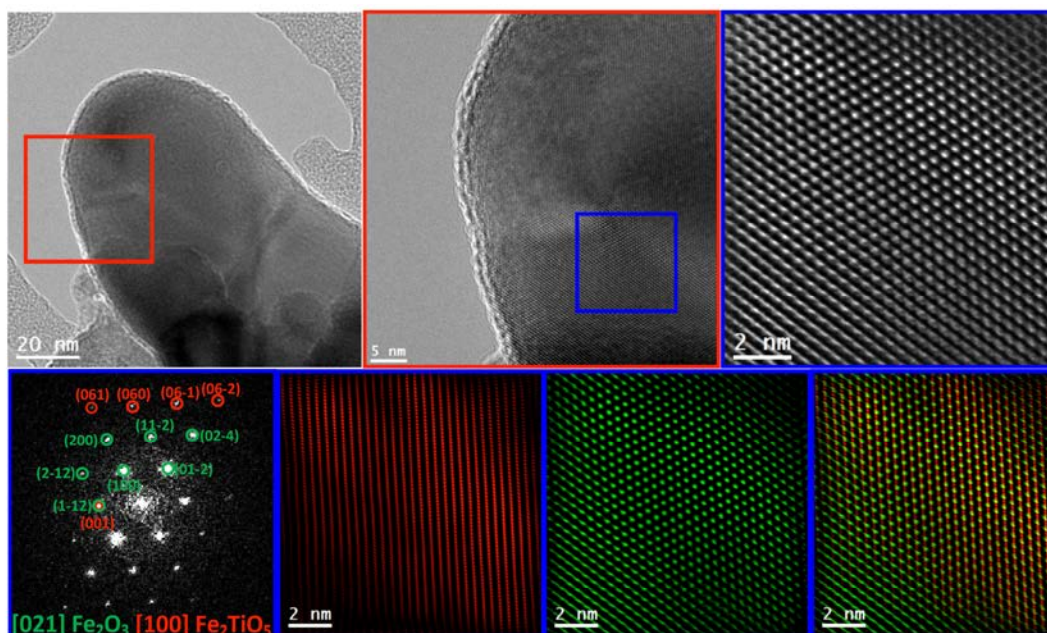


Figure S9. HRTEM and RGB IFFT images in the nanowires-like structure extracted from the ITO/Fe₂O₃/Fe₂TiO₅ electrode.

Top row: Left: low magnification TEM micrograph showing the edge of the nanowire; Middle: HRTEM detail corresponding to the red squared region; Right: detail of the structure in the blue rectangle region.

Bottom row: Left: the corresponding power spectrum of blue squared region indicating it is composed of hematite and pseudobrookite visualized along [021] and [100] directions, respectively; and the RGB IFFT images of hematite (green), pseudobrookite (red) and their composite, showing the atomic stack sequence of hematite and pseudobrookite.

As we can see from Figures S8 and S9, the low magnification IFFT RGB and the atomic IFFT RGB images together demonstrate the homogeneously coating of Fe₂TiO₅ onto Fe₂O₃ nanowires in the case of ITO/Fe₂O₃/Fe₂TiO₅ electrode.

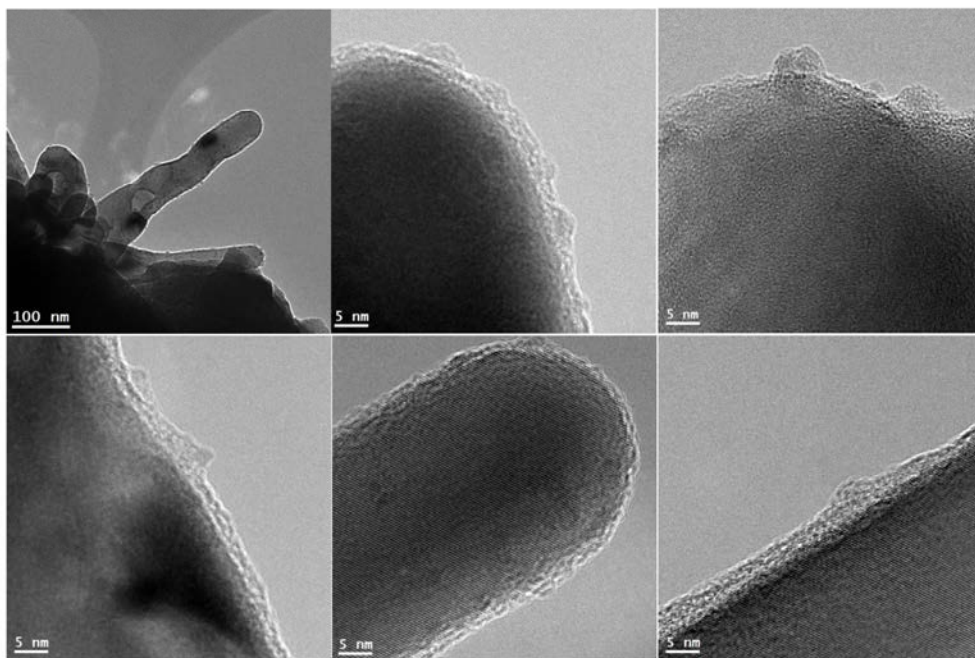


Figure S10. Several TEM images showing the distribution of FeNiOOH nanodots on the surface of $\text{Fe}_2\text{O}_3/\text{Fe}_2\text{TiO}_5$ composite nanowires of ITO/ $\text{Fe}_2\text{O}_3/\text{Fe}_2\text{TiO}_5/\text{FeNiOOH}$ electrode.

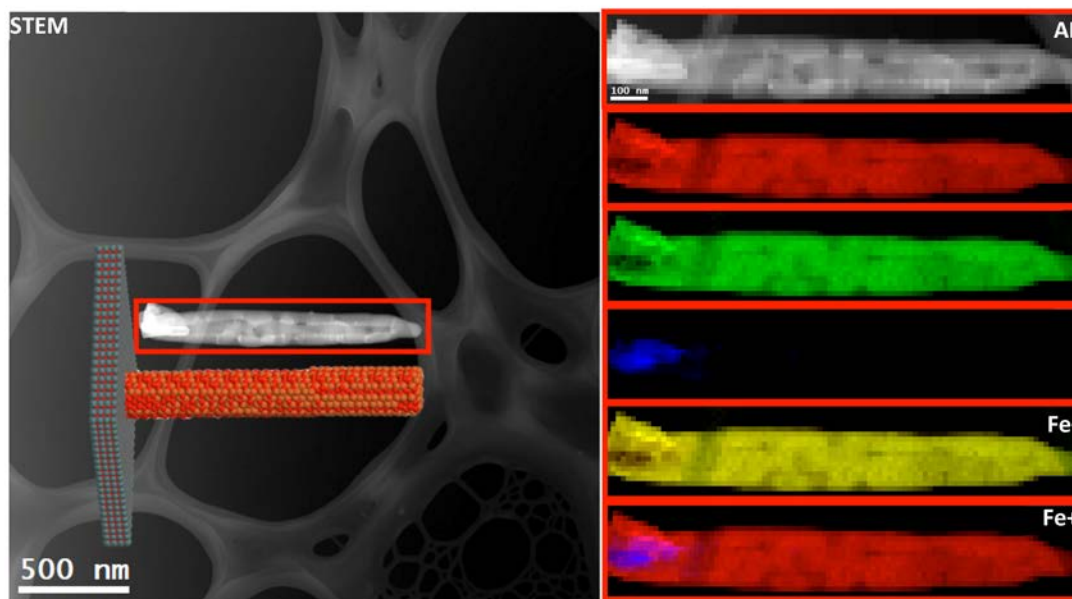


Figure S11. EELS chemical composition maps obtained from the red rectangled area of the ADF-STEM micrograph of a nanowire extracted from the Fe_2O_3 electrode. Individual Fe (red), O (green), Sn (blue) maps and their composite. (The inset of the ADF-STEM micrograph shows the atomic model for Fe_2O_3 electrode)

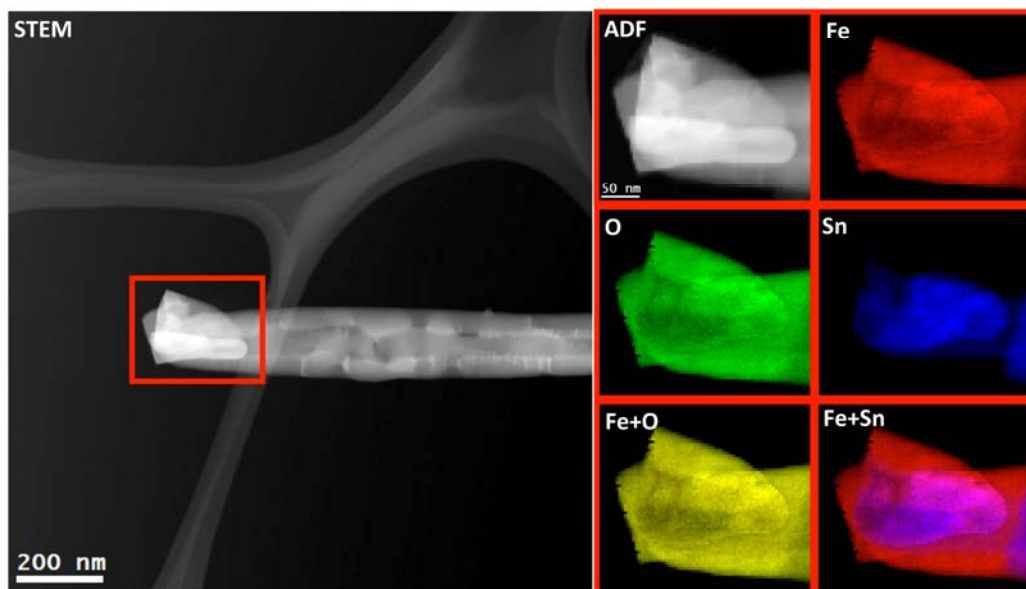


Figure S12. EELS chemical composition maps obtained from the red rectangled area of the ADF-STEM micrograph of a nanowire extracted from the Fe_2O_3 electrode. Individual Fe (red), O (green), Sn (blue) maps and their composite.

As displayed in Figures S11 and S12, the diameter and length of the Fe_2O_3 nanowires from the Fe_2O_3 electrode are estimated to be ca. 50 nm and 1 μm , respectively. The STEM-EELS mappings (Figures S11 and S12) reveal that the Sn elemental signal is only present at the bottom part of the Fe_2O_3 nanowire, the diameter of which is bigger than the top region of the nanowire. The Sn diffusion in the case of the Fe_2O_3 electrode is much weaker than that in the ITO/ Fe_2O_3 , ITO/ Fe_2O_3 / Fe_2TiO_5 , and ITO/ Fe_2O_3 / Fe_2TiO_5 / FeNiOOH electrodes, respectively, as we will see below in Figures S13- S17.

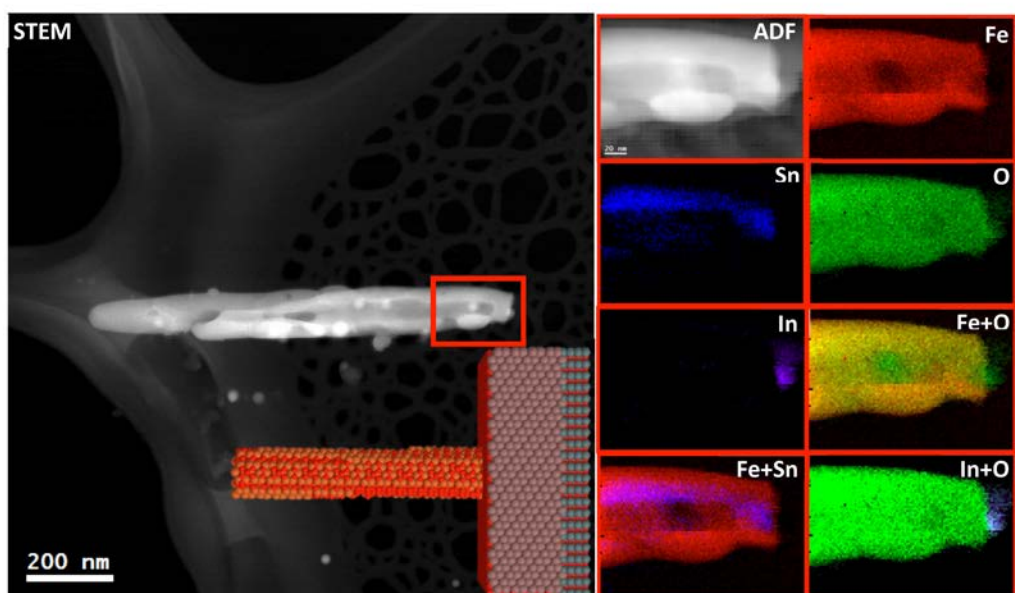


Figure S13. EELS chemical composition maps obtained from the red rectangled area of the ADF-STEM micrograph in the nanowire-like structure extracted from the ITO/Fe₂O₃ electrode. Individual Fe (red), O (green), Sn (blue) and In (purple) maps and their composite. (The inset of the ADF-STEM micrograph shows the atomic model for ITO/Fe₂O₃ electrode).

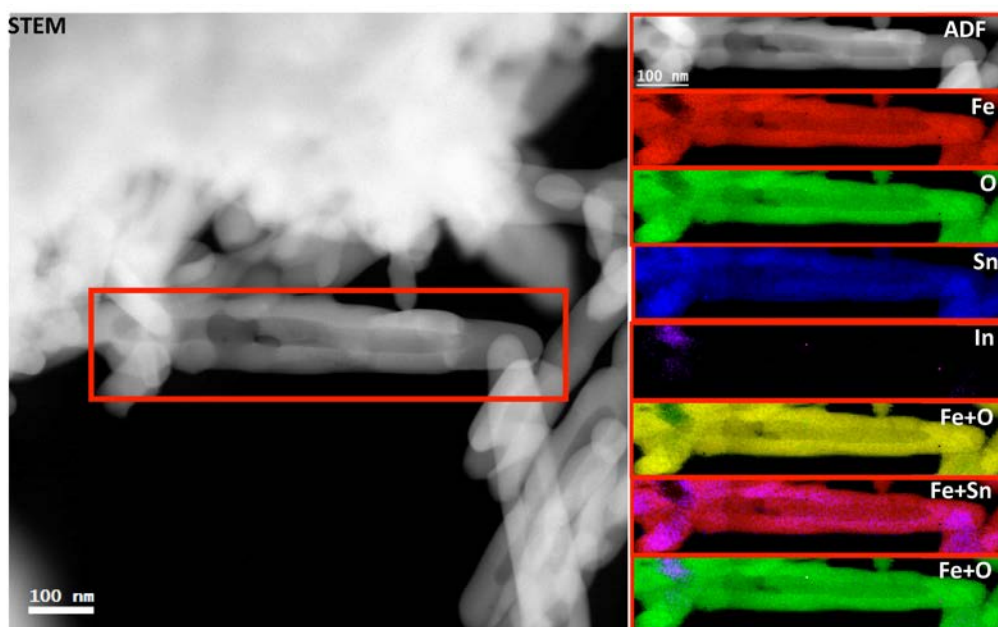


Figure S14. EELS chemical composition maps obtained from the red rectangled area of the ADF-STEM micrograph in the nanowire-like structure extracted from ITO/Fe₂O₃ electrode. Individual Fe (red), O (green), Sn (blue) and In (purple) maps and their composite.

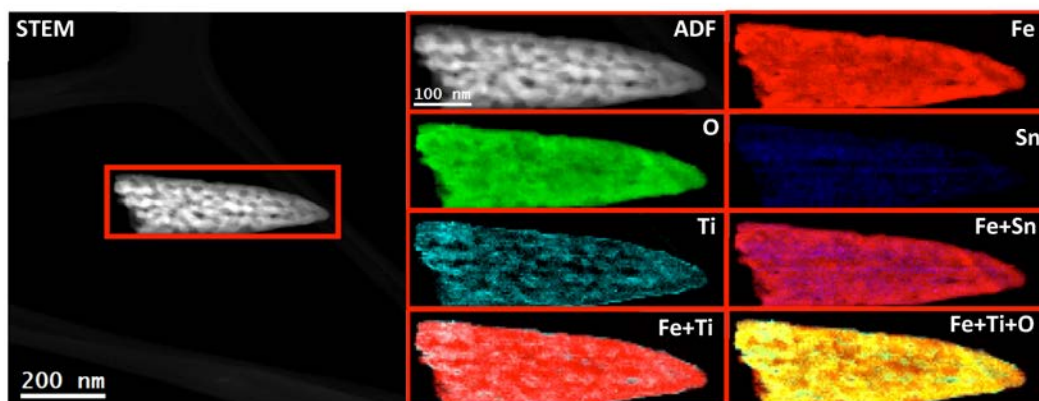


Figure S15. EELS chemical composition maps obtained from the red rectangled area of the ADF-STEM micrograph in the nanowire-like structure extracted from ITO/Fe₂O₃/Fe₂TiO₅ electrode. Individual Fe (red), O (green), Sn (blue) and Ti (indigo) maps and their composite.

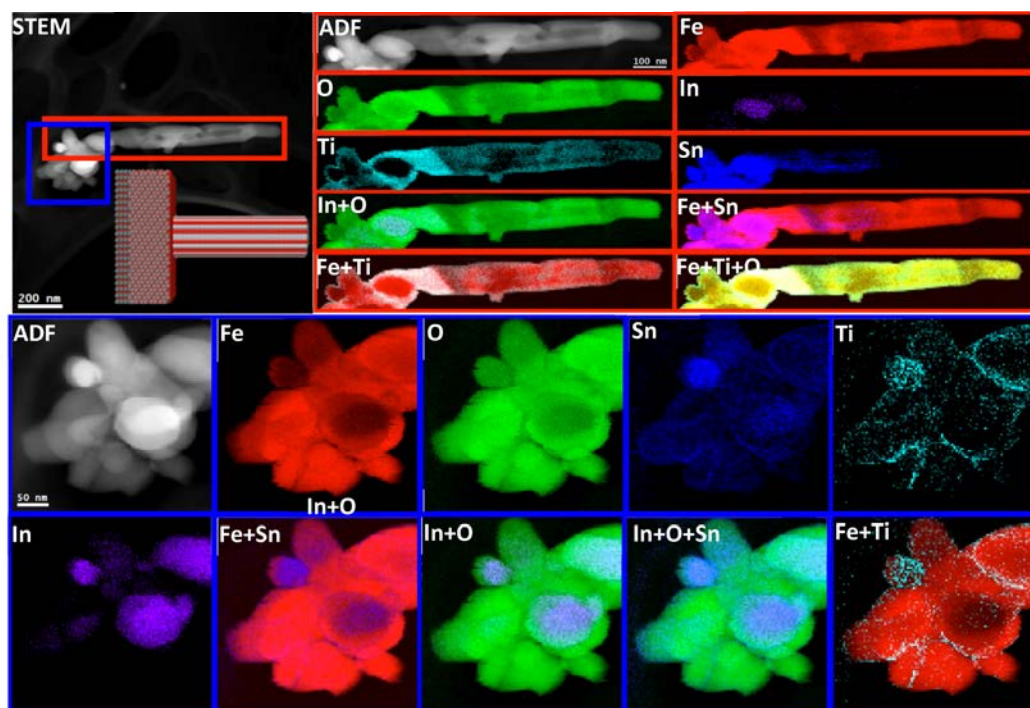


Figure S16. EELS chemical composition maps obtained from the red and blue rectangled area of the ADF-STEM micrograph in the nanowire-like structure extracted from ITO/Fe₂O₃/Fe₂TiO₅ electrode. Individual Fe (red), O (green), Sn (blue), In (purple) and Ti (indigo) maps and their composite. (The inset of the ADF-STEM micrograph shows the atomic model for ITO/Fe₂O₃/Fe₂TiO₅ electrode).

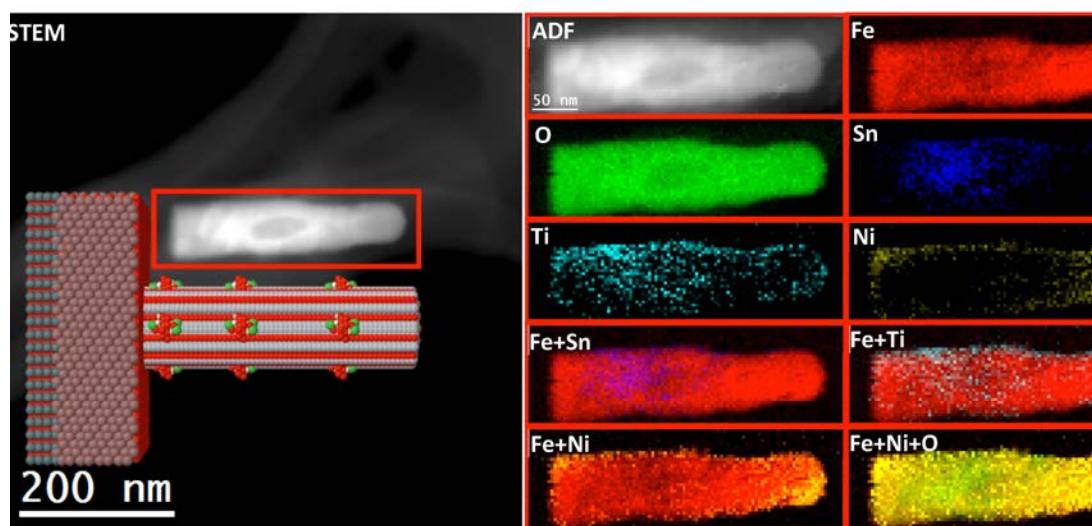


Figure S17. EELS chemical composition maps obtained from the red rectangled area of the ADF-STEM micrograph in the nanowire-like structure extracted from ITO/Fe₂O₃/Fe₂TiO₅/FeNiOOH electrode. Individual Fe (red), O (green), Sn (blue), Ti (indigo) and Ni (yellow) maps and their composite. (The inset of the ADF-STEM micrograph shows the atomic model for ITO/Fe₂O₃/Fe₂TiO₅/FeNiOOH electrode).

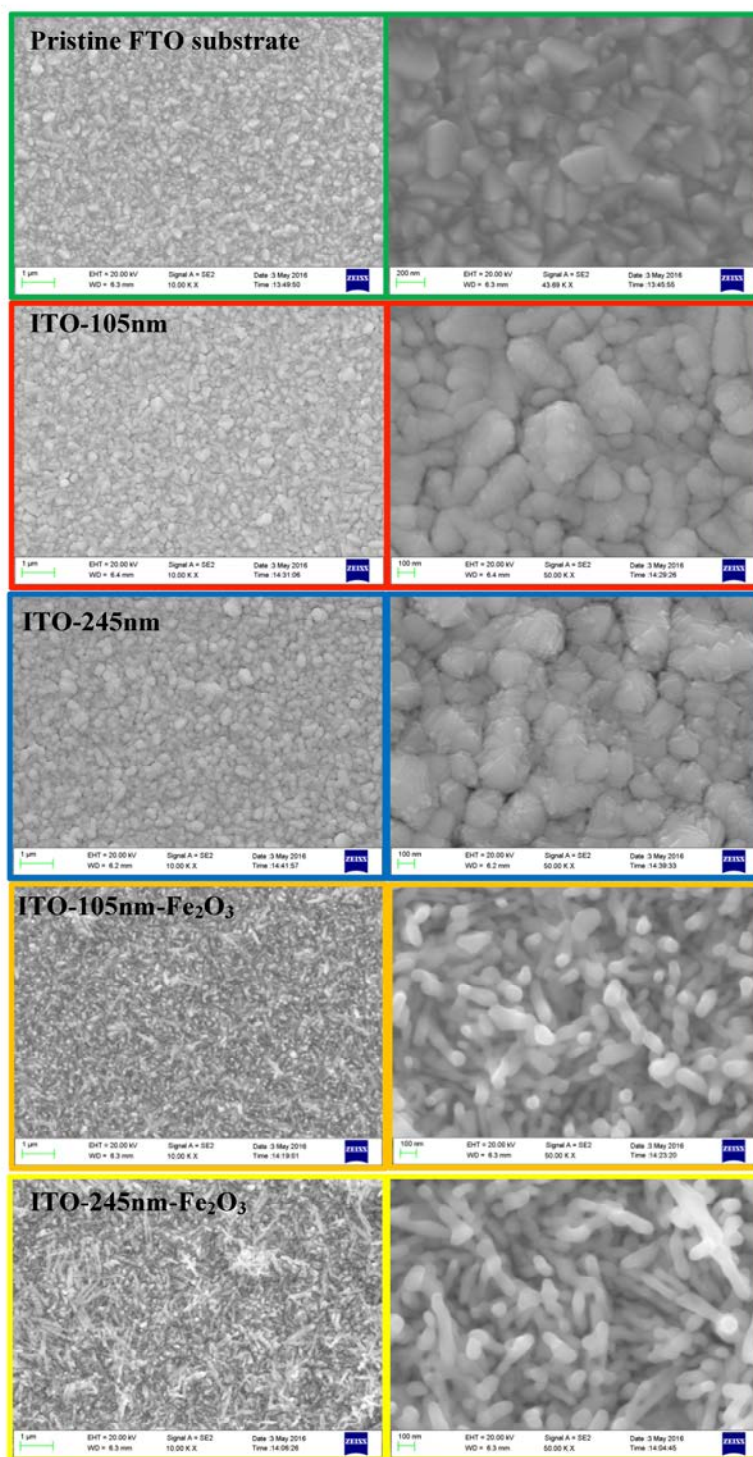


Figure S18. SEM images of the pristine FTO substrate, ITO-105 nm, ITO-245 nm, ITO-105 nm-Fe₂O₃ and ITO-245 nm-Fe₂O₃ electrodes.

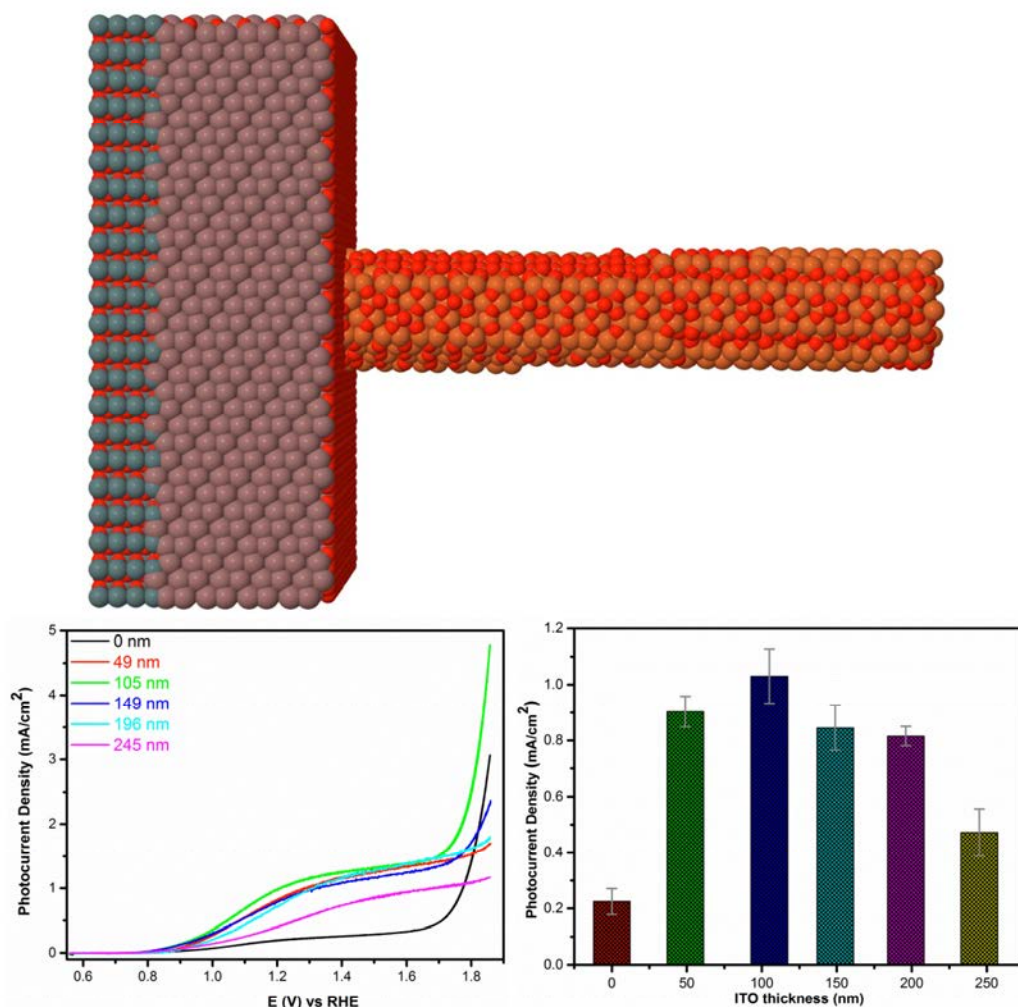


Figure S19. Top: the atomic model for optimized ITO/Fe₂O₃ electrodes. Bottom: Left: CV curves of the ITO/Fe₂O₃ electrodes with different ITO thickness sintering on 750 °C for 30min under illumination; Right: the photocurrent density at 1.23 V vs. RHE related to the ITO thickness (the error bar stemmed from the standard deviation of statistic data collected at least three repeated electrodes).

As displayed in Figure S19, with the increment of ITO deposition thickness from 0 nm to 105 nm, the photocurrent at 1.23 V vs. RHE gradually increases to 1.05 mA cm⁻². In stark contrast, the corresponding photocurrent at 1.23 V vs. RHE decreases intensively upon further extending ITO deposition thickness to 245 nm. This intensive reduction of photocurrent might be attributed to the deteriorated nanowire structure of hematite because of the exorbitantly doped Sn from the thick ITO matrix, which is evidenced by the randomly inclined hematite nanowires of ITO-245nm-Fe₂O₃ electrode as shown in Figure S18.

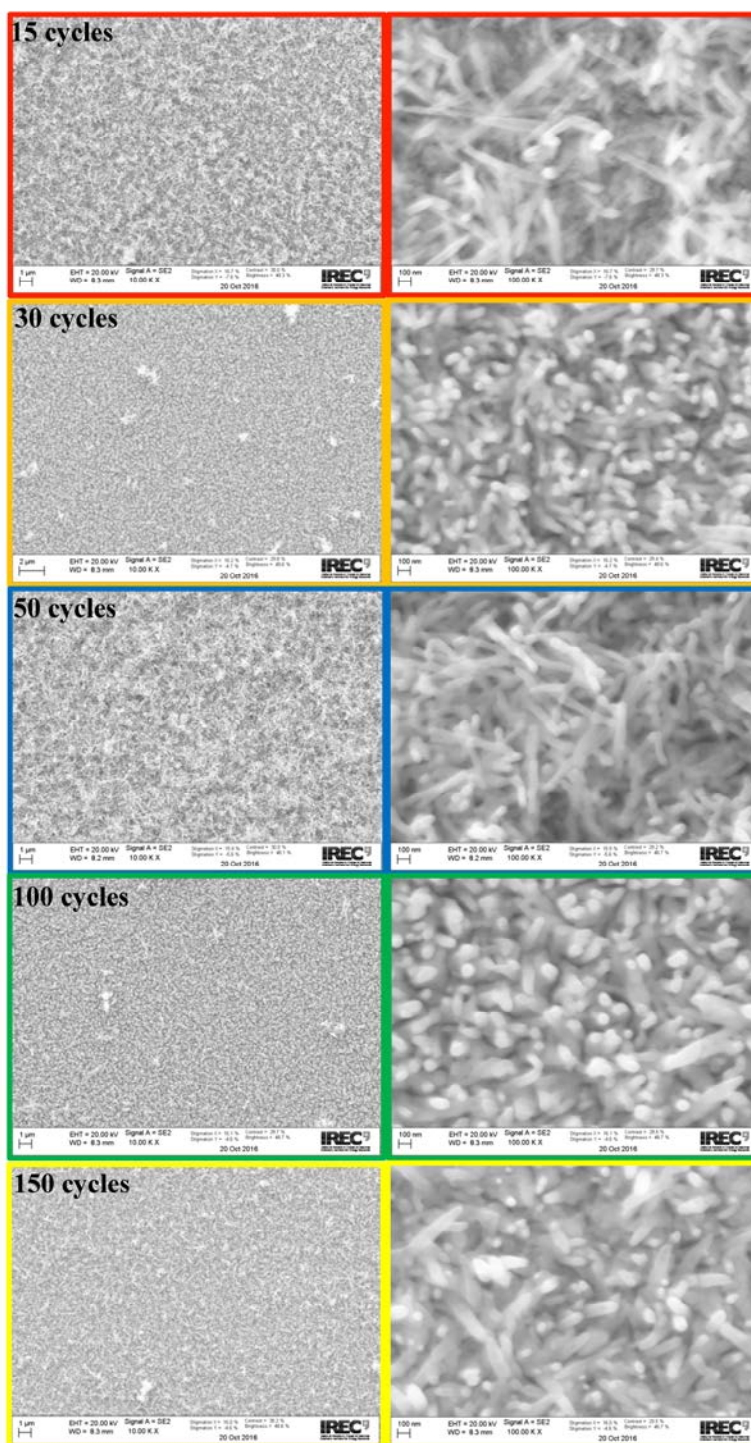


Figure S20. SEM images of the ITO/Fe₂O₃/Fe₂TiO₅ electrodes with different ALD cycles (TiO₂ thickness), e.g. 15 cycles, 30 cycles, 50 cycles, 100 cycles and 150 cycles.

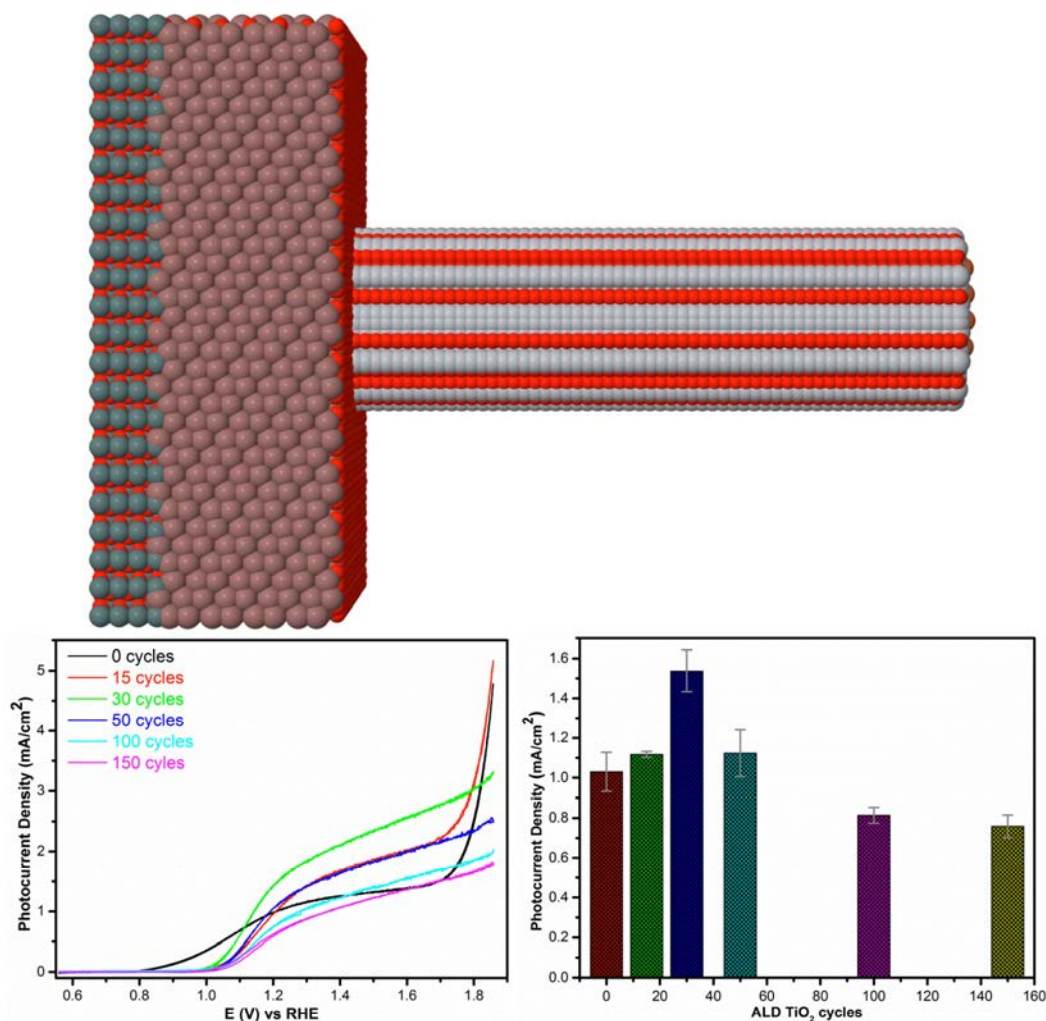


Figure S21. Top: the atomic model for optimized ITO/Fe₂O₃/Fe₂TiO₅ electrodes. Bottom: Left: CV curves of the ITO/Fe₂O₃/Fe₂TiO₅ electrodes with different ALD TiO₂ cycles (thickness) sintering on 750 °C for 30 min under illumination; Right: the photocurrent density at 1.23 V vs. RHE related to the ALD TiO₂ cycles (the error bar stemmed from the standard deviation of statistic data collected at least three repeated electrodes).

Figures S20 and S21 correlate the photocurrent response of the ITO/Fe₂O₃/Fe₂TiO₅ electrodes with the ALD TiO₂ deposition cycles. Figure S21 exhibits the photocurrent of the ITO/Fe₂O₃/Fe₂TiO₅ electrodes varies with the increment of ALD TiO₂ deposition cycles. At 30 ALD TiO₂ deposition cycles, the ITO/Fe₂O₃/Fe₂TiO₅ electrode possess the highest photocurrent of 1.56 mA cm⁻², indicating suitable coating of the Fe₂TiO₅ onto the ITO/Fe₂O₃ electrode, without residual TiO₂ on the surface of the ITO/Fe₂O₃/Fe₂TiO₅ electrode and the formation of deleterious heterojunction like the Fe₂O₃/Fe₂TiO₅/TiO₂,⁶ as confirmed by Figures S8-S9 and S15-S16.

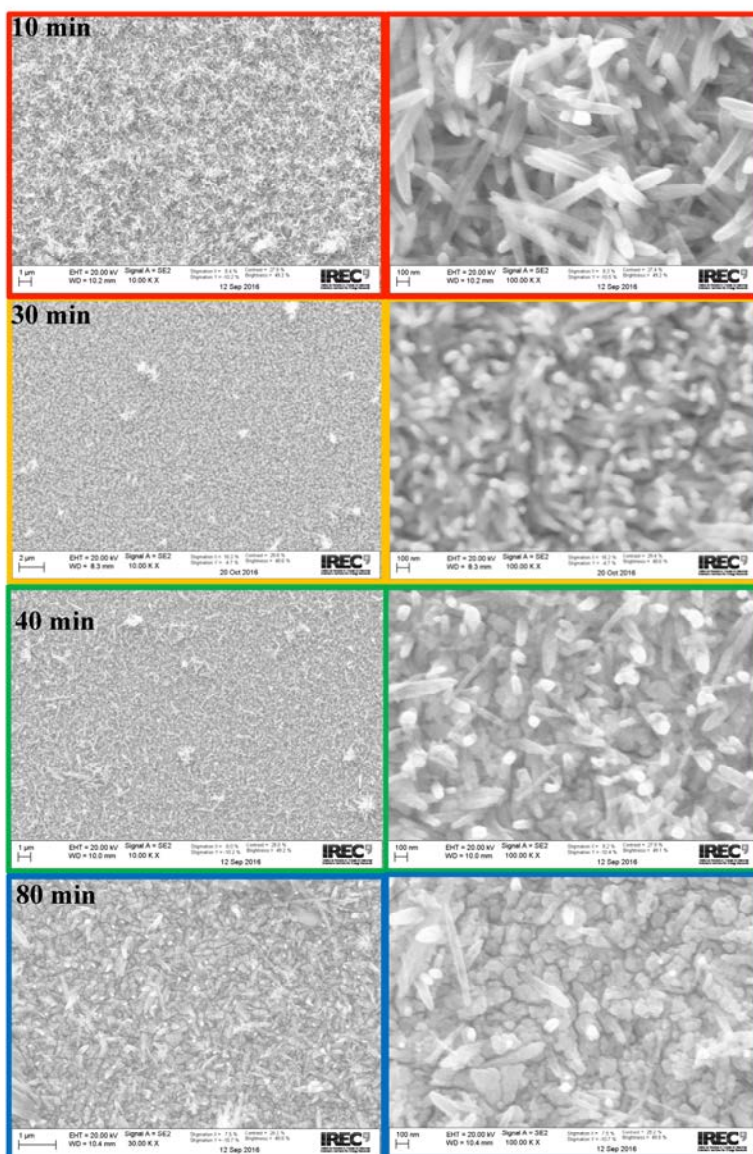


Figure S22. SEM images of the ITO/Fe₂O₃/Fe₂TiO₅-30 cycles electrodes with different sintering time at 750°C, e.g. 10 min, 30 min, 40 min and 80 min.

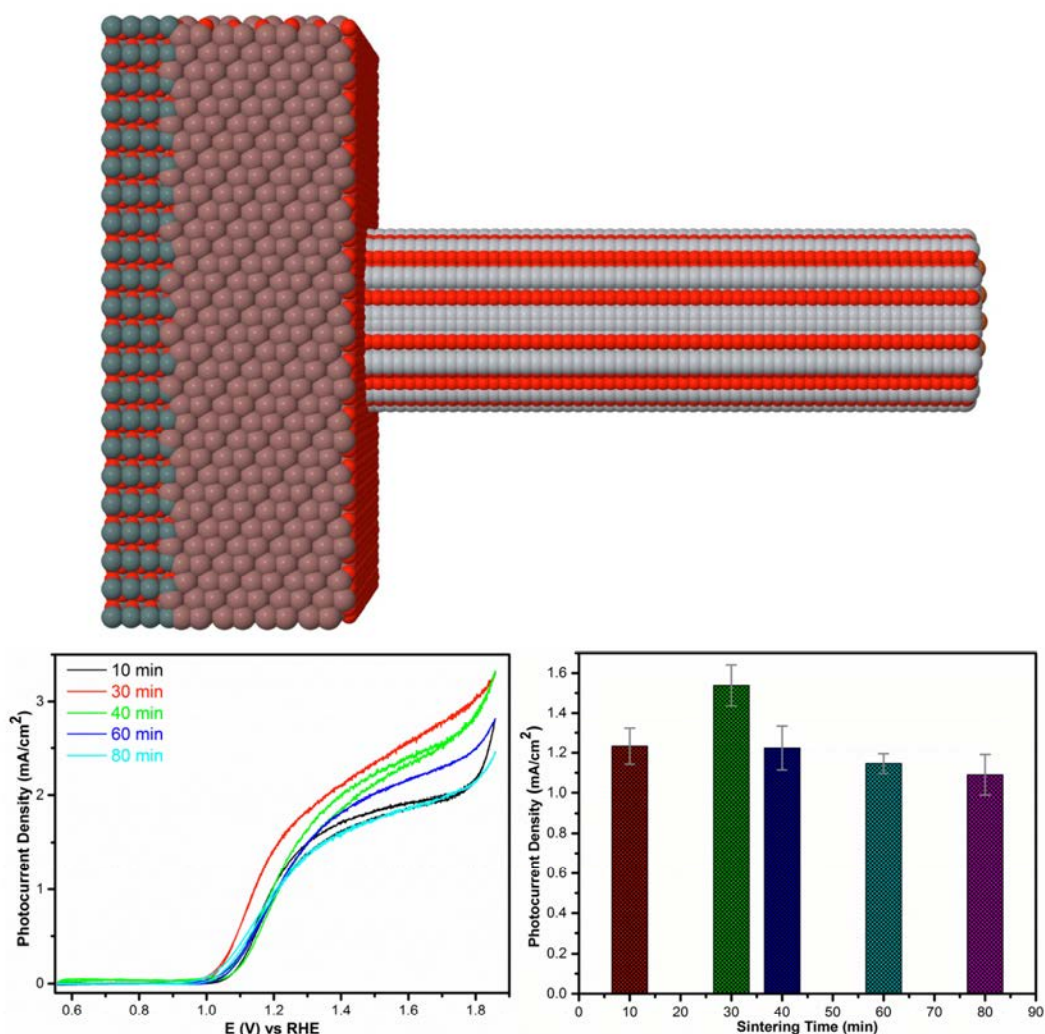


Figure S23. Top: the atomic model for optimized ITO/Fe₂O₃/Fe₂TiO₅ electrodes. Bottom: Left: CV curves of the ITO/Fe₂O₃/Fe₂TiO₅-30 cycles electrodes with different sintering time on 750 °C under illumination; Right: the photocurrent density at 1.23 V vs. RHE related to the sintering time (the error bar stemmed from the standard deviation of statistic data collected at least three repeated electrodes).

In order to reduce the surface defects, enhance the Sn doping and retain the nanostructure texturing of hematite nanowires at the same time, an optimization of sintering time for the ITO/Fe₂O₃/Fe₂TiO₅-30 cycles electrode has been performed, as shown in Figures S22 and S23. Figure S22 reveals the sintering time substantially affect the morphology of the Fe₂O₃/Fe₂TiO₅ nanowires. As the sintering time over 30 min at 750 °C, the Fe₂O₃/Fe₂TiO₅ nanowires initiate the deformation and finally evolve into a film-like structure, which somehow reduce the surface area exposure to electrolyte. The monitoring of the PEC performance in Figure S23 indicates the highest photocurrent response of the ITO/Fe₂O₃/Fe₂TiO₅-30 cycles electrode can be obtained with sintering parameter at 750 °C for 30min.

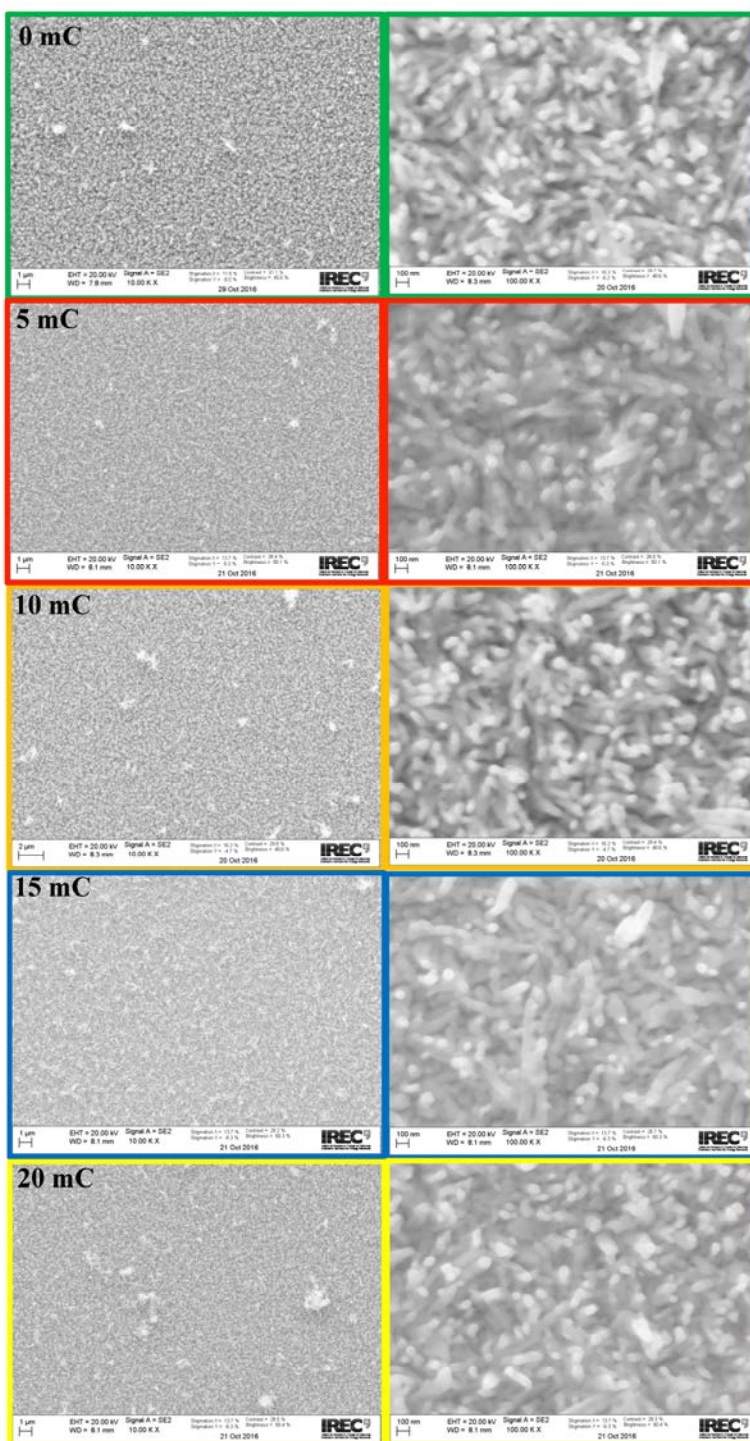


Figure S24. SEM images of the ITO/Fe₂O₃/Fe₂TiO₅/FeNiOOH electrodes with different FeNiOOH deposition charge, e.g. 0 mC, 5mC, 10 mC, 15 mC and 20 mC.

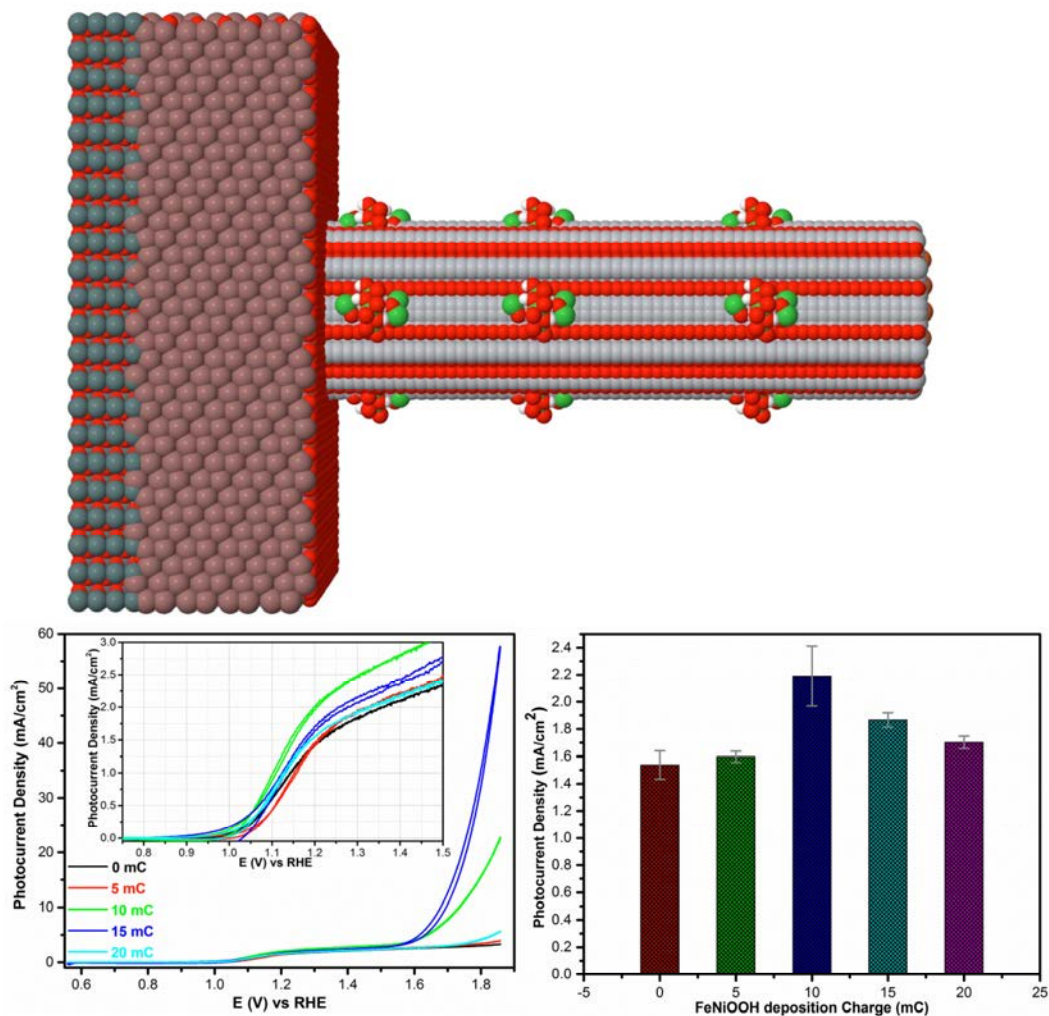


Figure S25. Top: the atomic model for the optimized ITO/Fe₂O₃/Fe₂TiO₅/FeNiOOH electrode. Bottom: Left: CV curves of the ITO/Fe₂O₃/Fe₂TiO₅/FeNiOOH electrodes with different FeNiOOH deposition charge under illumination; Right: the photocurrent density at 1.23 V vs. RHE related to the FeNiOOH deposition charge (the error bar stemmed from the standard deviation of statistic data collected at least three repeated electrodes).

It is well established that the OER activity of the FeNiOOH can be adjusted according to the OEC film thickness.⁷⁻⁹ In our case, the electrodeposition charges of FeNiOOH onto ITO/Fe₂O₃/Fe₂TiO₅ electrode have been optimized, as displayed in Figures S24 and S25. With the 10 mC decorations of the FeNiOOH nanodots, the photocurrent of the ITO/Fe₂O₃/Fe₂TiO₅ electrode can be further enhanced to 2.2 mA cm⁻². It reveals that coupling the FeNiOOH on the ITO/Fe₂O₃/Fe₂TiO₅ electrode effectively suppress the electron-hole pair recombination and accelerate reaction kinetics at the SEI.¹⁰⁻¹¹

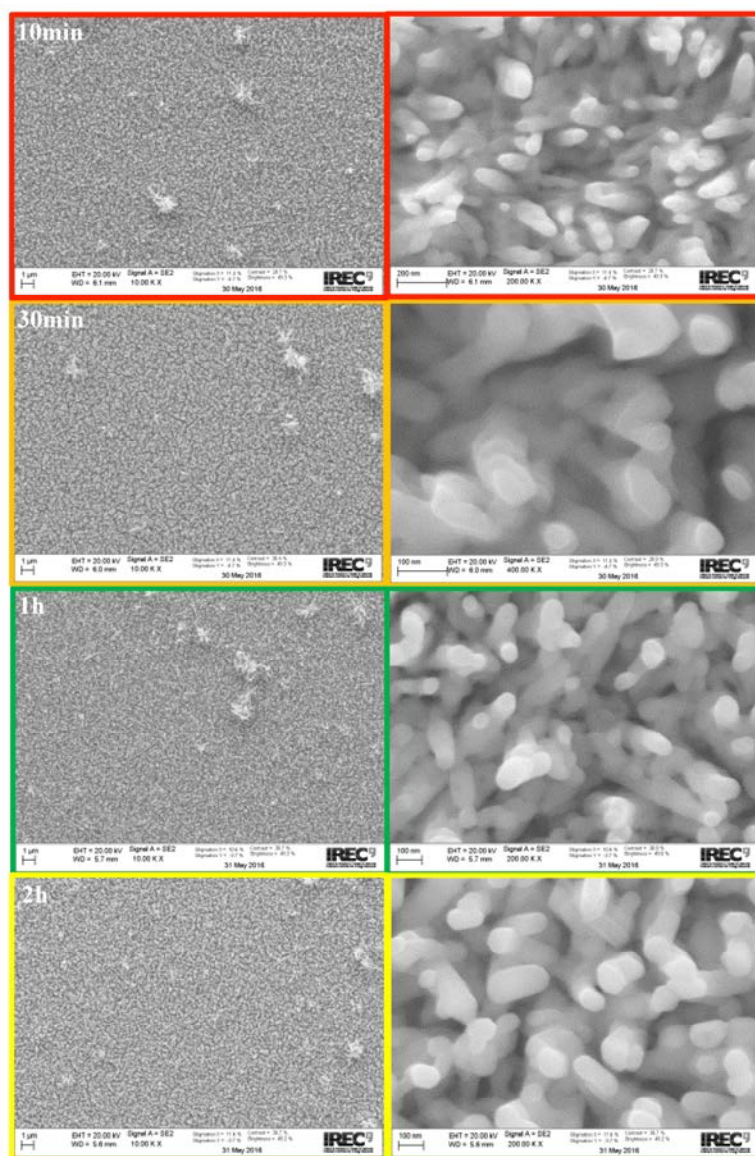


Figure S26. SEM images of the Fe₂O₃/Fe₂TiO₅-30 cycles electrodes with different sintering time at 750 °C, e.g. 10 min, 30min, 1 h and 2 h.

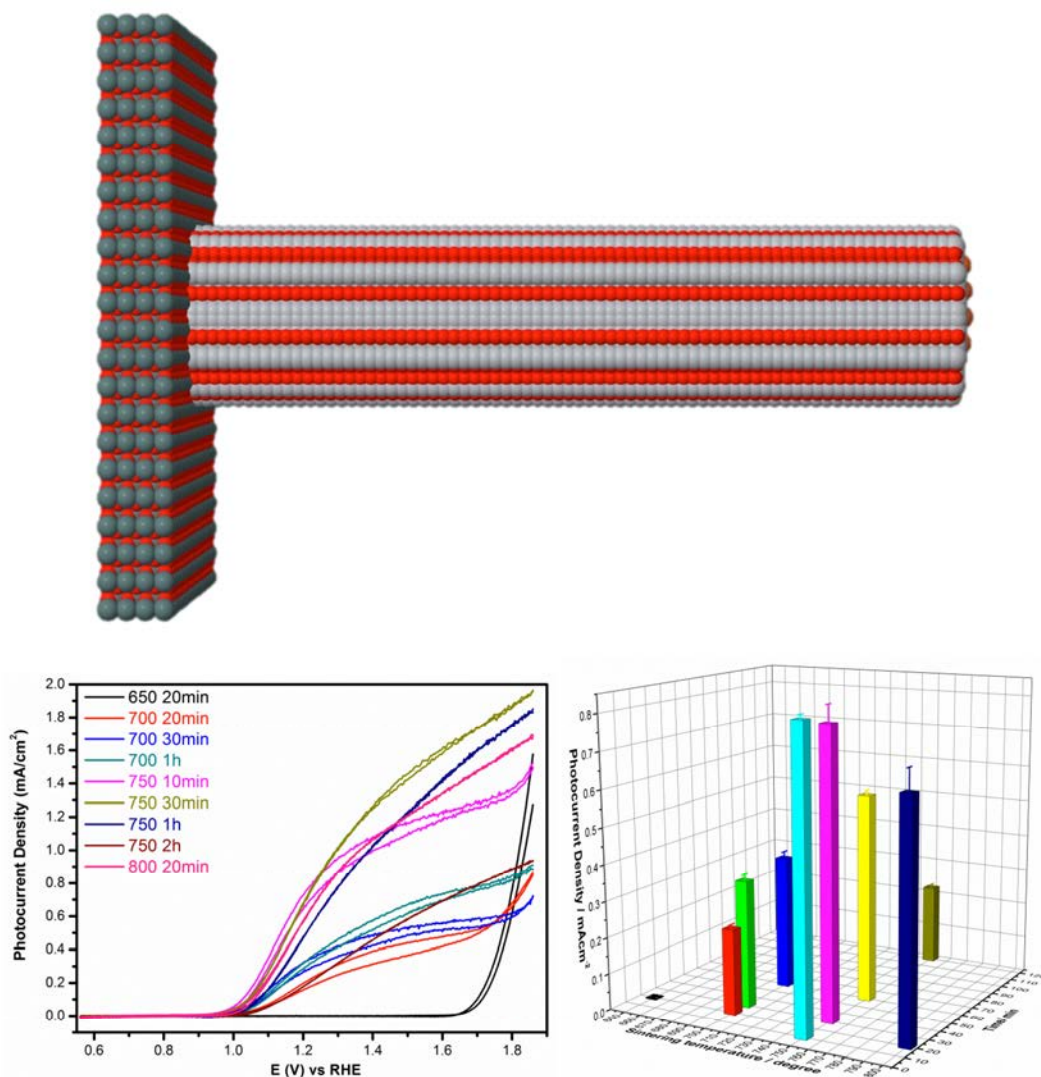
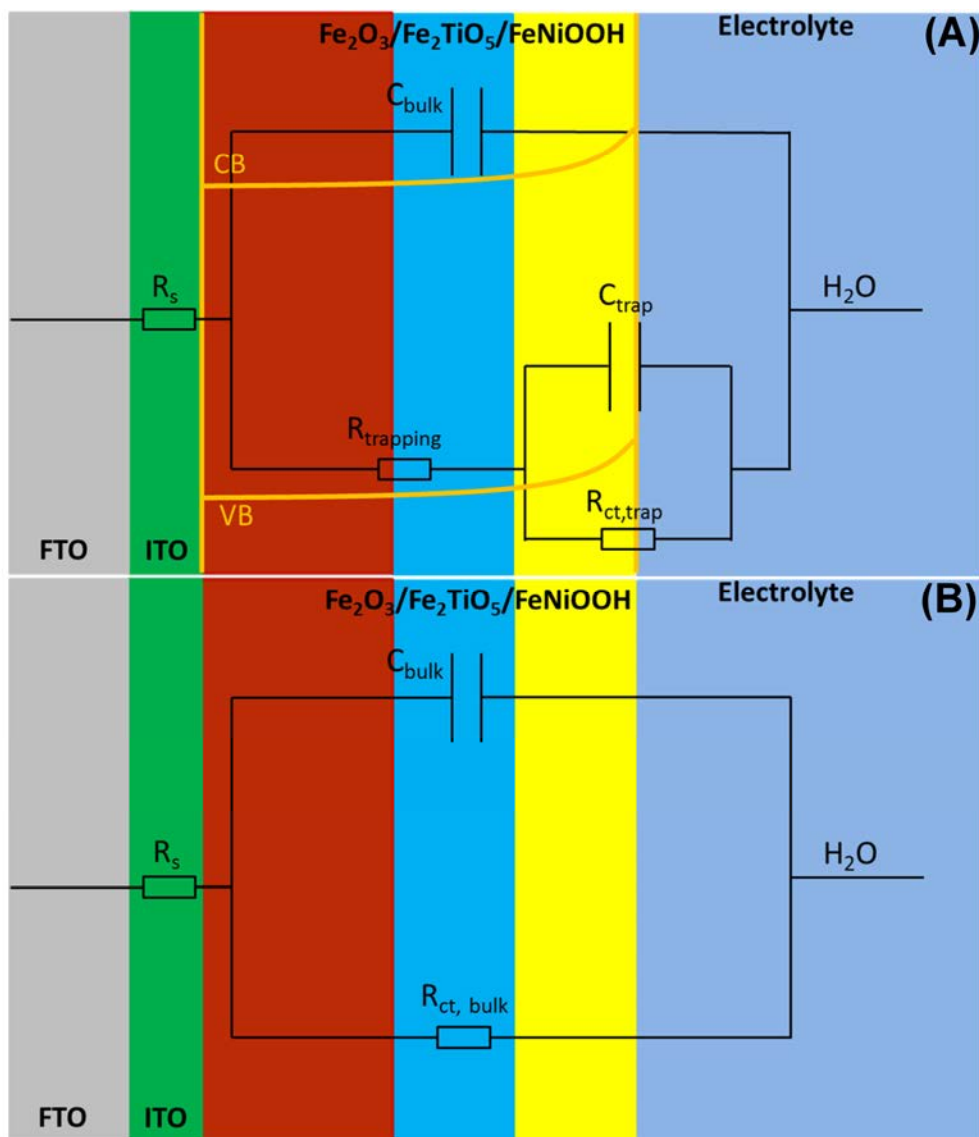


Figure S27. Top: the atomic model for the optimized $\text{Fe}_2\text{O}_3/\text{Fe}_2\text{TiO}_5$ -30 cycles electrode. Bottom: Left: CV curves of the $\text{Fe}_2\text{O}_3/\text{Fe}_2\text{TiO}_5$ -30 cycles electrodes with different sintering conditions under illumination; Right: the photocurrent density at 1.23 V vs. RHE related to the sintering conditions (the error bar stemmed from the standard deviation of statistic data collected at least three repeated electrodes).

As a proof of the necessity of ITO underlayer between FTO substrate and $\text{Fe}_2\text{O}_3/\text{Fe}_2\text{TiO}_5$ nanowires, the $\text{Fe}_2\text{O}_3/\text{Fe}_2\text{TiO}_5$ -30 cycles electrode was also fabricated and the sintering condition has been optimized, as presented in Figures S26 and S27. According to Figure S27, the optimization sintering condition for the $\text{Fe}_2\text{O}_3/\text{Fe}_2\text{TiO}_5$ -30 cycles electrode is 750°C for 30 min and the corresponding photocurrent is 0.81 mA cm⁻², which is much lower than 1.56 mA cm⁻² of the ITO/ $\text{Fe}_2\text{O}_3/\text{Fe}_2\text{TiO}_5$ -30 cycles electrode and thus further confirm the beneficial function of the ITO underlayer.



Schematic S1. A: Equivalent circuit (EC) for the charge transfer process of hematite composite under illumination, the hematite composite/electrolyte interface is mediated by surface states. R_s , resistance associated with the electric contacts of the electrode, electrolyte, etc. R_{trapping} , resistance associated with charge trapping at surface states. C_{bulk} , capacitance associated with charge accumulation in the bulk. $R_{\text{ct, trap}}$, resistance associated with the charge transfer process from surface states. C_{trap} , capacitance associated with charge accumulation on the surface states. B: simple Randles circuit for the charge transfer process of hematite composite under dark. R_s , resistance associated with the electric contacts of the electrode, electrolyte, etc. In this case, the $C_{\text{ct,trap}}$ and R_{ct} are eliminated because there is no surface states mediated process under dark.

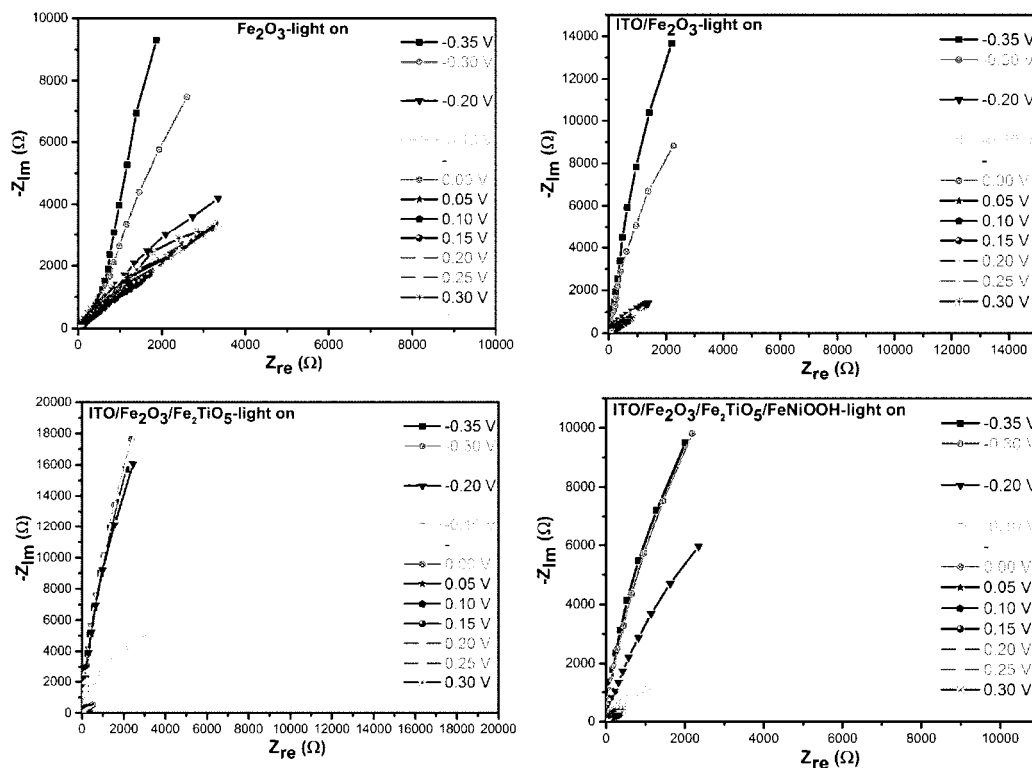


Figure S28. Nyquist (Imaginary vs. Real component of impedance) plots under light illumination of the Fe_2O_3 , ITO/Fe_2O_3 , $ITO/Fe_2O_3/Fe_2TiO_5$, and $ITO/Fe_2O_3/Fe_2TiO_5/FeNiOOH$ electrodes at -0.35, -0.3, -0.25, -0.2, -0.15, -0.1, -0.05, 0.00, 0.05, 0.10, 0.15, 0.20, 0.25, 0.30 and 0.35 V vs Ag/AgCl reference electrode. (Electrolyte: 1 M NaOH. AC amplitude: 5 mV. Frequency range: 100 mHz - 1MHz.)

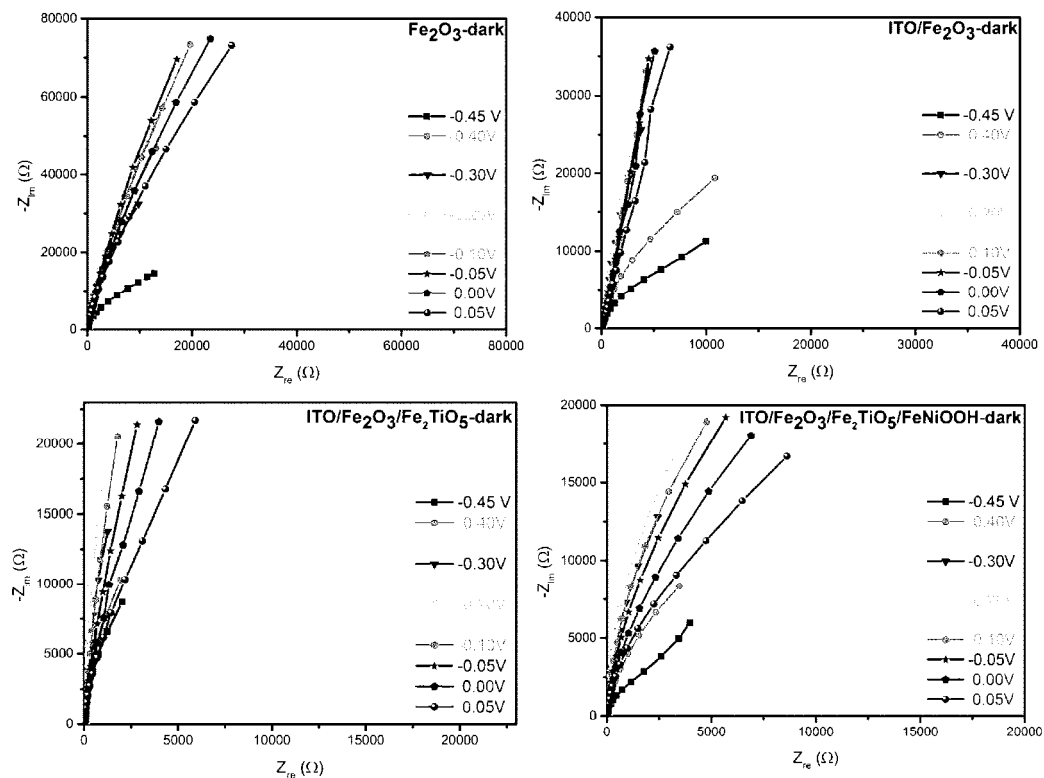


Figure S29. Nyquist (Imaginary vs. Real component of impedance) plots in the dark of the Fe_2O_3 , ITO/Fe_2O_3 , $ITO/Fe_2O_3/Fe_2TiO_5$, and $ITO/Fe_2O_3/Fe_2TiO_5/FeNiOOH$ electrodes at -0.45, -0.4, -0.35, -0.3, -0.25, -0.2, -0.15, -0.10, -0.05, 0.00 and 0.05 V vs Ag/AgCl reference electrode. (Electrolyte: 1 M NaOH. AC amplitude: 5 mV. Frequency range: 100 mHz - 1MHz.)

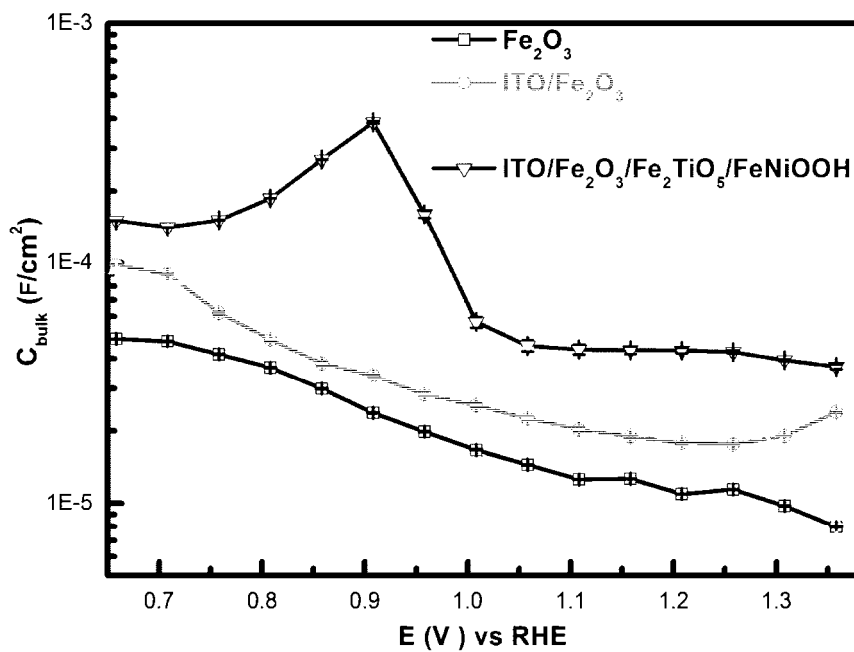


Figure S30. C_{bulk} of the Fe_2O_3 , $\text{ITO}/\text{Fe}_2\text{O}_3$, $\text{ITO}/\text{Fe}_2\text{O}_3/\text{Fe}_2\text{TiO}_5$, and $\text{ITO}/\text{Fe}_2\text{O}_3/\text{Fe}_2\text{TiO}_5/\text{FeNiOOH}$ electrodes as a function of the applied potential obtained from fitting EIS data in contact with 1M NaOH electrolytes under 1 sun illumination. Error bars stem from the goodness of the EIS data fittings.

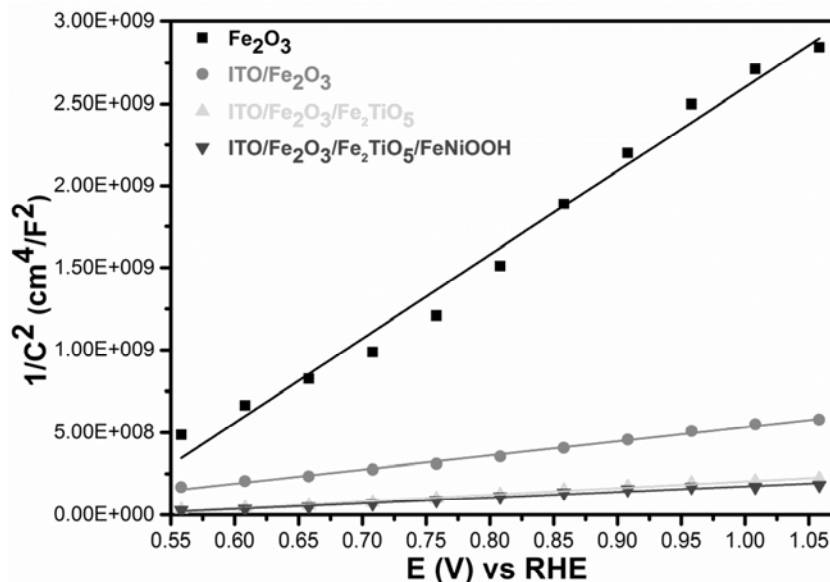


Figure S31. Mott-Schottky plots (C^{-2} vs. E) of the Fe_2O_3 , ITO/ Fe_2O_3 , ITO/ $\text{Fe}_2\text{O}_3/\text{Fe}_2\text{TiO}_5$, and ITO/ $\text{Fe}_2\text{O}_3/\text{Fe}_2\text{TiO}_5/\text{FeNiOOH}$ electrodes. Each point was obtained upon fitting the corresponding Nyquist plot at each potential in the dark to a classic Randles circuit (i.e. resistance and capacitance in parallel). Linear fittings (obtained in the 0.55-1.05 V vs. RHE potential range) are also depicted on each case. Electrolyte: 1 M NaOH. AC amplitude: 5 mV. Frequency range: 100 mHz - 1 MHz.

In order to gain further information on the bulk of hematite nanowires, impedance measurements were performed in the dark to derive the corresponding Mott-Schottky plots. Upon fitting the Nyquist plots to a Randles circuit (Schematic 1B), the potential-dependent capacitances were plotted following the Mott-Schottky model (C^{-2} vs. E , Fig. S31). When this model holds, equation (1) is used to fit the plots:⁶

$$\frac{1}{C^2} = \frac{2}{e\epsilon\epsilon_r N_D} (E - E_{fb} - \frac{kT}{e}) \quad (1)$$

where N_D is the charge donor density (cm^{-3}), E_{fb} is the flat band potential (V), ϵ is the vacuum permittivity ($8.85 \times 10^{-12} \text{ F m}^{-1}$), ϵ_r is the relative dielectric constant of hematite ($\epsilon_r = 32$), k is the Boltzmann constant ($1.38 \times 10^{-23} \text{ J K}^{-1}$) and T is the absolute temperature (K).

Table S1. Flat band potential values (E_{fb}), bulk donor densities (N_D) and total surface state density (N_{ss}) of the Fe_2O_3 , ITO/ Fe_2O_3 , ITO/ $\text{Fe}_2\text{O}_3/\text{Fe}_2\text{TiO}_5$, and ITO/ $\text{Fe}_2\text{O}_3/\text{Fe}_2\text{TiO}_5/\text{FeNiOOH}$ electrodes. E_{fb} and N_D values were respectively estimated from the x-intercepts (at $C^{-2} = 0$) and slopes of the Mott-Schottky plots (Figure S31).

Samples	N_D/cm^{-3}	$E_{fb}/\text{V vs. RHE}$	N_{ss}/cm^{-2}
Fe_2O_3	4.60E+18	0.465	9.53E+14
ITO/ Fe_2O_3	2.75E+19	0.353	1.54E+15
ITO/ $\text{Fe}_2\text{O}_3/\text{Fe}_2\text{TiO}_5$	5.80E+19	0.475	2.17E+15
ITO/ $\text{Fe}_2\text{O}_3/\text{Fe}_2\text{TiO}_5/\text{FeNiOOH}$	6.89E+19	0.468	1.23E+16

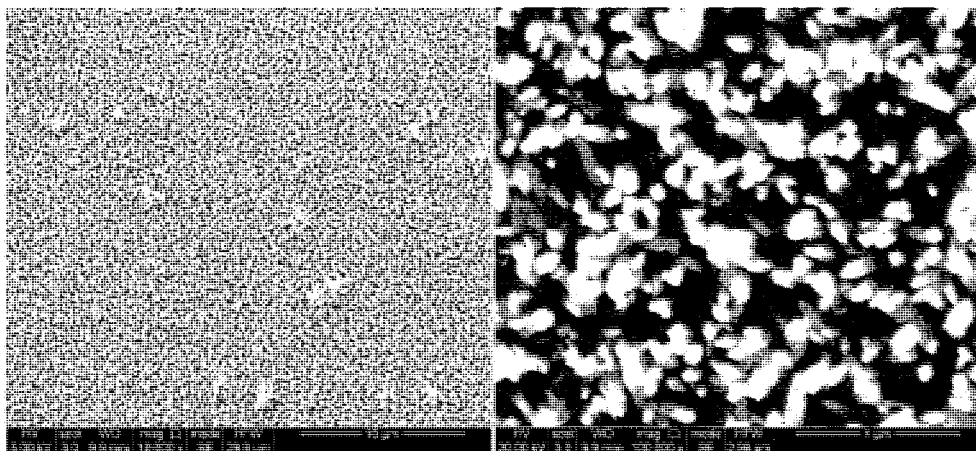


Figure S32. SEM images of FeOOH nanowires on FTO substrate.

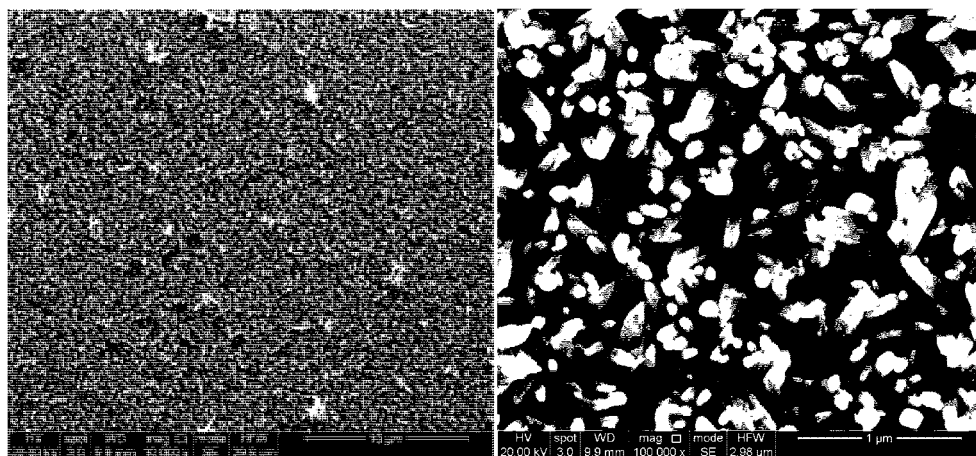
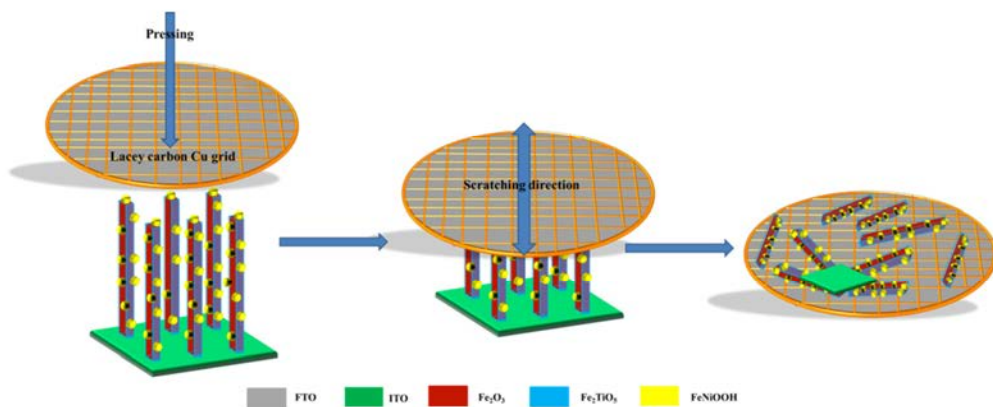


Figure S33. SEM images of FeOOH nanowires on FTO substrate after sintering at 550°C for 2h.



Schematic S2 The sample preparation process of FTO/ITO/Fe₂O₃/Fe₂TiO₅/FeNiOOH electrode for TEM and STEM-EELS characterization.

In order to avoid the chemical contamination from the solvent (ethanol, hexane etc.) and intensive mechanical damage (ultrasonic dispersion) during the TEM sample preparation, we directly scratched these nanowires from the as-prepared electrode. As displayed in schematic S2, the fragile nanowires were scratched and dispersed randomly on a lacy carbon Cu grid. It should be pointed out that some of the scratched nanowires disconnect from the ITO matrix, meanwhile other nanowires were still adhered to the ITO matrix.

Table S2. Photoelectrochemical performance comparison of hematite based electrodes.

Reference no.	Materials	Fabrication methods	Photocurrent at 1.23 V vs RHE (mA/cm ²)
[6]	Fe ₂ O ₃ /Fe ₂ TiO ₅	Sol-gel	1.35
[12]	Fe ₂ O ₃ /molecular Ir catalyst	Hydrothermal, soaking reaction	0.66
[13]	Fe ₂ O ₃ /NiO _x	Hydrothermal, photoelectrodeposition	0.6
[14]	Fe ₂ O ₃ /Fe-Pi	Hydrothermal, furnace heating	0.8
[15]	Fe ₂ O ₃ /TiO ₂	Hydrothermal, CBD	1.3
[16]	Fe ₂ O ₃ /graphene	Hydrothermal, CBD	0.5
[17]	Fe ₂ O ₃	Hydrothermal	0.8
[18]	C/Co ₃ O ₄ -Fe ₂ O ₃	Hydrothermal, electrodeposition	1.48
[19]	Fe ₂ O ₃ /TiO ₂	Thermal oxidation, lithography	0.45
[20]	Mesoporous Fe ₂ O ₃	Chemical etching	0.61
[21]	Fe ₂ O ₃ film	Spray pyrolysis	0.65
[22]	Fe ₂ O ₃ /FeOOH	PLD, photodeposition	0.85
[23]	TiO ₂ /Fe ₂ O ₃ /Ni(OH) ₂	ALD, hydrothermal, dipping	0.3
[24]	Fe ₂ O ₃ /TiO _x /FeOOH	Hydrothermal, electrodeposition	1.5
[25]	Co-N _x P doped carbon/graphene/Fe ₂ O ₃	Hydrothermal, chemical bath	2.15
[26]	Acid etched Fe ₂ O ₃	Chemical etching	1.0
[27]	Fe ₂ O ₃ /FeOOH	Hydrothermal, chemical bath	1.21
[28]	Fe ₂ O ₃ /TiO ₂	PE-CVD, ALD	1.8
[29]	Fe ₂ O ₃ /ZrO ₂ /Co-Pi	Hydrothermal, ALD, photo-electrodeposition	1.87
[30]	Fe ₂ O ₃ /IrO _x	Hydrothermal, Soaking	0.7
[31]	Fe ₂ O ₃	Electrodeposition	1.0
[32]	Fe ₂ O ₃ /Fe ₂ TiO ₅	Hydrothermal	1.4
[33]	Fe ₂ O ₃ /cobalt phosphate	Reactive ballistic and photo depositions	2.0
[34]	Fe ₂ O ₃ /NiO _x	Hydrothermal, photodeposition	0.6
[35]	Fe ₂ O ₃ /SiO ₂ /Sn doping	Hydrothermal, Chemical bath	2.0
Our work	ITO/Fe ₂ O ₃ /Fe ₂ TiO ₅ /FeNiOOH	Sputtering, Hydrothermal, ALD, photoelectrodeposition	2.20

References:

- [1] Q. H. Liu, J. F. He, T. Yao, Z. H. Sun, W. R. Cheng, S. He, Y. Xie, Y. H. Peng, H. Cheng, Y. F. Sun, Y. Jiang, F. C. Hu, Z. Xie, W. S. Yan, Z. Y. Pan, Z. Y. Wu, S. Q. Wei, *Nature Communications*, 2014, **5**, 5122.
- [2] J. Y. C. Chen, L. N. Dang, H. F. Liang, W. L. Bi, J. B. Gerken, S. Jin, E. E. Alp, S. S. Stahl, *J. Am. Chem. Soc.* 2015, **137**, 15090-15093.
- [3] F. Y. Ning, M. F. Shao, S. M. Xu, Y. Fu, R. K. Zhang, M. Wei, D. G. Evans, X. Duan, *Energy Environ. Sci.*, 2016, **9**, 2633-2643.
- [4] M. Görlin, P. Chernev, J. F. d. Araújo, T. Reier, S. Drespe, B. Paul, R. Krähnert, H. Dau, P. Strasser, *J. Am. Chem. Soc.* 2016, **138**, 5603-5614.
- [5] D. Friebe, M. W. Louie, M. Bajdich, K. E. Sanwald, Y. Cai, A. M. Wise, M. J. Cheng, D. Sokaras, T. C. Weng, R. Alonso-Mori, R. C. Davis, J. R. Bargar, J. K. Nørskov, A. Nilsson, A. T. Bell, *J. Am. Chem. Soc.* 2015, **137**, 1305-1313.
- [6] D. M. Satoca, M. Bartsch, C. Fabrega, A. Genç, S. Reinhard, T. Andreu, J. Arbiol, M. Niederberger, J. R. Morante, *Energy Environ. Sci.*, 2015, **8**, 3242-3254.
- [7] L. J. Han, P. Y. Tang, A. Reyes-Carmona, B. Rodriguez-Garcia, M. Torrens, J. R. Morante, J. Arbiol, J. R. Galan-Mascaros, *J. Am. Chem. Soc.*, 2016, **138**, 16037-16045.
- [8] F. Song, X. Hu, *Nat. Commun.* 2014, **5**, 4477.
- [9] Y. Zhao, X. Jia, G. Chen, L. Shang, G. I. Waterhouse, L. Z. Wu, C. H. Tung, D. O'Hare, T. Zhang, *J. Am. Chem. Soc.* 2016, **138**, 6517-6524.
- [10] T. W. Kim, K. S. Choi, *Science*, 2014, **343**, 990-994.
- [11] L. Wang, F. Dionigi, N. T. Nguyen, R. Kirchgeorg, M. Gliech, S. Grigorescu, P. Strasser, P. Schmuki, *Chem. Mater.* 2015, **27**, 2360-2366.
- [12] W. Li, S.W. Sheehan, D., Y. He, X. Yao, R. L. Grimm, G. W. Brudvig, D. W. Wang, *Angew. Chem. Int. Ed.* 2015 **54**, 11428-11432.
- [13] F. Malara, F. Fabbri, M. Marelli, A. Naldoni, *ACS Catal.* 2016, **6**, 3619-3628.
- [14] Z. F. Hu, Z. R. Shen, J. C. Yu, *Chem. Mater.* 2016, **28**, 564-572.
- [15] Y. G. Li, X. L. Wei, B. W. Zhu, H. Wang, Y. X. Tang, T. C. Sum, X. D. Chen, *Nanoscale*, 2016, **8**, 11284-11290.
- [16] S. X. Liu, L. X. Zheng, P. P. Yu, S. C. Han, X. S. Fang, *Adv. Funct. Mater.* 2016, **26**, 3331-3339.
- [17] Y. C. Zhang, H. N. Zhang, H. W. Ji, W. H. Ma, C. C. Chen, J. C. Zhao, *J. Am. Chem. Soc.*, 2016, **138**, 2705-2711.
- [18] P. Zhang, T. Wang, X.X. Chang, L. Zhang, J. L. Gong, *Angew. Chem. Int. Ed.* 2016, **55**, 5851-5855.
- [19] B. Iandolo, B. Wickman, E. Svensson, D. Paulsson, Anders Hellman, *Nano Lett.*, 2016, **16**, 2381-2386.
- [20] C. W. Wang, S. Yang, W. Q. Fang, P. Liu, H. J. Zhao, H. G. Yang, *Nano Lett.*, 2016, **16**, 427-433.
- [21] P. Dias, A. Vilanova, T. Lopes, L. Andrade, A. Mendes, *Nano Energy*, 2016, **23**, 70-79.
- [22] Q. Yu, X. G. Meng, T. Wang, P. Li, J. H. Ye, *Advanced Functional Materials*, 2015, **25**, 2686-2692.
- [23] L. Steier, J.S. Luo, M. Schreier, M. T. Mayer, T. Sajavaara, M. Grätzel, *ACS Nano*, 2015, **9**, 11775-11783.
- [24] I. S. Cho, H. S. Han, M. Logar, J. Park, X. L. Zheng, *Adv. Energy Mater.* 2015, 1501840.
- [25] Y. Hou, M. Qiu, T. Zhang, J. Ma, S. H. Liu, X. D. Zhuang, C. Yuan, X. L. Feng, *Advanced Materials*, 2017, **29**, 1604480.
- [26] Y. Yang, M. Forster, Y.C. Ling, G.M. Wang, T. Zhai, Y.X. Tong, A. J. Cowan, Y. Li, *Angew. Chem. Int. Ed.*, 2016, **55**, 3403-3407.
- [27] J. Y. Kim, D. H. Youn, K. Kang, J. S. Lee, *Angew. Chem. Int. Ed.*, 2016, **55**, 10854-10858.
- [28] A. Mettenbörgera, Y. Gönüllüa, T. Fischera, T. Heisiga, A. Sasinskaa, C. Maccatob, G. Carrarob, C. Sadac, D. Barrecad, L. Mayrhofere, M. Moselere, A. Helde, S. Mathur, *Nano Energy*, 2016, **19**, 415-427.
- [29] C. C. Li, A. Li, Z. B. Luo, J. J. Zhang, X. X. Chang, Z. Q. Huang, T. Wang, J. L. Gong, *Angew. Chem. Int. Ed.*, 2017, **56**, 4214-4219.
- [30] W. Li, D. He, S. W. Sheehan, Y.M. He, J. E. Thorne, X.H. Yao, G. W. Brudvig, D.W. Wang, *Energy Environ. Sci.*, 2016, **9**, 1794-1802.
- [31] O. Zandi, A. R. Schon, H. Hajibabaei, T.W. Hamann, *Chem. Mater.*, 2016, **28**, 765-771.
- [32] P. S. Bassi, R. P. Antony, P. P. Boix, Y.N. Fang, J. Barber, L. H. Wong, *Nano Energy*, 2016, **22**, 310-318.
- [33] Z.B. Luo, C.C. Li, S. S. Liu, T. Wang, J. L. Gong, *Chem. Sci.*, 2017, **8**, 91-100.
- [34] F. Malara, F. Fabbri, M. Marelli, A. Naldoni, *ACS Catal.* 2016, **6**, 3619-3628.
- [35] M. Y. Li, Y. Yang, Y. C. Ling, W. T. Qiu, F.X.Wang, T. Y. Liu, Y. Song, X. X. Liu, P. P. Fang, Y. X. Tong, Y. Li, *Nano Lett.*, 2017, **17**, 2490-2495.

Role of Bismuth in the Electrokinetics of Silicon Photocathodes for Solar Rechargeable Vanadium Redox Flow Batteries

Cristina Flox,^[a] Sebastián Murcia-López,^{*,[a]} Nina M. Carretero,^[a] Carles Ros,^[a] Juan R. Morante,^[a, b] and Teresa Andreu^[a]

The ability of crystalline silicon to photoassist the V^{3+}/V^{2+} cathodic reaction under simulated solar irradiation, combined with the effect of bismuth have led to important electrochemical improvements. Besides the photovoltage supplied by the photovoltaics, additional decrease in the onset potentials, high reversibility of the V^{3+}/V^{2+} redox pair, and improvement in the electrokinetics were attained thanks to the addition of bismuth. In fact, Bi^0 deposition has shown to slightly decrease the photocurrent, but the significant enhancement in the charge transfer, reflected in the overall electrochemical performance clearly justifies its use as additive in a photoassisted system for maximizing the efficiency of solar charge to battery.

The electrical conversion and storage of solar energy is a crucial target for assuring the world energy supply in the long term. Because of the current maturity of the photovoltaic (PV) technology, systems devoted to PV electricity or to photoelectrochemical (PEC) approaches for water splitting have been strongly developed in the last years.^[1,2] However, because of the sluggish kinetics associated to the water oxidation reaction^[3] and of inherent limitations in the H_2 economy, the possibility of storing energy by coupling PV systems to other kind of redox pairs has recently attracted more attention, giving rise to the so-called solar-powered electrochemical energy storage (SPEES),^[4] in which two systems, a PV and a battery, are integrated in a single device with potential advantages such as charging by using solar light.

Among other technologies, the vanadium redox flow batteries (VRFBs) are a robust alternative to be integrated into SPEES with several advantages: decoupling of energy and power, use of the same element in both half-reactions and possibility of large-scale development. Previously, some studies reported the combination of PEC systems in VRFBs, such as TiO_2 ^[5] and TiO_2/WO_3 photoanodes,^[6] and CdS thin films in tandem with dye-


sensitized solar cells.^[7] Particularly in the second case, an unbiased system reaching a promising state of charge was achieved, although the long-term stability in acid electrolyte and the low charge current attained by the semitransparent CdS film were substantial limitations. These systems also have significant restraints associated to the low photon absorption in comparison to other absorbers. Crystalline silicon has also been integrated as light absorber in a quinone/bromine bias-free redox flow battery.^[8] For that purpose, surface-buried junctions were used as photoelectrodes in both half-reactions attaining the necessary charge voltage upon illumination (photovoltage ≈ 1 V) in a system involving a PEC cell and a RFB. Despite the promising results, it should be pointed out that the associated cell voltage for these organic redox couples can only attain a maximum cell voltage of ≈ 0.89 V, which is lower than that of VRFBs.^[9]

One important aspect to consider in the design of this kind of SPEES is the overall cell voltage required to be supplied by the semiconductor. Interestingly, the photocharge process in VRFBs has only been applied to the anodic reaction (VO^{2+}/VO_2^+), even in full-cell configuration. Although both half-reactions have inherent limitations and the kinetics associated to each one strongly depends on the features of the used electrode, the negative reaction (V^{3+}/V^{2+}) can be a determining step because of parasitic reactions such as the hydrogen evolution reaction (HER),^[10] which is kinetically more favored and might cause imbalances and decrease in performance, and because of easy reoxidation of V^{2+} under normal operating conditions. Regarding this aspect, it is possible to improve the overall performance of SPEES systems by following the strategies developed in VRFBs, which is where electrochemical studies related to the interface control are essential. Bismuth-decorated graphitic felt was initially proposed by González et al. for improving the anodic reaction.^[11] However, most of the recent reports based on bismuth systems in VRFBs are focused in the negative rather than in the positive side.^[12] Bismuth species dissolved in aqueous acidic media were shown by Li et al.^[13] to improve the negative half-cell in VRFBs by promoting the redox reactions between the V^{3+}/V^{2+} pair. In particular, the intermediate BiH_x species formed in bismuth-decorated graphitic felt was proposed to catalyze the V^{3+}/V^{2+} pair rather than the HER.^[12]

Here, we report for the first time on the photoassisted negative half-reaction (V^{3+}/V^{2+}) in presence of bismuth and its role in the electrochemistry of the system, by using a photocathode based on a n^+ -p silicon buried junction (see the Sup-

[a] Dr. C. Flox, Dr. S. Murcia-López, Dr. N. M. Carretero, C. Ros, Prof. Dr. J. R. Morante, Dr. T. Andreu
IREC, Catalonia Institute for Energy Research
Jardins de les Dones de Negre 1, Sant Adrià de Besòs, 08930 (Spain)
E-mail: smurcia@irec.cat

[b] Prof. Dr. J. R. Morante
Faculty of Physics
University of Barcelona
Martí i Franquès 1, Barcelona, 08028 (Spain)

 Supporting Information and the ORCID identification number(s) for the author(s) of this article can be found under:
<https://doi.org/10.1002/cssc.201701879>.

porting Information for details), protected by a 100 nm TiO₂ layer deposited by atomic layer deposition (TiO₂/n⁺-p-Si).^[14] Initially, to analyze the effect of bismuth in the direct-charge injection, n⁺ degenerated silicon cathodes (TiO₂/n⁺-Si) were also evaluated in different media. These results under dark conditions are shown in Figure 1A. In the first situation, the mea-

E_{onset} for reaction 2 was found, moving to $-0.2 V_{\text{RHE}}$. Additionally, besides the obvious increase in the peak areas, a significant improvement in the reversibility of the V³⁺/V²⁺ redox pair is seen, increasing from the 13 to 69%.

After testing the electrocatalytic behavior of the cathodes in dark conditions, the TiO₂/n⁺-p-Si photocathodes were evaluated under illumination as shown in Figure 1B. First, a potential shift for all redox reactions toward the anodic direction was attained owing to the photovoltage (close to 0.6 V) provided by the TiO₂/n⁺-p-Si photocathode. Second, similar behaviors to the dark conditions were found in presence and absence of BiCl₃: poor reversibility for the V³⁺/V²⁺ redox pair in the oxidative part (reaction 2'), and a significant improvement after Bi³⁺ addition, increasing from 4.7 to 92.4% (see Table S2). The same improvement is translated into a decrease of the peak separation, changing from 0.76 to 0.22 V in presence of bismuth. Third, the redox peaks associated to the Bi³⁺/Bi⁰ reactions (in black) measured in absence of V³⁺ are clearly observed and besides the potential shift induced by the the photovoltage, a decrease in the separation of peaks is also evidenced in comparison to the dark test with the cathode, going from 0.31 to 0.08 V. Fourth, regarding the current differences between the dark current (*i*) and photocurrent (*j*), a significant variation can be observed in the voltammogram in absence of BiCl₃. On the one hand, a cathodic photocurrent of around 2.6 mA cm⁻² at the peak maximum for the V³⁺/V²⁺ reaction is attained, whereas the cathode in dark only provides 1.2 mA cm⁻² at much more negative potential. It is important to highlight that almost negligible currents are obtained with the TiO₂/n⁺-p-Si photocathode under dark (dotted line in Figure 1B), indicating that all the current is due to a photoactivation mechanism. On the other hand, in presence of bismuth, the differences in the current densities are less pronounced, changing from 2.6 to 2.5 mA cm⁻² under dark and light conditions, respectively, for the V³⁺/V²⁺ reduction. However, the reverse V²⁺/V³⁺ reaction is more positively affected by bismuth addition as previously stated and a concomitant effect with light is observed. In that sense, the anodic current for this reaction increases from 0.6 to 1.3 mA cm⁻² with the photocathode. It is worth noting that the Bi³⁺/Bi⁰ redox reactions also are promoted under illumination, which may have a concomitant effect on the vanadium cathodic processes. Despite this improvement it is obvious that the deposition of Bi⁰ on the surface of the electrode might limit the photon absorption and decrease the saturation photocurrent at more cathodic potentials. This effect is clearly seen in the inset of Figure 1B, where the two conditions are evaluated (without and with BiCl₃) at potentials reaching the HER. Therefore, photocurrents close to saturation of ≈11.8 and 8.6 mA cm⁻² at $-0.6 V_{\text{RHE}}$ were attained in absence and presence of Bi, respectively.

Blank voltammetries in the absence of V³⁺ were performed with the TiO₂/n⁺-p-Si photocathodes to determine the effect of Bi³⁺ on the HER. Under those conditions, the presence of BiCl₃ showed to increase the overpotential for HER with respect to the measurement with supporting electrolyte only (see Figure S1). Conversely, in a V³⁺ electrolyte, bismuth showed to have less effect on the HER (inset of Figure 1). The

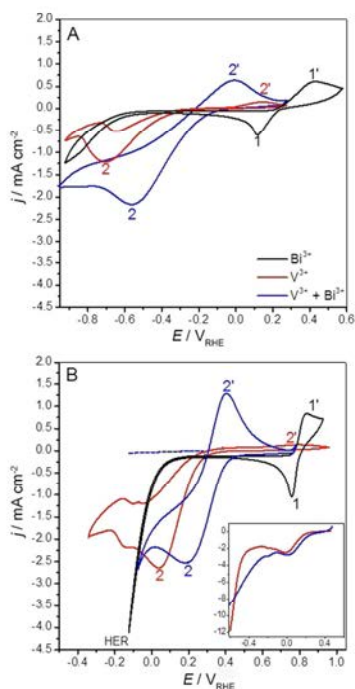


Figure 1. Voltammograms obtained with the TiO₂/n⁺-Si cathodes in dark (A) and with the TiO₂/n⁺-p-Si photocathodes under 1 sun illumination (B), in different media: 0.05 M V³⁺ or 0.05 M V³⁺ and 1 mM Bi³⁺ using 1 M H₂SO₄ as supporting electrolyte. The dotted line corresponds to the measurement with the TiO₂/n⁺-p-Si in dark conditions. Inset: curves obtained with the photocathodes in V³⁺ electrolyte without (red) and with (blue) Bi³⁺, at more negative potentials.

surement was performed with V³⁺ in H₂SO₄ electrolyte and without BiCl₃. Under that situation, the V³⁺/V²⁺ reaction (indicated by number 2) presents an onset potential (E_{onset}) of around $-0.45 V_{\text{RHE}}$ (see Table S1), whereas the reverse V²⁺/V³⁺ process (indicated as 2') is almost negligible, showing a significant peak separation. In this case, there is a very poor reversibility with the cathode. In presence of BiCl₃ dissolved in the supporting electrolyte (without any vanadium species), peaks corresponding to the Bi³⁺/Bi⁰ pair reactions (identified as 1 and 1' in black, occurring at potentials close to the expected value $E^0 \approx 0.05 V_{\text{Ag/AgCl}}$) are observed at relatively more anodic potentials, showing that in presence of Bi³⁺, the reduction and deposition of Bi⁰ on the cathode surface is the first step. When BiCl₃ was added to the V³⁺ electrolyte, an anodic shift in the

difference in both situations is the copresence of V^{3+} in the electrolyte. Therefore, the influence of bismuth on the HER depends also on the V^{3+} species. This situation can be explained through the reactions proposed by Suárez et al.,^[12] related to the electrochemical formation of BiH_x species, which possess high reducing power and are able to reduce V^{3+} and liberate H^+ , according to reactions (1) and (2). Therefore, this is not a competitive reaction with the HER. On the contrary, in absence of V^{3+} , the deposition of Bi^0 and even the possible formation of BiH_x do compete with the HER, besides passivating the electrode surface.



It is also clear that the TiO_2 passivation layer can also play a role on the HER. It has been demonstrated that it can effectively hinder this reaction thanks to the strong proton adsorption on the TiO_2 , which might restrict H_2 formation.^[10] However, besides having an effect in this aspect, TiO_2 layers have been used as protective layers of silicon photovoltaics, thanks to its good stability at different pH conditions, especially when it is not polarized at very negative potentials.^[14] Interestingly, the obtained results with the photocathode in presence of bismuth evidence that less negative voltages are necessary for performing the electrochemical reaction, so that less harsh conditions are necessary during cycling, assuring better stability for the photoelectrode and the TiO_2 protective layer.

After these tests, measurements with the photocathodes were performed under chopped illumination (Figure S2). Besides the shift in the potentials also previously observed, a sharp increase in the cathodic photocurrent at higher polarization in the absence of bismuth is seen. In fact, in the pulse represented in the inset of Figure S2, contributions from the two redox reactions (V^{3+}/V^{2+} and HER) can be distinguished at potentials below $-0.5 V_{RHE}$. The transient curves for this situation clearly show that despite the higher photocurrent in comparison to the electrolyte with Bi^{3+} , the system suffers important decays due to surface recombination. On the contrary, when bismuth is added, more stable transient curves are obtained as bismuth favors the V^{3+}/V^{2+} redox reaction. For instance, at around $-0.2 V_{RHE}$ in only 2 s, the photocurrent decays in 44 and 2% in the absence and presence of Bi^{3+} , respectively. So, even when the necessary potential for the V^{3+}/V^{2+} reduction decreases in the photoassisted process with the TiO_2/n^+-p-Si (the overpotential at the maximum is ≈ 200 mV lower), there is a stability matter with time.

Chronoamperometric measurements with chopped light at different potentials were also performed to evaluate the stability of the system. Initially, as seen in Figure 2, the zero current values correspond to the dark pulses in which no carriers are generated and no electrochemical reaction occurs. After this, when the illumination is on, it is possible to see that the presence of bismuth stabilizes the photocurrent even at more anodic potential ($0.05 V_{RHE}$). In the measurement without bismuth, the photocurrent shows a clear dependence on the po-

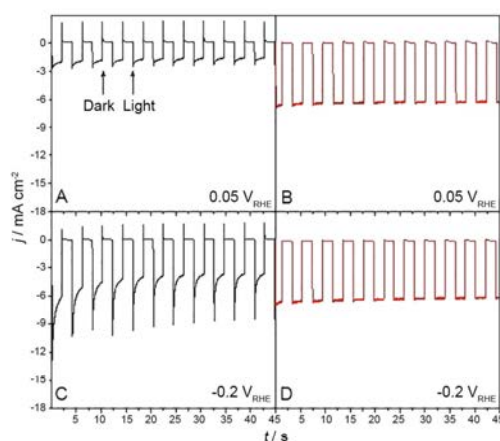


Figure 2. Chronoamperometric measurements at different potentials with chopped illumination in 1 M H_2SO_4 + 0.05 M V^{3+} electrolyte in absence (A), (C), and presence of Bi^{3+} (B), (D).

tential and the values tend to decrease with time. Moreover, the same transient behavior observed in the chopped voltammetry without bismuth is observed.

Bi^0 deposition on the surface of the TiO_2/n^+-p-Si photocathode after cycling is observed (see Figure S3) in the SEM images and EDX analysis. However, despite decreasing the saturation photocurrent, the values are more stable even at low polarization. This transient stability is ascribed to a faster V^{3+}/V^{2+} kinetics which attains for a better charge transfer from the photocathode to the electrolyte, thus decreasing recombination and maintaining the photocurrent with time.

To have a better understanding of the charge transfer after bismuth addition, potentiostatic electrochemical impedance spectroscopy (PEIS) measurements were performed (see the Supporting Information for details). As seen in the Nyquist plot in Figure 3 and Table 1, for the open circuit and illuminated conditions that represent the equilibrium situation, a significant decrease in the charge-transfer resistance (R_{ct}) is observed in presence of Bi^{3+} . Concomitantly, the rate constant (k) is boosted ninety times, indicating a much better electron transfer associated to Bi addition. Similarly, PEIS tests were performed (Figure S4) at the potentials corresponding to the maximum of the V^{3+}/V^{2+} redox reaction under dark and illumination. For both the TiO_2/n^+-p-Si photocathodes and TiO_2/n^+-Si cathodes, much lower R_{ct} values were observed in presence of bismuth (from the width of the semicircle corresponding to the surface charge transfer). In fact, a comparison of the two conditions indicates that the highest resistance enhancement takes place under illumination. In dark, the first semicircle corresponding to the diode is practically the same with and without bismuth, whereas the other one, related to the transfer from the electrode to the electrolyte, decreases in a lower proportion than in the test with light. These results prove that better electrokinetics for the V^{3+}/V^{2+} half-reaction occurs in

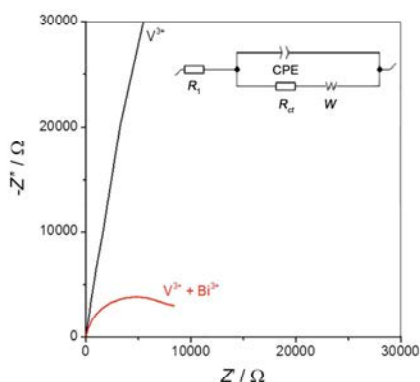


Figure 3. Potentiostatic electrochemical impedance spectroscopy performed with the $\text{TiO}_2/\text{n}^+\text{-p-Si}$ photocathodes under illumination and open circuit conditions, without and with Bi^{3+} . Inset: equivalent circuit used for calculations.

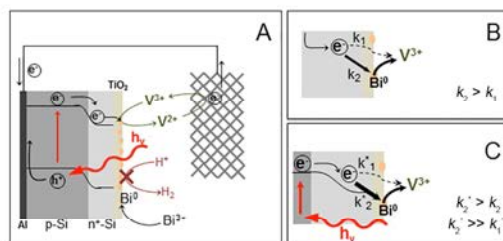
Table 1. Values obtained for R_{ct} , τ , and k from the Nyquist plot and equivalent circuit in Figure 3.

Conditions	R_{ct} [Ω]	$\tau^{[a]}$ [s]	k [s^{-1}]
V^{3+}	8331	0.27	3.60
$\text{V}^{3+} + \text{Bi}^{3+}$	694267	23.1	0.04

[a] Time constant, defined from the RC parallel circuit

presence of bismuth but also highlights that illumination positively contributes to the amelioration of these processes.

As a summary, a scheme illustrating the processes occurring under dark and illuminated conditions is included as Scheme 1. Two important aspects are highlighted: first, the illumination of the $\text{TiO}_2/\text{n}^+\text{-p-Si}$ buried junction leads to electron-hole pair generation, subsequently able to create a built-in photovoltage, which furthers aims to perform the reduction of V^{3+} to V^{2+} ; second, the deposition of Bi^0 on the surface of the electrode improves the electrokinetics of the $\text{V}^{3+}/\text{V}^{2+}$ redox reaction while probably hindering the H_2 formation. This is also beneficial for boosting the VFRB technology to the market as



Scheme 1. Schemes of the half-cell reaction in presence of bismuth with the $\text{TiO}_2/\text{n}^+\text{-p-Si}$ photocathode (A) and the charge-transfer mechanism under dark (B) and illumination (C) conditions.

one of the main drawbacks of this technology is the poor electrochemical activity performed by the negative reaction side. In current systems working without photoassisted processes, the HER directly competes with the $\text{V}^{3+}/\text{V}^{2+}$ reaction, causing imbalances in both compartments, increment of the overall cell polarization, loss of performance limiting the capability rate, and in consequence, low power values. For this reason, controlling the electrochemistry of the process becomes also important in a photoassisted system.

The electrochemical study of photoassisted cathodic side for a $\text{V}^{3+}/\text{V}^{2+}$ redox pair with crystalline silicon under simulated solar irradiation shows that the addition of bismuth leads to important improvements reflected in decreased onset potentials, higher reversibility, and more stable transient photocurrents. A significant enhancement of the electrokinetics is achieved in comparison to the system without bismuth. The importance of studying the interface and of assessing the underlying contributions of different components through electrochemical studies are clear and, in this case, validate the suitability of this kind of approach for operating solar-powered electrochemical energy storage based on vanadium redox flow batteries. The future challenges not only go through the integration of photovoltaics in full devices but also in applying known and new strategies for improving the performance of the storage systems.

Acknowledgements

Authors thank Generalitat de Catalunya for financial support through the CERCA Program, MINECO for additional support by coordinated project ENE2016-80788-C5-5-R and Fundaci3n Ram3n Areces partial funding through BAT-LIMET project. C.R. also thanks MINECO for his FPI grant (BES-2015-071618) and S.M.L. for his Juan de la Cierva, Formaci3n fellowship (FJCI-2014-19745).

Conflict of interest

The authors declare no conflict of interest.

Keywords: bismuth · photobatteries · photocathode · silicon · vanadium

- [1] J. Jia, L. C. Seitz, J. D. Benck, Y. Huo, Y. Chen, J. W. D. Ng, T. Biliir, J. S. Harris, T. F. Jaramillo, *Nat. Commun.* **2016**, *7*, 13237.
- [2] J. Gan, X. Lu, Y. Tong, *Nanoscale* **2014**, *6*, 7142–7164.
- [3] M. Biset-Peir3, S. Murcia-L3pez, C. F3brega, J. R. Morante, T. Andreu, *J. Phys. D* **2017**, *50*, 104003.
- [4] M. Yu, W. D. McCulloch, Z. Huang, B. B. Trang, J. Lu, K. Amine, Y. Wu, *J. Mater. Chem. A* **2016**, *4*, 2766–2782.
- [5] Z. Wei, Y. Shen, D. Liu, F. Liu, *Sci. Rep.* **2017**, *7*, 629.
- [6] D. Liu, Z. Wei, C. J. Hsu, Y. Shen, F. Liu, *Electrochim. Acta* **2014**, *136*, 435–441.
- [7] J. Azevedo, T. Seipp, J. Burfeind, C. Sousa, A. Bienten, J. P. Araujo, A. Mendes, *Nano Energy* **2016**, *22*, 396–405.
- [8] S. Liao, X. Zong, B. Seger, T. Pedersen, T. Yao, C. Ding, J. Shi, J. Chen, C. Li, *Nat. Commun.* **2016**, *7*, 11474.



- [9] P. Leung, A. A. Shah, L. Sanz, C. Flox, J. R. Morante, Q. Xu, M. R. Mohamed, C. P. de León, F. C. Walsh, *J. Power Sources* **2017**, *360*, 243–283.
- [10] J. Vázquez-Galván, C. Flox, C. Fábrega, E. Ventosa, A. Parra, T. Andreu, J. R. Morante, *ChemSusChem* **2017**, *10*, 2089–2098.
- [11] Z. González, A. Sánchez, C. Blanco, M. Granda, R. Menéndez, R. Santamaría, *Electrochem. Commun.* **2011**, *13*, 1379–1382.
- [12] D. J. Suárez, Z. González, C. Blanco, M. Granda, R. Menéndez, R. Santamaría, *ChemSusChem* **2014**, *7*, 914–918.
- [13] B. Li, M. Gu, Z. Nie, Y. Shao, Q. Luo, X. Wei, X. Li, J. Xiao, C. Wang, V. Sprenkle, W. Wang, *Nano Lett.* **2013**, *13*, 1330–1335.
- [14] C. Ros, T. Andreu, M. D. Hernández-Alonso, G. Penelas-Pérez, J. Arbiol, J. R. Morante, *ACS Appl. Mater. Interfaces* **2017**, *9*, 17932–17941.

Manuscript received: October 4, 2017

Revised manuscript received: November 14, 2017

Accepted manuscript online: November 14, 2017

Version of record online: December 18, 2017



Supporting Information

Role of Bismuth in the Electrokinetics of Silicon Photocathodes for Solar Rechargeable Vanadium Redox Flow Batteries

Cristina Flox,^[a] Sebastián Murcia-López,^{*[a]} Nina M. Carretero,^[a] Carles Ros,^[a]
Juan R. Morante,^[a, b] and Teresa Andreu^[a]

cssc_201701879_sm_miscellaneous_information.pdf

Experimental part

Photocathode preparation:

n^+ - p silicon buried junction with a thin layer of TiO_2 deposited by Atomic Layer Deposition (ALD) were used as photocathodes ($\text{TiO}_2/n^+-p\text{-Si}$). The preparation details of this sample is described elsewhere.¹ Briefly, Boron was implanted in a defined surface of a silicon p -type wafer (0.1-0.5 ohm-cm resistivity) and activated by rapid thermal annealing in order to create a 200 nm n^+ region. As back contact, an ohmic contact with a 1 μm Al/0.5%Cu was sputtered. Before the ALD process, a thin Ti film (5 nm) acting as buffer layer was deposited by thermal evaporation, after which the samples were sonicated for 5 min in a 1:1:1 isopropanol, acetone and water mixture. The TiO_2 deposition was carried out in a R200 Picosun ALD system, with TiCl_4 as Ti precursor and H_2O , used in successive pulses at 8 mbar in N_2 atmosphere, with 0.1 and 10 s pulses and purges, respectively. The temperature growth was 300°C and the thickness of the layer 100 nm.

Cathodes consisting in n^+ degenerately doped silicon with the TiO_2 layer were used ($\text{TiO}_2/n^+-\text{Si}$) for simulating the direct injection under dark conditions, during the blank tests.

Samples characterization:

The morphologic and EDX analyses of the samples after cycling were carried out in a Zeiss Auriga FESEM microscope.

(Photo)Electrochemical characterization:

All the electrochemical analyses were performed in a three-electrode cell with $\text{Hg}/\text{HgSO}_4/\text{K}_2\text{SO}_4$ (saturated) and Pt-mesh as reference and counter electrodes, using a VMP3 BioLogic potentiostat. For the photoelectrochemical measurements, a solar simulator with a 300W Xe arc lamp and AM 1.5G filter was used. The power density was calibrated for having $100\text{mW}\cdot\text{cm}^{-2}$ (1 Sun) irradiance.

Potentiostatic electrochemical impedance spectroscopy (PEIS) data were acquired with an alternate current (AC) perturbation of 10 mV in amplitude and a 100 mHz-1 MHz frequency range, both in the dark and under illumination, and under open circuit or selected direct current (DC) potentiostatic conditions.

Different conditions were used during the measurements, including the blank tests. In general, all the mixtures contained 1 M H_2SO_4 as base electrolyte, and some of them also had either 0.05 M V^{3+} , either 1 mM of BiCl_3 as Bi additive or both. All the electrolytes were deaerated before the tests and the (photo)electrochemical tests were performed under N_2 atmosphere.

The corresponding V^{3+} solution was prepared through an electrochemical process in a VREFB single-cell using as catholite and anolyte solution 1 M VOSO_4 (Alfa Aesar) in 3 M H_2SO_4 (Aldrich, 98%) solutions. The resulting solution in catholite part was 1 M V^{3+} in 3 M H_2SO_4 , which is

diluted to obtain the concentration 0.05 M V^{3+} in 1 M H_2SO_4 . The design of the VRFB single-cell has been described in previous published works.²

Table S1. Values obtained in the electrochemical measurements in dark with the $\text{TiO}_2/\text{n}^+\text{-Si}$ cathodes.

Electrolyte	$E_{\text{onset}} (\text{V}^{3+}/\text{V}^{2+}) / V_{\text{RHE}}$	$E_{\text{max}} (\text{V}^{3+}/\text{V}^{2+}) / V_{\text{RHE}}$	$Q (\text{V}^{3+}/\text{V}^{2+}) / \text{mC}\cdot\text{cm}^{-2}$	$Q (\text{V}^{2+}/\text{V}^{3+}) / \text{mC}\cdot\text{cm}^{-2}$	Reversibility (%)	$E_{\text{max}} (\text{Bi}^{3+}/\text{Bi}^0) / V_{\text{RHE}}$
$\text{H}_2\text{SO}_4 + \text{Bi}^{3+}$	-	-	-	-	-	0.12
$\text{H}_2\text{SO}_4 + \text{V}^{3+}$	-0.45	-0.70	6.0	0.8	13%	-
$\text{H}_2\text{SO}_4 + \text{V}^{3+} + \text{Bi}^{3+}$	-0.20	-0.56	8.7	6.0	69%	0.18

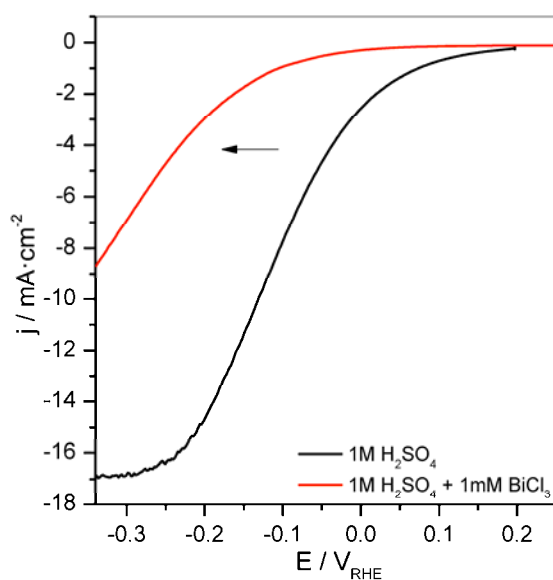


Figure S1. Voltammograms obtained with the $\text{TiO}_2/\text{n}^+\text{-p-Si}$ photocathodes during the blank tests with different electrolytes under illumination.

Table S2. Values obtained in the electrochemical measurements under illumination with the $\text{TiO}_2/\text{n}^+\text{-p-Si}$ photocathodes.

Electrolyte	$E_{\text{onset}} (\text{V}^{3+}/\text{V}^{2+}) / V_{\text{RHE}}$	$E_{\text{max}} (\text{V}^{3+}/\text{V}^{2+}) / V_{\text{RHE}}$	$Q (\text{V}^{3+}/\text{V}^{2+}) / \text{mC}\cdot\text{cm}^{-2}$	$Q (\text{V}^{2+}/\text{V}^{3+}) / \text{mC}\cdot\text{cm}^{-2}$	Reversibility (%)	Peak separation / V
$\text{H}_2\text{SO}_4 + \text{V}^{3+}$	0.2	0.04	10.6	0.5	4.7	0.76
$\text{H}_2\text{SO}_4 + \text{V}^{3+} + \text{Bi}^{3+}$	0.4	0.18	6.1	6.6	92.4	0.22

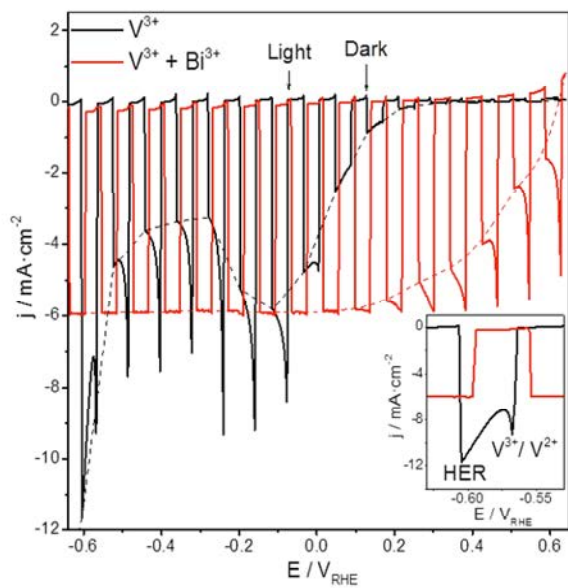


Figure S2. Linear scan voltammeteries under chopped light (dark/light pulses of 2 s) with the $\text{TiO}_2/\text{n}^+\text{-p-Si}$ photocathodes in 1 M H_2SO_4 + 0.05 M V^{3+} electrolyte, in absence and presence of 1 mM Bi^{3+} .

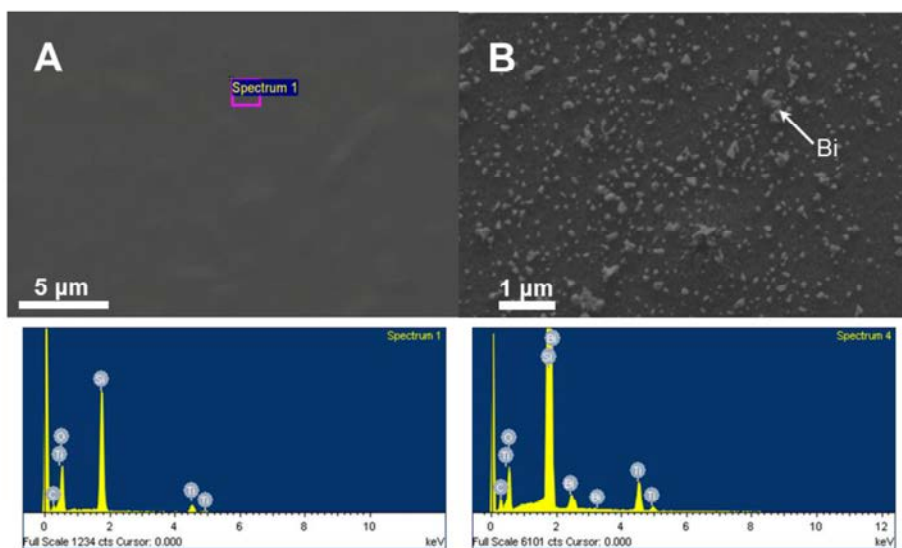


Figure S3. SEM and EDX analyses of the $\text{TiO}_2/\text{n}^+\text{-p-Si}$ photocathodes after measurements in absence (A) and presence (B) of Bi.

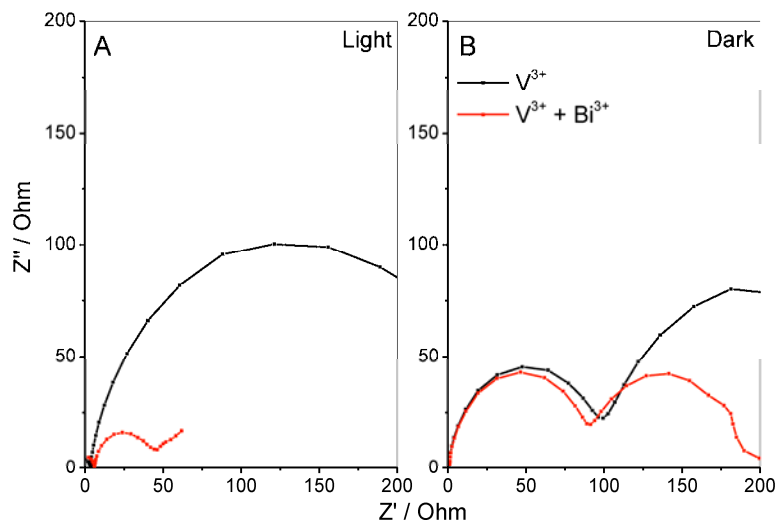


Figure S4. Potentiostatic electrochemical impedance spectroscopy in absence and presence of Bi^{3+} for different situations: illuminated photocathodes at $0.2 V_{RHE}$ (A) and cathodes in dark conditions at $-0.5 V_{RHE}$ (B).

References

1. C. Ros, T. Andreu, M.D. Hernández-Alonso, G. Penelas-Pérez, J. Arbiol, J.R. Morante, *ACS App. Mater. Interfaces* **2017**, 9, 17932-17941.
2. J. Vázquez-Galván, C. Flox, C. Fàbrega, E. Ventosa, A. Parra, T. Andreu, J.R. Morante, *ChemSusChem* **2017**, 10, 2089-2098.

(12) INTERNATIONAL APPLICATION PUBLISHED UNDER THE PATENT COOPERATION TREATY (PCT)

(19) World Intellectual Property Organization
International Bureau



(10) International Publication Number
WO 2017/109108 A1

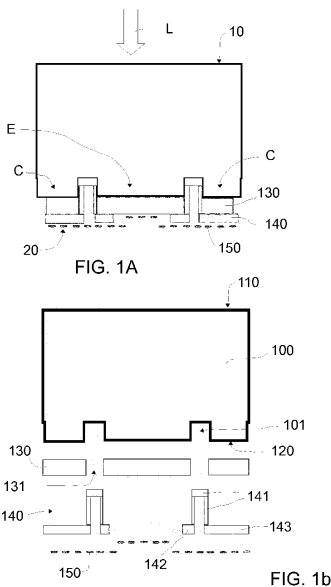
(43) International Publication Date
29 June 2017 (29.06.2017)

- (51) International Patent Classification:
C25B 1/00 (2006.01) H01L 31/068 (2012.01)
C25B 9/20 (2006.01)
- (21) International Application Number:
PCT/EP2016/082442
- (22) International Filing Date:
22 December 2016 (22.12.2016)
- (25) Filing Language: English
- (26) Publication Language: English
- (30) Priority Data:
15382658.1 23 December 2015 (23.12.2015) EP
- (71) Applicant: REPSOL, S.A. [ES/ES]; C. Méndez Álvaro, 44, 28045 Madrid (ES).
- (72) Inventors: PENELAS PÉREZ, Germán; Centro Tecnológico Repsol, Ctra. de Extremadura, km. 18, 28935 Móstoles (ES). HERNÁNDEZ ALONSO, María Dolores; Centro Tecnológico Repsol, Ctra. de Ex-

tremadura, km. 18, 28935 Móstoles (ES). ANDREU AR-BELLA, Teresa; Fundació Institut de Recerca en Energia de Catalunya, Jardins de les Dones de Negre, 1, planta 2, 08930 Sant Adrià De Besòs (ES). MORANTE LLEONART, Juan Ramón; Fundació Institut de Recerca en Energia de Catalunya, Jardins de les Dones de Negre, 1, planta 2, 08930 Sant Adrià De Besòs (ES). ROS FIGUERAS, Carles; Fundació Institut de Recerca en Energia de Catalunya, Jardins de les Dones de Negre, n.º 1, planta 2, 08930 Sant Adrià De Besòs (ES). CARRETERO GONZÁLEZ, Nina Magali; Fundació Institut de Recerca en Energia de Catalunya, Jardins de les Dones de Negre, n.1, pl.2, 08930 Sant Adrià De Besòs (ES). CALLE MARTIN, Eric; Electronic Engineering Department, (Universitat Politècnica De Catalunya), Edifici C4, C. Jordi Girona, 1-3, 08034 Barcelona (ES). ORTEGA VILLASCLARAS, Pablo; Electronic Engineering Department, (Universitat Politècnica De Catalunya), Edifici C4, C. Jordi Girona, 1-3, 08034 Barcelona (ES). ALCUBILLA GONZALEZ, Ramon; Electronic Engineering

[Continued on next page]

(54) Title: SUBSTRATE-ELECTRODE (SE) INTERFACE ILLUMINATED PHOTOELECTRODES AND PHOTOELECTRO-CHEMICAL CELLS



(57) Abstract: A photoelectrode for a photoelectrochemical cell is disclosed. The photoelectrode comprises a back-contact solar cell comprising emitter and collector contacts being spaced apart by first openings. The emitter and collector contacts are respectively collected in an emitter busbar and a collector busbar. The photoelectrode further comprises a contact passivation layer to separate the emitter and collector contacts from the electrolyte when in use. The contact passivation layer further comprises second openings in correspondence with the first openings. The photoelectrode further comprises a resin layer covering a portion of the contact passivation layer such that in use only charge carriers from the emitter contacts traverse the contact passivation layer in its way to the electrolyte while charge carriers from the collector contacts are collected in the collector busbar. An electrocatalyst layer is further provided covering respectively the resin layer and/or the contact passivation layer.

WO 2017/109108 A1

Figure A.3. Reprint of the WO/2017/109108 international patent.